Stratigraphic context and timing of sand supply to deep-marine Ainsa-Jaca basin, middle Eocene, Spanish Pyrenees: Constraints from geochemistry and sedimentology.

James Iain Scotchman

2012

UCL

Thesis submitted for examination for the award of Doctor of Philosophy (Ph.D)

Declaration

I, James Scotchman confirm that the work presented in this thesis is my own. Where information has been derived from other sources, I confirm that this has been indicated in the thesis.

Signed _____

Date _____

Abstract

The sediment flux to a basin is controlled by a complex combination of tectonics, climatic variability and stochastic events, thereby creating a cryptic geological record. Deconvolving the effects of individual factors controlling sedimentation can often be challenging, due to a variety of reasons including a lack of outcrop, a poor understanding of the regional tectonic framework and insufficiently detailed geological maps. However, many of these deficiencies can be overcome within the deep-marine Ainsa basin, South Central Pyrenees where detailed research over the last decade has provided an extensive knowledge base.

The Ainsa basin comprises ~4 km of middle Eocene deep-marine sediments. Basin stratigraphy consists of a succession of ~25 discrete sandy submarine fans and inter-fan deposits belonging to the Hecho Group. Recently it has been hypothesised that the supply of coarse-clastic sediment to the basin was paced by orbitally induced climate and/or sea level variability, whilst tectonics controlled the locus of deposition. This hypothesis is tested within the Upper Hecho Group using a refined basin age model and the creation of floating orbital time scales between submarine fans. Using calcareous nannofossil and large shallow benthic foraminifera, deposition of the Upper Hecho Group took place over a 6.0-8.3 Myr period between ~40.5-48.4 Ma, giving an average sediment accumulation rate (SAR) of 43.2±10.5 cm/kyr. Stratigraphic time series analyses of inter-fan fine-grained sediments indicate the presence of short eccentricity, obliquity and precession Milankovitch cycles. These floating time scales provide average SARs of 36, 28 and 25-33 cm/kyr for the Banaston, Ainsa and Guaso systems respectively. Applying these age models to the three systems suggest that submarine fan deposition potentially corresponds to specific eccentricity minima. As in the Pleistocene, such Milankovitch forcing could be linked with ephemeral glacio-eustatic low-stand conditions, associated with increased coarse sediment flux to the deep-marine Ainsa basin.

Table of contents

List of figures

List of plates

List of tables

List of equations

List of acronyms

AM	Amplitude modulation
AR	Autoregressive
ASM	Average spectral misfit
BW	Bandwidth
CCD	Carbonate compensation depth
CIE	Carbon isotope excursion
COI	Cone of influence
CPS	Counts per second
CWT	Continuous wavelet transform
DFT	Discrete Fourier transform
DJF	December, January and February
DOF	Degrees of freedom
ECORS	Etude Continentale et Océanique par Réflexion et Réfraction Sismique (Continental and Oceanic Study by Reflection Seismic Refraction)
EECO	Early Eocene climatic optimum
ED	Energy dispersive
ETM	Eocene thermal maximum
ETM2	Eocene thermal maximum 2
ETM3	Eocene thermal maximum 3
FFT	Fast Fourier transform
FM	Frequency modulation
FO	First occurrence
GCM	General circulation model
HCL	Hydrochloric acid
ICDD	International Centre for Diffraction Data
IRD	Ice rafted debris
JJA	June, July and August
LBF	Large benthic foraminifera
LO	Last occurrence
LSFT	Lomb-Scargle Fourier transform
MAR	Mass accumulation rate
MAT	Mean annual temperature
MATR	Mean annual temperature range
mbs	Metres below surface
MECO	Middle Eocene climatic optimum
MT	Megaturbidite

MTC	Mass transport complex
MTM	Multi-taper Method
N_f	Nyquist frequency
NGR	Natural gamma ray
NP	Nannofossil zonation of Martini (1971)
NPF	North Pyrenean Fault
NPTB	North Pyrenean thrust belt
OM	Organic matter
PDB	Peedee Belemnite
PETM	Paleocene-Eocene thermal maximum
R_f	Rayleigh frequency
SAR	Sediment accumulation rate
SBZ	Shallow benthic zonation of Serra-Kiel et al. (1998)
SCPU	South central Pyrenean unit
SGF	Sediment gravity flow
SGR	Spectral gamma ray
SI	Sampling interval
SMOW	Standard mean ocean water
SPMT	South Pyrenean main thrust
SPTB	South Pyrenean thrust belt
SST	Sea surface temperature
TC	Total carbon
TOC	Total organic carbon
TS	Tectono-sequence
TSU	Tectono-stratigraphic unit
UCL	University College London
VPDB	Vienna PeeDee Belemnite
WOSA	Weighted overlapped segment averaging
XRD	X-ray diffraction
XRF	X-ray fluorescence

Acknowledgements

I would like to thank my supervisors Prof. Kevin Pickering and Dr Stuart Robinson for their continuous support and guidance during my research. I am indebted to ExxonMobil and Dr Darren Box for providing funding, guidance and the internship at the ExxonMobil Upstream Research Company, Houston, USA.

Without the technical support discussions and guidance from the staff at the UCL and Birkbeck Earth Science departments, this thesis would not have been possible. I would especially like to thank: Tony Osborne for assistance in the measurement of calcium carbonate and TOC content; Dr Andrew Carter and Dr Andrew Beard for instructing me on the rock crushing process; Jim Davies for continuous help with most technical matters and the creation of thin-sections; Dr Alexandra Nederbragt and Prof. Jürgen Thurow for guidance and unlimited XRF analyses; Dr Paul Bowen and Dr Marcelle Boudagher-Fadel for the identification of palaeontological samples; Dorinda Ostermann for stable isotope analysis, and; Dr Ian Wood for XRD analysis. Also I thank Prof. Kristen St. John (James Madison University, USA) for supplying the IRD data.

Finally, I am forever grateful for the moral and financial support provided by my family, and especially to my grandparents for accommodating me whilst completing this thesis. Thank you to Harriet Jarlett for proving motivation and moral support for which I am forever grateful.

Chapter 1
Introduction, Geological and Climatic Setting

1.1 Introduction

The sediment flux to a basin is controlled by a complex combination of tectonics, climatic variability and random (stochastic) events (e.g., large-magnitude earthquakes), to create a cryptic geological record (Stow et al., 1984; Richards et al., 1998). Deconvolving the effects of individual factors upon sedimentation can often be challenging, due to a variety of reasons including a lack of outcrop, a poor understanding of the regional tectonic framework, insufficiently detailed geological maps and poorly understood stratigraphic sections.

Many of these deficiencies can be overcome within the deep-marine Ainsa basin, south central Spanish Pyrenees, (Fig. 1.1) where detailed geological mapping (Pickering and Corregidor, 2005; Pickering and Bayliss, 2009; Sutcliffe and Pickering, 2009), sedimentology (Mutti et al., 1972; Mutti, 1977; Mutti, 1983; Farrell, 1984; Fontana et al., 1989; Millington and Clark, 1995; Cronin et al., 1998; Pickering and Corregidor, 2000; Fernandez et al., 2004; Pickering and Corregidor, 2005; Das Gupta and Pickering, 2008; Heard et al., 2008; Labourdette et al., 2008; Mansurbeg et al., 2009; Breien et al., 2010; Caja et al., 2010), structural geology (Farrell et al., 1987; Holl and Anastasio, 1993; Munoz et al., 1994; Holl and Anastasio, 1995; Poblet et al., 1998; Mochales et al., 2010), bio- and magneto-stratigraphy (Bentham and Burbank, 1996; Heard and Pickering, 2008; Heard et al., 2008), geochemistry (Trave et al., 1997; Trave et al., 1998), seismic (Soto and Casas, 2001), reservoir and seismic modelling (Falivene et al., 2006a; Falivene et al., 2006b; Bakke et al., 2008; Falivene et al., 2010) along with unpublished conference field guides (Nijman and Nio, 1975; Mutti et al., 1985; Munoz et al., 1998; Remacha et al., 1998; Remacha et al., 2003) have accumulated over the last few decades. With such an extensive knowledge base, it has recently become possible to begin deconvolving the likely tectonic and climatic controls on deep-marine sedimentation within the Ainsa basin.

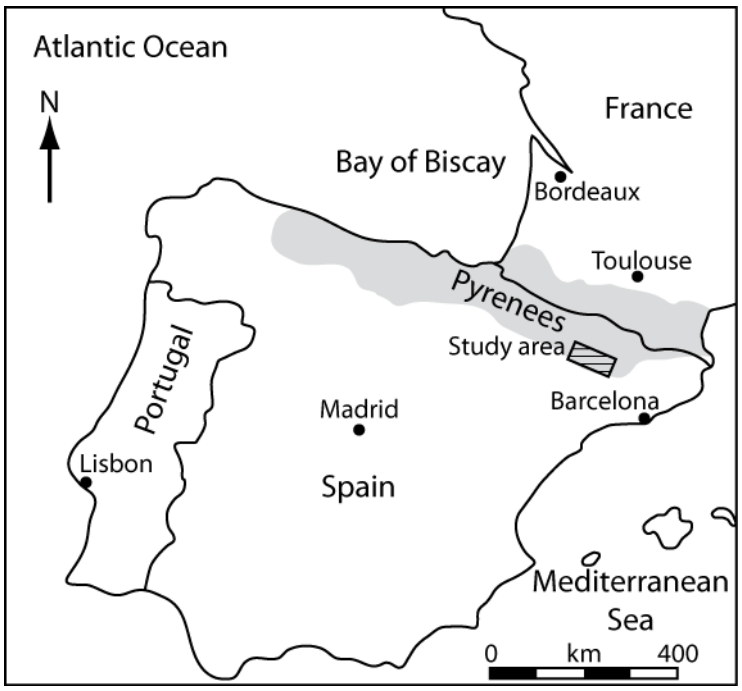

Figure 1.1 | Study area location map. The study area (Ainsa basin) for this research is located within the south-central Pyrenees, northern Spain.

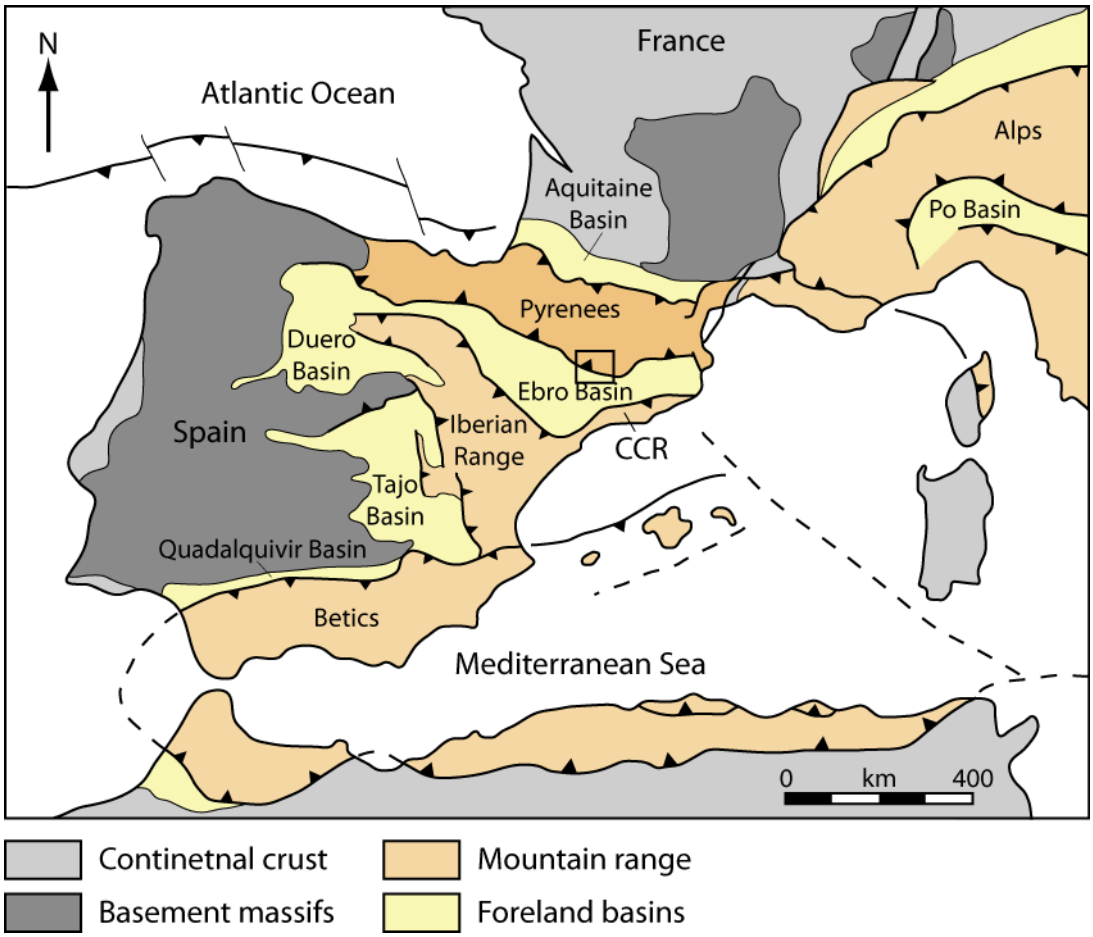

Figure 1.2 | Tectonic setting of southwest Europe (re-drawn from Verges et al, 2002). Study area within rectangle.

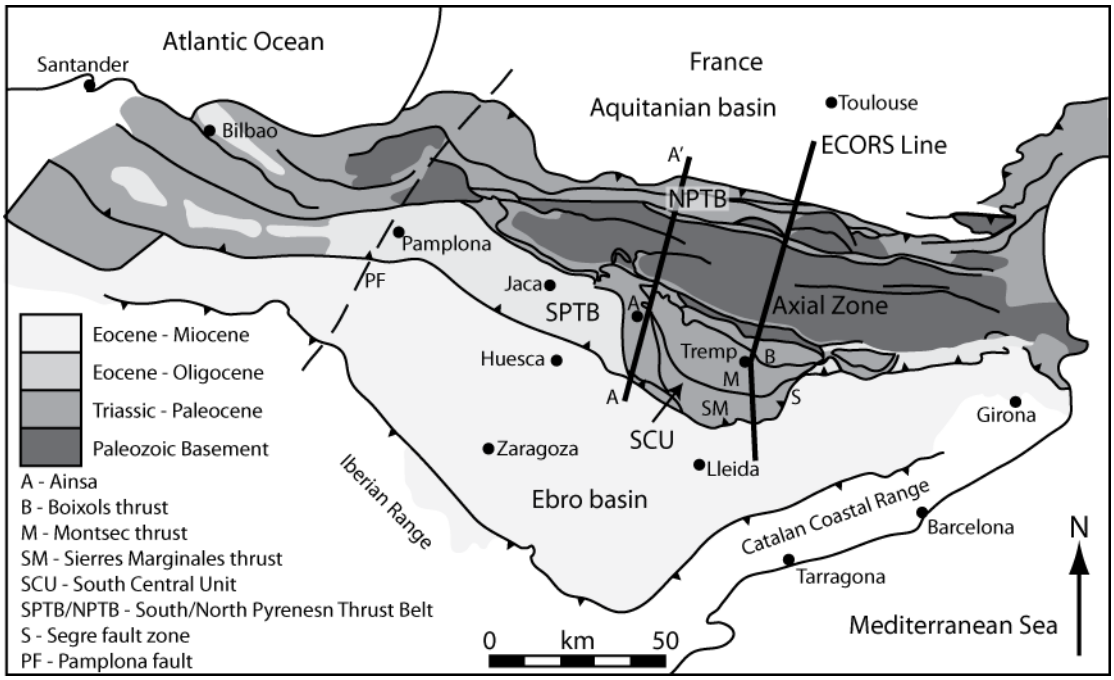

Figure 1.3 | Pyrenean tectonic zones and adjacent pro- and retro-foreland basins (re-drawn from Verges et al., 2002). The positions of the ECORS and A-A' cross sections of Figures 1.4 and 1.5 are shown.

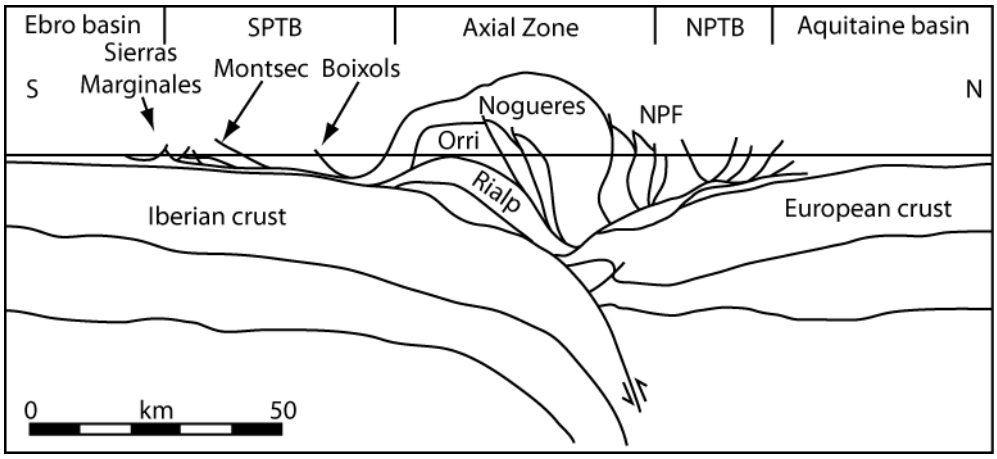

Figure 1.4 | Interpretation of the ECORS cross-section, re-drawn after Munoz et al. (1992).

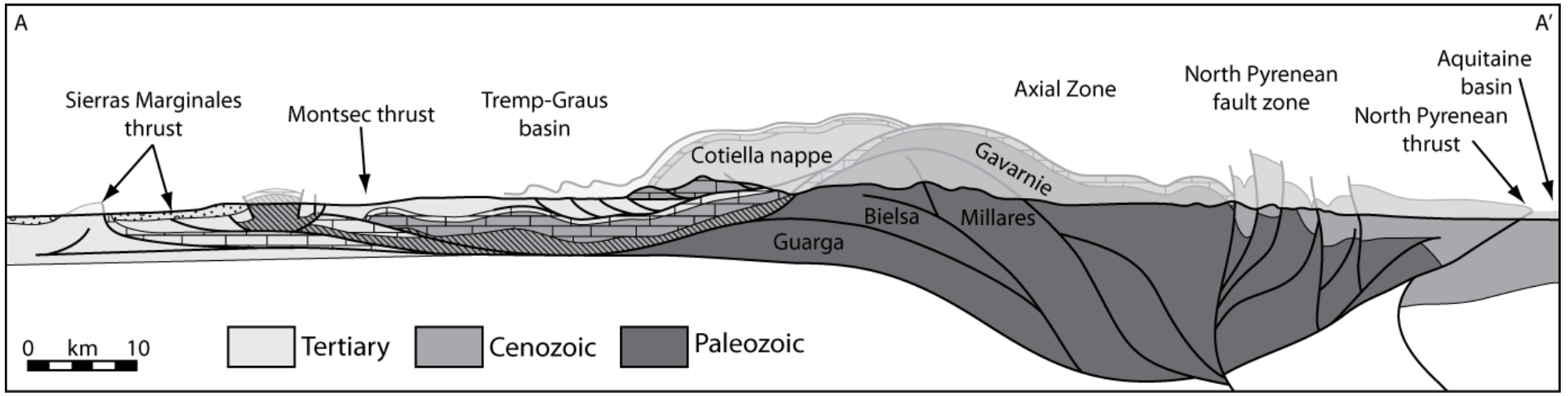

Figure 1.5 | North-south cross-section through the central Pyrenees re-drawn from Martinez-Pena and Casas-Sanz (2003). The Guarga, Bielsa and Millares Axial Zone thrust units are linked with the Rialp, Orri and Nogueres thrust units of Figure 1.4. The exact relationship between these units remains unclear.

1.2 Geological Setting

1.2.1 The Pyrenean Orogen

Today, the Pyrenean orogen is an E-W to ESE-WNW orientated, asymmetrical doubly-vergent wedge, flanked by thrust belts and foreland basins formed by the collision between the Iberian and European plates (Fig. 1.2). The evolution of the margin can be broken down into three main stages (Verges et al., 2002):

- extensional and trans-tensional tectonics associated with the opening of the Northern Atlantic created rift basins
- a collisional margin during the Tertiary
- a large-scale passive margin development during most of the Neogene

In almost all geological framework studies of the Pyrenees, the orogen has been divided into various sections from east to west and north to south. Divisions from east to west are: the Eastern Pyrenees from the Mediterranean Sea to the Segre fault zone; the Central Pyrenees between the Segre fault zone to the Pamplona fault; the Western Pyrenees from the Pamplona fault to the Atlantic (Verges et al., 2002). From north to south: the Aquitaine basin; the North Pyrenean thrust belt; the Axial Zone; the South Pyrenean thrust belt; and the Ebro basin (Choukroune, 1992; Verges et al., 1995; Morris et al., 1998; Verges et al., 2002) (Fig. 1.3).

Pre-collisional tectonic activity caused by the divergence of the Iberian and European plates has been cited as heavily influencing the subsequent Pyrenean orogen (Puigdefabregas and Souquet, 1986; Choukroune, 1992; Verges et al., 2002). Several phases of rifting associated with the opening of the Northern Atlantic took place between the Iberian and European plates during the Mesozoic (Puigdefabregas and Souquet, 1986). This extensional and trans-tensional tectonic regime led to the creation of pull-apart basins and associated thinning of the lithosphere, which are now part of the North Pyrenean Fault zone (NPF). Synchronously, the Iberian plate underwent a 35˚ anticlockwise rotation (Choukroune, 1992; Verges et al., 2002).

North-south compression commenced during the Mid-Late Cretaceous (Puigdefabregas and Souquet, 1986) and continued until late Oligocene times resulting in the inversion of previous rift structures culminating with the formation of a doubly-vergent orogenic wedge. Reconstructions indicate pre-collisional plate separation as being 100-150 km (Boillot, 1986). Continental collision commenced during the early Eocene (~55 Ma) leading to the partial subduction of the Iberian plate beneath the European plate (Choukroune and Team, 1989; Munoz, 1992; Pous et al., 1995; Gaspar-Escribano et al., 2001; Vacher and Souriau, 2001) (Fig. 1.4). Within the upper crust, thrusting resulted in the formation of the central Axial Zone antiformal stack

along with northward and southward foreland propagating thrust sheets. The most significant thrust system developed over the Iberian plate to the south. The resultant lithospheric loading led to a flexural response creating the southern and northern foreland basins (Brunet, 1986; Gaspar-Escribano et al., 2001). Total shortening of 147 km is calculated from balanced and restored cross-sections across the ECORS line, with a range between ~125 to ~165 km (Munoz, 1992; Verges et al., 1995; Beaumont et al., 2000). Regional shortening rates have been calculated as being 6 mm/yr at their maximum during the middle Eocene (~47 Ma) (Verges et al., 1995).

Discrete element models have been employed to identify and determine the timescale of thrust sheet propagation and accretion to a doubly vergent wedge such as the Pyrenees (Naylor and Sinclair, 2007). They identify cyclic pulses of thrust propagation away from the pro-wedge followed by accretion and subsequent internal thickening of the wedge orogenic growth/erosion. The maximum duration of each of these pulses is dependent upon the length, thickness and strength of the materials, which form the thrust sheet divided by the regional convergence rate. When applied to the Pyrenean orogen with a thrust sheet thickness of ~24 km and a regional convergence rate of 6 km/Myr then a maximum duration of 4 Myr results for thrust sheet accretion/propagation.

Deformation within the South Pyrenean Thrust Belt (SPTB) ended during the late Oligocene (~24.7 Ma) in a diachronous fashion migrating from east to west (Meigs et al., 1996; Verges et al., 2002).

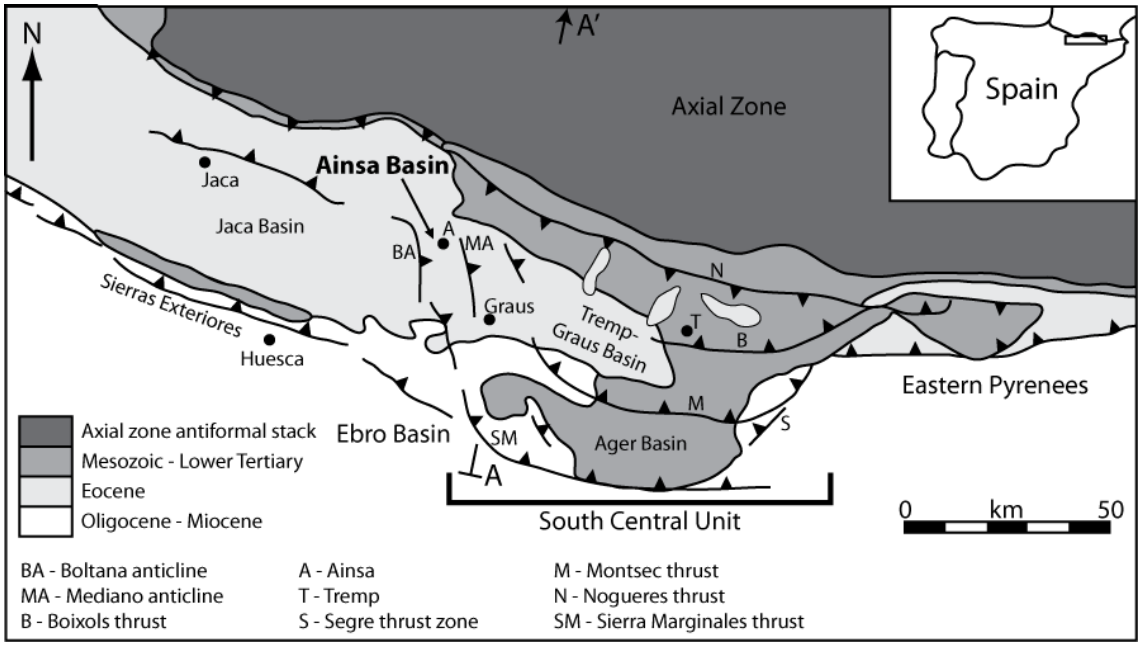

Figure 1.6 | Tectonic units and syn-tectonic sediments within the south-central Pyrenees re-drawn after Bentham et al. (1992b). Approximate position of Figure 1.5 A-A' cross-section shown.

1.2.2 Pyrenean zones

In a north to south transect, the orogen can be subdivided into five distinct zones: (i) the Aquitaine basin; (ii) the North Pyrenean Thrust Belt (NPTB); (iii) the Axial Zone; (iv) the South Pyrenean Thrust Belt (SPTB), and (v) the Ebro basin (Choukroune, 1992; Verges et al., 1995; Morris et al., 1998; Verges et al., 2002) (Figs. 1.3, 1.4).

The Aquitaine basin is the northern of the two foreland basins formed as a response to the flexural response to the loading of the lithosphere by the Axial Zone and the NPTB (Brunet, 1986). Confining the basin to the north is the Hercynian basement of Brittany and the Massif Central, and to the south by the Pyrenees. The basin fill consists of ~2 km of Tertiary sediments overlying ~10 km of Mesozoic sediments lying upon Hercynian basement (Curnelle et al., 1982). Syn-orogenic sedimentation commenced during the Late Cretaceous (Verges et al., 1995).

The North Pyrenean Thrust Belt (NPTB) is an imbricate system of N to NNE propagating thrust sheets including folded and thrust Mesozoic to lower Eocene cover rocks with tectonic windows into Hercynian basement (Fischer, 1984). Confining the NPTB to the north and south are the North Pyrenean Fault Zone (NPF) and the frontal anticline, respectively. Balanced and restored cross-sections indicate shortening across the NPTB to be ~36 km (Munoz, 1992; Verges et al., 1995). Shortening is believed to have been at a rate of ~1 mm/yr almost continuously throughout the Late Cretaceous to late Eocene with intensified deformation during the lower to middle Eocene (Verges et al., 1995).

Within the central Pyrenees is the E-W to WNW-ESE orientated Axial Zone, comprising an antiformal stack of Hercynian basement thrust sheets (Figs. 1.4, 1.5). Bounding the Axial Zone are the NPF and the Bóixols thrust to the north and south respectively. The NPF is marked by a narrow zone (1-5 km) of faulting and shearing, which developed during sinistral displacement in the mid-Cretaceous. Resultant crustal thinning allowed the upward transport of deep mantle material (granulities and lherzolites) toward upper crustal levels (Munoz, 1992). The NPF may represent the suture zone between the Iberian and European plates (Burbank et al., 1992a; Morris et al., 1998).

The Axial zone itself consists of up to 10 km of Cambrian and Carboniferous rocks affected by low- to high-grade metamorphism during the Hercynian orogeny which were later intruded by crustally-derived granitic bodies during the early Permian (Vissers, 1992). Unconformably overlying these deformed Palaeozoic rocks are late Carboniferous to Triassic rocks reaching 2.5 km in thickness (Verges et al., 1995).

During the Tertiary continental collision, three main tectonic units were thrust into an antiformal stack comprising of the Nogueres, Orri and Rialp thrust sheets

(Munoz, 1992; Verges et al., 1995) (Fig. 1.4). The resultant antiformal stack formed an orogenic wedge accounting for ~112 km of shortening in the Axial Zone (Munoz, 1992).

The South Pyrenean Thrust Belt (SPTB) lies to the south of the Axial Zone and was formed as the S to SSW propagating thrust sheets were detached along the evaporites of the Triassic Keuper Formation (Farrell et al., 1987; Verges et al., 1995; Teixell, 1996). The limits of the SPTB are marked by the Axial Zone Nogueres nappe and frontal thrust of the Sierras Marginales to the north and south respectively. Within the South Central Pyrenees (along the ECORS line) is the South Central Pyrenean Unit (SCPU; Fig. 1.6) (Farrell et al., 1987; Munoz, 1992; Meigs and Burbank, 1997; Sussman et al., 2004). The SCPU forms an arcuate part of the fold-thrust belt extending into the Ebro basin representing a salient (Sussman et al., 2004). The SCPU consists of three main tectonic units: the Sierras Marginales, Montsec, and Bóixols nappes comprising Mesozoic platform rocks and overlying Paleogene siliciclastics (Puigdefabregas and Souquet, 1986; Munoz, 1992; Puigdefabregas et al., 1992) (Fig. 1.6).

The Sierras Marginales thrust sheet occupies the area between the frontal South Pyrenean Main Thrust (SPMT) and the Montsec thrust to the north. The thrust sheet consists of upper Eocene-lower Oligocene conglomerates, sandstones and evaporites unconformably overlying Mesozoic and early Paleogene sediments (Munoz, 1992). Overlying the Sierras Marginales is the Montsec nappe comprising Mesozoic to Cenozoic stratigraphic units including ~2,000 m of Upper Cretaceous limestones (Muñoz, 1992). The thrust sheet is folded into a broad syncline supporting the Tremp-Graus basin (Fig. 1.4). The Bóixols thrust sheet is located between the Tremp basin and the northern back thrust against the Axial Zone antiformal stack consisting of over 5 km of mainly Lower Cretaceous sediments (Munoz, 1992). These three thrust sheets merge into the Segre Fault zone in the east of the SCPU whilst the western boundary is defined by an oblique ramp system (Farrell et al., 1987). The latter consists of the north-south trending Mediano, Añisclo and Boltaña fault detachment folds and associated southwest-vergent imbricate fan (Farrell et al., 1987; Holl and Anastasio, 1993, 1995; Poblet et al., 1998; Remacha et al., 2003).

The timing of thrust sheet emplacement has been estimated as being latest Cretaceous-Paleocene for the Bóixols (Puigdefabregas and Souquet, 1986; Verges and Burbank, 1996), early Eocene (Ypresian) for the Montsec (Farrell et al., 1987; Munoz, 1992; Verges and Burbank, 1996), and late Eocene (Bartonian; ~39.8 Ma) for the Sierras Marginales (Burbank et al., 1992b; Puigdefabregas et al., 1992; Meigs et al., 1996).

Within the eastern Pyrenees, thrusting commenced during the lower Eocene (~55 Ma) coeval with the SCPU resulting in rapid thrust propagation associated with

maximum shortening of ~4.5 mm/yr until the middle Eocene (~47 Ma) (Verges et al., 1995; Verges and Burbank, 1996). After the middle Lutetian (~47 Ma) shortening rates decreased to ~2 mm/yr until the end of thrusting during the late Oligocene (~25 Ma) (Verges et al., 1995; Meigs et al., 1996). Overall shortening within the SPTB was ~70 km (Verges et al., 1995).

The Ebro pro-foreland basin is a broadly triangular E-W trending asymmetrical sedimentary basin confined by the Pyrenees to the north and the Catalan and Iberian ranges to the SE and SW respectively (Fig. 1.3). Basin formation commenced around 55 Ma as a flexural response to loading from the South Pyrenean Thrust Belt and the Axial Zone (Puigdefabregas and Souquet, 1986; Millan et al., 1995; Gaspar-Escribano et al., 2001). Basin fill consists of Paleocene continental red beds and shallow-marine carbonates overlain by platform carbonates and evaporites of lower to middle Eocene age. During the middle to late Eocene, deposition of marls represent the distal facies of alluvial fans and deltas (Verges et al., 1995). Southward propagation of the deformation front during this period led to the southward migration of coarser-grained facies into the foreland. Non-marine sedimentation dominated after a major regression during the late Eocene (~37 Ma) resulting in widespread marine evaporite deposits (Cardona evaporite) marking the end of marine influence (Puigdefabregas and Souquet, 1986; Anadón and Roca, 1996). Tertiary fill within the basin reached a maximum thickness of 5,000 m in the north of the basin (Anadón and Roca, 1996). Final deformation in the Ebro basin took place during the late-Oligocene to Early Miocene leading to the current basin configuration (Anadón and Roca, 1996).

1.3 The South Central Pyrenees

The study area for this research, the Ainsa basin, is located in the south central Pyrenees, within the western oblique ramp of the South Central Pyrenean Unit (SCPU) (Fig. 1.6). The area is referred to, amongst others as the Eocene South-Central Pyrenean Basin (Remacha et al., 2003) or South Pyrenean basin (Farrell et al., 1987). The foreland basin developed in front of the migrating Pyrenean orogen within the SPTB representing an ideal area for the study of syn-tectonic evolution of sedimentary systems (Dreyer et al., 1999; Pickering and Corregidor, 2005; Heard and Pickering, 2008; Beamud et al., 2011).

The evolution of the south central Pyrenees can be divided into three main stages (Verges et al., 2002; Remacha et al., 2003). The first stage is characterised by the inversion of Mesozoic extensional structures forming the ancestral Pyrenean orogen (Munoz et al., 1986; Munoz, 1992; Remacha et al., 2003). Stage two includes the emplacement of the Upper and Lower Thrust Sheets (Munoz et al., 1986;

Puigdefabregas and Souquet, 1986; Munoz, 1992; Puigdefabregas et al., 1992), also referred to as the Upper and Lower thrusting complexes (Remacha et al., 2003). The final orogenic episode, stage three, is associated with the emergence of the Pyrenean Axial Zone and the infilling of the foreland basin (Puigdefabregas and Souquet, 1986; Puigdefabregas et al., 1992; Remacha et al., 2003).

Stage 1: Initiation of continental collision and the 'Ancestral Orogen'

The initiation of the Pyrenean orogen is associated with the start of north-south compression during the Late Cretaceous-Paleocene (Santonian-Thanetian). The presence and subsequent inversion of these Mesozoic extensional faults influenced the geometry and size of early thrust development (Farrell et al., 1987; Roure et al., 1989; Puigdefabregas et al., 1992; Teixell, 1996; McClay et al., 2004) including the Bóixols thrust sheet (Puigdefabregas and Souquet, 1986; Munoz, 1992; Verges and Burbank, 1996). Shortening rates during this stage were <0.5 mm/yr (Verges et al., 2002).

Subsidence associated with lithospheric loading from the 'ancestral' Pyrenees led to the formation of an east-west trending foreland basin deepening westward toward the Bay of Biscay. Uplift led to the emergence of the eastern Pyrenees which became a source area of clastics (Plaziat, 1981; Puigdefabregas and Souquet, 1986). Early foreland basin sediments are characterised by fluvial and lacustrine red beds (Garumnian Group) within the eastern and central Pyrenees (Puigdefabregas and Souquet, 1986; Puigdefabregas et al., 1992). Shallow marine conditions prevailed farther west with the deposition of the Gallinera Formation limestones (Plaziat, 1981; Puigdefabregas and Souquet, 1986).

Stage 2: The Upper and Lower thrust sheets and the deep-marine stage

The second stage of the area's tectonic development marked a major phase of reorganisation representing the start of the 'flysch' foreland basin stage of Remacha et al. (2003), here referred to as the "deep-marine stage". The initiation of this stage is characterised by an increase in shortening and thrust tip advancement rates from 55 Ma (Verges et al., 1995; Verges et al., 2002). Tectonic events during this stage commenced with the emplacement of the Upper Thrust Sheets involving the South Central Pyrenean Unit (SCPU) and the propagation of the ancestral orogen thrusts (Remacha et al., 2003) (Fig. 1.7).

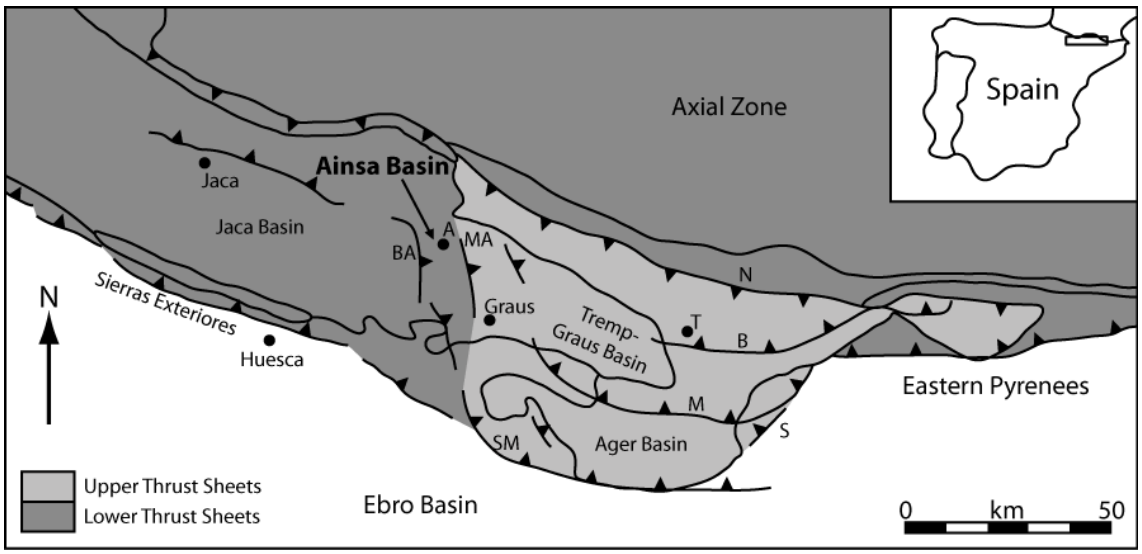

Figure 1.7 | South-central Pyrenean Upper and Lower Thrust Sheets of Stage 2. Upper Thrust Sheets involve the inversion of Mesozoic structures influencing the thrusts of the SCPU. The Lower Thrust Sheets formed the Axial Zone antiformal stack and under thrust the SCPU, Ainsa and Jaca basins creating piggyback basins. Lettering corresponds to that in Figure 1.6.

The SCPU consists, from north to south the Bóixols, Montsec and Sierras Marginales thrust sheets and these were progressively emplaced southward over the foreland. Emplacement of the SCPU commenced with the initiation of the Bóixols thrust which began during the latest Cretaceous-Paleocene (Puigdefabregas and Souquet, 1986; Verges and Burbank, 1996). Thrusting had ceased prior to the deposition of the Garumnian Group at ~55 Ma (Verges and Burbank, 1996). The geometry and extent of the Bóixols thrusting was influenced by the inversion of previous Mesozoic extensional structures (Munoz, 1992).

Compression continued into the early Eocene (Ypresian) leading to the southward emplacement of the Montsec thrust sheet along with initial formation of the Sierras Marginales thrust (Farrell et al., 1987; Munoz, 1992; Verges and Burbank, 1996). The emergence of the Montsec thrust continued into the Lutetian propagating from east to west (Farrell et al., 1987). The structure of the Montesc thrust sheet is a broad syncline creating the Tremp-Graus piggyback basin confined by the Bóixols and Montsec thrusts to the north and south respectively (Munoz, 1992). During emplacement of the Montsec thrust sheet, the western lateral ramp zone was expanded to form the Cotiella nappe, Mediano anticline, Los Molinos and Atiart thrusts (Munoz et al., 1986; Farrell et al., 1987; Munoz et al., 1994; Remacha et al., 2003). The development of the Mediano anticline marked the boundary between the terrestrial Tremp-Graus basin and marine Ainsa-Jaca basins to the west (Marzo et al., 1988; Puigdefabregas et al., 1992; Millington and Clark, 1995; Bentham and Burbank, 1996; Nijman, 1998).

Continued lithospheric loading from the Les Nogueres and Lakora thrust sheets led to an increase in foreland basin subsidence rates. Within the foreland basin, a marine transgression deposited shallow marine carbonates of the Alveolina Limestone Formation (Ager Group) upon the older Garumnian Group (Puigdefabregas and Souquet, 1986; Remacha et al., 2003). Overlying the Alveolina Limestone within the Tremp-Graus and Ainsa-Jaca basins are the first siliciclastic sediments of the coeval Lower-Middle Montanyana and Lower Hecho groups respectively (Nijman and Nio, 1975; Mutti, 1977; Mutti, 1983; Puigdefabregas and Souquet, 1986; Puigdefabregas et al., 1992; Nijman, 1998; Remacha et al., 2003; Pickering and Bayliss, 2009). These fluvio-deltaic (Lower-Middle Montanyana Group) and deep-marine (Lower Hecho Group) deposits represent the development of an east-west axial drainage system (Mutti, 1977; Mutti, 1983; Puigdefabregas and Souquet, 1986; Marzo et al., 1988; Puigdefabregas et al., 1992; Nijman, 1998). The developing Mediano anticline continued to represent the shelf break separating the Tremp-Graus and Ainsa-Jaca basins. Once across the shelf break, deep-marine sediments (Lower Hecho Group) were transported axially through the Ainsa basin transfer zone (submarine channels) to the Jaca basin floor (submarine lobes/fans) (Mutti, 1977; Mutti, 1983; Labaume et al., 1985). The south of the foreland basin saw the deposition of the Guara Formation shallow marine limestone (Labaume et al., 1985; Puigdefabregas and Souquet, 1986).

The second major phase of thrusting within stage two involved the emplacement of the Lower Thrust Sheets (Puigdefabregas and Souquet, 1986; Munoz, 1992; Puigdefabregas et al., 1992), Middle Thrust Sheets (Munoz et al., 1986) or Lower Thrusting Complex (Remacha et al., 2003), which commenced during the late Ypresian-Lutetian (Puigdefabregas and Souquet, 1986; Verges and Burbank, 1996; Remacha et al., 2003). This thrusting sequence marked the transformation of the east-west trending sedimentary trough from a simple foreland basin to a compartmentalised piggyback basin detached along the underlying Triassic Keuper evaporites (Munoz, 1992; Verges and Burbank, 1996; Remacha et al., 2003). Relative to the last phase of deformation, the basin is estimated to have migrated 30 km south over the foreland (Puigdefabregas and Souquet, 1986).

Initial thrusting involved the Larra-Boltaña thrust resulting in the formation of the north-south trending Boltaña anticline (Teixell, 1996). Later emplacement of the Gavarnie thrust and associated thickening of the Axial Zones antiformal stack, led to lithospheric loading along with the commencement of Iberian continental crust subduction (Puigdefabregas et al., 1992). Within the foreland basin this is characterised by a period of increased subsidence (Puigdefabregas and Souquet, 1986; Puigdefabregas et al., 1992). This is marked within the Ainsa basin by an

increase in subsidence from 15 cm/kyr to 40 cm/kyr whilst within the Tremp-Graus basin a simultaneous relative decrease is observed (Bentham and Burbank, 1996).

During this period the north-south trending Boltaña and Añisclo submarine highs developed along with further deformation of the Mediano detachment fold and lateral ramp zone (Farrell et al., 1987; Teixell, 1996; Remacha et al., 2003). These anticlines represent the reactivation and expansion of the western lateral ramp structures of the SCPU including the Arro, Los Molinos and Labuerda thrusts (Teixell, 1996; Remacha et al., 2003). The formation of the north-south trending Boltaña and Mediano anticlines further compartmentalised the east-west trending turbiditic trough into the Jaca, Ainsa and Tremp-Graus basins. The Mediano anticline continued to act as a shelf break separating the terrestrial Tremp-Graus basin from the deep-marine Ainsa basin (Marzo et al., 1988; Puigdefabregas et al., 1992; Millington and Clark, 1995; Bentham and Burbank, 1996; Nijman, 1998). The developing Boltaña anticline represented a submarine high dividing the deep-marine Ainsa and Jaca basins, restricting, but not preventing the westward transfer of Hecho Group siliciclastic sediments (Labaume et al., 1985; Farrell et al., 1987; Pickering and Corregidor, 2005).

The emplacement of the Lower Thrust Sheets influenced the deposition of the upper Hecho and Montanyana groups within the Ainsa-Jaca and Tremp-Graus basins respectively (Nijman and Nio, 1975; Puigdefabregas and Souquet, 1986; Nijman, 1998; Remacha et al., 2003). During this stage fluvio-deltaic and deep-marine sediments continued to be deposited within the Tremp-Graus and Ainsa-Jaca basins whilst southern carbonate shelf represented by the Guara Formation retreated southward (Puigdefabregas and Souquet, 1986; Remacha et al., 2003).

Stage 3: Emergence of the Axial Zone and the ‘post deep-marine’ stage

The final stage of foreland basin development (late Eocene-Oligocene) is associated with continued emplacement of the Gavarnie basement thrust, thus expanding the Axial Zone antiformal stack and eventually emerging as the Sierre Exteriores during the Oligocene (Puigdefabregas and Souquet, 1986; Puigdefabregas et al., 1992; Teixell, 1996). The foreland basin during this stage, even with increased thickening within the Axial Zone, experienced a decrease in subsidence and shortening rates (Verges et al., 1995; Bentham and Burbank, 1996; Verges et al., 2002) potentially due to sub-crustal thermal re-equilibrium or collapse of the subducting slab (Puigdefabregas et al., 1992).

During the late Lutetian-Bartonian, uplift of the Mediano anticline slowed and eventually ceased (Holl and Anastasio, 1993; Bentham and Burbank, 1996) whilst continued uplift of the Boltaña anticline eventually separated the Ainsa and Jaca basins

from ~42 Ma (Remacha et al., 2003). The reduction in subsidence rates, coupled with an increase in sediment supply from the uplifting Axial Zone, led to the shoaling of the foreland basin (Labaume et al., 1985; Puigdefabregas et al., 1992). Subsequent basin infill involved deltaic and fluvial sediments prograding westward and southward into the Ainsa and Jaca basins respectively (Bentham and Burbank, 1996; Hogan et al., 1996; Dreyer et al., 1999; Remacha et al., 2003).

Post-depositional deformation of Hecho Group sediments occurred during the emergence of a new basement thrust, folding the Gavarnie-Sierres Exteriores thrust sheet into a broad east-west trending syncline (Labaume et al., 1985; Teixell, 1996; Fernandez et al., 2004). This later deformation led to the accentuation of the southerly plunge of previous tectonic structures within the foreland basins (Fernandez et al., 2004).

1.4 The Hecho Group

The Hecho Group consists of a succession of clastic wedges filling the southern Pyrenean migrating foreland during the early-middle Eocene (Mutti et al., 1972; Mutti, 1977; Mutti, 1983). Sediments of the Hecho Group, along with the contemporaneous terrestrial Montanyana Group (Nijman and Nio, 1975; Nijman, 1998), are distributed within the genetically related Tremp-Graus, Ainsa and Jaca piggyback basins (Fig. 1.8).

Together, these deposits represent an east-west axial drainage system intimately related to the development of the south central Pyrenees (Mutti, 1983). From east to west the Montanyana Group of the Tremp-Graus basin consists of fluvial and shallow marine sediments, which prograded westward over the Mediano shelf break into the deep-marine Ainsa basin (Nijman and Nio, 1975; Marzo et al., 1988; Nijman, 1998; Caja et al., 2010). Ainsa basin sediments represent proximal deep-marine channelised sediment gravity flow (SGF) deposits confined by the developing Boltaña and Mediano anticlines. The Boltaña anticline marks the boundary with the Jaca basin where sediments comprise distal turbidite lobes.

Hecho Group sediments reach a maximum thickness of 4.5 km within the Ara Valley region of the Jaca basin (Remacha et al., 2003). Current distribution of the group extend 190 km axially and 10-45 km laterally (could be as much as 35-75 km; Remacha et al., 2003). Confining the Hecho Group today is the structurally complex region of the SCPU to the east, the Pamplona Fault to the west, the External Sierras to the south and Internal Sierras and Axial Zone to the north.

The Hecho Group has undergone several scales of sub-division within each sub-basin based upon the presence of unconformities or paraconformities and their

possible relation to syn-depositional tectonics (Mutti, 1983; Remacha et al., 2003; Heard et al., 2008; Pickering and Bayliss, 2009).

The first order division of the Hecho Group is based on the separation into the Upper and Lower Hecho groups (Remacha et al., 2003; Pickering and Bayliss, 2009; Bayliss, 2010). Within each basin this is based upon the identification of two major stages of deformation related to tectonic events within the growing Pyrenean orogen (Munoz et al., 1994; Teixell, 1996). The boundary between the Upper and Lower Hecho groups corresponds to the initiation of thrusts associated with the Lower Thrust Sheets (Larra-Boltaña and Gavarnie thrust sheets) during the latest Ypresian-Lutetian (Remacha et al., 2003; Bayliss, 2010).

Second order Hecho Group division involves the identification of unconformity or paraconformity bound allogroups or systems within the individual basins (Mutti, 1983; Remacha et al., 2003; Pickering and Bayliss, 2009). The origin of these allogroup-bounding unconformities has been proposed as tectonic enabling, the Hecho Group sediments being divided into tectono-sedimentary units (TSU's; Remacha et al., 2003; Fig. 1.9). However, the evidence linking allogroup-bounding unconformities to tectonic events does not appear within the peer-reviewed literature.

Basin-scale correlations of Hecho Group allogroups/systems have proved controversial due to the lack of preserved sediments upon the Boltaña anticline (Figs. 1.8, 1.9) (Das Gupta and Pickering, 2008; Caja et al., 2010). Correlations between the Hecho and Montanyana groups have been equally troublesome (Mutti, 1983; Mutti et al., 1985; Puigdefabregas and Souquet, 1986; Nijman, 1998; Bayliss, 2010).

1.5 The Ainsa basin

The Ainsa basin is a 1,000 km^2 (20 x 50 km), north to northwest orientated, piggyback basin located within the south central Spanish Pyrenees (Figs. 1.1, 1.6). Defining the eastern and western margins of the basin are the Mediano and Boltaña anticlines, which separate the Ainsa basin from the adjacent Tremp-Graus and Jaca basins respectively. The Cotiella thrust complex (Upper Thrust Sheets; Munoz et al., 1986) marks the northern edge of the basin whilst the frontal ramp of the Gavarnie nappe (Sierras Marginales thrust) lies to the south (Fig. 1.10). Syn-tectonic deposition within the basin records the upward facies evolution from early-mid Eocene marine slope sediment gravity flow deposits (SGFs) of the Hecho Group, through late Eocene-Bartonian prograding deltas (Sobrarbe Delta Complex; Sobrarbe Fm) and Bartonian fluvial (Escanilla Fm) and to finally, Oligocene alluvial fan conglomerates (Collegats Formation).

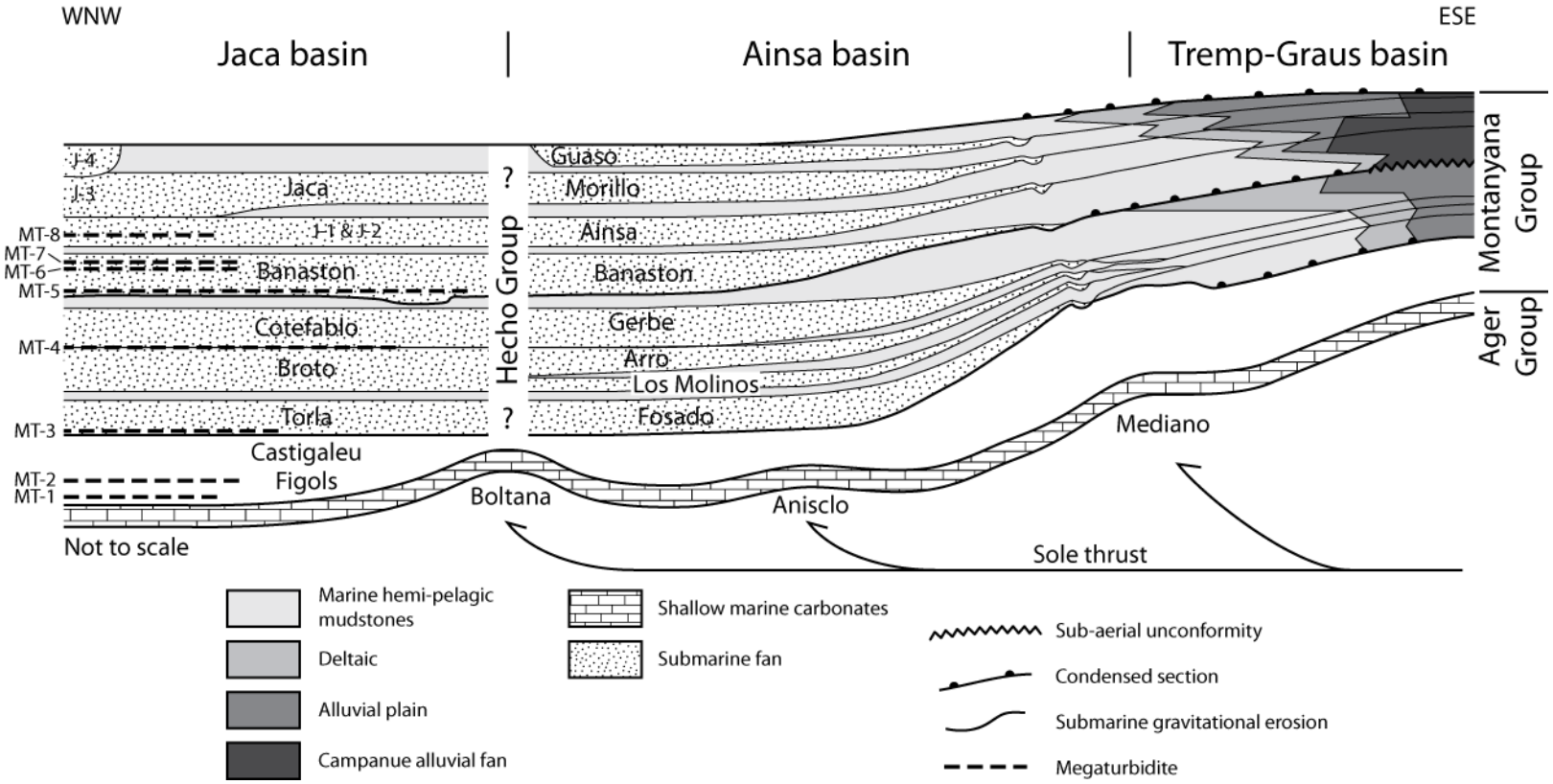

Figure 1.8 | Hecho and Montanyana group correlation between Tremp-Graus, Ainsa and Jaca piggyback basins. Sediments were supplied axially from the coeval Campanúe alluvial fan within the Tremp-Graus basin entering the Ainsa basin over the Mediano anticline. Coeval system sediments are identified within the distal Jaca basin containing several megaturbidites (MT-1 to MT-8). Correlations based upon various published papers, unpublished PhD theses and conference field guides (Nijman and Nio, 1975; Labaume et al., 1987; Munoz et al., 1998; Nijman, 1998; Remacha et al., 1998; Remacha et al., 2003; Bayliss, 2010). Correlations across the Boltaña anticline remain uncertain due to the lack of outcropping sediments.

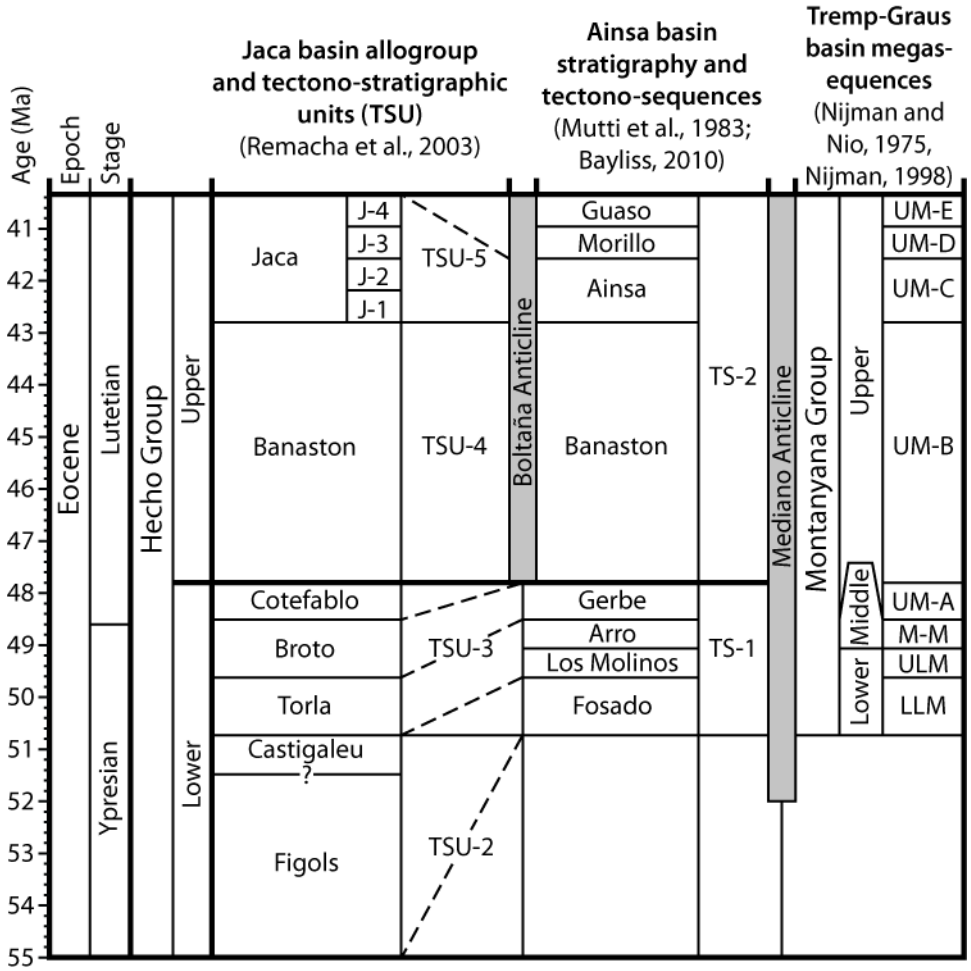

Figure 1.9 | Current stratigraphic, tectono-stratigraphic divisions and correlations within the coeval Tremp-Graus, Ainsa and Jaca basins. Timing of Jaca basin allogroups based upon Remacha et al. (2003) using the time scale of Gradstein et al. (2004). Application of this time scale to the adjacent Ainsa and Tremp-Graus basin sediments dependant upon accuracy of inter-basin correlation. Correlations between the Tremp-Graus and Ainsa basins proposed by Bayliss (2010). Dashed correlation lines between Ainsa and Jaca basin allogroups/systems and systems based upon Das Gupta and Pickering (2008) and Caja et al. (2010).

1.5.1 Tectonic setting

The deep-marine facies of the Ainsa basin formed during the second or 'flysch' stage of the Pyrenean orogen (Remacha et al., 2003). Initiation of this stage is characterised by the emplacement of the Upper and Lower thrust sheets (Figs. 1.6, 1.7) along with increased shortening and thrust tip advancement rates during the Ypresian (Munoz et al., 1986; Munoz, 1992; Puigdefabregas et al., 1992; Verges et al., 1995; Verges et al., 2002; Remacha et al., 2003). Increased lithospheric loading and possible subduction of the Iberian crust resulted in rapid foreland subsidence (Puigdefabregas et al., 1992). The result was an east-west trending axially draining sedimentary trough linked to the proto-Atlantic (Puigdefabregas et al., 1992).

Thrusting of the Upper Thrust Sheet began during the early Ypresian, resulting in the expansion of the SCPU (including the Cotiella nappe) and the associated western lateral ramp zone (Munoz et al., 1986; Farrell et al., 1987; Munoz, 1992; Holl and Anastasio, 1993; Munoz et al., 1994; Remacha et al., 2003). This expansion of the SCPU occurred by the southern and westward propagation of the Montsec thrust, creating the western oblique ramp of the SCPU (Farrell et al., 1987). The oblique ramp comprises a southwest verging imbricated thrust-fold system including the Cotiella, Los Molinos and Atiart thrusts and the north-south trending Mediano anticline (Figs. 1.10, 1.11, 1.12) (Farrell et al., 1987; Munoz et al., 1994; Trave et al., 1997; Trave et al., 1998). Formation of these structures is linked to the mid-late Ypresian Cotiella nappe emplacement inferred by the post- and syn-depositional of early Ypresian sediments (Farrell et al., 1987; Munoz et al., 1994). The Los Molinos thrust was important at this time as it accommodated both 7 km of shortening and 20˚ clockwise rotation (Remacha et al., 2003).

Transformation of the Ainsa basin to a piggyback basin commenced with the early Lutetian development of the Lower Thrust Sheet (Munoz et al., 1986; Munoz, 1992). The preliminary Larra-Boltaña thrust propagated along lower Triassic Keuper evaporites separating the basin from the underlying basement (Figs. 1.11, 1.12) forming the synchronous Boltaña and Añisclo anticlines (Farrell et al., 1987; Munoz, 1992; Teixell, 1996; Remacha et al., 2003). The former partially restricted the westward sediment transfer, and potentially ocean circulation, between the Ainsa and more distal Jaca basins (Labaume et al., 1985; Farrell et al., 1987; Heard et al., 2008).

After a short period the Gavarnie basement thrust internally deformed the Cotiella nappe during the formation of the Axial Zone antiformal stack (Fig. 1.5; Trave et al., 1997; 1998). During this time, structures within the lateral ramp zone were re-activated resulting in renewed uplift of the Mediano anticline along with the formation of out-of-sequence Arro and Labuerda or Gerbe thrusts (Remacha et al., 2003; Bayliss, 2010). Emplacement of the Gavarnie thrust and associated Axial Zone antiformal stack continued from the middle Lutetian to the middle Oligocene (Teixell, 1996). However, the Ainsa piggyback basin ‘flysch’ stage ended during the late Lutetian to early Bartonian with the basin infilling by prograding fluvio-deltaic deposits (Dreyer et al., 1999).

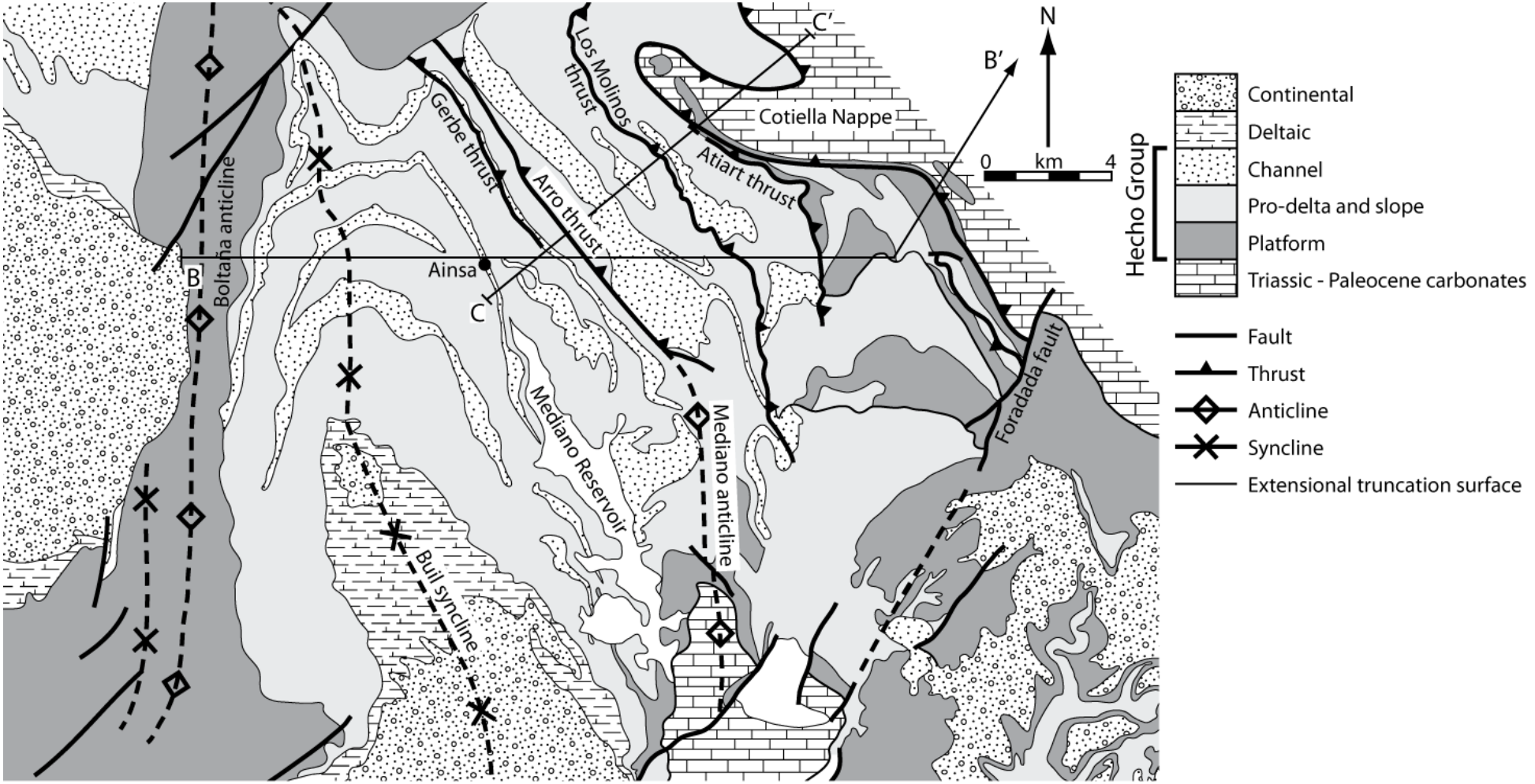

Figure 1.10 | Simplified geological map of the Ainsa basin re-drawn and modified from Munoz et al. (1994), Poblet (1998) and Pickering and Bayliss (2009). Cross sections B-B' and C-C' are shown in Figures 1.11 and 1.12.

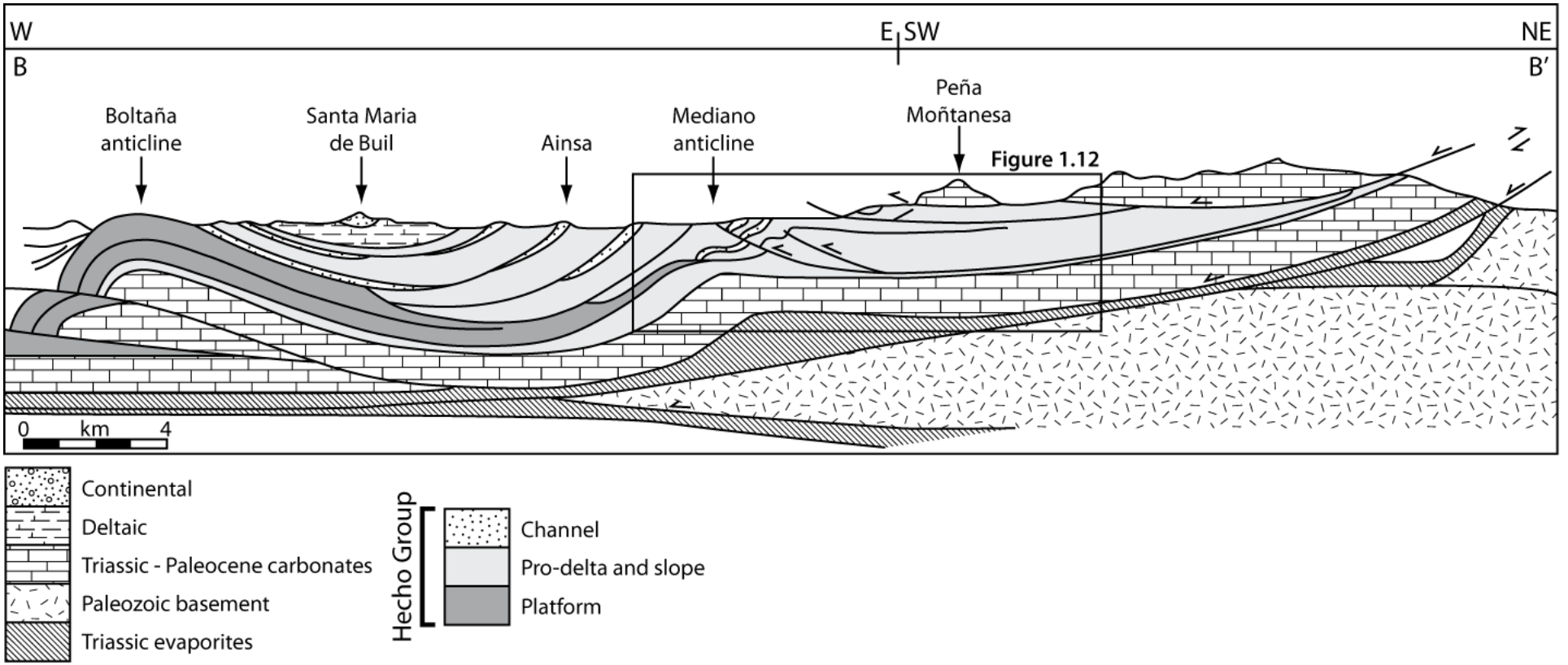

Figure 1.11 | Cross-section through the Ainsa basin redrawn from Dreyer et al. (1999). The E-W section illustrates the overall westward movement of the basins depocentre away from the western lateral ramp zone of the SCPU. Line of cross-section shown in Figure 1.10.

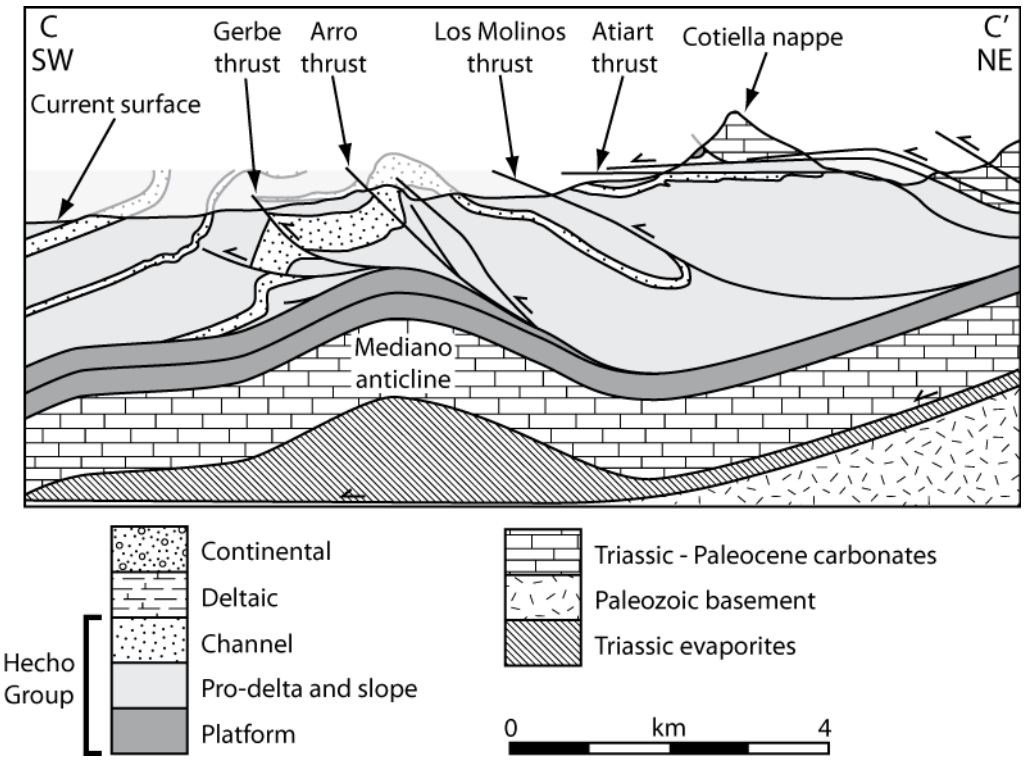

Figure 1.12 | Cross-section through the western boundary of the Ainsa basin redrawn from Poblet et al. (1998) and Munoz et al. (1994). Steeply dipping to overturned beds NE of the Arro thrust identified as an angular unconformity by Pickering and Bayliss (2009). Line of cross-section shown in Figure 1.10.

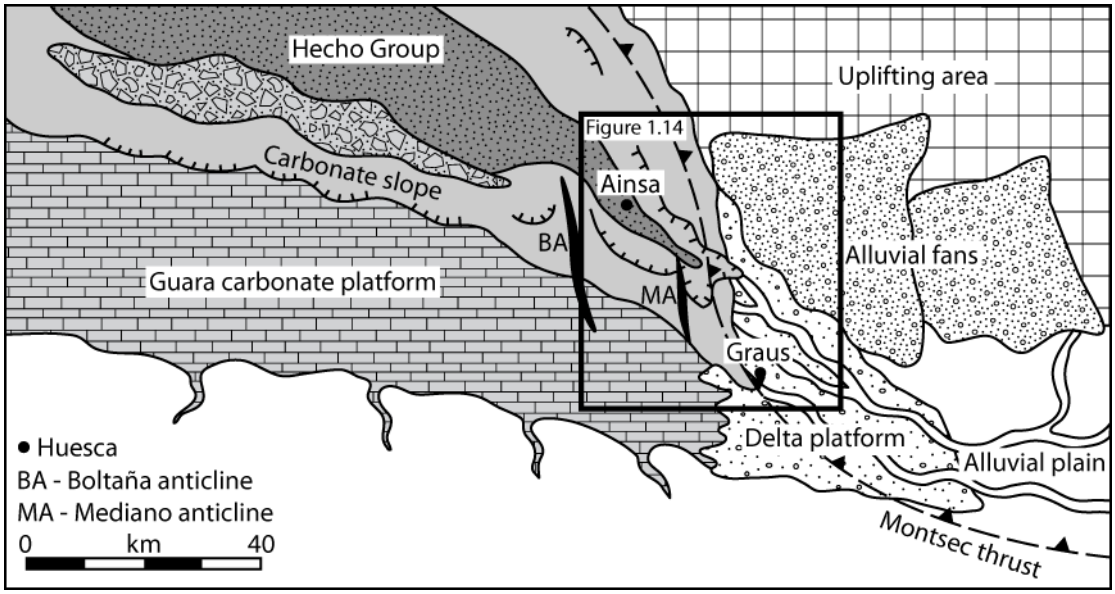

Figure 1.13 | Early Lutetian palaeogeographic reconstruction of the Tremp-Graus, Ainsa and Jaca basins (re-drawn from Dreyer et al. 1999). Sediments were sourced from the uplifting Axial Zone to the north and northeast and transported axially westward. Fluvio-deltaic conditions prevailed within the Tremp-Graus basin being supplied by the Campanúe alluvial fan. The Ainsa basin acted as a transfer zone transporting sediment to the distal lobes of the Jaca basin.

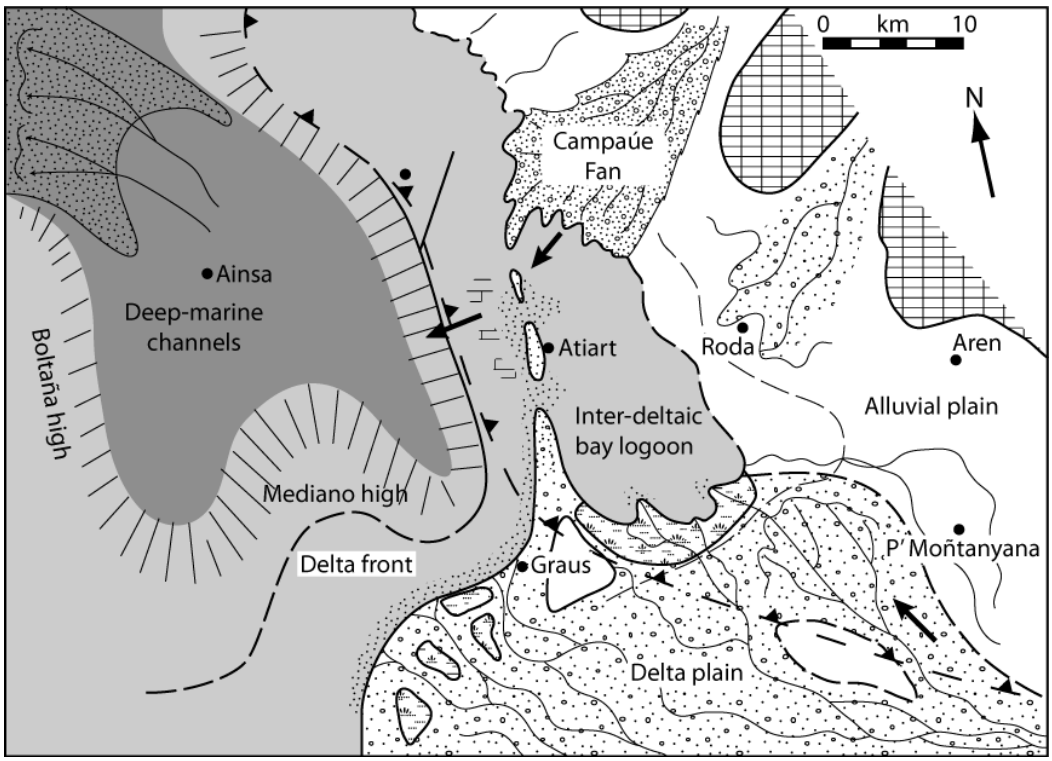

Figure 1.14 | Detailed early Lutetian palaeogeography of the eastern Tremp-Graus and Ainsa basins (re-drawn from Nijman and Nio, 1975).

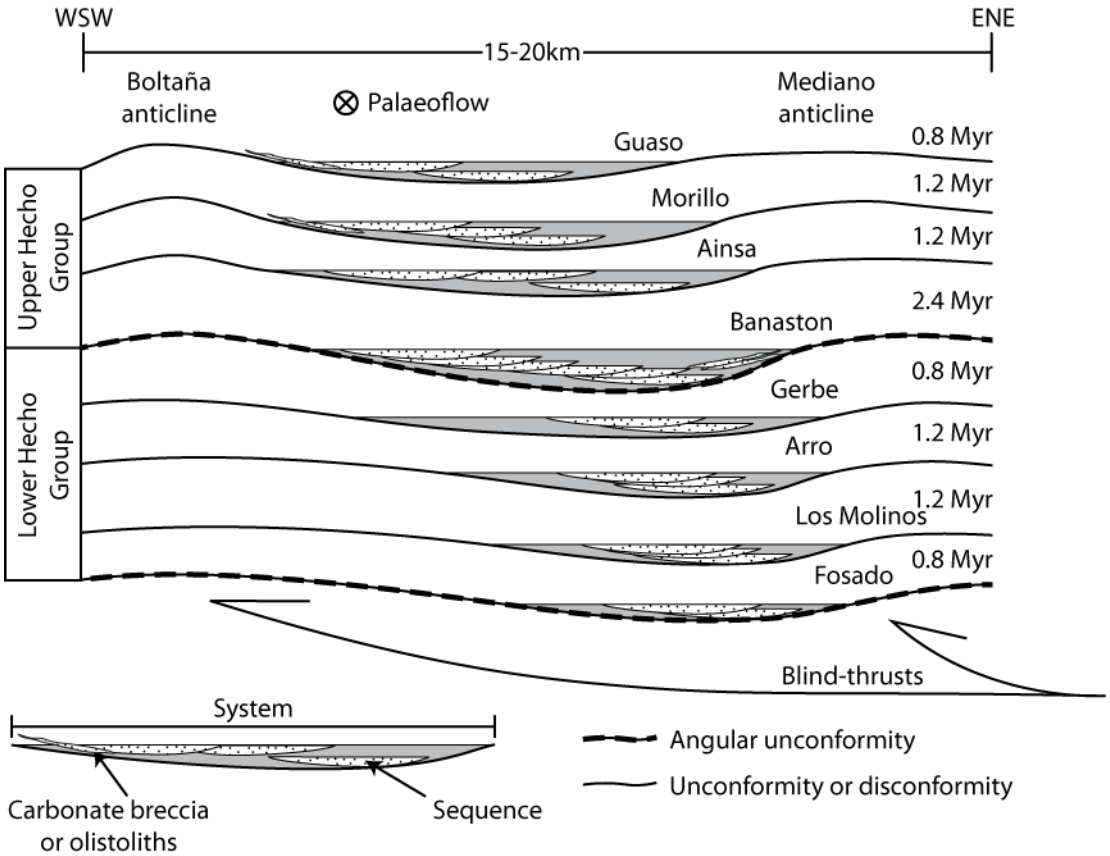

Figure 1.15 | Schematic of the proposed 'see-saw' stacking pattern of Ainsa basin systems (re-drawn from Pickering and Bayliss, 2010). Uplift of the flanking Boltaña and Mediano anticlines controlled the locus of basin deposition. Individual depositional sequences migrate away from the continuously growing Mediano anticline. Uplift of the Boltaña anticline proposed to have formed unconformities separating the depositional systems. Systems expanded for clarity. Durations for each system based upon the prediction that each sequence represents a 404 kyr long eccentricity cycle.

1.5.2 Basin stratigraphy

Since the 1970's the study of the sediments within the Ainsa basin has given rise to a broad range of stratigraphic nomenclature mainly within unpublished field guides and theses (Lunsen, 1970; Mutti et al., 1972; Nijman and Nio, 1975; Remacha et al., 1998; Soto and Casas, 2001; Remacha et al., 2003). Here the stratigraphic divisions of Pickering and Bayliss (2009) and the hierarchical scheme of Van Wagoner et al. (1990) applied to the Ainsa basin by Bayliss (2010) are used.

The deep-marine sediments of the Ainsa basin record a migratory transition zone delivering coarse clastic material from the more proximal Tremp-Graus basin to the more distal Jaca basin (Figs. 1.13, 1.14). Ainsa basin deep-marine sediments consist of ~4 km of siliciclastic turbiditic and hemipelagic deposits of the Hecho Group deposited within water depths >500 m (Nijman and Nio, 1975; Pickering and Corregidor, 2005). Within the Ainsa basin the Hecho Group has been divided into 7-8 unconformity bound systems each ~200-1,200 m thick (Fig. 1.15). From oldest to youngest these are named Fosado, Los Molinos (thrust duplicated?), Arro, Gerbe, Banaston, Ainsa, Morrilo and Guaso systems (Figs. 1.8, 1.9) (Das Gupta and Pickering, 2008; Heard et al., 2008; Pickering and Bayliss, 2009; Sutcliffe and Pickering, 2009). The systems are axially stacked in an overall south-westward direction migrating away from the deformation front (Fig. 1.15). These clastic systems have been interpreted as representing the proximal parts of topographically and structurally confined, coarse-grained and sand-rich, lower slope and axial basin floor submarine fans (Pickering and Corregidor, 2000; Pickering and Bayliss, 2009; Sutcliffe and Pickering, 2009).

Within each of these systems are 2-6 depositional sequences (individual submarine fans) with a total of 22-25 identified within the basin, each 30-100 m thick (Pickering and Bayliss, 2009; Bayliss, 2010). Axially, each depositional sequence consists of a number of complexes (basal MTCs, a thinning and fining upward sequence of submarine fan deposits topped by fine-grained hemipelagic inter-fan sediments). The development of this idealised sequence is divided into a 4-stage process outlined in detail below and within Pickering and Corregidor (2005) and illustrated in Figure 1.17. Individual sequences within a system are observed to be axially stacked in a south-westerly direction.

1.5.2.1 Typical Ainsa basin submarine fan development

Early submarine fan deposition shows an essentially passive (non-erosional) infill of pre-existing seafloor topography created by chaotic mass transport complex (MTC), debris flow and cohesive sediment slide deposits, interpreted as triggered by a fall in relative base-level (Pickering and Corregidor, 2000, 2005; Falivene et al., 2006a). These early deposits are relatively unconfined "channel mouth-bar" sheets, of ~5 m thick medium- to very coarse-grained, sandy turbidite and subordinate debris flow deposits.

After the initial submarine fan development, cyclic intra-fan channel incision, indicates that significant sediment bypass occurred (Pickering and Corregidor, 2000). These bypass stage sediments are typically associated with pebble-grade, high-concentration turbidity current deposits, debris flow deposits, coarse-grained flow-stripped turbidite deposits and tractional bedforms. In addition, erosional surfaces are associated with pebble-grade mud-clast conglomerate, extra-formational pebbles and coarse-grained sand material (Pickering and Corregidor, 2000).

Later stage channel infill is characterised by relatively less confined, and more heterolithic turbidite deposits, showing a thinning and fining upward sequence. Toward the top of each channel fill stage, more complete Bouma-type divisions are present. With the supply of coarse clastic sediment diminishing, the submarine fan is eventually abandoned and deposition returns to background hemipelagic mudstones.

The off-axis expression of these submarine fan sediments, generally consists of lateral-margin or levee-overbank successions of very thin- and thin-bedded Bouma T_{cd} and T_{de} sandy and silty turbidites, within a background of hemipelagic mudstones (Pickering and Corregidor, 2000).

Geological mapping shows that when the coarse clastic supply was much reduced to the Ainsa basin, inter-fan sediments were deposited as fine-grained, very thin- and thin-bedded turbidites and laminated to homogenised hemipelagic mudrocks. Coherent sediment slides and debris flow deposits are also present, with some containing larger benthic foraminifera. These deposits vary in thickness from decimetre to metre scales and are sourced from the mass wastage of upper to mid basin slope sediments due to seismic activity (Pickering and Corregidor, 2000). The thin-bedded and fine-grained turbidites are interpreted as due to storm processes redepositing fine-grained sediments into deep water (i.e., deep-marine "tempestites"), together with other processes, such as seismically triggered deposition (as "seismites"). Background pelagic and hemipelagic mudrocks are believed to be sourced from the flanking carbonate shelves, river mouths, and by the advection of suspended sediment over the shelf edge during storms (Pickering and Corregidor, 2000).

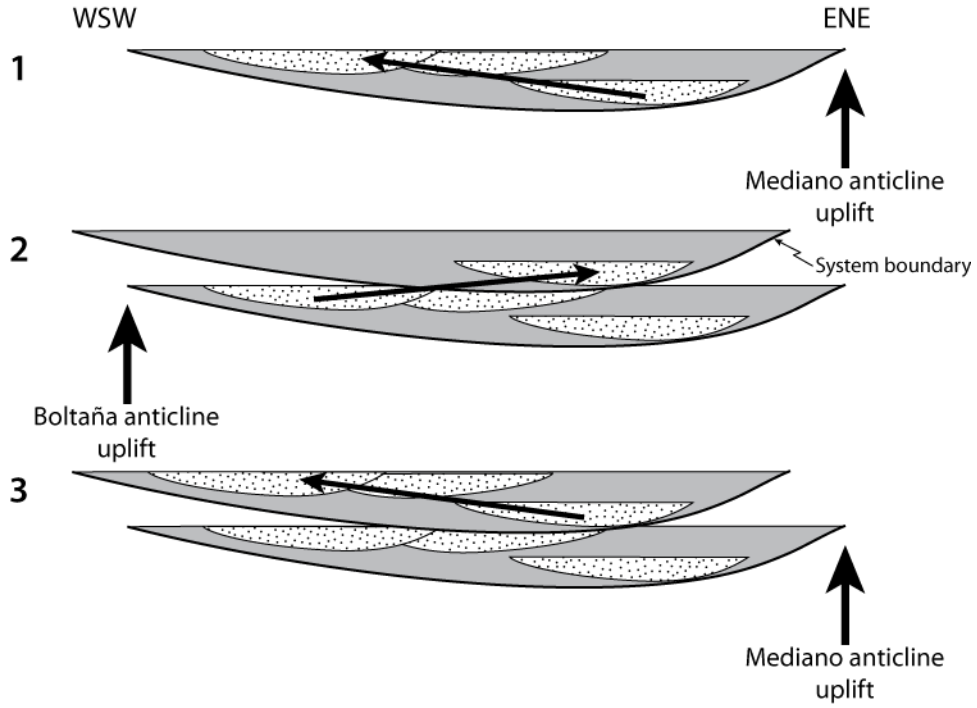

Figure 1.16 | The "see-saw" tectonic process. According to Pickering and Bayliss (2009), the syn-depositional activity of the blind-thrusts underlying the Mediano and Boltaña anticlines influenced the distribution of the deep-water depositional systems and sequences within the Ainsa basin (Fig. 1.15). The "see-saw" tectonic process is here outlined in 3 stages. Stage 1: The continuous uplift of the Mediano anticline is proposed to have forced the depositional sequences to migrate toward the west-southwest. Stage 2: Periodic activity of the blind-thrust beneath the Boltaña anticline is suggested to have forced the depositional axis back toward the east-northeast creating a system boundary. Step 3: Tightening of the Boltaña ceases/slows and Mediano anticline continues to grow forcing the depositional sequences to again migrate toward the west-southwest. However, with the Boltaña anticline forming during the early Lutetian, the "see-saw" tectonic process is unlikely to have influenced the deposition of the Ypresian Lower Hecho Group.

1.5.2.2 Syn-depositional tectonics

The effects of syn-depositional tectonics are prevalent within the Ainsa basin affecting both intra- and inter-system sedimentation. The largest scale of tectonic influence is the overall south-westward stacking of the individual Hecho Group systems away from the south central Pyrenean units (SCPUs) deformation front (Pickering and Bayliss, 2009) (Fig. 1.15).

On the system scale, two distinct stages of south central Pyrenean tectonic development enable the basins systems to be divided into two tectono-sequences (Pickering and Bayliss, 2009; Bayliss, 2010) (Fig. 1.9). The boundary between these tectono-sequences corresponds to the Upper and Lower Hecho group of Remacha et al. (2003) and the submarine truncation surface of Munoz et al. (1994; 1998).

The lower tectono-sequence (TS-1) contains the Fosado-Gerbe systems, which were deformed by the Los Molinos, Arro and Gerbe/Labuerda thrusts (Figs. 1.9, 1.18). The Los Molinos thrust has been related to the overturning (steep folding) of the Arro

Systems sediments (Munoz et al., 1994; Poblet et al., 1998) (Figs. 1.10, 1.12) creating the angular unconformity proposed by Pickering and Bayliss (2009). The initial Los Molinos thrust formed during the development of the Cotiella Nappe and the SW verging imbricated thrust system within its foreland (Upper Thrust Sheet; Munoz et al., 1986). The later Arro and Gerbe/Labuerda thrusts evolved during the initial stages of the Gavarnie basement thrusting (Lower Thrust Sheet; Munoz et al., 1986; Ramacha et al., 2003). The upper tectono-sequence (TS-2) comprises the Banaston-Guaso systems, which are comparatively un-deformed and therefore represent a stage of relative tectonic quiescence post initiation of the Lower Thrust Sheet. Each tectono-sequence has a proposed period of approximately 4 Myr based upon discrete element models of Pyrenean thrust sheets (Naylor and Sinclair, 2007; Heard et al., 2008; Pickering and Bayliss, 2009; Sutcliffe and Pickering, 2009).

Within the literature, the basin sediments have been further sub-divided into tectono-stratigraphic units (Fig. 1.9) (Remacha et al., 2003; Mansurbeg et al., 2009; Caja et al., 2010). Each tectono-stratigraphic unit (TSU) characterises similar types of sedimentary systems with sedimentation controlled by the same evolutionary tectonic framework (Remacha et al., 2003).

At the system scale, the south-westward stacking of individual systems and their constituent sequences illustrate the effects of syn-depositional tectonics. The position of the depositional axis of each system and their constituent sequences are believed to have been controlled by the uplift of the Boltaña and Mediano anticlines in a process described as “see-saw” tectonics (Figs. 1.15, 1.16) (Pickering and Bayliss, 2009). According to the “see-saw” tectonic process, continuous thrust-tip advancement of the blind thrust underlying the Mediano anticline led to syn-depositional uplift therefore forcing the basins depositional axis to migrate toward the southwest (Figs. 1.15, 1.16) (Pickering and Bayliss, 2009). Periodically this continuous south-westward migration was punctuated by activity of the thrust underlying the Boltaña anticline causing the basins depositional axis to migrate ~1 km toward the northeast. The resultant unconformities are utilised by Pickering and Bayliss (2009) to define the upper and lower boundaries of each system (Fig. 1.16).

With both of these anticlines being related to underlying thrusts (Figs. 1.8, 1.11), the “see-saw” hypothesis infers that thrust-tip advancement and hence anticlinal uplift was continuous and periodic for the Mediano and Boltaña anticlines, respectively. However, the Boltaña anticline did not develop until the early Lutetian with the initial thrusting (Larra-Boltaña thrust) of the Lower Thrust Sheets (Teixell, 1996). Only the Mediano anticline formed early enough to influence the deposition of the entire Hecho Group (mid-late Ypresian; Holl and Anastasio, 1993). It is therefore unlikely that the proposed “see-saw” tectonic process was active during the deposition of the Lower

Hecho Group. This may explain the limited lateral migration of the depositional axis within the Fosado, Los Molinos, Arro and Gerbe systems (Fig. 1.15). However, the later distribution of these systems remains unclear due to their poor exposure and tectonic deformation (Fig. 1.18).

With the early Lutetian development of the Boltaña anticline, the tectonic conditions were present for the “see-saw” tectonic mechanism to influence the deposition of the Upper Hecho Group. The increased lateral variability in the locus of submarine fan deposition, especially within the Banaston System, indicates the increased tectonic influence upon deep-marine sedimentation (Fig. 1.15).

Further supportive evidence supporting the effect of “see-saw” tectonics upon the Upper Hecho Group is provided by palaeomagnetic studies of the Boltaña and Mediano anticlines. Folding rates determined from the Mediano anticline indicate that uplift was continuous throughout the late Ypresian to early Bartonian (Chrons 22r to 18r) thereby supporting the hypothesis (Holl and Anastasio, 1993). However, Holl and Anastasio (1993) also identify periods of intensified uplift lasting periods of ~1.5 Myrs linked to the emplacement of the Cotiella thrust, which is not consistent with the “see-saw” tectonic hypothesis. Such periods of intensified uplift would theoretically force the deposition of the Ainsa basin toward the southwest.

The rate and timing of Boltaña anticline uplift is not clearly defined but may be estimated from the rotation of the underlying blind-thrust (Mochales et al., 2012). Thrust rotation data indicate that activity was continuous with an average of ~1.2˚/Myr during the Lutetian which increased to ~2.6˚/Myr during the late Lutetian to late Bartonian stages. Periods of intensified rotation are observed and potentially may relate to the timing of the observed unconformities separating the Hecho Group systems. However, without a detailed palaeomagnetic study determining the folding rates of the Boltaña anticline the proposed system bounding unconformities cannot be confidently linked to anticlinal uplift.

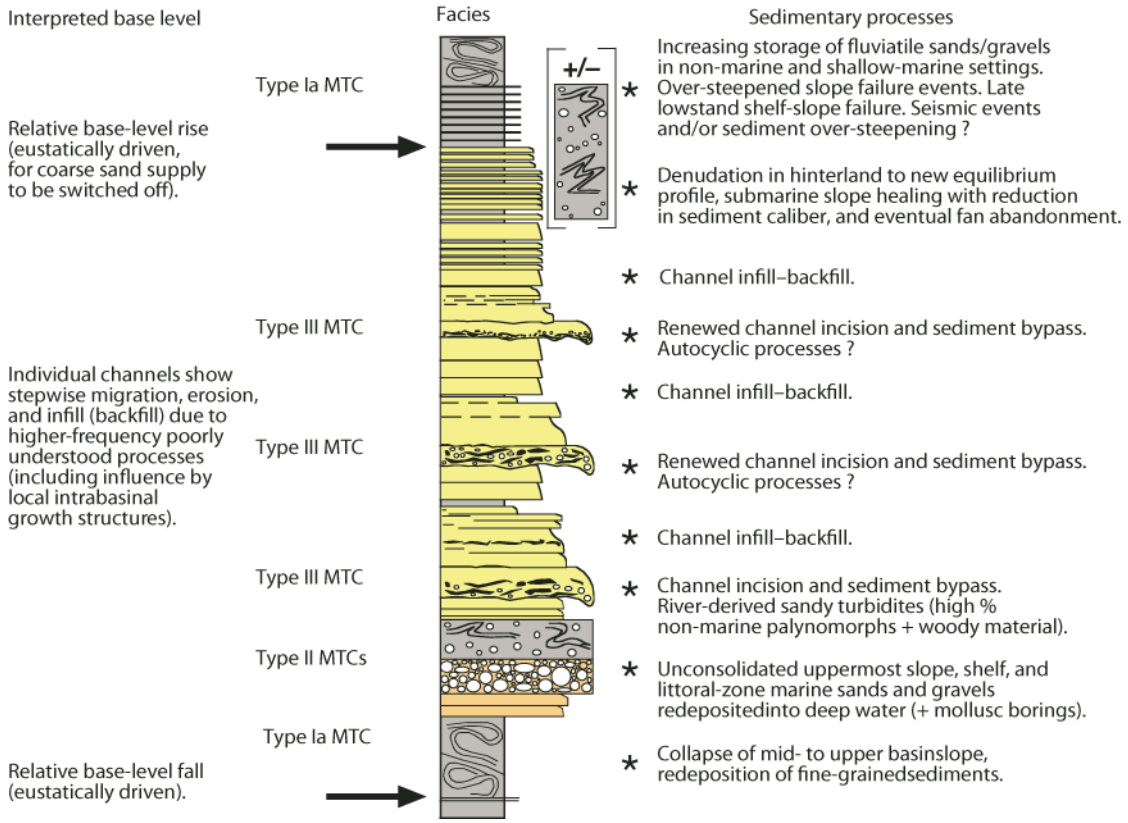

Figure 1.17 | Generalised Ainsa basin depositional sequence and interpretation (Pickering and Bayliss, 2009). Note, an earlier model of Pickering and Corregidor (2005) suggested tectonically forced base-level changes. For definitions of MTC deposits see Pickering and Corregidor (2005).

Figure 1.18 (next page) | Detailed geological map of the Ainsa basin (Pickering and Bayliss, 2009). The Banaston-Guaso systems (Upper Hecho Group; TS-2) show limited tectonic deformation and have been mapped with considerable detail. Below the Banaston System (Lower Hecho Group; TS-1) sediments are deformed by the Gerbe, Arro and Los Molinos thrusts part of the Peña Montañesa imbricate fan.

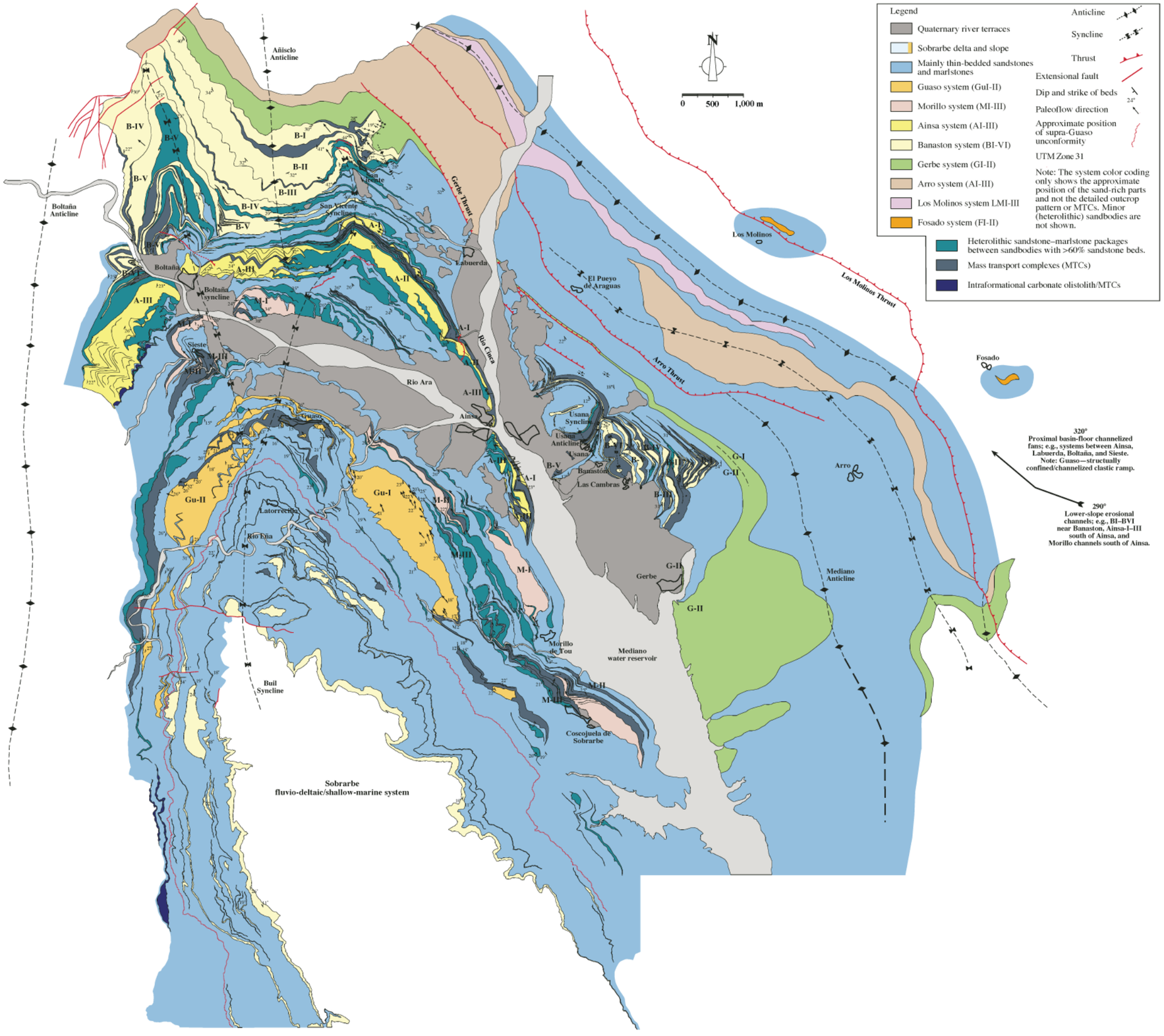
Legend
Quaternary river terraces
Sobrarbe delta and slope
Mainly thin-bedded sandstones and marlstones
Guaso system (GuI-II)
Morillo system (MI-III)
Ainsa system (AI-III)
Banaston system (BI-VI)
Gerbe system (GI-II)
Arro system (AI-III)
Los Molinos system LMI-III
Fosado system (FI-II)
Heterolithic sandstone–marlstone packages between sandbodies with >60% sandstone beds.
Mass transport complexes (MTCs)
Intraformational carbonate olistolith/MTCs
Anticline
Syncline
Thrust
Extensional fault
Dip and strike of beds
Paleoflow direction
Approximate position of supra-Guaso unconformity
UTM Zone 31
Note: The system color coding only shows the approximate position of the sand-rich parts and not the detailed outcrop pattern or MTCs. Minor (heterolithic) sandbodies are not shown.
N
0 500 1,000 m
320°
Proximal basin-floor channelized fans; e.g., systems between Ainsa, Labuerda, Boltaña, and Sieste. Note: Guaso—structually confined/channelized clastic ramp.
290°
Lower-slope erosional channels; e.g., BI–BVI near Banaston, Ainsa-I–III south of Ainsa, and Morillo channels south of Ainsa.
Añisclo Anticline
Boltaña Anticline
Gerbe Thrust
San Vicente
San Vicente Syncline
Boltaña
Boltaña syncline
Sieste
Labuerda
Río Cinca
Río Ara
Ainsa
Guaso
Latorrecilla
Río Ena
Buil Syncline
Sobrarbe fluvio-deltaic/shallow-marine system
Los Molinos
Los Molinos Thrust
El Pueyo de Araguas
Arro Thrust
Fosado
Usana Syncline
Usana Anticline
Usana
Banastón
Las Cambras
Arro
Gerbe
Mediano Anticline
Morillo de Tou
Mediano water reservoir
Coscojuela de Sobrarbe

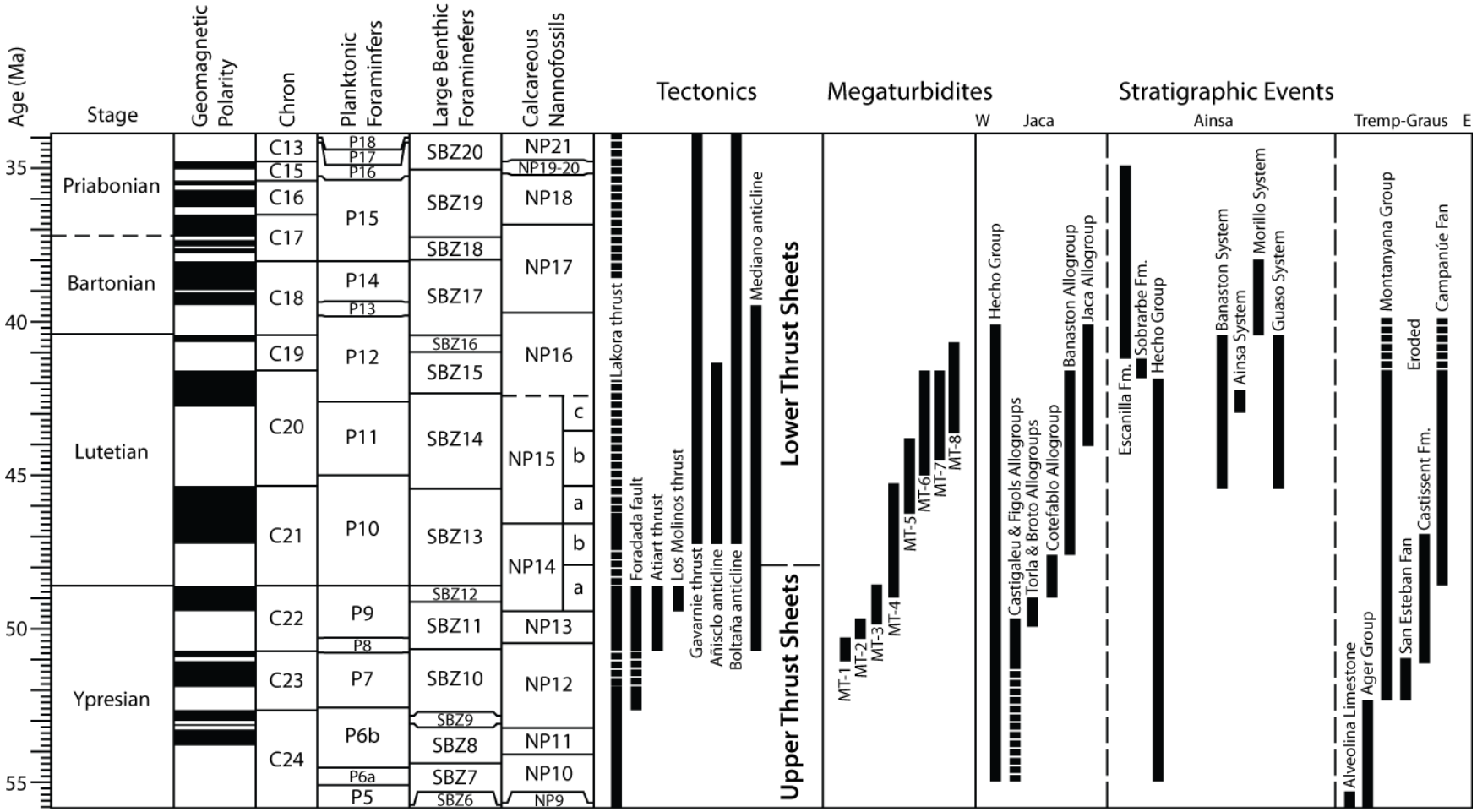

Figure 1.19 | Age ranges of tectonic and stratigraphic events within the south Pyrenean foreland basin. Tectonic data mainly from Remacha et al. (2003) with additional information from Farrell et al. (1987) and Holl and Anastasio (1993). Stratigraphic data collated from palaeontological (Kapellos and Schaub, 1973; Nijman and Nio, 1975; Labaume et al., 1985; Serra-Kiel et al., 1993; Payros et al., 1999; Oms et al., 2003; Pickering and Corregidor, 2005; Das Gupta, 2008) and magnetostratigraphic sources (Bentham et al., 1992; Bentham and Burbank, 1996; Hogan et al., 1996; Oms et al., 2003). Events placed upon the geological time scale of Gradstein et al. (2004).

1.5.3 Age of Ainsa basin sediments

Determining the duration of deep-marine sedimentation within the Ainsa Basin has proved difficult with a range of ages being present within the literature. Bio- and magneto-stratigraphic techniques have been employed to date the duration of Hecho Group sedimentation within the Ainsa and Jaca basins (Labaume et al., 1985; Bentham and Burbank, 1996; Payros et al., 1999; Oms et al., 2003; Jones et al., 2005; Pickering and Corregidor, 2005). These studies place the Ainsa basin deep-marine sediments within the early-middle Eocene (Ypresian-Bartonian) using the time scale of Gradstein et al. (2004). A synthesis of these data is provided in Figure 1.19.

Initial basin sediments are represented by the carbonate platform Alveolina Limestone upon which the first siliciclastic sediments were deposited. The age of the Alveolina Limestone has determined as 56 Ma from the adjacent Tremp-Graus basin (Serra-Kiel et al., 1993; Bentham and Burbank, 1996). The timing of the first system (Fosado) to be deposited can be determined using one of two proposed correlations with the Jaca basins allogroups and megaturbidites. Initially, Mutti et al. (1985) correlated the Fosado System with the Torla allogroup, the lower part of which contains megaturbidite 3 (MT-3) which was deposited during either NP13 or NP14 (Labaume et al., 1985; Payros et al., 1999). Alternatively, other authors either do not correlate the Fosado System with Jaca sediments (Das Gupta and Pickering, 2008), or associate them with the Figols allogroup (Caja et al., 2010). The Figols allogroup contains both MT-1 and MT-2 (Remacha et al., 2003), the lower of which (MT-1) is placed within NP12 (51 Ma; Labaume et al., 1985). Deep-marine sedimentation ceased with the progradation of the Sobrarbe delta complex into the basin at 41.8 Ma (Bentham and Burbank, 1996). Depending upon which basal Fosado correlations are correct, the deep-marine sediments of the Ainsa basin spanned 7-15 Myr.

Stable isotopic signatures of large benthic foraminifera have also been used to determine the age of the Ainsa basins sediments. A pilot study (Das Gupta, 2008) attempted to correlate the stable isotopic signature of 44 large benthic foraminifera, collected from throughout the basin stratigraphy, with the Cenozoic open ocean curve (Zachos et al., 2001). The study identified a tentative correlation between the $\delta^{13}C$ curves suggesting deep-marine sedimentation occurred over ~50-41 Ma. However, both the poor sampling resolution and the absence of stratigraphic spacing between samples leave this age determination lacking in credibility.

1.5.4 Pacing of Ainsa basin sediments

The pacing of coarse clastic sediment supply to the basin has been proposed as being controlled by either tectonics or orbital forcing (Pickering and Corregidor, 2000, 2005). Pickering and Corregidor (2005) proposed a 1.5 to 2 Myr tectonic control on the pacing of the individual systems associated with pulses of Mediano anticline deformation (Holl and Anastasio, 1993). An unspecified shorter scale tectonic driver is implied for supplying sediment to the individual sequences (Pickering and Corregidor, 2005).

However, following the identification of Milankovitch scale oscillations within the Ainsa System, it has been suggested that the timing of coarse clastic sediment supply was controlled by the orbital forcing of climate (Das Gupta and Pickering, 2008; Heard et al., 2008; Pickering and Bayliss, 2009; Sutcliffe and Pickering, 2009). The hypothesis is based upon the identification of 25 discrete submarine fan deposits within the Ainsa basin Hecho Group being deposited over a ~10-12 Myr period, giving an average duration for each submarine fan of 400-480 kyr, which is coincident with the 404-kyr duration of the long eccentricity Milankovitch cycle. Combining this with submarine fan accumulation being associated with low-stand conditions, fan deposition was assumed to be a 404 kyr paced glacio-eustatic mechanism.

Supporting the orbital influence upon regional sedimentation is the identification of the orbitally forced waxing and waning of coarse grained sediment supply within coeval the Montanyana Group (de Boer et al., 1991; Weltje et al., 1996; Nijman, 1998) and later Bartonian deltaic sediments within the Jaca basin (Kodama et al., 2010). Orbitally forced variations in climate have also been shown to influence sediment flux in fluvial and marine environments throughout the geological record (Goodwin and Anderson, 1985; Olsen, 1990; Olsen, 1994; Fischer, 1995; Pickering et al., 1999; Postma, 2001; Van der Zwan, 2002; Nador et al., 2003; Kodama et al., 2010) and specifically within deep-marine siliciclastic settings (van Tassell, 1987; Weltje and de Boer, 1993).

Within the study area these variations in coarse clastic sediment flux should propagate through to the deep-marine Ainsa basin as long as the sediments were directly sourced from the continent (van Tassell, 1987; Weltje and de Boer, 1993). However, the orbital signal may be lost where sediment is stored on a continental shelf then re-mobilised during a fall in base-level, which may or may not be orbitally forced (Posamentier et al., 1988; Posamentier and Vail, 1988; Van Wagoner et al., 1988). Submarine fan systems are additionally subjected to auto-cyclic, tectonic and intermittent erosion resulting in the possibility that evidence of orbital signals may be lost (de Boer and Smith, 1994).

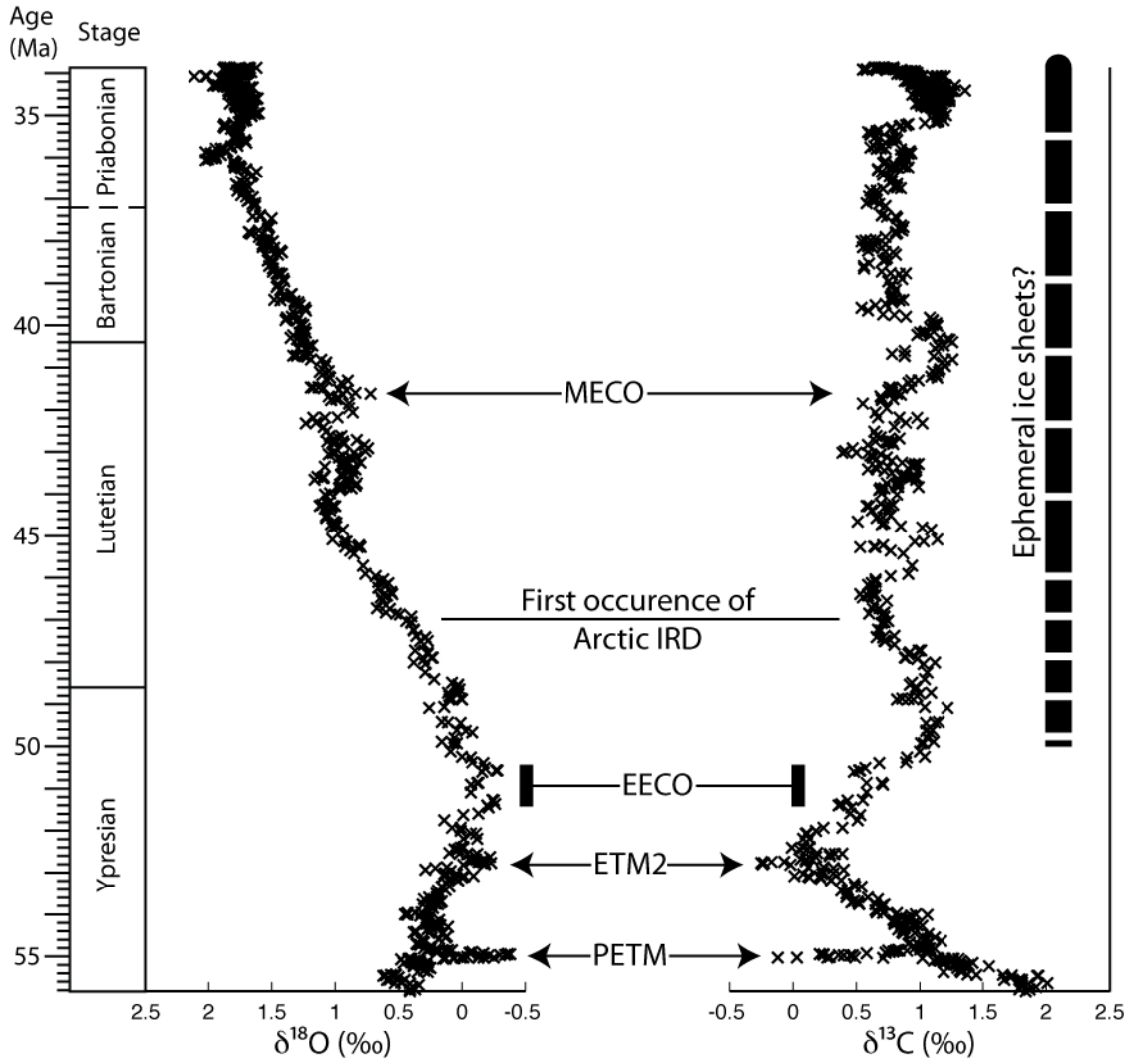

Figure 1.20 | Benthic foraminiferal stable isotopic variability during the Eocene epoch with major climatic events highlighted. Isotopic data 5-point moving average data from Zachos et al. (2001). Evidence for possible ephemeral ice accumulation discussed in text. MECO – Middle Eocene Climatic Optimum. IRD – Ice Rafted Debris. EECO – Early Eocene Climatic Optimum. ETM2 – Eocene Thermal Maximum 2. PETM – Paleocene-Eocene Thermal Maximum.

1.6 Climatic conditions

1.6.1 Global Eocene climate

The Eocene epoch marks a pivotal time in global climate evolution with the initiation of a long-term cooling trend leading to a substantial ice-sheet accumulation at the Oligocene-Eocene boundary (Zachos et al., 2001). The prevailing greenhouse climate represents the warmest epoch within the Cenozoic (Zachos et al., 1994; Zachos et al., 2001; Zachos et al., 2008). Global temperature gradients were considerably lower than today with warm high latitudes (Zachos et al., 1994; Greenwood and Wing, 1995; Andreasson and Schmitz, 2000; Huber and Sloan, 2001). Atmospheric CO_2 concentrations were greater with values between ~200-460 ppmv potentially linked to increased volcanic activity (Pearson and Palmer, 2000; Royer, 2006).

The early Eocene is characterised by an increase in global temperatures reaching a maximum with the Early Eocene Climatic Optimum (EECO) (Zachos et al., 2001). During this stage high latitude sea-surface and continental proxy records show temperatures of 19-25˚C (Bijl et al., 2009; Eberle et al., 2010). Lower latitude temperature estimates for the early Eocene show are believed ~27˚C (Keating-Bitonti et al., 2011).

Superimposed upon this early Eocene warming trend are the Paleocene Eocene Thermal Maximum (PETM), Eocene Thermal Maximum 2 (ETM2) and Eocene Thermal Maximum 3 (ETM3 or 'X') hyperthermal events (Zachos et al., 2001; Nicolo et al., 2007; Zachos et al., 2008; Agnini et al., 2009; Zachos et al., 2010). These events are short-lived (<10 kyr) global events where bottom water temperatures are believed to have increased by 2-6˚C, along with carbon and oxygen isotope excursions (CIE) (Kennett and Stott, 1991; Zachos et al., 2001; Stap et al., 2010). Recent studies show these events are paced by the 400 kyr eccentricity cycle except for the PETM which may be related to the 100 kyr eccentricity cycle (Cramer et al., 2003; Lourens et al., 2005; Röhl et al., 2007; Westerhold et al., 2007; Galeotti et al., 2010; Zachos et al., 2010; Sexton et al., 2011). Each of these hyperthermal events is characterised by a significant injection of isotopically depleted carbon into the climate system (Dickens et al., 1995; Lourens et al., 2005; Sexton et al., 2011), a shoaling of the carbonate compensation depth (Zachos et al., 2005) and perturbations of the hydrological cycle (Pagani et al., 2006). The source and mechanism of carbon addition to the ocean-atmosphere system remains uncertain (Dickens et al., 1995; Kurtz et al., 2003; Svensen et al., 2004; Zachos et al., 2010; Sexton et al., 2011).

Following the EECO, global temperatures began to decline indicating the initiation of climate deterioration culminating in the bi-polar accumulation of substantial polar ice by the Eocene-Oligocene boundary (Zachos et al., 2001). Atmospheric CO_2 levels also began to fall (Pearson and Palmer, 2000; Royer, 2006; Zachos et al., 2008). Interrupting this cooling trend is the Middle Eocene Climatic Optimum (MECO) event (Zachos et al., 2001) (Fig. 1.20). The MECO event involved the warming of both surface and deep ocean waters by 4-6˚C over a 500-kyr period (Bohaty and Zachos, 2003; Bohaty et al., 2009). Evidence suggests that a coeval increase in atmospheric CO_2 concentrations accompanied the temperature increase (Bijl et al., 2010). Climatic cooling continued further until the Eocene-Oligocene boundary where major bi-polar glaciations commenced (Zachos et al., 2001).

The potential presence and extent of polar ice during the Eocene greenhouse climate remains controversial. Increasing evidence suggests that bi-polar ephemeral ice formation may have commenced prior to the Eocene-Oligocene boundary, potentially as early as ~50 Ma (Miller et al., 2005; Westerhold and Röhl, 2009). Both

sedimentological (IRD) and proxy ($\delta^{18}O$) based evidence exists for the presence of ephemeral (possibly bi-polar?) ice accumulation during the middle Eocene from ~45 Ma (Cooper et al., 1991; Ehrmann and Mackensen, 1992; Pekar et al., 2005; Tripati et al., 2005; Moran et al., 2006; St. John, 2008; Tripati et al., 2008; Dawber and Tripati, 2011). Studies of Eocene marine sediments from the Arctic suggest that ephemeral sea-ice along with possible small isolated ice caps on higher Arctic elevations may have existed from ~47.5 Ma (Stickley et al., 2009). Once ice formation was initiated then its growth and decay was potentially orbitally controlled (Sangiorgi et al., 2008; St. John, 2008).

Initiation of substantial polar ice accumulation during this time has been linked to atmospheric CO_2 concentrations (DeConto and Pollard, 2003; DeConto et al., 2008). Empirical data suggest that for polar ice to form a minimum CO_2 threshold of ~280-750 ppmv must be crossed (Pearson and Palmer, 2000; Royer, 2006; DeConto et al., 2008). According to CO_2 reconstructions during the Eocene this threshold was potentially briefly crossed at ~50 Ma (Pearson and Palmer, 2000). However estimation of atmospheric CO_2 concentrations vary widely as illustrated by Lowenstein and Demicco (2006).

1.6.2 Eocene sea-level

Eustatic sea-level variability during the middle Eocene is suggested to have occurred over a range of temporal scales based upon stable isotopic and sequence stratigraphic observations (Haq et al., 1987; Miller et al., 2005; Pekar et al., 2005; Dawber et al., 2011). In the sequence stratigraphic context these sea-level changes correspond to 2nd (10-100 Myr), 3rd (1-10 Myr) and 4th (0.2-0.5 Myr) order cycles. During the Eocene, sequence stratigraphic evidence indicates long-term (2nd-order) sea-level variability occurred with sea-level reaching ~180 m above present day during the late Ypresian (sequence YP9). Following this high, sea-level gradually decreased to a low of ~40 m above present day during the Priabonian (sequence Pr1; Fig.1.21). Short-term (3rd-order) sea-level variability during the Ypresian indicate small amplitude, high frequency changes which then increase in amplitude and decrease in frequency after sequence YP9 (Fig. 1.21). Detailed stratigraphic studies of localised Eocene strata identify the presence of 4th-oder stratigraphic cycles interpreted as indicating sea-level variability of ~20-60 m during the Bartonian (Dawber et al., 2011).

Stable isotopic data ($\delta^{18}O$) have also been interpreted as possibly reflecting higher frequency eustatic sea-level variability with changes of >10 m (3rd and 2nd order; Miller et al. 2005; Pekar et al. 2005; Dawber et al. 2011). During the early Eocene sea-level variability is believed to have been ~20 m whilst during the middle Eocene this

increases to ~25-45 m (Pekar et al., 2005). However, others dispute the isotopic evidence for Eocene eustatic sea-level change suggesting that the observed changes in $\delta^{18}O$ are the result of temperature and hydrological affects (Burgess et al., 2008).

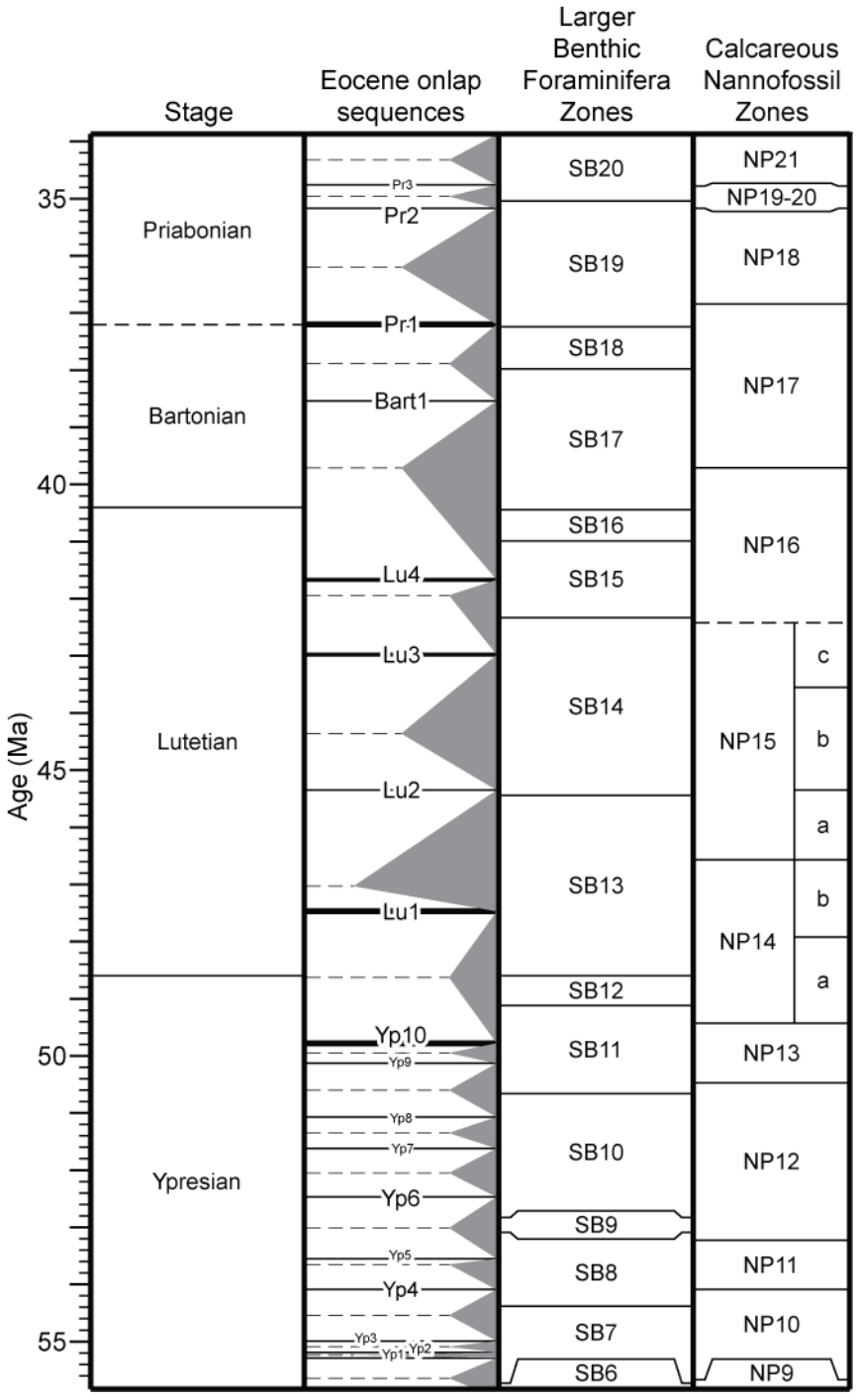

Figure 1.21 | Identified Eocene onlap sequences indicating eustatic sea-level variability. Sequence onlap curve of Hardenbol et al. (1998) and constructed using Time Scale Creator 4.2.5 (Ogg et al., 2010).

1.6.3 Pyrenean and Ainsa basin palaeoclimatic conditions

1.6.3.1 Regional climatic conditions

During the Eocene the study area was located at ~35˚N which is similar to the modern location of northern Morocco within the sub-tropics (Plaziat, 1981; Smith, 1996). Using General Circulation Models (GCMs) and geochemical data it is possible to estimate the predominant climatic conditions that prevailed over the study region. Sea surface temperatures (SST) predicted from GCM results for the eastern North Atlantic at during the Eocene are estimated as being 26-27˚C with precipitation rates being ~2.2 mm/day (Speelman et al., 2010; Tindall et al., 2010). Isotopic data obtained from shallow marine shell carbonate from middle Eocene deposits in southern England indicate that seasonality was similar to today with a 10-12˚C SST difference between summer and winter (Andreasson and Schmitz, 2000). However it is unclear whether this seasonal variation is due to temperature or precipitation changes (Keating-Bitonti et al., 2011).

Sedimentological studies within the distal Pamplona and basin also provide an insight into the regions palaeoclimate. Payros et al. (2010) use the sedimentology of the Urbasa-Andia Formation (southern edge of the deep-marine Pamplona basin, see their Fig. 1 for location) to indicate that tropical cyclone activity within the region was likely intensified in both power and frequency during the middle Eocene.

The study of early-middle Eocene planktonic foraminifera from the Pamplona and Basque basins indicate an alternation between high- and low-latitude species possibly indicating short-term changes in regional climate between warm and cool conditions (Payros et al., 2006). However, the variation in the dominance of high- or low-latitude species may alternately be the result of eutrophication of sea-water via the re-suspension of vast amounts of sediment rather than changes in climate. Despite this uncertainty, the general trend toward increased assemblages of high-latitude indices throughout the Ypresian-Lutetian reflect the post-EECO climatic deterioration (Fig. 1.20).

1.6.3.2 Ainsa basin and source area climatic conditions

Specific palaeoenvironmental conditions for the Ainsa basin are determined via palynofloral and microfaunal analyses obtained from unpublished Robertson Research reports based upon the Ainsa System (Unpublished Robertson Research report for UCL Ainsa Project; Fenton, 1999). These results suggest that tropical to sub-tropical conditions prevailed over the area during deposition of the Ainsa basin. This supports the findings of Greenwood and Wing (1995) who use terrestrial vegetation modelling to suggest that the climate of western Europe was tropical to sub-tropical with the

presence of palms indicating a largely frost free environment. Hinterland vegetation was dominated by coniferous vegetation (e.g., gymnospermous trees; Schmitz et al., 2001) on either upland and/or well drained lowlands. Based upon the paucity of pteridophyte and associated spores the limited development of fringing swamps and a possible minor development of a mangrove belt is suggested. Significant surface run-off into the basin due to moderately high rainfall patterns provided an abundance of biodegraded and physically abraded humic plant matter (vitrinite). Degradation of this organic material likely occurred during its storage on adjacent shelf and while on basin floor.

Marine conditions are believed to have prevailed throughout the accumulation of the Fosado-Guaso systems (e.g., as seen in the ubiquitous marine microfauna), with water depths estimated as 400 to 600 m (Pickering and Corregidor, 2005). The paucity of planktonic foraminifera, however, may have been due to poor connectivity of Ainsa basin waters with the open ocean currents and reduced salinities due to the presence of fresh water plumes. Alternatively, this may be due to poor preservation due to taphonomic effects as noted within the Jaca basin by Oms et al. (2003). The sediment-water interface is interpreted as being above the carbonate compensation depth (CCD). The presence of agglutinated and benthic foraminifera along with trace fossils (Heard and Pickering, 2008) suggest bottom waters contained some oxygen although these may have varied over time (Heard et al., 2008).

1.7 Milankovitch orbital cyclicity

1.7.1 Milankovitch theory

Milankovitch theory, initially proposed by Croll (1867) and subsequently refined by Milankovitch (1941), proposes a link between the Earth's orbital perturbations and periods of glacial climate. However, it was not until the work of Hays et al., (1976) that the theory became widely accepted, with Quaternary ice ages being linked to Milankovitch's (1941) orbital periods. Milankovitch proposed that the Earth's rotational axis and orbit around the Sun vary with three predictable periods, eccentricity, obliquity and precession (Fig. 1.22). Periodical perturbations to the Earth's orbit can be attributed to interactions between the Sun-Earth-Moon system and other planets in our solar system. Records of orbital forcing exist throughout the majority of the Phanerozoic (Hays et al., 1976; Olsen, 1990; Fischer et al., 1991; Olsen, 1994).

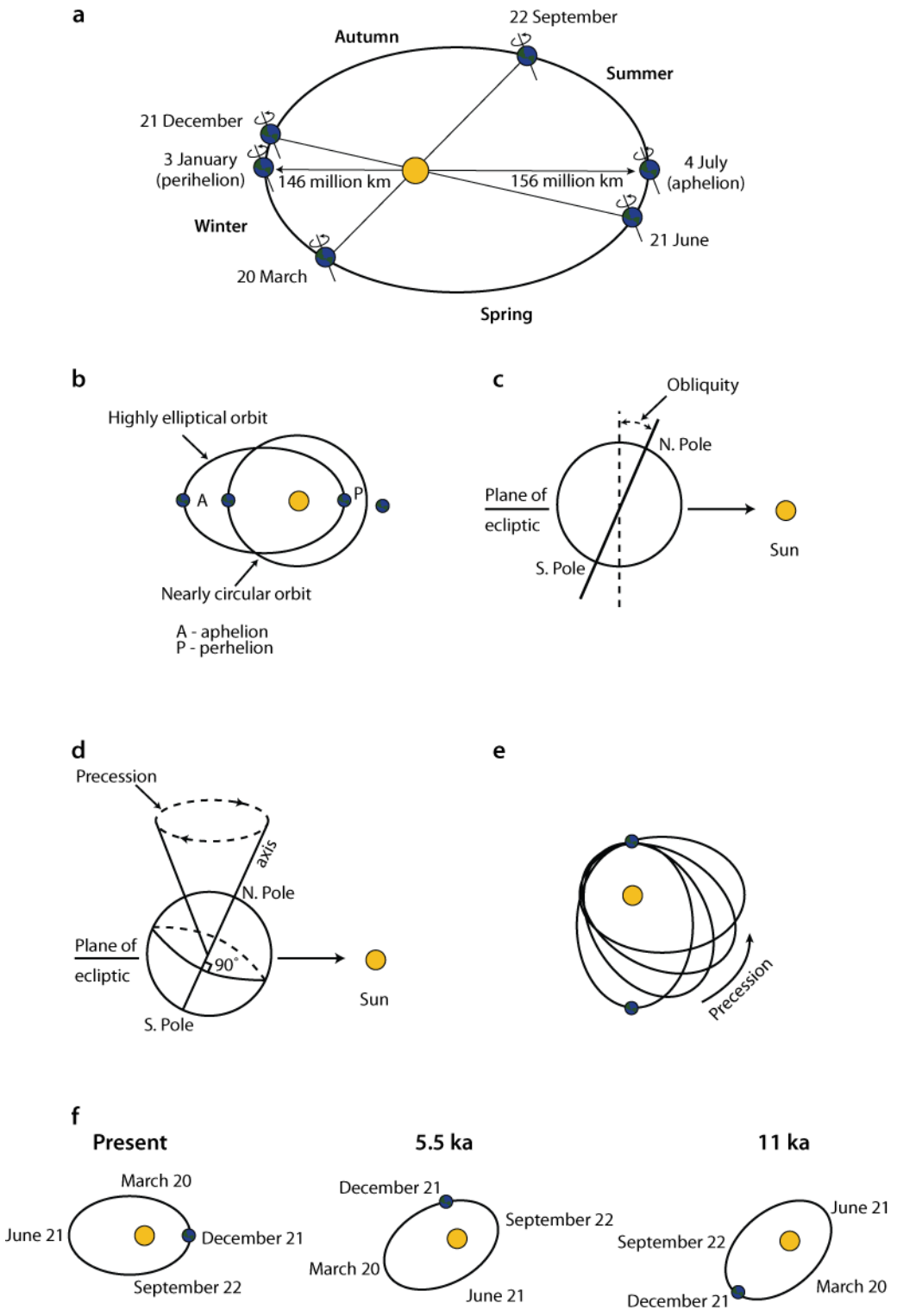

Figure 1.22 | Current orbital configuration and Milankovitch orbital variability. (a) Present day orbit and its relationship to the seasons, solstices and equinoxes. **(b)** Eccentricity is the change in Earth's orbit between near circular to an ellipse. **(c)** Obliquity involves the change in the angle of the Earth's tilt between 21.8˚ and 24.4˚. **(d and e)** The precession of the equinoxes is comprised of two factors, the precession of the Earth's rotational axis and the precession of the Earth's orbit. **(f)** The precession of the equinoxes is due to the combination of d & e. Today the Northern Hemisphere winter coincides with the perihelion and summer with the aphelion. A half-precession cycle into the past/future will result in Northern Hemisphere winter and summer coinciding with the aphelion and perihelion, respectively. Diagrams after Wilson et al. (2000).

1.7.2 Eccentricity

The Earth's orbit about the Sun varies from a near circular to an elliptical orbit with a period of 95 and 125 kyr with an additional long-eccentricity period of 404 kyr (Fig. 1.22). Driving eccentricity is the interaction between the angular momentum of the Earth as it orbits the Sun and periodic asymmetric torque applied by Jupiter and Venus.

Changes in eccentricity cause very minor changes of ~0.03% in the total annual insolation received by the earth and is by far weakest of all three orbital parameters. Despite this, eccentricity has a significant seasonal effect. The more elliptical the orbit becomes the more the season will be exaggerated in one hemisphere and moderated in the other. The current orbital configuration results in the Earth being closest to the Sun at a distance of 146 million km on January 3rd (perihelion) and furthest at 156 million km on July 4th (aphelion). At the perihelion the Earth receives ~351 Wm^{-2} compared to 329 Wm^{-2} during the aphelion thereby representing a difference of more than 6%. However, during periods of maximum eccentricity over the last 5 Ma, this difference may have been as much as 30% (Maslin and Ridgwell, 2005).

According to Milankovitch (1941) Northern Hemisphere ice-sheets were more likely to have formed during periods when the Northern Hemisphere summer is coincident with the aphelion thereby enabling snow from the previous winter to survive and accumulate over several seasons. The result being substantial ice accumulations observed during the Pleistocene (Hays et al., 1976).

1.7.3 Obliquity

Obliquity describes the tilt of the Earth's axis of rotation with respect to the plane of its orbit of the Sun (the plane of the ecliptic), which varies between 21.8˚ and 24.4˚ over a dominant period of 41 kyr (Fig. 1.22). The Earth's rotational axis precesses with a period of 1/26 kyr whilst the Earth's orbit precesses with a period of 1/70 kyr. Obliquity measures the difference between these two factors 1/26-1/70 = 1/41 kyr. Both of these precessional periods are quite regular leading to the 41 kyr obliquity period dominating with lesser periods of 29 and 53 kyr.

The tilt in the Earth's rotational axis is what gives rise to the seasons with the Northern and Southern hemispheres. The Northern Hemisphere experiences summer when it is tilted toward the Sun. During summer the hemisphere receives more than 12 hours of sunlight and the Sun is higher in the sky. The Southern Hemisphere at this time experiences winter with less then 12 hours of sunlight and the Sun is lower in the sky. With obliquity altering the angle of the hemisphere in relation to the Sun, during

periods of low obliquity (21.8˚), both summer and winter will be milder. During periods of high obliquity (24.2˚), summers will be warmer with cooler winters. Changes in obliquity over time therefore control the contrast between summer and winter. Milankovitch (1941) suggested that during periods of reduced obliquity, ice-sheets are more likely to accumulate in the Northern Hemisphere as snow will accumulate over several seasons. This provides an explanation for the dominance of the 41-kyr glacial-interglacial cycles prior to the mid-Pleistocene Revolution (MPR; Maslin and Ridgwell, 2005). Obliquity not only influences ice-sheet accumulation but global climate by affecting the amount of insolation received by the high and low latitudes. With this differential heating, obliquity influences the meridional atmospheric flux of heat, moisture and latent heat thereby affecting global climate (Raymo and Nisancioglu, 2003; Antico et al., 2010).

1.7.4 Precession

Precession consists of two components: axial precession and apsidal precession (Fig. 1.22). Axial precession involves the precession of the Earth's rotational axis over a period of 27 kyr. This results in the dates of the equinoxes to rotate about the Sun thereby changing the Earth-Sun distance for a particular season such as the Northern Hemisphere summer. Apsidal precession is the change in the Earth's elliptical orbit about the Sun, which rotates over a period of 105 kyr and controls the time of year when the Earth is closest to the Sun. Combining these two parameters results in the commonly identified precessional periods of 19 and 23 kyr. The shorter period 19 kyr periodicity occurs due to the combination of eccentricity and the precession of the axis of rotation. The longer 23 kyr period is due to the combination of the precession of the axis of rotation and the precessional changes in the Earth's orbit. The combined effect of these two periodicities is cause the perihelion to coincide with the summer season in each hemisphere on average 21.7 kyr but 180˚ out of phase.

Precession is greatly effected by the eccentricity of the Earth's orbit and results in either the amplification or muting of the insolation received over periods of ~100 and ~400 kyr. During periods of low eccentricity (more circular orbit) the effects of precession are muted as the difference in insolation received during the perihelion and aphelion is reduced. During periods of increased eccentricity (more elliptical orbit) the effects of precession are amplified with the difference in insolation received during the perihelion and aphelion is increased. The result is an amplitude modulation of the precessional insolation signal as illustrated in Figure 1.23.

Sub-Milankovitch cycles in insolation have also been proposed including half (~11 kyr) and quarter (~5 kyr) precession periods (Short et al., 1991; Berger and

Loutre, 1997; Berger et al., 2006). The identification of half precession cycles are linked to the twice-yearly passage of the Sun across equatorial sites during the spring and autumn equinox. The result is a twice-yearly maxima in insolation received within the tropics and sub-tropics when the Sun is over the equator resulting in the spring and autumn equinox, the magnitude of which is controlled by precession (Berger and Loutre, 1997; Berger et al., 2006).

Quarter precession cycles are also associated with the twice-yearly variation in the amount of insolation received within the tropics and sub-tropics (Berger et al., 2006). The maxima occur when the Sun is over the equator (spring and autumn equinox) whilst the minima occur when the Sun is over the Tropic of Cancer and Capricorn (summer and winter solstice). The result are four seasonal contrasts between the maxima and minima insolation received in the tropics occurring every ~5 kyr (Berger et al., 2006).

The sub-precessional variation in the amount of insolation received at the equator will alter the meridional temperature gradient thereby effecting atmospheric and oceanic circulation and exporting these changes to higher latitudes (Short et al., 1991; Crowley et al., 1992; Kukla and Gavin, 2004; Berger et al., 2006).

1.7.5 Combined affect upon climate

Variations in the Earth's orbital path by means of eccentricity, obliquity and precession control the amount of insolation received by the upper atmosphere. Using published algorithms it is possible to determine how insolation varies through time and with latitude (Berger, 1978a; Berger, 1978b; Ruddiman and McIntyre, 1984; Quinn et al., 1991; Berger et al., 1993; Laskar et al., 1993; Laskar et al., 2004; Laskar et al., 2011). Results indicate that eccentricity controls the total amount of insolation received by the Earth whilst obliquity and precession determine its latitudinal distribution (Berger, 1978a; Berger et al., 1993; Muller and MacDonald, 2000). Figure 1.23 uses the algorithms of Laskar et al. (2004) to demonstrate that precession dominates the lower latitudes whilst obliquity effects the insolation received at higher latitudes (Berger, 1978a). However, the climatic response to this differential forcing is far more complex (Short et al., 1991).

Eccentricity however, is not observed in the insolation spectra of Figure 1.23 but instead appears to modulate (amplitude modulation) the precessional cycle every ~100 kyr. The conspicuous absence of an eccentricity signal from the spectra is at odds with the strong evidence for eccentricity being responsible for Pleistocene ice ages (Hays et al., 1976; Laskar et al., 1993; Shackleton, 2000; Maslin and Ridgwell, 2005). This "100 kyr problem" illustrates the complexities of the global climatic

response to varying insolation and its encoding into the stratigraphic record (Short et al., 1991).

Although the effects of varying insolation on global climate remain poorly understood, the periods of orbital perturbations are clearly encoded within the stratigraphic record. A vast literature exists documenting orbitally forced climate covering an array of depositional settings and environmental proxies such as ice volume (Hays et al., 1976), bottom water oxygenation (Erba and Premoli Silva, 1994; ten Veen and Postma, 1996; Postma and ten Veen, 1999; Heard et al., 2008), atmospheric gases (Petit et al., 1999; Shackleton, 2000), aeolian material (Clemens et al., 1991), carbonate productivity (Herbert and Mayer, 1991), vegetation cover (Mommersteeg et al., 1995), ocean circulation (Kleiven et al., 2011), and precipitation (Kutzbach and Otto-Bliesner, 1982; Barron et al., 1989; Harris and Mix, 1999).

The period of the orbital variability is expected to vary through time. Using the equations of Berger et al. (1992) and Laskar et al. (2004; 2011) both the period (Table 1.1), orbital and insolation curves can be calculated for the middle Eocene.

Table 1.1 - Calculated orbital periods for the middle Eocene

Orbital Parameter	Period (kyr)*
Precession	18.82
Precession	22.64
Obliquity	40.01
Obliquity	52.29
Short Eccentricity	94.78
Short Eccentricity	123.82
Long Eccentricity	404.18

*Orbital periods calculated for 45 Ma using equations of Berger et al. (1992).

1.7.6 Orbital influence upon Eocene Northern Hemisphere and Pyrenean climate

Variation in the Earth's orbit will have resulted in changes of the prevailing regional oceanic and terrestrial climate within the Pyrenean region during the middle Eocene. The affect of orbital variation upon the regions climate can be estimated using general circulation models (GCMs) (Sloan and Morrill, 1998; Sloan and Huber, 2001; Lawrence et al., 2003). The more recent models of Sloan and Huber (2001) and Lawrence et al. (2003) are both based upon the two end members of the precessional cycle (MINS and MAXS) with suitable obliquity and eccentricity conditions.

The MINS setting produces the Northern Hemisphere perihelion during the Northern Hemisphere winter solstice and aphelion during the summer solstice leading to reduced seasonality within the Northern Hemisphere. The MAXS setting leads to the Northern Hemisphere perihelion during the Northern Hemisphere summer solstice and

aphelion during the winter solstice thereby leading to amplified seasonality within the Northern Hemisphere.

Combining the results from the two studies indicate that Northern Hemisphere SST, terrestrial mean annual temperatures (MAT), mean annual temperature range (MATR) are significantly influenced by precessional changes in insolation (Sloan and Huber, 2001; Lawrence et al., 2003).

The model of Sloan and Huber (2001) indicate that annual SST potentially varied by 6˚C in northern ocean regions (>60˚N) between the MINS and MAXS experiments. Below 60˚N, annual SST variability is negligible between the two orbital conditions. During the Northern Hemisphere winter (December, January and February; DJF) the difference in Arctic and northern Pacific SST is ~10˚C between experiments with MINS containing lowest temperatures. During the Northern Hemisphere's summer months of June, July and August (JJA) SSTs varied by 2-3˚C between MINS and MAXS settings. More importantly, the amount of insolation received at 80˚N during the summer is ~120 Wm^{-2} less during MINS compared to MAXS therefore enabling winter sea-ice to survive the summer and accumulate over several seasons.

The terrestrial GCM of Lawrence et al. (2003) suggests that continental January MATs for latitudes >75˚N differed by 10˚C between the two orbital configurations. Specifically to the Pyrenean region, the terrestrial model predicts that January and July temperatures differ by 2˚C and 6˚C, respectfully between the two orbital conditions. Pyrenean MATR between January and July indicate temperature variations of 10˚C between MINS and MAXS conditions.

Precipitation rates within the GCMs indicate a low to moderate sensitivity to precessional forcing with periods of greater seasonality leading to increased precipitation (Lawrence et al., 2003). Terrestrial estimates indicate that over the Pyrenean region precipitation changed by 7-9% between MINS and MAXS settings. The earlier model focussing upon the oceanic response suggests that surface run-off rates from the region varied by 12-17% between the precession end members (Sloan and Huber, 2001).

Both modelled oceanic and atmospheric circulation are also indicated to have been effected by the changing orbital conditions (Sloan and Huber, 2001). During MINS conditions, south-westerly surface winds in the North Atlantic are predicted to have increased by 30% during DJF compared to those during MAXS. During JJA, the south-westerly winds in the Northern Atlantic are shown to have intensified during MAXS conditions compared to MINS. The largest seasonal contrast in the North Atlantic south-westerly winds occurs during the MINS setting, with winter experiencing stronger winds compared to summer. The effect upon Pyrenean climate may have been an increased frequency of storms tracking toward the Iberian plate. The model

also indicates that wind-driven upwelling is highly sensitive to the changes in insolation with North Atlantic DJF upwelling being twice a strong and more widespread during MINS than during MAXS.

Overall the two models indicate that changes in precession affected the amount of insolation received by the Earth's upper atmosphere produced significant variability within Northern Hemisphere and Pyrenean climate. With the amplitude of precessional insolation changes being modulated by eccentricity, the latter will likely affect the Pyrenean climate via an intensified or muted precessional seasonal contrast hence modulating the climatic factors outlined above.

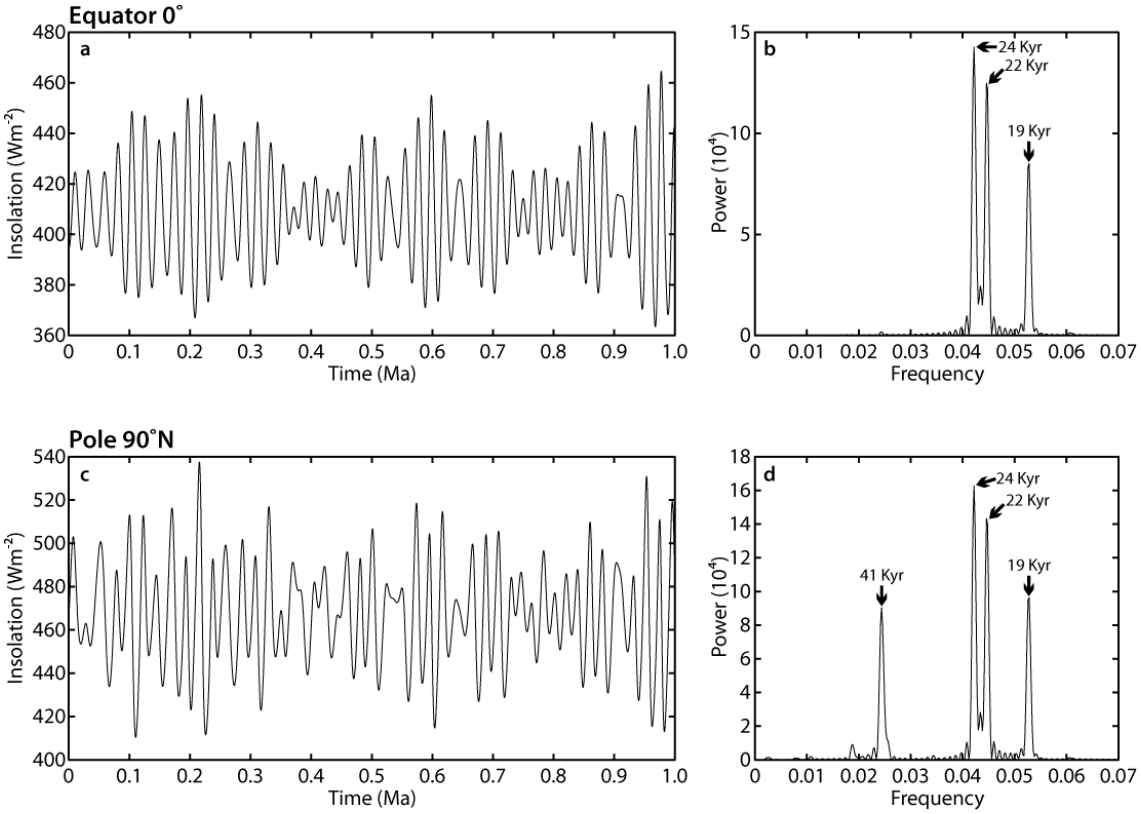

Figure 1.23 | Calculated insolation for the Equator (a) and N. Pole (c) using the equations of Laskar et al. (2004). From the spectra (b and d) it is apparent that the effect of obliquity is restricted to the poles. Additionally note the absence of any spectral peaks representing the eccentricity period but instead appear to amplitude modulate the amplitude of precession in a.

1.8 Research objectives

The main aim of this research is to investigate the hypothesis that the submarine fans of the Ainsa basin were paced by a 404 kyr glacio-eustatic cycle (Das Gupta and Pickering, 2008; Heard et al., 2008; Pickering and Bayliss, 2009; Sutcliffe and Pickering, 2009). The hypothesis presents a number of testable predictions:

- each of the basin sequences comprising a basal coarse-clastic submarine fan and overlying inter-fan deposits, span a 404-kyr long eccentricity cycle;
- the duration of a system can be estimated based upon the number of constituent sequences;
- the mechanism of coarse-clastic sediment supply to the basin is glacio-eustatic and therefore should coincide with periods of ice-sheet growth;
- tectonics controlled the locus of coarse-clastic sediment deposition;
- average sediment accumulation rate for Ainsa basin was ~40 cm/kyr.

This research aims to test these predictions via the construction of a basin age model (Chapter 3) and comparing the timing of basin events with tectonic and climatic records. The identification of Milankovitch orbital oscillations (i.e., eccentricity, obliquity and precession) within the hemipelagic inter-fan and off-axis fan sediments (Chapters 4, 5, 6 and 7), will enable the creation of floating orbital time scales in order to test the pacing of the submarine fan deposits and verify the biostratigraphic age model.

Validation of the proposed glacio-eustatic forcing mechanism shall be achieved by comparing the estimated ages of the submarine fans with the middle Eocene insolation curves of Laskar et al. (2004; 2011). This is based upon middle Eocene ephemeral (bi-polar?) ice-sheet accumulation being associated with orbitally forced periods of reduced insolation (Sangiorgi et al., 2008; St. John, 2008; Westerhold and Röhl, 2009). With the amount of insolation received by the Earth being controlled by the integration of the three Milankovitch orbital periods (Berger et al., 1993; Laskar et al., 2004), the latter can be utilised to estimate the timing of these insolation minima and hence periods of potential ice accumulation during the middle Eocene. Comparing these curves with the timing of the Upper Hecho Groups submarine fans should therefore enable the glacio-eustatic forcing mechanism to be tested.

Using more definitive indicators for the presence of ephemeral ice-sheets it may also be possible to verify whether these periods coincide with submarine fan deposition. Such definitive indicators for ice-sheet formation include the high resolution ice rafted debris and oxygen stable isotope records (St. John, 2008; Tripati et al., 2008; Zachos et al., 2008).

The affects of tectonics upon the basin will be tested using the age model to compare depositional events with published deformation histories for the basin bounding Mediano and Boltaña anticlines (Holl and Anastasio, 1993; Mochales et al., 2012). This will enable the “see-saw” tectonic model of Pickering and Bayliss (2009) to be validated and permit the affects of tectonics *versus* climatic controls upon sedimentation to be discerned.

Chapter 2
Analytical techniques

2.1 Introduction

It has been proposed that deposition of the ~25 discrete sandy submarine fans within the Ainsa basin was driven by the ~404 kyr Milankovitch long eccentricity cycle (Heard et al., 2008; Pickering and Bayliss, 2009; Sutcliffe and Pickering, 2009). Therefore, the hemipelagic sediments located between coarse-grained clastic submarine fans should contain a record of shorter Milankovitch orbital periods, i.e., eccentricity, obliquity and precession. Such variability has been shown to be well represented within hemipelagic sediments as their carbonate content, mineralogical and organic content are controlled by external factors such as climate (De Visser et al., 1989). Measurement of these, and additional geochemical signatures shall enable the orbital forcing hypothesis to be tested.

Research, therefore, focussed on the measurement of inter-fan sediment geochemistry using spectral gamma-ray, calcium carbonate content, total organic carbon content, inorganic stable isotopes and elemental profiles. From these data, stratigraphic time series have been created and analysed using various spectral techniques to determine the presence of any Milankovitch or sub-Milankovitch cycles.

2.2 Bulk rock geochemistry

2.2.1 Sample preparation

Bulk rock samples were collected for stable isotopic, calcium carbonate ($CaCO_3$), total organic carbon (TOC), mineralogical, and petrographic analyses. For stable isotopic, $CaCO_3$ and TOC analyses powdered samples were required. Prior to analysis the surface layer of each sample was removed using a grinding wheel to ensure the absence of any superficial contamination. Samples were rinsed with de-ionised water and dried overnight at ~50˚C. Crushing was achieved in a two-step process involving a jaw-crusher to create granule-sized fragments and a TEMA (vibrating tungsten-carbide crucible disc/ring mill) milling machine to powder the sample. Samples were milled at 960 RPM for 2-minutes.

2.2.2 Calcium carbonate

2.2.2.1 Background

The measurement of sediment calcium carbonate content has been widely used in the identification of orbital cycles (e.g., Mayer and Appel, 1999; Fischer et al., 1991). The carbonate content of hemipelagic sediments is known to be controlled by a combination of factors, including productivity, dilution, dissolution, diagenesis, and redox conditions (Einsele, 1982; Dean and Gardner, 1986; Fischer, 1986; Diester-Haass, 1991; Fischer et al., 1991; Westphal et al., 2010). It has been shown that these primary or secondary processes create cyclic records reflecting the orbital forcing of palaeoclimate.

Productivity cycles occur where the influx or biogenic carbonate supplied to the site of deposition varies within a background of relatively constant supply of terrigenous material. Cyclic changes of biogenic carbonate precipitation in surface waters has been linked to orbitally-forced variations in nutrient and/or sea surface temperature (SST) changes (Prell and Hays, 1976; Dean and Gardner, 1986; Herbert and Fischer, 1986; Fischer et al., 1991; Mayer and Appel, 1999).

Dilution cycles occur where the supply of terrigenous material varies within a background of relatively constant carbonate accumulation. Variations in terrigenous supply have been attributed to climatic factors including surface run-off, sea-level changes or current variations (Dean and Gardner, 1986; De Visser et al., 1989; Shimmield and Mowbray, 1991; Harris and Mix, 1999; Hyun et al., 2005; Laurin et al., 2005; Sagasti, 2005; Kodama et al., 2010).

Dissolution cycles are linked to variability in the depth of the lysocline or carbonate compensation depth (CCD). The lysocline represents the depth below which the effects of carbonate dissolution become noticeable. Below the CCD the carbonate content is reduced to <10% (Broecker, 2003). The depth of the lysocline/CCD has been shown to vary over orbital time-scales, therefore, creating cyclic changes in the preservation of marine carbonate (Volat et al., 1980; Dean et al., 1981; Dean and Gardner, 1986; Le and Shackleton, 1992; Bassinot et al., 1994). Dissolution is also affected by prevailing sea floor redox conditions at the time of carbonate deposition. Oxygen levels at the sea floor control the supply and preservation of organic matter (OM) within the sediment and its subsequent bacterial decomposition affecting carbonate dissolution (Einsele, 1982; Diester-Haass, 1991).

The effects of diagenesis have been shown to result in a non-primary mechanism for varying the carbonate content. During diagenesis carbonate sediments are subjected to carbonate dissolution and re-distribution. Within alternating limestone-marl rhythmites differential diagenesis results in the concentration of carbonate within

the limestone beds at the expense of the more clay rich layers leading to differential compaction (Ricken, 1985; Ricken, 1987; Westphal et al., 2000). A similar situation may exist for siliceous sediments (Fischer, 1986).

Which of the above processes is the primary control mechanism of carbonate content is often difficult to determine and it is likely to be a combination (Einsele, 1982; Fischer, 1986; Mayer and Appel, 1999). However, as long as the underlying cause of carbonate variability is primarily climatic then it is possible to confidently identify cyclicity (Mayer and Appel, 1999).

2.2.2.2 Methodology

To determine whether any orbital variability is recorded within the inter-fan sections carbonate content, powdered samples were analysed for total carbon (TC), TOC and $CaCO_3$ using a LECO CS-200 total carbon and sulphur analyser. Preparation of TC samples simply involved measuring ~250 mg of powdered sample placed into ceramic crucibles. The measurement of TOC required ~350 mg of powder placed into filter ceramic crucibles and repeatedly treated with 10% hydrochloric acid (HCl) to remove any inorganic carbonate ($CaCO_3$) until effervescence ceased (Equation 2.1). Samples were then rinsed three to four times using de-ionised water to remove any HCL residue.

Equation 2.1

$$Ca^{2+}CO_3^{2-} + 2H^+Cl^- \rightarrow CO_2 + H_2O + Ca^{2+}Cl_2^{2-}$$

During the reaction to remove the inorganic carbonate (Equation 2.1) a mass of carbon is included in the released CO_2 and needs to be corrected for when calculating the weight percentage of $CaCO_3$. Assuming all the $CaCO_3$ has been dissolved the mass proportion of carbon within $CaCO_3$ that will be lost to CO_2 can be calculated using:

Equation 2.2

$$x = \frac{CaCO_3}{C}$$

$$x = \frac{100.086}{12.011}$$

$$x = 8.333$$

With the corrective factor calculated the $CaCO_3$ can be determined using:

Equation 2.3

$$CaCO_3(\%) = (TC - TOC) \times 8.333$$

Standards of known concentrations of $CaCO_3$ were analysed prior to, during and after each batch of TC and TOC analyses enabling the effects of instrumental drift to be removed. Precision (standard deviation) of the standard is ±0.006% based upon 28 readings (Table 2.1).

Table 2.1 – Precision of carbon measurement

Total carbon of standard (%)	Difference from standard* (%)
0.426	0.008
0.433	0.001
0.434	0.000
0.435	0.001
0.437	0.003
0.438	0.004
0.439	0.005
0.439	0.005
0.439	0.005
0.439	0.005
0.440	0.006
0.441	0.007
0.442	0.008
0.442	0.008
0.442	0.008
0.443	0.009
0.443	0.009
0.443	0.009
0.443	0.009
0.443	0.009
0.444	0.010
0.444	0.010
0.444	0.010
0.445	0.011
0.446	0.012
0.447	0.013
0.448	0.014
0.459	0.025
Standard deviation	**0.006**

*Total carbon content of standard 0.434%.

2.2.3 Inorganic stable isotope analysis

2.2.3.1 Theory

The measurement of ratios between oxygen and carbon stable isotopes has become a common tool in the identification of past climate change. Isotopic variability within the geological past has been used to infer changes in sea-surface and bottom water temperatures (Shackleton and Boersma, 1981; Ruddiman et al., 1989; Zachos et al., 1994; Zachos et al., 2001), ice-volume (Hays et al., 1976; Raymo et al., 2006), orbital pacing of climate (Dansgaard et al., 1993; Petit et al., 1999) and major perturbations in global climate (Kennett and Stott, 1991; Bohaty and Zachos, 2003; Zachos et al., 2010).

Oxygen consists of three stable isotopes ^{16}O (99.757 %), ^{17}O (0.038 %) and ^{18}O (0.205 %). The measurement of the ratio between the ^{16}O and ^{18}O end members has become a standard tool in the investigation of past climates. Variation in this ratio is determined using the $\delta^{18}O$ notation, which compares the measured ratio to the Peedee Belemnite (PDB) international standard as represented by:

Equation 2.4

$$\partial^{18}O = \left[\frac{\left({}^{18}O/{}^{16}O \right)_{Sample}}{\left({}^{18}O/{}^{16}O \right)_{Standard}} - 1 \right] \times 1000$$

Variation with $\delta^{18}O$ values is caused by fractionation between the ^{16}O and ^{18}O isotopes during physical and bio-chemical processes. The former relates to kinetic isotope fractionation, which occurs during the evaporation of ocean waters. During this process, water vapour preferentially removes the lighter ^{16}O isotope leaving the surface waters enriched in ^{18}O. Precipitated water is isotopically heavier than the remaining vapour due to the favourable removal of ^{18}O. During glacial periods the isotopically light ^{16}O is stored in ice-sheets therefore leaving the oceans relatively enriched in ^{18}O. However, during periods of no substantial ice accumulation the precipitation of isotopically light water is returned to the oceans resulting in no overall change in $\delta^{18}O$. The above process allows the ice-volume of the past to be estimated via measuring seawater $\delta^{18}O$ values (Hays et al., 1976; Raymo et al., 2006).

The second process of fractionation is biological activity within the oceans, which preferentially removes ^{18}O during carbonate precipitation leaving the surrounding waters enriched in ^{16}O. The ambient temperature affects the degree of biological isotopic fractionation during precipitation. The measurement of carbonate precipitating organisms such as planktonic, benthic foraminifera and in some cases bulk sediment

enables changes in seawater $\delta^{18}O$ to be determined at the time of their growth. From these data it is then possible to estimate sea-surface and bottom water temperatures for the geological past (Shackleton et al., 1993; Zachos et al., 1994; Schrag et al., 1995).

Estimation of palaeo-temperatures from biogenically precipitated carbonate $\delta^{18}O$ values is calculated using the empirical equation determined by Anderson and Arthur (1983):

Equation 2.5

$$T = 16.0 - 14.4\left(\partial_c - \partial_{sw}\right) + 0.13\left(\partial_c - \partial_{sw}\right)^2$$

where T is temperature in ˚C, δ_c is the $\delta^{18}O$ values of carbonate in ‰ relative to VPDB and δ_{sw} is the $\delta^{18}O$ values of seawater in ‰ relative to SMOW (Anderson and Arthur, 1983).

Carbon consists of ^{12}C (98.93%) and ^{13}C (1.07%) stable isotopes the study of which enables the determination of past changes to the carbon cycle (Shackleton, 1987; Zachos et al., 2001). Variation in the ratio between these isotopes is determined using the $\delta^{13}C$ notation compared to the international standard (PDB) as represented as:

Equation 2.6

$$\partial^{13}C = \left[\frac{\left(^{13}C/^{12}C\right)_{Sample}}{\left(^{13}C/^{12}C\right)_{Standard}} - 1\right] \times 1000$$

Variations in $\delta^{13}C$ values are related to the isotopic fractionation during the transfer of carbon between different reservoirs. The two main carbon reservoirs are organic matter and sedimentary carbonate, each with a distinctive isotopic signature due to the effects of kinetic and equilibrium isotope fractionation (Schidlowski, 1988). Within the inorganic carbonate fractionation system, the transfer of carbon from the atmosphere, marine bicarbonate to carbonate sediments preferentially enriches ^{13}C within carbonate via equilibrium isotope fractionation.

The carbon within the organic matter (OM) reservoir is characterised by isotopically light $\delta^{13}C$ values, typically -26‰ (Schidlowski, 1988). The isotopically light nature of OM is due to the kinetic isotope effect that occurs during biological metabolism preferentially utilising the lighter ^{12}C isotope. During periods of increased burial of OM, large volumes of ^{12}C are sequestered within sediments therefore

enriching the remaining carbon reservoirs in ^{13}C resulting in more positive $\delta^{13}C$ values. Periods of erosion and subsequent release of this isotopically light OM leads to the replenishment of carbon reservoirs with ^{12}C shifting the recorded $\delta^{13}C$ toward more negative values.

The measurement of $\delta^{13}C$ and $\delta^{18}O$ preserved within planktonic and benthic foraminifera carbonate tests has enabled the identification of both long-term climate change (Shackleton, 1987; Veizer et al., 1999; Zachos et al., 2001) and orbitally-forced short-term variations (Hays et al., 1976; Ruddiman et al., 1989; Shackleton et al., 1992; Lisiecki and Raymo, 2005; Raymo et al., 2006). Specific to the Eocene, stable isotope analysis has successfully identified orbital variability (Wade et al., 2001; Cramer et al., 2003; Burgess et al., 2008) and climatic perturbations (Kennett and Stott, 1991; Wade and Kroon, 2002; Bohaty and Zachos, 2003; Sexton et al., 2006; Zachos et al., 2008; Stap et al., 2010; Dawber and Tripati, 2011).

Within this research the stable isotopes of bulk sediment shall be measured rather than foraminifera due to their poor preservation and paucity within the Ainsa basin. The reliability of bulk sediment isotope analysis is mainly linked to the amount of diagenesis the sediment has undergone. Studies suggest that the preservation of the primary isotopic composition is dependant upon the diagenetic openness of the pore-water system (Marshall, 1992). The openness of the system relates to the volume of pore-waters available during diagenesis. Only within a closed system where a relatively small volume of pore-water is present will the primary $\delta^{18}O$ values be retained (Marshall, 1992). However, the primary $\delta^{13}C$ values are more likely to be preserved as the pore-water $\delta^{13}C$ composition is solely affected by the dissolution of the original carbonate phase. Only within a completely open system will the primary $\delta^{13}C$ composition lost (Marshall, 1992).

Despite these potential issues, many researchers have utilised bulk sediment isotopic analysis to identify orbital cyclicity and climate perturbations within the Eocene (Cramer et al., 2003; Hollis et al., 2005; Lourens et al., 2005; Nicolo et al., 2007; Bohaty et al., 2009; Galeotti et al., 2010; Zachos et al., 2010). Here, variability within the preserved stable isotopic record is used to determine whether sediments retain a record of orbitally forcing.

2.2.3.2 Methodology

Inorganic isotopic analysis ($\delta^{13}C$ and $\delta^{18}O$) of bulk samples required the prior powdering and the amount of $CaCO_3$ to be determined as outlined above. Calcite vein samples collected from the A6 core were sampled using a hand-held drill to collect a small amount of powder. Each isotopic analysis requires between 300-500 mg of

carbonate ($CaCO_3$) to be present within each aliquot, which cannot exceed 1,000 mg. For the minimum amount of $CaCO_3$ (300 mg) to be present without exceeding 1000 mg only samples containing >30% $CaCO_3$ could be analysed.

Samples were analysed at the Bloomsbury Environmental Isotope Facility (BEIF) at University College London on a ThermoFinnigan Delta^{PLUS} XP stable isotope mass spectrometer attached to a ThermoScientific Gas Bench II device. Standards and sample powder (>100µg) were loaded into glass vials, rinsed with methanol and dried overnight at 70°C. For analysis, each vial was manually acidified with 100% phosphoric acid (0.1 ml) using a syringe injection via the screw cap septa. Precision of all internal (BDH, IAEA & IFC) and external standards (NBS19) is ±0.03 for $\delta^{13}C$ and ±0.08 for $\delta^{18}O$. All values are reported in the Vienna Pee Dee Bee notation (VPDB) relative to the international standard NBS-19.

2.3 Gamma-ray spectrometry

2.3.1 Theory

Outcrop spectral gamma-ray (SGR) detectors measure the levels of potassium ^{40}K, uranium (^{238}U) and thorium (^{232}Th) within sediment by counting the number of gamma ray emissions from their (^{40}K), or their daughter products ($^{232}Th \rightarrow {}^{208}Tl$ and $^{238}U \rightarrow {}^{214}Bi$) decay.

The use of SGR data within the Earth sciences has become increasingly common due to its ability for rapid data collection with minimal cost. A wide variety of sedimentary studies have utilised SGR for facies identification (Myers and Bristow, 1989; Slatt et al., 1992; Bristow and Williamson, 1998; North and Boering, 1999; Svendsen and Hartley, 2001), stratigraphic (Leeder et al., 1990; Aigner et al., 1995; Davies and Elliott, 1996; Parkinson, 1996; Andersson and Worden, 2004; Hampson et al., 2005; Koptikova et al., 2010) and palaeo-environmental (Myers and Wignall, 1987; Wignall and Myers, 1988; Jarrard and Arthur, 1989; ten Veen and Postma, 1996; Postma and ten Veen, 1999; Prokoph and Thurow, 2000; Ruffell and Worden, 2000) applications.

SGR detectors consist of a sodium-iodide (NaI) scintillator and a photo-multiplier tube. When gamma radiation interacts with the scintillator a pulse of light is emitted, the intensity of which indicates the energy of the incident radiation. The photo-multiplier converts the light energy into an electrical signal proportional to the incident radiations energy level. As the decay product of each isotope has a distinctive energy level, this allows the detector to allocate each gamma ray emission to an individual isotope. However, Compton scattering results in the isotopes energy signatures being progressively smeared resulting in a complex spectra spanning an energy range of 0-3

MeV (Rider, 1996). The detector therefore divides incident gamma ray energies into several pre-defined energy windows centred about the principle decay energies of 1.46 MeV for potassium, 1.76 MeV for thorium and 2.62 MeV for uranium (Lovborg et al., 1971; Rider, 1996). The spectra obtained by the SGR tool is then converted into quantitative abundances by comparison with spectra determined from calibration pads with known concentrations of K, U and Th (Lovborg et al., 1971).

The distribution of K, U and Th within sediments is complex due to the differential distributions and behaviours of these elements and their host minerals within the geological system. The concentrations of these radio-elements within common minerals are provided in Table 2.2. Within sedimentary systems, it has been suggested that abundances of K, U and Th within shales and sandstones should be interpreted separately due to their differing mineralogical constituents (Rider, 1996; Ruffell and Worden, 2000).

Of the three elements potassium is the most chemically active and abundant. Within the geological record K is found primarily within micas, micaceous clays (e.g., illite) and rock forming minerals such as microcline and orthoclase.

Thorium originates from acidic and intermediate igneous rocks and is extremely stable compared to U as it will not enter into solution. Within coarse-grained sediments Th is commonly concentrated within sand- and silt-sized grains of certain heavy minerals (e.g., zircon, thorite, monazite, epidote and sphene). Within finer-grained sediments these same Th bearing minerals are associated with terrestrial clays (Myers and Wignall, 1987; Rider, 1996).

The original source of U is mainly acidic igneous rocks. Uranium can be found within either the detrital and/or authigenic fraction due to it passing into sediments via three processes: chemical precipitation via acids or reducing environments (Adams and Weaver, 1958; Myers and Wignall, 1987; Van der Weijden et al., 1990; Lovley et al., 1991), adsorption by organic matter or living plants and animals (Veeh et al., 1974; Anderson et al., 1989; Klinkhammer and Palmer, 1991; Lüning and Kolonic, 2003), and chemical reaction with phosphorites (Rider, 1996). Increasing the heterogeneity of U within the sedimentary record is its solubility even in subsurface, rendering it susceptible to leaching and re-distribution (Adams and Weaver, 1958; Colley and Thomson, 1985).

Due to the heterogeneity of these elements within the sedimentary record (particularly U and Th), variations in their relative abundances expressed in Th/K and Th/U ratios have been used to interpret a variety of stratigraphic and environmental settings. However, sweeping generalisations are warned against as controls upon Th and U accumulation likely differ between depositional environments (Rider, 1996; Ruffell and Worden, 2000).

Within shale sediments, the Th/K ratio is generally used as an indicator for clay mineralogy, i.e., ratio of illite to kaolinite (Myers and Wignall, 1987; Van Buchem et al., 1992; Rider, 1996; Ruffell and Worden, 2000; Hesselbo et al., 2009). Generally, Th/K ratios <4 indicate shales are possibly dominated by illite whilst ratios >6 suggest the predominance of kaolinite (Rider, 1996). The Th/K ratio has been shown to decrease with increasing distance from the source area and bathymetry (Myers and Wignall, 1987; Parkinson, 1996; Andersson and Worden, 2004).

The ratio of Th/U has been used as an indicator for depositional oxygenation levels (Adams and Weaver, 1958; Myers and Wignall, 1987; Wignall and Myers, 1988). The average mudrock Th/U ratio is 3 to 6 with higher ratios indicating oxygenated environments and lower ratios reflecting reducing environments (Adams and Weaver, 1958; Wignall and Myers, 1988).

Sources of analytical error within the SGR technique involve instrumental drift and ambient temperature variation (Lovborg et al., 1971; Lovborg et al., 1980; Andersson and Worden, 2004). However, ratios of the elements will be unaffected by any instrumental drift and surface irregularities (Davies and Elliott, 1996; Parkinson, 1996; Andersson and Worden, 2004).

Table 2.2 – Radioelement concentrations of various minerals*

Mineral	K (%)	U (ppm)	Th (ppm)
Major			
Quartz	0.0	0.7	2.0
K-Feldspar†	11.8-14.0	3.0-7.0	0.2-5.0
Muscovite§	7.9·	2.0-8.0	6.0-25.0
Biotite**	8.5·	1.0-4.0	0.5-50.0
Calcite	0.0	1.5	0.0
Plagioclase	0.0	0.5-3.0	0.2-5.0
Pyroxene	0.0	2.0-25.0	0.0-40.0
Hornblende	0.0	1.0-30.0	5.0-50.0
Clay Minerals			
Illite	3.5-8.3	1.5	6.0-25.0
Glauconite	3.2-5.8	10.0	2-8
Montmorillonite	0.0-4.9	2.0-5.0	10-24
Chlorite	0.0-0.6	?	3.0-5.0
Kaolinite	0.0-6.0	1.5-9.0	6.0-42.0
Bauxite	?	?	8-132
Accessory Minerals			
Zircon	0.0	100-6000	50-4000
Sphene	0.0	100-700	100-600
Apatite	0.0	5-150	20-150
Monazite	0.0	500-3000	25000-200000
Ilmenite	0.0	1-50	?
Magnetite	0.0	1-30	0.3-20
Epidote	0.0	20-50	50-500

*Data collated from Myers and Wignall (1987), Rider (1996) and references within.
†K (%) for pure K-feldspar. Sedimentary K-feldspar probably lower.
§Pure muscovite does not contain Th but muscovite is often closely associated with Th-bearing accessory minerals in sediments.
·Average values.
**Th and U will be contained in heavy mineral inclusions such as zircon.

2.3.2 Methodology

Spectral gamma ray readings were taken using one of two portable gamma ray spectrometers over a number of field seasons. During April 2008 an Exploranium GR-320 and GPX-21 EnviSpec spectrometer was used during analysis of the Guaso (Chapter 4) and the lower ~114 m of the Ainsa (Chapter 5) inter-fan sediments. A Radiation Solutions Inc. (RSI) RS-125 Super-Spec spectrometer was used during two field seasons (August 2009 and April 2010) analysing the remaining Ainsa (Chapter 5) and Banaston (Chapter 6) inter-fan sections.

2.3.2.1 Exploranium GR-320

The Exploranium GR-320 spectrometer (no. 2077) equipped with a GPX-21 (no. 1887) detector is shown in Plate 2.1a. The detector records radiation using a 21 cubic inch Sodium Iodide (Thallium) [NaI(Tl)] crystal. Radiation is determined from a hemispheric sphere (Fig. 2.1a) 12-14cm depth and ~80cm diameter (Lovborg et al., 1971). A 3-minute sampling period is estimated to provide an instrument precision better then ±10% for all elements when readings taken from an ideal sampling plane (Lovborg and Mose, 1987; Van Buchem et al., 1992; Koptikova et al., 2010). Deviation away from perfect plane (Figs. 2.1c, 2.1d) has been shown to cause precision to vary from ±5-7%, ±10-15% and ±25-30% for K, Th and U respectively (Myers and Bristow, 1989; Parkinson, 1996). Temperature variation has also been suggested to affect gamma ray readings (Lovborg et al., 1971; Lovborg et al., 1980). However, limited field measurements using the GR-320 spectrometer suggest that temperature effects are minimal (Fig. 2.2; Table 2.3).

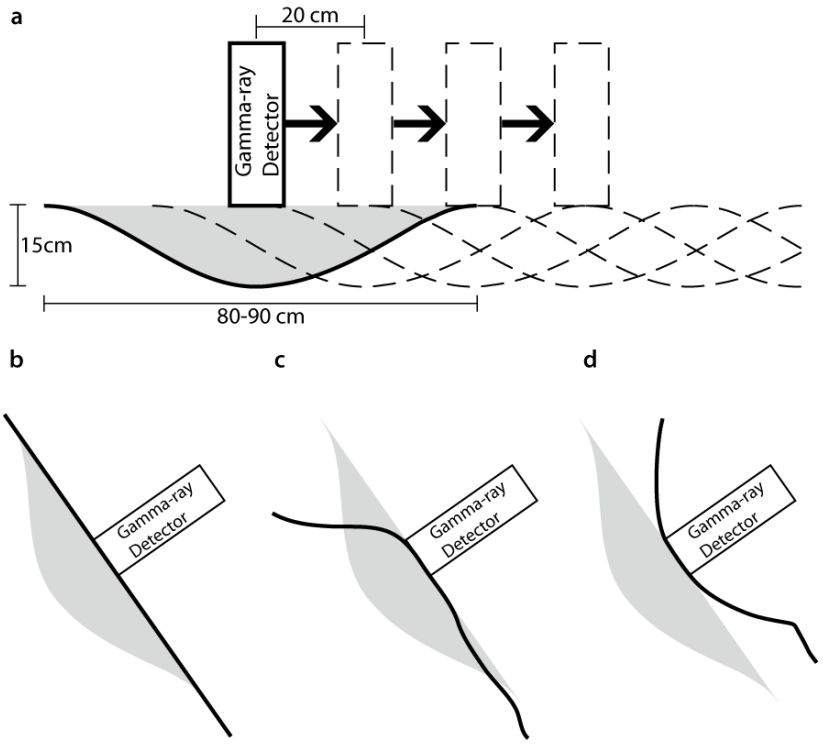

Figure 2.1 | Spectral gamma ray tool sampling area and non-ideal sampling positions. (a) Measurement spacing of less than the detection diameter will result in an average record of radioelement variability through stratigraphy. **(b-d)** Measurements taken from an ideal plane **(b)** will result in the greatest accuracy in radioelement measurement. Where measurements are taken from non-ideal planes then relatively less **(c)** or more **(d)** sediment will be sampled reducing the precision (Myers and Bristow, 1989; Parkinson, 1996).

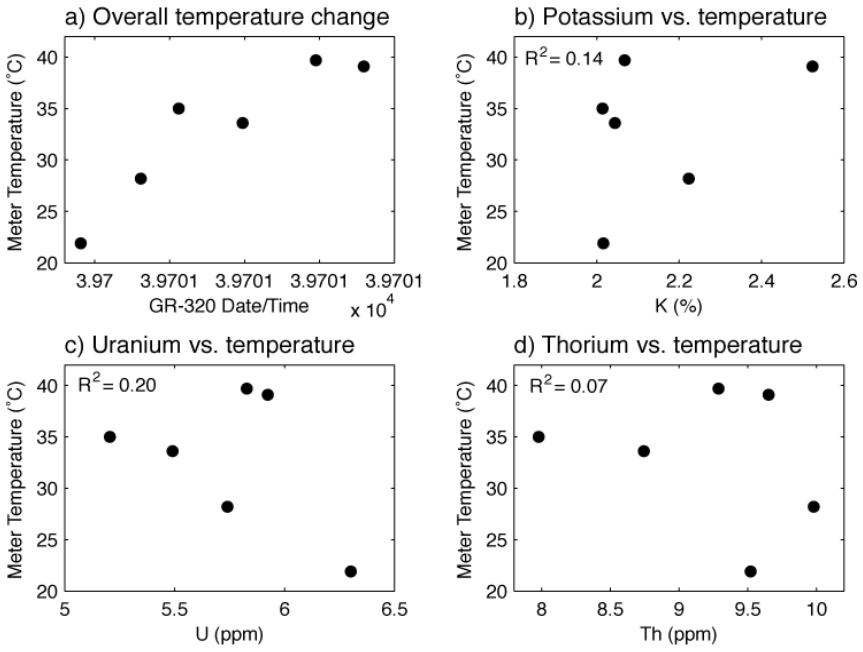

Figure 2.2 | Cross-plots showing the effect of temperature upon GR-320 spectrometer measurements. (a) Overall meter temperature change during sampling period. **(b-d)** Cross-plots and Pearson correlation coefficients (R^2) were produced to determine whether temperature influenced the recorded radioelement concentration. According to the R^2 values, no statistical relationship exists between temperature and reported radioelement concentration. Data used for cross-plots and R^2 values are provided in Table 2.3.

Plate 2.1 | GR-320 gamma ray spectrometer. (a) The GR-320 spectrometer and detector. **(b)** GR-320 spectrometer in use measuring an ideal plane (refer to Fig. 2.1).

Table 2.3 – GR-320 radioelement concentration and temperature change

Height (m)	GR-320 Date/time	K (%)	U (ppm)	Th (ppm)	Meter Temp. (˚C)
24.2	39700.44	2.02	6.30	9.52	21.9
27.6	39700.48	2.22	5.74	9.98	28.2
29.6	39700.51	2.01	5.21	7.98	35.0
31.8	39700.55	2.04	5.49	8.74	33.6
35.6	39700.60	2.07	5.83	9.29	39.7
38.4	39700.63	2.52	5.92	9.65	39.1
	R^{2}*	**0.14**	**0.20**	**0.07**	

*Pearson's correlation coefficient calculated between radioelement concentration and meter temperature.

Table 2.4 – RS-125 manufacturer precision estimates*

	1 Sigma K (%)	1 Sigma U (ppm)	1 Sigma Th (ppm)
K (%)			
0	0.000	0.000	0.000
0.1	0.030	0.041	0.006
1	0.096	0.130	0.019
5	0.214	0.291	0.042
10	0.303	0.412	0.060
U (ppm)			
0	0.000	0.000	0.000
1	0.043	0.307	0.027
10	0.135	0.970	0.087
100	0.427	3.067	0.274
1000	1.349	9.698	0.866
10000	4.270	30.67	2.740
Th (ppm)			
0	0.000	0.000	0.000
1	0.023	0.237	0.539
10	0.072	0.75	1.705
100	0.228	2.373	5.391
1000	0.721	7.504	17.04
10000	2.280	23.70	53.90

*Precision estimates based upon 2-minute count time and errors associated with counting statistics and background noise. Does not include calibration or geometry errors and therefore these values should be taken as relative rather than absolute. 1σ estimates decrease with increased count time. Data from RS-125 user manual.

Table 2.5 – RS-125 precision measurements at outcrop*

Sample I.D.	Time	Temp. (˚C)	Total (cpm)	K (%)	U (ppm)	Th (ppm)
3308	14:00:51	24.4	1650.5	2.2	3.1	9.7
3309	14:04:01	24.1	1637.5	2.0	3.4	9.3
3310	14:07:31	23.6	1638.6	2.1	2.4	10.5
3311	14:11:28	23.2	1589	1.8	2.5	11.1
3312	14:14:54	22.9	1650.3	2.1	3.6	9.1
3313	14:18:18	22.5	1614.1	2.1	3.0	12.1
3314	14:21:30	22.4	1628.8	2.0	2.2	11.0
3315	14:24:46	22.3	1683.5	2.0	3.8	11.2
3316	14:27:54	22.3	1618.7	1.9	2.3	10.8
3317	14:31:02	22.1	1615.6	2.3	1.8	9.6
3318	14:34:53	22.1	1650.8	2.0	3.8	9.3
	Standard deviation		**25.1**	**0.1**	**0.7**	**1.0**
	Mean		**1634.3**	**2.0**	**2.9**	**10.3**
	Difference (%)		**1.5**	**6.7**	**24.1**	**9.6**

*Measurements taken consecutively from the same position with a 3-minute sampling period.

2.3.2.2 Radiation Solutions RS-125

The Radiation Solutions Inc RS-125 Super-Spec uses a 6.3 cubic-inch Sodium-Iodide crystal to detect radiation from a ~0.9 m (3 ft) surface diameter. The manufacturer provides precision estimates for sample periods of 2-minutes (Table 2.4) and states that sampling periods of 3-minutes should provide "good" quality data. Repeated field measurements (11 readings using a 3-minute sampling time) from the same point suggest that precision is ±7%, ±24% and ±10% for K, U and Th respectively (Table 2.5). The effect of diurnal temperature variation was also tested with the result indicating no discernable effect upon total, K, U and Th readings (Warburton, 2011) (Fig. 2.3; data within the Appendix).

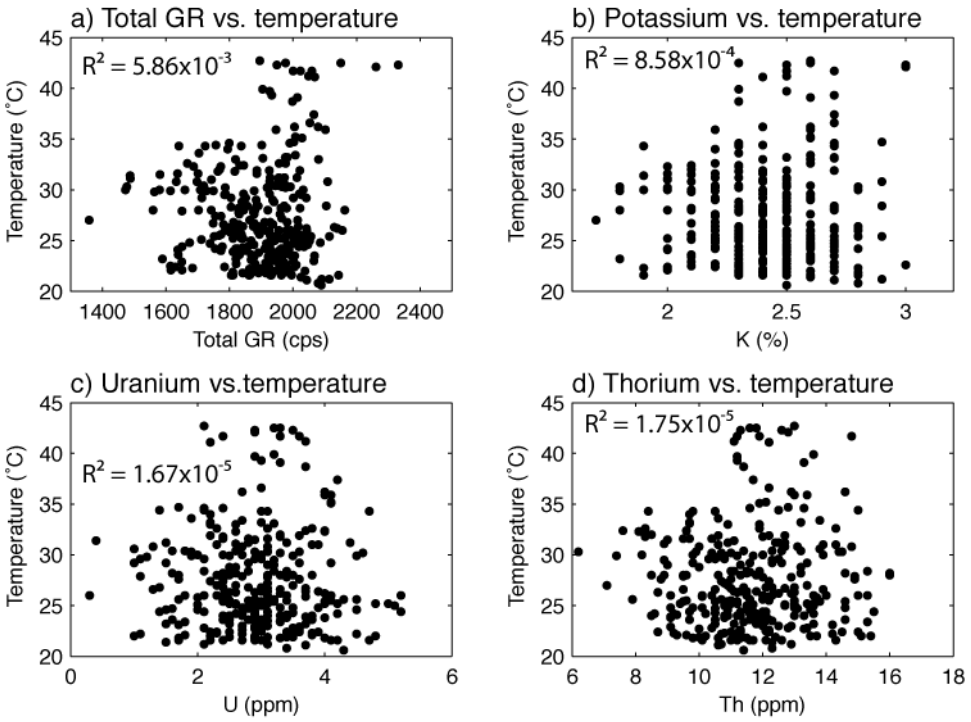

Figure 2.3 | Cross-plots showing the effect of temperature upon RS-125 spectrometer measurements from several field seasons. Cross-plots and Pearson correlation coefficients (R^2) were produced to determine whether temperature influenced the recorded concentration of radioelements. According to the R^2 values there is no statistical relationship between temperature and reported radioelement concentration. Data used for cross-plots and R^2 values are mainly from Warburton (2011) and are provided in the Appendix.

2.3.3 Field procedure

Where possible the sampling took place perpendicular to a 3 m-diameter flat rock surface with constant moisture content (Lovborg et al., 1971; Myers and Wignall, 1987; Parkinson, 1996). A sample interval of 20 to 40 cm (i.e., less than the detection radii of both machines) was used to create a moving average through the stratigraphy (Fig. 2.1a). At each sample point superficial material was removed prior to spectral measurements although little difference has been reported between cleaned and slightly weathered marlstone surfaces (Postma and ten Veen, 1999). Extensive weathering and pervasive vegetation of outcrops may result in leaching or possible concentration of certain elements and were identified and avoided where possible.

2.4 X-ray fluorescence core scanning

2.4.1 Theory

X-Ray Fluorescence (XRF) is a non-destructive analytical technique used to determine the relative abundance of elements within a material. The process is therefore ideal for the study of elemental variation within sedimentary split-cores. The development of commercial XRF split-core scanners (e.g., Avaatech and CORTEX XRF core scanners) has enabled high-resolution down-core geochemical data to be collected rapidly with minimal preparation. Determining down-core elemental variation using this method has proven useful in the study of past environmental change on a range of time-scales (Jansen et al., 1998; Norris and Röhl, 1999; Röhl and Abrams, 2000; Pälike et al., 2001; Lamy et al., 2004; Richter et al., 2006; Tjallingii et al., 2007; Westerhold et al., 2007; Sangiorgi et al., 2008; Weltje and Tjallingii, 2008; Itambi et al., 2009; Westerhold and Röhl, 2009; Grutzner and Higgins, 2010). Within this research the method is used to look for Milankovitch and sub-Milankovitch cyclicity within sections of sedimentary cores from the Ainsa basin.

XRF analysis determines the relative abundance of elements within a material by exposing it to x-ray radiation. Subsequently, atoms within the irradiated area are ionised due to the excitation of an inner orbital electron. Depending on the position of the missing electron, a limited number of electronic transitions are able to occur. For example, if the missing electron originated from the K-shell then it can be replaced by an electron from either the L- or M-shells, resulting in K_{α} or K_{β} transitions respectively. During each transition a photon of energy is released. Atoms within the material are therefore said to fluoresce, a process where the atoms absorb higher energy x-rays and emit lower energy x-rays. An example of the fluorescence of a calcium atom is illustrated in Figure 2.4. As each element has its own distinctive orbital structure they

fluoresce with different energies. The energies of the emitted photons are equal to the energy difference between the two orbital positions involved (i.e., the distances between an elements K, L, M and N shells vary, producing distinctive values for K_{α}, K_{β}, L_{α}, L_{β}, etc.). With this information it is therefore possible to identify each element by their distinctive K_{α}, K_{β}, L_{α}, L_{β}, etc. energies.

Counting the number of fluorescent photons emitted using energy dispersion (ED) analysis enables the determination of the relative abundance of each element within an irradiated area. Counting occurs by directing the fluorescent x-rays into a solid-state detector (beryllium x-ray window), which produces a continuous current that is proportional to the detected photon energies. A multi-channel analyser collects the data and produces an accumulating spectrum. Spectra are subsequently converted into semi-quantitative data by comparison with model spectra. During this process, energy spectra are converted into x-ray intensity data by subtracting the background continuum, applying statistical corrections for physical processes in the detector, deconvolving overlapping peaks and the calculation of peak integrals. The quality of this processing can be determined using provided chi-squared values.

Output data corresponds to the relative abundance of each element within the fluoresced area and presented in counts per second (CPS). XRF split core scanning is a semi-quantitative technique dependant upon the energy of the incident x-rays, attenuation of fluoresced x-rays, count time, and the physical properties of the sediment such as water content, grain-size, surface-roughness and density (Jenkins and De Vries, 1970; Richter et al., 2006; Tjallingii et al., 2007). Due to these factors, it is difficult to determine absolute elemental abundances. However, the relative change in elemental abundance should be faithfully recorded (Richter et al., 2006).

The use of XRF count data cannot be used to compare elemental abundances or directly determine mineralogy within a sample due to varying detection depths and detection limits (Table 2.6). Both of these variables are determined by an elements fluoresced x-ray energy and its attenuation by the material being analysed (Jenkins and De Vries, 1970). Minerals with a greater elemental mass fluoresce with a higher energy compared to those of lower mass. This enables their detection through a greater thickness of material before the signal is significantly degraded via attenuation. As a result, the fluorescence x-rays from elements of greater mass will be measured from a larger volume of material compared to lighter elements (Fig. 2.5). Therefore, within raw count data heavier elements will be relatively enriched compared to lighter elements making the determination of mineralogy from count data difficult.

Table 2.6 – Detection limits and depths for selected elements*

Element	Atomic weight	Kα line (keV)	Detection limit (ppm)	Detection depth (mm)
Mg	24	1.25	20000	
Al	27	1.49	2000	0.05
Si	28	1.74	1000	
P	31	2.01	500	
S	32	2.31	500	
K	39	3.31	400	
Ca	40	3.69	200	0.5
Ti	48	4.51	500	
Mn	55	5.89	100	
Fe	56	6.40	45	1
Sr	88	14.14	5	1-2
Zr	91	15.74	20	
Ba	137	32.19	40	2-4
Pb	207	10.84 (Lα)	10	

*Values based upon average marine sediments composed of significant amounts of Si, Al and/or Ca (Richter et al., 2006).

2.4.2 Avaatech split-core scanner

The Avaatech split-core scanner (Richter et al., 2006) used in this research is based within the UCL Environmental Sedimentology Facility. The machines incident x-rays originate from a rhodium source enabling the study of elements within the Al-Bi range. The solid-state detector uses a beryllium x-ray window with 2,048 channels with a resolution of 20 eV per channel. The irradiated area is controlled by an adjustable 16 mm (y-axis) x 1-10 mm (z-axis) aperture. Varying the irradiated area affects the amount of incident radiation received by the sediment surface and subsequently the amount of fluorescence. To prevent the incident and fluoresced x-rays being scattered by air, the area between the radiation source, sediment surface and detector is flushed with helium.

To enable the maximum range of elements to be analysed both the 10 kV (Al-Rh) and 30 kV (Zn-Bi) settings were used. The 30 kV analyses required a Pb-thick filter to prevent the accumulating spectra being overwhelmed by emissions from lighter elements of lesser excitation energies. The lower 10 kV analyses required no filter as the incident x-rays were of insufficient energies to cause the heavier elements to fluoresce.

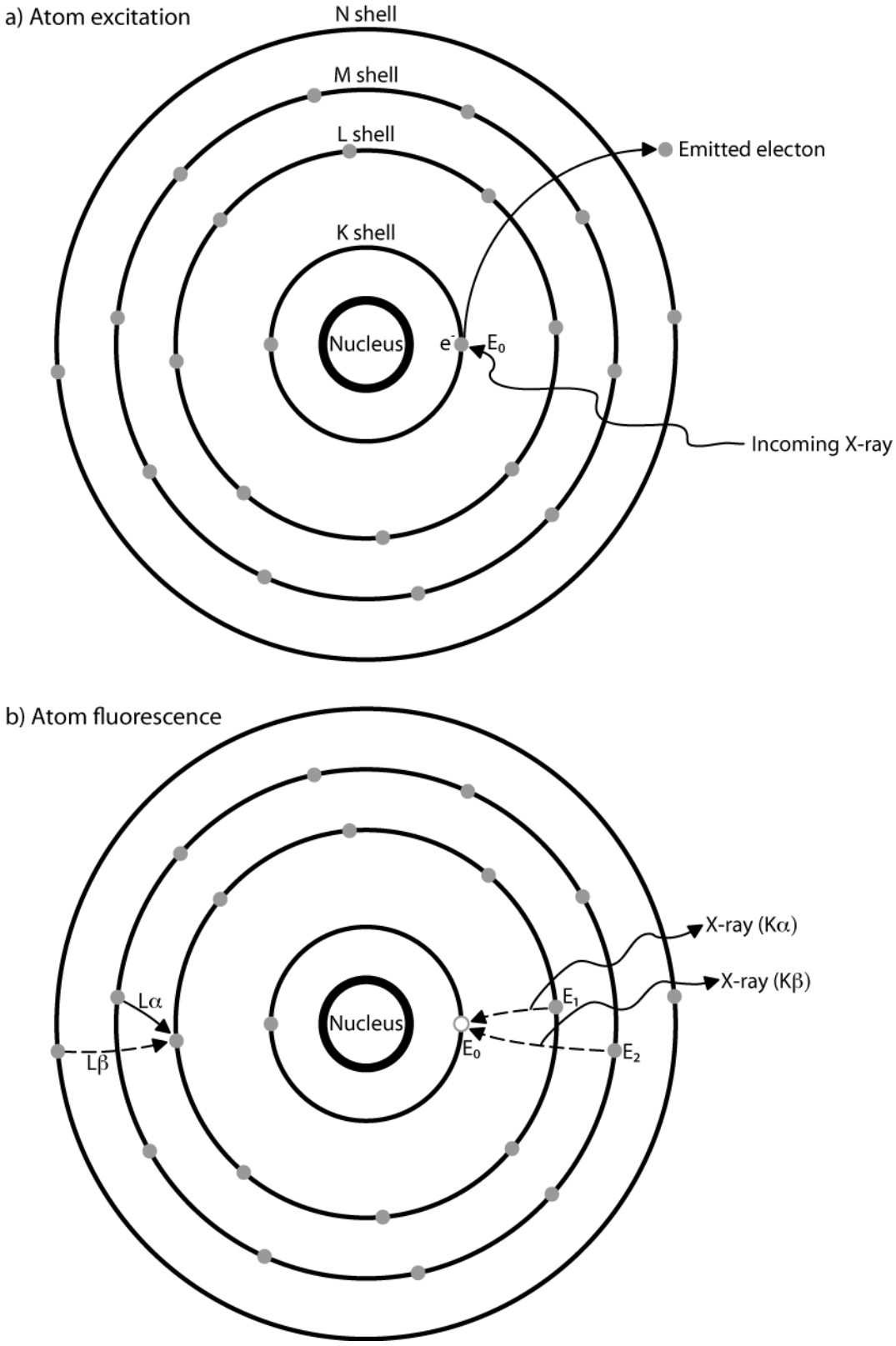

Figure 2.4 | X-ray fluorescence of a Ca atom. (a) Incoming x-ray excites electron within atoms K-shell and subsequently expelled. **(b)** Electron falls from higher orbital level to replace lost electron and releases an x-ray with energy representative of the distance between orbital shells. The replacement electron may originate from several orbital levels and therefore have different energies. As each element consists of a unique atomic structure it must also have characteristic x-ray energy, which can be used to identify its relative concentration.

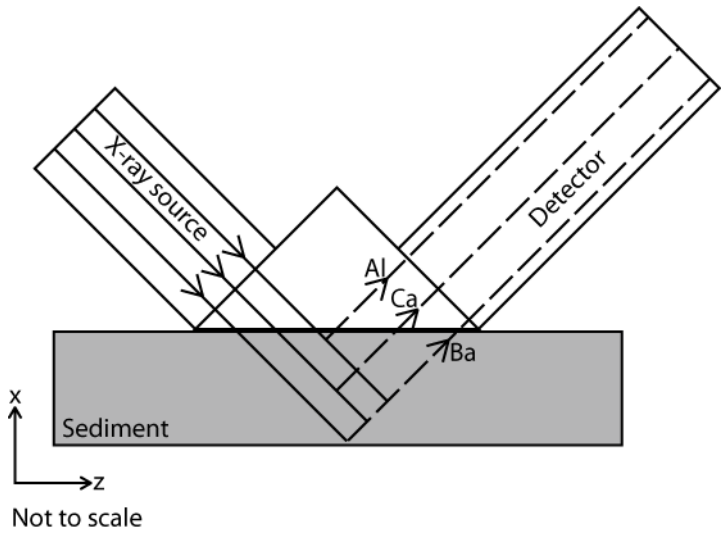

Figure 2.5 | Differential element x-ray penetration depths. The volume of sediment sampled for each element is dependant upon atomic mass. Elements of larger mass fluoresce with higher energy and therefore can be determined from greater depth. An example of this is provided in Table 2.7.

In an attempt to quantify the relationship between elemental mass and x-ray detection depths, a crystal of orthoclase ($KAlSi_3O_8$) was scanned using a 10 kV setting (600 μA; no filter; 30 s count time). Results are displayed in Table 2.7. From these data, the ratio of Al:K is ~1:10 when according to the chemical formula of orthoclase it should be ~1:1. The explanation for this can be found by comparing the penetration depths of Al and K (K will likely have similar penetration depth to Ca due to similar atomic mass; Table 2.6), which is approximately ten times that of Al.

Table 2.7 – Orthoclase XRF scan results*

Measurement position (mm)	Al_Area	K_Area†
55	5656	58403
60	5379	56181
65	5323	55173
70	5372	54839
Average§	**5433**	**56149**

*XRF measurements taken using 10 kV, 600 μA; no filter; 30 s count time. Additional relative elemental concentrations can be located within Appendix.

†Relative elemental concentration results with chi-squared values >3 excluded.

§The ratio between the relative concentrations of K and Al is ~1:10 which is similar to their 1:10 detection depth ratio.

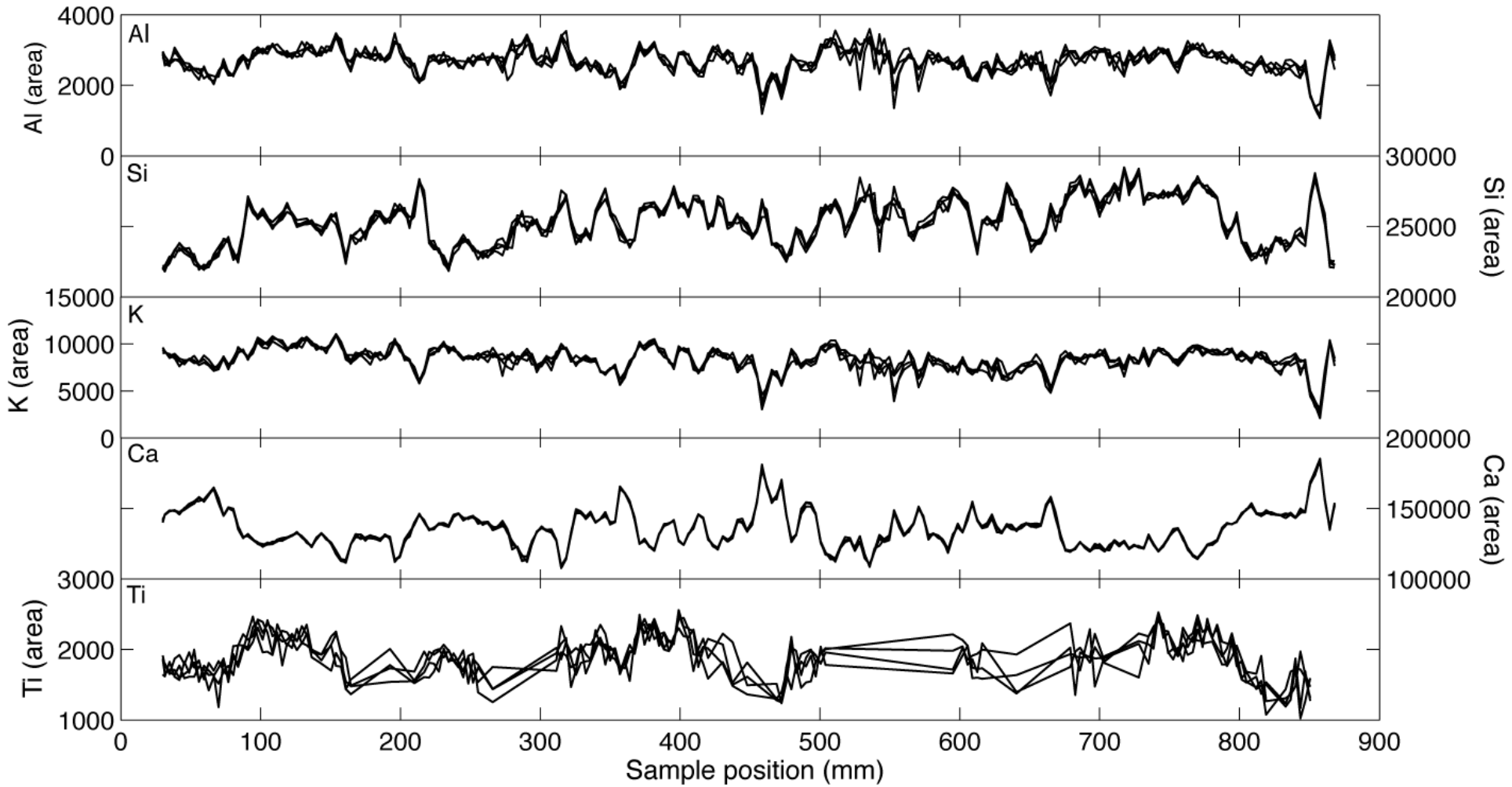
Al
Si
K
Ca
Ti
Al (area)
Si (area)
K (area)
Ca (area)
Ti (area)
4000
2000
0
30000
25000
20000
15000
10000
5000
200000
150000
100000
3000
1000
0
100
200
300
400
500
600
700
800
900
Sample position (mm)

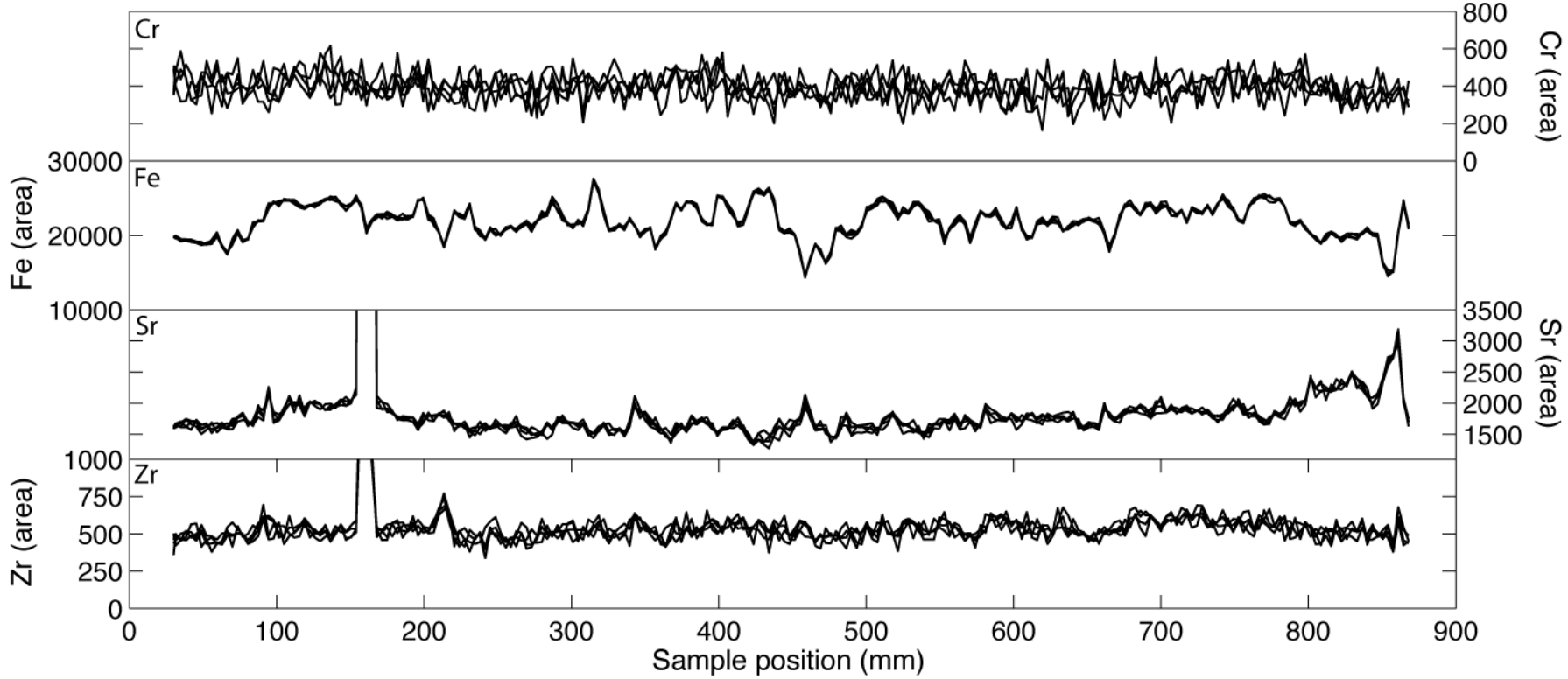

Figure 2.6 | Selected element profiles for A6/8-5 core interval. Scanning at both 10 kV and 30kV created 5 depth profiles for each element. Profiles do not contain data positions with chi-squared values >3. Elements with large standard deviation differences from the mean have more varied profiles.

To test the precision between consecutive scans, a core section (A6/8-5) was scanned 10 times consecutively (Fig. 2.6; Appendix). The standard deviation was calculated for each element and measurement position (Table 2.8). Comparisons between runs reveal that only Al, Si, K, Ca, Ti, Fe, Sr and Zr elements are strongly reproducible to ±10% when chi-squared values >3 are removed (Table 2.8). However, 40% of Ti values were associated with chi-squared values >3 suggesting that Ti results should be considered with caution or that an alternate processing model is required.

Table 2.8 – XRF precision using A6/8-5 core interval*

Element	Standard deviation	Mean	Percent difference (%)†	Percent chi-squared >3 (%)
Al	115	2691	4.4	0
Si	252	25321	1.0	4
S	147	787	22.3	0
K	335	8375	4.2	0
Ca	825	135753	0.6	0
Ti	146	1910	7.8	40
V	41	68	62.9	97
Cr	62	394	15.9	0
Mn	54	125	48.8	0
Fe	221	21968	1.0	0
Zn	18	81	22.3	0
Sr	55	2089	3.0	0
Zr	40	542	7.4	0
Mo	33	156	21.2	0

*XRF precision determined from 5 consecutive scans using 10 kV (600 μA; no filter) and 5 scans at 30 kV (1,000 μA; Pd thick filter), 30 s sampling time and 3.5 mm sample spacing. A total of 241 data points scanned. Scan positions with chi-squared values >3 removed prior to calculations. Element profiles of selected elements shown in Figure 2.6.

†Percent difference between mean and standard deviation.

2.5 X-ray powder diffraction

X-ray diffraction (XRD) of powdered samples is commonly used for mineral identification, especially fine-grained lithologies where petrological methods are unsuitable. For this research, the XRD method was used to identify qualitative mineralogical changes within proposed orbital cycles. Previous studies have used the method to identify changes in abundance or type of mineralogy associated with climate change (Ruffell and Worden, 2000; Nador et al., 2003; Hesselbo et al., 2009).

The mineralogy of an unknown powdered substance was ascertained using the PANalytical X'pert PRO powder diffractometer at the UCL Earth Sciences X-Ray Diffraction Laboratory. Prior to analysis the sample to be analysed required crushing to a fine powder as outlined in Section 2.2.1.

Each specimen is placed with a holder and assumed randomly orientated. The specimen is then exposed to monochromatic x-rays generated from a cobalt anode with a 1.79 Å wavelength. Interaction between the incident x-rays and the specimen creates secondary diffracted x-rays (in the form of cones). Diffraction of the incident x-

rays will occur when a certain set of parameters, defined by Bragg's Law, is fulfilled. Bragg's Law is defined as:

Equation 2.7

$$n\lambda = 2d\sin\theta$$

where *n* is an integer, λ is the wavelength of incident x-rays (Å), *d* is the inter-planar spacing generating the diffraction (Å) and θ is the diffraction angle. When Bragg's Law is satisfied, constructive interference between diffracted x-rays within a minerals crystal lattice creates diffraction maxima. As each mineral contains a different lattice structure and therefore varying inter-planar spacing, Bragg's Law will be fulfilled over varying diffraction angles. To achieve the maximum range of diffraction angles the sample is rotated relative to the incident x-ray beam. Where diffraction maxima occur both the angle (recorded as 2θ) and the intensity are recorded in a spectrum by the X'PERT-Pro software. Positions of intensity peaks within the spectrum are characteristic of the minerals involved. The identification of the individual mineral species present is achieved by comparing measured peaks and intensities with those within a database of standard data provided by International Centre for Diffraction Data (ICDD). The intensity of the individual spectral peaks can also be used to determine the relative abundance of that mineral.

2.6 Stratigraphic time series analysis

A time series is a sequence of observations taken over discrete intervals ordered by a single variable such as time. Within the stratigraphic record, a time series can be created by oscillations ranging from yearly to orbital (Milankovitch) time scales leading to variation in sediment properties (e.g., grain-size, mineralogy, geochemistry, etc.). These climatically driven oscillations are ideally recorded within the stratigraphic record as a series of sine or cosine waves differing in wavelength and amplitude. When these signals are combined a far more complex signal is created (Fig. 2.7). With the addition of random noise and the environmental background, a simple visual identification of individual oscillations becomes difficult, if not impossible (Fig. 2.7). In addition, amplitude and frequency modulation along with non-linear distortion of the time series can further complicate the interpretation of cyclostratigraphic signals. Enabling the examination of these cryptic oscillations within a time series is a process called spectral analysis.

2.6.1 Cyclostratigraphic time series

Cyclostratigraphic time series are constructed by measuring variations in stratigraphic variables ordered by increasing depth or time. Subsequent spectral analysis reveals whether any periodic (stationary) or quasi-periodic (near stationary) oscillations are present.

When creating a time series from stratigraphic variables there are, however, limits to the amount of data that can be realistically collected. Ideally, a cyclostratigraphic time series would involve an infinitesimal sample interval enabling all stratigraphic data to be recorded. Unfortunately, this approach is not practical resulting in continuous signals being sampled discretely. Discrete sampling of a continuous record limits the amount of data and hence, the highest frequency that can be recorded by the time series, which is known as the Nyquist frequency (N_f):

Equation 2.8

$$N_f = {}^{1}\!/_{2SI}$$

where *SI* the sampling interval. The Nyquist frequency is based upon a constant sample interval and states that the smallest sine or cosine wave that can be reconstructed must be sampled twice per oscillation. If the highest frequency of interest is not sampled twice per oscillation then an aliased signal may result. Aliased oscillations result in the creation of spurious frequencies leading to the possible

incorrect interpretation of the original signal (Pisias and Mix, 1988). It has been suggested that 4 samples taken per oscillation of the smallest wavelength being studied is adequate to avoid aliasing of a simple sinusoid (Weedon, 2003). However, in the case where the signal does not comprise a simple sinusoid, a minimum of 8 samples per oscillation are required (Herbert, 1994). It is therefore apparent that when studying discretely sampled oscillations, it is preferable for the sampling interval to be as small as practicable to avoid the complications of aliasing.

For spectral analysis to accurately determine oscillations, a time series must be of adequate length to resolve individual frequencies. Random fluctuations in accumulation rates and non-stationary climate forcing can result in the accurate identification of oscillations from short time series difficult. To overcome these difficulties Weedon (2003) suggested that the adequate length of a time series can be determined using:

Equation 2.9

$$N = \frac{0.75\upsilon \cdot \lambda}{SI}$$

where N is the number of data points, υ is the number of degrees of freedom, λ is the longest wavelength to be analysed and SI is the sampling interval. In the case of many palaeoclimatic studies where eight degrees of freedom are used (Weedon, 2003), six oscillations of the longest wavelength are required before the times series will be of adequate length.

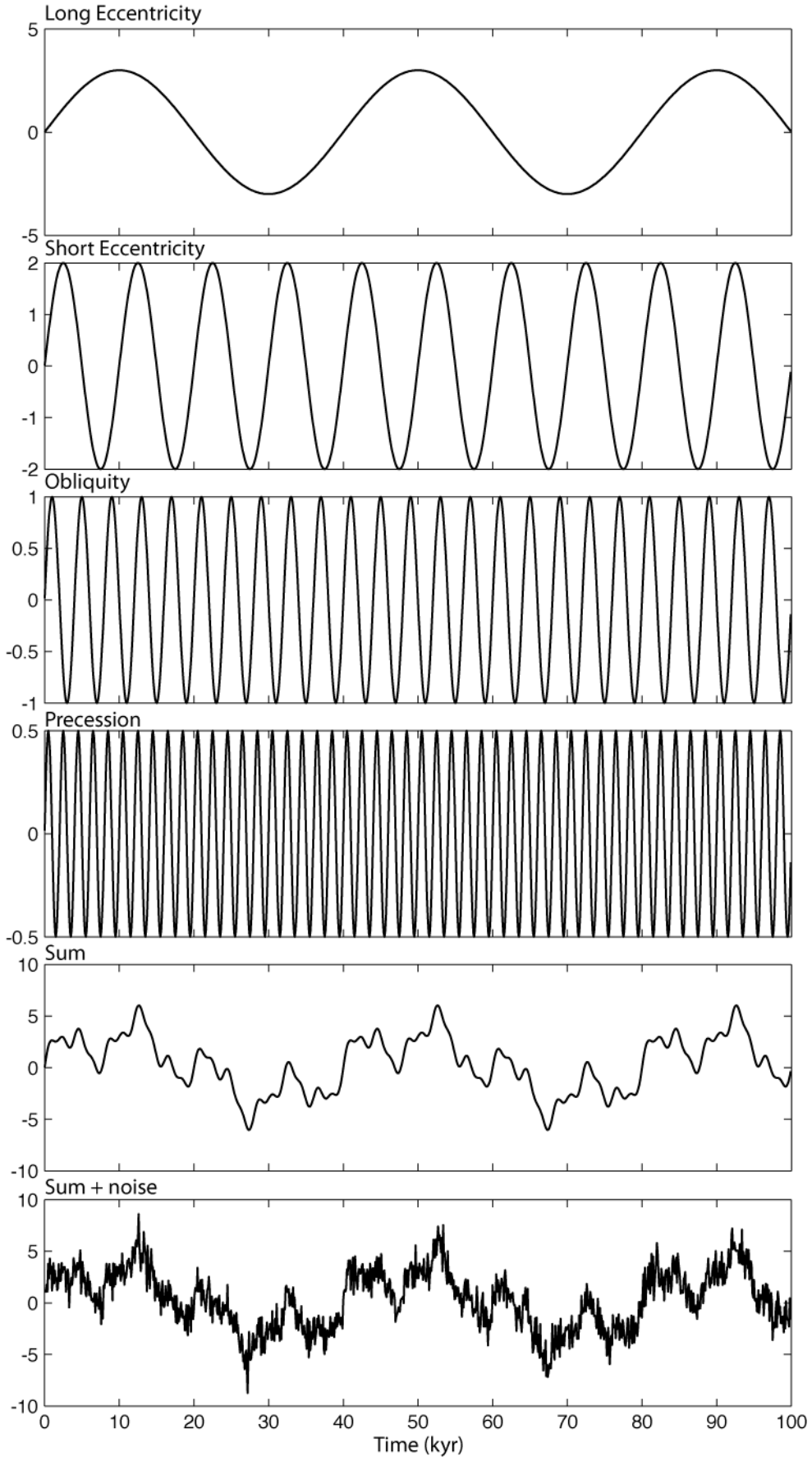

Figure 2.7 | Synthetic time series composed of individual sine waves. The Milankovitch signal is composed of individual sine waves and when combined create a more complex record. With the addition of random noise, the identification of the shorter wavelength signals becomes difficult.

2.6.2 Time series pre-processing

Prior to applying a spectral analysis technique, the stratigraphic time series will require pre-processing to prohibit the creation of artefacts during the Fourier transform. Without this processing spurious and/or distorted spectral peaks may be interpreted as being significant.

2.6.2.1 Mean subtraction and de-trending

During spectral analysis the spectral power is determined by calculating the mean square deviation from zero for each frequency component examined. Each time series therefore requires a mean of zero, which is achieved by subtracting the mean of the entire time series from each data point. The result should be a mean subtracted time series with a zero mean thus avoiding an erroneous estimation of spectral power.

If the mean value of a time series contains a progressive increase or decrease along its length it is inferred to contain a trend. During spectral analysis, the Fourier transform treats the data as if it were continuous (i.e., repeated indefinitely). As a result, any trend within the data would lead to a spectral peak with a wavelength equal to the length of the time series. The trend can be removed by fitting a least squares regression line through the data then subtract the line point by point from the time series (Weedon, 2003). Helpfully, the process of subtracting the trend results in the time series oscillating about the zero line therefore performing mean subtraction. Where the data contains a stepped change in the mean (e.g., a change in sedimentation rate) the time series can be split into two sections at the point of the step change with each segment de-trended individually (Weedon, 2003).

2.6.2.2 Outliers

Data points positioned well outside the range of adjacent time series values are deemed as outliers. During the Fourier transform outliers appear as an unit impulse. The unit impulse can itself be reconstructed from an infinite number of sine and cosine waves which are represented in a spectra as a straight line. This has the effect of raising the background level of the spectrum resulting in the apparent reduction in signal power of real peaks. Outliers can also cause ringing at higher frequencies (Percival and Walden, 1993). Removal of outliers from time series data is subjective care should therefore be taken.

2.6.2.3 Interpolation

Many spectral estimation algorithms require evenly spaced data. Often within a stratigraphic section a constant sampling interval is not always possible leading to missing or irregularly spaced data. The method of interpolation provides estimates of these missing data points based upon adjacent data.

Commonly either linear or cubic spline interpolation techniques are used within time series analysis (Yiou et al., 1996). If values vary smoothly from point to point then simple linear interpolation will suffice. This method works by estimating a straight line between the two data points and calculates the mid-point value between the two. Such a process assumes a linear transition between the data points, which can introduce spectral artefacts such as the loss of high frequency components (Yiou et al., 1996; Schulz and Stattegger, 1997; Weedon, 2003).

Interpolation of a time series however, introduces artefacts to both the time and frequency domain. To limit these possible artefacts it is advisable to: preserve the number of data points before and after interpolation (Trauth, 2007); use a sample interval close to the mean spacing of the original data (Weedon, 2003); and explore the effect of the method used upon the relative spectral amplitudes, as illustrated in figure 3 of Schulz and Statteger (1997). The choice of new sampling interval is important. If too large, the original data is smoothed resulting in the loss of power in higher frequencies: if too fine, then an unrealistic Nyquist frequency is created but would not add new information to the time series (Yiou et al., 1996). To avoid the complications caused by interpolation, methods based upon the Lomb-Scargle spectral estimation technique (Press et al., 1992; Schulz and Stattegger, 1997) have been developed to work with unevenly spaced data (Section 2.7.3).

2.6.2.4 Data tapering

The Fourier transformation of a finite observational time series will not only produce a spectral peak, but also sidelobes due to spectral leakage, which is the result of how the Fourier transform treats the finite nature of observational time series. During the Fourier transform the abrupt edges of the time series are represented using additional sine and cosine components creating sidelobes. Each of these spurious frequencies are assigned power at the expense of each real spectral peak. The resultant spectral estimate is therefore underestimated and it is said to exhibit bias. Spectral leakage within red noise environmental data re-distributes power away from lower frequencies therefore swamping higher frequency components (Weedon, 2003).

To reduce spectral leakage, a taper or data window can be applied to remove the abrupt edges of the time series. Tapering is achieved by multiplying the time series data by a window function that starts at one in the centre and is reduced to zero at the edges. Different tapers exist, each with their own characteristic spectral sidelobes associated with each real spectral peak (Harris, 1978). The size of these sidelobes depends upon the choice of taper and proportion of the data tapered (Ifeachor and Jervis, 2002). Use of spectral windows has the effect of smoothing the data therefore increasing the degrees of freedom (DOF), bandwidth (BW) and altering confidence levels (Bloomfield, 2000). The statistical effects of various data tapers are well documented (Jenkins and Watts, 1968; Harris, 1978; Percival and Walden, 1993).

2.7 Spectral Estimation Techniques

Spectral estimation involves the deconvolution of a time series into its constituent sine and cosine waves based upon Fourier's Theorem. According to Fourier's Theorem, oscillations within any time series can be re-created by combining together regular sine and cosine waves of different wavelengths and amplitudes. As sine and cosine waves are orthogonal functions, they can be added together to describe any time series but none of the individual component waves can be constructed from combinations of other waves in the group.

2.7.1 The periodogram

To apply Fourier's Theorem to a time series, the discrete Fourier transform (DFT) is utilised to calculate a raw form of spectra, the periodogram. The periodogram forms the basis for many spectral estimation techniques, therefore a brief explanation of the process is provided. A more detailed description can be found within the literature (Jenkins and Watts, 1968; Percival and Walden, 1993; Bloomfield, 2000; Ifeachor and Jervis, 2002; Weedon, 2003).

The DFT operates by using paired regular sine and cosine waves to determine the relative importance of each frequency. The frequencies analysed are restricted to integer divisors of the number of time series points multiplied by the sample interval (*SI*). The resultant frequency range spans from infinity (0 Hz) to the Nyquist frequency (N_f) and is known as Fourier harmonic frequencies. Each harmonic frequency is represented by a cosine wave and used to multiply the individual data points within the time series. The sum of the results is multiplied by a constant (2/N where *N* is the number of data points in the time series), which yields average amplitude for that frequency. This process is repeated for the same frequency sine wave. When

combined, the relative average amplitudes of the sine and cosine waves represent the oscillation of that frequency and phase. To convert these values into periodogram power, the sum of the squared sine and cosine average amplitudes of each Fourier harmonic frequency is calculated. Plotting the power vs. frequency creates the periodogram.

Prior to modern computers the DFT was computationally slow to perform. In response the fast Fourier transform (FFT) was developed to calculate the DFT with reduced execution time (Cooley and Tukey, 1965; Press et al., 1992). The FFT, similar to the DFT, divides the times series into two pieces of size N/2 at each step and is therefore limited to blocks of a power of two. This restricts the time series length to be an integer power of two points (e.g., N = 256, 512, 1024 etc.). Where necessary, zeros can be supplemented to the time series (zero padding) to fulfil this constraint. Zero padding has the useful effect of increasing the number of Fourier harmonic frequencies analysed (Bloomfield, 2000), therefore increasing the frequency resolution of the spectral estimate (Muller and MacDonald, 2000). However, zero padding needs to be compensated for when calculating the spectral estimates DOF and BW (Press et al., 1992) and has been shown to contribute toward spectral leakage (Bloomfield, 2000).

Limitations of both the DFT and FFT are that evenly spaced data is required and that the examinable frequencies are restricted to the Fourier harmonics. If the frequency of an oscillation does not match that of a Fourier harmonic frequency, then scalloping or picket fencing may occur (Harris, 1978; Ifeachor and Jervis, 2002). This results in the corresponding peak being slightly reduced in size compared to what would be expected. Zero padding of the data to reduce the spacing between spectral estimates can be used to help reduce the effect of scalloping.

Independent of which algorithm is employed, the periodogram is said to produce a poor approximation of the expected spectrum (Ifeachor and Jervis, 2002). Problems caused by spectral leakage (re-distribution of spectral power from the spectral peak to sidebands), and a low statistical stability due to the power values being randomly distributed about the expected spectral background (Priestly, 1981; Scargle, 1982; Press et al., 1992; Ifeachor and Jervis, 2002), have resulted in the periodogram being rarely applied to climatic time series.

To mitigate these issues, modifications to the data and the periodogram spectral estimation technique are applied. Spectral leakage can be suppressed by applying a data taper to the time series prior to implementing the Fourier transform (Press et al., 1992). Improving the statistical reliability of the spectral estimates is achieved by averaging several periodogram estimates together creating a smoothed periodogram (Percival and Walden, 1993). Several methods of periodogram smoothing exist, including the Bartlett (Bartlett, 1948) and Welch (Welch, 1967) techniques. These

smoothed periodograms, including other spectral estimation techniques that better approximate the theoretical spectrum than the periodogram, are known as power spectra. Unfortunately, both of these techniques have the effect of altering the statistical properties of the spectral estimate and therefore require consideration during degrees of freedom, bandwidth and confidence level estimation (Bloomfield, 2000). Despite this, many texts exist documenting the modified statistical properties of tapered and smoothed periodograms (Jenkins and Watts, 1968; Percival and Walden, 1993).

In a raw periodogram each spectral estimate is dependent upon two values (the sum of the squared mean cosine and sine amplitudes), which results in there being 2 degrees of freedom (DOF). When smoothing the periodogram, the DOF are increased as each spectral estimate includes more data from adjacent frequencies. Usually within cyclostratigraphic time series it is common for 8 to 14 degrees of freedom to be used (Weedon, 2003). Along with increasing the number of degrees of freedom, smoothing also increases the bandwidth, reducing the ability of individual frequency components to be identified from one another and the spectral background. It is therefore important to strike a compromise between the amount of smoothing and its effect upon bandwidth when creating a spectral estimate.

Although well understood, the periodogram is thought to be unsuitable for the analysis of time series associated with red noise backgrounds such as palaeoclimatic data (Percival and Walden, 1993). Other authors suggest that the periodogram is preferable over other spectral estimation methods in these circumstances (MacDonald, 1989; Muller and MacDonald, 2000).

2.7.2 Welch and Bartlett methods

Smoothing the periodogram can be achieved by calculating the periodogram from individual sub-sections of the time series then averaging them together to create a spectral estimate. Two slightly differing methods exist, the Bartlett (1948) and Welch (1967) techniques. The Bartlett method simply involves the splitting of the time series into sections of equal length; uses a FFT to compute the periodogram for each section; then estimates the spectrum by averaging together the individual periodograms.

An improvement upon the Bartlett spectral estimation technique is the Welch method of spectral estimation or weighted overlapped segment averaging (WOSA). Instead of splitting the time series into contiguous blocks of data, the Welch method involves the time series being split up into equal length overlapping segments. By overlapping the data segments, a spectral estimator with better variance properties is produced than when using non-overlapping segments. Each data segment is tapered using a spectral window thereby reducing potential bias due to leakage in the

periodogram. Overlapping the tapered subsections compensates somewhat for the effect of tapering, i.e., data values that are down weighted in one segment can have a higher weight in another segment (Percival and Walden, 1993). The degree of smoothing achieved using this method is determined by the amount of overlap between segments and the number of segments used. To obtain the best results a 50% overlap of the subsections is required (Percival and Walden, 1993; Ifeachor and Jervis, 2002).

Both methods are efficient when using the FFT algorithm and can effectively handle very long time series (Percival and Walden, 1993). The Welch method of spectral estimation is a favoured over the Bartlett method as for the same degrees of freedom it produces better quality spectra and reduces the variance of the power spectral density estimates (Ifeachor and Jervis, 2002). Drawbacks associated with the reduction in variance are that the spectral bandwidth is increased (Ifeachor and Jervis, 2002).

2.7.3 Normalised Lomb-Scargle Fourier transform

Whilst collecting palaeo-environmental data it is often difficult to collect data at regular intervals necessary for the spectral analyses methods discussed so far. Problems introduced by the necessary interpolation to an evenly spaced time scale can be avoided by using the Lomb-Scargle Fourier Transform (Lomb, 1976; Scargle, 1982). The Lomb-Scargle Fourier Transform (LSFT) is an improvement upon the periodogram enabling unevenly spaced data to be analysed whilst retaining the statistical properties of the power obtained from evenly spaced data.

The LSFT evaluates the sines and cosines only at points where data exists therefore removing the requirement for evenly spaced data. First the mean and variance of the data is determined followed by calculating the power as a function of angular frequency. By using the constant (τ) the spectral power estimates become independent from shifting data points along the time axis by any constant (Scargle, 1982). When power estimates are calculated for evenly spaced data, the constant is removed and the equation reverts back to the original. Additionally, this particular choice of offset makes the resultant spectral estimation the equivalent to the least square fit of sine and cosine functions to the time series (Scargle, 1982). As this least squares fit had been previously investigated by Lomb (1976) the method is known as the Lomb-Scargle Fourier Transform.

Unlike other methods the Lomb-Scargle method carries out the Fourier transform on a point-by-point rather than per-time basis. These points correspond to the frequencies that are to be analysed by the LSFT and need to be defined. To

determine the highest frequency to be analysed (*fhi*) we use the Nyquist frequency (N_f) that would be obtained if the number of data points were evenly spaced over the length of the time series. The lowest frequency to be analysed is simply the equivalent to the spacing between frequency scale points. The number of frequencies analysed by the LSFT is controlled by the over sampling factor (*ofac*) which has a similar to zero-padding in other techniques. In most cases the *ofac* is usually set to 4 to compromise computing time and smoothness of the periodogram (Press et al., 1992; Schulz and Stattegger, 1997; Trauth, 2007). Prior to applying the LSFT the time series require linear trends to be removed and centred about zero.

Detailed descriptions of the LSFT method can be found within Scargle (1982), Press et al. (1992) and Schulz and Stattegger (1997). MATLAB code to apply the LSFT is found within Trauth (2007) and Muller and MacDonald (2000).

2.7.4 REDFIT

The REDFIT algorithm (Schulz and Mudelsee, 2002) is based upon the earlier SPECTRUM algorithm (Schulz and Stattegger, 1997), which combines the Lomb-Scargle (Lomb, 1976; Scargle, 1982) and Welch Overlapped Segment Averaging (Welch, 1967) spectral analyses techniques. The combination of these techniques enables the spectral analysis of unevenly spaced time series data avoiding the need for interpolation and its associated limitations (Schulz and Stattegger, 1997). The REDFIT algorithm additionally enables the robust determination of the autoregressive (AR1) spectral background directly from the analysed data enabling confidence levels to be accurately applied.

Applying the method to a time series first requires the removal of any linear trend which will also act to centre the data about zero. REDFIT spectral analyses require several parameters to be defined including the over-sampling factor (*ofac*), number of WOSA segments of 50% overlap (n_{50}) and the shape of the spectral window (*iwin*) to be applied to each WOSA segment. Where sufficient bandwidth would be retained, these variables were varied until eight degrees of freedom were achieved. Once the power spectrum is calculated the algorithm determines the red noise (AR1) spectral background from the spectrum and multiplies this by various χ^2-probability distribution values to create 80%, 90%, 95%, 99% and critical confidence levels. An example REDFIT spectrum calculated from insolation over the last 1 million years is illustrated in Figure 2.8.

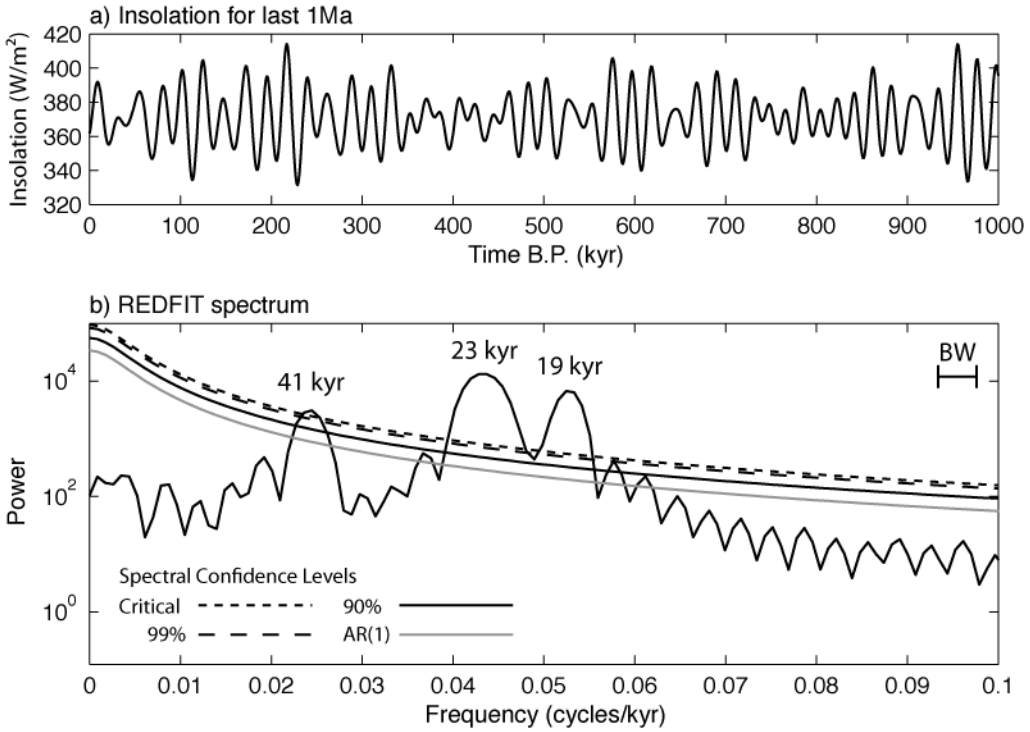

Figure 2.8 | Example REDFIT spectrum of insolation time series since 1 Ma. REDFIT spectrum was calculated using an *ofac* of 4, 6 rectangular windows resulting in 8 degrees of freedom. Bandwidth is ±0.002 cycles/kyr. **(a)** Mean insolation time series (*N*=1001 & *SI*=1 kyr) calculated for 65˚N using the algorithm of Laskar (2004). **(b)** The spectrum identifies the 41 kyr, 23 and 19 kyr Milankovitch periods to above the critical level (99.7%).

2.7.5 Multi-Taper Method

The multi-taper method (MTM) proposed by Thomson (1982) is another spectral technique based upon the periodogram and has been successfully utilised within palaeoclimatic studies (Thomson, 1990a; Thomson, 1990b; Olsen and Kent, 1999; Melice et al., 2001; Grutzner et al., 2002; Meyers and Sageman, 2007; Boulila et al., 2008; Machlus et al., 2008; Meyers, 2008). Here the method is briefly outlined whilst detailed mathematical descriptions and modifications of the MTM and F-test can be found within the literature (Thomson, 1982; Thomson, 1990a; Percival and Walden, 1993; Lees and Park, 1995; Yiou et al., 1996; Ghil et al., 2002).

The MTM involves applying a series of orthogonal discrete prolate spheroidal sequence (or Slepian sequence) data tapers to a time series. After each data taper is applied a periodogram is calculated. Subsequently, these periodograms are averaged to create a power spectrum. Due to the ability of discrete prolate tapers to suppress periodogram leakage, MTM spectra posses well suppressed side-lobes, good smoothing and high frequency resolution (Weedon, 2003). However, MTM spectra produce flat topped rather than sharp spectral peaks (Fig. 2.9). The number of tapers applied is typically within the ranges of 4 to 8 (Weedon, 2003).

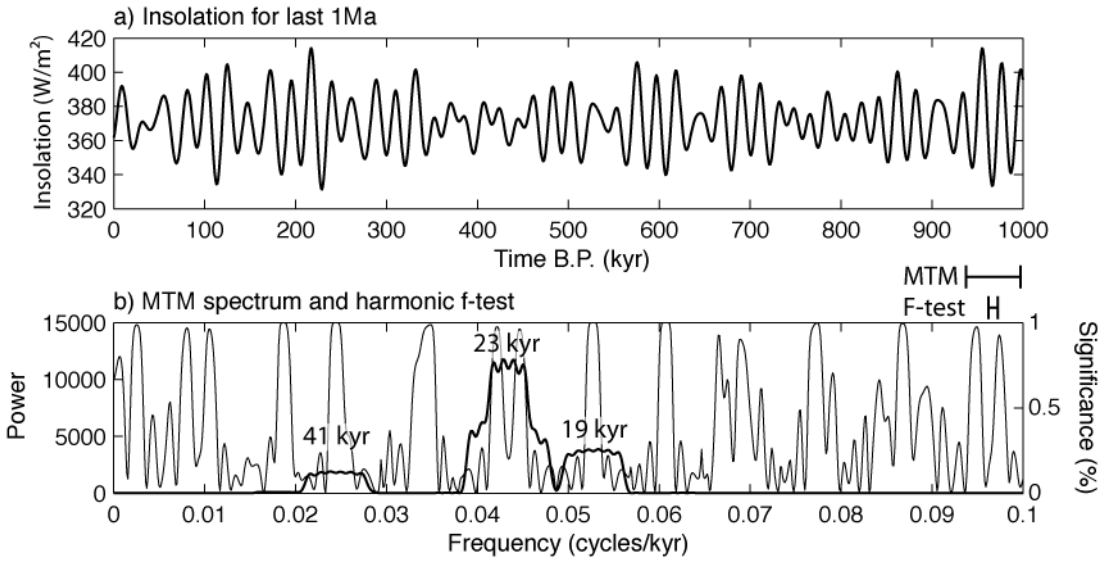

Figure 2.9 | Example MTM spectrum calculated from insolation time series since 1 Ma. (a) Mean insolation time series the same as that for Figure 2.8. **(b)** MTM (bold line) and harmonic F-test (fine line) spectra for insolation time series. MTM spectrum create flat topped peaks representing identifying the 41 kyr, 23 and 19 kyr Milankovitch periods. F-test spectrum splits the 23 kyr spectral peak into a 24 and 22 kyr precession periods. MTM bandwidth = ±0.003 cycles/kyr. F-test bandwidth = ±0.0005 cycles/kyr.

The MTM additionally enables a statistical F-test (Fig. 2.9) for the presence of pure sinusoidal components within a time series (Thomson, 1990a). The F-test is independent from amplitude so can identify low amplitude peaks that are statistically significant and high amplitude peaks that are not (Yiou et al., 1996; Ghil et al., 2002). The main benefit of this technique is that its bandwidth is equal to the minimum resolution bandwidth, which is identical to the Rayleigh frequency (R_f).

The major assumption of this technique is that the time series must contain periodic and separated components. If not then a continuous spectrum (e.g., red noise) will be broken down into spurious spectral peaks at arbitrary frequencies with potentially high significance levels (Yiou et al., 1996; Ghil et al., 2002). Therefore to avoid this possibility it is necessary to verify the presence of F-test frequencies using an additional spectral technique.

MTM spectral analysis within this research is performed within Analyseries 2.0.4.2 (Paillard et al., 1996). Prior to the calculation of MTM spectrum, time series were pre-processed to remove any linear trend, mean subtracted and linearly interpolated. MTM spectra were calculated once the time-bandwidth product (*NW*) and number of data tapers (*K*) were inputted. The number of tapers (*K*), according to Ghil et al. (2002), should be less than $2NW - 1$. The number of degrees of freedom (*DOF*) is simply twice the number of tapers (Thomson, 1982; Percival and Walden, 1993) whilst the bandwidth (*BW*) is the Rayleigh frequency multiplied by the number of tapers (Thomson, 1982; Ghil et al., 2002).

2.7.6 Wavelet spectral analysis

The inability of traditional periodogram spectral estimate techniques to identify temporal variations in non-stationary climate data (i.e., time series with temporal changes in frequency), led to the development of wavelet analysis (Farge, 1992; Meyers et al., 1993; Lau and Weng, 1995; Torrence and Compo, 1998). Instead of averaging the signal power over the entire length of the time series, the wavelet transform creates signal power estimates temporally. The method has become widely used within stratigraphic and palaeoclimatic studies (Prokoph and Barthelmes, 1996; Prokoph and Agterberg, 2000; Rial and Anaclerio, 2000; Turney et al., 2005; Berger et al., 2006; Westerhold et al., 2007; Machlus et al., 2008; Westerhold and Röhl, 2009; Grutzner and Higgins, 2010; Zachos et al., 2010). For this research, the continuous wavelet transform (CWT) algorithm is used to determine temporal changes in signal variance. Here the method is outlined with further mathematical details on the method are outlined within Torrence and Compo (1998).

The continuous wavelet transform works by using finite wavelets in the same way that the Fourier transform uses infinite sine and cosine waves. Wavelets are small packets of waves, which rapidly decay to zero at either end. These wavelets, like sine and cosine waves, are orthogonal functions meaning that wavelets of different scales and positions can be combined together to create any signal. These scaled and translated wavelets are referred to as baby wavelets, which originate from a mother wavelet. Whilst many different mother wavelets exist, the Morlet wavelet with a wave number of 6 is commonly used within the Earth Sciences community (Torrence and Compo, 1998; Prokoph and Agterberg, 2000; Lu et al., 2003; Grinsted et al., 2004; Keener et al., 2010).

The wavelet transform is calculated by multiplying a time series by a series of baby wavelets, which are repeatedly translated along the time scale. At each position a correlation coefficient is calculated for that scale. The scale of the wavelet is then increased (dilated) and translated along the time scale with correlation coefficients calculated for each position. This process is repeated for a range of defined scales resulting in coefficients existing for each scale and position. Frequency values are subsequently obtained by converting the scaled wavelets into pseudo-frequencies. To produce the wavelet power spectrum the time, period and power (squared magnitude of the amplitude), are calculated and are plotted in a contoured plot as illustrated in Figure 2.10.

If a vertical slice were taken through the wavelet power spectra, a spectrum illustrating period and power would result specific to that time or depth. Time averaging these individual wavelet spectra creates a global wavelet spectrum yielding information

upon the average power of oscillations throughout the time series (Fig. 2.10). This provides an unbiased and consistent estimation of the true power spectrum of a time series (Percival, 1995).

To determine significance levels within a wavelet power spectra, a method similar to that of the Periodogram based spectral estimates are utilised. Firstly, the spectral background needs to be determined which, in the case of environmental data corresponds to red noise (Shackleton and Imbrie, 1990; Weedon, 2003). Assuming that the mean spectral background within the analysed time series corresponds to red noise, its position is estimated using a Fourier power spectrum. The background spectrum is then multiplied by the chi-squared value corresponding to the appropriate confidence level (Gilman et al., 1963; Bloomfield, 2000). Once the confidence level has been calculated for each scale, they can be represented as a contour line within the wavelet power spectrum (Torrence and Compo, 1998).

As the continuous wavelet transform is applied to a finite time series, the abrupt edges will cause the Fourier transform to create discontinuities within the wavelet power spectrum. Torrence and Compo (1998) have suggested that by zero padding the time series to the next power-of-two these edge effects are dampened. However, zero padding introduces its own problems by decreasing the amplitudes at larger scales near to the edges of the wavelet power spectrum. To define the areas influenced by this amplitude dampening, the cone of influence (COI) is identified (Torrence and Compo, 1998).

Wavelet spectral analysis were accomplished using the online tool (http://paos.colorado.edu/research/wavelets/) based upon the algorithms of Terrence and Compo (1998). Prior to analysis, data requires any linear trend to be removed, mean subtraction and linear interpolation. Wavelet analyses were performed using the Morlet mother wavelet with a time parameter of 6. Start scales defining the minimum wavelet scale analysed were varied until desired frequency range was found. The resolution of the wavelet spectra is defined by the scale width (δj). The value of δj were again varied until the adequate resolution was reached but remained below the maximum of ~0.5 (Torrence and Compo, 1998). The number of scales (J) used during the wavelet analysis is determined by the number of powers-of-2, which remained at 11. The type of spectral background was selected as red noise as this most likely corresponds to the background climatic spectrum (Shackleton and Imbrie, 1990; Weedon, 2003).

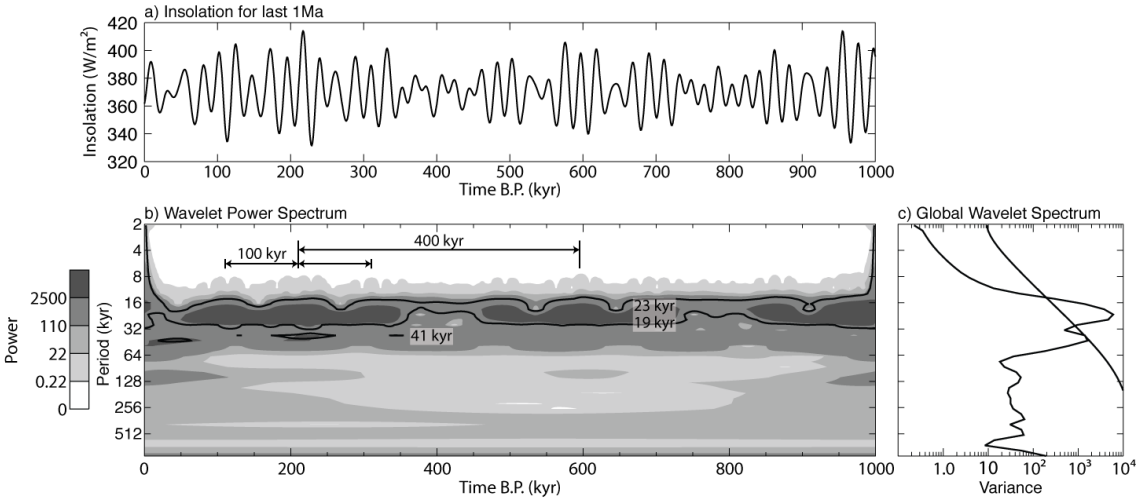

Figure 2.10 | Wavelet spectrum for insolation time series since 1 Ma. (a) Mean insolation time series same as that for Figures 2.8 and 2.9. **(b)** Calculated using scale width of 0.2, 11 powers-of-two and a start scale of 2. The 90% red-noise confidence levels in a and c represented by solid bold lines. Unlike the REDFIT and MTM methods, the wavelet spectrum provides evidence for the presence of both long and short eccentricity cycles. The varying power in the precession band indicates that the amplitude is being modulated by eccentricity (i.e., amplitude modulation). **(c)** Global wavelet spectrum showing the average power spectrum for length of time series.

2.8 Interpretation of power spectra

2.8.1 Cyclostratigraphic spectra

Cyclostratigraphic time series produce mixed spectra consisting of periodic and quasi-periodic oscillations. Mixed spectra produce spectral peaks along with irregular fluctuations creating a sloping spectral background (Priestly, 1981; Weedon, 2003). To allow the identification of periodic and quasi-periodic components within the spectra it is necessary to differentiate them from the spectral background (Section 2.8.2). The spectral background is comprised of random fluctuations considered the result of stochastic processes along with random measurement errors (Weedon, 2003). Three main types of spectral background exist; random (white) noise; autoregressive (red) noise; and moving average noise and are outlined in Weedon (2003). Commonly environmental spectra contain autoregressive (red) noise (Gilman et al., 1963; Hays et al., 1976; Shackleton and Imbrie, 1990; Weedon, 2003).

Red noise consists of random numbers with the addition of a positive or negative weighting from the previous time series value therefore representing an autoregressive (AR) process. The natural system represents an AR process as it contains an environmental inertia, i.e., it possesses a memory of past events therefore, creating a red noise spectral background. First order AR processes [AR(1)] creates each successive value based upon the immediately preceding value (has a 'memory' of one step) plus a random component. AR(1) spectral backgrounds contain their

greatest value at zero frequency and decrease down to the Nyquist frequency. Higher order AR processes involve increased 'memories' which has the effect of creating oscillations within the time series (Schwarzacher, 1975). These higher order AR processes have their maximum value at non-zero frequencies making the spectra difficult to interpret (Priestly, 1981). Various methods exist within the literature on the modelling of AR spectral backgrounds, many of which are outlined by Weedon (2003).

2.8.2 Significance of spectral results

Mixed spectra, such as those obtained from palaeoenvironmental time series, contain a combination of random noise fluctuating about a spectral background and environmentally induced oscillations. Identification of these significant oscillations is achieved by calculating confidence levels.

When spectral estimates are obtained using periodogram smoothing techniques such as REDFIT and MTM, the scale of erratic fluctuations can be estimated assuming that the uncertainties of the spectral estimates follow a chi-squared (χ^2) distribution (Priestly, 1981; Percival and Walden, 1993). To determine the spectral confidence level, the number of degrees of freedom of the spectral estimate technique is divided by the chi-squared distribution appropriate to the confidence level required (Priestly, 1981). However, the degrees of freedom depend upon the spectral estimation method used, type of spectral window, whether the data was tapered and the degree of zero-padding (Bloomfield, 2000). In the case of commonly used spectral windows, their modified degrees of freedom can be found within Table 269 of Jenkins and Watts (1968).

Prior to determining the confidence levels, the position of the red noise spectral background needs to be identified. Methods of estimating the position of the spectral background vary depending upon the technique used. When using the periodogram and Blackman-Tukey methods the simplest method is to use a log power versus a log frequency plot and fit a straight line to the estimates (Wunsch, 2000). However, methods such as this should not be used when analysing unevenly spaced data as the required interpolation reddens the spectrum thereby enhancing low frequency spectral components (Weedon, 2003). To overcome this the REDFIT technique (Fig. 2.8) is able to estimate the AR(1) background directly from an unevenly spaced time series (Schulz and Mudelsee, 2002).

With the location of the spectral background identified, upper confidence levels are calculated by multiplying the spectral background by the appropriate multiplicative factor. These confidence levels correspond to the limits of confidence intervals i.e., the upper limit of the 90% confidence level is equivalent to the 95% confidence level

(Bloomfield, 2000). Spectral peaks with power greater than that confidence level are significant to that level and are not associated with climatic red-noise background.

2.8.3 Spectral resolution and bandwidth

Spectral resolution is the spacing between successive spectral estimates influencing the ability of individual frequencies to be identified. Power spectra have a finite spectral resolution controlled by the spectral estimation technique and the length of the time series. When using the DFT, the spacing of successive spectral estimates is known as the Rayleigh frequency R_f:

Equation 2.10

$$R_f = 1 / (N \times SI)$$

where SI is the sampling interval and N is the number of data points in the time series. Hence, by increasing the number of data points within a time series, the more spectral information can be packed into the frequency range between the zero and the Nyquist frequency. As a result more spectral estimates can be performed and the spectral resolution is increased.

The frequency resolution within a power spectrum is known as resolution bandwidth. Bandwidth (BW) corresponds to the width of the narrowest detectable spectral peak in the spectral estimate. Each spectral peak or frequency within a power spectrum has an uncertainty of ±1/2BW so it is desirable for bandwidth to be narrow. Bandwidth is dependent upon the spectral estimation technique used, the data length and whether the time series was tapered prior to the spectral estimation. The simplest method of decreasing the bandwidth is to increase the length of the data by zero-padding prior to applying the Fourier transform.

2.8.4 Filtering

The filtering of a time series is employed to remove high-frequency noise (low-pass filter) or isolate a frequency band of interest (band-pass filter). These filtering techniques result in the retention of a selective frequency band identified within a power spectrum. Prior to filtering of the time series, the filter design is considered.

Filtering requires the definition of the pass-, stop- and transition-bands, which represent the frequency range that will be retained, removed and the transition between, respectively (Fig. 2.11). To retain the original signal amplitude, the gain within the pass-band should be close to one, whilst within the stop-band gain should be close to zero. The transition between the two should ideally be abrupt, however the use of Fourier techniques requires a more gradual transition. Together, these features represent the filters gain function. Application of the filter to the time series is achieved via convolution. During convolution a phase shift can occur when a filter is asymmetric but can be avoided using forward and reverse filtering (Trauth, 2007).

Band-pass filtering (Fig. 2.11) within this research was applied within Analyseries 2.0.4.2 (Paillard et al., 1996). Only significant frequencies of interest were filtered using a Gaussian shaped filter. The bandwidth of the spectral analysis technique was used to define the filter bandwidth.

Low-pass filtering (Fig. 2.11) was used to isolate only the low frequency components of time series. Filtering was performed within MathWorks MATLAB using the `lowpass.m` script (Appendix) modified from that of Trauth (2007). The use of the `filtfilt` function within the script enabled any phase shift caused by the asymmetric filter design to be removed from the output signal.

Figure 2.11 (next page) | Example low- and band-pass filters applied to synthetic Milankovitch signal. (a) Synthetic Milankovitch sinusoidal signal containing 400, 100, 41 and 20 kyr periods as in Figure 2.7. **(b)** Simple periodogram spectrum of time series clearly identifying the frequencies present. **(c)** Frequency response of low-pass filter design showing pass-, transition- and stop-bands. This example is a 12^{th} order filter with a cut off frequency of 0.25 cycles/kyr. **(d)** Frequency response of a 4^{th} order band-pass filter with a pass-band between 0.095 and 0.15 cycles/kyr. **(e)** Frequencies within the pass-band are retained within the filter output whilst those in the stop-band are discarded. In this low-pass example both eccentricity frequencies are retained. **(f)** Output from the band-pass filtering of the 0.1 cycles/kyr frequency. Ideally the output should represent the original signal in Figure 2.7.

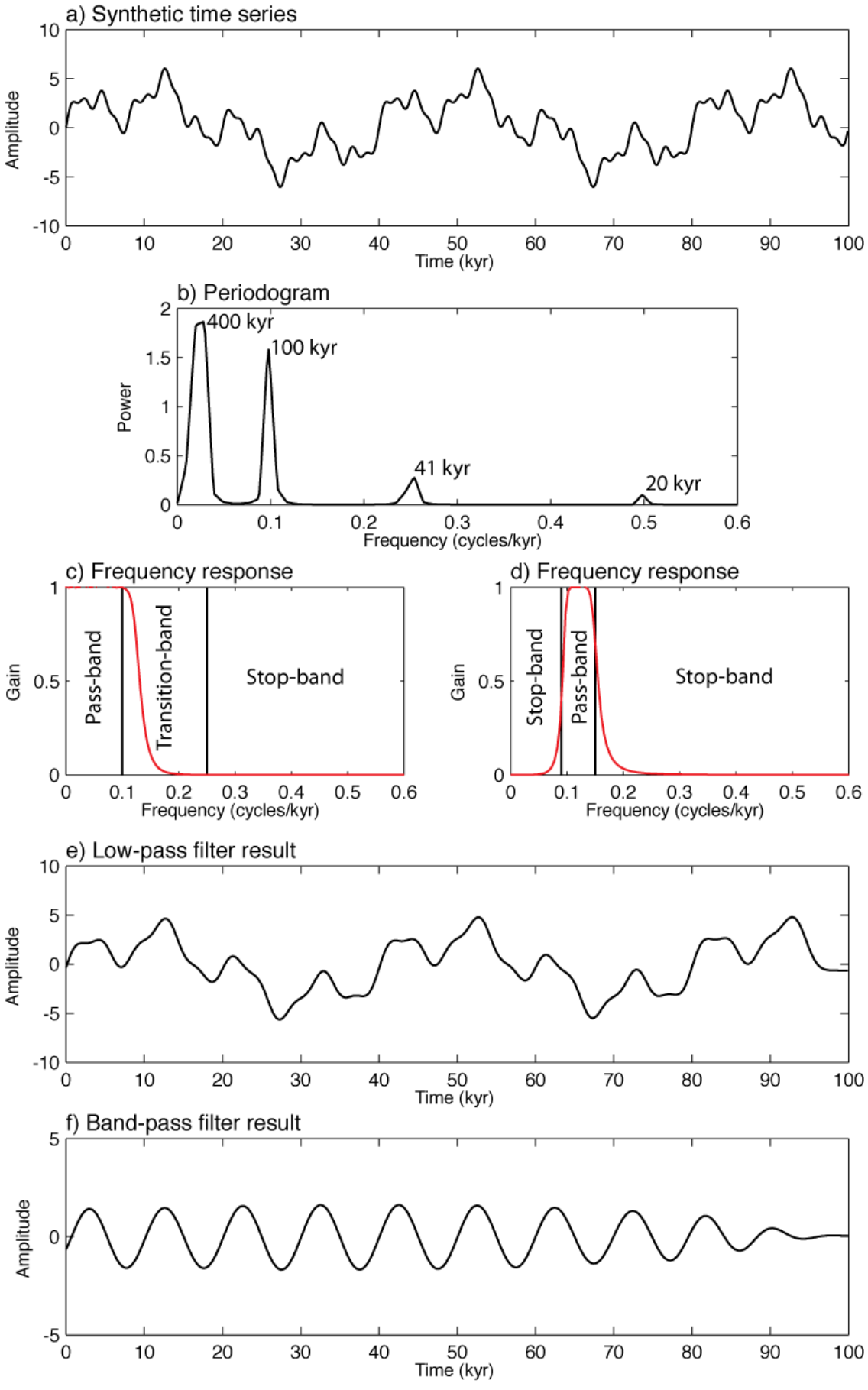
a) Synthetic time series
Amplitude
Time (kyr)
b) Periodogram
400 kyr
100 kyr
41 kyr
20 kyr
Power
Frequency (cycles/kyr)
c) Frequency response
Pass-band
Transition-band
Stop-band
Gain
Frequency (cycles/kyr)
d) Frequency response
Stop-band
Pass-band
Stop-band
Gain
Frequency (cycles/kyr)
e) Low-pass filter result
Amplitude
Time (kyr)
f) Band-pass filter result
Amplitude
Time (kyr)

2.9 Distortions within the orbital signal

Variability in the insolation received by the Earth is primarily controlled by three main orbital perturbations outlined in Section 1.7. The stratigraphic records of these oscillations commonly contain distortions caused by either interaction between the different orbital parameters and/or due to changes in the sediment accumulation rate (SAR). Within the measured stratigraphic time series these changes are present as amplitude or frequency modulation. The modulation of the insolation signal is similar in principle to modulation within electronics, which involves the distortion of a carrier signal by a modulating signal causing variation in the carrier signals amplitude and frequency.

Imposed amplitude modulation (referred to from here as AM) occurs when the amplitude of a carrier frequency is amplified of muted by a modulating frequency of longer wavelength (Fig. 2.12). Frequency modulation (FM) occurs when the frequency of a carrier signal of fixed amplitude is distorted by a modulating frequency (Fig. 2.12). These modulations have been shown to occur via the interaction between Milankovitch orbital cycles (King, 1996; Rial, 1999; Hinnov, 2000; Rial and Anaclerio, 2000; Melice et al., 2001; Rodriguez-Tovar and Pardo-Iguzquiza, 2003; Huybers and Aharonson, 2010). An example of AM is illustrated in Figures 1.20 and 2.10 where insolation changes forced by precession are amplitude modulated by the short eccentricity.

The modulation of orbital cycles may also occur during their signals transfer into the stratigraphic record via changes in sediment accumulation rates (Schiffelbein and Dorman, 1986; Hagelberg and Pisias, 1990; Hinnov and Park, 1998; Weedon, 2003; Laurin et al., 2005). Variations in SAR, and hence the time-depth relationship, can be characterised as being: random, cyclic, having a long-term trend, or abrupt (Weedon, 2003). Each of these styles of SAR change have their own characteristic spectral signature (Weedon, 2003).

Spectral analysis of AM and FM Milankovitch derived signals create complex spectra with multiple peaks (Fig. 2.12). Spectra obtained from both AM and FM spectra will contain spectral peaks representing the carrier frequency and numerous spectral artefacts known as combination tones. The modulating frequency is not represented within the spectra as a peak but, instead as the spacing between combination tones. The spectral position of combination tones can be predicted using:

Equation 2.11

$$c = \left| f_c \pm n f_m \right|$$

where c is the combination tone position on the frequency axis, f_c is the carrier frequency, n is the integer 1, 2, 3, 4, 5,…, and f_m is the modulating frequency (Chowning, 1973). Combination tones with negative positions are 180˚ out of phase and will be represented as positive frequencies. Constructive and destructive interference between these phases will result in not all combination tones being present within the spectrum. Additionally, as the number of combination tones increases with the modulation intensity, spectral power is lateral redistributed from the carrier frequency to combination tones (Chowning, 1973).

The effect of varying SAR upon spectral analysis depends upon the magnitude of the time-depth distortion. If SAR variability is too great then any cyclic component will be lost. In the case where SAR is cyclic (e.g., forced by an orbital oscillation) or contain a trend then the effects are similar to FM (Schiffelbein and Dorman, 1986). Where an abrupt change occurs then two sets of spectral peaks will be present each corresponding to the different sedimentation rates. Random fluctuations will result in the broadening of spectral peaks, therefore, reducing spectral power. Distortions within time series are more clearly identified when using wavelet spectral analysis with examples given within the literature (Lau and Weng, 1995; Prokoph and Barthelmes, 1996).

Figure 2.12 (next page) | Examples of amplitude and frequency modulation and their effect upon calculated power spectra. (a) The synthetic short eccentricity (100 kyr) and precession (20 kyr) Milankovitch cycles used in this example (from Figure 2.7). **(b)** Example of an amplitude modulated (AM) signal. In this example the amplitude of the precession signal is being amplified or attenuated by the short eccentricity cycle. **(c)** REDFIT power spectrum of the AM signal indicating the presence of the precession carrier frequency (0.5 cycles/kyr) and two flanking combination tones (0.4 and 0.6 cycles/kyr). The modulating frequency is not represented by a spectral peak but as the distance between the combination tones and carrier frequency. **(d)** Example of a frequency modulated (FM) signal. Here the eccentricity cycle is causing the precession carrier frequency to either dilate or contract. **(e)** REDFIT power spectrum of the FM signal illustrating the presence of the carrier frequency (0.5 cycles/kyr) and several symmetrically distributed combination tones. The modulating frequency is not represented as a spectral peak but as the spacing between the combination tones. See the Appendix for MathWorks MATLAB `AM.m` and `FM.m` scripts for the creation of above AM and FM signals.

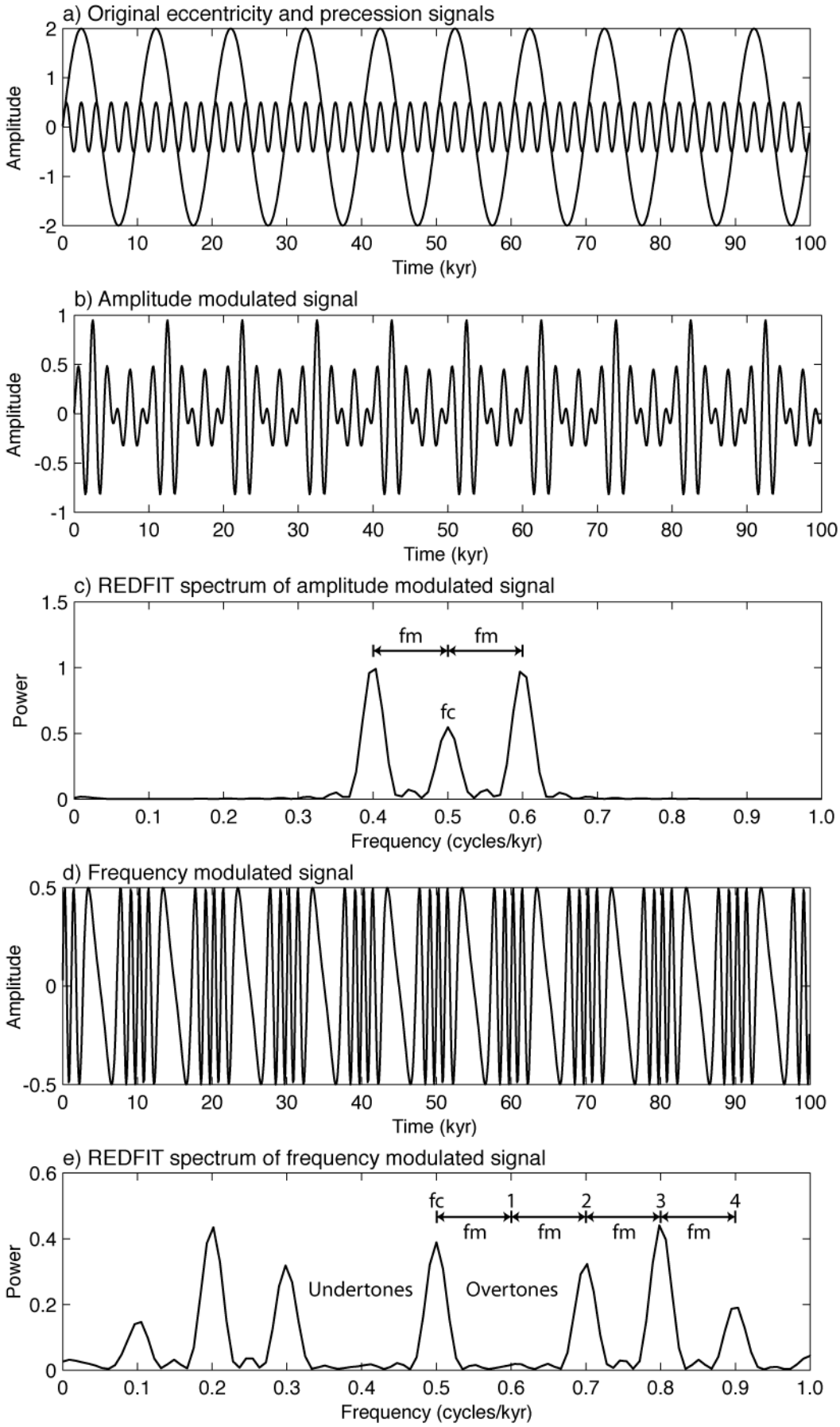
a) Original eccentricity and precession signals
Amplitude
Time (kyr)
b) Amplitude modulated signal
Amplitude
Time (kyr)
c) REDFIT spectrum of amplitude modulated signal
Power
fm
fm
fc
Frequency (cycles/kyr)
d) Frequency modulated signal
Amplitude
Time (kyr)
e) REDFIT spectrum of frequency modulated signal
Power
fc
1
2
3
4
fm
fm
fm
fm
Undertones
Overtones
Frequency (cycles/kyr)

2.10 Identification of orbital signals

2.10.1 Ratio Method

Identification of orbital signals within stratigraphic records that lack absolute age constraint is commonly achieved by using the ratios between significant frequencies. Within power spectra the ~5:2.5:1 ratio between peaks has traditionally been used as evidence for their presence of the short eccentricity (~100 kyr), dominant obliquity (~41 kyr) and precession (~23 kyr) orbital periods (e.g., Hays et al., 1976). However, the presence of harmonics and combination tones within power spectra caused by distortions to time series may also result in the identification of similar ratios (Hinnov, 2000; Meyers and Sageman, 2007). A prime example of the problems created by the combination of orbital and non-orbital forcing is depicted by the Latemar Controversy outlined by Meyers (2008).

2.10.2 Average Spectral Misfit

To overcome the limitations of the ratio method, Meyers and Sageman (2007) provide the average spectral misfit (ASM) algorithm. The ASM method objectively estimates an optimal sediment accumulation rate (SAR) for a stratigraphic time series containing orbital periods. The method also provides a formal statistical test for rejecting the null hypothesis (H_o) of no Milankovitch periods being present. The ASM method relies upon the multi taper method (MTM) harmonic F-test (Thomson, 1982; Thomson, 1990a) to identify significant frequencies. The MTM F-test provides a statistical test (F-test) for presence of pure sinusoidal components within the stratigraphic series with good frequency resolution. F-test significance results are independent of amplitude so the method is able to identify low amplitude peaks that are statistically significant as well as high amplitude peaks that are not. Meyers and Sageman (2007) advocate the method is ideal for cases where the orbitally controlled insolation signal is distorted during encoding within the sedimentary record.

The ASM method is achieved by firstly analysing the stratigraphic time series using the MTM and MTM harmonic F-test techniques. Frequencies exceeding the 90% MTM F-test confidence level, within a frequency range corresponding to ~80% of the total variance (area under the MTM spectrum curve), are isolated. Based upon these frequencies, objective SAR estimates are calculated for the stratigraphic time series. Each ASM simulation requires the input of the number of steps (max 200) and range of SARs to be analysed, the stratigraphic series Nyquist (N_f) and Rayleigh (R_f) frequencies, the age of the stratigraphic section (Ma), the orbital terms to be analysed (eccentricity, obliquity and/or precession) and the number of Monte Carlo simulations

to perform to determine null hypothesis significance levels (H_o). Application of the ASM was preformed in two steps with a wide SAR range and resolution, which were increased around regions of interest. The ASM process and results are illustrated in Figure 2.13 and Table 2.9.

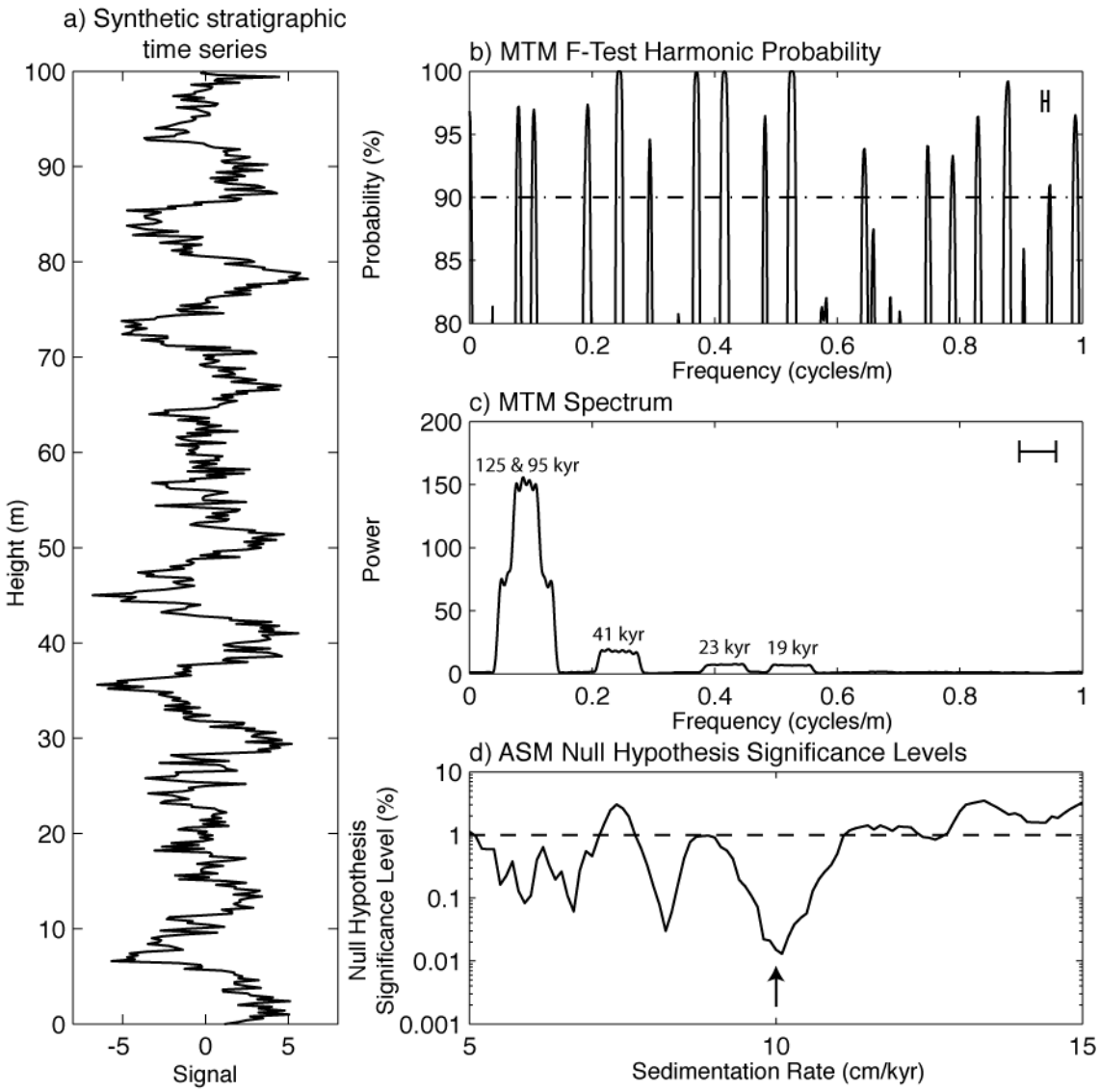

Figure 2.13 | Synthetic stratigraphic time series and ASM analysis. (a) Synthetic stratigraphic series containing 19, 24, 41, 95 and 125 kyr oscillations plus random noise. The stratigraphic series contains 501 data points with a sampling interval of 0.2 m yielding Rayleigh (R_f) and Nyquist (N_f) frequencies of 0.00998004 and 2.5 cycles/m respectively. The SAR is 10 cm/kyr. **(b)** Harmonic F-test showing the significance of frequencies within the 0 to 1 cycles/m range. Only those above 90% are considered for ASM analysis. Bandwidth (horizontal bar) is 0.00998004 cycles/m. **(c)** MTM spectrum calculated using 6 data tapers and a time-width product of 4 providing 12 degrees of freedom. The area under the curve represents the variance of the spectrum. Approximately 90% of the total variance is present between 0 to 1 cycles/m and is used to determine the frequency range to be analysed. MTM bandwidth (horizontal bar) is 0.05988024 cycles/m. **(d)** ASM analysis of the 16 significant frequencies within the 0 to 1 cycles/m frequency range provides 5 significant SAR estimates (Table 2.9). The most significant is 10.1 cm/kyr. Arrow represents 10 cm/kyr position of input SAR.

Table 2.9 – ASM results from synthetic stratigraphic time series

	SAR (cm/kyr)	5.9	6.7	8.2	10.1	12.6
	H_o (%)*	0.083	0.061	0.030	0.013	0.841
Frequency (cycles/m)†	F-test Significance (%)	Temporal Period (kyr)§				
0.081	97.2	210	185	151	**123**	99
0.105	97.0	161	142	116	**94**	76
0.193	97.3	88	77	63	51	41
0.244	100.0	69	61	50	**41**	33
0.294	94.6	58	51	41	34	27
0.370	99.9	46	40	33	27	21
0.416	100.0	41	36	29	**24**	19
0.482	96.4	35	31	25	21	16
0.526	100.0	32	28	23	**19**	15
0.645	93.8	26	23	19	15	12
0.747	94.1	23	20	16	13	11
0.789	93.3	21	19	15	13	10
0.830	96.4	20	18	15	12	10
0.879	99.2	19	17	14	11	9
0.947	91.0	18	16	13	10	8
0.989	96.5	17	15	12	10	8

*H_o significance level represents the probability that the null hypothesis of there being no orbital periods present at that SAR would be rejected in error. In other words, the probability of orbital period being present at that SAR estimate is H_o significance level subtracted from 100. Only those SAR estimates exceeding the critical level of 0.990099% are presented.

†Frequencies between 0-1 cycles/m selected as contains ~90% of total MTM spectral variance.

§Temporal periods in bold represent those expected from synthetic stratigraphic time series in Figure 2.13.

2.11 Application of spectral analysis techniques

Due to the various techniques of data collection the recovered time series within this research will in most cases be unevenly spaced. In these instances, interpolation shall be applied to create an evenly spaced time series by following the process outlined in Section 2.6.2.3. The evenly spaced time series will be subsequently analysed using the MTM, MTM F-test and Wavelet techniques outlined above and in Figure 2.14. Any possible spurious spectral results introduced by interpolation shall be avoided by also using the REDFIT spectral analysis technique as this is suited to unevenly spaced data. With each of these spectral analysis techniques using differing processes to calculate the Fourier transform, consistent results between methods shall indicate the reliability of spectral results.

The estimation of SARs will be achieved following the method of Meyers and Sageman (2007) who use the ASM algorithm. This is based upon the spectral results obtained from the MTM F-test. Although the majority of the time series are likely to be unevenly spaced, only the MTM F-test method has an adequately small bandwidth to work with the ASM method. The possible introduction of spurious spectral results due to interpolation within the ASM results will therefore require consideration.

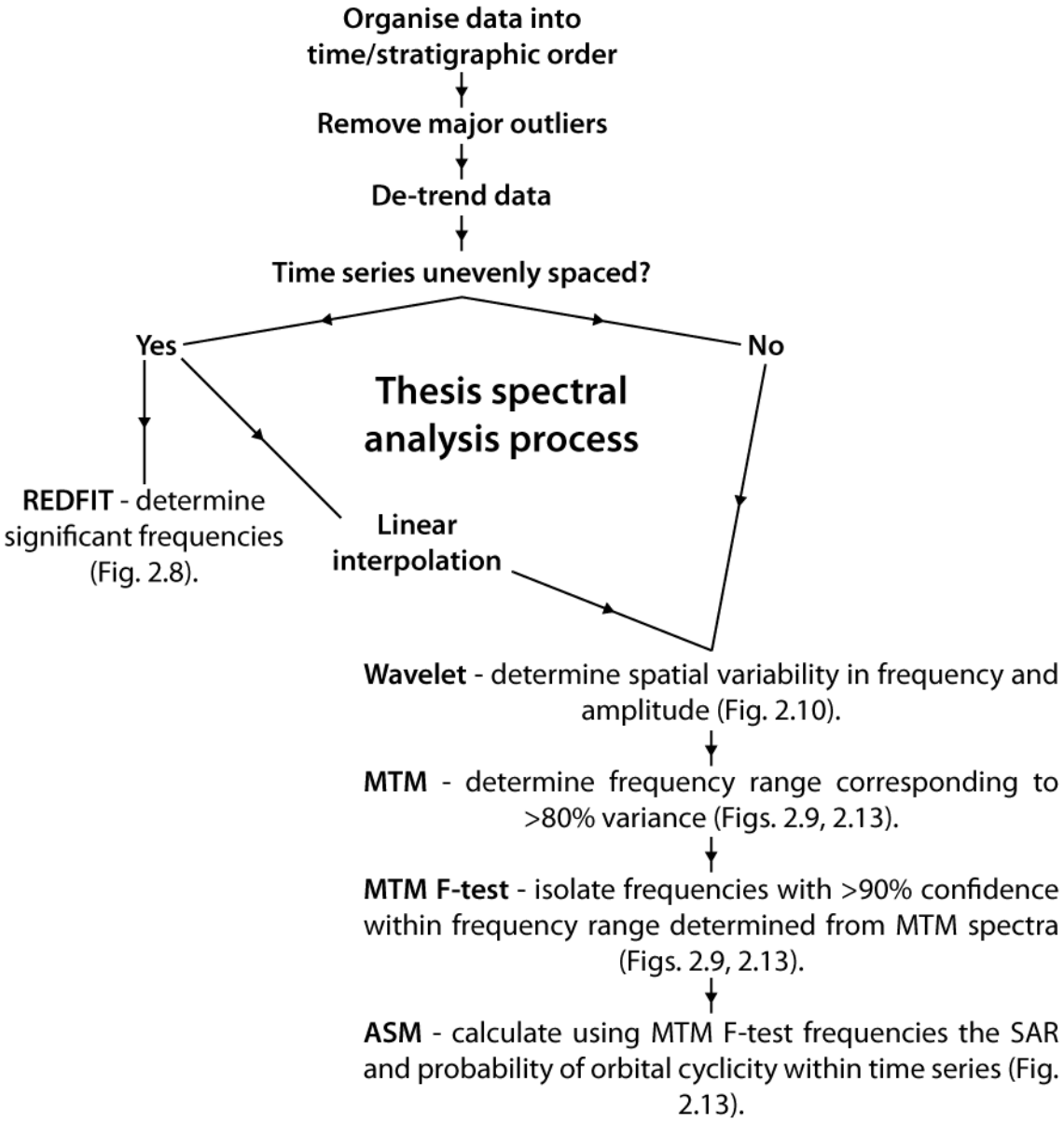

Figure 2.14 | The general process of time series analysis within this thesis. Using a range of spectral analysis techniques, significant frequencies can be confidently determined from both evenly and unevenly spaced data. The end result is the ability to identify orbital signals using both the ratio method and statistically using the ASM technique. The latter additionally provides an independent estimate for the sediment accumulation rate (SAR) for the time series. Details upon all of these techniques can be found within the text.

Chapter 3
Age Model for Ainsa basin

3.1 Introduction

3.1.1 Chapter objectives

Recently, it has been proposed that each sequence within the Ainsa basin was paced by a long eccentricity (404 kyr) glacio-eustatic cycle (Das Gupta and Pickering, 2008; Heard et al., 2008; Pickering and Bayliss, 2009; Sutcliffe and Pickering, 2009). This hypothesis provides a number of testable predictions, namely that:

- each sequence spans 404 kyrs;
- the duration of each depositional system can be estimated based upon the number of constituent sequences;
- the base of each sequence should coincide with a period of eccentricity minima;
- tectonics controlled the locus of coarse-clastic sediment deposition;
- the average sedimentation rate for the basin was ~40 cm/kyr.

Within this chapter, biostratigraphic data collected from the Upper Hecho Group of the Ainsa basin is used to construct an age model, thereby enabling the rigorous testing of the above predictions.

3.1.2 Biostratigraphic nomenclature

Within this chapter the standard calcareous nannofossil zonations (NP) of Martini (1971) and the large foraminiferal shallow benthic zonation (SBZ) of Serra-Kiel et al. (1998) are used. The ages for these biostratigraphic schemes are taken from Time Scale Creator 4.2.5 (Ogg et al., 2010), which is based upon the updated GTS2004 time scale (Gradstein et al., 2004), unless stated otherwise.

3.1.3 Previous dating of the Upper Hecho Group

Current dating of the Upper Hecho Group within the Ainsa basin is limited (Bentham and Burbank, 1996; Dreyer et al., 1999; Jones et al., 2005; Pickering and Corregidor, 2005), being based mainly upon stratigraphic correlations with the equivalent down-dip Jaca basin sediments (Figs. 1.8, 3.1) (Labaume et al., 1985; Payros et al., 1999; Oms et al., 2003; Remacha et al., 2003). The accuracy of these correlations has proven controversial due to the lack of Hecho Group preservation across the Boltaña anticline (Das Gupta and Pickering, 2008; Caja et al., 2010).

The base of the Upper Hecho Group within the Ainsa basin is represented by the initiation of the Banaston System. The down-dip equivalent within the Jaca basin contains megaturbidite-5 (MT-5) which resides within nannofossil zone NP15 (Labaume et al., 1985), Chron 20r (Oms et al., 2003) and around the planktonic foraminiferal P10-11 zone boundary (Payros et al., 1999). These data suggest the maximum age of the Banaston System is 45.4 Ma. However, other authors date the base of the Banaston Allogroup within the Jaca basin (TSU-4) as 47.8 Ma (Remacha et al., 2003; Remacha et al., 2005).

The upper limit of the Upper Hecho Group within the Ainsa basin is represented as the 'unconformity' between the top of the Guaso System and overlying Sobarbe Formation (Dreyer et al., 1999; Sutcliffe and Pickering, 2009). In the field this unconformity is represented as a horizon of dark grey marl. Dating of this transition places it within Chron 20n (Bentham and Burbank, 1996) and SBZ15 (Dreyer et al., 1999) therefore indicating an age between 41.6-42.3 Ma.

A combination of the above magneto- and bio-stratigraphic studies (Fig. 3.1) suggests that the Upper Hecho Group was deposited between 41.6-42.3 and 45.3-47.8 Ma, therefore, spanning 3.7-6.2 Myr.

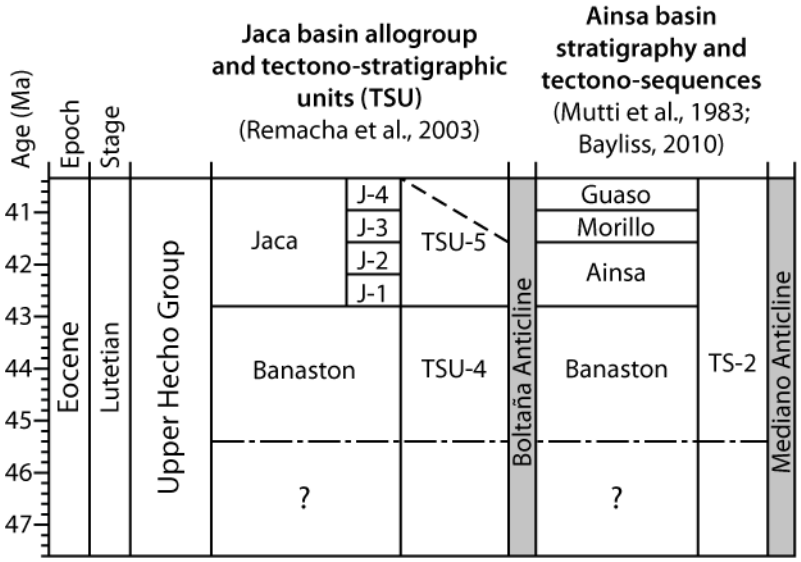

Figure 3.1 | Current Upper Hecho Group stratigraphic and tectono-stratigraphic correlations across the Boltaña anticline. Timing of Jaca basin allogroups based upon Remacha et al. (2003). Application of this time scale to the adjacent Ainsa basin sediments dependant upon accuracy of inter-basin correlation. Correlation lines between Ainsa and Jaca basin allogroups and systems based upon Das Gupta and Pickering (2008) and Caja et al. (2010). The base of the Banaston System (base Upper Hecho Group) remains uncertain at either 45.4 or 47.8 Ma (see text).

3.2 Materials and methods

3.2.1 Palaeontological sampling

As part of this research, palaeontological samples were collected along various transects throughout the basin during several field seasons (Fig. 3.2; Table 3.1). Large benthic foraminiferal (LBF) samples were collected as either individual tests taken directly from outcrop or as LBF-rich sediment samples. LBF samples were commonly associated with mass transport complexes (MTCs) and turbiditic deposits (Plates 5.1; 3.1). Hemipelagic sediments stratigraphically contiguous to these MTCs and turbiditic deposits were collected at each location for calcareous nannofossil analysis. Additional bulk sediment samples were collected during later field seasons (those with G1/2 and NS prefix) and from the Ainsa core (A6 prefix).

A composite basin stratigraphy (Fig. 3.4; Table 3.2) was partly compiled from detailed measured sections (Chapters 4, 5 and 6) and Ainsa well data from Pickering and Clark (2012). The remaining estimates were obtained from the measurement of the horizontal distances from the geological map of the Ainsa basin (Pickering and Bayliss, 2009), which were converted to stratigraphic thickness using measured dips (Fig. 3.2). The lower and upper limits of the measured stratigraphy are taken as the base of the Gerbe System (Pickering and Bayliss, 2009) and the Buil Nummulite banks of the Sobrarbe deltaic complex (Dreyer et al., 1999), respectively.

Palaeontological samples were located within the basin stratigraphy using either their GPS location or known positions within the measured sections. Where collected away from measured sections, samples were positioned within the basin stratigraphy based upon their location relative to laterally extensive deposits, usually submarine fans.

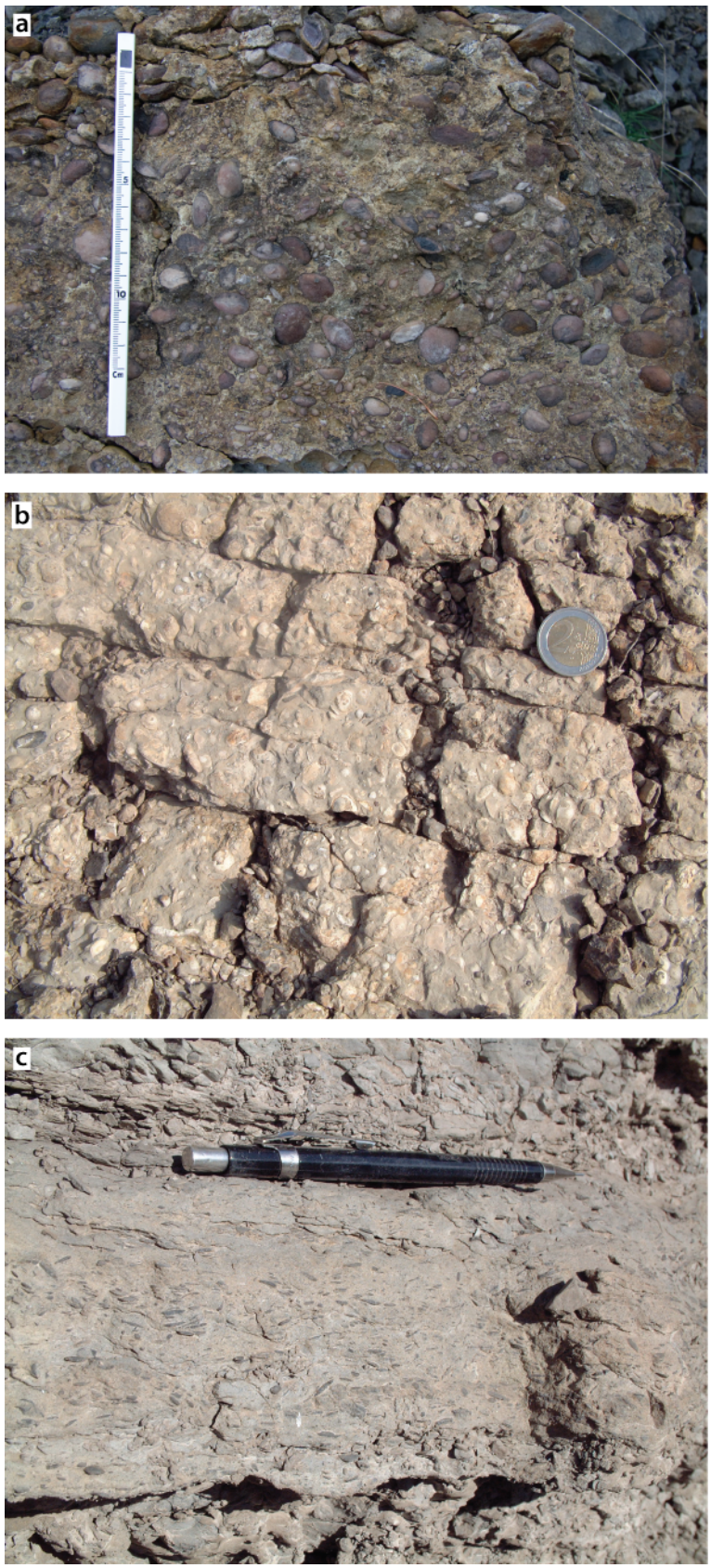

Plate 3.1 | Examples of Nummulite-rich sediments at outcrop from throughout the basin. (a) Nummulite wackestones of the Buil Nummulite banks of Dreyer et al. (1999) observed at location D007. **(b)** Bioclastic wackestone sampled at location AI013 containing a variety of marine fauna. Two Euro coin for scale. **(c)** Nummulite wackestone showing preferred alignment during deposition within the Fosado System.

Table 3.1a – Upper Hecho Group palaeontological samples

Height (m)*	UTM Coordinate†	Sample	System & Sequence		Notes
2266.0	0261332 4694762	BUIL-3, 4, 5, D007	DELTA		Buil Nummulite bank
2211.7	0259097 4695432	D004	DELTA		Estimated position
2104.1	0262117 4696234	D003	DELTA		Estimated position
2052.1	0258512 4695245	D002	DELTA		Estimated position
2015.4	0258357 4695319	D001	DELTA		Estimated position
1994.0	0260437 4686614	MFS-4 (+1m)	GUASO		MFS-4 equates to top Guaso / base delta unconformity
1841.7	0262383 4696972	GU015, GUB015	GUASO	G2	G2 fan
1829.0	0260210 4700041	GU017	GUASO	G2	G2 fan
1829.0	0262636 4697312	GU014, GUB014	GUASO	G2	G2 fan
1795.8		G1/2-208	GUASO	G1	42.75m above top G1 sand
1781.8		G1/2-133	GUASO	G1	28.75m above top G1 sand
1770.1	0261775 4698851	MFS-2 (0m) / MFS-1	GUASO	G1	17.03m above top G1 sand
1768.6	0261775 4698851	MFS-2 (-1.5m)	GUASO	G1	16.03m above top G1 sand
1765.9		G1/2-071	GUASO	G1	12.83m above top G1 sand
1762.3		G1/2-049	GUASO	G1	9.28m above top G1 sand
1757.8		G1/2-026	GUASO	G1	4.78m above top G1 sand
1755.5		G1/2-013	GUASO	G1	2.46m above top G1 sand
1738.0	0263219 4697625	GU012	GUASO	G1	Mid G1 sand
1728.0	0261873 4699270	NS-14	MORILLO	M3	0.4m below base G1 sand
1725.5	0261873 4699270	NS-15	MORILLO	M3	2.5m below NS-14
1692.0	0263690 4697625	M005	MORILLO	M3	Top M3 sand
1667.0	0263763 4697692	M004, MB004	MORILLO	M3	Base M3 sand
1597.8	0264786 4696242	M009	MORILLO	M2	Upper 1/3 M2
1583.0	0263993 4697974	AI023	MORILLO	M2	Mid M2
1560.0	0265357 4695369	M002, MB002	MORILLO	M1	Base M2
1466.2	0258590 4701671	M012	MORILLO	M1	Base M1
1460.0	0264469 4698237	AI021	MORILLO	M1	Base M1
1425.0	0262948 4701632	AI014, AIB014	AINSA	A3	Top MTC of Forcaz Stream
1425.0	0262962 4701692	NS-10	AINSA	A3	Same estimated horizon as AI014
1421.0	0263035 4701577	AI013	AINSA	A3	2-3m above AI011
1419.0	0263008 4701620	AI011 / AI011B	AINSA	A3	~20m above AI008
1413.0	0263038 4701624	AI012, AIB012	AINSA	A3	6m below AI011
1398.4	0263145 4701629	AI008	AINSA	A3	261.4m above top A2 sand
1398.4		Ainsa-228.4m	AINSA	A3	Same as AI008, 261.4m above top A2 sand
1361.5		Ainsa-191.5m	AINSA	A3	224.5m above top A2 sand
1360.7	0263153 4701693	AI007, AIB007	AINSA	A3	~1m below 76.9m sample
1345.7		Ainsa-175.69m	AINSA	A3	208.69m above top A2 sand
1323.2		Ainsa-153.18m	AINSA	A3	186.18m above top A2 sand
1284.0	0263354 4701662	NS-09	AINSA	A3	146.96m above top A2 sand
1274.0	0263236 4701775	AI015	AINSA	A3	137m above top A2 sand
1274.0	0263373 4701663	NS-17	AINSA	A3	137m above top A2 sand
1210.0		A6/37-3	AINSA	A2	~73m above top A2 sand
1197.3	0263578 4701710	NS-13	AINSA	A2	60.3m above top A2 sand
1183.6	0263620 4701704	NS-11	AINSA	A2	46.28m above top A2 sand
1182.7	0263620 4701704	NS-12	AINSA	A2	45.32m above top A2 sand
1118.0	0263713 4701908	AI003	AINSA	A2	7m above AIB003
1111.0	0263739 4701916	AI002, AIB002	AINSA	A2	Base A2 sand
1111.0	0263740 4701917	NS-08	AINSA	A2	Same estimated horizon as AI002
1111.0	0263740 4701917	NS-07	AINSA	A2	Same estimated horizon as AI002
1109.0	0265268 4698472	NS-03	AINSA	A1	2m below base A2 sand
1106.0	0265268 4698472	NS-02	AINSA	A1	5m below base A2 sand
1074.5	0263956 4702018	AI016, AIB016	AINSA	A1	
1028.0	0265309 4698555	NS-04	AINSA	A1	5m above top A1 fan
1027.0	0265289 4698581	NS-01	AINSA	A1	2m above top A1 fan
1027.0	0265270 4698614	AI028	AINSA	A1	2m above top A1 fan
1025.0	0265291 4698603	AI027, AIB027	AINSA	A1	Very top A1 sand
1016.6	0265399 4698410	NS-05	AINSA	A1	Basal hemipelagic
1016.1	0265399 4698410	NS-06	AINSA	A1	0.5m below NS-05
1001.0	0262643 4704269	NS-27	BANASTON	B6	~15m below A1 fan

Table 3.1b – Upper Hecho Group palaeontological samples

Height (m)*	UTM Coordinate†	Sample	System & Sequence		Notes
974.3	0262730 4704278	NS-26	BANASTON	B6	199.7m above base B5 sand
953.1	0262806 4704299	NS-25	BANASTON	B6	178.6m above base B5 sand
929.0	0267559 4698297	B005	BANASTON	B5	Top B5 sequence
929.0	0267225 4698473	B004, BB004	BANASTON	B5	Top B5 sequence, same as B005
897.4	0262978 4704295	NS-24	BANASTON	B5	122.9m above base B5 sand
878.2	0267618 4698345	B006B, BB006	BANASTON	B5	50.82m below B005
816.8	0263217 4704320	NS-23	BANASTON	B5	42.3m above base B5 sand
775.0	0263283 4704319	Ban-134.5m	BANASTON	B5	Base B5 sand
774.0	0263281 4704321	NS-22	BANASTON	B4	0.85m below base B5 sand
767.0	0263322 4704328	NS-21	BANASTON	B4	7.5m below base B5 sand
749.0	0263413 4704340	NS-20	BANASTON	B4	25.5m below base B5 sand
680.0	0263499 4704375	NS-19	BANASTON	B3	94.92m below base B5 sand
651.0	0263583 4704375	NS-18	BANASTON	B3	123.9m below base B5 sand
619.0	0268098 4698432	B013, BB013	BANASTON	B3	Position measured from map§, ~62m from base Ban-3
589.0	0268112 4698461	B014	BANASTON	B3	Position measured from map, ~32m from base Ban-3
552.4	0268158 4698498	B015	BANASTON		8-10m below B014, ~top B2
470.0	0268283 4698518	B016, BB016	BANASTON	B2	Position measured from map, ~87m from top Ban-2
366.0	0268643 4698557	B022	BANASTON	B1	Position measured from map, ~18m from top Ban-1
334.0	0268768 4698640	B026	BANASTON	B1	Position measured from map, ~32m below BB022
135.1	0268533 4697219	NS-28	GERBE		Estimated position on log
108.6	0268577 4697283	NS-29	GERBE		3m above top Gerbe sands
105.0	0268289 4696090	GB001	GERBE		Very top Gerbe-2
76.1	0269446 4696228	GB004	GERBE		

*Height position relative to base of Gerbe System.
†GPS positions using WGS84 datum and un zone UTM 31T.
§Positions measured using horizontal distances corrected for dip obtained from Ainsa basin geological map (Pickering and Bayliss, 2009).

Figure 3.2 (next page) | Sample and measured section positions marked upon the Ainsa basin geological map of Pickering and Bayliss (2009). Palaeontological samples collected from throughout the Upper Hecho Group. Details are provided within Table 3.1. Detailed logging (Chapters 4-6) and drilling of the Ainsa wells (Pickering and Corregidor, 2005; Pickering and Clark, 2012) provide accurate stratigraphic thickness estimates of several sections. Several of these are presented in Figure 3.3. The thickness of remaining intervals was estimated using distances and dips obtained from the geological map.

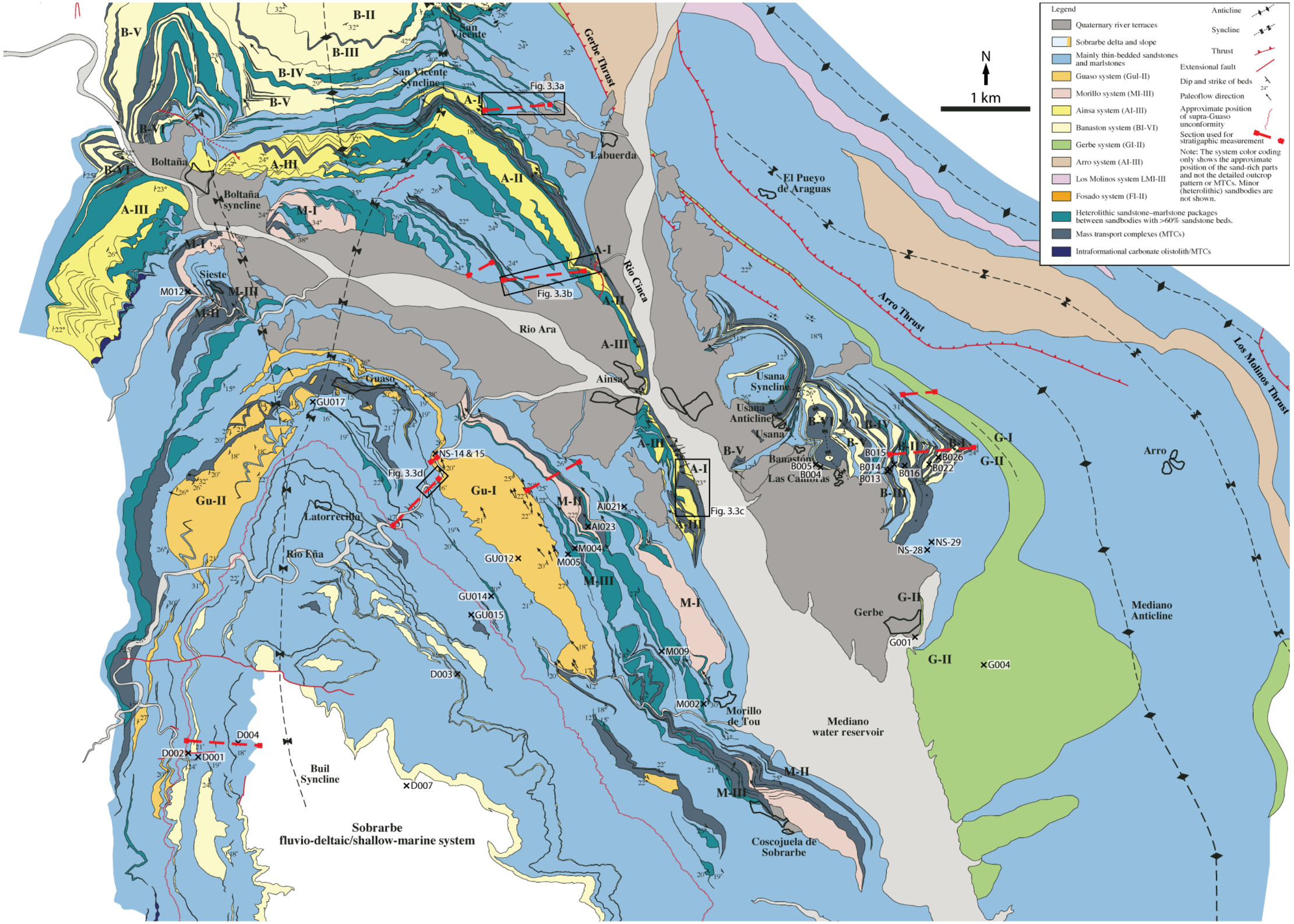
Legend
Quaternary river terraces
Sobrarbe delta and slope
Mainly thin-bedded sandstones and marlstones
Guaso system (Gul-II)
Morillo system (MI-III)
Ainsa system (AI-III)
Banaston system (BI-VI)
Gerbe system (GI-II)
Arro system (AI-III)
Los Molinos system LMI-III
Fosado system (FI-II)
Heterolithic sandstone–marlstone packages between sandbodies with >60% sandstone beds.
Mass transport complexes (MTCs)
Intraformational carbonate olistolith/MTCs
Anticline
Syncline
Thrust
Extensional fault
Dip and strike of beds
Paleoflow direction
Approximate position of supra-Guaso unconformity
Section used for stratigaphic measurement
Note: The system color coding only shows the approximate position of the sand-rich parts and not the detailed outcrop pattern or MTCs. Minor (heterolithic) sandbodies are not shown.
N
1 km
Gerbe Thrust
San Vicente
San Vicente Syncline
Fig. 3.3a
Labuerda
El Pueyo de Araguas
Arro Thrust
Los Molinos Thrust
Boltaña
Boltaña syncline
Sieste
Río Cinca
Fig. 3.3b
Río Ara
Ainsa
Usana Syncline
Usana Anticline
Usana
Banastón
Las Cámaras
Arro
Guaso
Fig. 3.3d
Fig. 3.3c
Gu-II
Gu-I
Latorrecilla
Río Ena
Gerbe
Mediano Anticline
Mediano water reservoir
Morillo de Tou
Coscojuela de Sobrarbe
Buil Syncline
Sobrarbe fluvio-deltaic/shallow-marine system
B-V
B-IV
B-III
B-II
A-III
A-II
A-I
M-III
M-II
M-I
G-II
G-I
M012
GU017
NS-14 & 15
AI021
AI023
M004
M005
GU012
GU014
GU015
D003
M009
M002
G001
G004
NS-28
NS-29
B015
B014
B013
B016
B026
B022
B005
B004
D004
D002
D001
D007

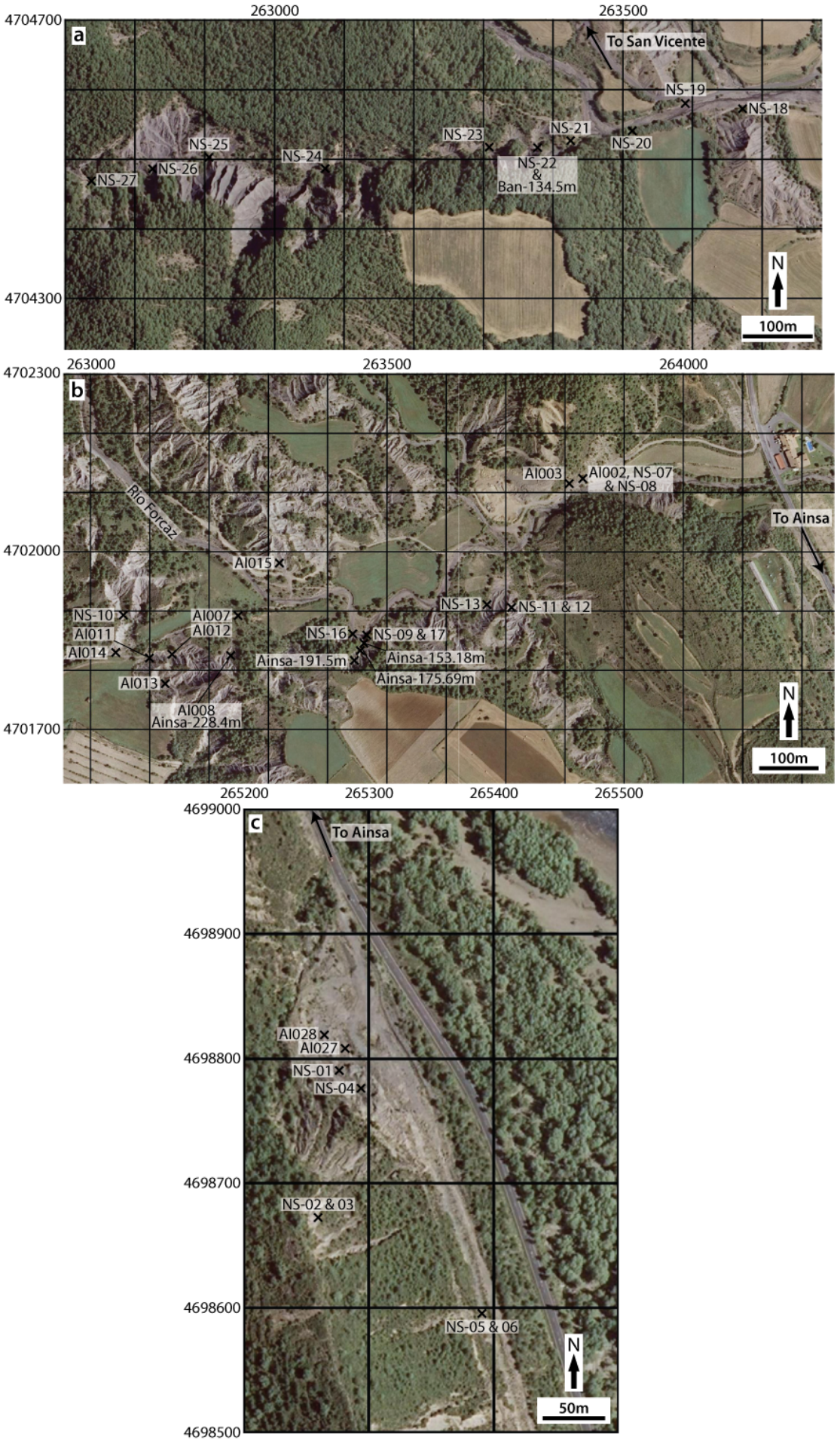
a
263000
263500
4704700
4704300
To San Vicente
NS-19
NS-18
NS-21
NS-20
NS-23
NS-25
NS-24
NS-22
&
Ban-134.5m
NS-26
NS-27
N
100m
b
263000
263500
264000
4702300
4702000
4701700
Río Forcaz
AI003
AI002, NS-07
& NS-08
To Ainsa
AI015
NS-13
NS-11 & 12
NS-10
AI007
AI012
AI011
AI014
NS-16
NS-09 & 17
Ainsa-191.5m
Ainsa-153.18m
Ainsa-175.69m
AI013
AI008
Ainsa-228.4m
N
100m
c
265200
265300
265400
265500
4699000
4698900
4698800
4698700
4698600
4698500
To Ainsa
AI028
AI027
NS-01
NS-04
NS-02 & 03
NS-05 & 06
N
50m

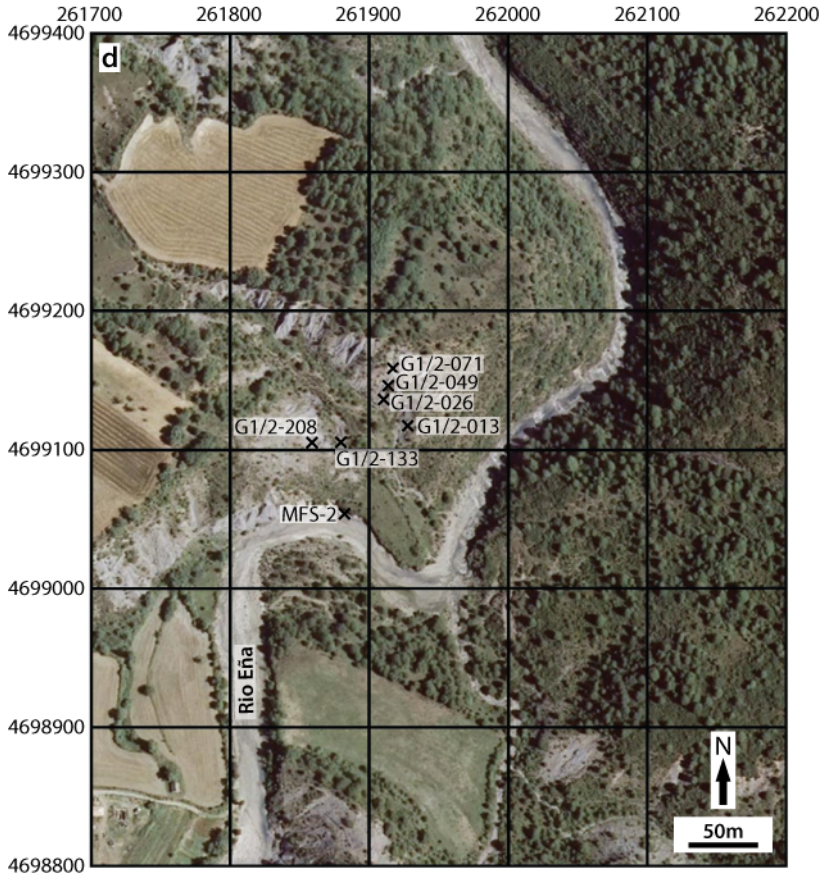

Figure 3.3 (above and previous page) | Areas of intensive sampling within the Upper Hecho Group of the Ainsa basin. In association with several detailed measured sections taken through the Banaston **(a)**, Ainsa **(b)** and Guaso **(d)** systems (Chapters 4-6), bulk sediment samples were collected to constrain their age and duration. The Ainsa Quarry **(c)** outcrop was also intensively sampled. UTM zone 31 coordinates are used, aerial images from http://sigpac.mapa.es/fega/visor/.

3.2.2 Sample preparation

LBF samples requiring disaggregation were initially fragmented using a hammer and placed in boiling water for ~1 hour and subsequently passed through a very-fine sieve to remove clay- and silt-sized particles. Samples were placed within crucibles and dried overnight at ~50˚C. Liberated tests were hand picked from the sediment and the residue set aside. Thin sections were created using randomly selected tests from each sample or directly from bulk sediment sample (e.g., Plates 3.1, 5.1). Nannofossil smear slides were made from cleaned bulk sediment samples in the standard manner (Bown and Young, 1998).

3.2.3 Basin age model construction

Large benthic foraminiferal and nannofossil assemblages were analysed by Drs M. BouDagher-Fadel and P. Bown, respectively, at University College London. The upper and lower bounds of each SBZ is positioned mid-point between adjacent sample points

representing contrasting assemblages. Nannofossil event positions represent midpoints between samples containing the first (FO) or last (LO) occurrence of a specific species and adjacent samples including or excluding that species.

The Upper Hecho Group age model was constructed using the NP events as these represent discrete data points relative to the broad shallow benthic zones (Fig. 3.5). Age error envelopes were estimated from the height error bars. The gradients and intercepts determined from the age error envelopes and midpoints were used to estimate the age for each system, sequence and complex. Sediment accumulation rates (SAR) are determined between each pair of NP data midpoints. Minimum and maximum SAR values were determined for each interval based upon the height errors.

Table 3.2 – Upper Hecho Group thickness estimates

System / Complex	Thickness (m)	Cumulative Thickness (m)	Source
Delta	273	2266	Estimated*
Guaso-2 marl	163	1993	Estimated
Guaso-2 sand	2	1830	Outcrop logging 2008
Guaso-1 marl	75	1828	Outcrop logging 2008[†]
Guaso-1 sand	25	1753	Estimated
Morillo-3 marl	36	1728	Estimated
Morillo-3 sand	25	1692	Estimated
Morillo-2 marl	57	1667	Estimated
Morillo-2 sand	50	1610	Estimated
Morillo-1 marl	79	1560	Estimated
Morillo-1 sand	21	1481	Estimated
Ainsa-3 marl	194	1460	Outcrop logging 2008/10[§] and estimation
Ainsa-3 sand	56	1266	Outcrop logging 2008/10
Ainsa-2 marl	73	1210	Outcrop logging 2008/10, A6 Well
Ainsa-2 sand	26	1137	L2 Well (Pickering and Clark, 2012)
Ainsa-1 marl	86	1111	L1 Well (Pickering and Clark, 2012)
Ainsa-1 sand	9	1025	L1 Well (Pickering and Clark, 2012)
Banaston-6 marl	46	1016	Warburton Logging 2010[#]
Banaston-6 sand	41	970	Warburton Logging 2010
Banaston-5 marl	140	929	Warburton Logging 2010
Banaston-5 sand	14	789	Warburton Logging 2010
Banaston-4 marl	75	775	Quarmby Logging August 2009[#]
Banaston-4 sand	15	700	Quarmby Logging August 2009
Banaston-3 marl	35	685	Quarmby Logging August 2009
Banaston-3 sand	93	650	Estimated
Banaston-2	173	557	Estimated
Banaston-1	218	384	Estimated
Gerbe Marl	61	166	Estimated
Gerbe-1 & 2	105	105	Estimated
Base Gerbe		0	

*Thickness estimated from converting horizontal distance measured from the Ainsa basin geological map into stratigraphic thickness using dips obtained from Figure 3.2.
[†]Details within Chapter 4 – Guaso System.
[§]Details within Chapter 5 – Ainsa System.
[#]Details within Chapter 6 – Banaston System.

3.3 Results

3.3.1 Upper Hecho Group stratigraphic thickness

A composite stratigraphy for the Upper Hecho Group was constructed around the measured sections marked in Figure 3.2. The total stratigraphic section measures 2,266 m and spans from the base of the Gerbe System to the top of Sobrarbe Formation. Individual system and complex height estimates are provided in Table 3.2.

3.3.2 Biostratigraphic markers

Within the Upper Hecho Group, nine NP datum events are identified (Table 3.3). Sediments of the lowermost Gerbe System contained the FO of *Blackites piriformis* placing the system within Zone NP14. The Banaston System spans both subzones NP14b and 15a based upon the FO and LO of *Blackites inflatus* and the single occurrence of *Nannotetrina fulgens*. The overlying Ainsa System contains the FO of *Sphenolithus furcatolithoides* along with the FO and LO of *Chiasmolithus gigas* placing the system within Subzone NP15b. Guaso System sediments yielded the FO of *Reticulofenestra umbilicus* and the LO of *S. furcatolithoides*, which are dated as occurring at 41.4 and 40.1 Ma (Agnini et al., 2011), respectively. Also present throughout the studied section are numerous reworked Cretaceous species. The full results table and images of individual taxa (Appendix Plate 1.1) are provided within the Appendix.

Analysis of the large benthic foraminifera place the Banaston System specimens within SBZ13 based upon the presence of an assembalge including *Nummulites laevigatus, N. obesus, N.* spp., N. syrticus, *Assilina* spp. *Assilina abrardi, N. lehneri, N. messinae, Alveolina elliptica,* and *Discocyclina* sp. The Ainsa System is placed within SBZ14 derived from an assemblage containing *N. beneharnenesis,* cf. *N. crassus, N. obesus, N. boussaci, Assilina spira, A. exponens, A. suteri, N. perforatus, Discocyclina* sp. and *Alveolina munieri.* The Morillo System contained *N. perforatus, Assilina exponens, N. aturicus, Discocyclina balatonica, N. boussaci* and *N. crassus* indicating the system spans both SBZ15 and 16. The youngest assemblages contain *N. perforatus, N. brongniarti,* and *N. Lyelli*, which place the Guaso System and Sobrarbe Formation deposits within SBZ17.

Table 3.3 – Upper Hecho Group palaeontological results

Height (m)	Sample	SBZ*	SB Marker	SBZ Event Age (Ma)	NP	NP Marker Event	NPZ Event Age (Ma)†
2266.0	BUIL-3, 4, 5, D007	17	*N. Lyelli, N. brongniarti*				
1994.0	MFS-4 (+1m)				16	LO *S. furcatolithoides*	40.1
1841.7	GU015, GUB015	17			16		
1829.0	GU017	17					
1829.0	GU014, GUB014	17	*N. brongniarti*		16		
1738.0	GU012	17	Base SBZ17	40.44			
1725.5	NS-15					FO *R. umbilicus*	41.4
1692.0	M005	16	*N. aturicus, A. exponens*	40.44			
1667.0	M004, MB004	16	*N. aturicus,* A. exponens				
1597.8	M009	15/16					
1583.0	AI023	15/16					
1560.0	M002, MB002	15/16					
1466.2	M012	15/16					
1460.0	AI021	15/16	Base SBZ15	42.33			
1425.0	AI014, AIB014				15b	LO *C. gigas*	43.55
1421.0	AI013	16	*N. aturicus*				
1419.0	AI011 / AI011B	14	Top SBZ14	42.33			
1413.0	AI012, AIB012				15b	*C. gigas*	
1398.4	AI008	15	*N. crassus,* A. exponens				
1398.4	Ainsa-228.4m	14					
1361.5	Ainsa-191.5m	14					
1360.7	AI007, AIB007				15b	FO *S. furcatolithoides*	45.1
1345.7	Ainsa-175.69m	14					
1323.2	Ainsa-153.18m	14					
1274.0	AI015	14	*N. beneharnensis, A. exponens*				
1210.0	A6/37-3				15b	FO *C. gigas*	45.35
1118.0	AI003	14					
1111.0	AI002, AIB002	14					
1027.0	AI028	14					
1025.0	AI027, ABI027	14	Base SBZ14	45.44			
929.0	B005	13	Top SBZ13	45.44			
878.2	B006B, BB006	13					
775.0	Ban-134.5m				15a	FO *N. fulgens*	46.57
619.0	B013, BB013	13			14b	LO *B. inflatus*	46.67
589.0	B014	13					
552.4	B015	13	*N. laevigatus*				
470.0	B016, BB016	13			14b	FO *B. inflatus*	47.92
366.0	B022	13					
334.0	B026	13	Lowermost SBZ13	48.6			
105.0	GB001				14	FO *B. piriformis*	48.02

*Shallow benthic zonation (SBZ) of Serra-Kiel et al. (1998).
†Nannofossil zoneation of Martini (1971). Nannofossil event ages for the LO of *B. inflatus* and FO B. of *B. piriformis* are of Molina et al. (2011). LO of *S. furcatolithoides* from Agnini et al. (2011).

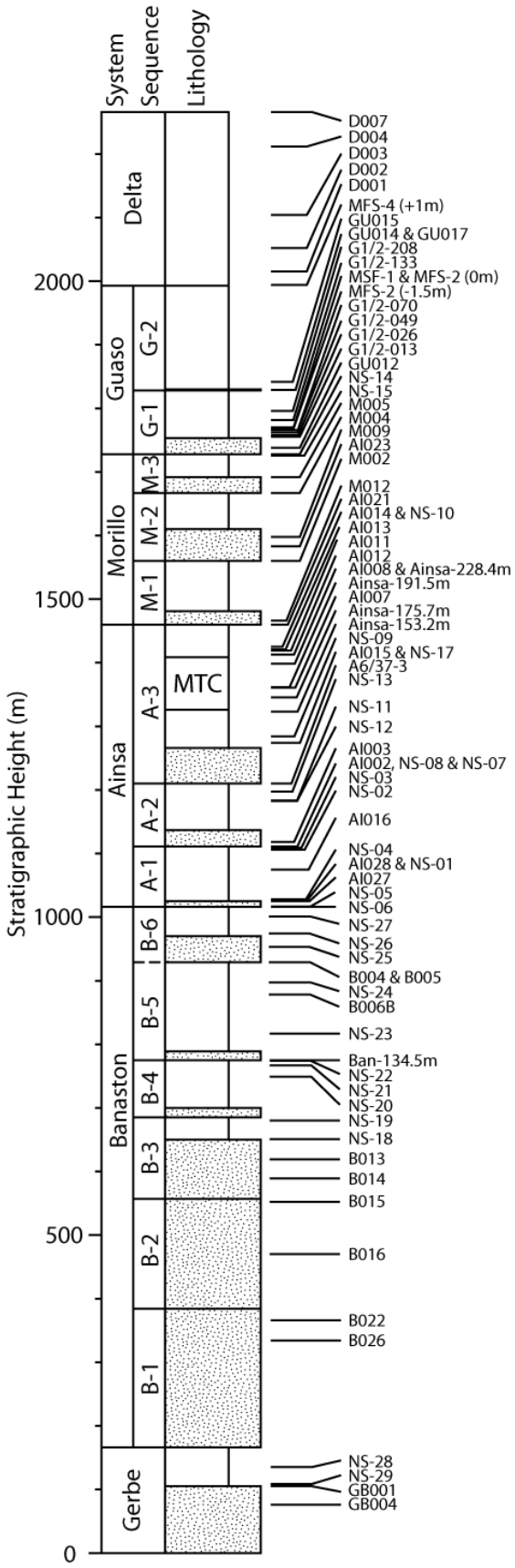

Figure 3.4 | Composite Upper Hecho Group stratigraphy determined from detailed measured sections and basin geological map. Palaeontological samples collected from throughout the Upper Hecho Group and placed within stratigraphy to enable the construction of an age model (Fig. 3.5).

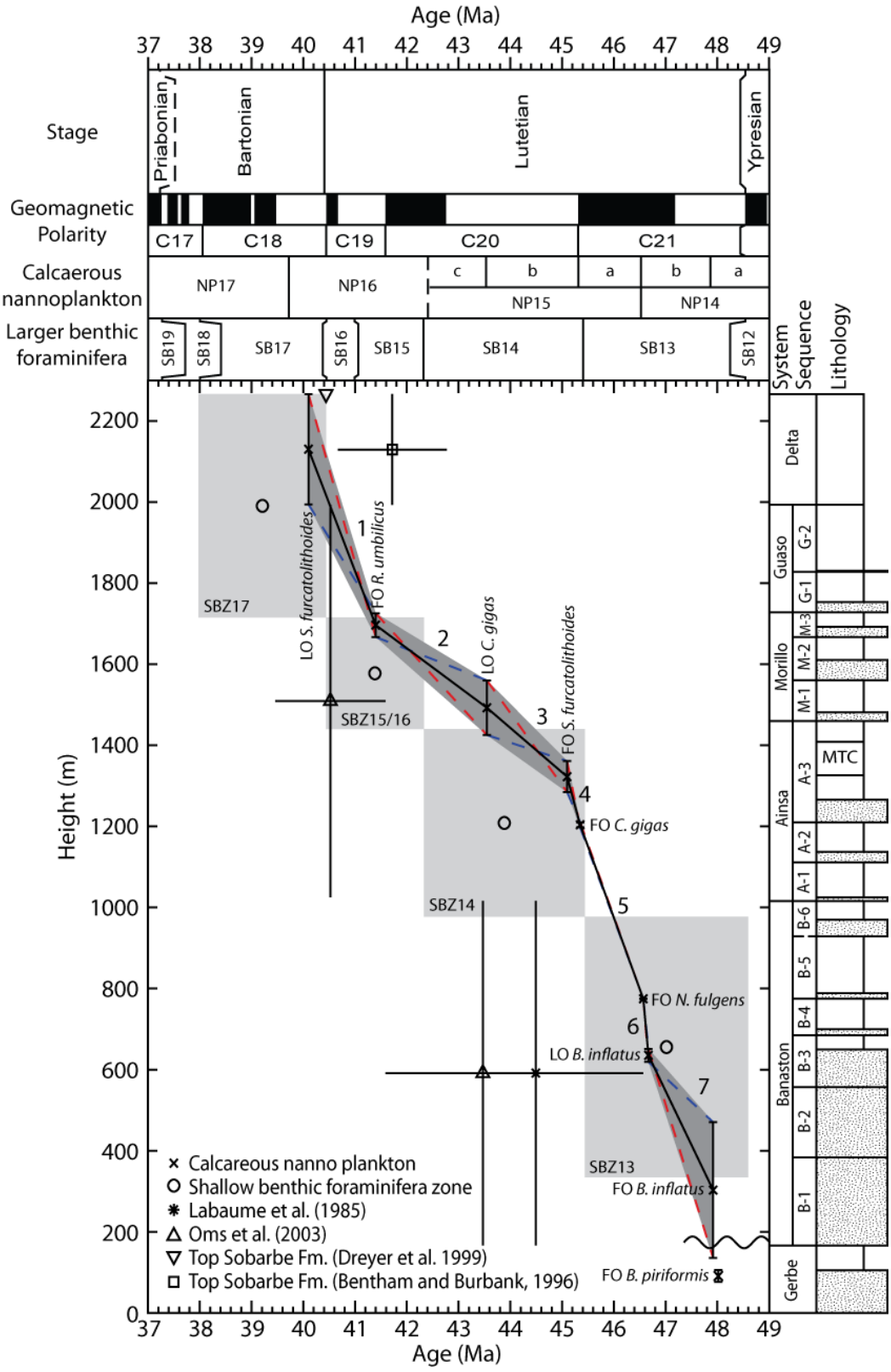

Figure 3.5 | Upper Hecho Group age model. Using the composite Upper Hecho Group stratigraphy (Fig. 3.4) and biostratigraphic events (Table 3.1) an age model is constructed. Nannofossil events are here utilised to construct the age model as these represent discrete points in time rather than broad shallow benthic zones (grey boxes). Mean (black solid line), minimum (blue dashed line) and maximum (red dashed line) sediment accumulation rates are determined from height error bars for each numbered interval (1-7). Dark grey shaded area represents age uncertainty. The equations of the lines (Table 3.4) representing the upper and lower bounds of the age uncertainty along with the mid point line are used to date the Upper Hecho Group.

Table 3.4 – Equations used to estimate Upper Hecho Group ages*

	Lower		Mid		Upper	
Interval†	Slope	Intercept	Slope	Intercept	Slope	Intercept
1	-251.54	12080.73	-333.65	15509.56	-415.77	18938.39
2	-112.56	6326.95	-94.77	5619.66	-76.98	4912.38
3	-90.99	5387.81	-109.79	6273.91	-128.59	7160.01
4	-346.64	16917.46	-474.70	22731.34	-602.76	28545.21
5	-347.01	16934.16	-351.80	17157.97	-356.60	17381.78
6	-1549.90	72952.83	-1394.95	65737.31	-1240.00	58521.79
7	-387.10	18685.14	-265.95	13046.79	-144.79	7408.43

*Equations of the lines representing the upper, mid and lower age bounds within the age model (dark grey shading and black solid line in Figure 3.5) are used to calculate the ages in Tables 3.5, 3.6.
†Intervals correspond to those in Figure 3.5.

Table 3.5 – Calculated complex durations

Complex	Height to top (m)	Age (Ma)*			Duration (Myr)		
		Min	Mid	Max	Min	Mid	Max
Delta	2266			40.10	0.00		
Guaso-II marl	1993	40.10	40.51	40.76	0.00	0.49	1.04
Guaso-II sand	1830	40.75	41.00	41.15	0.00	0.01	0.40
Guaso-I marl	1828	40.76	41.01	41.15	0.00	0.22	0.57
Guaso-I sand	1753	41.06	41.23	41.33	0.00	0.07	0.34
Morillo-III marl	1728	41.16	41.30	41.39	0.00	0.14	0.68
Morillo-III sand	1692	41.30	41.45	41.84	0.00	0.26	0.86
Morillo-II marl	1667	41.40	41.71	42.16	0.00	0.60	1.50
Morillo-II sand	1610	41.91	42.31	42.90	0.00	0.53	1.64
Morillo-I marl	1560	42.35	42.84	43.55	0.00	0.83	2.23
Morillo-I sand	1481	43.05	43.67	44.58	0.00	0.17	1.28
Ainsa-III marl	1460	43.24	43.85	44.33	0.82	1.37	2.02
Ainsa-III sand	1266	45.15	45.22	45.26	0.06	0.12	0.20
Ainsa-II marl	1210	45.31	45.34	45.35	0.17	0.20	0.24
Ainsa-II sand	1137	45.52	45.54	45.55	0.04	0.07	0.10
Ainsa-I marl	1111	45.60	45.61	45.63	0.22	0.24	0.27
Ainsa-I sand	1025	45.85	45.86	45.87	0.00	0.03	0.05
Banaston-VI marl	1016	45.87	45.88	45.89	0.11	0.13	0.15
Banaston-VI sand	970	46.01	46.01	46.02	0.10	0.12	0.13
Banaston-V marl	929	46.12	46.13	46.14	0.39	0.40	0.41
Banaston-V sand	789	46.53	46.53	46.53	0.04	0.04	0.04
Banaston-IV marl	775	46.57	46.57	46.57	0.05	0.05	0.06
Banaston-IV sand	700	46.62	46.62	46.63	0.00	0.01	0.02
Banaston-III marl	685	46.63	46.63	46.64	0.01	0.03	0.04
Banaston-III sand	650	46.65	46.66	46.67	0.00	0.30	0.67
Banaston-II	557	46.50	46.96	47.32		0.65	
Banaston-I	384	46.59	47.61				
Gerbe Marl	166	46.83	48.43				

*Age estimates calculated from the equations of intervals containing the top of the relevant complex (Table 3.4).

3.3.3 Upper Hecho Group age model

Using the above results, it is possible to construct an age model for the Upper Hecho Group within the Ainsa basin (Fig. 3.5). The age model suggests the Upper Hecho Group accumulated over a 6.0-8.3 Myr period spanning ~40.5-48.4 Ma whilst individual system and complex ages are also approximated (Tables 3.5 and 3.6). Sediment accumulation rates (SAR) are determined between adjacent NP points and range between 9.5±4.5 and 139.5±16.5 cm/kyr (Table 3.7).

Table 3.6 – Calculated sequence and System durations

	Duration (Myrs)*			
	Min	**Mid**	**Max**	**Expected†**
Sequence				
Guaso-II	0.00	0.49	1.05	0.40
Guaso-I	0.00	0.30	0.63	0.40
Morillo-III	0.01	0.40	1.00	0.40
Morillo-II	0.19	1.13	2.15	0.40
Morillo-I	0.00	1.01	1.98	0.40
Ainsa-III	0.99	1.49	2.11	0.40
Ainsa-II	0.25	0.28	0.31	0.40
Ainsa-I	0.24	0.27	0.30	0.40
Banaston-VI	0.23	0.25	0.27	0.40
Banaston-V	0.43	0.44	0.45	0.40
Banaston-IV	0.06	0.07	0.08	0.40
Banaston-III	0.00	0.33	0.69	0.40
Banaston-II	0.00	0.95		0.40
Banaston-I	0.00	1.47		0.40
Mean	**0.17**	**0.63**	**0.92**	
Std. Dev.	**0.27**	**0.48**	**0.76**	
System				
Guaso	0.40	0.79	1.29	0.80
Morillo	1.85	2.54	3.17	1.20
Ainsa	1.54	2.04	2.65	1.20
Banaston	0.94	2.55		2.40
Mean	**1.18**	**1.98**	**2.37**	
Std. Dev.	**0.64**	**0.83**	**0.97**	

*Durations calculated from complex age estimates in Table 3.4.

†Expected durations those predicted by Pickering and Bayliss (2009).

Table 3.7 – Interval SAR estimates

Interval	SAR (cm/kyr)			SAR Error* (± cm/kyr)	Expected SAR (cm/kyr)
	Min	**Mid**	**Max**		
1	20.65	33.37	46.08	12.71	32†
2	4.98	9.48	13.98	4.50	
3	4.15	10.98	17.81	6.83	
4	29.58	47.47	65.36	17.89	30§
5	34.62	35.18	35.74	0.56	30§
6	123.00	139.49	155.99	16.49	
7	11.92	26.59	41.27	14.67	
Mean	**32.70**	**43.22**	**53.75**	**10.52**	40#
Std. Dev.	**41.49**	**44.54**	**48.31**	**6.60**	

*SAR error calculated relative to midpoint estimate.

†SAR estimate from Dreyer et al. (1999).

§SAR estimate from Heard et al. (2008).

#Mean SAR for entire Ainsa basin Hecho Group from Pickering and Bayliss (2009).

3.4 Discussion

3.4.1 Age model

The construction of the age model using the above method should produce a reliable estimate of the Upper Hecho Group age and duration. The age and SAR estimates for individual systems and sequences within the Upper Hecho Group are, however, potentially subject to substantial errors associated with the method of stratigraphic thickness determination. Intervals where detailed stratigraphic measurements were taken (Chapters 4, 5 and 6) are likely to be subject to reduced errors.

Substantial uncertainty will also likely exist due to the technique used to place samples within the compiled stratigraphy. The collection of samples away from the location where stratigraphic thickness was measured, their placement will likely have a relatively low accuracy, especially where no distinctive marker horizon is present (see Fig. 3.2). The marker horizons used for correlation are assumed to be isochronous. Samples with likely the lowest accuracy are those obtained from the Morillo System.

The association of LBF samples with MTC and turbiditic deposits indicates reworking into the deep-marine basin. LBF habitats are believed to have been shallow marine environments (Boudagher-Fadel, 2008) such as those existing in the adjacent coeval Tremp-Graus basin (Figs. 1.13, 1.14). Although these LBF specimens are allogenic, their delivery and deposition was likely relatively instantaneous during storm and slope failure events and therefore can be considered biostratigraphically reliable. The corroboration between the independent NP and SBZ data suggests that the allogenic effects upon these data are likely to be negligible.

Although nannofossil analyses indicate the presence of reworked Cretaceous taxa, the youngest identified (those of middle Eocene age) are most likely in situ and therefore can be considered reliable. The presence of Cretaceous taxa is supportive of the Upper Hecho Group sediments being derived from the Mesozoic carbonate sediments from the Tremp-Graus basin (Nijman and Nio, 1975).

3.4.2 Comparison with previous age estimates

The new biostratigraphic age model corresponds well with previous dating of the Upper Hecho Group. Dating of the base of the group indicates an age of 46.8-48.4 Ma that is in agreement with the 47.8 Ma age suggested by the interpretation of unspecified magneto- and bio-stratigraphic data (Remacha et al., 2003; Remacha et al., 2005). The remaining basal ages for Upper Hecho Group originate from the Jaca basin. Here, the base of the group is marked by megaturbidite-5 (MT-5; Fig. 1.8) which has been suggested to reside within Chron 20r (Oms et al., 2003). However, the P10/11

boundary (Payros et al., 1999) and NP15 (Labaume et al., 1985) indicates a younger age than the ~45 Ma suggested by Oms et al. (2003).

The cessation of marine deposition within the Ainsa basin (top Upper Hecho Group) is currently dated as occurring between 41.6-42.3 Ma based upon the basal Sobrarbe deltaic sediments belonging to SBZ15 and Chron 20n (Bentham and Burbank, 1996; Dreyer et al., 1999). The age model constructed here, however, indicates a ~1 Myr younger age of 40.1-40.8 Ma.

Existing dating of the Ainsa basins deep-marine systems is limited, with only the Ainsa System being subjected to both published (Jones et al., 2005; Pickering and Corregidor, 2005) and unpublished planktonic foraminiferal and nannofossil analyses (based upon unpublished reports for the UCL Ainsa Project; Fenton, 1999; Pickering and Boudagher-Fadel, 2004). These studies place the Ainsa System around the P11/12 boundary (~43 Ma), which is in agreement with the system age range of 43.2-45.9 Ma (Table 3.6) predicted by the new age model.

The corroboration between the new Ainsa basin age model (Fig. 3.5) and previous independent magneto- and bio-stratigraphic studies indicates that the age-depth relationship is likely to be reliable.

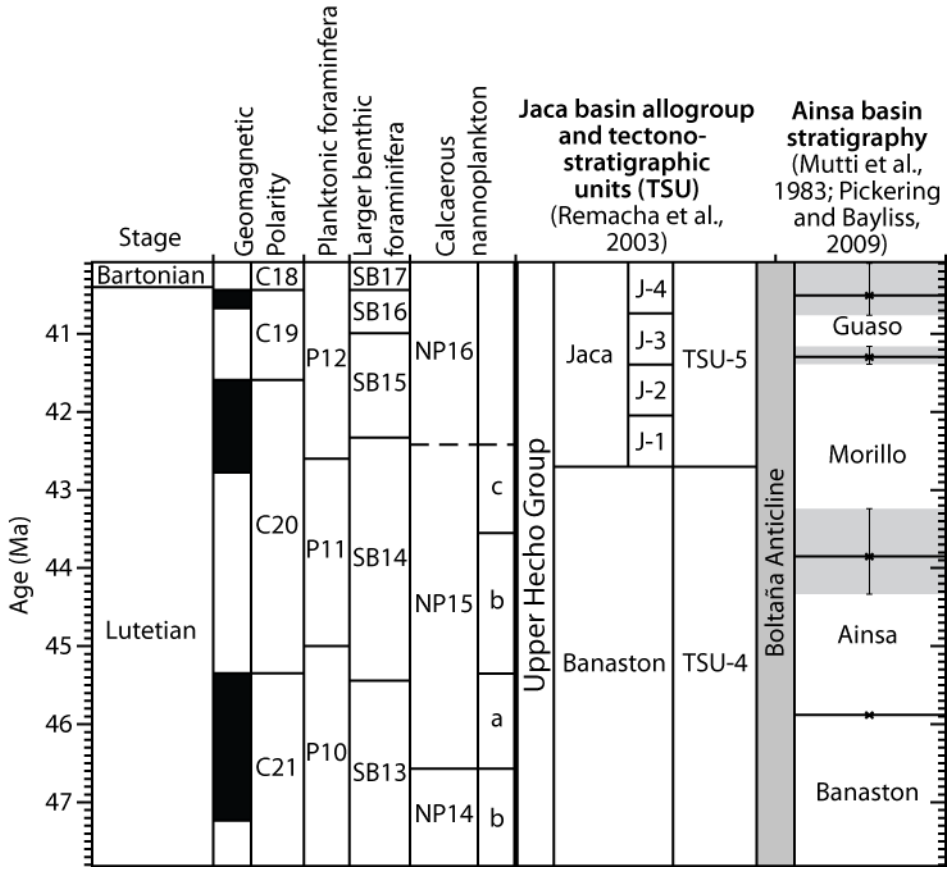

Figure 3.6 | Updated inter-basin system/allogroup age comparison. Based upon the Ainsa basins Upper Hecho Group age model it is apparent that inter-basin correlations proposed in Figure 3.1 require review. Ainsa basin stratigraphy are dated using the mid point values from Table 3.5 whilst upper and lower limits are represented by horizontal grey bars.

3.4.3 Inter-basin correlations

The newly available age constraints and the age model, from within the Ainsa basin presented here, enable the inter-basin stratigraphic correlations to be assessed via comparison with Jaca and Tremp-Graus basin age estimates (Fig. 1.8). Based upon these correlations, the Banaston System and Allogroup of the Ainsa and Jaca basins are believed coeval (Fig. 3.1). Comparison between the Ainsa and Jaca basin age models however indicates that, although the system/allogroup initiation was relatively isochronous (~47 Ma), the system/allogroup cessation appears diachronous (Fig. 3.6). However, as suggested by Oms et al. (2003), the top of the Jaca basins Banaston Allogroup may coincide with the top of Chron 21n rather than 20n when using the alternative biostratigraphic calibration of Payros et al. (1999). Such a calibration would result in the Banaston/Jaca allogroup boundary being isochronous with the Banaston/Ainsa system transition at ~45 Ma.

The remaining correlations within the Upper Hecho Group suggest that the Ainsa-Guaso systems and Jaca Allogroup (TSU-5) are coeval (Figs. 1.8, 3.1). Based upon the appropriate basin age models, the cessation of the Upper Hecho Group within the Ainsa and Jaca basins appear isochronous at 40.1-40.8 and ~40 Ma respectively. However, when using the alternative magnetostratigraphic Jaca basin calibration suggested by Oms et al. (2003), deposition of the Upper Hecho Group would have ceased within the Jaca basin (~41 Ma; lower Chron 19r) prior to the Ainsa basin (40.1-40.8 Ma). With the Hecho Group system infilling axially from the west (Bentham and Burbank, 1996; Dreyer et al., 1999), it would be expected that the proximal Ainsa basin would infill prior to the more distal Jaca basin therefore, rendering the alternative magnetostratigraphic calibration of Oms et al. (2003) unlikely.

Based upon the above age dating, the upper and lower limits of the Upper Hecho Group appear isochronous across the Ainsa and Jaca basins supporting their current intra-basin correlation. Stratigraphic correlations within Ainsa and Jaca basin systems/allogroups however, appear unreliable as correlated systems/allogroups appear be seen to be diachronous. To account for these chronological disparities the current intra-basin Upper Hecho Group correlations require review.

A correlation between the Ainsa basin systems (Pickering and Bayliss, 2009) and Tremp-Graus basin megasequences (Nijman, 1998) has been proposed by Bayliss (2010) (Fig. 1.9). Within the Lower Hecho Group the Castissent Sandstone (Megasequence MM) is correlated with the Charro canyon (Arro System) (Millington and Clark, 1995; Nijman, 1998). The overlying 5 megasequences may, therefore, correlate with the overlying 5 Ainsa basin systems. Verification of these correlations is beyond the scope of this study and is not considered further.

3.4.4 Ainsa basin sediment accumulation rates

The biostratigraphic age model suggests that the Ainsa basins sediment accumulation rates (SAR) varied between 9.5±4.5 and 139.5±16.5 cm/kyr with a mean of 43.2±10.5 cm/kyr (Table 3.7). The minimum and maximum SAR values determined here exceed the 15 to 40 cm/kyr range previously suggested for the basin (Bentham and Burbank, 1996; Heard et al., 2008; Pickering and Bayliss, 2009). The mean SAR estimate, however, corresponds well with the ~40 cm/kyr SAR predicted for the Hecho Group post ~43 Ma (Bentham and Burbank, 1996) and the entire Ainsa basin (Pickering and Bayliss, 2009).

Where sections within the Upper Hecho Group have previously been studied in detail it is possible to compare their SARs with those predicted within the age model. Such an interval exists within the Ainsa System where Heard et al. (2008) used the orbital pacing of bioturbation intensity to estimate an SAR of 30 cm/kyr for the A6 core. The laterally equivalent outcrop to these sediments is represented within sections 4 and 5 of the basin age model (Fig. 3.5). Within these intervals SAR estimates are calculated as 35.2±0.6 and 47.5±17.9 cm/kyr, both of which are similar to that predicted (Table 3.7).

The SAR estimate for the Sobrarbe deltaic complex has previously been estimated to have been 32 cm/kyr based upon the study of LBF (Dreyer et al., 1999). The basin age model supports this estimate with an SAR of 33.4±12.7 cm/kyr for the Guaso System and Sobrarbe Formation (Table 3.7).

The magnetostratigraphic study of the Ainsa basin sediment by Bentham and Burbank (1996) suggest SAR rates increased from ~15 to ~40 cm/kyr at the base of Chron 20n (42.77 Ma). Such a shift in SAR values, although younger in age at ~41.4 Ma, is also observed within the age model between the Morillo and Guaso systems (Fig. 3.5; Table 3.7). Comparison between the Mediano measured section of Bentham and Burbank (1996) and the Ainsa basins geological map (Pickering and Bayliss, 2009), indicate the magnetostratigraphic data for their study was likely collected from the Morillo and Guaso systems. Despite the age discrepancy, it is, therefore, likely that the more than two fold increase in SAR observed by Bentham and Burbank (1996) is coincident with that observed within the basin age model.

3.4.5 Testing the orbital forcing hypothesis

Applying the age model outlined here to the Upper Hecho Group enables the orbital forcing hypothesis to be tested by estimating system and sequence duration and age. These temporal features are compared to their predicted durations along with orbital,

sea-level, stable isotopic and ice-rafted debris (IRD) curves to test the proposed 404 kyr paced glacio-eustatic mechanism.

Dating the base of each sequence indicates that their individual durations ranged between <0.01 and 2.15 Myr (Table 3.6). Although the mean and standard deviation of these estimates suggest 404-kyr duration, only 8 of the 14 sequences (~57%) actually correspond to this period. Calculated system durations indicate that only the Banaston and Guaso systems correspond to their predicted durations (Table 3.6). The remaining Ainsa and Morillo system durations exceed those predicted by ~1 Myr.

With the Upper Hecho Group spanning 6.0-8.3 Myrs, it is therefore apparent that if the deposition of each submarine fan was paced by the 404 kyr Milankovitch cycle, then 15-20 would be expected compared to the 14 observed. However, the missing siliciclastic deposits may be represented by the less voluminous and numerous heterolithic accumulations, which have received far less attention than the voluminous fan deposits.

The irregular pacing of the Upper Hecho Groups submarine fan complexes thereby appears initially inconsistent with the orbital forcing model of Pickering and Bayliss (2009). Despite this, the proposed orbitally paced glacio-eustatic mechanism for the supply of coarse clastics to the basin may still be valid. Such a mechanism would predict that submarine fan deposition coincided with periods of ice accumulation and subsequent sea-level low-stand conditions as observed within more recent deep-marine sediments (Shanmugam and Moiola, 1982; Weaver and Kuijpers, 1983; Manley and Flood, 1988; Feeley et al., 1990; Pickering et al., 1999; Ridente and Trincardi, 2002; Marsaglia et al., 2004; Normark et al., 2006; Covault and Graham, 2010).

During the middle Eocene, despite this being understood to be a “greenhouse world”, ephemeral ice accumulation is believed to have occurred during orbitally forced periods of reduced insolation (Sangiorgi et al., 2008; St. John, 2008; Westerhold and Röhl, 2009). With the amount of insolation received by the Earth being controlled by the integration of the three Milankovitch orbital periods (Berger et al., 1993; Laskar et al., 2004), the latter can be utilised to estimate the timing of these insolation minima and hence periods of potential ice accumulation during the middle Eocene.

Orbital conditions resulting in periods of insolation minima require a combination of, low eccentricity and angle of obliquity reducing the seasonal contrast and the northern hemispheres summer to coincide with the aphelion (greatest Earth-Sun distance). The integration of these conditions reduces the total insolation received, thereby enabling the formation of winter ice at high latitudes. The reduced seasonality enables the ice to survive the following summer and accumulate over consecutive seasons. Using the orbital equations of Laskar et al. (2004; 2011) it is possible to

predict when in the geological past these conditions coexisted and hence enable the timing of ice accumulation and subsequent low-stand conditions to be predicted. Comparing these events with the timing of the Upper Hecho Groups submarine fan complexes should therefore enable the glacio-eustatic forcing mechanism to be tested (Fig. 3.7).

Comparison between the orbital parameters and the dating of the Upper Hecho Groups submarine fan complexes (Fig. 3.7) indicate that several do coincide with certain eccentricity minima at irregular intervals. However, with the average age uncertainty of the Upper Hecho Group age model being ±180 kyr, and the apparent variability within the calculated eccentricity curves (Fig. 3.7), it remains impossible to confidently assign submarine fan complexes to individual eccentricity minima. Only the age estimates for the Banaston System are well enough resolved to enable a reliable correlation but even so they do not consistently correspond to eccentricity minima.

Comparing the timing of each sequence with the global eustatic sea-level record of Haq et al. (1987) (Fig. 3.7) reveals a poor correlation between their initiation and sea-level low-stand and off-lap events. If the deposition of each sequence is related to glacio-eustasy, then sea-level changes must have occurred at a higher frequency than those indicated by available records.

Other more direct indicators of ice accumulation are the $\delta^{18}O$ and IRD records available for the middle Eocene. Comparing the timing of submarine fan complexes within the Upper Hecho Group and these records should enable the glacio-eustatic mechanism to be more reliably tested (Fig. 3.8). However, the $\delta^{18}O$ record of Zachos et al. (2008) lacks sufficient resolution especially prior to ~43.9 Ma for the accurate determination of potential ice-sheet formation. Despite this, the deterioration in global climate represented by the steady increase of $\delta^{18}O$ values supports the potential for ephemeral ice-sheet accumulation. The IRD data however, from the Greenland Sea (Tripati et al., 2008) and central Arctic Lomonosov Ridge (St. John, 2008) can be used to identify the timing of Northern Hemisphere ephemeral ice-sheet formation and hence potential glacio-eustatic low-stand conditions. The comparison between the timing of IRD and submarine fan complex deposition indicate that icebergs were being discharged into the proto North Atlantic and Arctic seas during the majority of Upper Hecho Group deposition (Fig. 3.8). Several clusters of IRD events coincide with submarine fan deposition (e.g., Guaso-II, Morillo-II, Ainsa-III MTC, Ainsa-I to -III and Banaston-VI) thereby supporting the hypothesised glacio-eustatic control on sediment supply.

The role of tectonic processes upon the development of the Upper Hecho Group is proposed to have influenced the locus of coarse-clastic sediment deposition via a “see-saw” tectonic mechanism (Fig. 1.16; Pickering and Bayliss, 2009). This

hypothesis can be verified using the Upper Hecho Group age model to compare the timing of system and sequence deposition with the timing of Mediano and Boltaña anticline deformation (Fig. 3.7) (Holl and Anastasio, 1993; Mochales et al., 2012). The continuous syn-depositional uplift of the Mediano anticline, illustrated in Figure 6 of Holl and Anastasio (1993), likely caused the overall south-westward migration of the systems and sequences away from the deformation front. Periods of increased activity within the Boltaña anticline are attributed to the north-eastward shift in the depositional axis creating the unconformable surfaces separating each system (Pickering and Bayliss, 2009). Based upon the age model, these surfaces formed between 45.85-45.89, 43.05-44.33 and 41.06-41.39 Ma for the Banaston-Ainsa, Ainsa-Morillo and Morillo-Guaso system boundaries, respectively (Table 3.5). Only the timing of the surfaces separating the Ainsa-Morillo and Morillo-Guaso systems correspond with periods of increased rotation of the blind-thrust underlying the Boltaña anticline, which potentially represent periods of increased anticline tightening and uplift (Fig. 3.7). Insufficient thrust rotational data exists to test the initiation of the Ainsa System. Despite this, the timing of these events lends support to the "see-saw" tectonic process proposed by Pickering and Bayliss (2009) (Figs. 1.15, 1.16).

Using the age model for the Upper Hecho Group it has been possible to discern the affects of tectonics *versus* climate upon the deposition of submarine fans. Within other deep-marine basins where the combined affects of climatic and tectonic forcing have been studied within glacial climates, researchers identify a similar pattern with glacio-eustasy being the dominant control on the timing of coarse-clastic sediment supply whilst tectonics influenced their spatial distribution (Manley and Flood, 1988; Feeley et al., 1990; Pickering et al., 1999; Prins and Postma, 2000; Normark et al., 2006).

Figure 3.7 (next page) | Comparison between eccentricity, obliquity, anticlinal tectonic activity, eustatic sea-level and global stratigraphic sequences with Upper Hecho Group age estimates. The initiation of each submarine fan complex according to the glacio-eustatic mechanism should coincide with insolation minima during periods of low eccentricity. Despite several submarine fan complexes being coincident with eccentricity minima, the majority remain ambiguous due to the relatively large uncertainties within the age model. The eccentricity and obliquity curves were calculated using the equations of Laskar et al. (2004). The additional eccentricity curves are those from Laskar et al. (2011). Possible periods of Boltaña anticline uplift possibly linked to the rotation of the blind-thrust underlying the anticline (Mochales et al., 2012). Periods of intensified rotation within the limbs of the Mediano anticline are also represented (∗) (Holl and Anastasio, 1993). Sea-level, relative to today, is that of Haq et al. (1987) and SEPM global sequences of Hardenbol et al. (1998). The basal age of each of the Upper Hecho Groups identified submarine fan complexes are marked along with their error estimates corresponding to those in Table 3.5.

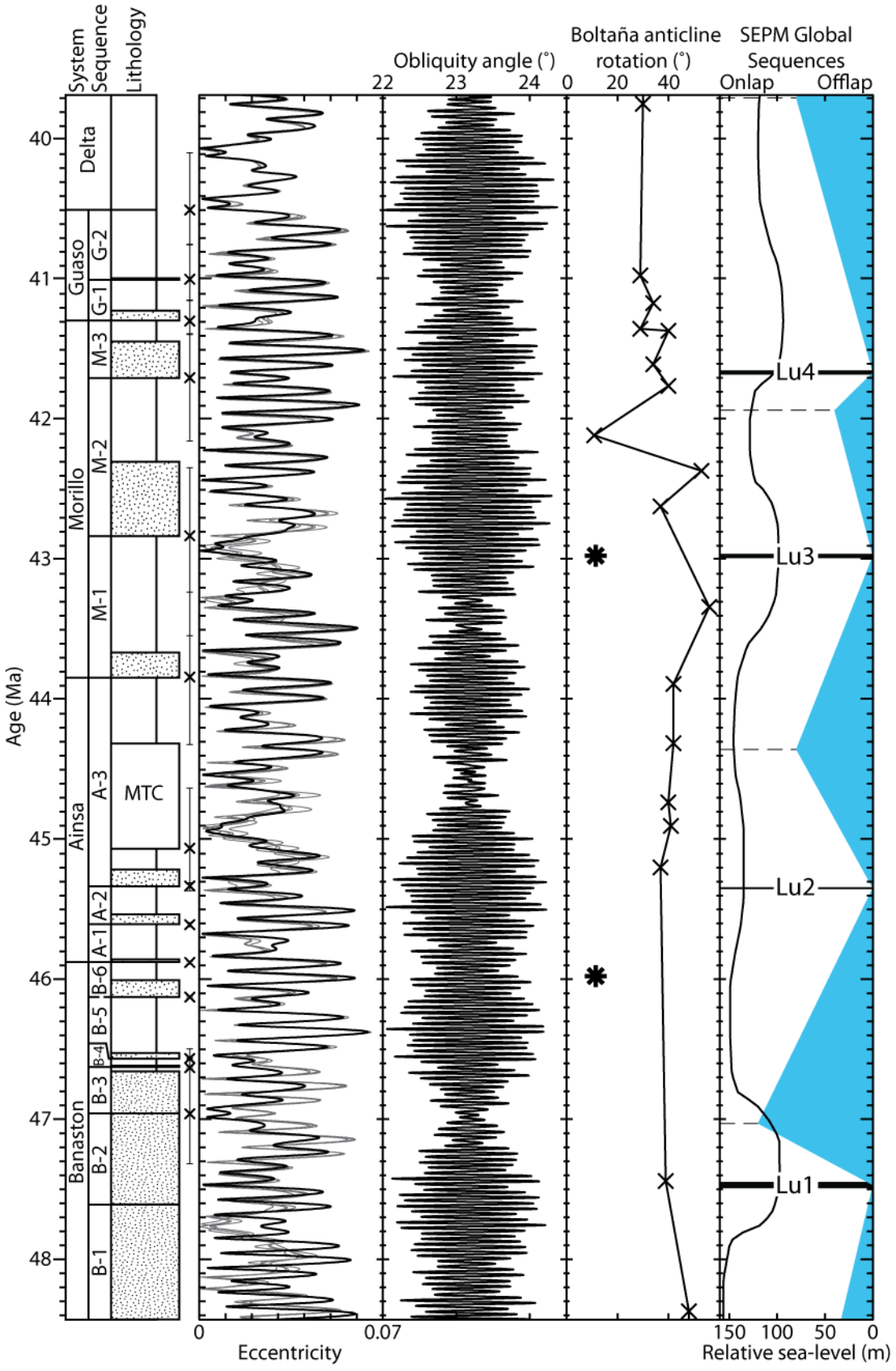
System
Sequence
Lithology
Obliquity angle (°)
22
23
24
Boltaña anticline
rotation (°)
0
20
40
SEPM Global
Sequences
Onlap
Offlap
Age (Ma)
40
41
42
43
44
45
46
47
48
Delta
Guaso
G-2
G-1
Morillo
M-3
M-2
M-1
Ainsa
A-3
MTC
A-2
A-1
Banaston
B-6
B-5
B-4
B-3
B-2
B-1
Lu4
Lu3
Lu2
Lu1
0
0.07
Eccentricity
150
100
50
0
Relative sea-level (m)

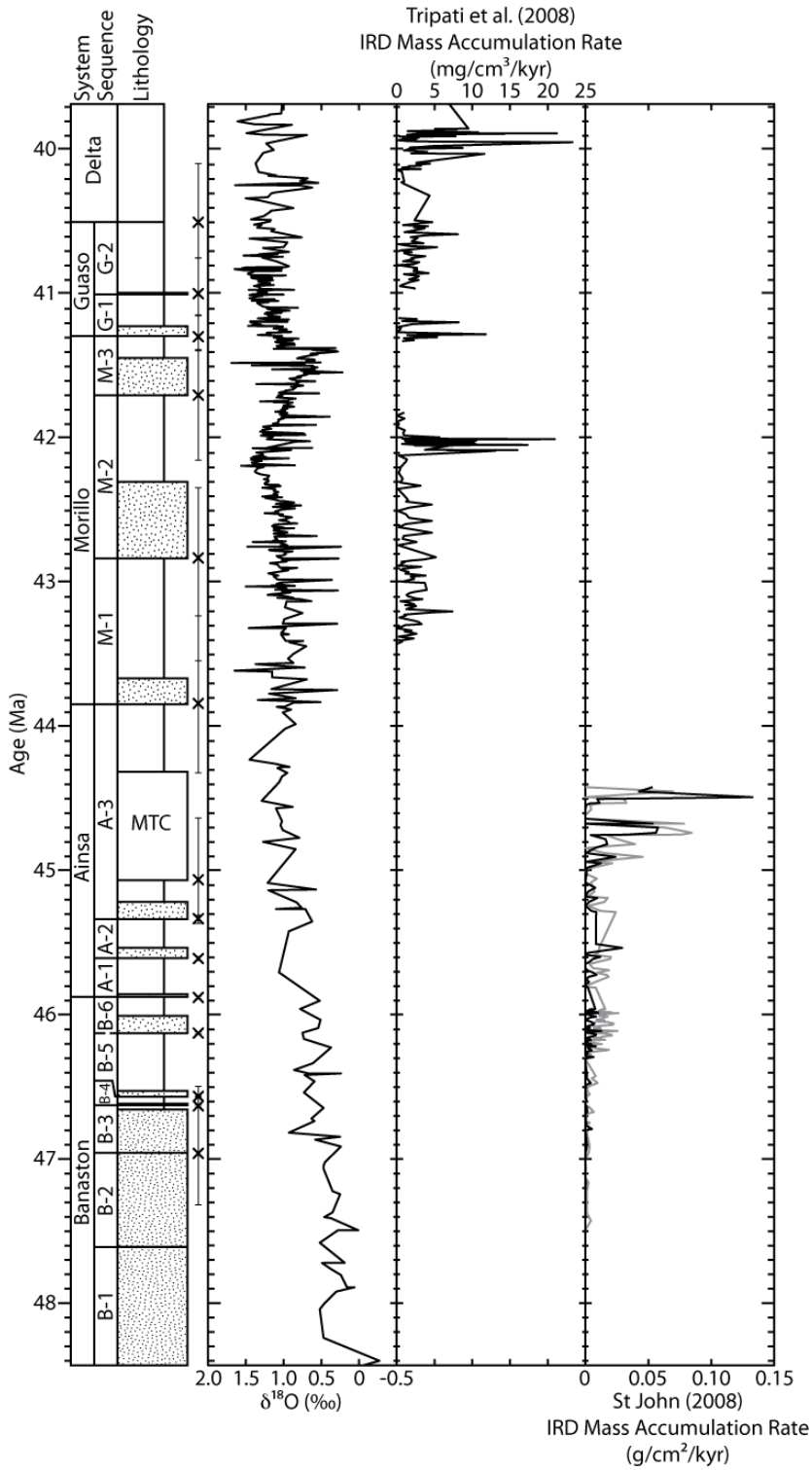

Figure 3.8 | Timing of Upper Hecho Group submarine fan deposition compared with coeval $\delta^{18}O$ and IRD data. The $\delta^{18}O$ record is determined from benthic deep-marine foraminifera (Zachos et al., 2008). Ice rafted debris (IRD) mass accumulation rate (MAR) data obtained from Eocene Greenland Sea and Lomonosov Ridge sediments. These data are interpreted as reflecting periods of potential Northern Hemisphere ephemeral ice-sheet formation (St. John, 2008; Tripati et al., 2008). IRD data represented by the solid black line is that >250um in size whilst the grey line the MAR of sediment 150-250um. With the low-resolution $\delta^{18}O$ data it is uncertain whether submarine fan deposition coincided with periods of increased $\delta^{18}O$ values, which could indicate ice-sheet growth. The IRD data however, clearly indicate the presence of northern hemisphere ice during the deposition of the Upper Hecho Group.

3.5 Summary

Within this chapter, an Upper Hecho Group age model has been constructed based upon the identification of calcareous nannofossil and larger benthic foraminifera. The age model suggests that the Upper Hecho Group accumulated over a 6.0-8.3 Myr period spanning ~40.5-48.4 Ma. These age estimates correspond well with those previously proposed for systems within the Ainsa basin and the Upper Hecho Group within the adjacent Jaca basin. Although the Upper Hecho Group inter-basin correlations are isochronous, those between the systems and allogroups appear diachronous indicating they require further review.

The Upper Hecho Group age model enabled the age and duration of each system and sequence to be estimated, thus allowing the predictions made by the orbital forcing hypothesis to be tested. Applying the 404-kyr orbital forcing hypothesis to the 6.0-8.3 Myr Upper Hecho Group duration would suggest that 15-20 sequences should exist, each corresponding to insolation minima every 0.4 Myr. With only 14 sequences being identified and their durations mainly exceeding the predicted 0.4 Myr, the orbital forcing hypothesis appears uncertain. However, when taking into account the less voluminous heterolithic deposits, the number of sequences and their durations may more closely correspond to those predicted.

Comparing the timing of submarine fan deposition with periods of potential ephemeral ice-sheet formation (orbital curves, $\delta^{18}O$ and IRD), indicate that several tentative correlations may exist thereby supporting the glacio-eustatic forcing mechanism. However, the uncertainty within the age model and calculated orbital curves must be addressed before the hypothesis can be adequately tested.

Using the Upper Hecho Group age model, the proposed “see-saw” tectonic model is here potentially validated. Comparison between the timing of the north-eastward migration of the basins depositional axis likely corresponds periods of intensified rotation of the thrust underlying the Boltaña anticline. The overall south-westward migration of the depositional systems and sequences within the Upper Hecho Group is here associated with the continuous syn-depositional uplift of the Mediano anticline. Further palaeomagnetic work is required before the “see-saw” process can be fully verified.

Although the Upper Hecho Group age model may initially refute the orbital forcing hypothesis, its further refinement should enable the predictions to be more rigorously tested. Improvement of the age model may be obtained from the identification of orbital cyclicity within the sediments allowing orbital time scales to be constructed for systems and between sequences. With an improved age model the

timing of submarine fan complexes and events can be more accurately determined and compared to middle Eocene climatic and tectonic indicators.

Chapter 4
The Guaso System

4.1 Introduction

4.1.1 Chapter objectives

In the Ainsa basin, the Guaso System records the final deep-marine deposition within the Upper Hecho Group. The system represents a delta-fed, structurally-confined, low-gradient clastic system prior to the onset of mainly deltaic conditions across the basin (Sutcliffe and Pickering, 2009). According to recent work it is hypothesised that the pacing of coarse clastic sediment supply to the system is controlled by a long eccentricity (404 kyr) driven glacio-eustatic process (Pickering and Bayliss, 2009; Sutcliffe and Pickering, 2009). Within this chapter, new inter-fan chemo-stratigraphic data are analysed using spectral analysis techniques to isolate orbital components and create a floating time scale between the Guaso submarine fans. Incorporation of this into the basin age model should allow the 404 kyr glacio-eustatic forcing hypothesis to be tested.

4.1.2 The Guaso System

The Guaso System is the youngest of the eight, unconformity-bound, genetically-linked, depositional systems within the Ainsa basin (Fig. 1.8). The system consists of a 250-350 m succession of deep-marine deposits divided into the Guaso-I and Guaso-II sequences (Pickering and Bayliss, 2009; Sutcliffe and Pickering, 2009). Each sequence consists of a basal submarine fan and MTC deposits overlain by inter-fan fine-grained marlstone and additional MTC deposits. The system represents a low-gradient (prodeltaic) clastic slope confined by the flanking Boltaña and Mediano anticlines (Fig. 4.1) (Sutcliffe and Pickering, 2009). Deposition of the Guaso System is thought to have been within upper bathyal depths based upon foraminiferal and ichnofossil assemblages (Sutcliffe and Pickering, 2009; Bayliss, 2010). Today, the Guaso System sediments are located within the core of the southerly plunging Buil Syncline, bound to the east and west by the Mediano and Boltaña anticlines, respectively (Figs. 1.18, 4.2).

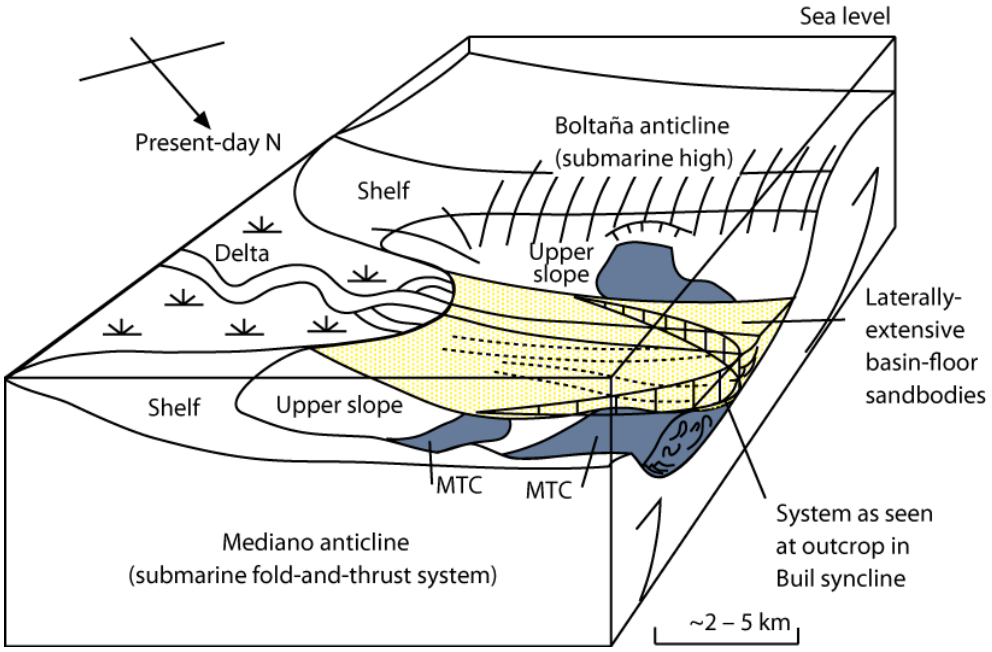

Figure 4.1 | Guaso System depositional model as proposed by Sutcliffe and Pickering (2009). The Guaso System is interpreted as representing a low-gradient (prodeltaic) clastic slope confined by the flanking Boltaña and Mediano anticlines.

Deposition of each submarine fan complex follows the generic template proposed for the basin (Fig. 1.17). The initiation of each fan complex (and hence sequence) is marked by a ~5-10 m thick basal Type-Ia and -Ib MTCs (intra-formational marly sediments) and contain suspended minor amounts of medium- to coarse-grade sandstone. Overlying these initial deposits are thick-bedded and amalgamated sandstones, followed by a fining-upward trend in each submarine fan that may be overlain by multi-event MTCs or minor heterolithic sandbodies (Sutcliffe and Pickering, 2009). Following submarine fan abandonment, fine-grained hemipelagic inter-fan sediments and rare type-I MTCs accumulated. The depositional axis of the subsequent Guaso-II sequence is observed to erode into the inter-fan sediments of the Guaso-I sequence whilst off-axis positions appear unaffected.

The cessation of the Guaso System, and hence deep-marine deposition within the Ainsa basin, occurred with the progradation of the Sobrarbe deltaic complex infilling the basin with shallow-marine deltaics (Sobrarbe Formation) and subsequent fluvial sediments (Escanilla Formation). Marking the boundary between the deep-marine and deltaic sediments is a submarine degradation surface created by compressional uplift of the study area (Dreyer et al., 1999). Within the basin this surface is represented by mudstone-supported carbonate breccias along the basin flanks and by bluish upper slope marls above the Hecho Group in the central part of the basin (Dreyer et al., 1999).

4.1.3 System dating

The study of calcareous nannofossil and large benthic foraminifera collected from the Guaso System suggests deposition occurred during nannofossil zone NP16 and shallow benthic zone SBZ17. This places the system within the latest Lutetian to earliest Bartonian (refer to Chapter 3 for details). Previous studies favour a slightly older age for the system based upon overlying sediments of the Sobrarbe deltaic complex being placed within SBZ15 and SBZ16 (Dreyer et al., 1999). Magneto-stratigraphy suggests the base of the Sobrarbe Formation coincides with the top of Chron 20n (Bentham and Burbank, 1996).

4.1.4 Tectonic setting

Deposition of the Guaso System coincided with the latter stages of the Ainsa basin tectono-sequence 2 (TS-2) of Bayliss (2010) which involved continued emplacement of the Gavarnie basement thrust. Regionally this thrusting resulted in the thickening of the Pyrenean Axial Zone and the transformation of the southern foreland into a series of compartmentalised piggyback basins (Munoz, 1992; Verges and Burbank, 1996; Remacha et al., 2003). Emplacement of the Gavarnie basement thrust resulted in regional uplift leading to an overall shoaling of the Ainsa basin.

The Ainsa basin during this phase of tectonic activity became increasingly confined due to the continued growth and tightening of the bounding Boltaña and Mediano anticlines (Farrell et al., 1987; Teixell, 1996; Remacha et al., 2003). These structures represented a growing submarine high and intra-slope lineament respectively (Das Gupta and Pickering, 2008; Heard et al., 2008; Sutcliffe and Pickering, 2009). Continued growth of these anticlines represented the continued expansion of the western lateral ramp structures of the South Central Pyrenean Unit (SCPU) (Teixell, 1996; Remacha et al., 2003). Although the region was undergoing uplift, the developing Buil syncline located between these structures provided adequate accommodation space for the deposition of the Guaso System and Sobrarbe delatic complex (Bayliss, 2010). During deposition of the latter, sediment accumulation rates (SAR) are estimated at 32 cm/kyr (Dreyer et al., 1999).

The intra-basinal tectonic setting during the Guaso System deposition considerably influenced the deep-marine sediment distribution. The Mediano anticline continued to act as a shelf break with the terrestrial Tremp-Graus basin over which sediment was supplied in an easterly direction (Nijman and Nio, 1975; Sutcliffe and Pickering, 2009). Once entering the basin, the relief of the Boltaña anticline was sufficient to deflect the sediment flow northwards prior to passing into the Jaca basin

(Labaume et al., 1985; Das Gupta and Pickering, 2008). The growth of these bounding anticlines also led to the south-westward shift in the depositional axis of the Guaso System corresponding to the “see-saw” tectonic model of Pickering and Bayliss (2009) depicted in Figures 1.15 and 1.16.

4.1.5 Sediment petrography

Sediments supplying the Guaso System submarine fan sandstones originated from the Campanùe alluvial fan which comprises conglomerates and sandstones derived from Mesozoic and Palaeozoic source rocks, 65% of which originate from Mesozoic carbonates (Weltje et al., 1996; Caja et al., 2010). The Guaso System submarine fan sandstones consist of feldspathic litharenites with a mean $Q_{50}F_{19}L_{31}$ composition (Das Gupta and Pickering, 2008). Disagreement, however, exists over the analysis of the clastic carbonate grains with the Guaso System’s sediments, either being described as carbonate extra-basinal arenites (enriched carbonate extra-basinal carbonate grains; Das Gupta and Pickering, 2008) or hybrid arenites (enriched carbonate intra-basinal carbonate grains; Caja et al., 2010).

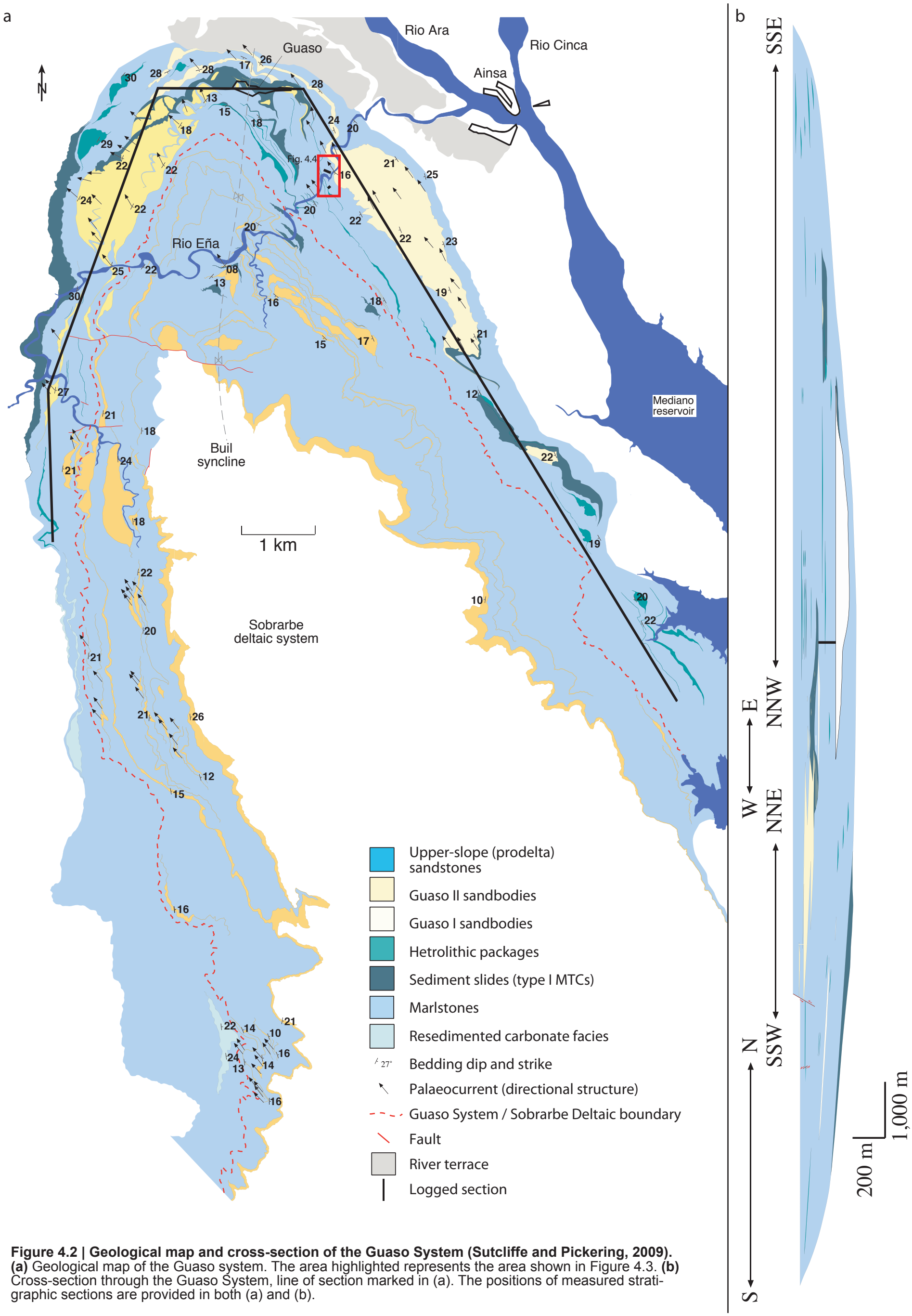

Figure 4.2 | Geological map and cross-section of the Guaso System (Sutcliffe and Pickering, 2009). **(a)** Geological map of the Guaso system. The area highlighted represents the area shown in Figure 4.3. **(b)** Cross-section through the Guaso System, line of section marked in (a). The positions of measured stratigraphic sections are provided in both (a) and (b).

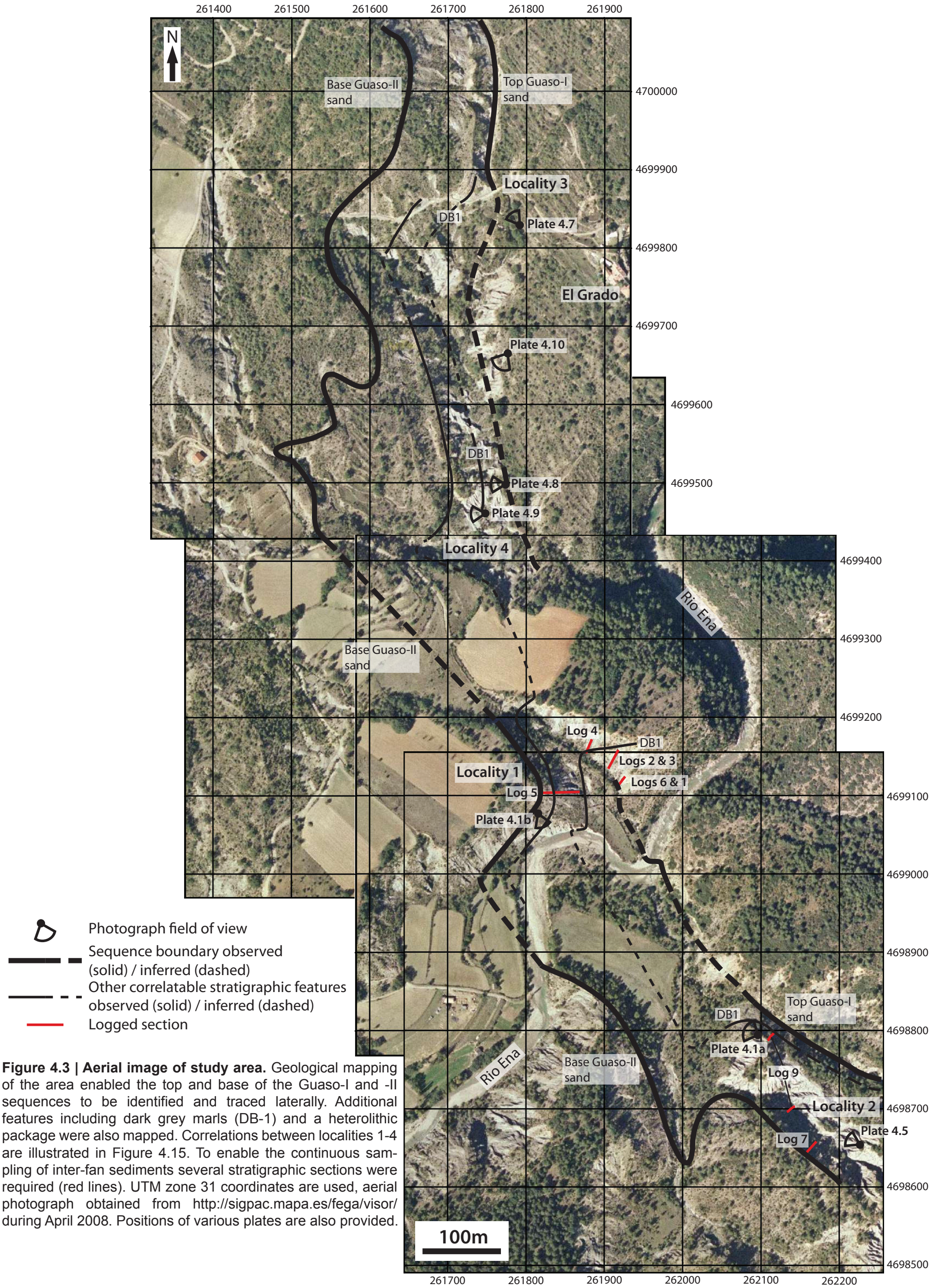

Figure 4.3 | Aerial image of study area. Geological mapping of the area enabled the top and base of the Guaso-I and -II sequences to be identified and traced laterally. Additional features including dark grey marls (DB-1) and a heterolithic package were also mapped. Correlations between localities 1-4 are illustrated in Figure 4.15. To enable the continuous sampling of inter-fan sediments several stratigraphic sections were required (red lines). UTM zone 31 coordinates are used, aerial photograph obtained from http://sigpac.mapa.es/fega/visor/ during April 2008. Positions of various plates are also provided.

Figure 4.4 | Measured sections (1-7 and 9) obtained from localities 1 and 2. Numerous laterally offset stratigraphic sections were measured to ensure the entire inter-fan stratigraphy was sampled (Figure 4.3). Bulk sediment and spectral gamma ray samples were collected every 0.2 m where possible. Several bulk sediment samples were used for XRD (*), petrographic (#) and palaeontological (†) analysis. Full scale version of this figure is available within the Appendix.

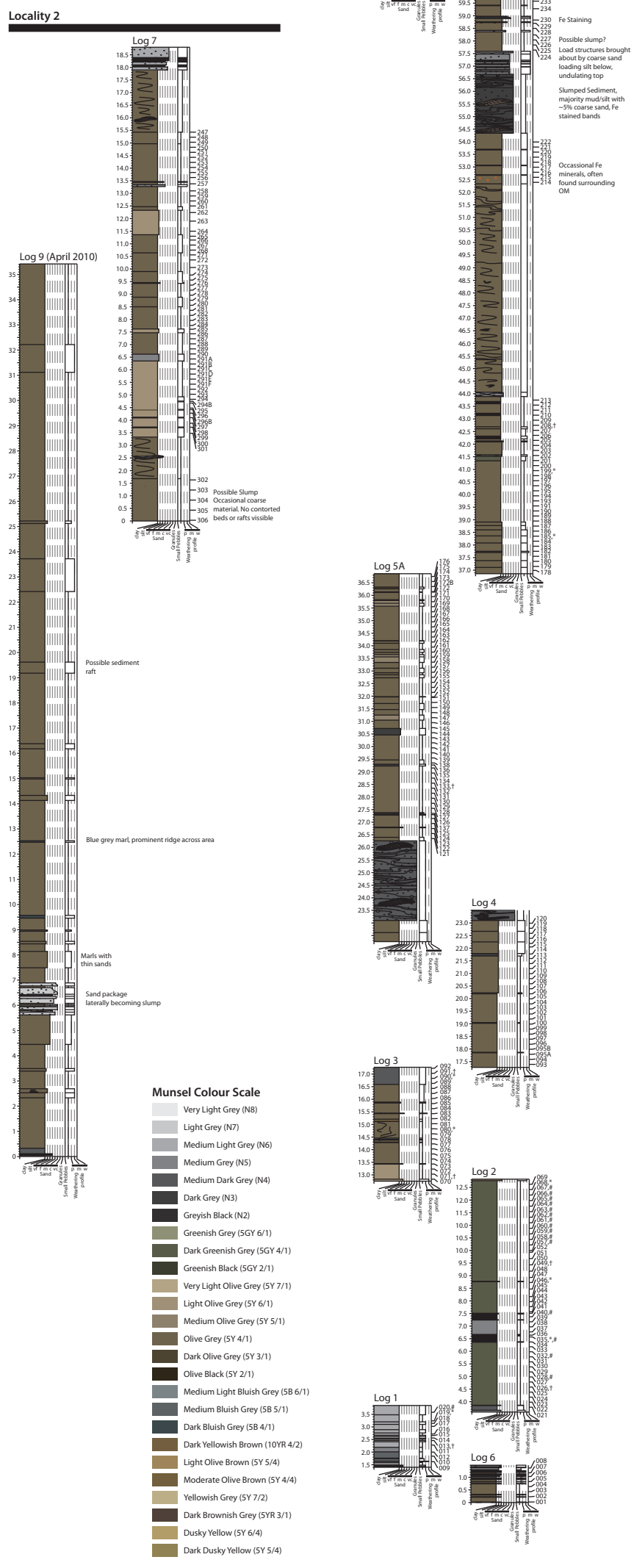

Plate 4.1 | Panoramic image of localities 1 and 2. (a) View of outcropping stratigraphy of Locality 1. Guaso church lies upon the Guaso-II submarine fan complex and can be correlated laterally with the ~1 m thick present within localities 1 and 2. (b) View of sediments at Locality 2 and positions of measured sections (red lines). Position of photograph marked within Figure 4.3.

4.2 Materials and methods

4.2.1 Study location

Inter-fan sediments of the Guaso System were studied in detail within an area south of El Grado (O'Grau) village (Fig. 4.3). Two marl sections, correlated across the Rio Eña, were studied to ensure the complete stratigraphic coverage between Guaso-I and Guaso-II submarine fan complexes. Locality 1 (UTM 31T coordinates 0261797, 4698920) is located adjacent to the Rio Eña ~600 m south of El Grado (Plate 4.1). Locality 2 (UTM 31T coordinates 0262050, 4698549) is located adjacent to a tributary of the Barranco de las Pueyos, ~480 m SSE from Locality 1 (Plate 4.1). Two further sections located ~250 m southwest (Locality 4; UTM 31T coordinates 0261606, 4699253) and ~200 m northwest (Locality 3; UTM 31T coordinates 0261595, 4699656) of El Grado village were studied to determine lateral stratigraphic variability of the sediments.

Prior to sample collection, a detailed sedimentary log was constructed (Fig. 4.4). Samples were collected, where possible, at 0.2 m intervals. Sediment slides, slumps and bedded heterolithic packages were not sampled as these were assumed to be instantaneous events. Spectral gamma ray and bulk rock samples were as far as possible, taken from the same position. In total 306 samples were collected from localities 1 and 2.

4.2.2 Geochemical sampling

Spectral gamma ray readings were taken using an Exploranium GR-320 (no. 2077) and GPX-21 (no. 1887) EnviSpec Portable Gamma Ray Spectrometer following the method outlined in Chapter 2. With a ~0.2 m between readings a moving average was created running through the section. Readings were taken over a 3-minute period giving an instrument precision of ±10% for all elements (Lovborg and Mose, 1987).

Bulk rock samples were collected for geochemical analyses from below the weathered surface. These samples were cleaned, dried in an oven overnight at 50˚C before being crushed to a fine powder to be utilised for total carbon (TC), total organic carbon (TOC), total inorganic carbonate ($CaCO_3$), stable isotopic ($\delta^{13}C$ and $\delta^{18}O$) and x-ray diffraction (XRD) analyses. Methodologies and background to these analytical techniques are provided in Chapter 2. Petrographic thin-sections were also made for selected sample points.

To enable comparison between Guaso bulk rock and diagenetic calcite, additional A6 core bulk sediment (Heard et al., 2008) and calcite vein samples were sampled for their $\delta^{13}C$ and $\delta^{18}O$ compositions. Bulk rock samples, previously analysed

by Heard et al. (2008), which were taken from the archive half of the A6 core were crushed to a fine powder using a pestle and mortar. Calcite vein samples were obtained from the archive half of the core using a hand drill. Stable isotope values were obtained using the methods outlined in Chapter 2.

XRD analyses were performed upon eight specimens from selected minima, maxima and intermediate $CaCO_3$ values. Measurements were taken using 30 mA and 40 kV tube current and voltage respectively. Scanning was carried out at room temperature (25˚C) using a 2θ start and end positions of 5˚ and 60˚, a step size of 0.0170˚ scanned over a 275 s period.

4.2.3 Spectral analysis

Sediments selected for stratigraphic time series analysis were between sample positions 001 (0.02 m) and 213 (43.75 m). Stratigraphy above 43.75 m contained frequent sediment slides and was therefore not suitable for inclusion within the stratigraphic time series. The deformed sediments between 23.10 m and 26.25 m were removed from the stratigraphic section as this type-Ib MTC event is treated as instantaneous. The de-trended stratigraphic time series used for spectral analyses is provided in Figure 4.5.

With the majority of the stratigraphic time series being unevenly spaced, the REDFIT algorithm (Schulz and Mudelsee, 2002) was utilised (see Section 2.6.4) to determine statistically significant frequencies. REDFIT spectral analyses were performed using an over-sampling factor (ofac) of 6 and a hifac of 1. To maintain the required 8 degrees of freedom 6 WOSA rectangular segments were used. However, due to the short time series, the resultant insufficient spectral resolution required the number of WOSA segments to be reduced to 2, thereby providing 3 degrees of freedom.

To determine the spatial distribution of regular oscillations within these stratigraphic series, the online tool (http://paos.colorado.edu/research/wavelets/) was utilised, which applies the continuous wavelet algorithms (CWT) of Torrence and Compo (1998). The continuous wavelet spectra were calculated using the de-trended and interpolated outcrop stratigraphic series. CWT calculations used a Morlet mother wavelet with a parameter of 6, a start scale of 2, a scale width of 0.1, 11 powers-of-2 with no zero padding therefore, not requiring a cone of influence.

The stratigraphic series, although short, would be expected to contain records of orbital cyclicity however, their objective identification remains difficult. An objective method is although provided by the Average Spectral Misfit (ASM) method of Meyers and Sageman (2007). The ASM method provides a null hypothesis significance level of

there being no orbital periods present. The method also provides an objective sediment accumulation rate (SAR) based upon significant frequencies identified by the MTM harmonic F-test (Thomson, 1982; Thomson, 1990). Further details are provided within Chapter 2.

MTM analyses were performed upon the interpolated and de-trended stratigraphic series within Analyseries 2.0.4.2 (Paillard et al., 1996) using a time bandwidth product of 4 and 6 data tapers. F-test frequencies of ≥90% confidence were isolated within a frequency range corresponding to ≥80% total variance within each stratigraphic series MTM spectra. Based upon these frequencies, the ASM was calculated for each stratigraphic series based upon their Rayleigh (R_f) and Nyquist (N_f) frequencies (Table 4.1). The range of SARs used was 5-100 cm/kyr with a step size of 0.95 cm/kyr resulting in 100 ASM and H_o estimates for each analysis. The number of orbital terms used during ASM analyses was varied to include all terms and exclude the eccentricity terms for reasons discussed later. ASM calculations were calculated for 41 Ma (Table 4.2) based upon available dating for the Guaso System (Chapter 3).

Once significant frequencies are assigned orbital durations, their visualisation was achieved via frequency selective filtering. To isolate individual frequencies of interest, a Gaussian band-pass filter, with bandwidths corresponding to the MTM harmonic F-test, was applied using Analyseries 2.0.4.2 (Paillard et al., 1996). All orbital filters were subsequently summed to create comb-filters.

Table 4.1 – Stratigraphic time series statistics

Stratigraphic Time Series*	N	Sample Interval (m)†	Nyquist Frequency (cycles/m)§	Rayleigh Frequency (cycles/m)#
$CaCO_3$	203	0.200	2.500	0.025
TOC	203	0.200	2.500	0.025
$\delta^{13}C$	203	0.200	2.500	0.025
$\delta^{18}O$	203	0.200	2.500	0.025
K	193	0.211	2.370	0.025
U	193	0.211	2.370	0.025
Th	193	0.211	2.370	0.025
Th/K	193	0.211	2.370	0.025
Th/U	193	0.211	2.370	0.025

*Stratigraphic time series statistics after removal of major outliers from the Guaso outcrop data. No data were removed from the radioelement outcrop data.
†Sample interval applied during linear interpolation for wavelet and MTM F-test algorithms.
§Nyquist frequency represents the maximum discernable frequency based upon the sampling interval.
#Rayleigh frequency represents the minimum spacing within the fast Fourier transform frequency grid. Calculated from the number of data points and sample interval.

Figure 4.5 (next page) | Stratigraphic time series constructed from de-trended Locality 1 data. The time series includes samples 1-213 (0.02-43.75 m) collected from Locality 1. Any linear trend and major outliers were removed where necessary. The subsequent time series were utilised during spectral analyses. Statistics for each time series is provided in Table 4.1.

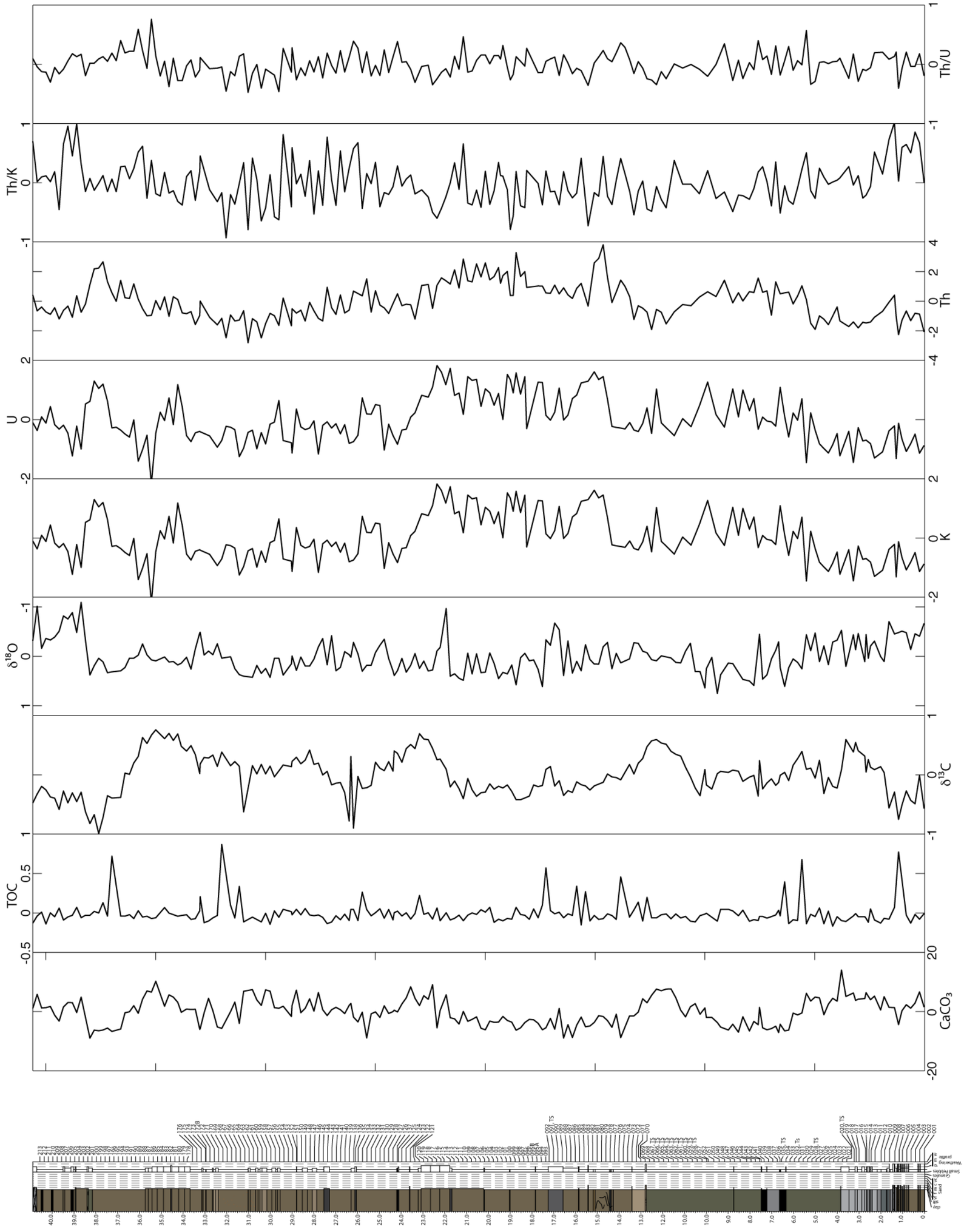
Th/U
Th/K
Th
U
K
δ18O
δ13C
TOC
CaCO3

Table 4.2 – Calculated orbital periods for the Guaso System

Orbital Parameter	Period (kyr)*
Precession	18.84
Precession	22.67
Obliquity	40.10
Obliquity	52.44
Short Eccentricity	94.78
Short Eccentricity	123.82
Long Eccentricity	404.18

*Orbital periods calculated for 41 Ma using equations of Berger et al. (1992).

4.3 Results

4.3.1 Inter-fan sedimentology

The sedimentary succession measured at Locality 1 comprises eight individual stratigraphic sections, each laterally offset by several metres (Fig. 4.4; Plates 4.2, 4.3, 4.4). The base of the section immediately overlies the last sandstone bed of the Guaso-I sequence. The overlying ~75 m section includes mainly olive grey, fine-grained inter-fan marlstones, medium (DB-2 and 3) and dark grey (DB-1) marl beds and type-Ia and -Ib MTC deposits as defined by Pickering and Corregidor (2005). Type-Ia MTCs here comprise deformed intra-formational marls whilst type-Ib MTCs contains additional decimeter-scale sandstone olistoliths. Only two significant sandstone beds are present at 57 m and 74.5 m, each immediately overlying substantial (>10 m) type-Ib MTC deposits. Palaeocurrent directions obtained from these sandstones suggest palaeocurrent directions of ~304˚.

The stratigraphy of Locality 2 was compiled from two measured sections (Fig. 4.4; Plates 4.5, 4.6). The ~44 m section consists of olive grey marlstones, with subordinate medium-dark grey marlstones, type-Ib MTCs and medium-coarse sandstones. Three laterally continuous prominent ridges (~1-2 m thick) consisting of well-lithified olive grey marl are apparent at outcrop (Plate 4.6). Sole structures measured at Locality 2 indicate palaeocurrent directions of ~326˚.

Locality 3 (Fig. 4.3; Plate 4.7) includes a series of olive grey marls directly overlying the final sandstone beds of the Guaso-I sequence. The top of the exposed section includes a package of inter-bedded, rippled sandstones and marlstones. Similar to the previous localities, a horizon of dark grey marlstone is located several metres below the sandstone/marlstone package. No stratigraphic section was measured at Locality 3.

Plate 4.2 | Position of logs 1, 3 and 6 measured at Locality 1. The base of the section in the bottom right corner represents the final sandstone beds of the Guaso-I submarine fan complex. The overlying inter-fan sediments were measured in several logs offset by several metres to enable continuous stratigraphic coverage. The dark grey marl horizon can be clearly seen in this view and can be correlated across the area (Fig. 4.3).

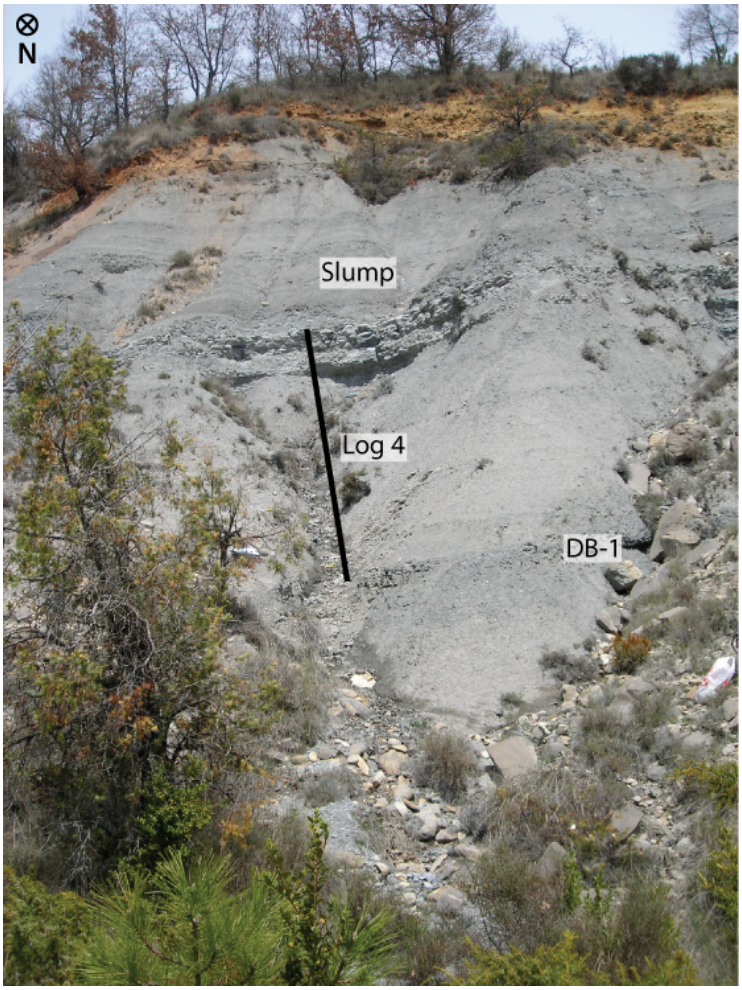

Plate 4.3 | Position of log 4 measured at Locality 1. The dark grey marlstone (DB-1) bed was utilised to correlate between logs 3 and 4. The top of the log corresponds to the base of the overlying type-Ib MTC (Fig. 4.4).

Plate 4.4 | Positions of log 5 at Locality 1. The base of the section shown here consists of the type-Ib MTC identified at the top of log 4. The lateral equivalent sandstone of the Guaso-II submarine fan complex marks the top of the section.

Stratigraphy at Locality 4 (Fig. 4.3) consists of a short section of olive-grey marlstones with three medium-dark grey marl beds similar to those identified at the other localities (Plates 4.8). The top of the outcrop at Locality 4 consists of a package of sandstones directly overlying a type-Ia MTC deposit (Plate 4.9).

Mapping of the identified features between the 4 localities revealed the lateral extent and facies changes of several distinct beds. Tracing sediments between localities 3 and 4 identified the DB-1 dark grey marl bed as being laterally extensive across the area. Lateral facies changes were also observed with an inter-bedded sand/marlstone package transforming to slumped sands/marlstones and well-lithified marl beds between localities 3 and 4 (Plate 4.10; Fig. 4.15).

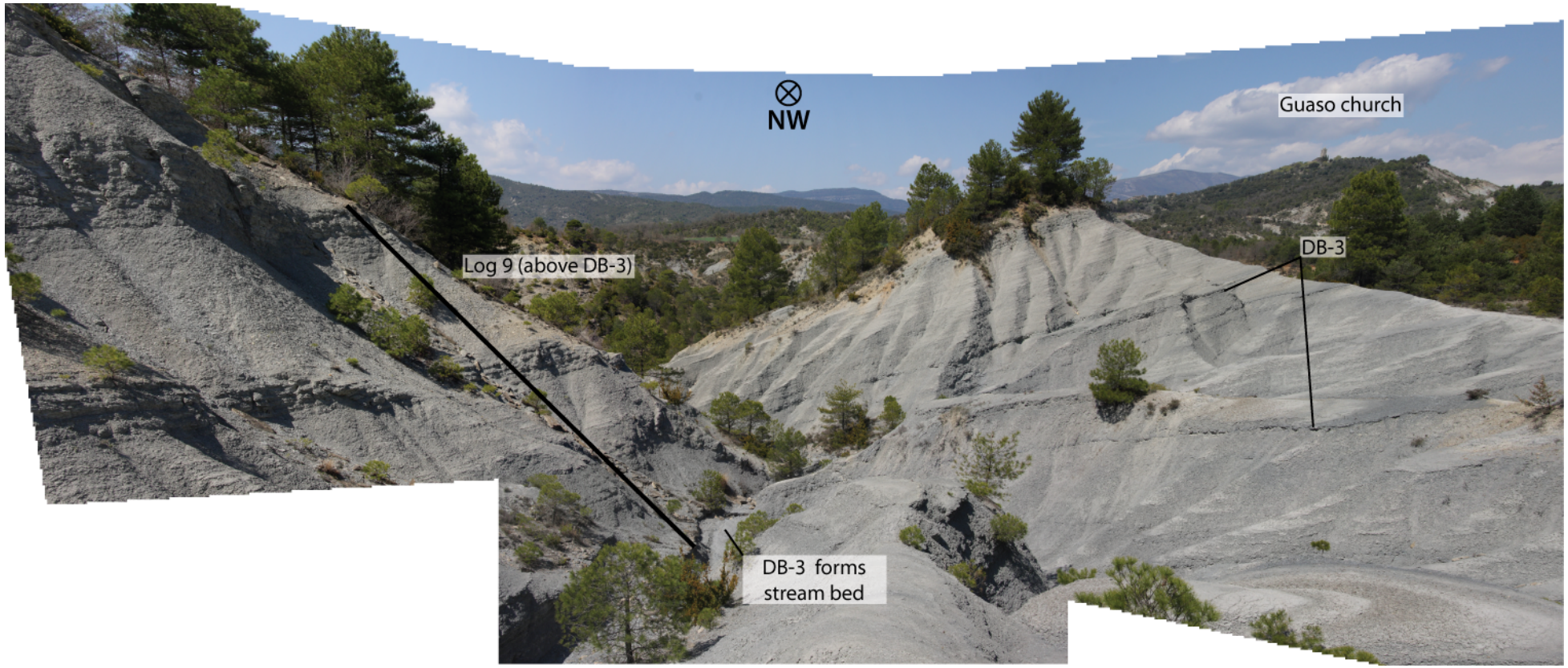

Plate 4.5 | Locality 2 contained two measured sections, logs 7 and 9. The dark grey marlstone (DB-3) bed was used to correlate between the two parts of log 9.

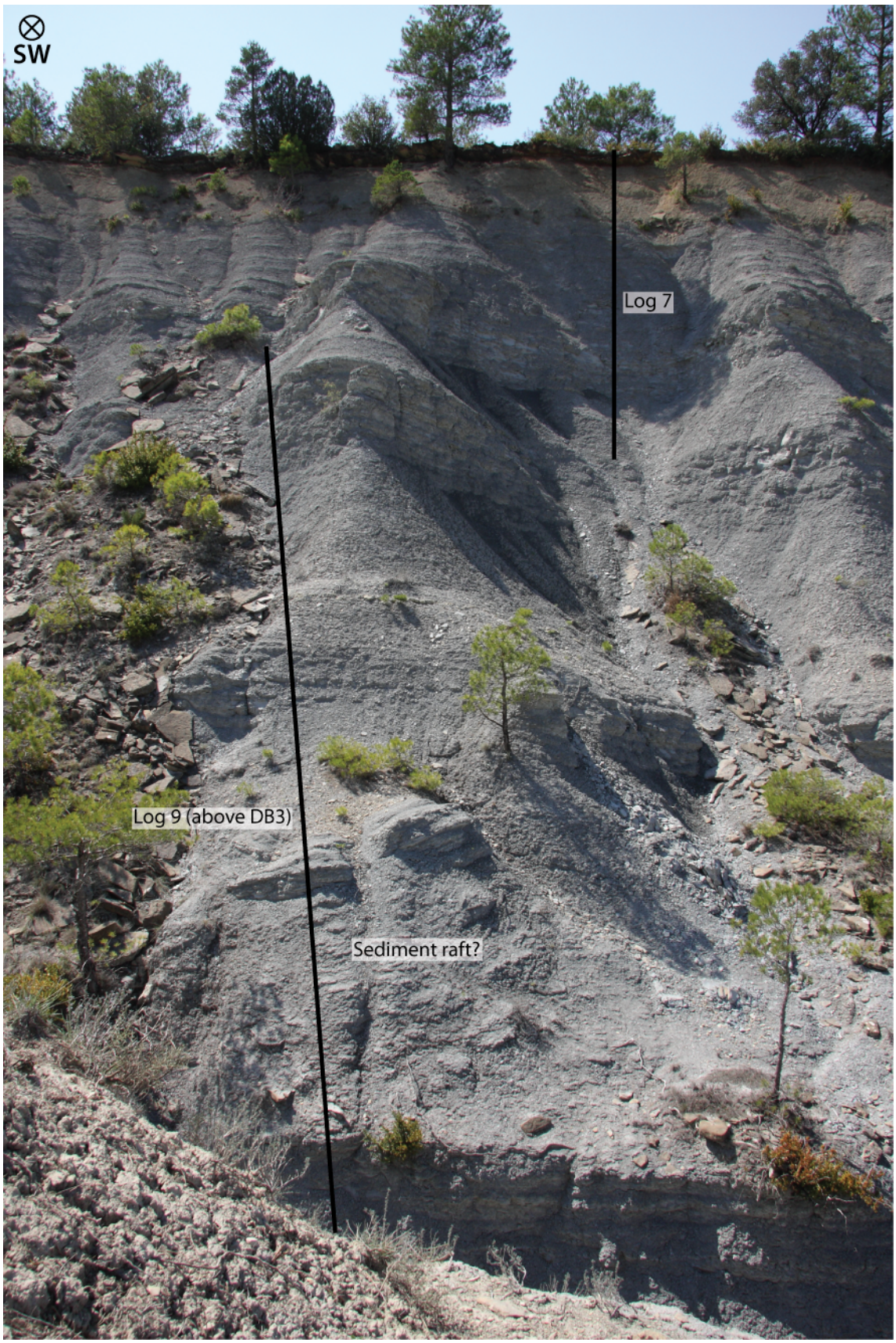

Plate 4.6 | View containing the positions of the top of log 9 and log 7 at Locality 2. Geochemical data only collected from log 7 whilst log 9 was used for correlation purposes.

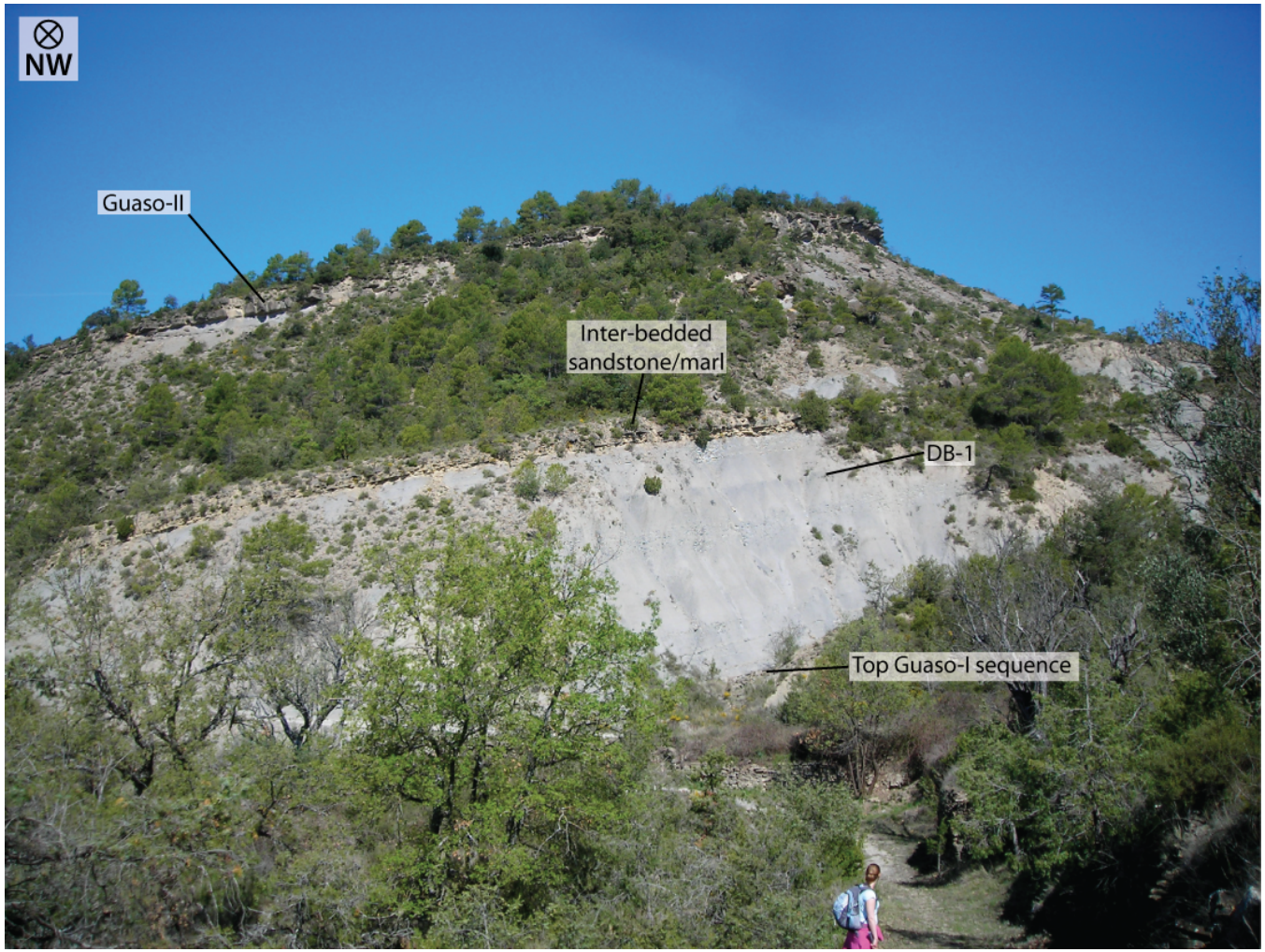

Plate 4.7 | View showing the stratigraphy present at Locality 3. No stratigraphic section was measured at Locality 3. The presence of DB-1 enabled correlation localities 1-3. The inter-bedded sandstone/marlstone package is traced toward the southwest and undergoes a lateral facies change into a MTC deposit.

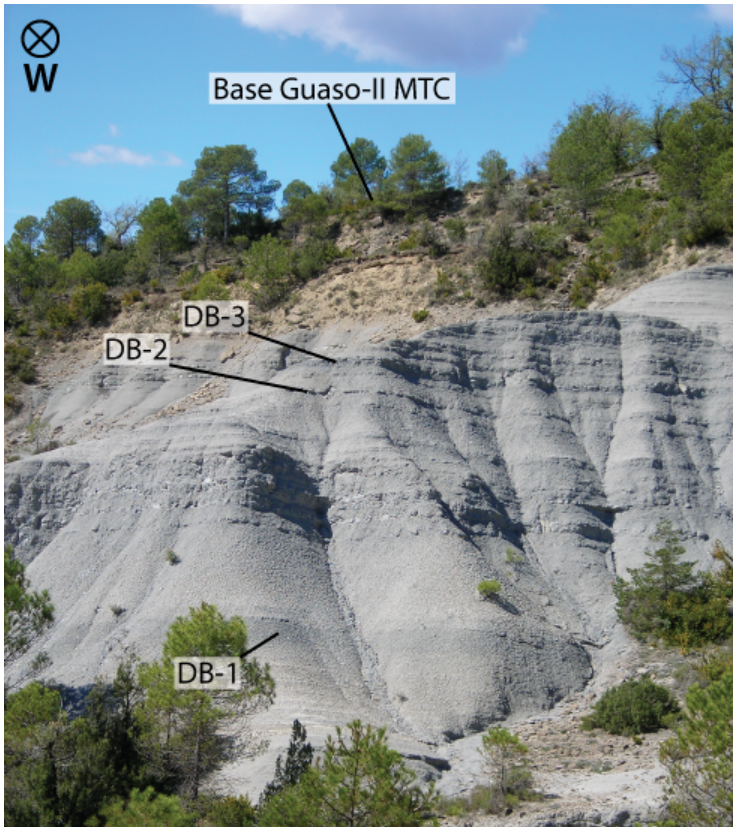

Plate 4.8 | View showing stratigraphy present at Locality 4. The package of sediments, which appears more resistant to weathering, is the lateral equivalent to the inter-bedded sandstone/marlstone package shown in Plate 4.7. The package shows a lateral sandstone/marlstone-MTC-marl facies change in a southerly direction.

Plate 4.9 | Type-Ib MTC located directly beneath heterolithic package at Locality 4. The presence of the MTC deposit beneath the sandy heterolithic package is consistent with the sediments observed at Locality 1 at ~44-57 m and the generic sand deposition model (Fig. 1.17).

Plate 4.10 | Panoramic view of the stratigraphy present between localities 3 and 4. Correlation of the stratigraphy within this interval illustrates the lateral facies changes from inter-bedded sandstone/marlstone (Locality 3)-MTC-marlstone (Locality 4).

Figure 4.6 (next page) | Geochemical results obtained from Locality 1. Both bulk sediment samples and spectral gamma ray readings were collected, where possible, every 0.2 m throughout the section. MTC and sandstone deposits were not sampled, as these are assumed instantaneous events. Several bulk sediment samples were used for XRD (*), petrographic (#) and palaeontological (†) analysis.

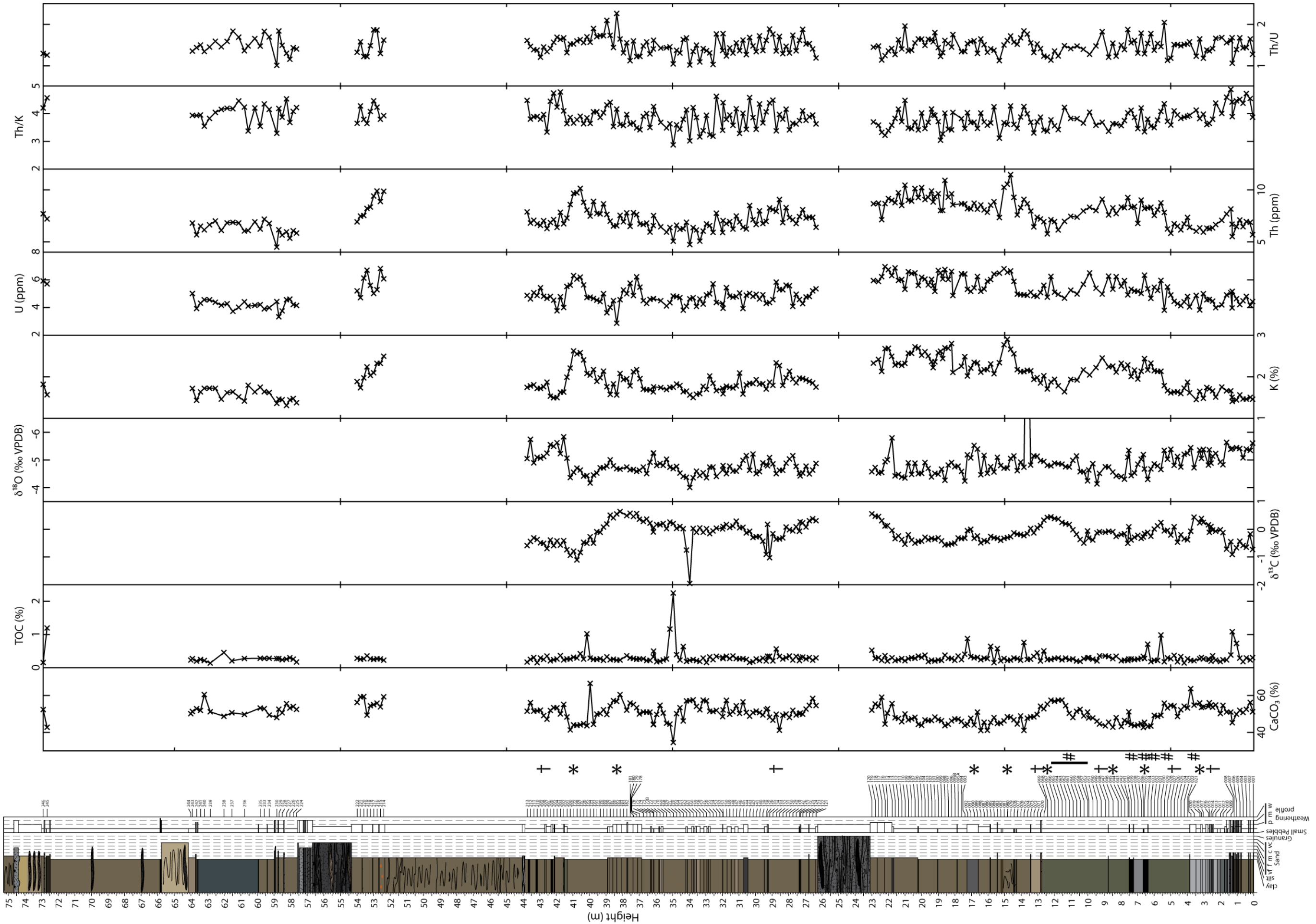
Th/K
Th/U
U (ppm)
Th (ppm)
δ18O (‰ VPDB)
K (%)
TOC (%)
δ13C (‰ VPDB)
CaCO3 (%)
Height (m)
clay
silt
vf f m c vc
Sand
Granules
Small Pebbles
w m d
Weathering profile

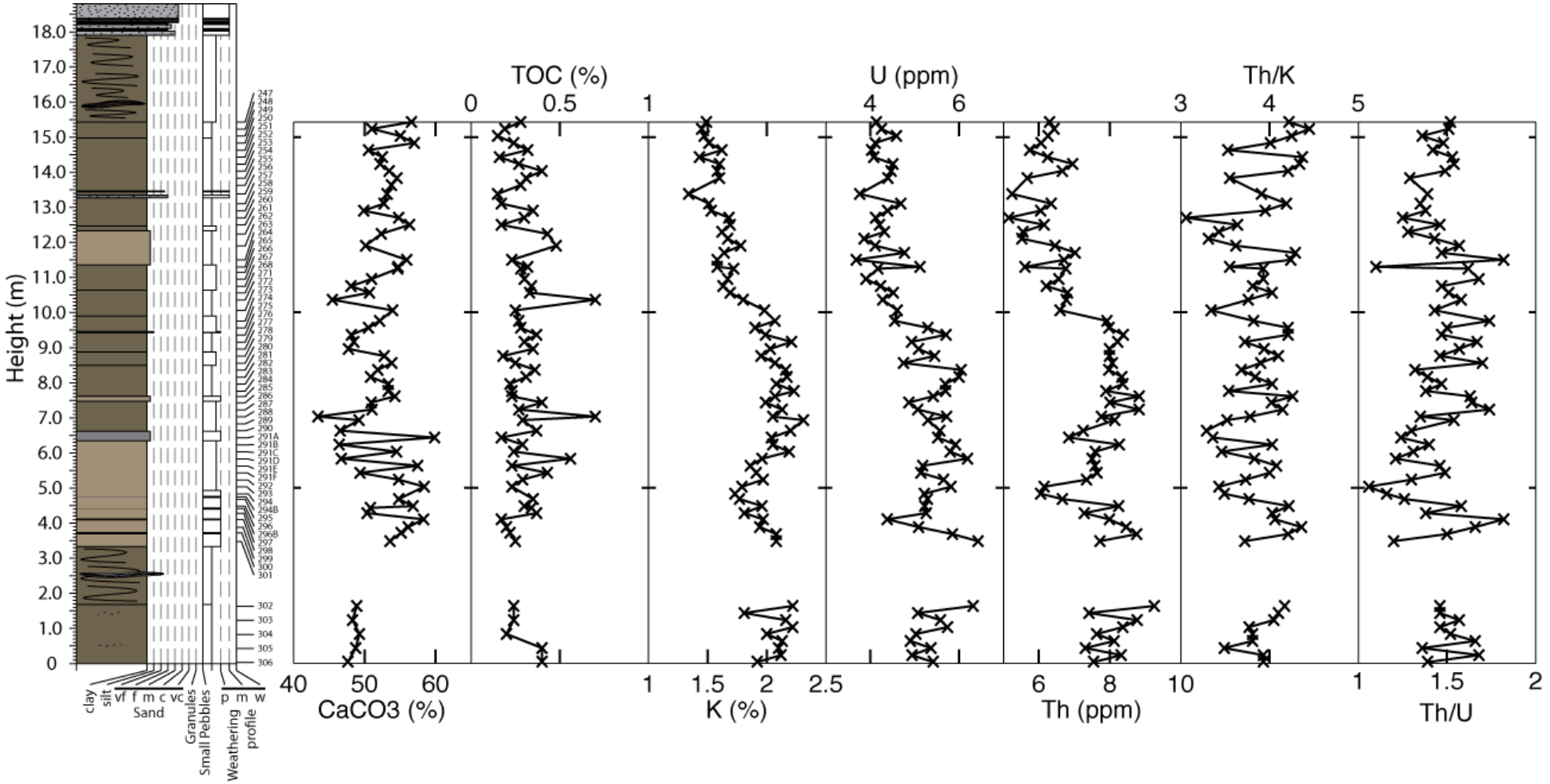

Figure 4.7 | Geochemical results obtained from Locality 2. Both bulk sediment samples and spectral gamma ray readings were collected, where possible, every 0.2 m throughout the section. MTC and sandstone deposits were not sampled, as these are assumed instantaneous events.

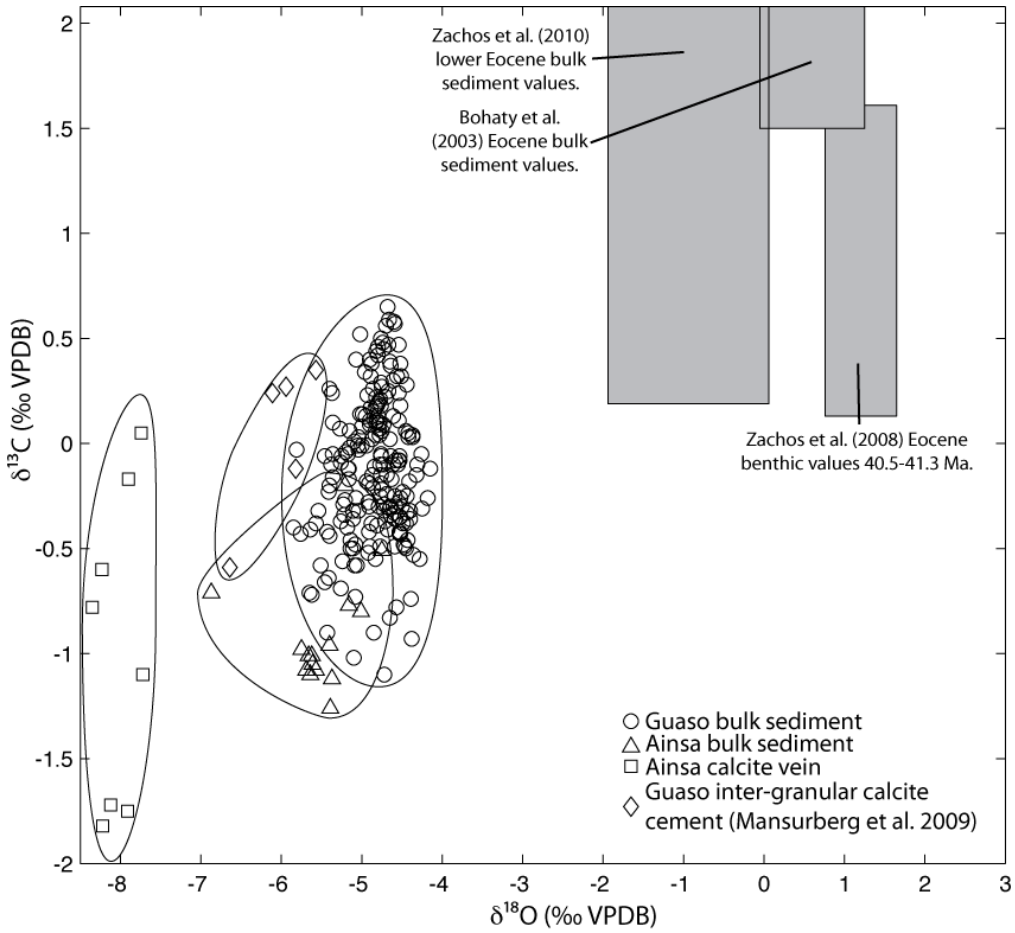

Figure 4.8 | Stable isotope cross-plot comparing Guaso results with existing Eocene data. Compared to existing Eocene data (Zachos et al., 2008), the stable isotopic composition of the Guaso sediments show a marked depletion in $\delta^{18}O$ and a lesser depletion in $\delta^{13}C$. The position of the Guaso samples between the diagenetic (diamond) and benthic seawater values suggests their $\delta^{18}O$ and $\delta^{13}C$ values have been affected by diagenesis. The Guaso $\delta^{13}C$ compositions are considered less prone to diagenetic alteration thereby explaining their closer similarity with existing Eocene data. Despite alteration the trends identified within the isotopic data may enable orbital forcing to be identified.

4.3.2 Sediment geochemistry

Bulk sediment geochemistry and SGR data from localities 1 and 2 are shown in Figures 4.6 and 4.7 whilst Table 4.3 provides their summary statistics. Sediments from both localities display little TOC variation from the mean value of 0.30%. Greater variability is observed within the measured $CaCO_3$ content with gradual fluctuations in Locality 1 about a 50% mean. Sediment $CaCO_3$ content at Locality 2 appears more erratic than Locality 1.

Table 4.3 – Summary statistics of geochemical data*

	N	Min	Max	Mean	Variance
Locality 1					
$CaCO_3$ (%)	236	34.58	63.75	50.33	20.89
TOC (%)	237	0.15	2.26	0.31	0.04
$\delta^{13}C$ (‰)	206	-1.10	0.65	-0.13	0.12
$\delta^{18}O$ (‰)	206	-5.85	-4.02	-4.84	0.12
K (%)	227	1.32	2.92	1.96	0.13
U (ppm)	227	2.91	7.00	5.12	0.66
Th (ppm)	227	4.55	11.53	7.57	1.57
Th/K	227	2.90	4.91	3.88	0.14
Th/U	227	1.02	2.27	1.49	0.04
Locality 2					
$CaCO_3$ (%)	63	43.43	59.87	52.15	12.16
TOC (%)	63	0.15	0.70	0.30	0.01
K (%)	68	1.34	2.31	1.87	0.06
U (ppm)	68	3.68	6.43	4.98	0.48
Th (ppm)	68	5.15	9.25	7.24	1.03
Th/K	68	3.06	4.45	3.88	0.10
Th/U	68	1.06	1.82	1.46	0.03

*Single outlier removed from $CaCO_3$, $\delta^{13}C$ and $\delta^{18}O$ data prior to calculation of statistics.

Carbonate isotopic results from Locality 1 bulk sediments have a relatively narrow range of $\delta^{18}O$ values compared to $\delta^{13}C$ (Fig. 4.8). Carbon and oxygen isotopic results obtained from the Ainsa System's A6 core are also included in Figure 4.8. A6 bulk sediments appear depleted by ~0.5‰ in both $\delta^{13}C$ and $\delta^{18}O$ compositions compared to the Guaso sediments. The isotopic compositions of A6 vein calcites when compared with those obtained from the bulk sediment, share similar $\delta^{13}C$ but significantly depleted (~2.5‰) $\delta^{18}O$ values.

Stratigraphically, carbon isotopic values obtained from Locality 1 show smooth variation about a mean $\delta^{13}C$ value -0.13‰ whilst $\delta^{18}O$ values are characterised by more erratic behavior especially within the lower 23 m (Fig. 4.6).

Spectral gamma ray (SGR) K, U and Th data co-vary throughout both localities. Statistically (Fig. 4.9; Table 4.4) this is confirmed with R^2 correlation coefficients being significant (>0.6) for relationships involving K. The relationship between U and Th however is less significant with a R^2 value of 0.4. Th/K and Th/U values show little variability throughout both sections with mean values of 3.9 and 1.5, respectively.

The semi-quantitative mineralogical composition of 8 bulk sediment samples obtained from XRD analyses, indicate the dominance of calcite, muscovite and quartz with lesser amounts of chlorite, rutile, dolomite and pyrite (Fig. 4.10; Table 4.5). Comparison between these data and bulk sediment geochemistry indicate few significant correlation coefficients (Fig. 4.11; Table 4.6). Only calcite, quartz and muscovite vs. $CaCO_3$ content suggest significant correlation coefficients (R^2) of >0.8.

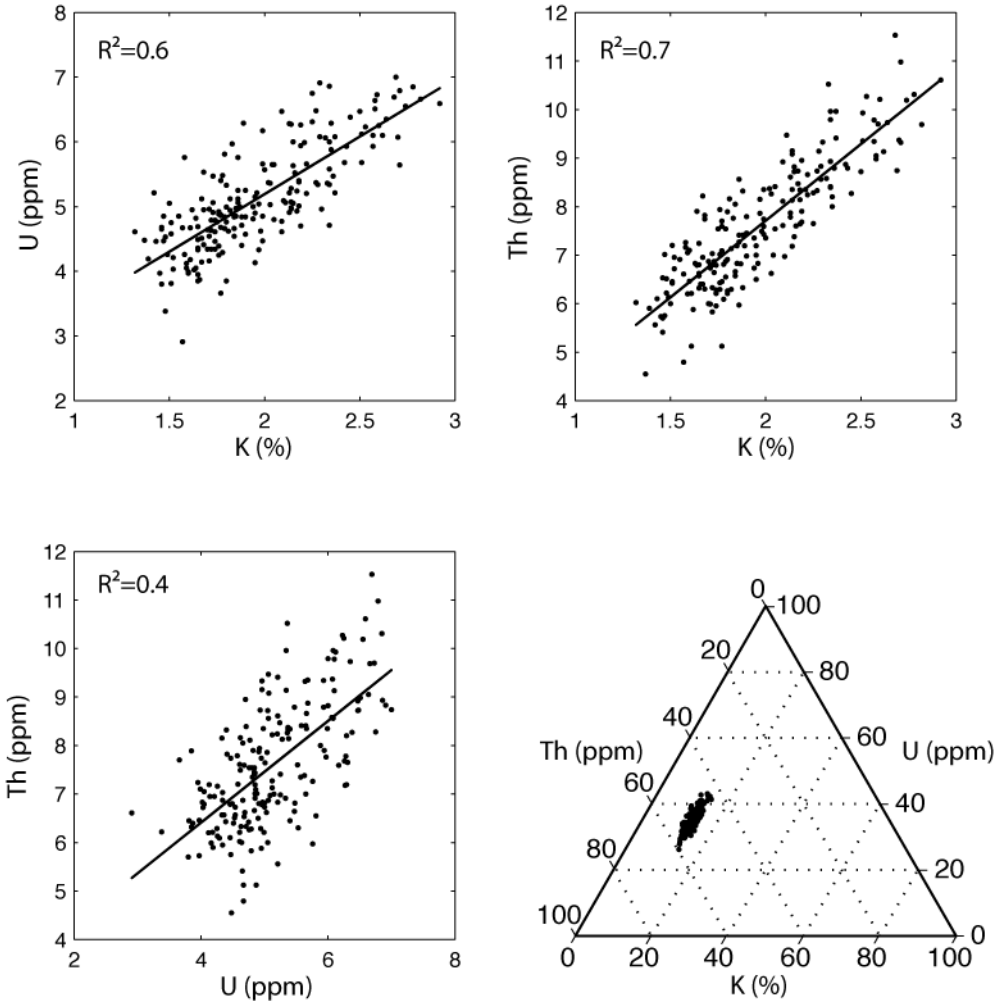

Figure 4.9 | Spectral gamma ray cross-plot and ternary diagram. Positive correlations exist between the individual radioelements measured during spectral gamma ray logging. See also Table 4.4 for additional correlation coefficients.

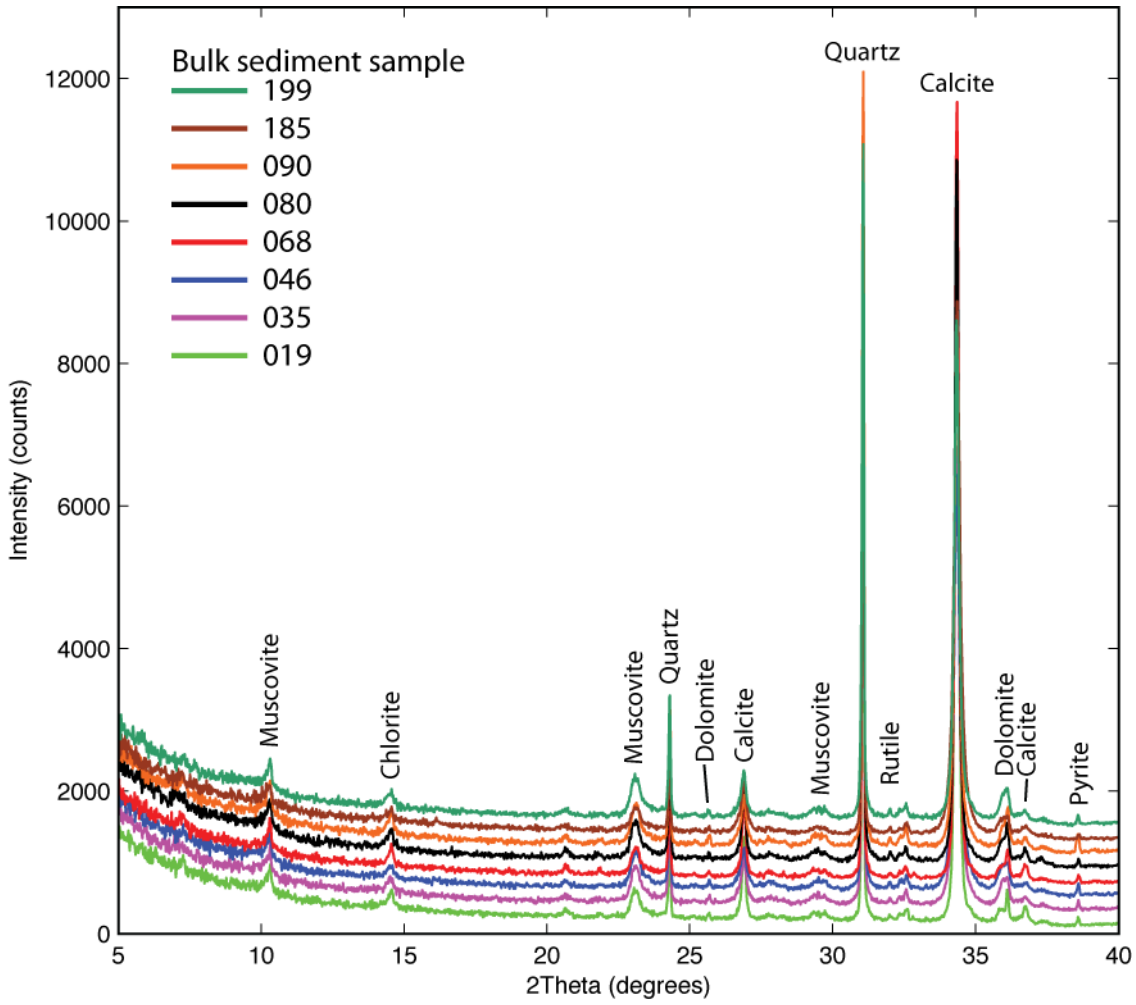

Figure 4.10 | XRD spectra obtained from 8 bulk sediment samples. Analyses of bulk sediment samples using X-ray powder diffractometery enabled their constituent mineralogy to be identified. The intensity of each peak is proportional to the abundance of that mineral, therefore, enabling semi-quantitative mineralogical concentrations to be determined (Table 4.5). Each XRD spectra are artificially spaced by 200 counts.

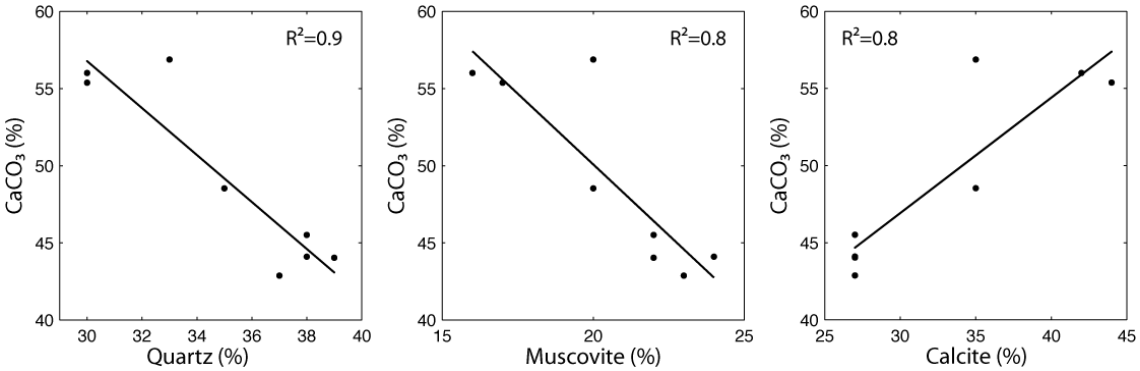

Figure 4.11 | Cross-plots comparing XRD determined mineralogy and bulk sediment carbonate content. Y-axis values are from bulk sediment analysis whilst x-axis data from bulk sediment XRD analysis (refer to Chapter 2 for relevant methodologies). The positive correlation between the carbonate content indicators suggests the estimates are likely reliable. The negative correlations between carbonate content and terrigenous indicators (quartz and muscovite) are indicative of dilution affects.

Table 4.4 – Pearson correlation coefficients

	$\delta^{13}C$	TOC %	CaCO3 (%)	K (%)	U (ppm)	Th (ppm)	Th/K	Th/U
N=165								
$\delta^{13}C$	1.000	0.000	0.238	0.039	0.032	0.108	0.051	0.019
$\delta^{18}O$	0.031	0.000	0.053	0.168	0.101	0.107	0.062	0.001
N=195								
TOC %		1.000	0.153	0.001	0.002	0.008	0.012	0.026
$CaCO_3$ (%)			1.000	0.206	0.117	0.168	0.015	0.007
K (%)				1.000	0.613	0.746	0.119	0.022
U (ppm)					1.000	0.424	0.095	0.127
Th (ppm)						1.000	0.028	0.216
Th/K							1.000	0.320
Th/U								1.000

Table 4.5 – XRD and relevant bulk sediment results

	XRD Run							
	XU915	**XU864**	**XU922**	**XU877**	**XU907**	**XU908**	**XU920**	**XU914**
Bulk Sample	199	185	90	80	68	46	35	19
Height (m)	37.79	35.19	16.83	14.83	12.42	8.47	6.57	3.24
XRD*								
Calcite (%)	27.00	35.00	27.00	35.00	44.00	27.00	27.00	42.00
Chlorite (%)	5.00	6.00	5.00	5.00	4.00	7.00	6.00	5.00
Muscovite (%)	24.00	20.00	22.00	20.00	17.00	23.00	22.00	16.00
Quartz (%)	38.00	33.00	39.00	35.00	30.00	37.00	38.00	30.00
Rutile (%)	1.00	1.00	1.00	1.00	1.00	1.00	3.00	3.00
Dolomite (%)	2.00	1.00	2.00	2.00	2.00	2.00	2.00	2.00
Pyrite (%)	3.00	4.00	4.00	2.00	2.00	4.00	3.00	2.00
Bulk Sediment								
TOC %	0.32	0.23	0.30	0.23	0.25	0.28	0.28	0.28
CaCO3 (%)	44.10	56.87	44.04	48.53	55.38	42.87	45.52	56.01
$\delta^{13}C$ (‰)	-0.78	0.56	-0.32	-0.29	0.44	-0.08	-0.15	0.24
$\delta^{18}O$ (‰)	-4.57	-4.70	-5.54	-4.72	-4.82	-4.58	-4.69	-5.37
K (%)	2.64	1.57	2.36	2.92	1.72	2.27	2.45	1.66
U (ppm)	6.35	2.91	5.47	6.59	4.79	5.37	6.38	3.87
Th (ppm)	9.73	6.61	8.79	10.61	5.83	8.33	8.27	6.40
Th/K	3.69	4.20	3.72	3.64	3.39	3.67	3.37	3.85
Th/U	1.53	2.27	1.61	1.61	1.22	1.55	1.30	1.65

*XRD mineralogical concentrations are semi-quantitative.

Table 4.6 – XRD and bulk sediment correlation coefficients*

	XRD		
	Calcite (%)	**Muscovite (%)**	**Quartz (%)**
XRD			
Calcite (%)	1.00		
Muscovite (%)	0.92	1.00	
Quartz (%)	0.95	0.87	1.00
Bulk sediment			
TOC (%)	0.33	0.28	0.32
$CaCO_3$ (%)	0.79	0.75	0.85
$\delta^{13}C$ (‰)	0.50	0.53	0.60
$\delta^{18}O$ (‰)	0.04	0.16	0.02
K (%)	0.40	0.43	0.54
U (ppm)	0.29	0.32	0.43
Th (ppm)	0.42	0.46	0.54
Th/K	0.01	0.01	0.03
Th/U	0.00	0.00	0.01

*Pearson correlation coefficients calculated using 8 samples.

4.3.3 Sediment petrography

Petrographic analyses of 17 inter-fan sediment samples (Appendix Plate 1.2; Figs. 4.4, 4.6) reveal they are mainly composed of pale brown, clay sized particles below the resolution of a petrographic analysis. Samples 060 and 058 contain the greatest abundance of well-sorted, angular, very-fine sand sized grains of mainly calcite and quartz. Grains are either well distributed throughout the thin-section or concentrated within discontinuous bands. The remaining samples were essentially homogeneous in relation to the distribution of these grains. Irregularly shaped opaque minerals are pervasive throughout the samples with proportions remaining relatively constant. Micro-bioturbation is pervasive throughout the samples with the largest burrows (~2 mm diameter) visible in sample 091.

Samples contain frequent bioclasts including miliolids, *Ostracod sp.*, *Echinoid sp.*, algae fragments and planktonic and benthic foraminifera, which are commonly infilled with sparitic calcite. Comparison between the 17 thin-sections reveals that samples 035, 040, 058 and 061, which contain the least $CaCO_3$ (44-49%) contents, contain fewer bioclasts when compared to samples 064, 065, 066 and 067 with greater $CaCO_3$ (~57%) contents. Although not entirely consistent, those samples with lower $CaCO_3$ content appear to be those with a greater proportion of detrital grains.

4.3.4 Spectral results

Results from REDFIT and MTM F-test spectral analyses of the lower 43.75 m of the Locality 1 section reveal the presence of regular cyclicity above the 90% confidence (Table 4.7; Figs. 4.12, 4.13). Within the 0.023-0.186 cycles/m frequency range, several distinct frequency bands are commonly identified above the 90% confidence level. These are positioned at 0.032-0.037, 0.080-0.111 and 0.160-0.186 cycles/m. Taking both REDFIT (±0.022 cycles/m) and MTM F-test (±0.012 cycles/m) bandwidth into account these frequency variations are minimal.

Wavelet spectral results identify frequencies within similar bands to REDFIT and MTM F-test spectra (Fig. 4.14). Spatially, the ~0.025 cycles/m (~1/40 m) frequency is present to above the 90% confidence level throughout the majority of the time series except for TOC, $\delta^{13}C$ and Th/U. The ~0.087 cycles/m (~1/12 m) frequency is spatially variable and identified within all but the TOC, K and U time series to >90% confidence level. The spatial distribution of the ~0.087 cycles/m (~1/11.5 m) frequency within the $\delta^{13}C$ and $\delta^{18}O$ time series, persistently exceeds the 90% confidence level throughout whilst the remaining spectra indicate the frequency is spatially sporadic. The ~0.171

cycles/m (~1/5.9 m) frequency is only identified as exceeding the 90% confidence level intermittently within the CaCO3, $\delta^{13}C$, $\delta^{18}O$ and Th/U time series.

ASM analyses including and excluding eccentricity terms identify significant SAR values ranging between 6.90-76.25 cm/kyr (Table 4.8; Fig. 4.13). No significant results were determined for TOC, U and Th/K time series. F-test results from K contained only one significant frequency, which was insufficient for the ASM to be calculated. Only $CaCO_3$, $\delta^{13}C$, $\delta^{18}O$, Th and Th/U F-test results provided significant SAR estimates when including and excluding eccentricity terms. The most consistent ASM results are the SAR estimates between 23-27 cm/kyr with null hypothesis levels between 0.176-0.014% (Table 4.8). Applying the significant SAR values to the MTM F-test frequencies used yield a range of potential temporal periods (Table 4.9).

Table 4.7a – Spectral results

Spectral Estimation Method	Frequency (cycles/m)*	Period (m)	Confidence Level (%)	Temporal Period (kyr)†
Th/U				
Wavelet	0.050	20.15	90.0	80.8
	0.100	10.05	90.0	40.3
	0.173	5.80	90.0	23.2
REDFIT§	0.111	9.02	Critical (99.2)	36.1
	0.173	5.80	95.0	23.2
	0.327	3.06	95.0	12.3
	0.413	2.42	95.0	9.7
MTM F-test#	0.056	18.01	87.7	72.2
	0.102	9.82	90.8	39.4
	0.273	3.66	85.9	14.7
	0.319	3.13	91.8	12.6
	0.417	2.40	99.8	9.6

*Frequencies between 0-0.5 cycles/m provided. Full results are located within the digital Appendix.
†Temporal period determined using the average SAR of 24.95 cm/kyr identified from ASM analyses.
§All REDFIT analyses have bandwidth (BW) = ±0.022 cycles/m.
#All MTM F-test analyses have bandwidth (BW) = ±0.012 cycles/m.

Table 4.7b – Spectral results

Spectral Estimation Method	Frequency (cycles/m)	Period (m)	Confidence Level (%)	Temporal Period (kyr)
$CaCO_3$				
Wavelet	0.024	42.41	90.0	170.0
	0.096	10.37	90.0	41.6
	0.171	5.86	90.0	23.5
REDFIT	0.025	40.67	Critical (99.3)	163.0
	0.098	10.17	Critical (99.3)	40.8
	0.160	6.26	90.0	25.1
MTM F-test	0.098	10.24	86.79	41.0
	0.161	6.21	91.55	24.9
	0.264	3.79	97.04	15.2
	0.396	2.53	91.36	10.1
	0.439	2.28	98.84	9.1
$\delta^{13}C$				
Wavelet	0.047	21.14	90.0	84.7
	0.096	10.46	90.0	41.9
	0.170	5.90	90.0	23.6
REDFIT	0.006	162.68	Below R_f	652.0
	0.098	10.17	95.0	40.8
	0.160	6.26	95.0	25.1
MTM F-test	0.039	25.60	80.8	102.6
	0.098	10.24	91.4	41.0
	0.186	5.39	90.3	21.6
	0.347	2.88	80.9	11.6
	0.366	2.73	80.4	10.9

Spectral Estimation Method	Frequency (cycles/m)	Period (m)	Confidence Level (%)	Temporal Period (kyr)
TOC				
Wavelet	0.209	4.78	90.0	19.2
	0.372	2.69	90.0	10.8
REDFIT	0.252	3.97	90.0	15.9
	0.357	2.80	80.0	11.2
	0.418	2.39	80.0	9.6
MTM F-test	0.059	17.07	88.5	68.4
	0.122	8.19	89.4	32.8
	0.161	6.21	89.5	24.9
	0.259	3.86	97.7	15.5
	0.352	2.84	97.5	11.4
	0.425	2.35	82.4	9.4
$\delta^{18}O$				
Wavelet	0.023	42.60	90.0	170.7
	0.047	21.38	90.0	85.7
	0.072	13.94	90.0	55.9
REDFIT	0.006	162.68	Below R_f	652.0
	0.080	12.51	Critical (99.3)	50.2
	0.172	5.81	90.0	23.3
MTM F-test	0.088	11.38	95.2	45.6
	0.186	5.39	96.4	21.6
	0.376	2.66	94.9	10.7
	0.532	1.88	98.1	7.5

Table 4.7c – Spectral results

Spectral Estimation Method	Frequency (cycles/m)	Period (m)	Confidence Level (%)	Temporal Period (kyr)
K				
Wavelet	0.025	40.60	90.0	162.7
	0.076	13.12	80.0	52.6
REDFIT	0.012	81.14	Below R_f	325.2
	0.080	12.48	90.0	50.0
MTM F-test	0.032	30.87	90.5	123.7
	0.162	6.17	80.4	24.7
	0.259	3.86	85.9	15.5
	0.319	3.13	83.7	12.6
	0.421	2.37	88.9	9.5
Th				
Wavelet	0.025	40.35	90.0	161.7
	0.049	20.49	90.0	82.1
REDFIT	0.018	54.09	Below R_f	216.8
MTM F-test	0.037	27.01	93.2	108.2
	0.264	3.79	91.0	15.2
	0.356	2.81	92.3	11.2
	0.467	2.14	86.9	8.6

Spectral Estimation Method	Frequency (cycles/m)	Period (m)	Confidence Level (%)	Temporal Period (kyr)
U				
Wavelet	0.025	40.31	90.0	161.6
REDFIT	0.012	81.14	Below R_f	325.2
	0.080	12.48	95.0	50.0
	0.265	3.77	80.0	15.1
	0.314	3.18	90.0	12.8
MTM F-test	0.032	30.87	93.4	123.7
	0.157	6.35	86.9	25.5
	0.259	3.86	82.0	15.5
	0.319	3.13	91.5	12.6
	0.417	2.40	99.3	9.6
	0.463	2.16	85.7	8.7
Th/K				
Wavelet	0.025	40.66	90.0	163.0
	0.049	20.31	90.0	81.4
	0.074	13.50	90.0	54.1
REDFIT	0.012	81.14	Below R_f	325.2
	0.080	12.48	95.0	50.0
	0.314	3.18	95.0	12.8
	0.407	2.46	80.0	9.9
MTM F-test	0.083	12.00	89.0	48.1
	0.120	8.31	83.9	33.3
	0.315	3.18	97.7	12.7
	0.421	2.37	99.0	9.5

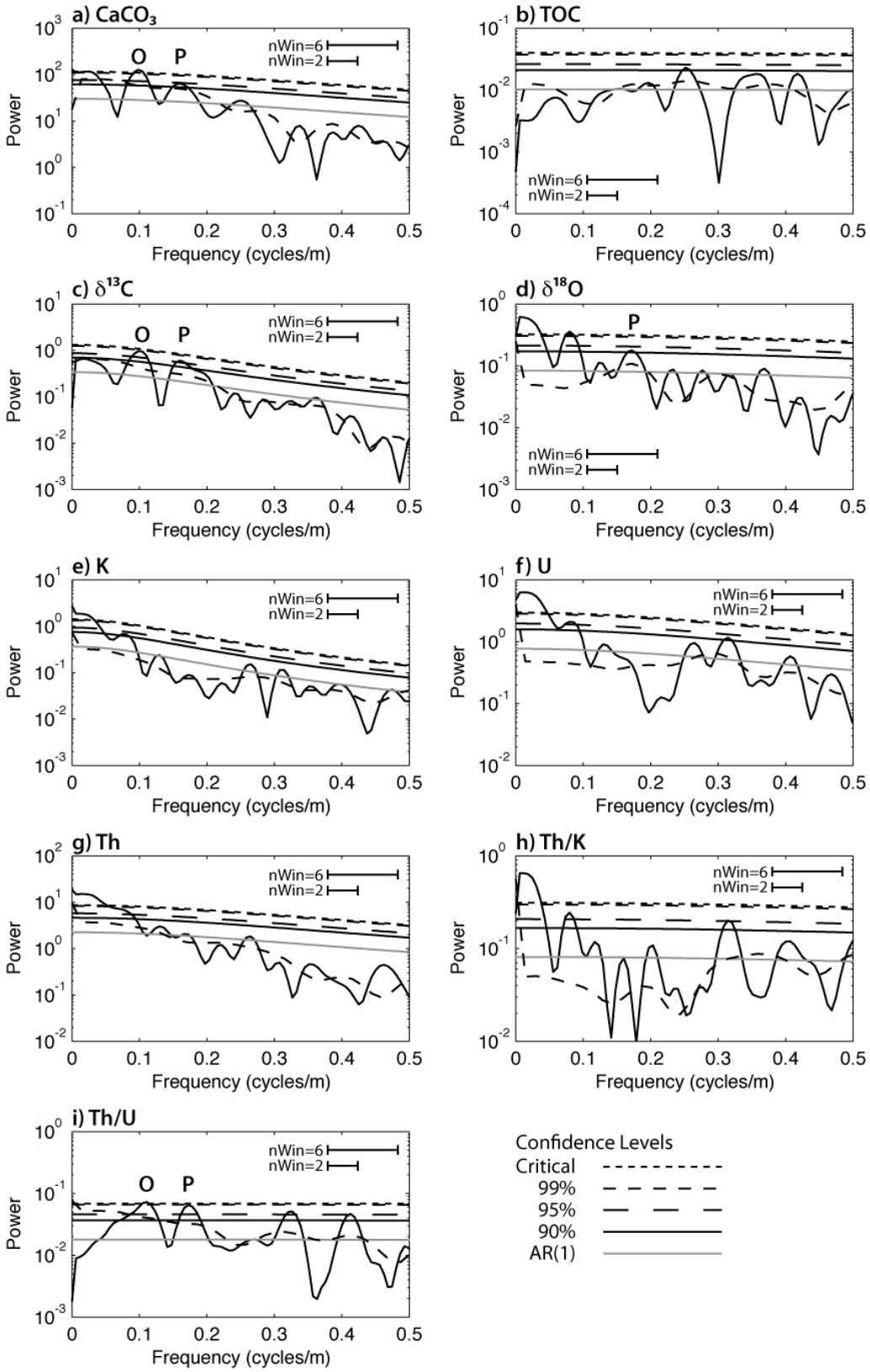

Figure 4.12 | REDFIT spectrum determined from each time series. Spectra for each time series were calculated twice using 2 (dashed line) and 6 (solid line) WOSA windows. Spectra calculated using 6 WOSA windows had 8 degrees of freedom but resulted in poor spectral resolution (large BW). Increased resolution was achieved using only 2 WOSA windows, which resulted in 3 degrees of freedom. Although below the recommended 8 degrees of freedom the higher resolution spectra are assumed reliable.

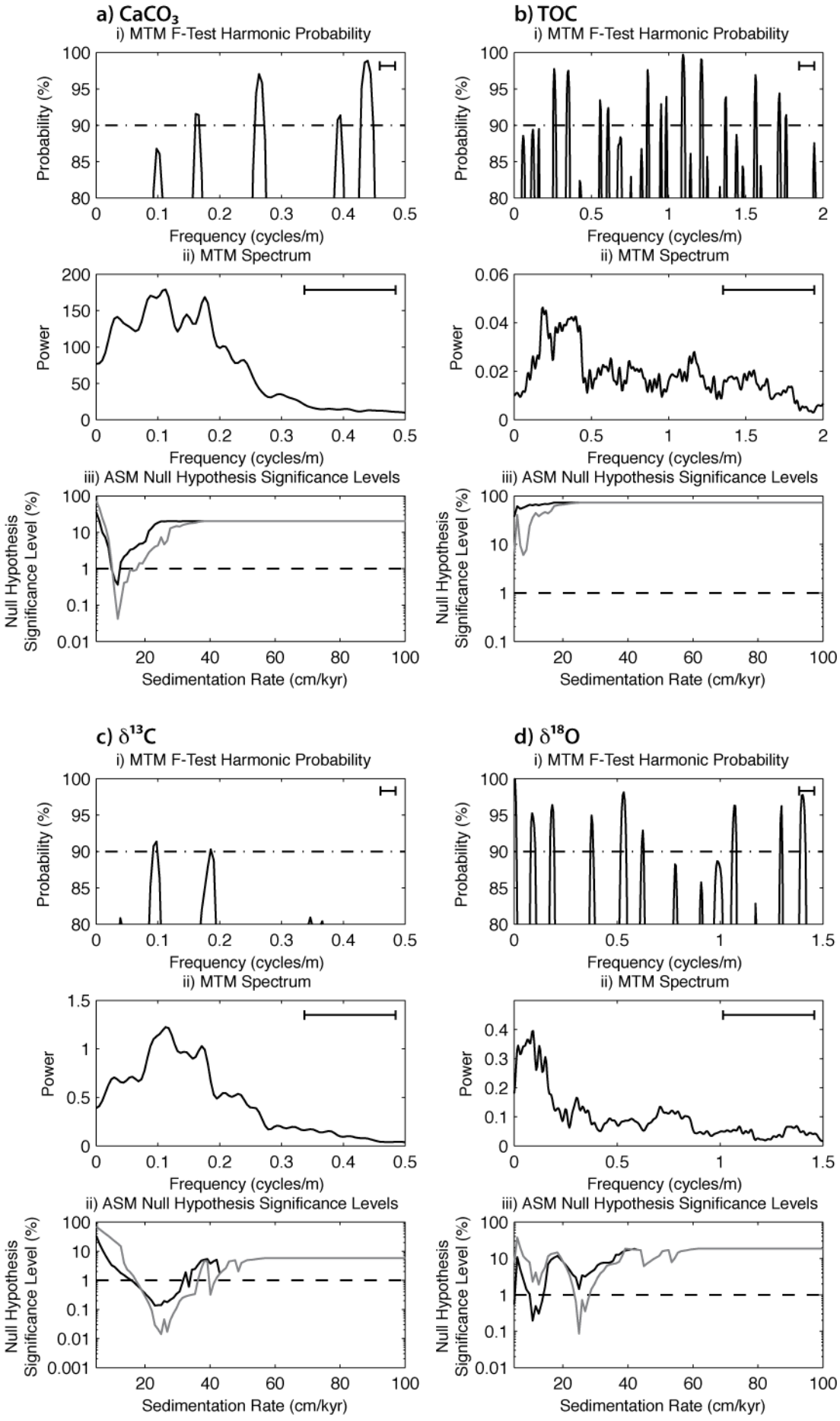
a) CaCO3
i) MTM F-Test Harmonic Probability
Probability (%)
Frequency (cycles/m)
ii) MTM Spectrum
Power
Frequency (cycles/m)
iii) ASM Null Hypothesis Significance Levels
Null Hypothesis Significance Level (%)
Sedimentation Rate (cm/kyr)
b) TOC
i) MTM F-Test Harmonic Probability
Probability (%)
Frequency (cycles/m)
ii) MTM Spectrum
Power
Frequency (cycles/m)
iii) ASM Null Hypothesis Significance Levels
Null Hypothesis Significance Level (%)
Sedimentation Rate (cm/kyr)
c) δ13C
i) MTM F-Test Harmonic Probability
Probability (%)
Frequency (cycles/m)
ii) MTM Spectrum
Power
Frequency (cycles/m)
ii) ASM Null Hypothesis Significance Levels
Null Hypothesis Significance Level (%)
Sedimentation Rate (cm/kyr)
d) δ18O
i) MTM F-Test Harmonic Probability
Probability (%)
Frequency (cycles/m)
ii) MTM Spectrum
Power
Frequency (cycles/m)
iii) ASM Null Hypothesis Significance Levels
Null Hypothesis Significance Level (%)
Sedimentation Rate (cm/kyr)

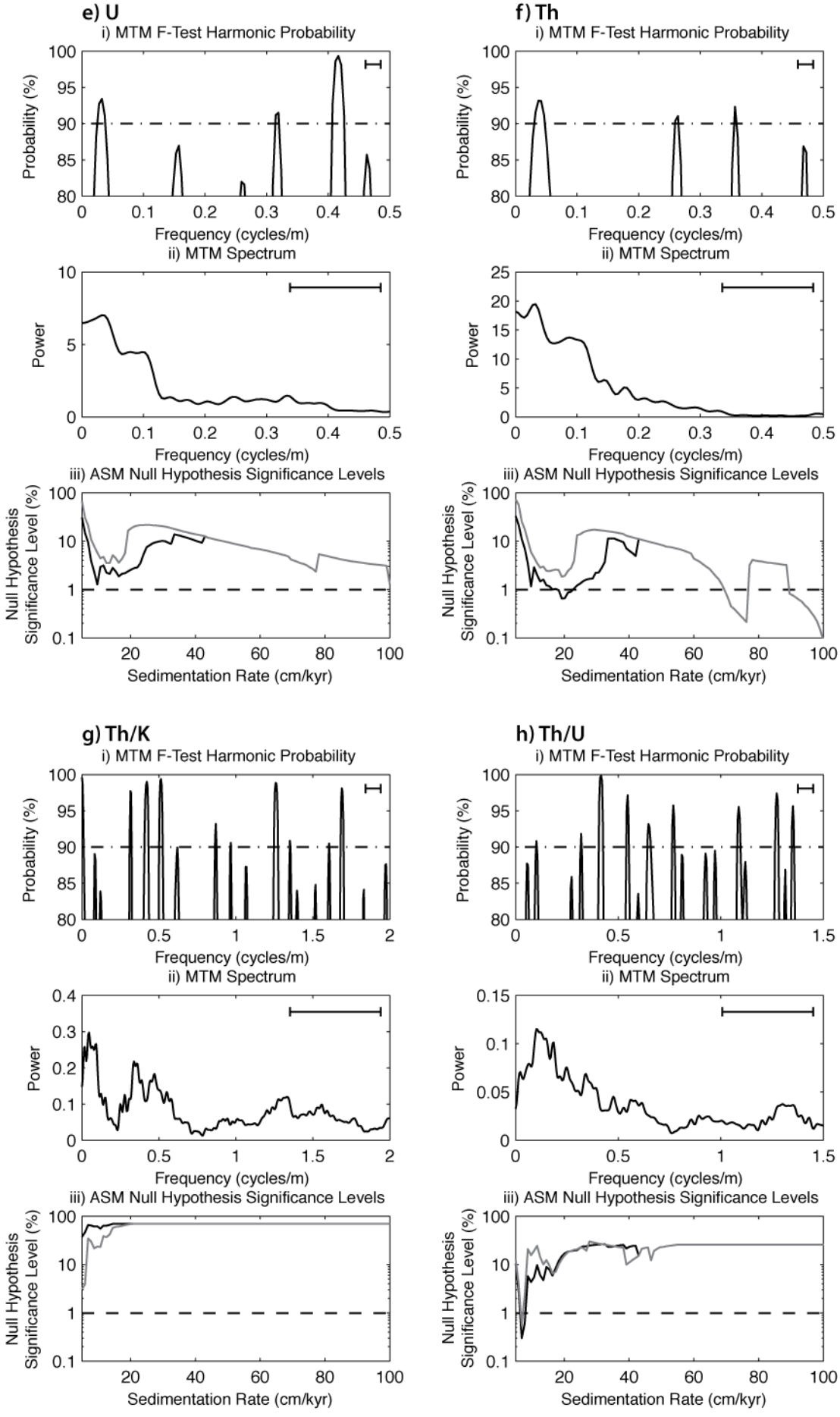
e) U
i) MTM F-Test Harmonic Probability
Probability (%)
Frequency (cycles/m)
ii) MTM Spectrum
Power
Frequency (cycles/m)
iii) ASM Null Hypothesis Significance Levels
Null Hypothesis Significance Level (%)
Sedimentation Rate (cm/kyr)
f) Th
i) MTM F-Test Harmonic Probability
Probability (%)
Frequency (cycles/m)
ii) MTM Spectrum
Power
Frequency (cycles/m)
iii) ASM Null Hypothesis Significance Levels
Null Hypothesis Significance Level (%)
Sedimentation Rate (cm/kyr)
g) Th/K
i) MTM F-Test Harmonic Probability
Probability (%)
Frequency (cycles/m)
ii) MTM Spectrum
Power
Frequency (cycles/m)
iii) ASM Null Hypothesis Significance Levels
Null Hypothesis Significance Level (%)
Sedimentation Rate (cm/kyr)
h) Th/U
i) MTM F-Test Harmonic Probability
Probability (%)
Frequency (cycles/m)
ii) MTM Spectrum
Power
Frequency (cycles/m)
iii) ASM Null Hypothesis Significance Levels
Null Hypothesis Significance Level (%)
Sedimentation Rate (cm/kyr)

Figure 4.13 (previous 2 pages) | Multi-Taper Method spectral and Average Spectral Misfit results. (i) Significant frequencies (>90%) were identified from each time series using the MTM harmonic F-test (Table 4.7). Bandwidth represented by horizontal bar. (ii) The MTM spectra were utilised to determine frequency range whilst the variance (area below the curve) was calculated in 0.5 cycles/m increments. The maximum frequency corresponded to ~80% variance in accordance with Meyers et al. (2008). Bandwidth represented by horizontal bar. (iii) ASM calculations were run using all orbital terms (black solid line) and without eccentricity terms (grey solid line). Only those SAR estimates with H_o significance levels below the critical level (0.99009901%; dashed line) are included within Tables 4.8 and 4.9. ASM analyses were not performed as insufficient significant frequencies were identified (Table 4.7).

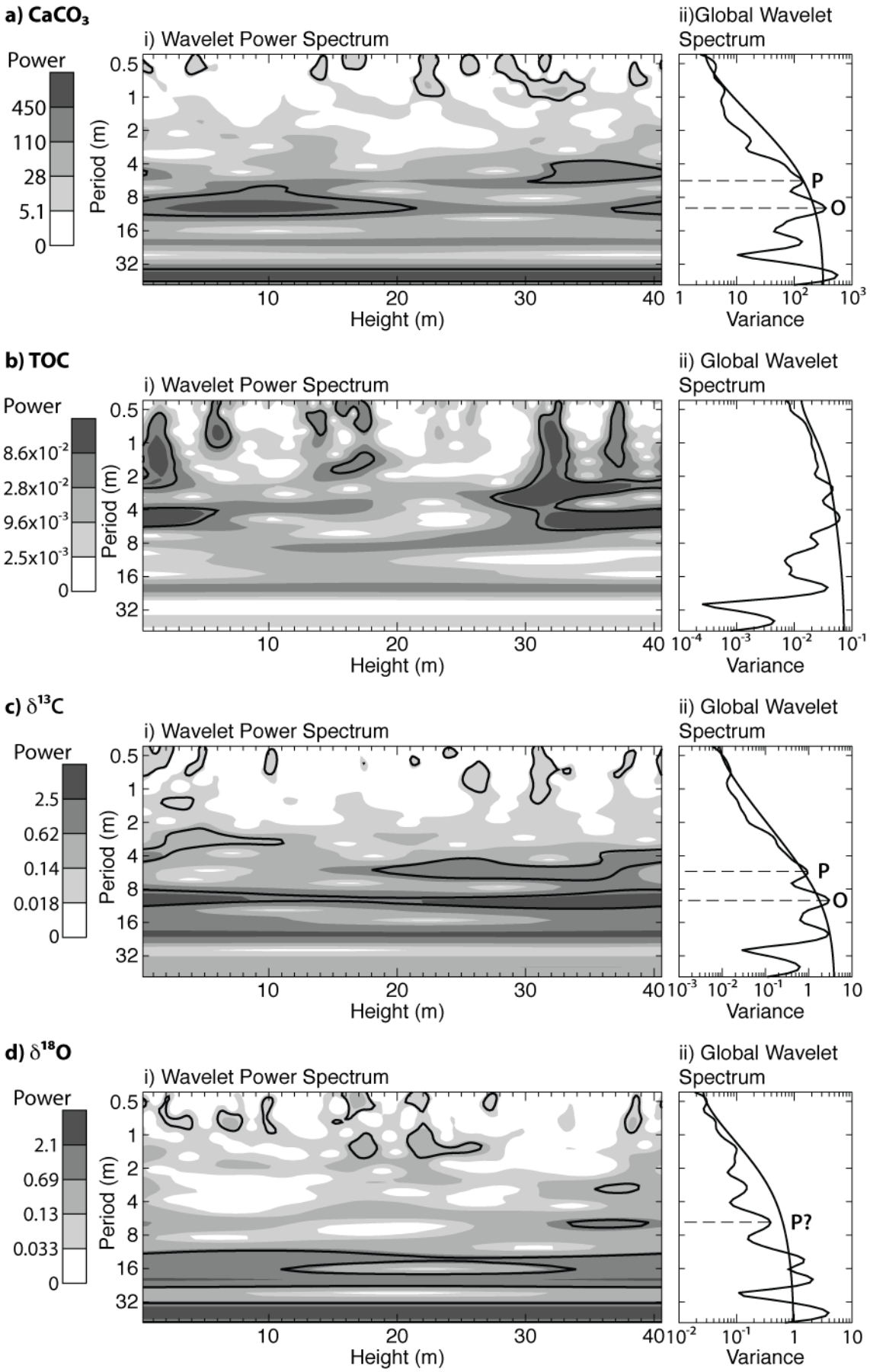
a) CaCO3
i) Wavelet Power Spectrum
ii)Global Wavelet Spectrum
Power
450
110
28
5.1
0
Period (m)
0.5
1
2
4
8
16
32
10
20
30
40
Height (m)
P
O
1
10
10^2
10^3
Variance
b) TOC
i) Wavelet Power Spectrum
ii) Global Wavelet Spectrum
Power
8.6x10^-2
2.8x10^-2
9.6x10^-3
2.5x10^-3
0
Period (m)
Height (m)
10^-4
10^-3
10^-2
10^-1
Variance
c) δ13C
i) Wavelet Power Spectrum
ii) Global Wavelet Spectrum
Power
2.5
0.62
0.14
0.018
0
Period (m)
Height (m)
P
O
10^-3
10^-2
10^-1
1
10
Variance
d) δ18O
i) Wavelet Power Spectrum
ii) Global Wavelet Spectrum
Power
2.1
0.69
0.13
0.033
0
Period (m)
Height (m)
P?
10^-2
10^-1
1
10
Variance

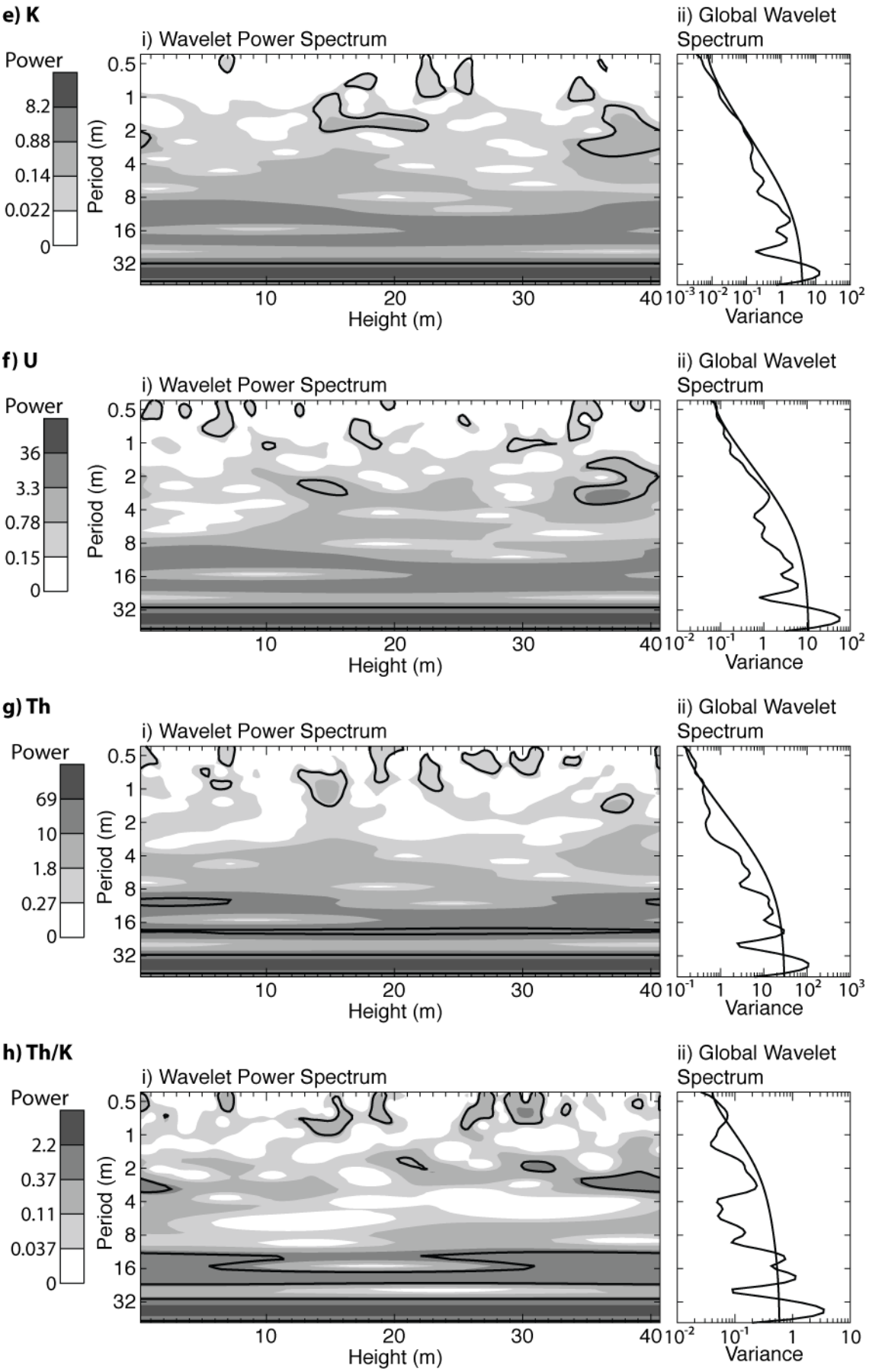
e) K
i) Wavelet Power Spectrum
ii) Global Wavelet Spectrum
Power
8.2
0.88
0.14
0.022
0
Period (m)
0.5
1
2
4
8
16
32
10
20
30
40
Height (m)
10^{-3} 10^{-2} 10^{-1} 1 10 10^{2}
Variance
f) U
i) Wavelet Power Spectrum
ii) Global Wavelet Spectrum
Power
36
3.3
0.78
0.15
0
Period (m)
0.5
1
2
4
8
16
32
10
20
30
40
Height (m)
10^{-2} 10^{-1} 1 10 10^{2}
Variance
g) Th
i) Wavelet Power Spectrum
ii) Global Wavelet Spectrum
Power
69
10
1.8
0.27
0
Period (m)
0.5
1
2
4
8
16
32
10
20
30
40
Height (m)
10^{-1} 1 10 10^{2} 10^{3}
Variance
h) Th/K
i) Wavelet Power Spectrum
ii) Global Wavelet Spectrum
Power
2.2
0.37
0.11
0.037
0
Period (m)
0.5
1
2
4
8
16
32
10
20
30
40
Height (m)
10^{-2} 10^{-1} 1 10
Variance

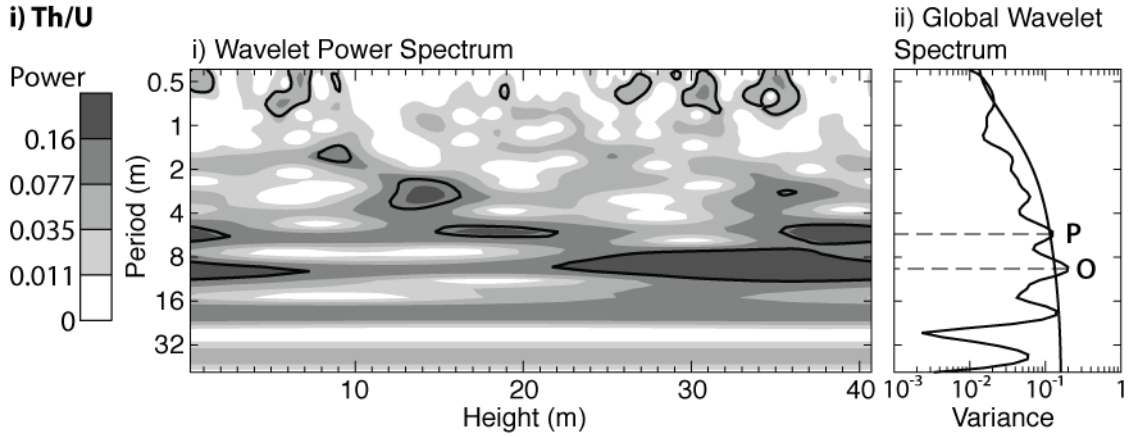

Figure 4.14 | Wavelet spectra for each time series shown in Figure 4.5. (i) Wavelet spectra illustrate the spatial distribution of frequencies throughout the individual time series. Bold contours represent the 90% confidence level. (ii) Global wavelet spectra represent the average variance throughout the entire time series. Those frequencies exceeding the 90% confidence level (solid line) and corresponding to the predicted obliquity (O) and precession (P) periods are marked.

Table 4.8 – ASM results

	All Orbital Terms				No Eccentricity Terms			
Stratigraphic time series*	**SAR (cm/kyr)**	**Ho Level (%)**	**ASM (cm/kyr)**	**No. of Orbital Terms**	**SAR (cm/kyr)**	**Ho Level (%)**	**ASM (cm/kyr)**	**No. of Orbital Terms**
$CaCO_3$	11.65	0.363	4.78E-03	6	11.65	0.042	2.45E-03	4
					16.40	0.869	4.28E-03	4
$\delta^{13}C$	23.05	0.135	6.71E-03	6	24.95	0.014	3.02E-03	4
	26.85	0.176	7.85E-03	6	26.85	0.017	3.27E-03	4
	33.50	0.594	1.29E-02	5	40.15	0.318	1.21E-02	4
$\delta^{18}O$	5.00	0.553	2.20E-03	7	24.95	0.086	1.67E-03	4
	10.70	0.195	2.35E-03	6	26.85	0.353	2.60E-03	4
	12.60	0.303	2.73E-03	6				
Th	19.25	0.652	6.65E-03	6	76.25	0.212	1.02E-02	4
	76.25	0.212	1.02E-02	4				
Th/U	6.90	0.299	2.14E-03	7	6.90	0.546	1.47E-03	4

*Only stratigraphic time series with significant SAR estimates are provided.

Table 4.9 – Temporal duration of MTM F-test frequencies

$CaCO_3$ SAR Estimate (cm/kyr)		All terms	No ecc. terms	
SAR (cm/kyr)		11.65	11.65	16.40
Frequency (cycles/m)*	Confidence Level (%)	Temporal period when applying SAR estimate†		
0.161	91.5	53.3	53.3	37.8
0.264	97.0	32.6	32.6	23.1
0.396	91.4	21.7	21.7	15.4
0.439	98.8	19.5	19.5	13.9

$\delta^{13}C$ SAR Estimate (cm/kyr)		All terms			No ecc. terms		
SAR (cm/kyr)		23.05	26.85	33.50	24.95	26.85	40.15
Frequency (cycles/m)	Confidence Level (%)	Temporal period when applying SAR estimate					
0.098	91.4	44.4	38.1	30.6	41.0	38.1	25.5
0.186	90.3	23.4	20.1	16.1	21.6	20.1	13.4

$\delta^{18}O$ SAR Estimate (cm/kyr)		All terms			No ecc. terms	
SAR (cm/kyr)		5.00	10.70	12.60	24.95	26.85
Frequency (cycles/m)	Confidence Level (%)	Temporal period when applying SAR estimate				
0.088	95.2	227.6	106.3	90.3	45.6	42.4
0.186	96.4	107.8	50.4	42.8	21.6	20.1
0.376	94.9	53.2	24.9	21.1	10.7	9.9
0.532	98.1	37.6	17.6	14.9	7.5	7.0
0.625	92.9	32.0	15.0	12.7	6.4	6.0
1.069	96.3	18.7	8.7	7.4	3.7	3.5
1.299	96.2	15.4	7.2	6.1	3.1	2.9
1.401	97.8	14.3	6.7	5.7	2.9	2.7

Th SAR Estimate (cm/kyr)		All terms		No ecc. terms
SAR (cm/kyr)		19.25	76.25	76.25
Frequency (cycles/m)	Confidence Level (%)	Temporal period when applying SAR estimate		
0.037	93.2	140.3	35.4	35.4
0.264	91.0	19.7	5.0	5.0
0.356	92.3	14.6	3.7	3.7

Th/U SAR Estimate (cm/kyr)		All terms	No ecc. terms
SAR (cm/kyr)		6.90	6.90
Frequency (cycles/m)	Confidence Level (%)	Temporal period when applying SAR estimate	
0.102	90.8	142.3	142.3
0.319	91.8	45.4	45.4
0.417	99.8	34.8	34.8
0.546	97.1	26.5	26.5
0.648	93.2	22.4	22.4
0.768	95.7	18.9	18.9
1.088	95.5	13.3	13.3
1.273	97.4	11.4	11.4
1.351	95.6	10.7	10.7

*Frequencies determined from the MTM F-test. Frequency ranges represent ~80% of total variance within the MTM spectrum.

†Using significant SAR values identified from ASM analyses it is possible to establish the frequency that each orbital period was assigned.

4.4 Interpretation

4.4.1 Stratigraphic correlations

Correlations between localities 1 and 2 are provided in Figure 4.15. Lateral correlations are based upon the presence of various dark-coloured marlstone (DB1-3) beds, type-Ib MTCs, sand packages and colour between localities 1, 2 and 4. Local mapping identifies the DB-1 marl bed as being laterally extensive, which therefore provides an excellent local marker horizon (Fig. 4.2). Thinner dark grey marl horizons (DB-2 & 3) are relatively limited in aerial extent but remain relatively useful markers.

The observation of lateral facies changes from inter-bedded sandstone to MTCs and lithified marlstones enable further correlations between localities to be made. The sand-MTC-marl sequence located ~5 m above DB-1 can therefore be identified occurring over a ~860 m distance between localities 1, 2 and 4 (Figure 4.15). Such sandstone-MTC-lithified marl transitions have been interpreted as representing a channel-axis to more off-axis depositional setting (Pickering and Corregidor, 2000, 2005).

The medium-coarse grained sandstones and underlying type-Ib MTC, which mark the top of localities 1 and 2, are laterally correlative with the off-axis deposit of the Guaso-II submarine fan complex (Figs. 4.2, 4.3). The base of the section at Locality 1 consists of the uppermost sandstones of the Guaso-I submarine fan complex. The measured section at Locality 1 therefore includes the entire inter-fan sediments between the two Guaso submarine fans. The stratigraphy at Locality 1 is assumed relatively complete despite the presence of several type-Ia and -Ib MTCs, which either duplicate or represent missing stratigraphy.

Figure 4.15 | Proposed correlations between measured sections taken from localities 1, 2 and 4. With the DB-1 bed being present at each section it was used as a datum. The remaining correlations are based upon colour, mapping or expected lateral facies variations. Full scale version of the figure can be found within the Appendix.

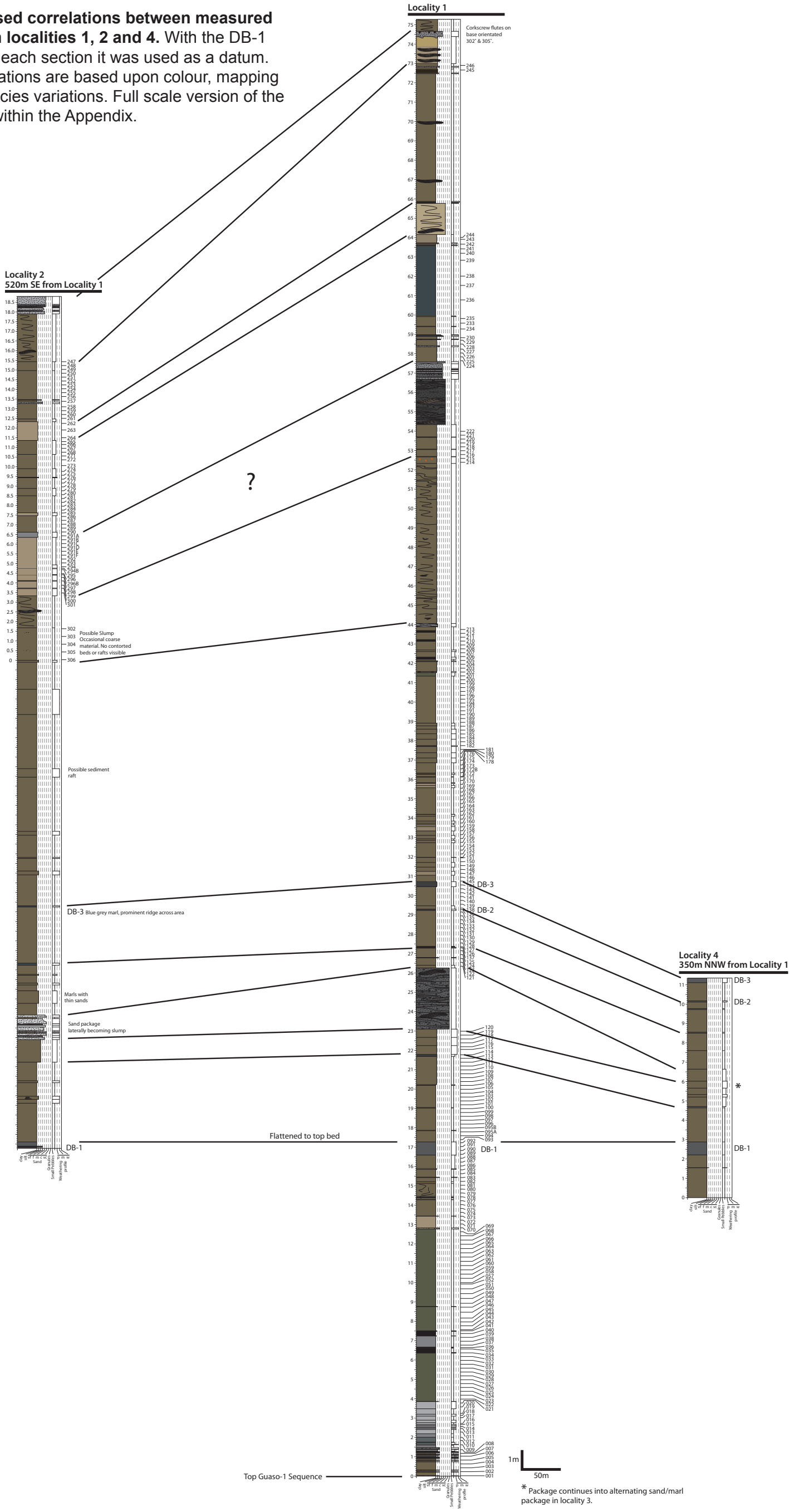

4.4.2 Sediment geochemistry

4.4.2.1 Calcium carbonate content

The ~20% variability in carbonate content could be attributable to productivity, dissolution, dilution or to diagenetic processes (Einsele, 1982; Fischer, 1986; Westphal et al., 2010). Of the possible primary factors, the sediment carbonate content was likely to have been controlled by dilution cycles (Dean and Gardner, 1986; De Visser et al., 1989; Shimmield and Mowbray, 1991; Harris and Mix, 1999; Hyun et al., 2005; Laurin et al., 2005; Sagasti, 2005). Although limited (N=8), the inverse correlations (R^2=0.75-0.85) between terrigenous components (quartz and muscovite) and carbonate content strongly indicate dilution controlled the carbonate content (Figure 4.11). Additional evidence, although statistically insignificant (Table 4.4), is provided from an inverse relationship between carbonate content and K radioelement concentrations. Limited petrographic thin-section analyses also suggest that periods of increased detrital supply correspond to depleted $\delta^{13}C$ and carbonate contents (Figs. 4.4, 4.6, 4.16).

The remaining primary factors for carbonate variation that include productivity and dissolution remain unlikely based upon the observed geochemical relationships and observations. Productivity can be dismissed as a primary control upon carbonate content due to the poor correlation between carbonate and $\delta^{13}C$ (R^2=0.2) and the lack of TOC variability. Variability within marine productivity should result in positive correlations between $CaCO_3$, TOC and $\delta^{13}C$ (Scholle and Arthur, 1980; Marshall, 1992; Kump and Arthur, 1999; Jarvis et al., 2002; Morse, 2003; Wade and Pälike, 2004). Due to the lack of positive correlations between $CaCO_3$, TOC and $\delta^{13}C$ it is assumed that productivity was not the primary driver of carbonate variation. However, the absence of significant TOC variability may be due to the lack of preservation via oxidisation during sub-aerial exposure or diagenetic decomposition.

Dissolution is unlikely to have affected the carbonate content as water depth estimates of 300-800 m (Sutcliffe and Pickering, 2009) place the sediment-water interface well above the Eocene CCD of ~2.7-3.0 km (Zachos et al., 2005; Bohaty et al., 2009; Pälike et al., 2009; Dawber and Tripati, 2011). Dissolution associated with the redox-controlled oxidisation of organic matter (Einsele, 1982; Diester-Haass, 1991) is also unlikely based upon relatively consistent reducing conditions at the sediment-water interface (see below).

Post-depositional diagenetic processes may have produced carbonate variability either by infilling of porosity or re-distribution (Ricken, 1985; Ricken, 1987; Westphal et al., 2000). Carbonate content is unlikely to be related to porosity as where increased grain-size is observed carbonate content is reduced (Fig. 4.16). Alternately,

the diagenetic re-distribution of carbonate from the more clay rich layers to the more pure carbonate layers could be responsible (Fischer, 1986; Westphal et al., 2010). However, within the studied inter-fan sediments, there is little major lithological disparity between the sediments unlike the limestone-marl couplets where this was originally proposed e.g., Einsele (1982). Without further analyses the possibility of secondary diagenetic processes leading to the observed variation in carbonate cannot be dismissed.

Although additional work is required to further constrain the responsible forcing mechanism(s), available evidence suggests dilution was most likely the dominant controlling factor on inter-fan carbonate content. The affects of productivity variation and diagenetic processes are also likely to have contributed but to a lesser extent.

4.4.2.2 Stable isotopes and diagenesis

Prior to interpretation of the isotopic results, it is necessary to determine the potential affects of diagenetic alteration to the primary isotopic signal. The reliability of bulk sediment isotope analysis is mainly linked to the amount of diagenesis the sediment has undergone. Previous studies indicate the differential affects of diagenesis upon preserved isotope compositions (Scholle and Arthur, 1980; Shackleton, 1987; Marshall, 1992). These studies indicate that $\delta^{13}C$ is affected to a lesser extent during diagenetic processes whilst $\delta^{18}O$ values are more readily depleted. The disparity between isotopic values obtained from the Ainsa basin and published Eocene seawater/bulk sediment isotopic compositions are likely indicative of such diagenetic alteration (Fig. 4.8). The least altered isotopic compositions are those obtained from benthic foraminifera whilst the Ainsa core vein calcites represent the most diagenetically altered values. Guaso and Ainsa system bulk sediment isotopic values occupy the zone between these two end members therefore indicating a moderate level of diagenetic alteration.

The observed $\delta^{13}C$ disparity between Guaso hemipelagic and published pelagic bulk sediments are potentially due to differing OM concentrations. Compared to pelagic sediments, hemipelagic sediments are more likely to contain increased levels of marine and terrestrial OM, which contain isotopically light carbon ($\delta^{13}C$ -25‰). During the diagenetic breakdown of OM, isotopically light carbon is liberated and released into pore-waters from which calcite cement is precipitated. The resulting isotopic composition of the calcite will therefore be depleted relative to the amount of OM present (Marshall, 1992; Voigt and Hilbrecht, 1997). Reinforcing this model is the increased amount of OM (mean TOC of 1.29%) present within the slightly more depleted A6 core sediments (Heard et al., 2008).

Based upon the trend within Figure 4.8 diagenesis is likely responsible for the observed $\delta^{13}C$ contrast between Guaso and published Eocene values. The ~1‰ depletion in Guaso System $\delta^{13}C$ values, and the lack of covariance between $\delta^{13}C$ and $\delta^{18}O$ within Figure 4.8, is suggestive of a relatively closed pore water system (Marshall, 1992). Within such a system, the $\delta^{13}C$ composition of pore-waters are influenced by the isotopic composition of the detrital calcite undergoing dissolution (Marshall, 1992). With such a scenario, a "memory" of primary $\delta^{13}C$ values will likely be retained and therefore orbital variability may be recorded.

The significant depletion of Guaso System bulk sediment $\delta^{18}O$ values compared to those expected of the Eocene (Fig. 4.8) is indicative of diagenetic dissolution, and subsequent re-precipitation of calcite occurring at elevated depths, temperatures and the possible presence of meteoric waters (Emery, 1987; Marshall, 1992; Schrag et al., 1995; Trave et al., 1997). Using this interpretation, the distribution of results in Figure 4.8 suggests that the A6 calcite vein samples record diagenetic $\delta^{18}O$ values from a greater depth than the lesser-depleted Guaso bulk sediments. The resultant $\delta^{18}O$ values precipitated during diagenesis will, therefore, record a secondary $\delta^{18}O$ composition of the pore-waters and the temperature of precipitation. Although $\delta^{18}O$ compositions have been diagenetically altered there is still potential for primary trends to be retained (Schrag et al., 1995).

To confirm whether the mean $\delta^{18}O$ values reflects primary (temperature) or secondary (diagenetic) affects, a palaeotemperature estimate is determined using Equation 2.5. Calculations were based upon a mean Guaso (-4.84‰ VPDB) and A6 core vein calcite (-8.02‰ VPDB) values (δ_c) whilst the Eocene seawater (δ_w) $\delta^{18}O$ value was assumed -1.0‰ (SMOW) for an ice-free world. The resultant Guaso and A6 core vein calcite palaeotemperature estimates of 34˚C and 51˚C, respectively, far exceed the expected Eocene benthic 4-14˚C (Zachos et al., 2001; Bohaty et al., 2009) and sea surface temperatures of ~25-27˚C (Bijl et al., 2009; Keating-Bitonti et al., 2011). The $\delta^{18}O$ depletion is therefore indicative of precipitation under elevated temperatures during diagenesis. The distribution of Guaso bulk sediment isotopic values in Figure 4.8 can, therefore be explained in terms of diagenetic alteration between low (benthic foraminifera) and high (A6 core vein calcite) levels of diagenetically altered end members.

Validation of whether the $\delta^{18}O$ and $\delta^{13}C$ values reflect primary climatic change can be determined using the other geochemical data obtained from the inter-fan section (Figs. 4.5, 4.6; Tables 4.4, 4.6). Of the two isotopic variables the $\delta^{18}O$ data is here less likely to reflect a primary climatic signal based upon the lack of any relationships with the other geochemical or mineralogical data (Table 4.6). Carbon

isotopic data, however, demonstrates a reasonable positive relationship with $CaCO_3$ and the mineralogical data (Table 4.6). Assuming that $CaCO_3$ and mineralogy reflect a primary climatic signal then it suggests that $\delta^{13}C$ data, although diagenetically altered, likely retains a 'memory' of climate change. Considering the differing susceptibility of $\delta^{18}O$ and $\delta^{13}C$ values to diagenetic alteration, the $\delta^{13}C$ values are more likely to contain a 'memory' of climate change compared to $\delta^{18}O$ values which are more prone to alteration (Marshall, 1992). Only the use of $\delta^{13}C$ values is therefore justified to identify orbitally forced climatic variability. Any cyclicity within the $\delta^{18}O$ time series is therefore considered unreliable and shall not be considered further.

4.4.2.3 Stable isotopic variation

Mechanisms potentially influencing $\delta^{13}C$ compositions are a differential supply of extra-basinal carbonate and diagenesis. Stratigraphic variation in concentrations of extra-basinal carbonate potentially influenced the isotope composition of the Guaso System carbonates. The source area for the Guaso System clastic sediments is believed to be the Campanúe alluvial fan, which consists of 65% Cretaceous-Paleocene carbonates (Weltje et al., 1996; Caja et al., 2010). Studies of Cretaceous sediment isotopic compositions (Stoll and Schrag, 2000; Veizer and Mackenzie, 2003) indicate similar $\delta^{13}C$ values compared to those of the middle Eocene (Bohaty et al., 2009). Variation in the supply of these carbonates could therefore differentially influence carbon isotopic compositions.

Stratigraphic changes in grain-size conceivably resulted in $\delta^{13}C$ variation via differential diagenesis. Changes in grain-size could lead to relative increases in porosity promoting precipitation of relatively depleted diagenetic calcite (Marshall, 1992). Very limited petrographic observations indicate samples with increased abundance of coarse-grains correspond to depleted isotopic values (Fig. 4.16). Further detailed petrographic analyses would be required before any relationship can be determined.

Specific to the $\delta^{13}C$ isotope system, variability within Guaso stratigraphy may be the result of oscillations within the carbon cycle, differential diagenesis or the varying supply of extra-basinal carbonate. Carbon isotope variation is commonly interpreted as representing differential burial of OM (Shackleton, 1987; Jenkyns et al., 2002). During periods of increased productivity, the deposition of OM removes isotopically light carbon from the marine reservoir. The marine reservoir, therefore, becomes relatively depleted in ^{12}C resulting in more positive $\delta^{13}C$ carbonate values. Periods of OM erosion and subsequent oxidisation will result in isotopically light carbon being returned to the marine reservoir.

Variation in OM concentrations and source (terrestrial vs. marine) within the sediment can also affect $\delta^{13}C$ values. During the diagenetic decomposition of OM isotopically light carbon is released into the pore-waters and subsequently incorporated into precipitated cements resulting in more depleted $\delta^{13}C$ values (Marshall, 1992). However, the lack of significant TOC variation renders this scenario unlikely, but cannot be ruled out (Table 4.3).

The amount of fluvial input to be basin could affect the recorded $\delta^{13}C$ carbonate compositions. Variation in fluvial input would affect the amount of terrestrially derived dissolved inorganic carbon (DIC) supplied to the basin. Modern $\delta^{13}C$ compositions of fluvial DIC is -6.5‰ (Scholle and Arthur, 1980). With increased concentrations of terrestrially sourced DIC, basin waters would become relatively enriched in ^{12}C, which would be recorded within $\delta^{13}C$ compositions of coeval carbonate deposits.

Without further investigation, the discussed mechanisms for the inter-fan $\delta^{13}C$ variation within the Guaso System remain inconclusive. However, as long as the relative change in isotope compositions are based upon primary (environmental) factors, then it remains possible to identify climatic forcing even if the absolute value is secondary (Mayer and Appel, 1999).

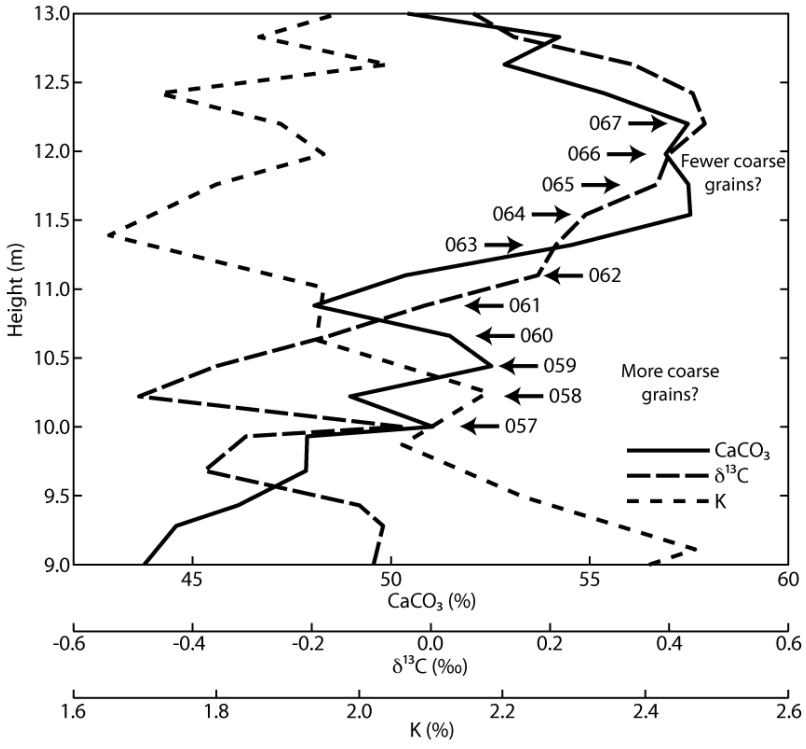

Figure 4.16 | Petrographic thin-section positions and selected geochemical variation within the Locality 1 measured section. Although variable, the thin-sections containing the coarsest grains appear to correspond to increased K and decreased $CaCO_3$ and $\delta^{13}C$ values.

4.4.2.4 Spectral gamma ray

Within pure carbonate sediments, concentrations of K, U and Th radioelements are negligible (Myers, 1989). However, the hemipelagic sediments of the Guaso System contain additional terrestrial siliciclastic minerals including significant concentrations of muscovite and quartz (Table 4.5; Fig. 4.10). Contained within, or associated with these minerals, are varying levels of K, U and Th (Table 2.2). Possible support for this interpretation is provided from the positive correlation coefficients calculated from the comparison between radioelement concentrations and identified quartz and muscovite abundance (Table 4.6). The relative sample volume of each method could explain the observed poor correlation coefficients between mineral and radioelement concentrations. XRD analyses incorporate information from a relatively small sample volume from an exact stratigraphic position. However, the GR-320 gamma ray detector includes radiation from a larger volume of sediment, (±0.4 m from the sample position) leading to averaging of sediment properties over several sample points (Fig. 2.1). Variation observed within radioelement concentrations, especially K and Th are therefore assumed to represent the supply of terrigenous detrital material to the basin.

The relative mobility of U within sediments complicates its interpretation (Rider, 1996). Reduced correlation coefficients of U vs. mineralogical abundance and the lack of association with TOC content (Tables 4.4, 4.6) can be explained by several possible mechanisms: the diagenetic breakdown of OM; differential redox conditions resulting in the authigenic precipitation of U (Myers and Wignall, 1987); U leaching from the exposed sediments (Adams and Weaver, 1958; Colley and Thomson, 1985); or by the allogenic supply of U from detrital clays and heavy minerals (Rider, 1996).

Calculated Th/K and Th/U ratios obtained from the sediments can also be used to identify mineralogical and palaeoenvironmental conditions. The average Th/K ratio of 3.9 suggests the dominant clay within the sediments is illite and/or muscovite (Myers, 1989; Rider, 1996). However, the negligible correlation coefficient between Th/K and muscovite may suggest the dominance of illite (Table 4.6). Mean Th/U values of 1.5 are below the average mudrock values of 3-6 which suggests sediments were deposited within a restricted environment (Wignall and Myers, 1988) supporting the conclusions of Heard et al. (2008) for the Ainsa System. The relative stability of each of these ratios indicates both clay type and benthic redox conditions did not differ significantly.

4.4.3 Sediment cyclicity

Using the SAR estimates from the ASM method it is possible to statistically determine whether orbital cyclicity is recorded within the inter-fan stratigraphy of the Guaso System. However, it is first necessary to determine the number of orbital terms that will provide the most reliable SAR estimate. The reliability of the SAR estimates is dependant upon the precision of the input frequencies. With the precision of these frequencies contingent upon the number of complete oscillations, it is necessary to ensure that the time series is of adequate length. If the time series is insufficient in length then ASM calculations can be performed using a reduced number of orbital terms.

Previous SAR estimates can be utilised to estimate whether this is sufficient length to reliably identify each of the orbital terms. Available SAR estimates of 27.5-33.3 cm/kyr (Dreyer et al., 1999; Heard et al., 2008) suggest wavelengths of 33.7 m (eccentricity; 110 kyr), 12.5 m (obliquity; 41 kyr) and 7.0 m (precession; 23 kyr). With the length of the time series being 40.59 m, the number of eccentricity, and potentially obliquity, cycles will be inadequate to produce a precise frequency estimates. ASM analyses performed without eccentricity terms are therefore considered more reliable.

ASM analyses produce a wide range of SAR estimates (Table 4.8; Fig. 4.13). To determine which of these values represents a realistic inter-fan SAR, comparison is made with available biostratigraphic data (Chapter 3). Using the calcareous nannofossil markers identified at the base and top of the Guaso System, a linear SAR of 33.4±12.7 cm/kyr is estimated (Table 4.10; Fig. 4.17). With the stratigraphic thickness of the Guaso System including events of increased SAR (submarine fans and MTCs) values are likely to be below this estimate. The only SAR estimates to remain within these parameters are 24.95 and 26.85 cm/kyr. Of these the 24.95 cm/kyr is considered the inter-fan SAR based upon the lower H_o and average spectral misfit estimates (Table 4.8).

Applying the 24.95 cm/kyr SAR estimate to the REDFIT, wavelet and MTM F-test significant frequencies provides their temporal estimates (Table 4.7). REDFIT and MTM F-test spectral data identify the 0.080-0.111 and 0.160-0.186 cycles/m frequency ranges as representing temporal periods of 22-25 and 36-50 kyr respectively. According to the predicted Milankovitch orbital periods for 41 Ma (Table 4.2), these likely correspond to orbital precession and obliquity. Variability within these temporal estimates are likely due to spectral bandwidth and the short time series and possibly slight variations within the SAR (Weedon, 2003). The lower 0.032-0.037 cycle/m frequency range is assigned a temporal period of 108-124 kyr corresponding to orbital

eccentricity (95 and 125 kyr). However, as less than one complete oscillation is present, the presence of eccentricity should be considered with caution.

Spatially only $CaCO_3$, $\delta^{13}C$ and Th/U time series contain evidence for the spatial continuity of these orbital periods (Fig. 4.14). Evidence for amplitude modulation of the precession band 0.173 cycles/m (5.80 m) is provided within the Th/U wavelet spectrum. The increased power every ~20 m may be indicative of modulation by eccentricity but without a longer time series this remains uncertain. The remaining time series contains evidence for both obliquity and precession but below the 90% confidence level.

With orbital periods assigned to MTM F-test frequencies, their visualisation is achieved by band-pass filtering (Figs. 4.18, 4.19). Band-pass filters of the 0.080-0.111 and 0.160-0.186 cycles/m bands correspond well to only the $CaCO_3$ and $\delta^{13}C$ time series data (Fig. 4.18).

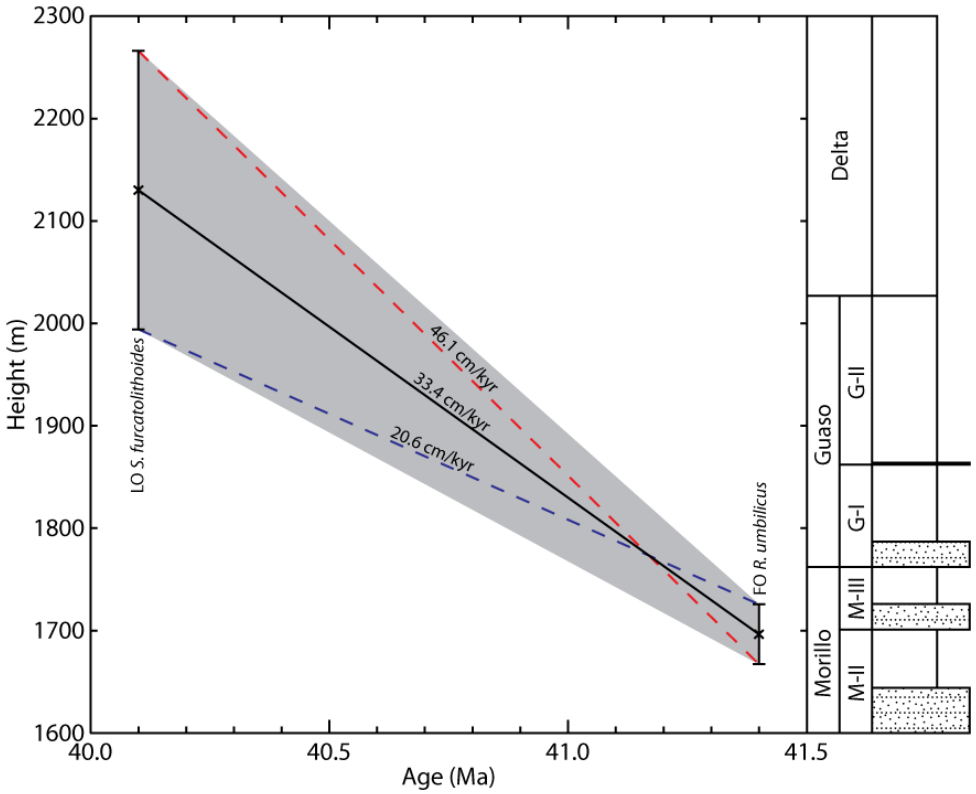

Figure 4.17 | Guaso System biostratigraphic data and estimated age. The two calcareous nannofossil data points are used to calculate the approximate age and duration of the Guaso System and its constituent complexes. Height error bars enable age error envelope (grey shaded area), minimum (blue dashed line), and maximum (red dashed line) SAR values to be calculated. Mid point values age and SAR values are represented by black solid line. Details upon the age model are available in Chapter 3.

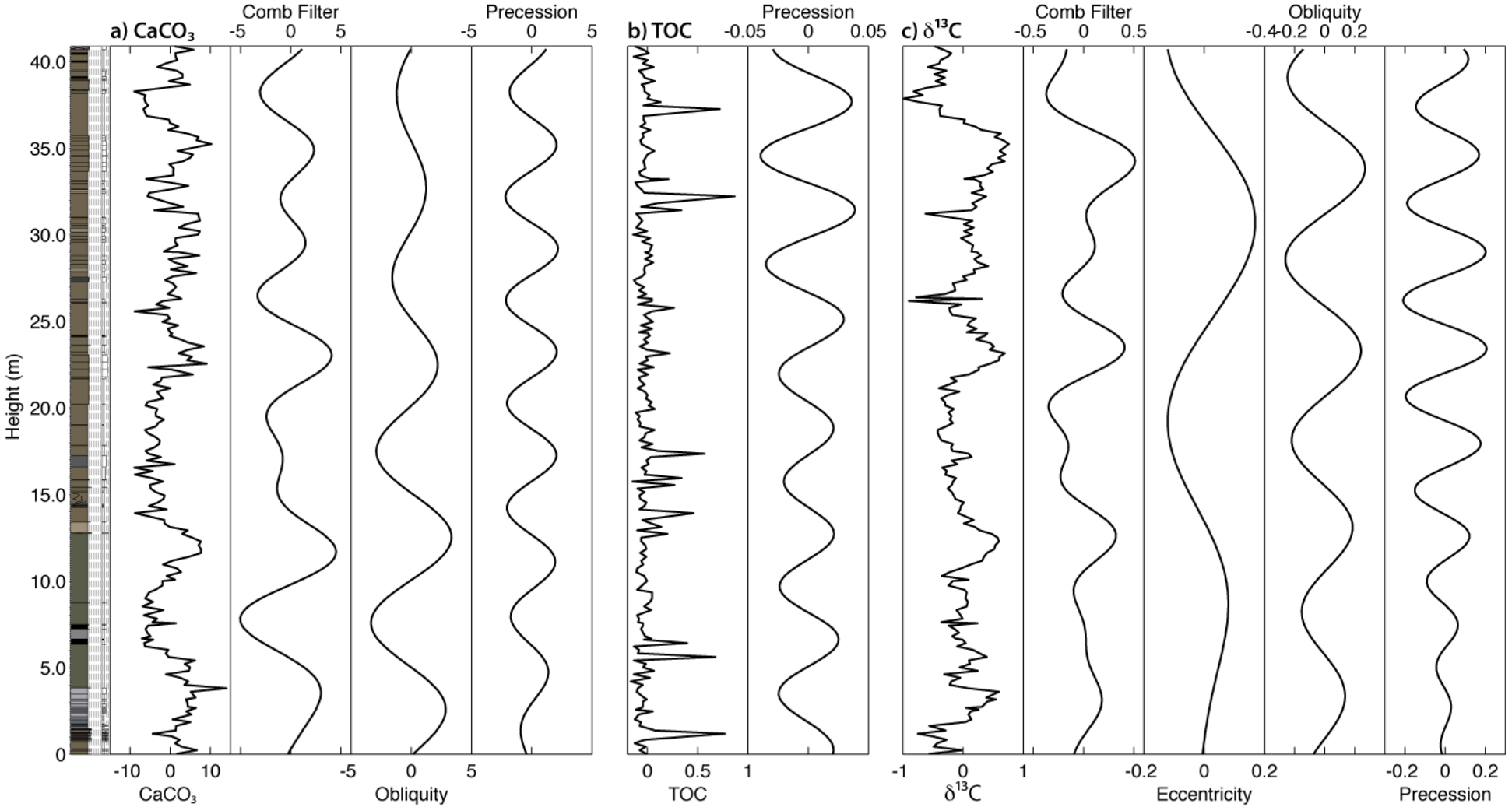
a) CaCO3
Comb Filter
Precession
b) TOC
Precession
c) δ13C
Comb Filter
Obliquity
Height (m)
40.0
35.0
30.0
25.0
20.0
15.0
10.0
5.0
0
-10 0 10
CaCO3
-5 0 5
Obliquity
0 0.5 1
TOC
-1 0 1
δ13C
-0.2 0 0.2
Eccentricity
-0.2 0 0.2
Precession

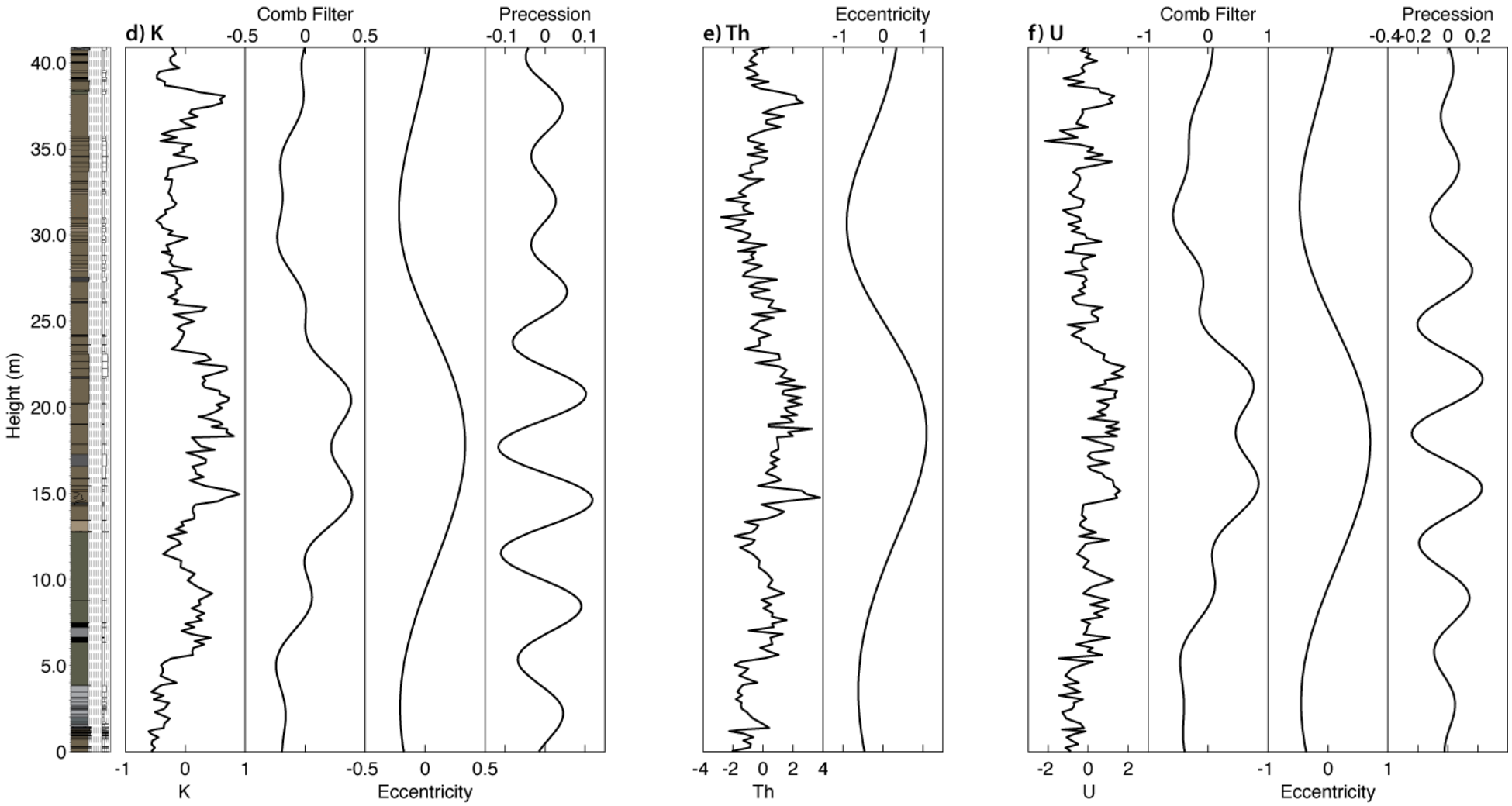
d) K
Comb Filter
Precession
-0.5 0 0.5
-0.1 0 0.1
Height (m)
40.0
35.0
30.0
25.0
20.0
15.0
10.0
5.0
0
-1 0 1
K
-0.5 0 0.5
Eccentricity
e) Th
Eccentricity
-1 0 1
-4 -2 0 2 4
Th
f) U
Comb Filter
Precession
-1 0 1
-0.4 -0.2 0 0.2
-2 0 2
U
-1 0 1
Eccentricity

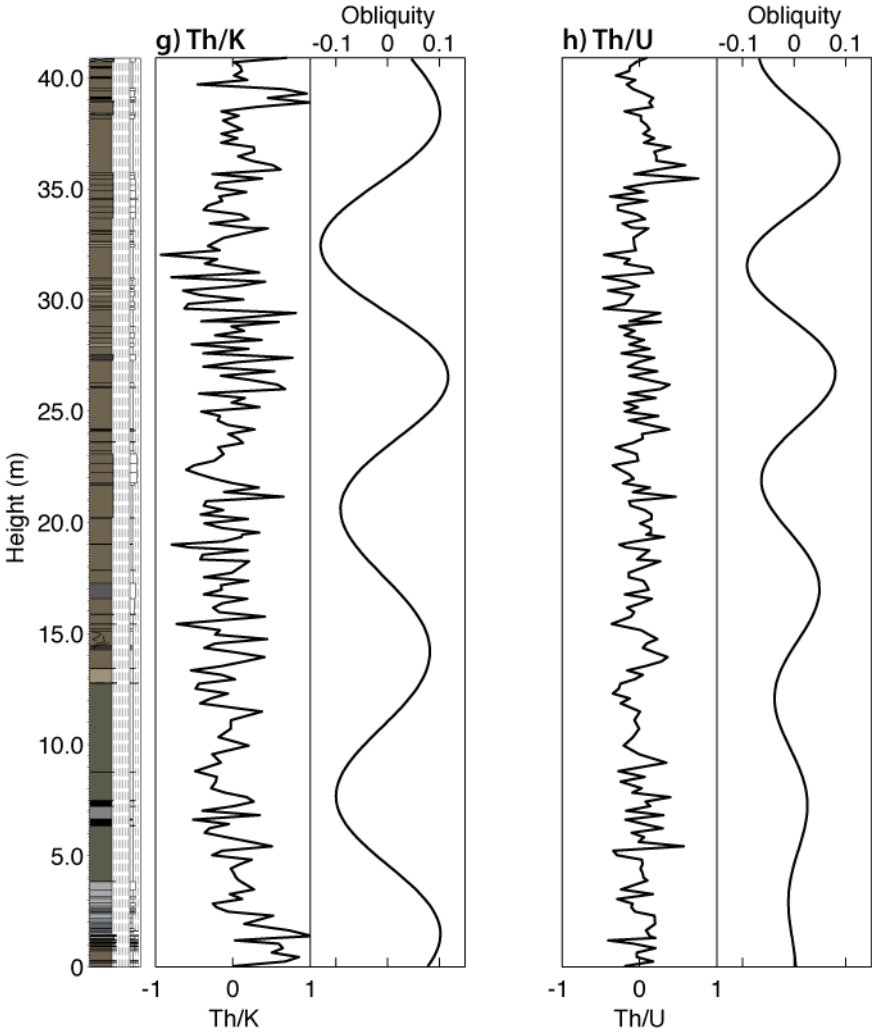
g) Th/K
h) Th/U
Obliquity
-0.1
0
0.1
Height (m)
40.0
35.0
30.0
25.0
20.0
15.0
10.0
5.0
0
-1
0
1
Th/K
Th/U

Figure 4.18 (previous 3 pages) | Band-pass filters of proposed orbital periods compared to stratigraphic series and lithologic column. Significant MTM harmonic F-test frequencies were isolated using band-pass filtering performed within Analyseries 2.0.4.2 (Paillard et al., 1996). Band-pass filter positions are illustrated in Figure 4.19. Comb-filters represent the sum of the individual band-pass filters. Filters for $\delta^{18}O$ not performed due to likely significant diagenetic alteration.

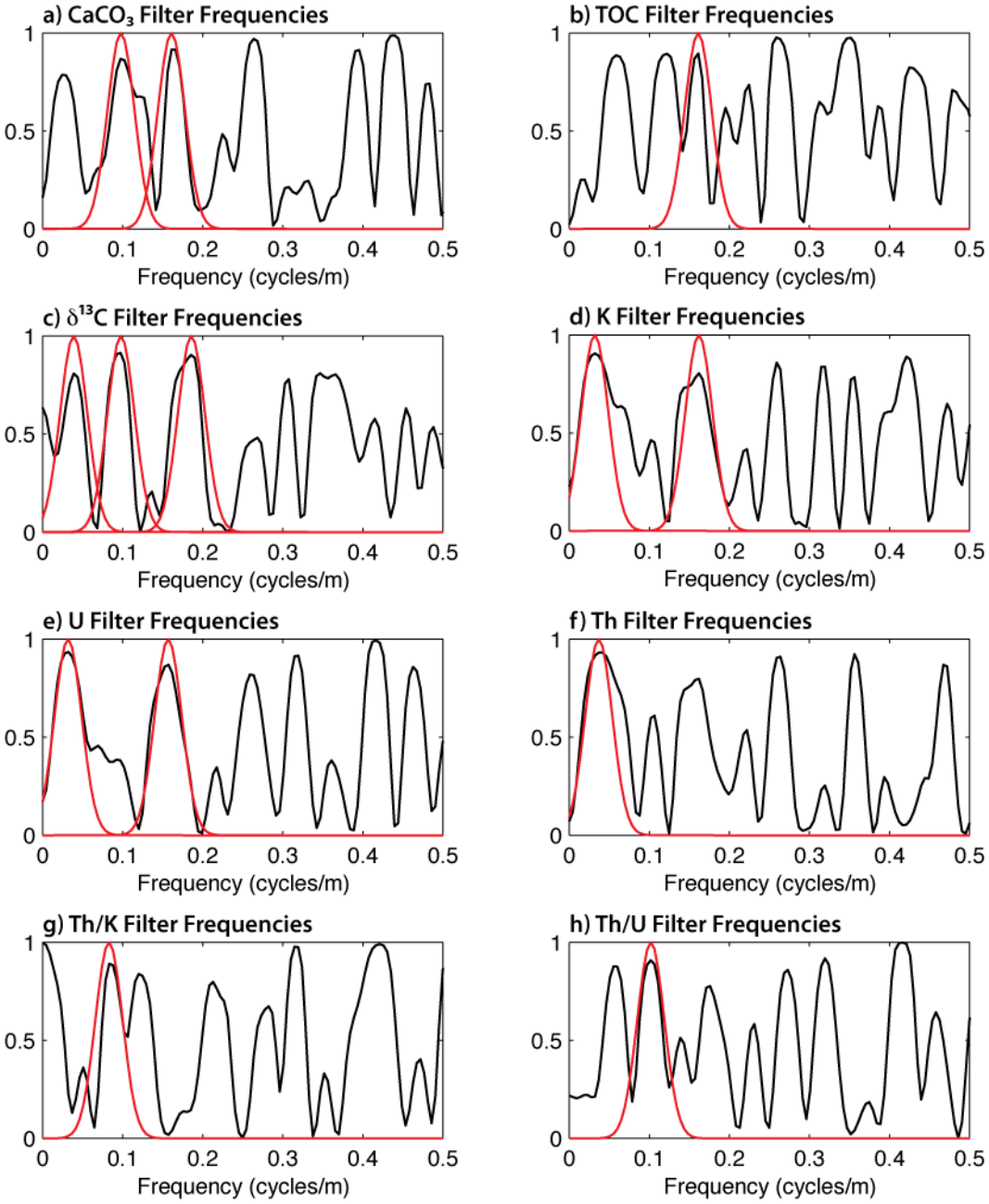

Figure 4.19 | Band-pass filter gain functions applied to Guaso System time series. Pass-band filters were applied to each stratigraphic time series within Analyseries 2.0.4.2 (Paillard et al., 1996). The Gaussian pass-band (red solid line) is centred about the frequency to be filtered. The width of the pass-band is determined by the bandwidth of the MTM harmonic F-test. Filtered frequencies and bandwidth information for each stratigraphic time series are provided within Table 4.7.

Table 4.10 – Guaso System biostratigraphic age model

	Height (m)*	Age (Ma)†			Duration (Myr)		
		Min	Mid	Max	Min	Mid	Max
Sequence							
Guaso-II	1993	40.10	40.51	40.76	0.00	0.49	1.05
Guaso-I	1828	40.76	41.01	41.15	0.00	0.30	0.63
Morillo-III	1728	41.16	41.30	41.39			
Complex							
Guaso-II marl	1993	40.10	40.51	40.76	0.00	0.65	1.04
Guaso-II sand	1830	40.75	41.00	41.15	0.00	0.01	0.40
Guaso-I marl	1828	40.76	41.01	41.15	0.00	0.30	0.57
Guaso-I sand	1753	41.06	41.23	41.33	0.00	0.10	0.34
Morillo-III marl	1728	41.16	41.30	41.39			

*Height estimates obtained from Chapter 3.
†Age estimates determined from equations for min, mid and max age lines in Figure 4.17.

4.5 Discussion

4.5.1 Guaso System depositional model

Consolidation of the above interpretations enables a depositional model for the inter-fan sediments of the Guaso System to be constructed. Orbitally paced (precession and obliquity) variation in river discharge could explain the majority of the features displayed by the relationships between the geochemical data. The inverse relationship between carbonate and terrigenous input indicators (quartz and muscovite) suggest the inter-fan sediments were affected by orbitally-paced dilution cycles. The associated supply of terrestrially derived DIC introduced to the basin could account for the variation observed within $\delta^{13}C$ compositions. However, the values reported here are most likely secondary values with the identified orbital frequencies being the result of a 'memory' of relative climatic change.

Support for this model is provided by the identification of orbitally-paced dilution cycles within coeval (Arguis Formation; Lutetian-Priabonian) Jaca basin sediments (Kodama et al., 2010). Eocene precipitation and continental run-off rates, which control terrestrial input to the basin, are shown to be strongly influenced by orbital precession (Sloan and Huber, 2001; Westerhold and Röhl, 2009).

Deposition of the Guaso System coincided with the final stages of deep-marine sedimentation within the Ainsa basin. The Guaso System accumulated during a period of increased tectonic uplift, reduced subsidence rates and increasing overall sediment supply to the basin (Labaume et al., 1985; Puigdefabregas et al., 1992). Despite this background of regional uplift, accommodation space was still being created within subsiding synclines located between uplifting thrust-related anticlines, thereby enabling the deposition of the overlying Sobrarbe deltaic complex (Dreyer et al., 1999). It is therefore reasonable to assume that during the deposition of the Guaso System,

similar growth structures existed within the basin allowing the accumulation of deep-marine sediments (Bayliss, 2010).

The affects of intra-basinal tectonics, mainly the continuous uplift of the Mediano anticline (Holl and Anastasio, 1993), are suggested to have caused the observed south-westward stacking of the Guaso-I and Guaso-II sequences via a "see-saw" tectonic process (Figs. 1.15, 1.16) (Pickering and Bayliss, 2009). The Boltaña anticline is assumed to have created the truncation surface separating the Morillo and Guaso systems. Based upon the age model (Fig. 4.18) it is possible to estimate the timing of this truncation surface and therefore, the timing of Boltaña anticline uplift as having occurring between 41.1 and 41.4 Ma (Table 4.10). The timing of this activity is coincident with the increase in rotation of the blind-thrust beneath the Boltaña anticline at ~41 Ma (Mochales et al., 2012) (Fig. 3.7).

4.5.2 Guaso System sequence timing and duration

To determine the timing and duration of the constituent sequences within the Guaso System, both the orbital and biostratigraphic age models are applied. Application of the biostratigraphic age model (Fig. 4.17; Table 4.10) suggests that the individual sequences within the Guaso System accumulated over periods of 0.30 and 0.49 Myrs, respectively.

The time separating the two Guaso submarine fan complexes can be determined using the orbital and biostratigraphic age models. Application of the orbitally derived SAR to the 49.74 m of inter-fan stratigraphy (without the MTC and significant sand package deposits) measured at Locality 1 yields a duration of 199 kyr. The stratigraphic completeness of Locality 1 however, may contain missing stratigraphy associated with the large type-Ia MTC located >44 m. To obtain an alternative stratigraphic thickness estimate, a combined thickness is obtained from the correlations between localities 1 and 2 (Fig. 4.15). Using the 54.69 m of combined stratigraphy (without MTC and sand package deposits), application of the SAR yields a temporal duration of 219 kyr. Both these temporal estimates are consistent with the 0.22 Myr period determined from the system's age model (Table 4.10). The corroboration between the independent biostratigraphic and orbital age models suggests that the age model proposed for the Guaso System is reliable.

The relative timing of other basin events can also be determined using the orbital age model. The base of the two major coarse-grained events (at 23.1 and 56.7 m) in the inter-fan section measured at Locality 1 are separated by 31.2 m of stratigraphy including ~8.4 m of type-Ia MTC (43.9-52.3m). Using the SAR this stratigraphic distance represents 125 kyr. However, with the assumption that MTCs

represent instantaneous events, only 22.8 m of stratigraphy is assumed continuous which represents ~91 kyr. Both of these durations correspond closely to eccentricity orbital periods (Table 4.2).

4.5.3 Orbital pacing of the Guaso System

Constructing a temporal framework for the Guaso System (Fig. 4.17) enables the orbital forcing hypothesis to be tested (Pickering and Bayliss, 2009; Sutcliffe and Pickering, 2009). The hypothesis predicts that submarine-fan complexes were paced by a long eccentricity controlled glacio-eustatic mechanism (Chapter 1). Pickering and Bayliss (2009) apply this model to the Guaso System and predict that each sequence spanned 404 kyr whilst the entire system was deposited over 808 kyr.

The biostratigraphic age model indicates that the Guaso System spanned 0.79 Myr with a range between 0.40-1.29 Myr. The system's constituent Guaso-I and -II sequences were deposited over <0.63 and <1.05 Myr periods, respectively. Although large errors exist within the age model, these estimates are potentially consistent with the predicated sequence (0.4 Myr) and system (0.8 Myr) durations of Pickering and Bayliss (2009).

The orbital forcing hypothesis also suggests that glacio-eustatic processes control the supply of coarse clastics to the basin. As in Chapter 3, testing this hypothesis is achieved by comparing the timing of Guaso submarine fan deposits (Table 4.10) relative to the calculated mean insolation received at 65˚N during June/July, orbital curves (Laskar et al., 2004; Laskar et al., 2011), $\delta^{18}O$ (Zachos et al., 2008) and ice-rafted debris data (Tripati et al., 2008) which can be used to indicate the presence of ephemeral ice-sheets.

Using the system age model it is possible to compare the timing of the Guaso deposits with the calculated orbital curves (Fig. 4.20). Despite uncertainty existing within the age model, the Guaso-I and Guaso-II coarse-grained siliciclastic fan deposits potentially coincide with periods of eccentricity minima spaced by ~400 kyrs. During these periods of insolation minima, glacio-eustatic low-stands would be expected to occur as during the Pleistocene (Hays et al., 1976). The association and timing of these events therefore support the hypothesis being tested. However, the uncertainty within the age model does not exclude the alternative interpretation of submarine fans being deposited during eccentricity maxima (Fig. 4.20). This relationship would be consistent with previous studies and climatic models from the region linking orbitally forced insolation with variations in continental run-off (Sloan and Huber, 2001; Kodama et al., 2010).

Further validation of the hypothesis is achieved by comparing the timing of submarine fan deposits with high-resolution sedimentological and geochemical indicators of ice accumulation (Fig. 4.21). The record of ice rafted debris (IRD) provide a more reliable measure of Arctic ice, thereby potentially indicating the timing of potential glacio-eustatic sea-level changes during the middle Eocene (Tripati et al., 2008). The timing of IRD and submarine fan deposition suggest that Guaso-I submarine fan deposition coincided with a peak in IRD mass accumulation rate (MAR) at ~41.3 Ma (Fig. 4.21). The presence of IRD prior and subsequent to the Guaso-II fans deposition supports the coeval presence of ephemeral northern hemisphere ice sheets indicating a potential glacio-eustatic depositional mechanism.

Another indicator of potential ice-sheet formation is the oxygen isotope record available for the middle Eocene (Zachos et al., 2008). During the Pleistocene oxygen isotopes have been successfully utilised to determine the timing of glacial-interglacial and associated sea-level cycles (Hays et al., 1976; Mix and Ruddiman, 1984). During glacial intervals $\delta^{18}O$ composition of seawater have been shown to become heavier (enriched in ^{18}O compared to ^{16}O). Applying this principle to the middle Eocene record should therefore enable the testing of the glacial-eustatic mechanism proposed for the Guaso System. Comparison between the timing of submarine fan deposition and the oxygen isotope record appears inconclusive mainly due to the poor resolution of the isotope record. Despite this, the deposition of the Guaso-I fan does coincide with a <0.5‰ decrease in $\delta^{18}O$ values (Zachos et al., 2008), which would be consistent with fan deposition coinciding with periods of ice accumulation.

Considering the above discussion, the timing of coarse-clastic sand supply during deposition of the Guaso System appears to coincide with periods of expected ice-sheet formation. Such a scenario would lower sea-level enabling the supply of coarse clastic material to the Ainsa basin (Shanmugam and Moiola, 1982; Howell and Vedder, 1983; Weaver and Kuijpers, 1983; Pickering et al., 1999; Normark et al., 2006). With the pacing of these depositional events being ~400 kyr, such a relationship would support the proposed 404-kyr paced glacio-eustatic driver controlling the siliciclastic flux to the basin (Pickering and Bayliss, 2009; Sutcliffe and Pickering, 2009). Further testing of the hypothesis is however required mainly via the construction of an improved age model along with higher resolution middle Eocene IRD and stable isotope records.

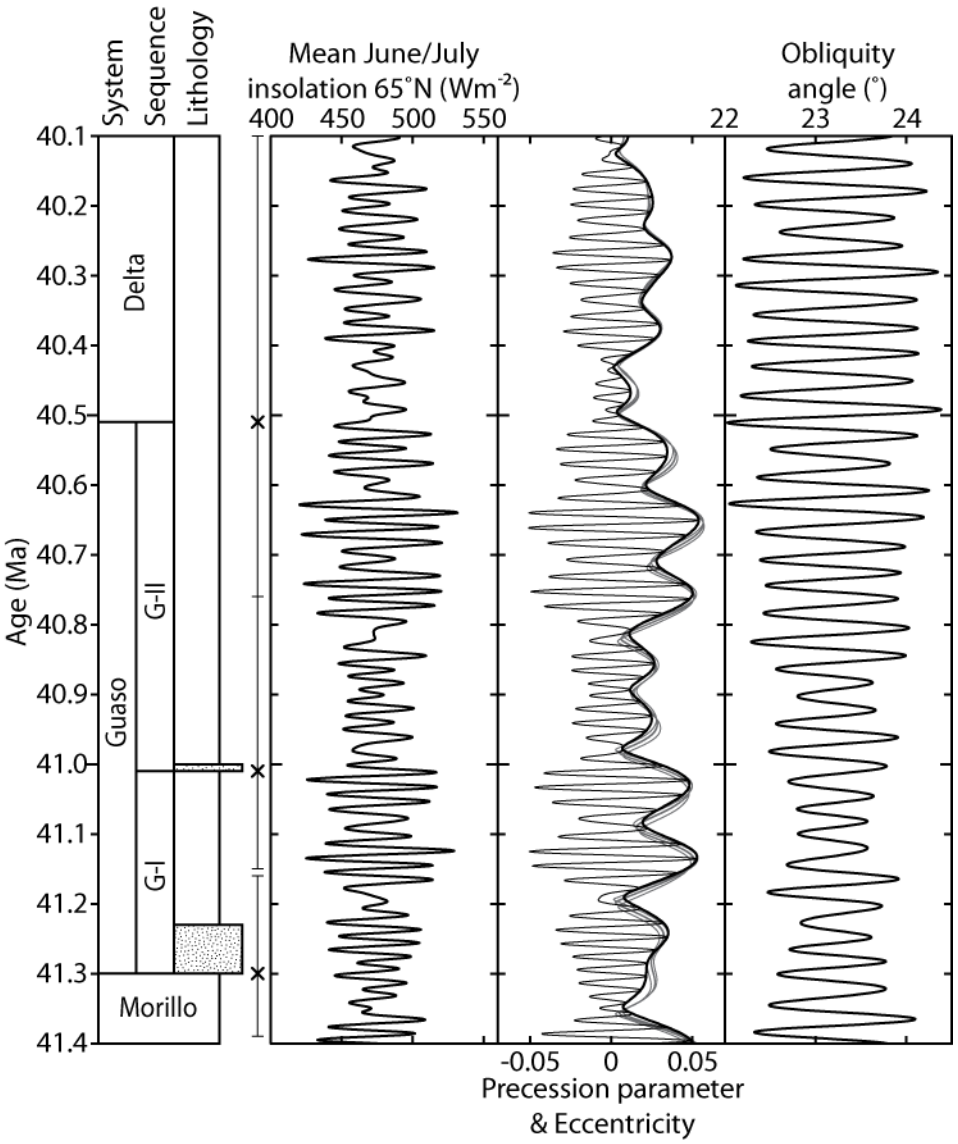

Figure 4.20 | Comparison between Guaso System estimated age and calculated insolation and eccentricity curves. The estimated age of the Guaso System and its constituent complexes are based upon mid-point ages. Uncertainty within age represented by error bars based upon the minimum and maximum age (Table 4.10). The mean insolation curve represents the insolation received during at 65˚N during June/July between 40.1 and 41.4 Ma. Both the mean insolation and eccentricity components were calculated within Analyseries 2.0.4.2 (Paillard et al., 1996) using the equation of Laskar et al. (2004). Additional eccentricity curves (grey curves) are from the updated calculation of Laskar et al. (2011).

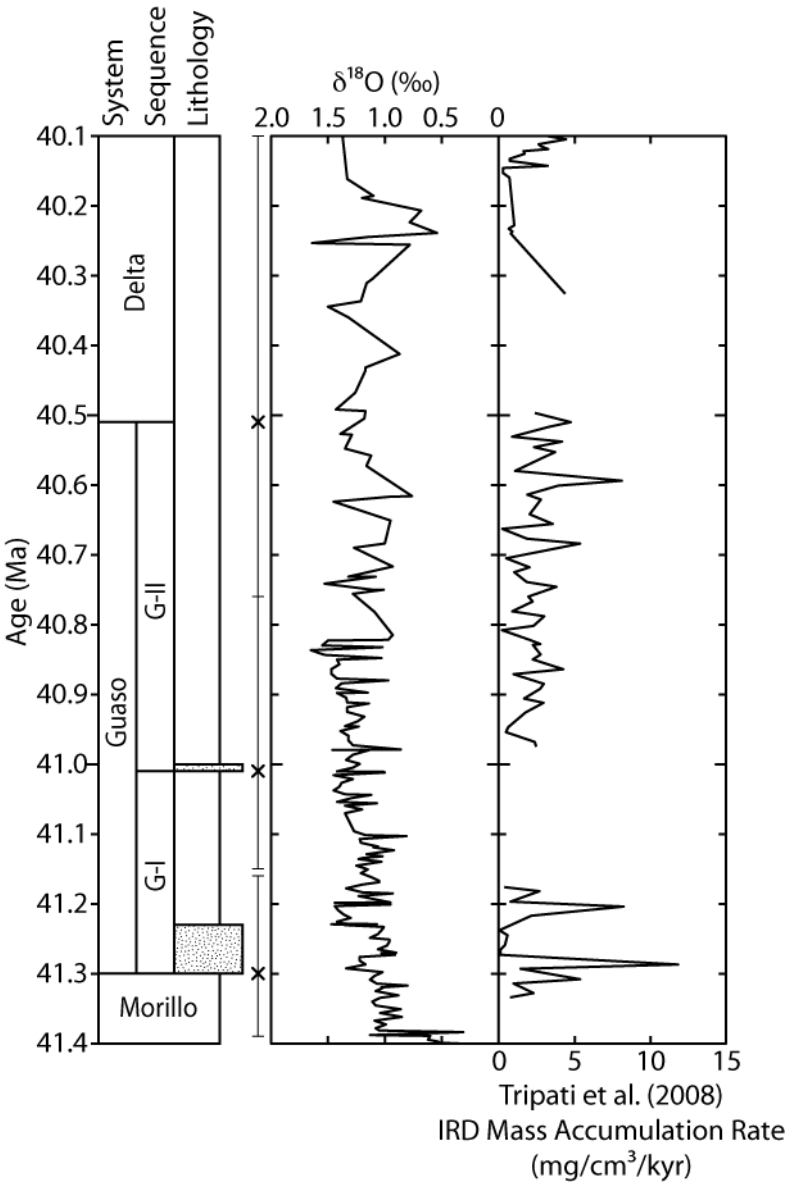

Figure 4.21 | Guaso System submarine fan timing compared to coeval $\delta^{18}O$ and IRD data. The timing of submarine fan deposits identical to those in Figure 4.20. The $\delta^{18}O$ record is determined from benthic deep-marine foraminifera (Zachos et al., 2008). Ice rafted debris (IRD) mass accumulation rate (MAR) data is that obtained from Eocene Greenland Sea sediments and are interpreted as reflecting periods of glaciation in the North Atlantic (Tripati et al., 2008). IRD data is that >250um in size. With the low-resolution $\delta^{18}O$ data it is uncertain whether submarine fan deposition coincided with periods of increased $\delta^{18}O$ values. The IRD data however, clearly indicate the presence of northern hemisphere ice during the deposition of the Guaso System.

4.6 Summary

The immediate conclusions from this chapter are outlined here. Further detailed discussion can be found in Chapter 8. Inter-fan sediments of the Guaso System appear to contain cyclic components consistent with both orbital precession and obliquity. Both of these orbital periods appear to have influenced the supply of terrigenous material to the deep-marine Ainsa basin creating carbonate dilution and stable isotopic cycles.

Identification of orbital cyclicity provides independent validation of the biostratigraphic age model proposed for the Guaso System. Application of both age models to the inter-fan sediments separating the submarine fan complexes provided a duration of ~200 kyr, potentially representing half a 400 kyr sea-level cycle. Average sediment accumulation rates calculated for the inter-fan and entire Guaso System are 24.95 cm/kyr and 33.4±12.7 cm/kyr, respectively.

The biostratigraphic age model enabled the temporal duration of the Guaso System, Guaso-I and Guaso-II stratigraphic components to be identified as 0.40-1.29, <0.63 and <1.05 Myr, respectively. Despite large errors within the age model, these estimates are consistent with the predicated sequence (404 kyr) and system (808 kyr) durations of Pickering and Bayliss (2009).

The timing of submarine fan deposition within the Guaso System appears to coincide with periods of ephemeral ice-sheet formation, at least within the Northern Hemisphere. This, along with the ~400 kyr pacing of submarine fan deposition is consistent with the proposed orbital forcing hypothesis (Pickering and Bayliss, 2009; Sutcliffe and Pickering, 2009). However, until a higher resolution age model and geochemical data spanning the entire Guaso System are available, it will remain difficult to determine precisely the mechanism for coarse clastic supply to the basin.

Whilst the timing of submarine fan deposition is believed controlled by climate, tectonics potentially influenced their spatial distribution via the “see-saw” mechanism. The role of tectonics within the development of the Guaso System is demonstrated by the correspondence between the timing of the unconformity at the base of the system and increased tectonic activity of the Boltaña anticline.

Chapter 5
The Ainsa System

5.1 Introduction

5.1.1 Chapter objectives

The Ainsa System is amongst the most studied deep-marine submarine fan system within the Ainsa basin (Cronin et al., 1998; Pickering and Corregidor, 2000; Fugelli and Olsen, 2005; Pickering and Corregidor, 2005; Falivene et al., 2006; Bakke et al., 2008; Heard et al., 2008; Schuppers, 2009; Falivene et al., 2010). Within this chapter, new chemo-stratigraphic and existing ichnological data are obtained from the systems sediments at both outcrop and the laterally equivalent subsurface. Using spectral analysis techniques to isolate the short eccentricity, obliquity and precession orbital periods, it should be possible to test this hypothesis by the creation of a floating time scale and the calculation of a sediment accumulation rate (Chapter 2). The resultant orbital age model shall be compared to the previously defined biostratigraphic age model (Chapter 3). Ultimately, it should be possible to test the predictions of the orbital forcing hypothesis, mainly that the Ainsa Systems submarine fans were paced by a 404-kyr paced glacio-eustatic cycle (Heard et al., 2008; Pickering and Bayliss, 2009).

5.1.2 The Ainsa System

The Ainsa System is one of the eight, unconformity-bound submarine fan systems within the Ainsa Basin (Fig. 1.8). The Ainsa System contains a succession of submarine fan and related inter-fan complex deposits belonging to the middle Eocene Hecho Group (Mutti, 1983; Remacha et al., 2003). This group contains a sequence of deep-marine sediment gravity-flow deposits, compartmentalised between the Ainsa and adjacent Jaca deep-marine basins. The Ainsa System contains ~180 m of stratigraphy consisting of three linear submarine fan complex deposits (Ainsa-I, Ainsa-II and Ainsa-III), interpreted as representing lower-slope and basin-floor fans. Each submarine fan complex is on average tens of metres thick, and laterally stacked in an east-west foreland stepping direction (Figs. 1.8, 5.1). Today, the Ainsa System sediments are located within the southerly plunging Buil Syncline, and are bound to the east and west by the Mediano and Boltaña anticlines respectively (Fig. 5.2).

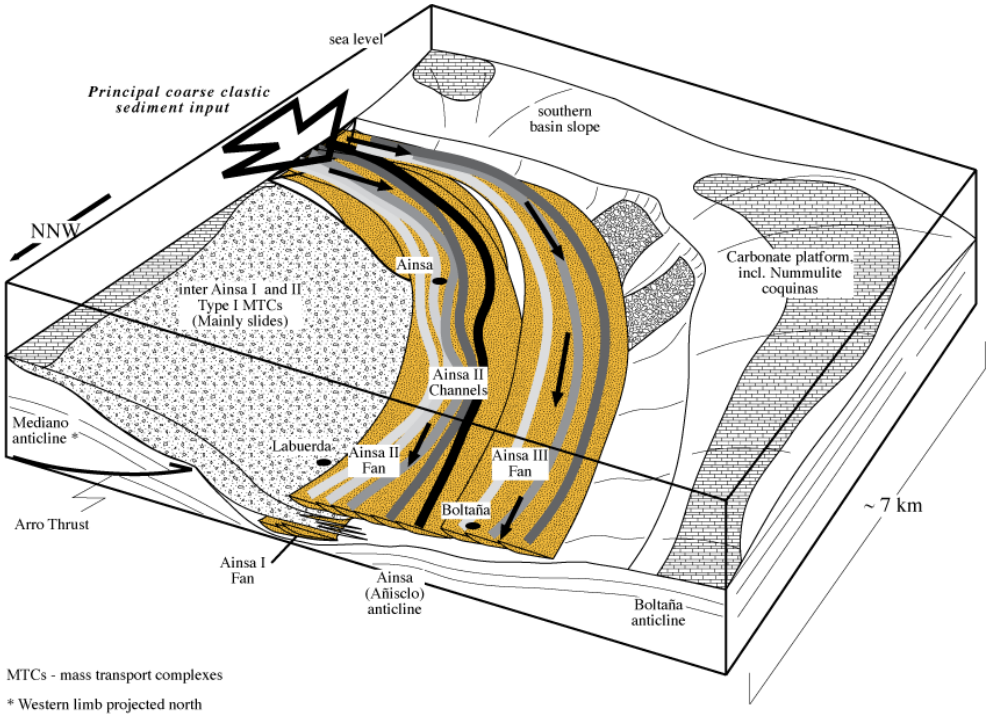

Figure 5.1 | Ainsa System depositional model (Pickering and Bayliss, 2009). Syn-depositional activity of the Añisclo, Boltaña and Mediano anticlines affected distribution the Ainsa Systems submarine fan sediments.

5.1.3 Tectonic setting

The submarine fan complexes of the Ainsa System accumulated during the second stage of major tectonic activity within the South Central Pyrenees associated with emplacement of Lower Thrust Sheets (Munoz, 1992). Tectonic activity during this time involved the Larra-Boltaña cover thrust system (Teixell, 1996; Teixell, 1998) and the early development of the Gavarnie-Sierres basement thrust (Labaume et al., 1985; Puigdefabregas and Souquet, 1986; Remacha et al., 2003). Regionally this is believed to have transformed the Tremp-Ainsa-Jaca basins from a simple foreland basin to a piggyback basin, which was detached along underlying Triassic Keuper evaporites (Labaume et al., 1985; Remacha et al., 2003).

During the Lower Thrusting Sheet emplacement, tectonic activity within the Ainsa Basin involved the expansion of the South Central Pyrenean Unit (SCPU) lateral ramp zone. Associated intra-basin deformation included the continued growth of the Mediano anticline and the development of the Boltaña and Añisclo fault-propagation folds (Remacha et al., 2003; Tavani et al., 2006). As a result, these structures segmented the Ainsa Basin from the terrestrial Tremp-Graus basin in the east and the deep-marine Jaca Basin to the west. Within the basin, this period of increased deformation is represented by an angular unconformity at the base of the Banaston

System, which enables the basins subdivision into two tectono-sequences (Heard et al., 2008; Pickering and Bayliss, 2009; Bayliss, 2010).

The accumulation of the Ainsa System coincided with the Mediano anticlines continuous uplift, leading to the westward syn-depositional lateral offset stacking of the individual submarine fans (Holl and Anastasio, 1993; Pickering and Bayliss, 2009). The termination of the Ainsa System was marked by a shift of the basin depositional axis eastward, marking the initiation of the overlying Morillo System, is attributed to renewed growth of the Boltaña anticline (Pickering and Bayliss, 2009). Intra-fan deposition was also affected by the syn-depositional Añisclo submarine high, which affected the spatial distribution of the Ainsa-I and Ainsa-III fan deposits (Pickering and Corregidor, 2000).

5.1.4 Palaeogeographic conditions

During the accumulation of the Ainsa System, the active Mediano and Boltaña anticlines shaped the regional palaeogeography, including palaeobathymetry (Figs. 1.13, 1.14). The Mediano anticline acted as the shelf break that separated the deep-marine Ainsa Basin from the shallow-marine and terrestrial Tremp-Graus Basin (Marzo et al., 1988; Puigdefabregas et al., 1992; Munoz et al., 1994; Millington and Clark, 1995; Bentham and Burbank, 1996). Farther west the Boltaña anticline represented a submarine high separating the Ainsa and Jaca deep-marine basins.

Sediments supplying the Ainsa System originated from the submarine and subaerial erosion of deltaic, shallow marine and alluvial sediments of the Montanyana Group (Fig. 1.8) (Marzo et al., 1988; Nijman, 1998; Caja et al., 2010). Once within the basin, both the Mediano and Boltaña anticlines confined channel deposition into a SSE-NNW trending linear system as recorded by the 320˚ palaeocurrent directions (Mutti, 1983; Pickering and Corregidor, 2000, 2005). The Boltaña anticlines submarine topography was not believed sufficient to prevent sediments westward transfer to the Jaca Basin although it may have been enough to cause periodic changes in bottom-water redox conditions (Heard et al., 2008).

Palaeoclimatic conditions during the deposition of the Ainsa System are outlined in Section 1.6.3.

Figure 5.2 (next page) | Geological map of the Ainsa System (Pickering and Corregidor, 2000, 2005). The sediments located between the Ainsa and Morillo systems were sampled within the Rio Forcaz valley. Spectral gamma ray data were collected from the logged section marked between the top of the Ainsa-II submarine fan and MTC deposits marking the top of the Ainsa System.

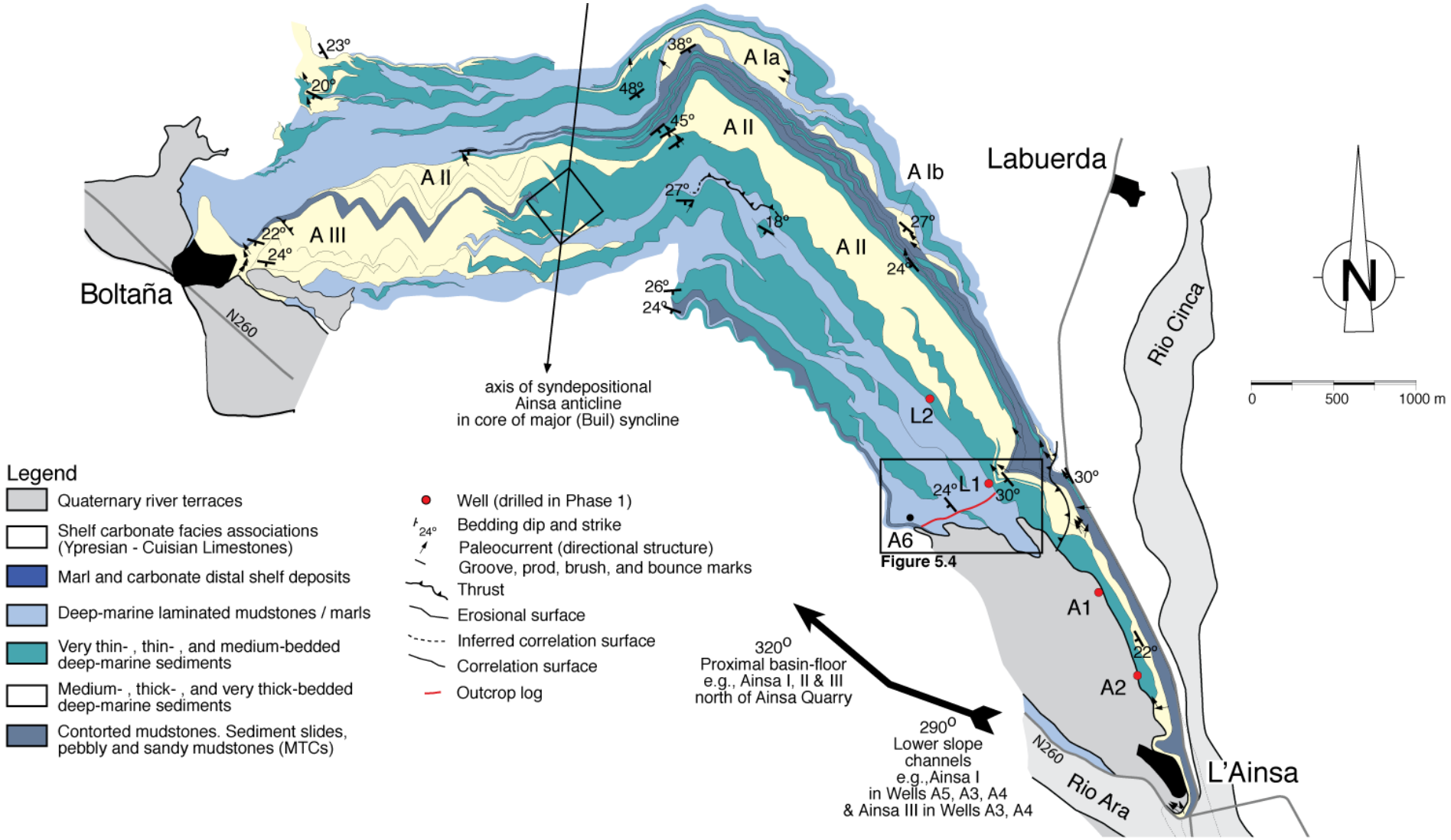
Boltaña
N260
A III
A II
A Ia
A II
A Ib
A II
Labuerda
Rio Cinca
axis of syndepositional
Ainsa anticline
in core of major (Buil) syncline
L2
L1
A6
Figure 5.4
A1
A2
320°
Proximal basin-floor
e.g., Ainsa I, II & III
north of Ainsa Quarry
290°
Lower slope
channels
e.g.,Ainsa I
in Wells A5, A3, A4
& Ainsa III in Wells A3, A4
N260
Rio Ara
L'Ainsa
N
0
500
1000 m
Legend
Quaternary river terraces
Shelf carbonate facies associations
(Ypresian - Cuisian Limestones)
Marl and carbonate distal shelf deposits
Deep-marine laminated mudstones / marls
Very thin- , thin- , and medium-bedded
deep-marine sediments
Medium- , thick- , and very thick-bedded
deep-marine sediments
Contorted mudstones. Sediment slides,
pebbly and sandy mudstones (MTCs)
Well (drilled in Phase 1)
Bedding dip and strike
Paleocurrent (directional structure)
Groove, prod, brush, and bounce marks
Thrust
Erosional surface
Inferred correlation surface
Correlation surface
Outcrop log

5.1.5 Dating of system

The deposition of the Ainsa System, based upon the biostratigraphic age model (Chapter 3; Fig. 5.3), occurred between 43.9-45.9 Ma on the time-scale of Gradstein et al. (2004). Analyses of calcareous nannofossil assemblages indicate that the systems sediments contain the first occurrence (FO) of both *Chiasmolithus gigas* and *Sphenolithus furcatolithoidesis* dated at 45.35 and 45.10 Ma, respectively. The identification of these marker species indicates that the Ainsa Systems deposition was coincident with nannofossil zone NP15 of Martini (1971).

Large benthic foraminifera collected from the system indicate deposition occurred within the coeval shallow benthic zones SBZ14 and 15 of Serra-Kiel et al. (1998). The assembalge identified within the system includes *Nummulites beneharnenesis, N.* cf. *crassus, N. obesus, N. boussaci, N. perforatus, Assilina spira, A. exponens, A. suteri, A. spira, Discocyclina* sp. and *Alveolina munieri.*

The new Ainsa System age model (Fig. 5.3) corroborates well with existing Lutetian age estimates for the Ainsa System. Biostratigraphic data obtained from the Ainsa-I and Ainsa-II submarine fans suggest they accumulated during the Lutetian Stage of the Middle Eocene, some time between 43.5 and 47.6 Ma (Unpublished Robertson Research report for UCL Ainsa Project (1999)). Pickering and Corregidor (2005) use planktonic foraminifera to infer that the Ainsa System sediments were deposited between ~45 to 47 Ma around the P11 to P12 zone boundary (calcareous nannofossil zones NP14 and NP15). Other workers suggest similar age ranges but are far less constrained, e.g., Jones et al. (2005).

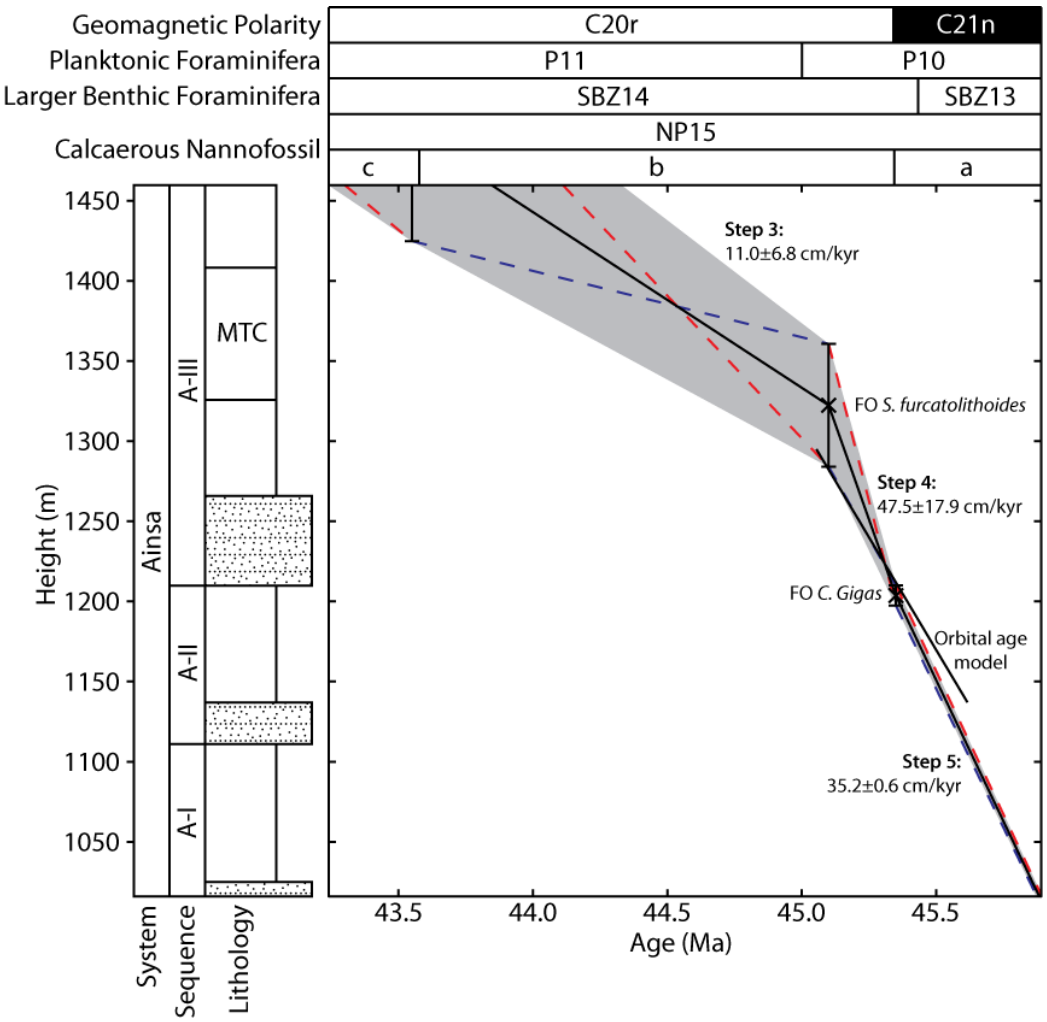

Figure 5.3 | Ainsa System age model determined from nannofossil data. Detailed description of age model provided in Chapter 3. Solid lines between nannofossil data points represent mid-point ages whilst grey shaded areas constitute age error envelope. The additional solid line between the two nannofossil tie points represents the orbitally derived age model for the studied sediments within this chapter. The 28.12 cm/kyr SAR estimate closely corresponds with the lower 29.6 cm/kyr SAR estimate of Step 4 within the biostratigraphic age model.

Figure 5.4 (next page) | Aerial photograph of studied area. For continuous stratigraphic coverage several lateral shifts in stratigraphy were required using distinctive beds and slumps for correlation. Start position and end positions (0 and 243.44 m) for outcrop measurement marked by red line. UTM zone 31 coordinates are used, aerial image from http://sigpac.mapa.es/fega/visor/. Points a to c represent the position and direction of the photographs shown in Plate 5.3.

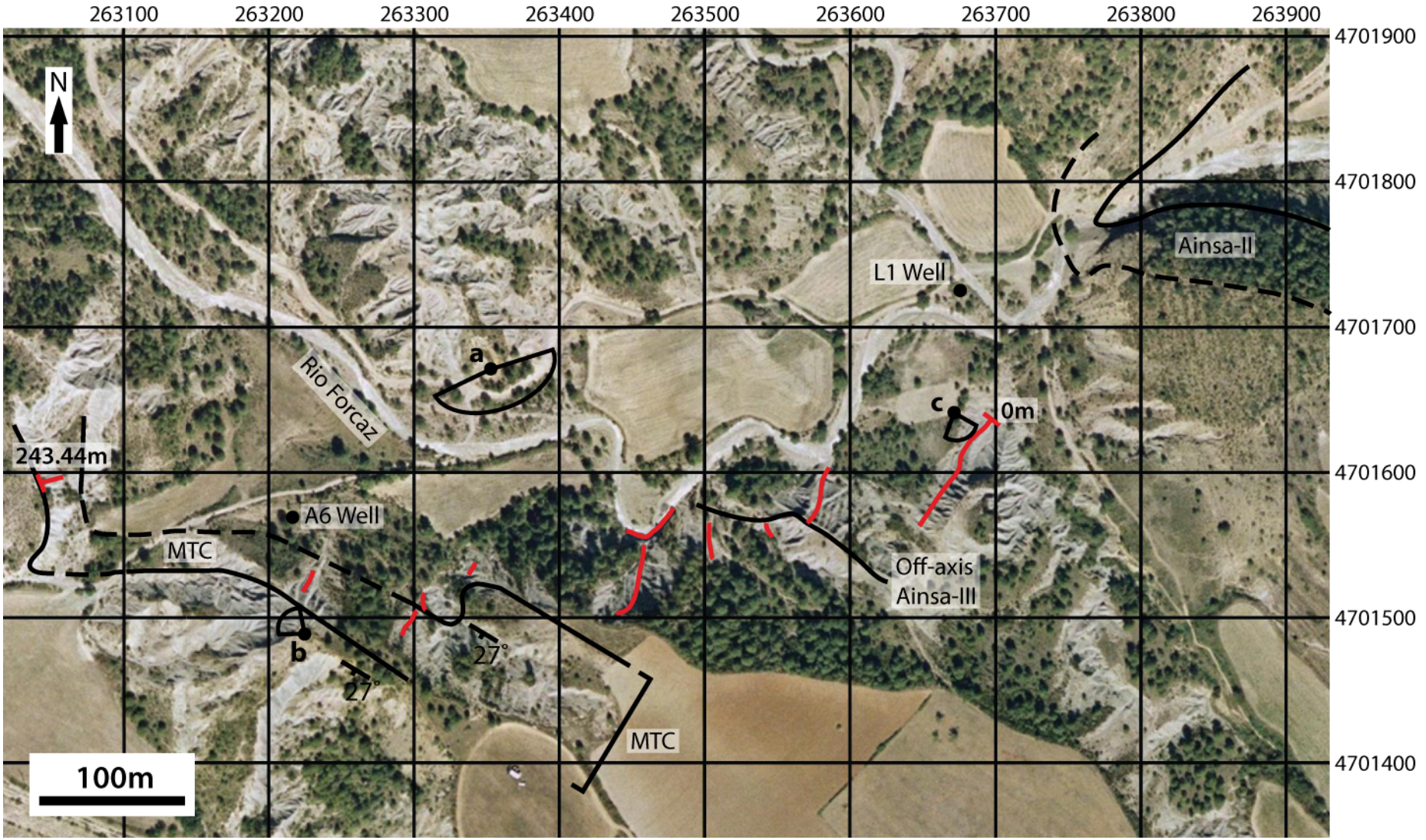
263100
263200
263300
263400
263500
263600
263700
263800
263900
4701900
4701800
4701700
4701600
4701500
4701400
N
Ainsa-II
L1 Well
Rio Forcaz
a
c
0m
243.44m
A6 Well
MTC
Off-axis
Ainsa-III
b
27°
27°
MTC
100m

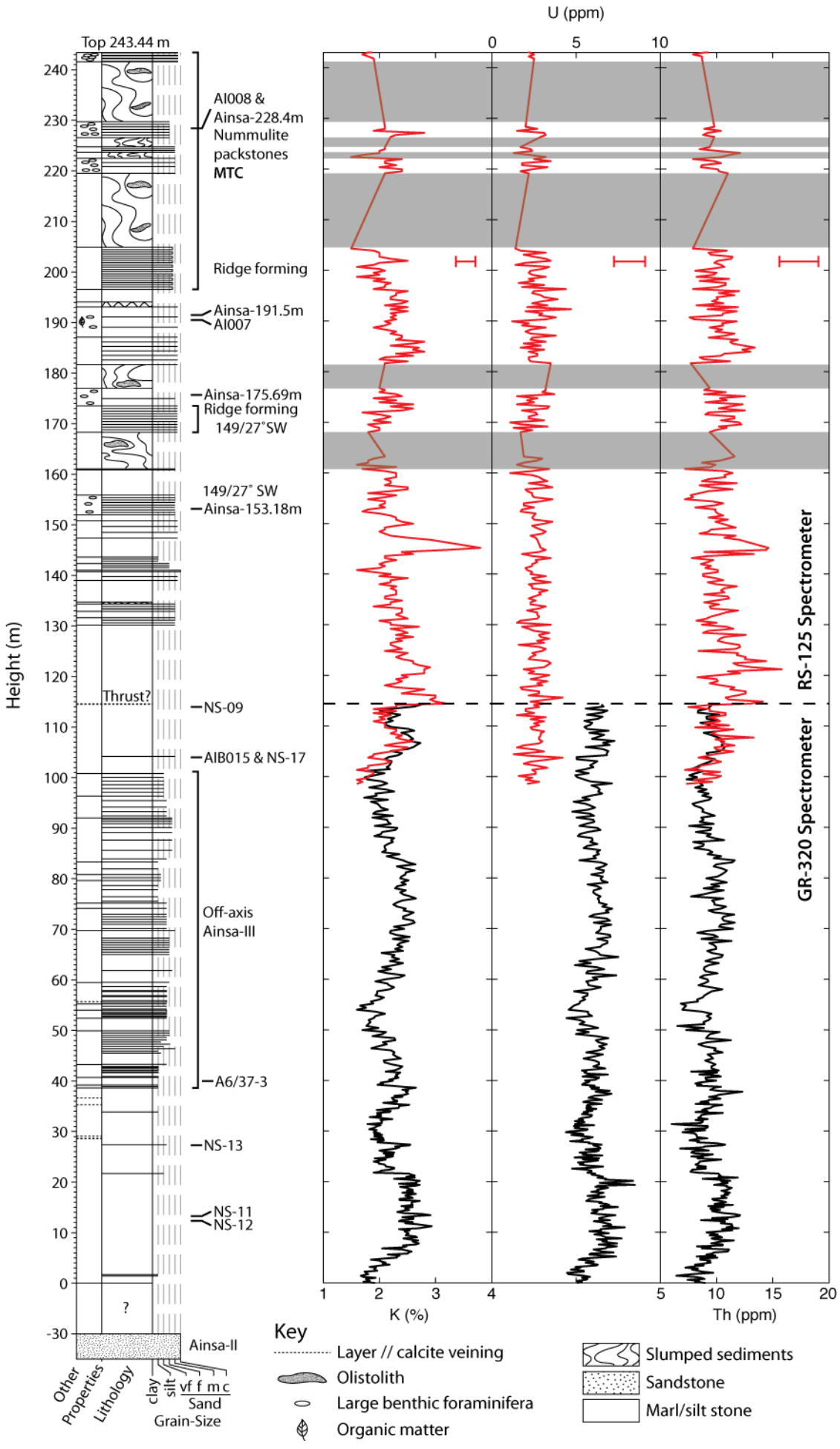
U (ppm)
0
5
10
Top 243.44 m
Height (m)
240
230
220
210
200
190
180
170
160
150
140
130
120
110
100
90
80
70
60
50
40
30
20
10
0
-30
AI008 &
Ainsa-228.4m
Nummulite
packstones
MTC
Ridge forming
Ainsa-191.5m
AI007
Ainsa-175.69m
Ridge forming
149/27°SW
149/27° SW
Ainsa-153.18m
Thrust?
NS-09
AIB015 & NS-17
Off-axis
Ainsa-III
A6/37-3
NS-13
NS-11
NS-12
?
Ainsa-II
Other Properties
Lithology
clay
silt
vf f m c
Sand
Grain-Size
RS-125 Spectrometer
GR-320 Spectrometer
1
2
3
4
5
10
15
20
K (%)
Th (ppm)
Key
Layer // calcite veining
Olistolith
Large benthic foraminifera
Organic matter
Slumped sediments
Sandstone
Marl/silt stone

Figure 5.5 (previous page) | Stratigraphic log of studied section at outcrop. Two portable gamma ray spectrometers were utilised over two field seasons to log the ~240 m of stratigraphy between the top of the Ainsa-II fan to the MTC deposits toward the top of the Ainsa System. The lower interval (0 to 114.4 m) was measured using the Exploranium GR-320 spectrometer (black data) whilst the upper interval (98.7 to 243.44 m) used a Radiation Solutions RS-125 spectrometer (red data). Average 1σ levels estimated for 2-minute sampling times for the RS-125 spectrometer are shown as horizontal lines (Table 2.4). These are likely to be overestimated as here a 4-minute sampling time was utilised for RS-125 measurements. Position of palaeontological samples used to construct age model are also shown (see Chapter 3).

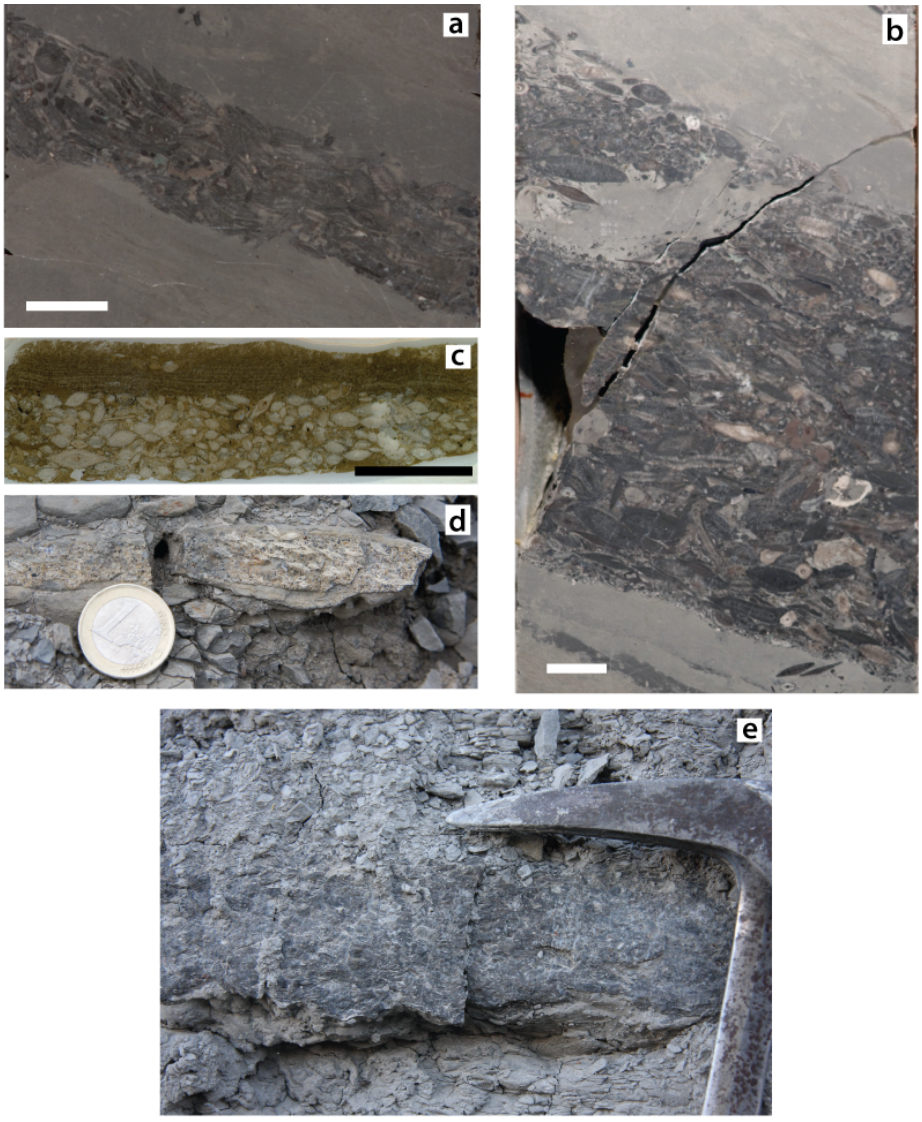

Plate 5.1 | Examples of Nummulites in coarse fraction of turbidites and Nummulite packstones. a and b) Within the A6 core several Nummulite packstones are present representing a probable collapse of nearby Nummulite banks. **c and d)** Nummulites included within coarse fraction of turbidites in thin-section (c) and at outcrop (d). These examples are located at 173.69 m and 153.18 m within the litho-stratigraphic log (Fig. 5.5). One euro coin for scale. **(e)** Size and abundance of Nummulite packstones increase toward top of section indicating possible instability of Nummulite bars within the adjacent Tremp-Graus basin.

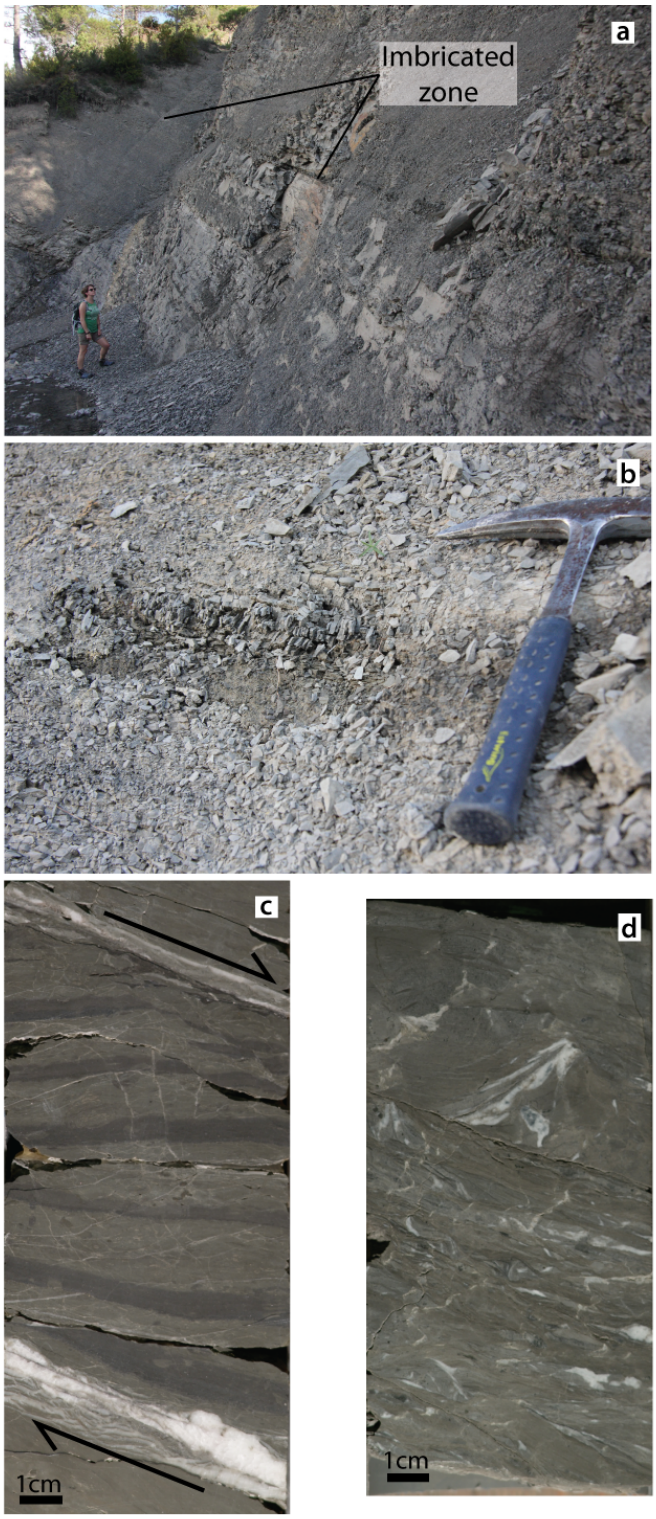

Plate 5.2 | Thrust planes observed both at out outcrop and in the A6 core sediments. (a) The layer parallel thrust plane at outcrop located at 114.6 m height. At outcrop the thrust plane consists of a 10 cm zone of imbricated marls with ~1 cm thick calcite veins above and below. **(b)** Close up of thrust plane at outcrop with imbrication of marls apparent. **(c)** Thrust plane within the A6 core at 71.2 m. The scale and appearance of the thrust plane is similar to that observed at outcrop. **(d)** An additional thrust horizon was identified at 156 m again with calcite veins above and below.

5.2 Materials and methods

5.2.1 Study location and sediments

In order to identify potential orbital cyclicity, outcropping sediments between the Ainsa-II submarine fan and the Morillo System were studied (Figs. 5.2, 5.4). Representative sediments within this interval are illustrated in Figure 5.5 and represent a combination of inter-fan, off-axis fan and MTC deposition. Initial sediments (0 to 40 m) consist of inter-fan, colour laminated mudstones and siltstones with rare thin silty turbidites. An increased frequency in thin very-thin and thin-bedded silty turbidites at ~40 m, likely correspond to off-axis deposits of the Ainsa-III submarine fan (Pickering and Bayliss, 2009). Higher parts of the section (~160 to 240 m) record an abundance of cohesive slides, MTCs and increasingly common centimetre-scale *Nummulite* rich turbidites and packstones (Plate 5.1). At ~114 m, a layer parallel shear horizon represents the potential for missing or duplication of sediments (Fig. 5.5; Plate 5.2).

The A6 well and its recovered sediments sample this same stratigraphic interval but laterally offset (Fig. 5.6). The A6 well is one of eight wells drilled within the Ainsa Basin, which took place as part of the FORCE Deep Water clastic Workgroup project, based at University College London (Pickering and Corregidor, 2000, 2005). Wells were drilled at 400 to 500 m intervals through the Ainsa Systems submarine fan deposits (wells A1, A2, A3, A4, A5, L1 and L2), as this represents typical inter-well space in a producing oilfield. The A6 well was drilled through the off-axis and inter-fan sediments separating the Ainsa and Morillo systems (Figs. 5.2, 5.4). Recovered sediments have previously been subdivided into three stratigraphic sections by Heard et al. (2008). The base of the core (230 to 209.9 m) comprises thin-bedded sandstones, siltstone-mudstone laminae and intervals of intensely bioturbated siltstone and silty mudstone, which are associated with the waning of Ainsa-II fan deposition (Pickering and Corregidor, 2005). The middle section (~210 to 64 m) is described as containing packets of siltstone-mudstone laminae, stratified siltstones, graded mudstones and thin biogenic mudstones. Separating these packets are generally more intensely bioturbated intervals of mottled siltstones and mudstones. The upper part of the core contains decimetre- to metre-scale sediment slides and debris flows, thin-bedded sandstones and siltstone-mudstone laminae. Two potential thrusts intersect the well at 71.2 mbs (metres below surface) and 156.6 mbs (Plate 5.2).

Figure 5.6 (next page) | Litho-stratigraphic correlation between outcrop and well sections. Distinctive horizons such as sediment slides enable the correlation between the sediments at outcrop and recovered from the subsurface. Other features such as layer parallel thrust planes appear more mobile.

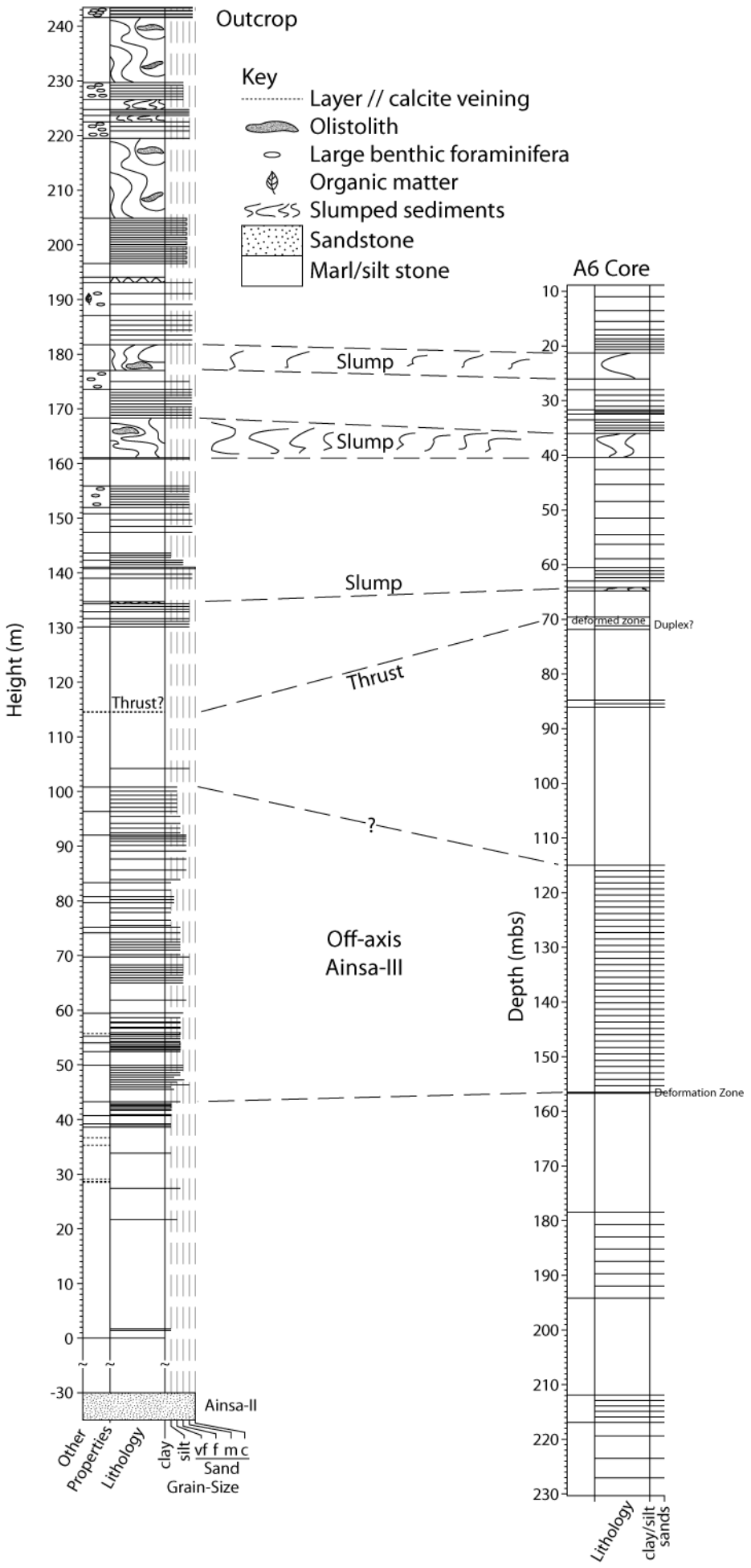
Outcrop
Key
Layer // calcite veining
Olistolith
Large benthic foraminifera
Organic matter
Slumped sediments
Sandstone
Marl/silt stone
A6 Core
Slump
Slump
Slump
Thrust
Thrust?
?
deformed zone
Duplex?
Deformation Zone
Off-axis
Ainsa-III
Height (m)
Depth (mbs)
Ainsa-II
Other Properties
Lithology
clay
silt
vf f m c
Sand
Grain-Size
Lithology
clay/silt
sands

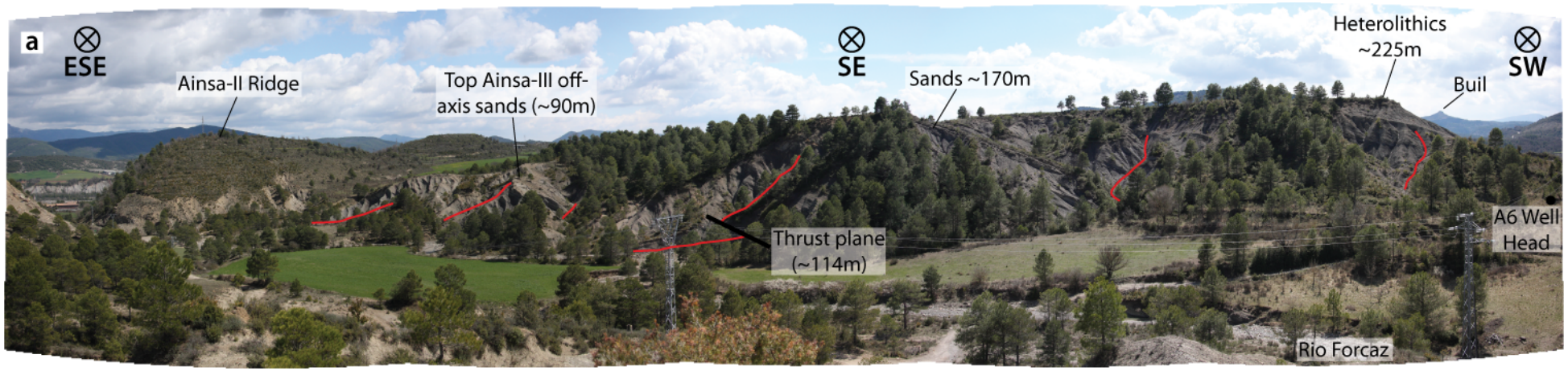
a
ESE
Ainsa-II Ridge
Top Ainsa-III off-axis sands (~90m)
SE
Sands ~170m
Heterolithics ~225m
Buil
SW
Thrust plane (~114m)
A6 Well Head
Rio Forcaz


b
NW
Heterolithics ~220m
Slump 205-220m
Rio Forcaz

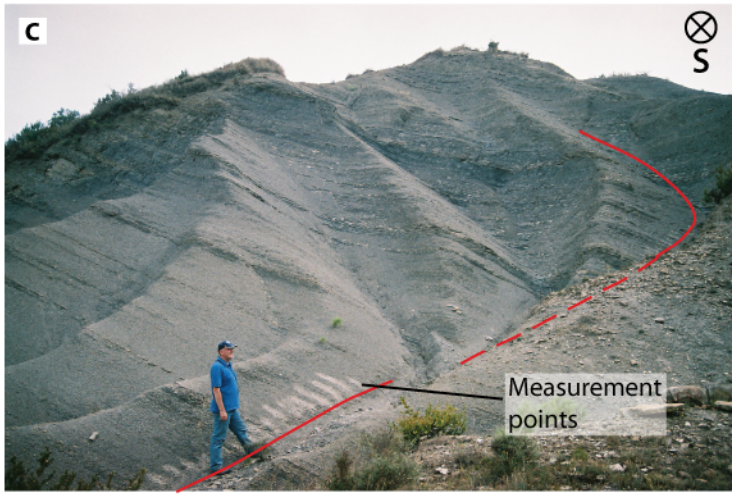
c
S
Measurement points

Plate 5.3 (previous page) | Outcrop images illustrating the logged sections within the Rio Forcaz valley. The locations and direction of these photographs are shown in Figure 5.4. **(a)** Photo-mosaic showing the approximate locations of the individual logged intervals (red lines), which were subsequently combined to create the outcrop stratigraphic series. Some sections are out of view. The ridge to the ESE represents the Ainsa-II submarine fan deposits above which logging commenced. **(b)** View from the ridge at the southwest end of the valley showing the heterolithic and MTC deposits toward the top of the studied section. **(c)** An individual interval toward the base of the studied stratigraphy. The termination of the red line corresponds to ~42 m height. SGR measurement points are visible due to cleaning of surface material.

5.2.2 Data collection

5.2.2.1 Outcrop spectral gamma ray

Spectral gamma ray (SGR) measurements of the Ainsa-II to Morillo-I outcropping stratigraphy were taken over two field seasons (April, 2008 and April, 2010) logging a total of 243.44 m. To enable continuous sampling along the section, it was necessary to join smaller vertical sections by lateral correlation of a distinct “marker” bed/interval: in general, such sections were in the order of up to a few tens of metres (Fig. 5.4, Plate 5.3). Measurements were started from the first available outcrop ~30 m above the Ainsa-II submarine fan sediments and continued into thick MTC and heterolithic deposits to the southwest (Fig. 5.4; Plate 5.3). Where possible, relatively flat, un-weathered surfaces were measured in an attempt to reduce measurement errors (Myers and Wignall, 1987; Parkinson, 1996). At outcrop, superficial material was removed prior to spectral measurements being taken. Initially, a sample interval of 0.2 m was used but was increased to 0.4 m after ~40 m. By using a sample interval less than the detection radii of the GR-320 and RS-125 machines the resultant SGR data therefore records a moving average though the section. SGR readings from both machines consist of K (%), U (ppm) and Th (ppm) whilst the RS-125 Super-Spec additionally records total gamma (CPS). Further details upon SGR are discussed in Chapter 2.

During the April 2008 sampling season (0 to 114.4 m) spectral gamma-ray readings were taken using an Exploranium GR-320 (no. 2077) and GPX-21 (no. 1887) EnviSpec Portable Gamma Ray Spectrometer. Spectral gamma-ray readings during the April 2010 sampling season (98 to 240 m) were obtained using a Radiation Solutions RS-125 Super-Spec spectrometer. Measurements for both machines were taken using a 3- to 4-minute sampling periods, respectively.

The use of differing spectrometers to collect outcrop SGR data may introduce artificial SGR variations between data sets. An attempt to quantify the differences between the GR-320 and RS-125 SGR spectrometers was achieved via measuring the same short section between 98 to 114 m with each machine. Despite this, only outcrop

data below 114.4 m shall be used for spectral analyses thus avoiding any potential issues due to the use of different spectrometers and potential thrusting.

5.2.2.2 A6 well spectral gamma ray, core ichnological and geochemical data

A6 downhole measurements collected by Robertson Geologging Limited (collected 13th May 1999) provide spectral gamma ray (SGR), natural gamma ray (NGR) and caliper data with a sampling resolution of 0.1 m (Table 5.1; Fig. 5.7). Generally, radiation from the subsurface is collected from 20 cm above and below the spectrometer and 10 cm horizontally but will vary depending upon lithology (Rider, 1996). Details on the logging speed and composition of drilling mud are unavailable. Sediment recovery from the A6 well was ~97%, which enabled Heard et al. (2008) to measure bioturbation intensity and bulk sediment geochemistry [total organic carbon (TOC) and calcium carbonate ($CaCO_3$)] data from 0.1 m and 1 m intervals respectively between 4.3 to 209 mbs (metres below surface; Table 5.1; Fig. 5.8).

Subsurface data for spectral analysis below 72 mbs is here utilised to avoid the potential thrust horizon at 71.2 mbs. Sediments above 72 mbs were not analysed as they contain numerous mass movement deposits, which may represent either missing or duplicated sections and are therefore unsuitable for spectral analysis.

Table 5.1 – Outcrop and A6 well data properties

Data Set*	N	Mean	Min	Max	Standard Deviation	Percentage Difference (%)†	Height / Depth below surface (m)	
							Min	Max
Outcrop								
Potassium	385	2.24	1.60	2.93	0.27	11.84	0.00	114.40
Uranium	385	6.05	4.39	8.49	0.67	11.14	0.00	114.40
Thorium	385	9.40	6.01	12.28	1.10	11.70	0.00	114.40
Th/K	385	4.21	2.94	5.51	0.38	9.03	0.00	114.40
Th/U	385	1.56	1.05	2.23	0.18	11.54	0.00	114.40
A6 Well 72 – 229m								
Potassium	1531	1.56	0.03	4.02	0.74	47.37	72.10	229.40
Uranium	1297	3.88	0.01	13.12	2.35	60.45	72.30	229.40
Thorium	1561	7.36	0.11	23.05	3.68	49.92	72.10	229.40
Total Gamma	1574	145.16	113.70	193.00	9.74	6.71	72.10	229.40
Natural Gamma	1559	62.98	39.40	96.23	8.81	13.99	72.20	228.00
Th/K	1473	5.38	0.16	19.29	3.35	62.24	72.10	229.40
Th/U	1223	2.73	0.01	19.94	3.13	114.74	72.30	229.40
Bioturbation	1371	79.79	8.33	100.00	20.12	25.22	72.00	209.00
TOC	136	1.23	0.11	2.37	0.42	33.98	72.00	209.00
$CaCO_3$	136	34.20	19.50	49.86	5.62	16.44	72.00	209.00

*Only the A6 well data has had outliers and negative values removed. Properties for data prior to de-trending or interpolation.

†Percentage difference between mean and standard deviation.

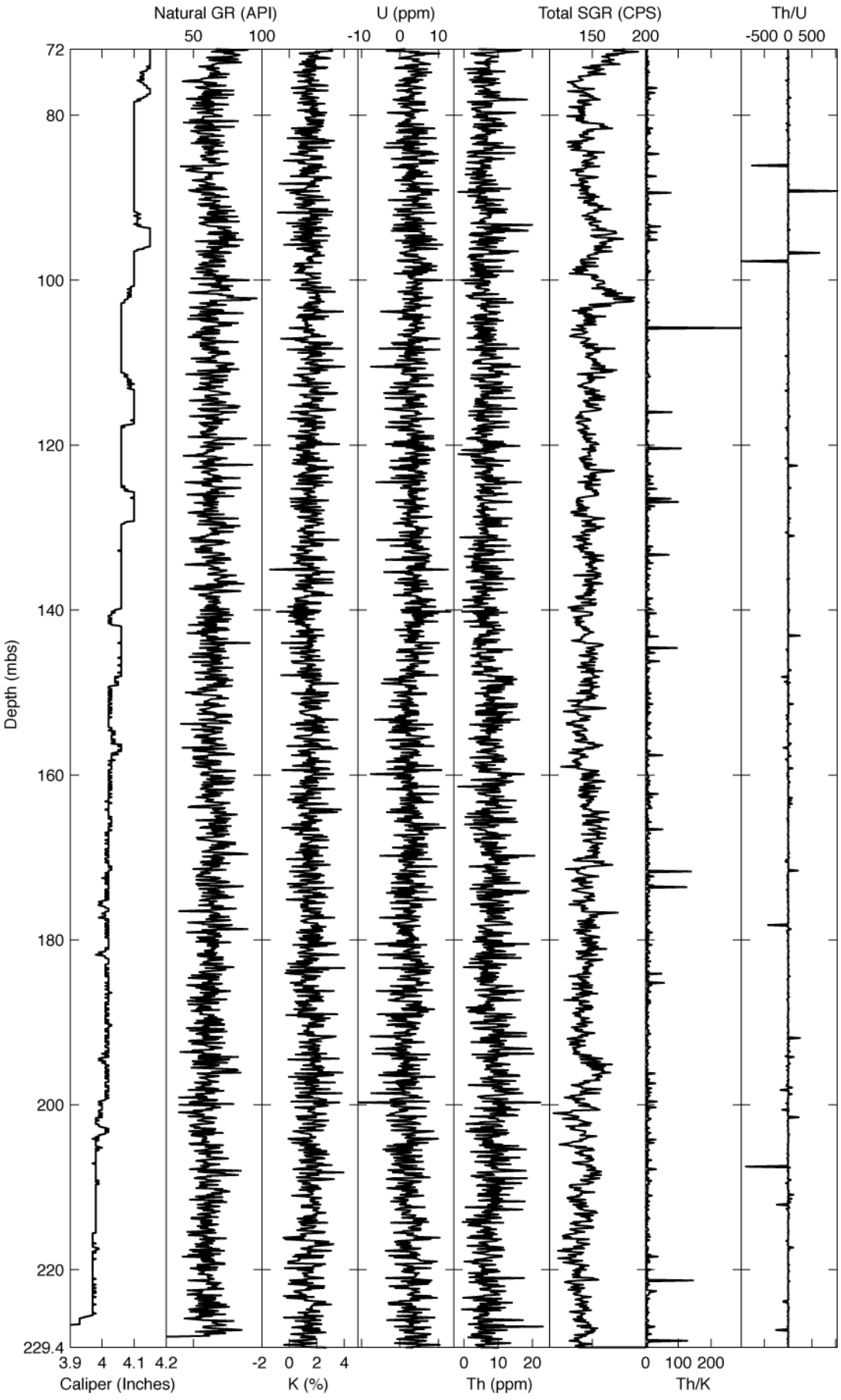
Natural GR (API)
50
100
U (ppm)
-10
0
10
Total SGR (CPS)
150
200
Th/U
-500 0 500
72
80
100
120
140
160
180
200
220
229.4
Depth (mbs)
3.9
4
4.1
4.2
Caliper (Inches)
-2
0
2
4
K (%)
0
10
20
Th (ppm)
0
100
200
Th/K

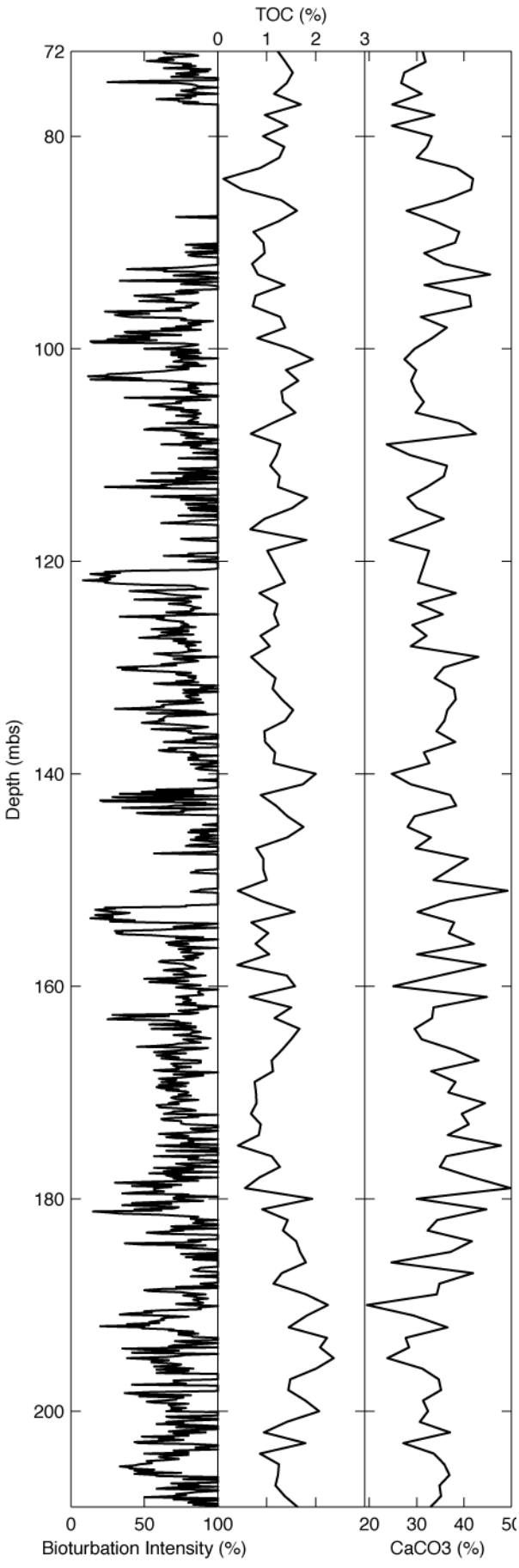

Figure 5.7 (previous page) | A6 wireline log data for 72-229.4 mbs prior to processing. These data were later processed to create a stratigraphic time series by removing outliers and negative values.

Figure 5.8 (left) | A6 bioturbation intensity, $CaCO_3$ and TOC data from Heard et al. (2008). Excellent core recovery enabled the bioturbation intensity to be measured throughout the length of the A6 core. Bulk sediment samples were also analysed for $CaCO_3$ and TOC content at a much lower resolution and are unsuitable for statistical analysis.

Table 5.2 – Outcrop and A6 well stratigraphic time series properties

Stratigraphic Series Data*	N	Sample Interval† (m)	Nyquist Frequency (cycles/m)§	Rayleigh Frequency (cycles/m)#
A6 well				
Potassium	1531	0.1028	4.8638	0.0064
Uranium	1297	0.1212	4.1254	0.0064
Thorium	1561	0.1008	4.9603	0.0064
Th/K	1473	0.1068	4.6816	0.0064
Th/U	1223	0.1285	3.8911	0.0064
Total	1574	0.1000	5.0000	0.0064
NGR	1559	0.1000	5.0000	0.0064
Bioturbation	1371	0.1000	5.0000	0.0073
Outcrop				
Potassium	385	0.2979	1.6784	0.0087
Uranium	385	0.2979	1.6784	0.0087
Thorium	385	0.2979	1.6784	0.0087
Th/K	385	0.2979	1.6784	0.0087
Th/U	385	0.2979	1.6784	0.0087

*Stratigraphic series data here show statistics after the removal negative and major outliers from the A6 well data. No data were removed from the outcrop data.

†Mean sample intervals determined for the wavelet and MTM F-test algorithms, which require evenly spaced data.

§Nyquist frequency represents the maximum discernable frequency based upon the sampling interval.

#Rayleigh frequency represents the minimum spacing within the fast Fourier transform frequency grid. Calculated from the number of data points and sample interval.

5.2.3 Data processing

Prior to spectral analysis, each data set requires pre-processing to create a stratigraphic time series. During this process, major outliers, negative values and any linear trends were removed and, depending upon the spectral technique, linear interpolated to create an evenly spaced depth/height-scale (Table 5.2). Due to the differing spectral analysis algorithm requirements, two data sets were created for each stratigraphic series, one for analysis using the REDFIT algorithm (Schulz and Mudelsee, 2002) and another for the continuous wavelet (Torrence and Compo, 1998) and multi-taper method (MTM) and F-test algorithms (Thomson, 1982; Thomson, 1990).

5.2.4 Spectral analyses

With the majority of the stratigraphic time series being unevenly spaced, the REDFIT algorithm (Schulz and Mudelsee, 2002) was utilised (Section 2.6.4) to determine statistically significant frequencies. REDFIT spectral analyses were performed using an over-sampling factor (ofac) of 4 and a hifac of 1. To maintain the required 8 degrees of freedom 6 WOSA rectangular segments were used when analysing both outcrop and A6 well time series. However, using this setting resulted in a poor spectral resolution

within the outcrop SGR time series due to the reduced number of data points. To overcome this REDFIT analyses were calculated using 2 WOSA segments providing 3 degrees of freedom.

To determine the spatial distribution of regular oscillations within these stratigraphic series, the online tool (http://paos.colorado.edu/research/wavelets/) was utilised, which applies the continuous wavelet algorithms (CWT) of Torrence and Compo (1998). The continuous wavelet spectra were calculated using the de-trended and interpolated outcrop and well stratigraphic series. CWT calculations used a Morlet mother wavelet with a parameter of 6, a scale width of 0.1, 11 powers-of-2 with no zero padding therefore not requiring a cone of influence. A6 well and outcrop analysis used start scales of 5 and 2 respectively.

With the stratigraphic time series potentially containing records of orbital cyclicity, their objective identification and quantification is achieved using the Average Spectral Misfit (ASM) method of Meyers and Sageman (2007). Based upon significant frequencies identified by the MTM harmonic F-test (Thomson, 1982; Thomson, 1990), the ASM method provides a null hypothesis significance level of there being no orbital periods present. An objective sediment accumulation rate (SAR) is also provided.

MTM analyses were performed upon the interpolated and detrended stratigraphic series within Analyseries 2.0.4.2 (Paillard et al., 1996) using a time bandwidth product of 4 and 6 data tapers. F-test frequencies of ≥90% confidence were isolated within a frequency range corresponding to ≥80% total variance within the relevant MTM spectra. Based upon these frequencies, the ASM was calculated for each stratigraphic series based upon their Rayleigh (R_f) and Nyquist (N_f) frequencies (Table 5.2). The range of SARs used was 5 to 100 cm/kyr with a step size of 0.95 cm/kyr resulting in 100 ASM and H_o estimates for each analysis. All 7 orbital periods were utilised during the ASM calculation for 45 Ma (Table 1.1) based upon available dating for the Ainsa System (Pickering and Corregidor, 2005). Where less than 6 complete short eccentricity cycles were present within the stratigraphic time series, the ASM analyses were preformed without this frequency.

5.2.5 Band-pass and low-pass filtering

To remove high frequency noise, and to enable clearer comparison with comb-filter results, a 5th order Butterworth low-pass filter (cut-off frequency of 0.5 cycles/m) was applied to A6 well stratigraphic time series following the MATLAB routine (`lowpass.m`; Appendix) of Trauth (2007).

With persistent frequencies assigned orbital durations, their visualisation is achieved via frequency selective filtering. To isolate individual frequencies of interest, a

Gaussian band-pass filter with bandwidths corresponding to the MTM harmonic F-test were applied using Analyseries 2.0.4.2 (Paillard et al., 1996). Individual precession and all orbital filters were subsequently summed to create comb-filters.

5.3 Results

5.3.1 Outcrop SGR

SGR measurements taken between the top of the Ainsa-II sandbody and the MTCs and heterolithics marking the base of the Morillo system are shown in Figure 5.5. Within the lower 160 m of stratigraphy the SGR data, especially K radioelement concentrations, appear to vary over a 30 to 40 m period. Trends within the SGR data obtained above 160 m are ambiguous due to the numerous type-Ia and -Ib MTC deposits.

Comparisons between the data obtained from the different SGR detectors show that K and Th are adequately reproduced whilst U is offset by ~3.6 ppm (Fig. 5.9). Radioelement relationships appear to vary between spectrometers, main differences are apparent within the K/U and Th/U correlations, which switch from positive in GR-320 data to no correlation for RS-125 data. Th/K however, show a consistently positive correlation between spectrometers. Ternary diagrams (Fig. 5.10a) show that compared to the GR-320 spectrometer, the RS-125 spectrometer reports less U and increased Th with the outcrop. SGR K, U and Th values appear to decrease with the increased occurrence of cm-scale silt and sandstone beds through the section. Anomalously high peaks within mudstone sections occur at ~115 m and ~145 m within the K and Th data.

Statistical properties of the data used for spectral analysis (0 to 114.4 m) are provided in Table 5.2. Cross-plot relationships between the SGR elements within this range show reasonable positive R^2 correlation coefficients (Fig. 5.10a).

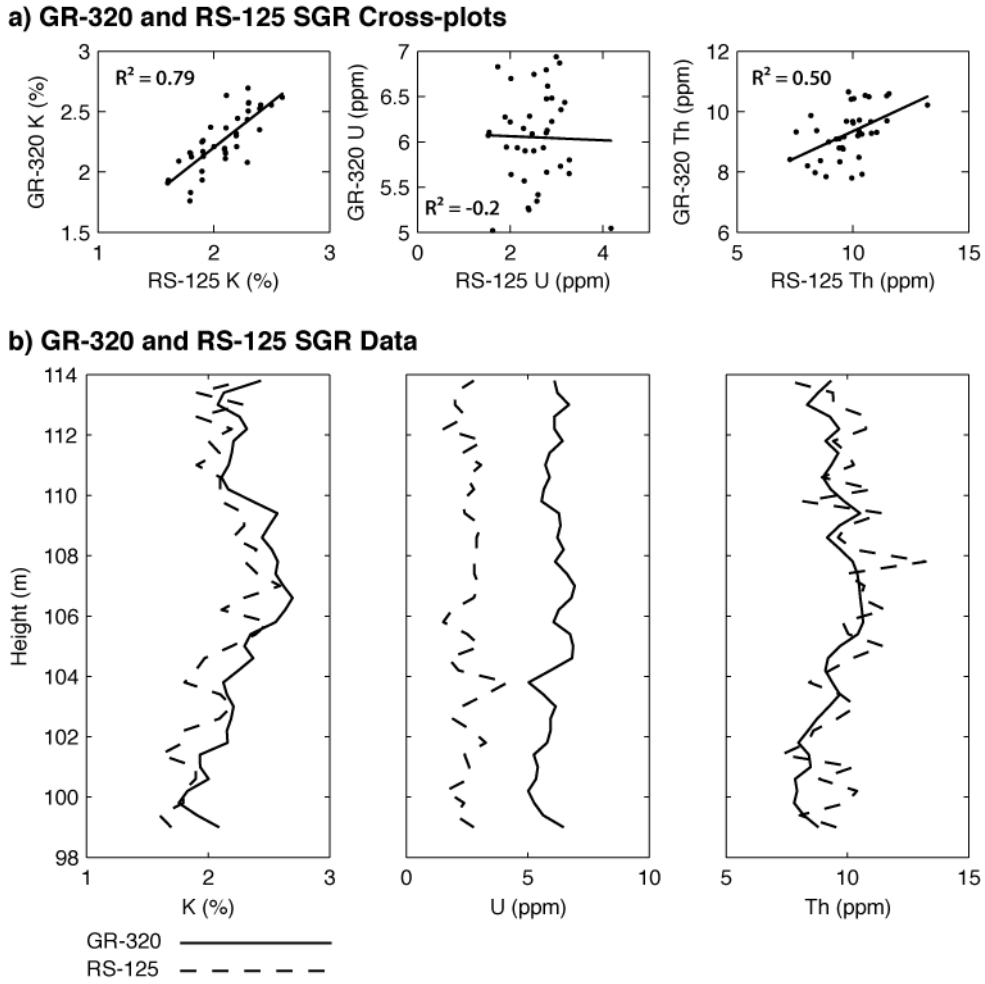

Figure 5.9 (above) | Comparison between SGR data collected using different spectrometers. Logging the same 16 m of stratigraphy with both the GR-320 and RS-125 spectrometers it is possible to test the reproducibility between machines. To enable statistical comparison between the GR-320 and RS-125 SGR spectrometers, overlapping measurements taken between two tie points (98 to 114 m) were linearly interpolated ('`interp1.m`' MATLAB function). **(a)** Cross-plots and Pearson correlation coefficients for SGR data. **(b)** SGR data interpolated to the same scale to enable statistical comparison. Readings were taken using GR-320 and RS-125 spectrometers every 40 cm with 3 and 4-minute periods respectively. Results indicate that K and Th are reasonably reproduced whilst U is poor.

Figure 5.10 (next page) | Cross-plots and ternary diagrams for outcrop and A6 SGR data. (a) Cross-plots and ternary diagrams show SGR data obtained using the GR-320 and RS-125 spectrometers. Radioelement relationships vary widely between the two spectrometers with only Th/K recording similar trends. The ternary diagram supports the poor reproducibility of U illustrated in Figures 5.5 and 5.9 with the RS-125 values being consistently lower. **(b)** Cross-plots and ternary diagrams showing SGR data for A6 well with negative values removed. Trends within the A6 SGR data show opposite correlations to those obtained from outcrop. Ternary diagram illustrates that A6 well data have a far greater range than outcrop data.

a) Outcrop GR-320 and RS-125 SGR data

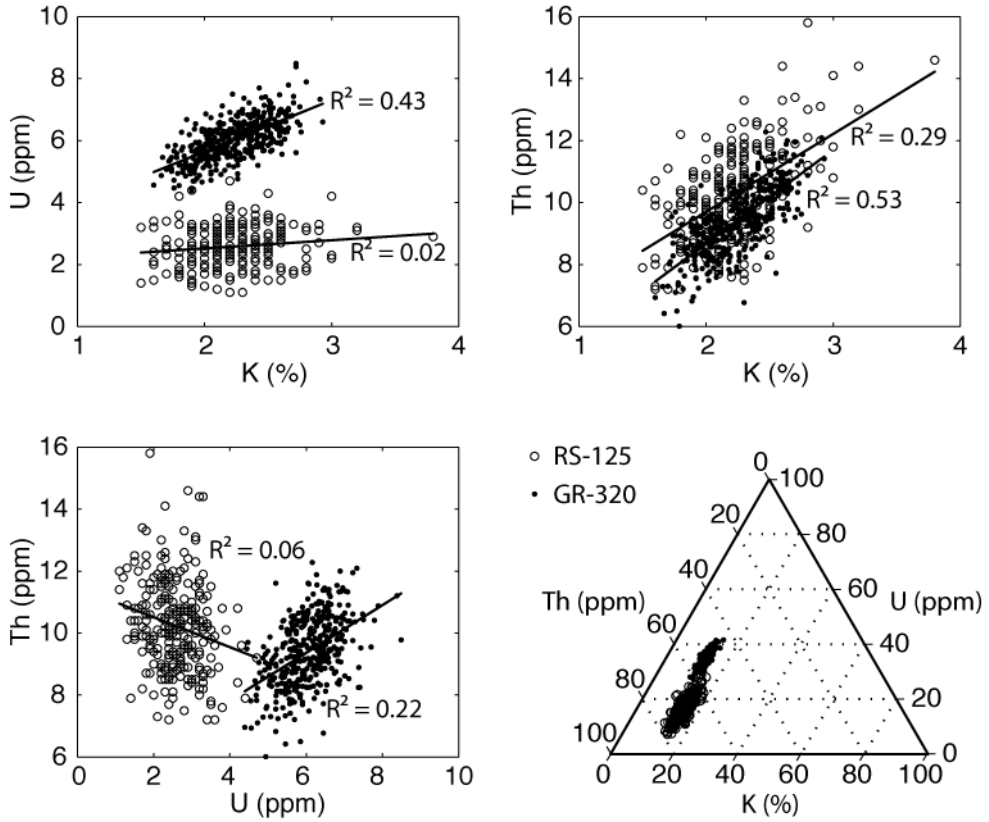

b) A6 SGR data

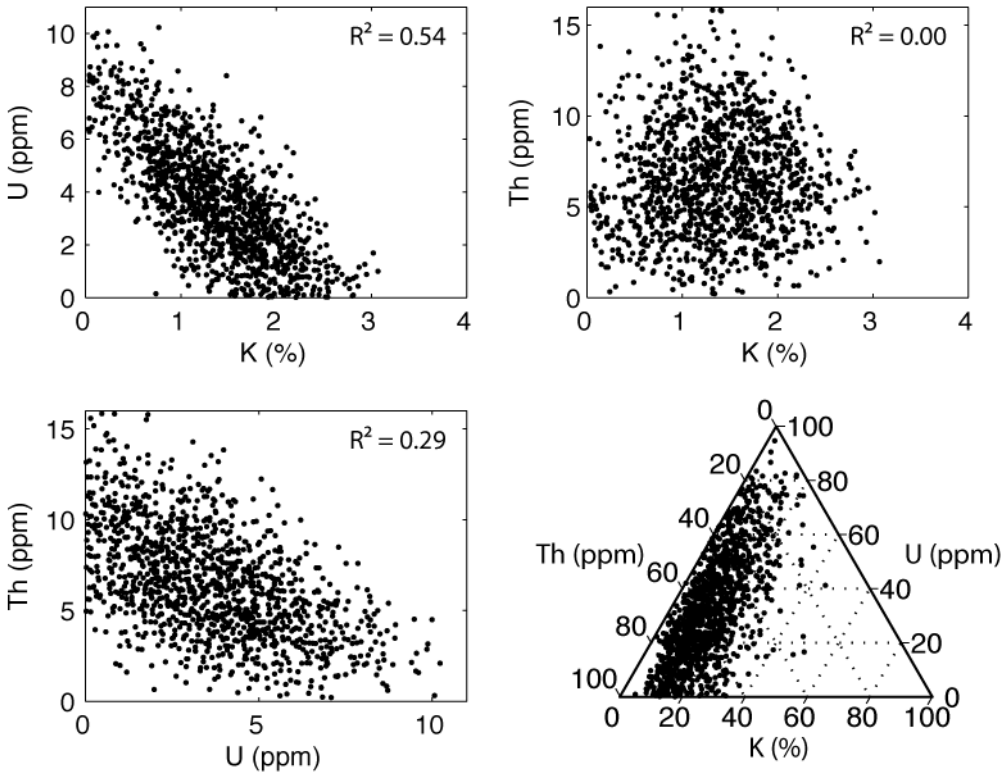

5.3.2 Outcrop spectral and ASM analyses

REDFIT analyses of the outcrop time series between 0 to 114.4 m (Fig. 5.11) using 6 WOSA segments reveal few significant frequencies >90% confidence within the 0 to 0.5 cycles/m range. The most consistent is the 0.015 (BW±0.018) cycles/m frequency, which consistently exceeds the critical confidence level of 99.1% within all but the Th/U spectrum.

Spectral results obtained at higher resolution (2 WOSA segments) REDFIT analyses reveal persistent frequencies between 0.023-0.039 (BW±0.008) cycles/m that exceed the critical confidence level of 99.6% (Table 5.3; Fig. 5.12) again in all but the Th/U spectra. Other persistent frequencies are within the 0.056-0.098 cycles/m band which exceed the 90-95% confidence levels. The significance of these frequency bands is confirmed by the MTM F-test analyses of the interpolated data indicating the presence of similar 0.021-0.043 and 0.062-0.095 (BW±0.004) cycles/m frequencies (Table 5.3; Fig. 5.13).

Spatially, the above frequency bands appear to vary with stratigraphic height from ~0.043 (1/23 m) to ~0.021 (1/47 m) cycles/m, generally above the 95% confidence level (Fig. 5.14). Additionally, this frequency appears to diminish in power between ~60-90 m. The most spatially persistent frequency is identified at ~0.017 (1/58 m) cycles/m. Spatially this frequency appears the most continuous throughout the section with confidence levels remaining above 95%. Other persistent significant frequencies are identified within the 0.07-0.09 and 0.128-0.182 cycles/m bands. Spatially, the latter of these frequency ranges within the U and Th wavelet spectra reveal intervals of increased power at ~25, ~60-80 and ~100 m. Additional significant frequencies within the 0-0.5 cycles/m range are shown in Table 5.3.

ASM results obtained using all and no eccentricity terms contain a wide range of SAR estimates between 6.90-71.50 cm/kyr that exceed the minimum null hypothesis significance level of 0.99% (Table 5.4; Fig. 5.2). The most significant SAR values identified between the outcrop time series are those between 20 and 35 cm/kyr.

Figure 5.11 (next page) | Outcrop SGR stratigraphic series and low-pass filters. Outcrop SGR data required little processing prior to spectral analysis. The grey line shows SGR data for analysis whilst the black line represents the low-pass filter. The key for the lithostratigraphic log can be found in Figure 5.5.

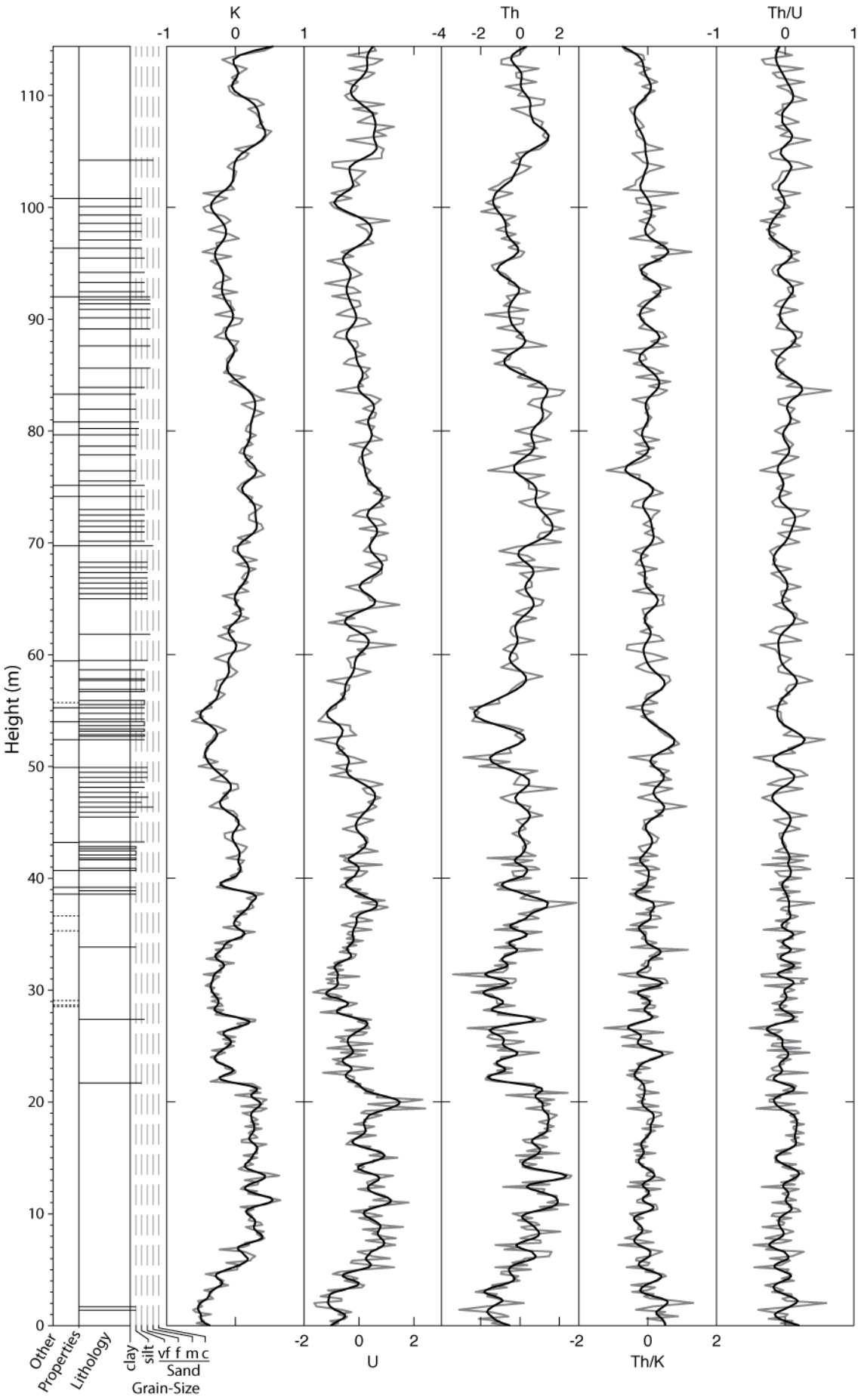
K
Th
Th/U
-1
0
1
-4
-2
0
2
-1
0
1
Height (m)
0
10
20
30
40
50
60
70
80
90
100
110
Other Properties
Lithology
clay
silt
vf f m c
Sand
Grain-Size
-2
0
2
U
-2
0
2
Th/K

Table 5.3a – Outcrop spectral results

Spectral estimation method	Frequency (cycles/m)*	Period (m)	Confidence level (%)	Temporal period (kyr)†
K				
Wavelet	0.017	58.65	95.0	208.6
	0.037	26.72	95.0	95.0
REDFIT§	0.039	25.42	Critical	90.4
MTM F-test#	0.018	55.46	90.0	197.2
	0.031	32.11	90.0	114.2
	0.128	7.82	99.0	27.8
	0.197	5.08	95.0	18.1
	0.267	3.74	95.0	13.3
	0.341	2.93	95.0	10.4
	0.384	2.61	95.0	9.3
	0.447	2.23	99.0	7.9
	0.482	2.08	95.0	7.4
U				
Wavelet	0.017	58.46	95.0	207.9
	0.034	29.45	95.0	104.7
REDFIT	0.010	101.69	90.0	361.6
	0.033	30.51	Critical	108.5
	0.075	13.26	95.0	47.2
	0.098	10.17	90.0	36.2
MTM F-test	0.033	30.50	95.0	108.5
	0.082	12.20	95.0	43.4
	0.128	7.82	95.0	27.8
	0.182	5.50	95.0	19.5
	0.218	4.59	95.0	16.3
	0.267	3.74	95.0	13.3
	0.295	3.39	90.0	12.1
	0.341	2.93	90.0	10.4
	0.388	2.57	90.0	9.2
	0.446	2.24	99.0	8.0

Spectral estimation method	Frequency (cycles/m)	Period (m)	Confidence level (%)	Temporal period (kyr)
Th				
Wavelet	0.017	57.58	95.0	204.8
	0.037	27.33	95.0	97.2
REDFIT	0.007	152.53	95.0	542.4
	0.033	30.51	Critical	108.5
MTM F-test	0.031	32.11	95.0	114.2
	0.082	12.20	90.0	43.4
	0.128	7.82	95.0	27.8
	0.154	6.49	90.0	23.1
	0.200	5.00	95.0	17.8
	0.279	3.59	95.0	12.8
	0.318	3.14	95.0	11.2
Th/K				
Wavelet	0.009	116.7	95.0	415.0
	0.041	24.1	95.0	85.7
REDFIT	0.003	305.1	Critical	1,084.9
	0.023	43.6	Critical	155.0
	0.062	16.1	95.0	57.1
	0.318	3.1	90.0	11.2
	0.338	3.0	90.0	10.5
	0.452	2.2	90.0	7.9
MTM F-test	0.021	46.93	95.0	166.9
	0.062	16.06	90.0	57.1
	0.151	6.63	95.0	23.6
	0.220	4.55	90.0	16.2
	0.234	4.27	90.0	15.2
	0.252	3.96	90.0	14.1
	0.279	3.59	95.0	12.8
	0.320	3.13	90.0	11.1
	0.387	2.59	95.0	9.2
	0.454	2.20	99.0	7.8

Table 5.3b – Outcrop spectral results

Spectral estimation method	Frequency (cycles/m)	Period (m)	Confidence level (%)	Temporal period (kyr)
Th/U				
Wavelet	0.040	24.8	95.0	88.2
REDFIT	0.043	23.5	90.0	83.5
	0.056	17.9	95.0	63.8
	0.256	3.9	95.0	13.9
	0.279	3.6	95.0	12.8
	0.367	2.7	90.0	9.7
MTM F-test	0.043	23.47	95.0	83.4
	0.095	10.52	95.0	37.4
	0.167	5.98	90.0	21.3
	0.200	5.00	95.0	17.8
	0.279	3.59	95.0	12.8
	0.336	2.98	90.0	10.6
	0.388	2.57	95.0	9.2
	0.446	2.24	99.0	8.0

*Frequencies between 0 and 0.5 cycles/m provided. Full results located within the Appendix.
[†]Temporal period determined using the average SAR of 28.12 cm/kyr identified from ASM analyses.
[§]REDFIT spectral results for 2 WOSA segments. All REDFIT analyses have bandwidth (BW) = ±0.008 cycles/m. REDFIT critical level = 99.6%.
[#]All MTM F-test analyses have bandwidth (BW) = ±0.004 cycles/m.

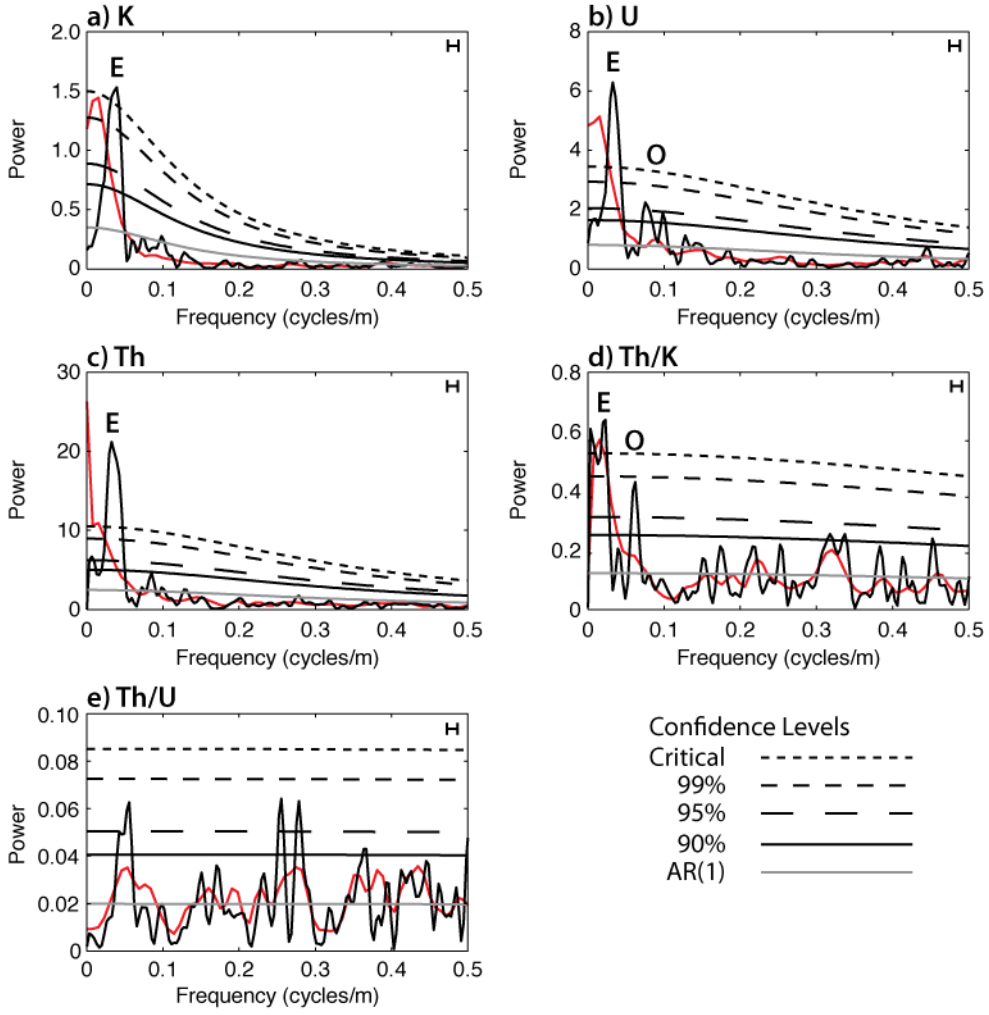

Figure 5.12 (previous page) | REDIFT spectra calculated from outcrop SGR stratigraphic time series. Spectra calculated using two settings. The red line spectra represent REDFIT analyses using an ofac of 4 and 6 WOSA segments. Due to the low spectral resolution of these results analysis was repeated using an ofac of 4 and 2 WOSA segments providing 3 degrees of freedom (black line spectra). Confidence levels and bandwidth (0.016 cycles/m) values are those calculated for analyses using 2 WOSA segments. Significant frequencies thought to represent the main eccentricity (E), obliquity (O) and precession (P) Milankovitch periods are marked.

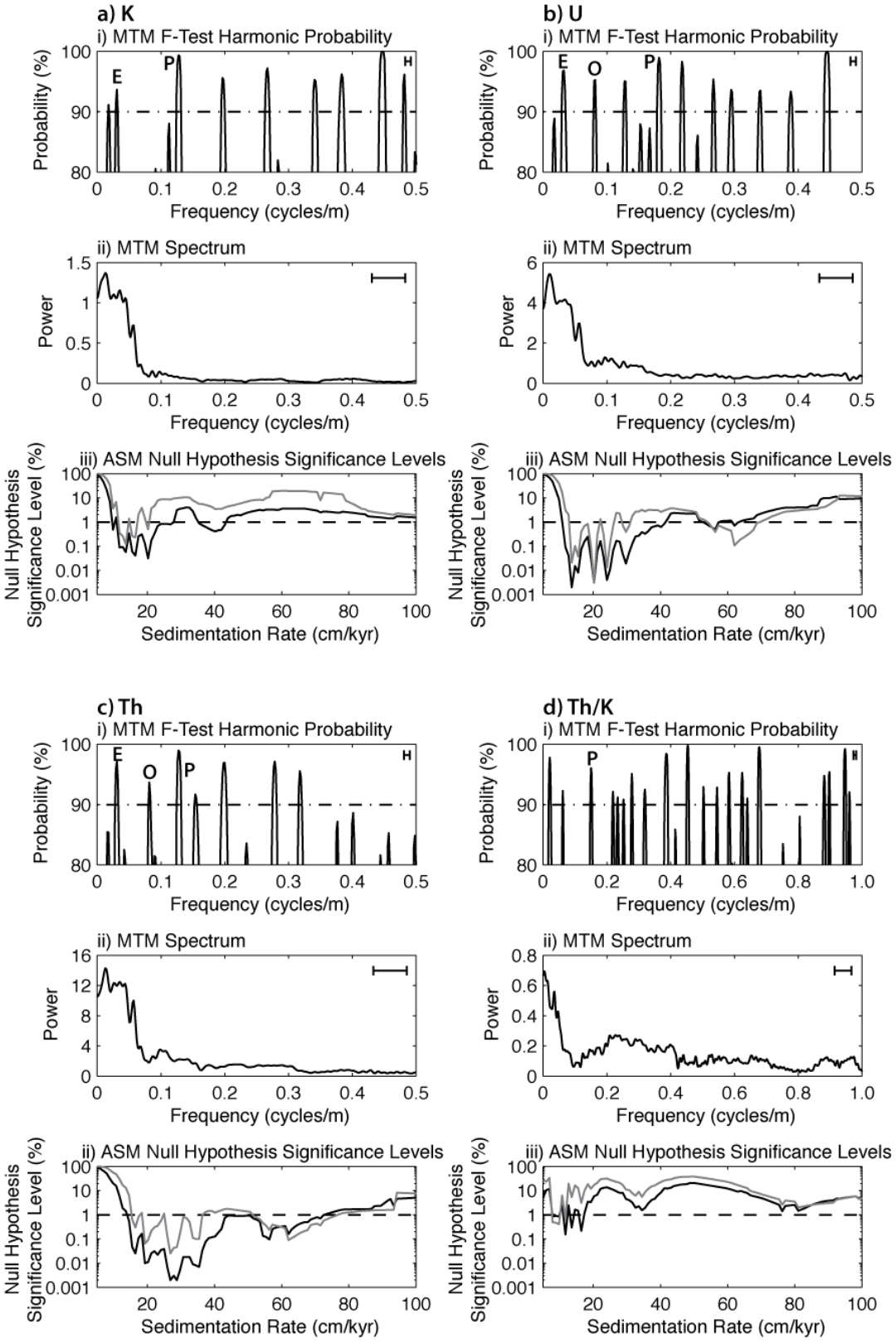

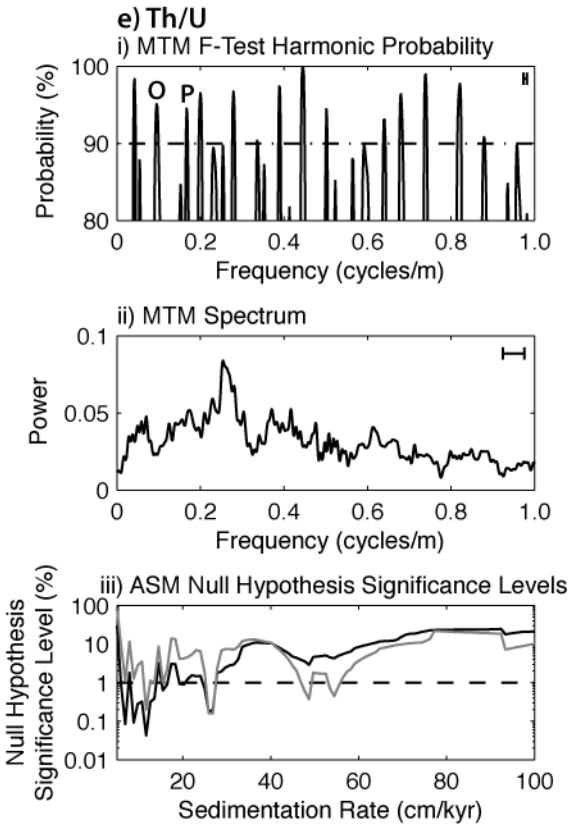

Figure 5.13 (previous two pages) | Multi-Taper Method spectral and Average Spectral Misfit results. (i) Significant frequencies (>90%) were identified from each time series using the MTM harmonic F-test (Table 5.3). Bandwidth of 0.009 cycles/m represented by horizontal bar. Significant peaks thought to represent the main eccentricity (E), obliquity (O) and precession (P) Milankovitch periods are marked. (ii) The MTM spectra was utilised to determine the frequency range that corresponded with ~80% of the total variance. The variance (area below the curve) was calculated for every 0.5 cycles/m increment. Bandwidth of 0.052 cycles/m represented by horizontal bar. (iii) ASM calculations were run using all orbital terms (black solid line). Only those SAR estimates with H_o significance levels below the critical level (0.99009901%; dashed line) are included within Table 5.3.

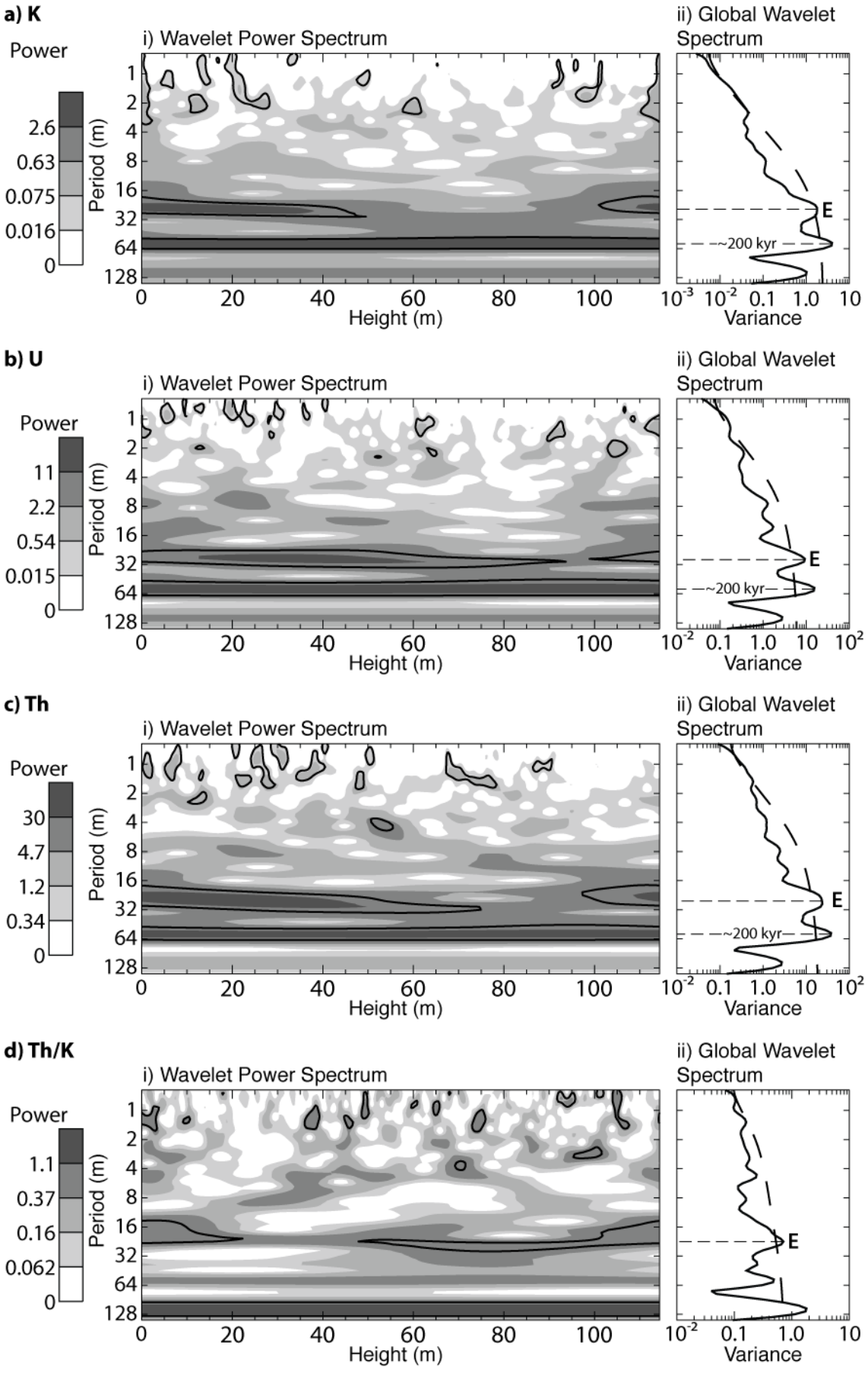
a) K
i) Wavelet Power Spectrum
ii) Global Wavelet Spectrum
Power
2.6
0.63
0.075
0.016
0
Period (m)
1
2
4
8
16
32
64
128
0
20
40
60
80
100
Height (m)
E
~200 kyr
10-3
10-2
0.1
1.0
10
Variance
b) U
i) Wavelet Power Spectrum
ii) Global Wavelet Spectrum
Power
11
2.2
0.54
0.015
0
Period (m)
Height (m)
E
~200 kyr
10-2
0.1
1.0
10
102
Variance
c) Th
i) Wavelet Power Spectrum
ii) Global Wavelet Spectrum
Power
30
4.7
1.2
0.34
0
Period (m)
Height (m)
E
~200 kyr
10-2
0.1
1.0
10
102
Variance
d) Th/K
i) Wavelet Power Spectrum
ii) Global Wavelet Spectrum
Power
1.1
0.37
0.16
0.062
0
Period (m)
Height (m)
E
10-2
0.1
1.0
10
Variance

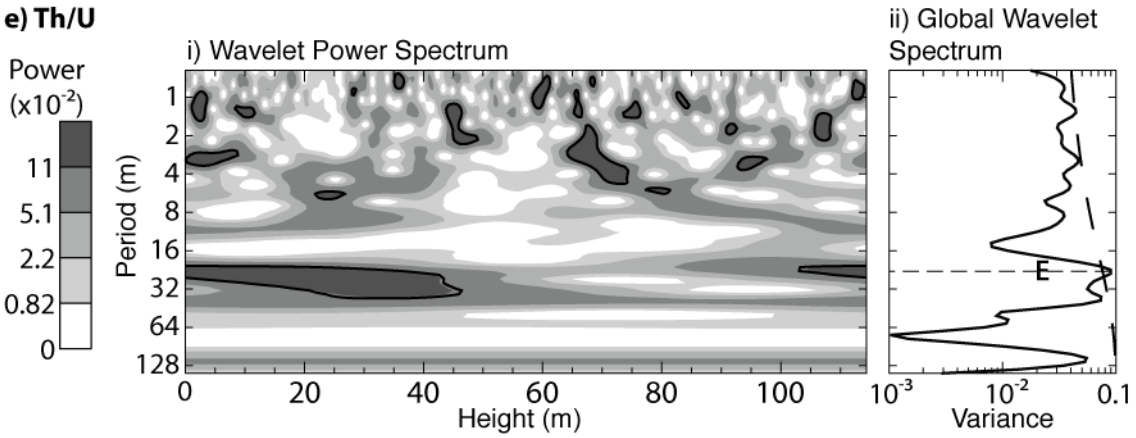

Figure 5.14 | Outcrop time series wavelet spectra. (i) Wavelet spectra illustrate the spatial distribution of frequencies throughout the individual time series. Bold contours represent the 95% confidence level. (ii) Global wavelet spectra represent the average variance throughout the entire time series. Those frequencies exceeding the 95% confidence level (dashed line) and corresponding to the predicted eccentricity (E), obliquity (O) and precession (P) periods are marked.

Table 5.4 – Outcrop ASM results

	With all orbital terms				Without eccentricity terms				
	SAR (cm/kyr)	H_o Level (%)*	ASM (cm/kyr)	No. of Orbital Terms		SAR (cm/kyr)	H_o Level (%)	ASM (cm/kyr)	No. of Orbital Terms
K	9.75	0.483	2.58E-03	7	**K**	13.55	0.122	1.65E-03	4
	11.65	0.088	2.33E-03	7		16.40	0.228	2.16E-03	4
	13.55	0.057	2.41E-03	7		20.20	0.500	2.78E-03	4
	16.40	0.041	2.45E-03	7					
	20.20	0.031	2.62E-03	7	**U**	13.55	0.021	9.54E-04	4
	26.85	0.797	4.78E-03	7		15.45	0.037	1.13E-03	4
	40.15	0.412	4.72E-03	6		20.20	0.003	6.40E-04	4
						24.00	0.013	1.33E-03	4
U	13.55	0.002	1.26E-03	7		29.70	0.388	2.85E-03	4
	15.45	0.008	1.75E-03	7		56.30	0.387	3.35E-03	4
	20.20	0.003	1.72E-03	7		62.00	0.106	2.80E-03	4
	24.00	0.004	1.91E-03	7					
	29.70	0.019	2.18E-03	6	**Th**	16.40	0.299	2.71E-03	4
	35.40	0.322	3.82E-03	6		19.25	0.064	2.25E-03	4
	40.15	0.620	4.82E-03	6		26.85	0.025	2.17E-03	4
	56.30	0.491	5.32E-03	6		56.30	0.237	3.63E-03	4
	62.00	0.706	5.58E-03	6		62.00	0.090	3.11E-03	4
						71.50	0.365	4.99E-03	4
Th	16.40	0.025	2.76E-03	7					
	19.25	0.010	2.74E-03	7	**Th/K**	9.75	0.411	5.81E-04	4
	23.05	0.022	3.08E-03	7		11.65	0.636	7.71E-04	4
	26.85	0.002	2.40E-03	7					
	28.75	0.002	1.98E-03	6	**Th/U**	11.65	0.199	9.76E-04	4
	35.40	0.007	2.51E-03	6		13.55	0.964	1.74E-03	4
	47.75	0.899	6.42E-03	6		26.85	0.160	1.60E-03	4
	56.30	0.095	5.13E-03	6		48.70	0.374	2.73E-03	4
	62.00	0.162	5.38E-03	6		54.40	0.450	2.94E-03	4
	71.50	0.710	7.61E-03	6					
Th/K	7.85	0.853	1.04E-03	7					
	9.75	0.855	1.28E-03	7					
	11.65	0.153	1.04E-03	7					
	13.55	0.298	1.36E-03	7					
	16.40	0.218	1.47E-03	7					
Th/U	6.90	0.084	9.87E-04	7					
	8.80	0.092	1.25E-03	7					
	11.65	0.043	1.42E-03	7					
	15.45	0.632	2.44E-03	7					
	20.20	0.893	2.98E-03	7					
	25.90	0.179	2.65E-03	7					

*H_o significance level represents the probability that the null hypothesis of there being no orbital periods present at that SAR would be rejected in error. In other words, the probability of orbital period being present at that SAR estimate is the H_o significance level subtracted from 100. Only those SAR estimates exceeding the critical level of 0.99009901% are presented.

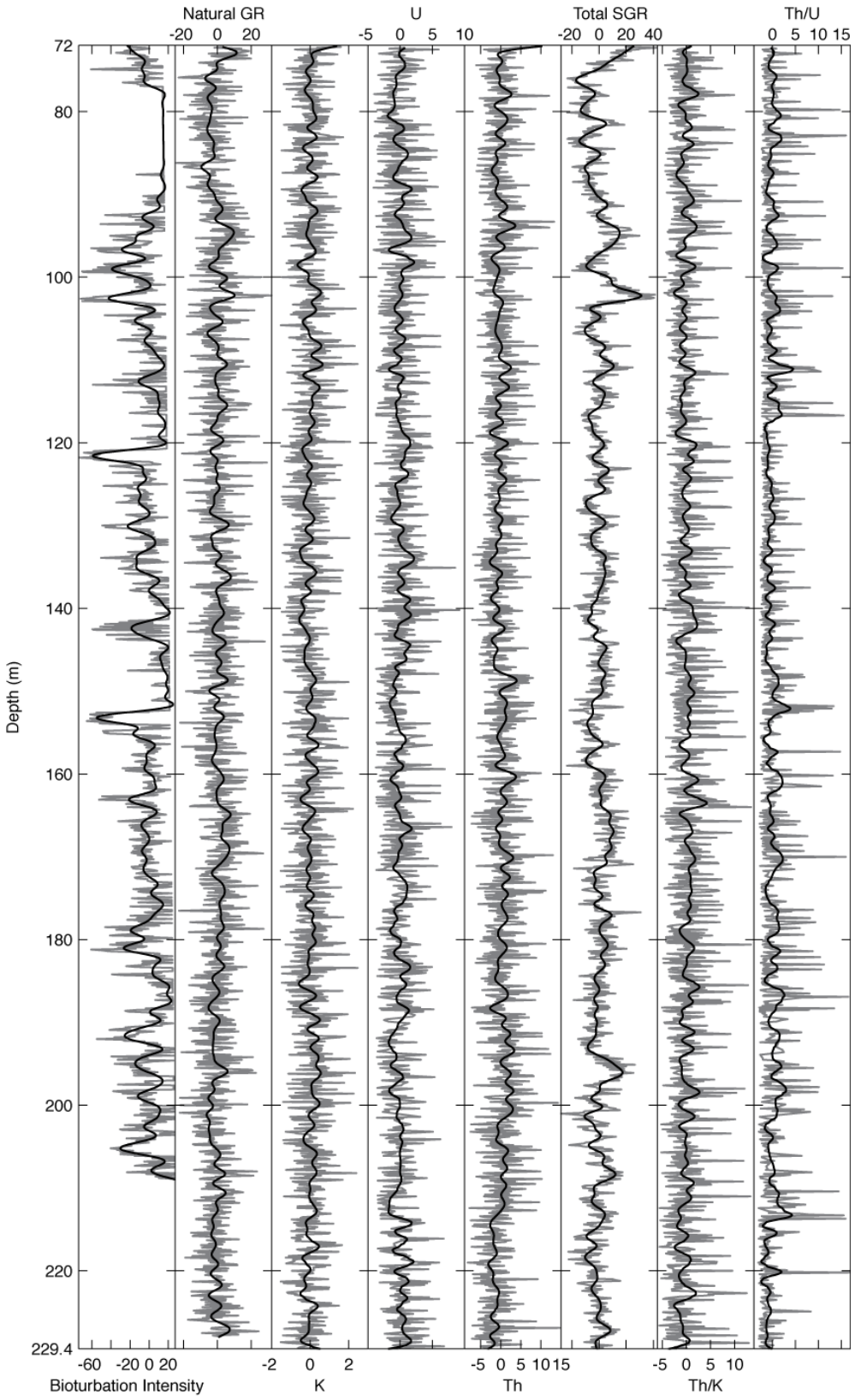

Figure 5.15 | A6 well SGR, natural GR and bioturbation intensity stratigraphic time series. Prior to spectral analysis the raw data obtained from the A6 well was processed to remove outliers, negative values, the mean and long-term trends. The grey solid line represents the resultant stratigraphic time series. Application of a low-pass filter (5^{th} order Butterworth filter, cut-off frequency 0.5 cycles/m) enables the visualisation of the underlying variability within the stratigraphic time series (black solid line).

5.3.3 A6 geophysical and bioturbation data

Calliper results indicate that the width of the A6 well gently decreases with depth from 4.15” to 3.98” with a reduction in significant width deviations below ~160 m. Noise levels within the SGR and NGR data are generally high. Only total SGR exhibits a low noise level (Table 5.2). Contributing to the high noise levels are the abundance of negative values which account for 2.7%, 14.4% and 0.8% of the total number of data points within K, U and Th data respectively. Lowpass filtering of these data show that underlying variations are present (Fig. 5.15).

Bioturbation intensity of the core generally shows clear variations with average values ranging between ~70 to 100% with perturbations every ~20 to 30 m where values decrease to ~20%. These large variations cease below ~160 mbs. The lower resolution TOC and $CaCO_3$ data also appear to vary with a similar period, although do not appear to correlate with the bioturbation data.

Statistical relationships between data prior to processing are limited to poor inverse correlations between $CaCO_3$ and TOC (R^2 = 0.52), K and U (R^2 = 0.54) and Th and U (R^2 = 0.29). The remaining correlation coefficients between data are negligible.

5.3.4 A6 spectral and ASM results

Spectral results obtained from the well and core time series (Figs. 5.16, 5.17, 5.18) indicate a dominance of frequencies within the 0.011-0.012, 0.023-0.045 and 0.061-0.096 cycle/m bands similar to those obtained from the equivalent outcrop (Tables 5.3, 5.5). REDFIT spectra obtained from the bioturbation intensity, total SGR and NGR time series suggest the 0.032-0.045 cycles/m frequency exists above the critical confidence level (Fig. 5.16). The higher frequencies also exceed the critical confidence level within the total SGR data. Spatially, the lower of these frequency bands (0.011-0.012 cycles/m) appear the most continuous whilst the higher 0.061-0.096 cycle/m frequencies are more variable (Fig. 5.18). Other significant frequencies identified between the 0 and 0.5 cycles/m are provided in Table 5.5 and up to the Nyquist frequency in the Appendix.

Applying the ASM method to the A6 stratigraphic time series using all orbital and no eccentricity terms (Fig. 5.17) produce a range of significant SAR estimates ranging between 5.0 and 96.2 cm/kyr (Table 5.6). The most consistent SAR estimates to exceed the critical level are those within the total SGR, bioturbation and NGR ASM results where significant values range between 26.85 and 30.65 cm/kyr. The ASM results obtained from the remaining individual spectral SGR data are highly variable.

Table 5.5a – A6 spectral results

Spectral Estimation Method	Frequency (cycles/m)*	Period (m)	Confidence Level (%)	Temporal Period (kyr)†	Spectral Estimation Method	Frequency (cycles/m)	Period (m)	Confidence Level (%)	Temporal Period (kyr)
Bioturbation					**Total SGR**				
Wavelet	0.032	31.48	95.0	111.9	**Wavelet**	0.012	82.96	95.0	295.0
	0.083	12.03	95.0 (110-195m)	42.8		0.032	31.3	95.0 (72-150, 200-229m)	111.3
	0.254	3.94	95.0 (110-160m)	14.0		0.063	15.94	95.0	56.7
						0.092	10.86	95.0	38.6
REDFIT§	0.038	26.07	Critical	92.7	**REDFIT**	0.033	29.93	Critical	106.4
Critical=99.7	0.083	12.03	Critical	42.8	Critical=99.8	0.072	13.82	Critical	49.1
BW=±0.015					BW=±0.013	0.100	9.98	Critical	35.5
						0.139	7.18	Critical	25.5
						0.173	5.79	95.0	20.6
						0.217	4.61	90.0	16.4
MTM F-test	0.032	31.51	95.0	112.0	**MTM F-test**	0.005	204.80	95.0	728.3
BW±0.004	0.073	13.65	90.0	48.6	BW±0.003	0.029	34.13	90.0	121.4
	0.104	9.64	90.0	34.3		0.061	16.38	90.0	58.3
	0.157	6.35	90.0	22.6		0.095	10.50	95.0	37.3
	0.193	5.18	90.0	18.4		0.106	9.42	90.0	33.5
	0.281	3.56	90.0	12.7		0.117	8.53	90.0	30.3
	0.315	3.18	95.0	11.3		0.150	6.66	95.0	23.7
	0.356	2.81	99.0	10.0		0.170	5.89	95.0	21.0
	0.392	2.55	95.0	9.1		0.255	3.92	90.0	13.9
						0.348	2.87	95.0	10.2
						0.376	2.66	95.0	9.5
						0.386	2.59	90.0	9.2
						0.398	2.51	90.0	8.9
						0.444	2.25	99.0	8.0
						0.470	2.13	90.0	7.6
						0.480	2.08	99.0	7.4

Table 5.5b – A6 spectral results

Spectral Estimation Method	Frequency (cycles/m)	Period (m)	Confidence Level (%)	Temporal Period (kyr)	Spectral Estimation Method	Frequency (cycles/m)	Period (m)	Confidence Level (%)	Temporal Period (kyr)
NGR					**K**				
Wavelet	0.024	41.69	95.0	148.3	**Wavelet**	0.012	82.22	95.0	292.4
	0.044	22.92	95.0 (72-120, 190-229m)	81.5		0.024	42.28	95.0	150.4
	0.093	10.81	95.0 (72-105, 220-229m)	38.4		0.046	21.71	95.0 (140-210m)	77.2
	0.183	5.46	95.0 (patchy)	19.4		0.155	6.47	95.0 (85-110m)	23.0
REDFIT	0.045	22.25	Critical	79.1	**REDFIT**	0.045	22.46	90.0	79.9
Critical=99.8	0.101	9.89	90.0	35.2	Critical=99.8	0.145	6.91	90.0	24.6
BW=±0.014	0.140	7.12	90.0	25.3	BW=±0.013	0.172	5.80	95.0	20.6
	0.197	5.09	95.0	18.1		0.323	3.10	95.0	11.0
	0.478	2.09	90.0	7.4		0.367	2.72	90.0	9.7
						0.434	2.30	95.0	8.2
MTM F-test	0.005	204.80	90.0	728.3	**MTM F-test**	0.011	93.57	90.0	332.8
BW=±0.003	0.070	14.37	95.0	51.1	BW=±0.003	0.023	44.32	95.0	157.6
	0.096	10.37	95.0	36.9		0.047	21.05	99.0	74.9
	0.137	7.31	99.0	26.0		0.114	8.77	90.0	31.2
	0.149	6.71	90.0	23.9		0.142	7.02	95.0	25.0
	0.200	5.00	95.0	17.8		0.173	5.77	95.0	20.5
	0.236	4.24	95.0	15.1		0.194	5.17	95.0	18.4
	0.286	3.50	95.0	12.4		0.233	4.30	99.0	15.3
	0.319	3.14	90.0	11.2		0.303	3.30	90.0	11.7
	0.332	3.01	90.0	10.7		0.327	3.06	99.0	10.9
	0.359	2.79	90.0	9.9		0.368	2.72	99.0	9.7
	0.369	2.71	95.0	9.6		0.394	2.54	95.0	9.0
	0.387	2.58	90.0	9.2		0.432	2.31	95.0	8.2
	0.408	2.45	90.0	8.7		0.469	2.13	99.0	7.6
	0.471	2.12	95.0	7.5					

Table 5.5c – A6 spectral results

Spectral Estimation Method	Frequency (cycles/m)	Period (m)	Confidence Level (%)	Temporal Period (kyr)	Spectral Estimation Method	Frequency (cycles/m)	Period (m)	Confidence Level (%)	Temporal Period (kyr)
U					**Th**				
Wavelet	0.025	40.27	95.0	143.2	**Wavelet**	0.012	81.06	95.0	288.3
	0.042	24.02	95.0	85.4		0.024	41.69	95.0	148.3
	0.082	12.13	95.0 (115-175m)	43.1		0.051	19.53	95.0 (80-115, 160-190m)	69.5
	0.164	6.11	95.0 (130-210m)	21.7		0.091	11	95.0 (80-170m)	39.1
REDFIT	0.011	89.70	Critical	319.0	**REDFIT**	0.011	89.94	Critical	319.9
Critical=99.7	0.050	19.93	Critical	70.9	Critical=99.8	0.056	17.99	99.0	64.0
BW=±0.013	0.084	11.96	95.0	42.5	BW=±0.013	0.100	9.99	95.0	35.5
	0.145	6.90	90.0	24.5		0.422	2.37	95.0	8.4
	0.424	2.36	95.0	8.4		0.450	2.22	95.0	7.9
MTM F-test	0.023	43.17	95.0	153.5	**MTM F-test**	0.024	41.29	90.0	146.8
BW=±0.003	0.046	21.58	95.0	76.8	BW=±0.003	0.048	20.64	90.0	73.4
	0.121	8.27	95.0	29.4		0.061	16.52	90.0	58.7
	0.145	6.89	99.0	24.5		0.103	9.71	99.0	34.5
	0.200	4.99	95.0	17.7		0.134	7.44	90.0	26.5
	0.234	4.28	95.0	15.2		0.159	6.30	95.0	22.4
	0.277	3.61	90.0	12.8		0.246	4.07	95.0	14.5
	0.314	3.18	90.0	11.3		0.344	2.91	99.0	10.3
	0.343	2.91	90.0	10.4		0.421	2.37	95.0	8.4
	0.365	2.74	95.0	9.8		0.448	2.23	90.0	7.9
	0.423	2.36	95.0	8.4		0.460	2.17	90.0	7.7
	0.487	2.05	90.0	7.3					
	0.496	2.02	95.0	7.2					

Table 5.5d – A6 spectral results

Spectral Estimation Method	Frequency (cycles/m)	Period (m)	Confidence Level (%)	Temporal Period (kyr)	Spectral Estimation Method	Frequency (cycles/m)	Period (m)	Confidence Level (%)	Temporal Period (kyr)
Th/K					**Th/U**				
Wavelet	None				**Wavelet**	0.012	81.4	95.0	289.5
						0.032	31.2	95.0 (72-110m)	111.0
REDFIT	0.468	2.14	95.0	7.6		0.071	14	95.0 (195-220m)	49.8
Critical=99.8						0.101	9.934	95.0 (157-185m)	35.3
BW=±0.013									
MTM F-test	0.008	124.99	90.0	444.5	**REDFIT**	0.011	89.73	95.0	319.1
BW=±0.003	0.102	9.83	95.0	35.0	Critical=99.7	0.084	11.96	90.0	42.5
	0.138	7.23	99.0	25.7	BW=±0.013	0.106	9.45	95.0	33.6
	0.173	5.79	95.0	20.6		0.412	2.43	95.0	8.6
	0.233	4.29	99.0	15.3					
	0.326	3.07	95.0	10.9	**MTM F-test**	0.059	16.98	95.0	60.4
	0.368	2.72	99.0	9.7	BW=±0.003	0.266	3.76	95.0	13.4
	0.392	2.55	95.0	9.1		0.344	2.91	99.0	10.3
	0.432	2.31	90.0	8.2		0.391	2.56	95.0	9.1
	0.461	2.17	90.0	7.7		0.414	2.41	95.0	8.6
	0.498	2.01	95.0	7.1		0.486	2.06	95.0	7.3

*Frequencies between 0-0.5 cycles/m provided. Full results located within the Appendix.
[†]Temporal period determined using the average SAR of 28.12 cm/kyr identified from ASM analyses.
[§]REDFIT spectral results for 6 WOSA segments.

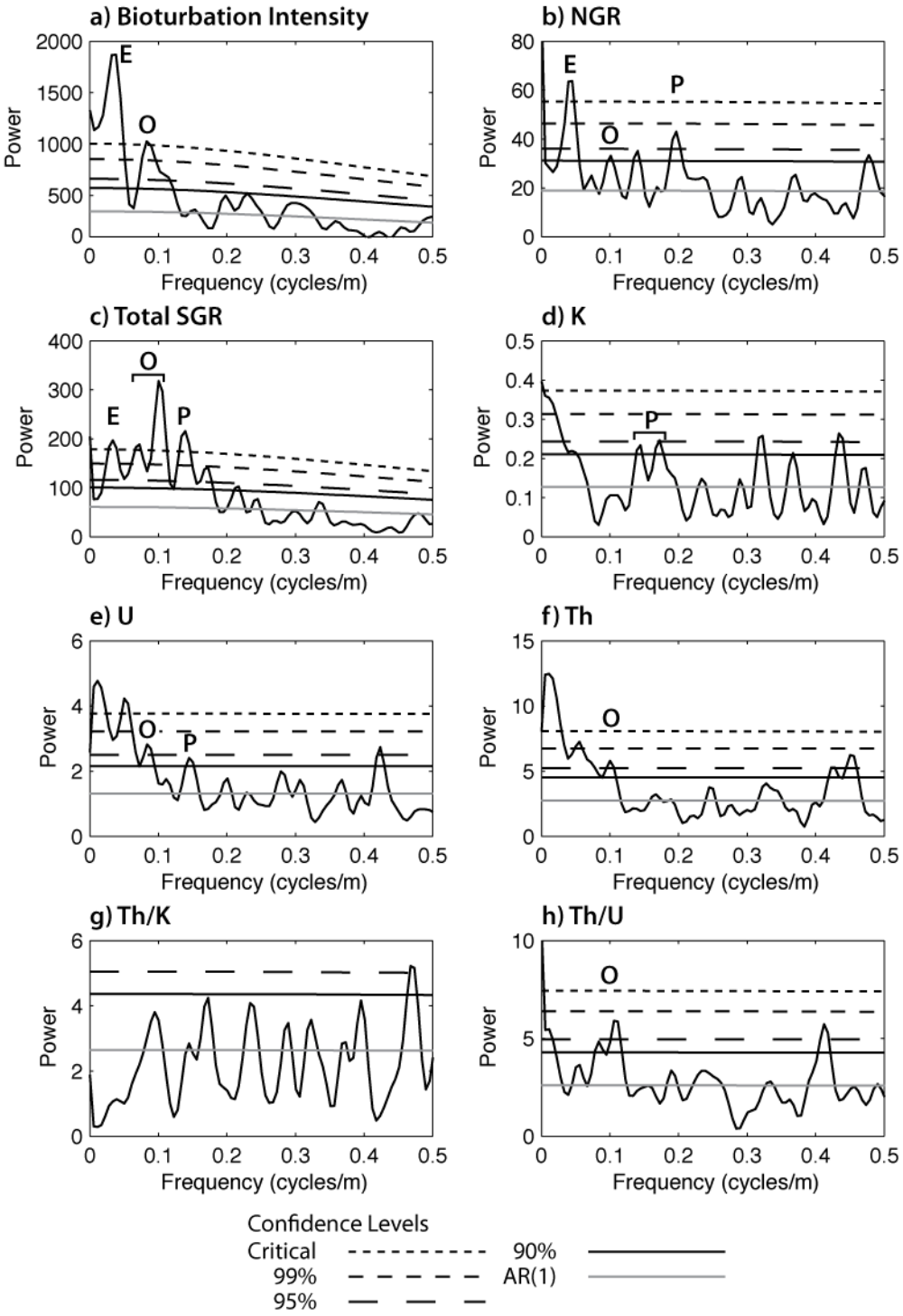

Figure 5.16 | REDIFT spectra calculated from A6 well and core time series. Spectra calculated using ofac of 4 and 6 WOSA segments providing 8 degrees of freedom. Significant frequencies thought to represent the main eccentricity (E), obliquity (O) and precession (P) Milankovitch periods are marked. The horizontal bar in each spectrum represents a bandwidth (Table 5.5).

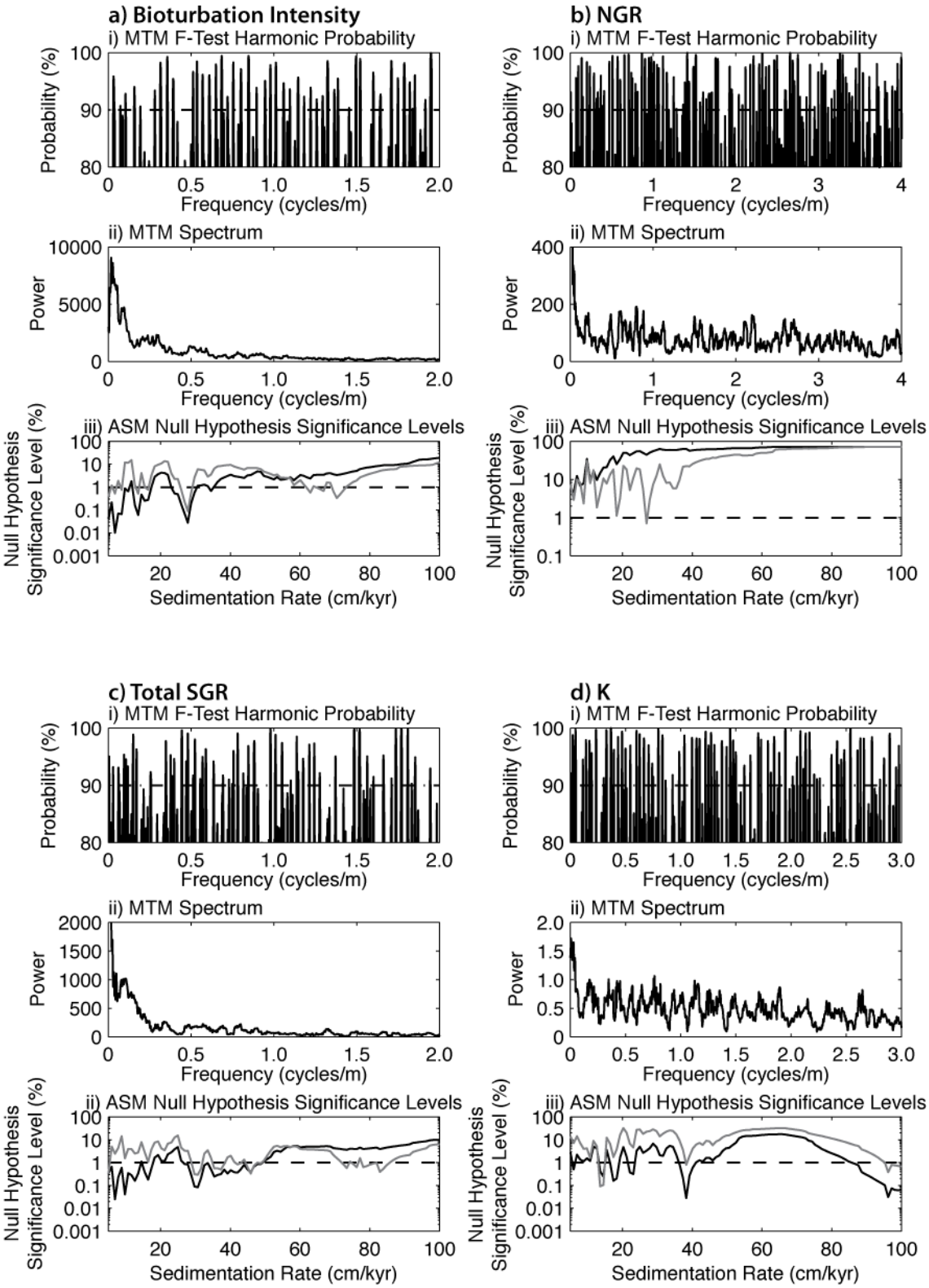
a) Bioturbation Intensity
i) MTM F-Test Harmonic Probability
Probability (%)
Frequency (cycles/m)
ii) MTM Spectrum
Power
iii) ASM Null Hypothesis Significance Levels
Null Hypothesis Significance Level (%)
Sedimentation Rate (cm/kyr)
b) NGR
c) Total SGR
d) K

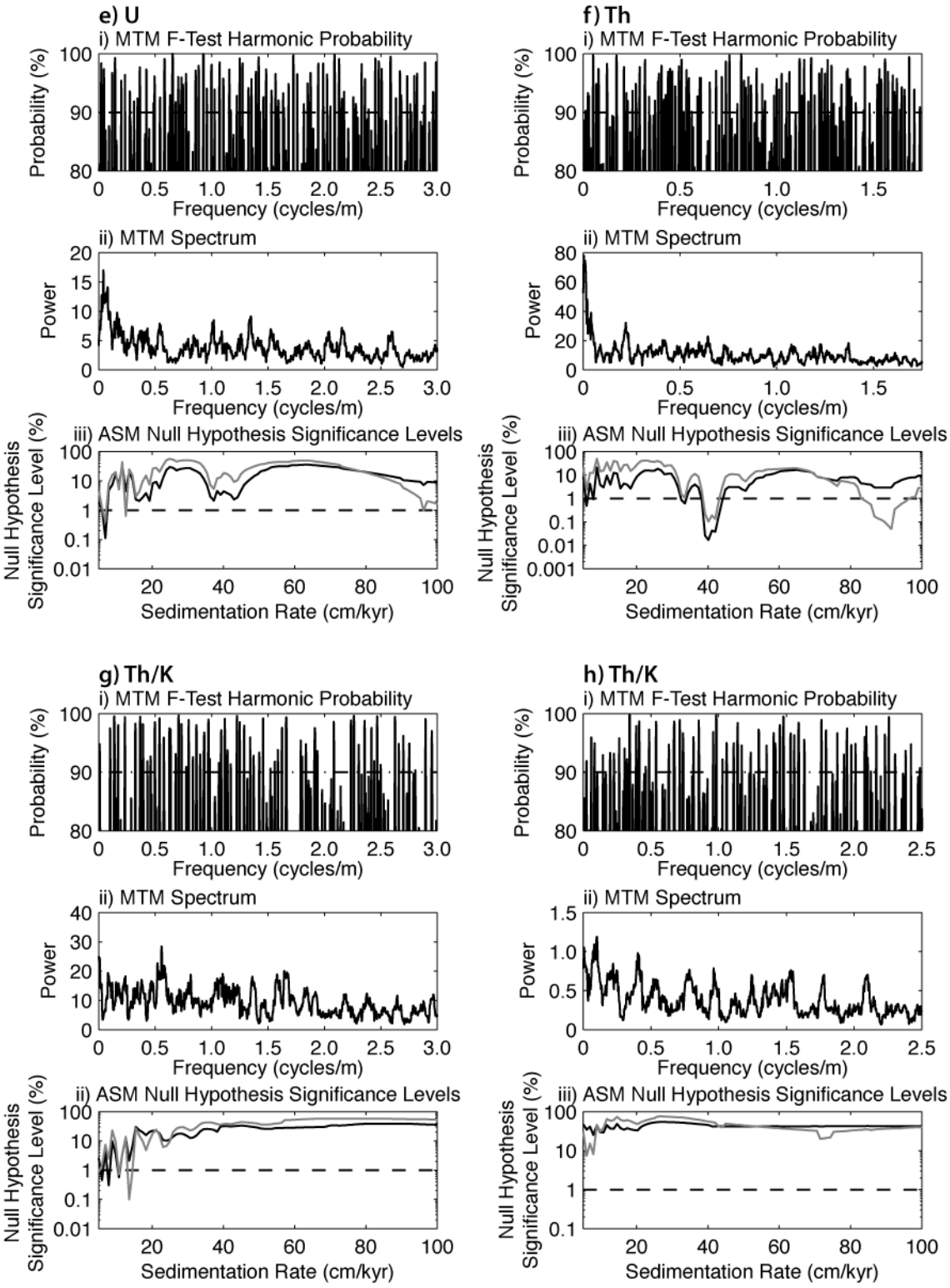

Figure 5.17 | Multi-Taper Method spectral and Average Spectral Misfit results of A6 well and core time series. (i) Significant frequencies (>90%) were identified from each time series using the MTM harmonic F-test (Table 5.5). Bandwidth represented by horizontal bar. (ii) The MTM spectra was utilised to determine the frequency range that corresponded with ~80% of the total variance. The variance (area below the curve) was calculated for every 0.5 cycles/m increment. Bandwidth represented by horizontal bar. (iii) ASM calculations were run using all orbital terms (black solid line). Only those SAR estimates with H_o significance levels below the critical level (0.99009901%; dashed line) are included within Table 5.6.

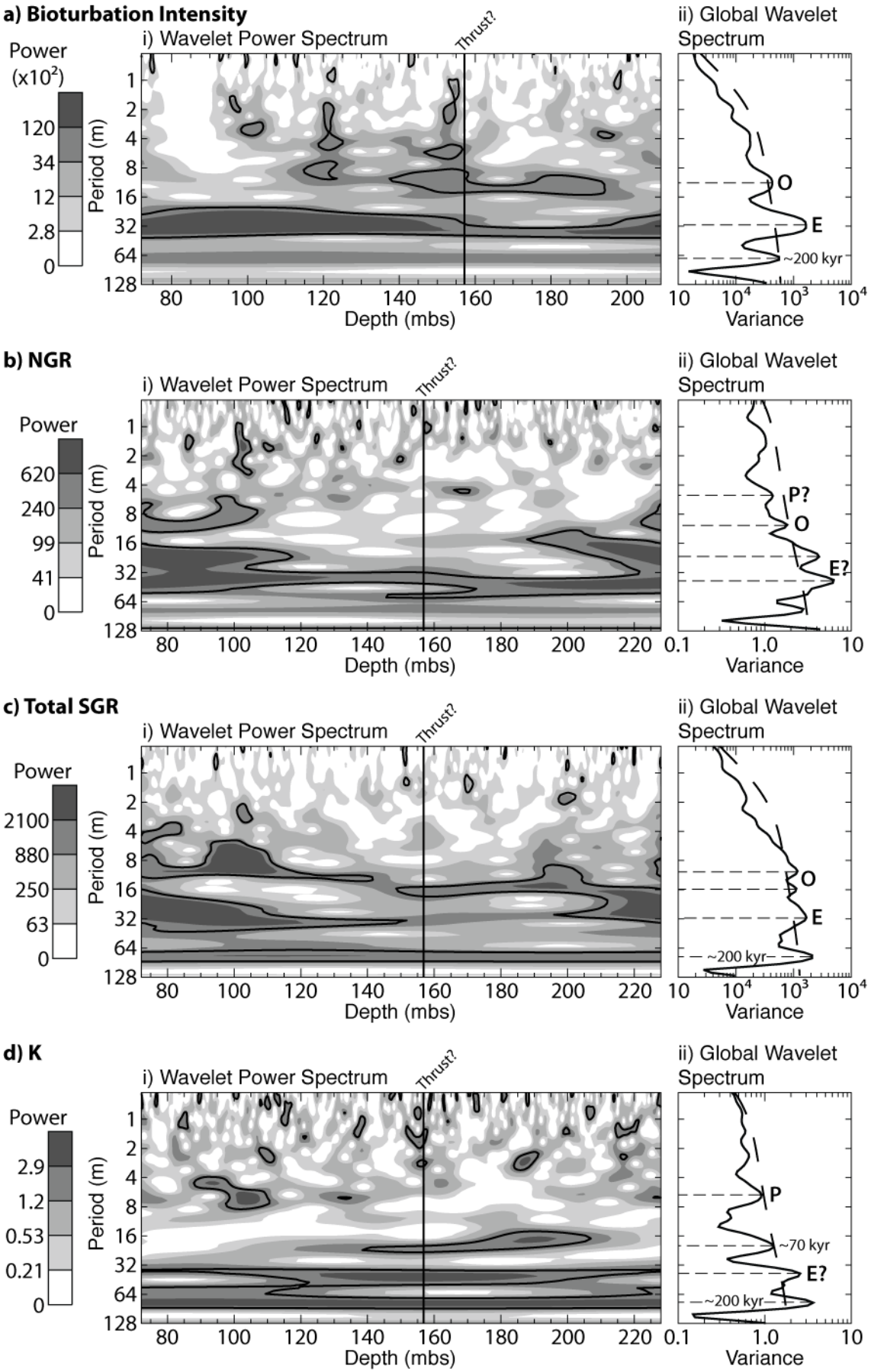
a) Bioturbation Intensity
i) Wavelet Power Spectrum
Thrust?
ii) Global Wavelet Spectrum
Power (x10²)
120
34
12
2.8
0
Period (m)
1
2
4
8
16
32
64
128
80
100
120
140
160
180
200
Depth (mbs)
O
E
~200 kyr
10
10⁴
10³
10⁴
Variance
b) NGR
i) Wavelet Power Spectrum
Thrust?
ii) Global Wavelet Spectrum
Power
620
240
99
41
0
Period (m)
80
100
120
140
160
180
200
220
Depth (mbs)
P?
O
E?
0.1
1.0
10
Variance
c) Total SGR
i) Wavelet Power Spectrum
Thrust?
ii) Global Wavelet Spectrum
Power
2100
880
250
63
0
Period (m)
80
100
120
140
160
180
200
220
Depth (mbs)
O
E
~200 kyr
10
10⁴
10³
10⁴
Variance
d) K
i) Wavelet Power Spectrum
Thrust?
ii) Global Wavelet Spectrum
Power
2.9
1.2
0.53
0.21
0
Period (m)
80
100
120
140
160
180
200
220
Depth (mbs)
P
~70 kyr
E?
~200 kyr
0.1
1.0
10
Variance

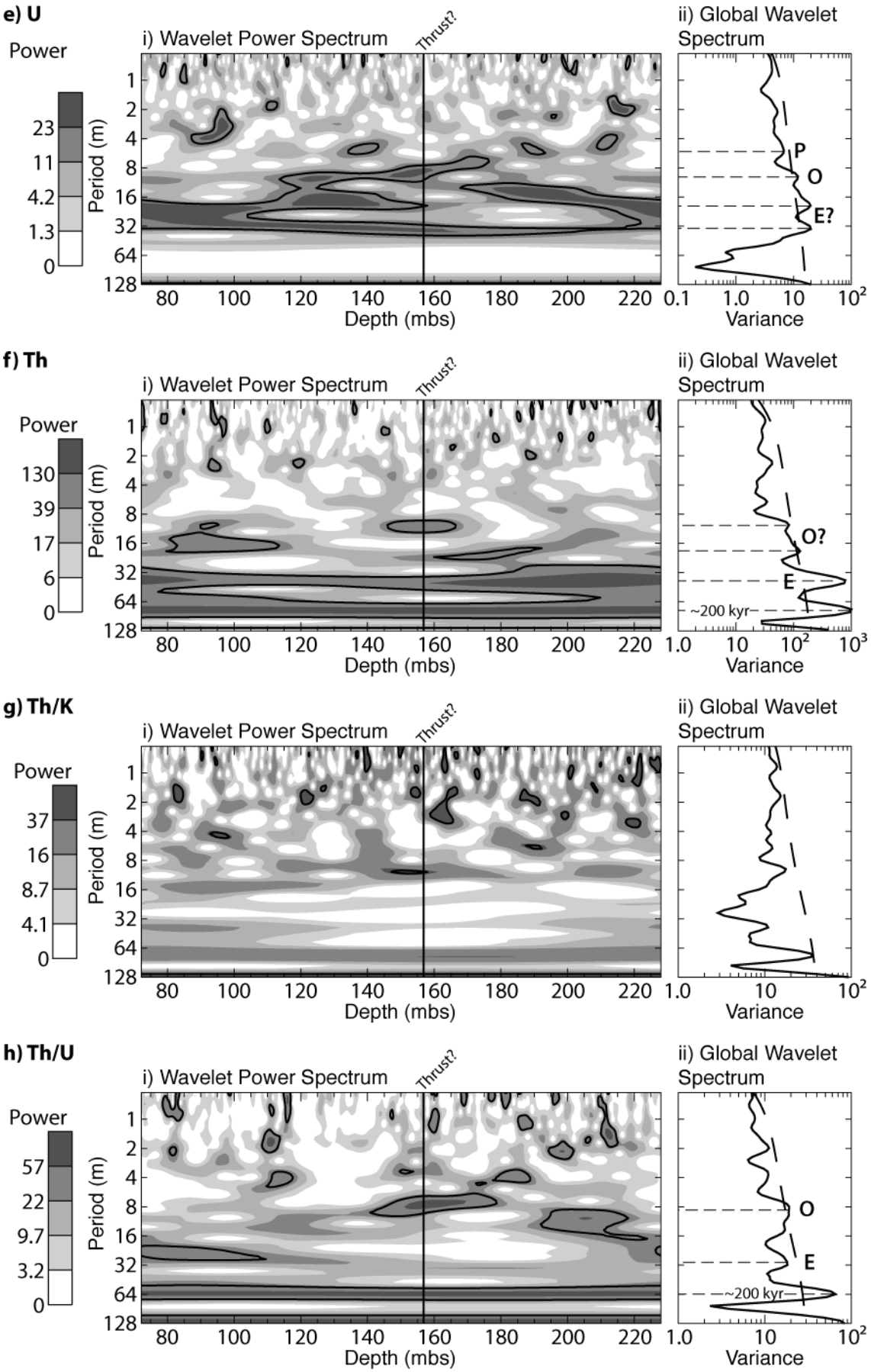
e) U
Power
23
11
4.2
1.3
0
i) Wavelet Power Spectrum
Thrust?
Period (m)
1
2
4
8
16
32
64
128
80
100
120
140
160
180
200
220
Depth (mbs)
ii) Global Wavelet Spectrum
P
O
E?
0.1
1.0
10
10²
Variance
f) Th
Power
130
39
17
6
0
i) Wavelet Power Spectrum
Thrust?
Period (m)
Depth (mbs)
ii) Global Wavelet Spectrum
O?
E
~200 kyr
1.0
10
10²
10³
Variance
g) Th/K
Power
37
16
8.7
4.1
0
i) Wavelet Power Spectrum
Thrust?
Period (m)
Depth (mbs)
ii) Global Wavelet Spectrum
1.0
10
10²
Variance
h) Th/U
Power
57
22
9.7
3.2
0
i) Wavelet Power Spectrum
Thrust?
Period (m)
Depth (mbs)
ii) Global Wavelet Spectrum
O
E
~200 kyr
1.0
10
10²
Variance

Figure 5.18 (previous two pages) | A6 well and core time series wavelet spectra obtain from A6 well and core. (i) Wavelet spectra illustrate the spatial distribution of frequencies throughout the individual time series. Bold contours represent the 95% confidence level. (ii) Global wavelet spectra represent the average variance throughout the entire time series. Those frequencies exceeding the 95% confidence level (dashed line) and corresponding to the predicted eccentricity (E), obliquity (O) and precession (P) periods are marked.

Table 5.6 – A6 ASM results

	All orbital terms				No eccentricity terms				
	SAR (cm/kyr)	Ho Level (%)*	ASM (cm/kyr)	No. of Orbital Terms		SAR (cm/kyr)	Ho Level (%)	ASM (cm/kyr)	No. of Orbital Terms
Bioturbation	5.00	0.042	5.16E-04	7	**Bioturbation**	5.00	0.384	4.03E-04	4
	6.90	0.010	5.52E-04	7		6.90	0.519	6.04E-04	4
	8.80	0.065	9.00E-04	7		8.80	0.747	8.71E-04	4
	10.70	0.648	1.59E-03	7		13.55	0.517	1.20E-03	4
	13.55	0.060	1.30E-03	7		16.40	0.767	1.55E-03	4
	15.45	0.253	1.82E-03	7		27.80	0.088	1.27E-03	4
	27.80	0.028	1.88E-03	7		62.95	0.568	3.01E-03	4
	34.45	0.670	2.89E-03	6		66.75	0.677	3.15E-03	4
						70.55	0.328	2.70E-03	4
NGR	None								
					NGR	26.85	0.702	1.04E-03	4
Total	5.00	0.328	6.31E-04	7					
	6.90	0.025	5.70E-04	7	**Total**	5.00	0.328	3.42E-04	4
	9.75	0.041	8.35E-04	7		30.65	0.293	1.74E-03	4
	12.60	0.162	1.28E-03	7		35.40	0.556	2.16E-03	4
	16.40	0.179	1.58E-03	7		37.30	0.500	2.17E-03	4
	30.65	0.083	2.15E-03	7		42.05	0.826	2.62E-03	4
	35.40	0.243	2.66E-03	7		45.85	0.337	2.20E-03	4
	39.20	0.331	2.57E-03	6		48.70	0.925	2.95E-03	4
	42.05	0.365	2.70E-03	6		73.40	0.574	3.02E-03	4
	45.85	0.381	2.79E-03	6		76.25	0.631	3.12E-03	4
						78.15	0.627	3.13E-03	4
K	5.95	0.507	5.40E-04	7		82.90	0.394	2.83E-03	4
	14.50	0.244	1.05E-03	7					
	17.35	0.160	1.13E-03	7	**K**	13.55	0.091	3.23E-04	4
	23.05	0.318	1.60E-03	7		38.25	0.799	1.75E-03	4
	38.25	0.028	1.50E-03	7		96.20	0.378	1.98E-03	4
	96.20	0.031	1.32E-03	6					
					U	6.90	0.431	2.08E-04	4
U	6.90	0.111	3.36E-04	7		12.60	0.629	4.51E-04	4
						96.20	0.978	2.22E-03	4
Th	5.95	0.486	4.36E-04	7					
	7.85	0.922	6.38E-04	7	**Th**	40.15	0.103	7.04E-04	4
	33.50	0.610	1.99E-03	7		42.05	0.134	8.03E-04	4
	40.15	0.017	7.29E-04	6		91.45	0.050	7.61E-04	4
	42.05	0.038	8.71E-04	6					
					Th/K	5.00	0.862	3.27E-04	4
Th/K	5.95	0.454	5.93E-04	7		10.70	0.716	6.67E-04	4
	7.85	0.304	7.27E-04	7		13.55	0.099	3.88E-04	4
	10.70	0.573	1.07E-03	7					
Th/U	None				**Th/U**	None			

*H_o significance level represents the probability that the null hypothesis of there being no orbital periods present at that SAR would be rejected in error. In other words, the probability of orbital period being present at that SAR estimate is the H_o significance level subtracted from 100. Only those SAR estimates exceeding the critical level of 0.99009901% are presented.

5.4 Interpretation

5.4.1 SGR variation

Interpretation of spectral and natural gamma ray variability can be determined using the results obtained from the younger Guaso System (Chapter 4). With the Ainsa and Guaso systems residing within the same tectono-stratigraphic unit (Mansurbeg et al., 2009; Caja et al., 2010), and sharing the same source areas (Marzo et al., 1988; Nijman, 1998; Caja et al., 2010), it is reasonable to assume that the systems mineralogy are comparable. Based upon the limited petrographic and XRD analyses of the Guaso Systems inter-fan sediments, it appears that the amount of quartz and muscovite weakly correlate with K, U and Th SGR values (Table 4.6). Such a relationship would suggest that radioelement concentrations were influenced by variation in terrigenous run-off from the Tremp-Graus basin. The variation in SGR at both outcrop and the subsurface therefore reflect changes in the mineralogical assemblage of the inter-fan sediments rather than grain-size (Myers and Bristow, 1989).

The link between U and organic matter (OM) can be shown here as unlikely. The absence of correlation between TOC and U from either the Guaso System (Chapter 4) or the A6 well, suggests that U variability was more likely due to changes in authigenic precipitation rates rather than OM as suggested by Heard et al. (2008). The authigenic precipitation of U requires reducing conditions at the sediment-water interface (Myers and Wignall, 1987). Using the mean outcrop and A6 Th/U ratios of 1.56 and 2.73 respectively, which lie below the ‘normal’ 3-6 mudrock values (Rider, 1996), supports the prevalence of reducing conditions. Variations in Th/U within the Ainsa System therefore likely reflect changing redox conditions at the sediment-water interface. However, U may have been leached thereby destroying any existing relationship with the low resolution TOC data.

The Th/K ratio is commonly interpreted as reflecting the proportion of illite to kaolinite contained within fine-grained sediments (Myers and Wignall, 1987; Van Buchem et al., 1992; Rider, 1996; Ruffell and Worden, 2000; Hesselbo et al., 2009). Mean outcrop and A6 Th/K values of 4.21 and 5.38 lie within the mean 4 to 6 range indicating that neither illite nor kaolinte dominate the inter-fan Ainsa sediments.

Variations within the total spectral and natural gamma obtained from the A6 well record the total radiation emitted by the decay of K, U and Th radioelements. It can therefore be assumed that they respond to the potential enrichment in minerals bearing these elements and the authigenic precipitation of U.

Other factors that may cause variability within the SGR data are layer parallel fault zones which have been observed to relatively enrich K, U and Th elements

(Ruffell et al., 2004). Anomalous K and Th SGR values are here observed within the SGR data collected from outcrop at 114.4 m (Fig. 5.5), which corresponds to the ~10 cm thick duplex zone (Plate 5.2). The enrichment in K, U and Th within this zone suggests increased secondary mineralisation has occurred.

5.4.2 Spectral interpretation

To determine whether any of the significant frequencies identified within SGR and bioturbation intensity correspond to expected orbital periods, the ASM results are utilised (Chapter 2). However, the outcrop and A6 well ASM results appear ambiguous with a wide range of significant SARs being identified. Instead consistency between the most significant results shall be used to identify a realistic SAR for the studied section.

Within the outcrop ASM results two SARs are consistently identified as being the most significant at 20.20 and 26.85 cm/kyr (Fig. 5.13; Table 5.4). Of these only the 26.85 cm/kyr SAR estimate assigns orbital periods to the significant MTM F-test frequencies (Table 5.7). Where identified, the 26.85 cm/kyr SAR assigns the eccentricity, obliquity and precession orbital periods to the significant 0.031-0.033, 0.082-0.095 and 0.154-0.200 cycles/m frequency bands, respectively.

The most significant SARs identified from the A6 spectral results are again variable (Fig. 5.17; Table 5.6). Of these data, only the bioturbation intensity, NGR and total SGR ASM results contain consistent SAR values between 26.85 and 30.65 cm/kyr. Applying these SAR estimates to the frequencies from which they were determined, indicates that the eccentricity, obliquity and precession orbital periods are assigned similar frequency bands as those proposed for the outcrop time series (Table 5.8). Similar frequencies within these bands are sporadically identified within the remaining A6 SGR data. Reasons for this are likely due to that the total SGR, bioturbation intensity and NGR data are considered more reliable as they are least likely to be distorted by borehole effects or geophysical processing artefacts. Of these data, the bioturbation record is likely to be the most accurate due to the discrete nature of sampling (Heard et al., 2008), therefore avoiding boundary smearing and borehole affects (Rider, 1996). The individual SGR radioelement data generally are inconsistent with the majority of the other spectral results most likely due to the high levels of noise within the data along with additional possible artefacts of processing which are impossible to quantify without additional information.

Although no unique SAR is identified, the consistent assignment of orbital periods to near identical frequency bands, suggests that the SAR estimates between 26.85 and 30.65 cm/kyr are reliable. The null hypothesis significance levels (H_o) of these SARs indicate that orbital cyclicity is present with a confidence level between

99.30-99.98%. However, these SAR estimates are slightly below the 47.5±17.9 and 35.2±0.6 cm/kyr SAR values obtained from the biostratigraphic age model for the same section (Fig. 5.3). The discrepancy between these values is likely due to the biostratigraphic age models method of construction. The age models SAR estimates for the studied interval are calculated from stratigraphy containing a combination of inter-fan, submarine fan and MTC sediments (Fig. 3.2). Of these sediments the submarine fan and MTC deposits are expected to have been rapidly deposited compared to the finer grained inter-fan deposits. The resultant SARs predicted by the biostratigraphic age model, therefore, are an average of these differing depositional settings. With this in mind, the SAR expected for the studied inter-fan sediments are likely less than the 47.5±17.9 and 35.2±0.6 cm/kyr estimates. The average inter-fan SAR of 28.12 cm/kyr suggested from the identification of orbital cyclicity is therefore likely reliable and is subsequently used to estimate the temporal periods of the significant frequencies identified in Tables 5.7 and 5.8.

Table 5.7 – Applying outcrop SAR estimates to significant frequencies

K SAR Estimate (cm/kyr)		13.55	16.40	20.20				
Frequency (cycles/m)*	**Confidence Level (%)**	**Temporal Period (kyr)†**						
0.018	90.0	409.3	338.2	274.6				
0.031	90.0	237.0	195.8	159.0				
0.128	99.0	57.7	47.7	38.7				
0.197	95.0	37.5	31.0	25.2				
U SAR Estimate (cm/kyr)		13.55	15.45	20.20	24.00	29.70	56.30	62.00
Frequency (cycles/m)	**Confidence Level (%)**	**Temporal Period (kyr)**						
0.033	95.0	225.1	197.4	151.0	127.1	102.7	54.2	49.2
0.082	95.0	90.1	79.0	60.4	50.8	41.1	21.7	19.7
0.128	95.0	57.7	50.6	38.7	32.6	26.3	13.9	12.6
0.182	95.0	40.6	35.6	27.2	22.9	18.5	9.8	8.9
Th SAR Estimate (cm/kyr)		16.40	19.25	26.85	56.30	62.00	71.50	
Frequency (cycles/m)	**Confidence Level (%)**	**Temporal Period (kyr)**						
0.031	95.0	195.8	166.8	119.6	57.0	51.8	44.9	
0.082	90.0	74.4	63.4	45.4	21.7	19.7	17.1	
0.128	95.0	47.7	40.6	29.1	13.9	12.6	10.9	
0.154	90.0	39.6	33.7	24.2	11.5	10.5	9.1	
0.200	95.0	30.5	26.0	18.6	8.9	8.1	7.0	
Th/K SAR Estimate (cm/kyr)		9.75	11.65					
Frequency (cycles/m)	**Confidence Level (%)**	**Temporal Period (kyr)**						
0.021	95.0	481.3	402.8					
0.062	90.0	164.7	137.8					
0.151	95.0	68.0	56.9					
Th/U SAR Estimate (cm/kyr)		11.65	13.55	26.85	48.70	54.40		
Frequency (cycles/m)	**Confidence Level (%)**	**Temporal Period (kyr)**						
0.043	95.0	201.4	173.2	87.4	48.2	43.1		
0.095	95.0	90.3	77.6	39.2	21.6	19.3		
0.167	90.0	51.3	44.1	22.3	12.3	11.0		
0.200	95.0	42.9	36.9	18.6	10.3	9.2		

*Frequencies between 0 and 0.2 cycles/m determined from the MTM F-test of the outcrop stratigraphic series.

†Using significant SAR values identified from ASM analyses it is possible to establish the frequency that each orbital period was assigned.

Table 5.8a – Applying A6 SAR estimates to significant frequencies

Bioturbation intensity SAR Estimate (cm/kyr)		5.00	6.90	8.80	13.55	16.40	27.80	62.95	66.75	70.55
Frequency (cycles/m)*	**Confidence Level (%)**	**Temporal Period (kyr)†**								
0.032	95.0	630.2	456.6	358.0	232.5	192.1	113.3	50.1	47.2	44.7
0.073	90.0	273.1	197.9	155.2	100.8	83.3	49.1	21.7	20.5	19.4
0.104	90.0	192.8	139.7	109.5	71.1	58.8	34.7	15.3	14.4	13.7
0.157	90.0	127.0	92.0	72.2	46.9	38.7	22.8	10.1	9.5	9.0
0.193	90.0	103.7	75.1	58.9	38.3	31.6	18.7	8.2	7.8	7.3

NGR SAR Estimate (cm/kyr)		26.85
Frequency (cycles/m)	**Confidence Level (%)**	**Temporal Period (kyr)**
0.005	90.0	762.8
0.070	95.0	53.5
0.096	95.0	38.6
0.137	99.0	27.2
0.149	90.0	25.0
0.200	95.0	18.6

Total SGR SAR Estimate (cm/kyr)		5.00	30.65	35.40	37.30	42.05	45.85	48.70	73.40	76.25	78.15	82.90
Frequency (cycles/m)	**Confidence Level (%)**	**Temporal Period (kyr)**										
0.005	95.0	4,096.0	668.2	578.5	549.1	487.0	446.7	420.5	279.0	268.6	262.1	247.0
0.029	90.0	682.7	111.4	96.4	91.5	81.2	74.4	70.1	46.5	44.8	43.7	41.2
0.061	90.0	327.7	53.5	46.3	43.9	39.0	35.7	33.6	22.3	21.5	21.0	19.8
0.095	95.0	210.1	34.3	29.7	28.2	25.0	22.9	21.6	14.3	13.8	13.4	12.7
0.106	90.0	188.3	30.7	26.6	25.2	22.4	20.5	19.3	12.8	12.3	12.0	11.4
0.117	90.0	170.7	27.8	24.1	22.9	20.3	18.6	17.5	11.6	11.2	10.9	10.3
0.150	95.0	133.2	21.7	18.8	17.9	15.8	14.5	13.7	9.1	8.7	8.5	8.0
0.170	95.0	117.9	19.2	16.6	15.8	14.0	12.9	12.1	8.0	7.7	7.5	7.1

Table 5.8b – Applying A6 SAR estimates to significant frequencies

K SAR Estimate (cm/kyr)		13.55	38.25	96.20
Frequency (cycles/m)	**Confidence Level (%)**	**Temporal Period (kyr)**		
0.011	90.0	690.6	244.6	97.3
0.023	95.0	327.1	115.9	46.1
0.047	99.0	155.4	55.0	21.9
0.114	90.0	64.7	22.9	9.1
0.142	95.0	51.8	18.3	7.3
0.173	95.0	42.6	15.1	6.0
0.194	95.0	38.1	13.5	5.4
Th SAR Estimate (cm/kyr)		40.15	42.05	91.45
Frequency (cycles/m)	**Confidence Level (%)**	**Temporal Period (kyr)**		
0.024	90.0	251.8	214.5	153.8
0.048	90.0	125.9	107.2	76.9
0.061	90.0	100.7	85.8	61.5
0.103	99.0	59.2	50.5	36.2
0.134	90.0	45.4	38.6	27.7
0.159	95.0	38.4	32.7	23.5
U SAR Estimate (cm/kyr)		6.90	12.60	96.20
Frequency (cycles/m)	**Confidence Level (%)**	**Temporal Period (kyr)**		
0.023	95.0	625.6	342.6	44.9
0.046	95.0	312.8	171.3	22.4
0.121	95.0	119.9	65.7	8.6
0.145	99.0	99.9	54.7	7.2
0.200	95.0	72.3	39.6	5.2
Th/K SAR Estimate (cm/kyr)		5.00	10.70	13.55
Frequency (cycles/m)	**Confidence Level (%)**	**Temporal Period (kyr)**		
0.008	90.0	2,499.7	1,168.1	922.4
0.102	95.0	196.6	91.9	72.5
0.138	99.0	144.6	67.6	53.4
0.173	95.0	115.9	54.2	42.8

*Frequencies between 0 and 0.2 cycles/m determined from the MTM F-test of the outcrop stratigraphic series.

†Using significant SAR values identified from ASM analyses it is possible to establish the frequency that each orbital period was assigned.

5.4.3 Band-pass filtering

Band-pass filtering of the significant MTM F-test components believed to correspond to orbital periods are presented in Figure 5.19. The band-pass gain functions used in the calculation of the filters are provided in Figure 5.20. These band-pass filters reasonably correspond to the majority of features within the outcrop and A6 stratigraphic series. Within the A6 total SGR and bioturbation intensity and outcrop K, U and Th filters, the dominance of the proposed eccentricity frequency (~0.03 cycles/m) is clearly demonstrated. Higher frequency periods dominate the Th/K and Th/U outcrop stratigraphic series.

Evidence for amplitude modulation of the precession band (0.157-0.200 cycles/m) is provided within the outcrop Th/U and A6 bioturbation intensity (Fig. 5.19). Within these records amplitude increases every ~30 m broadly coincident with period of the ~0.03 cycles/m filter. The A6 total spectral gamma also demonstrates similar amplitude increases but over a longer ~50 m period. Such amplitude modulation of the precession frequency is consistent with Milankovitch theory and climatic records (Hinnov, 2000; Pälike et al., 2001; Huybers and Aharonson, 2010) therefore providing strong supporting evidence for the presence of orbital forcing within Ainsa inter-fan sediments.

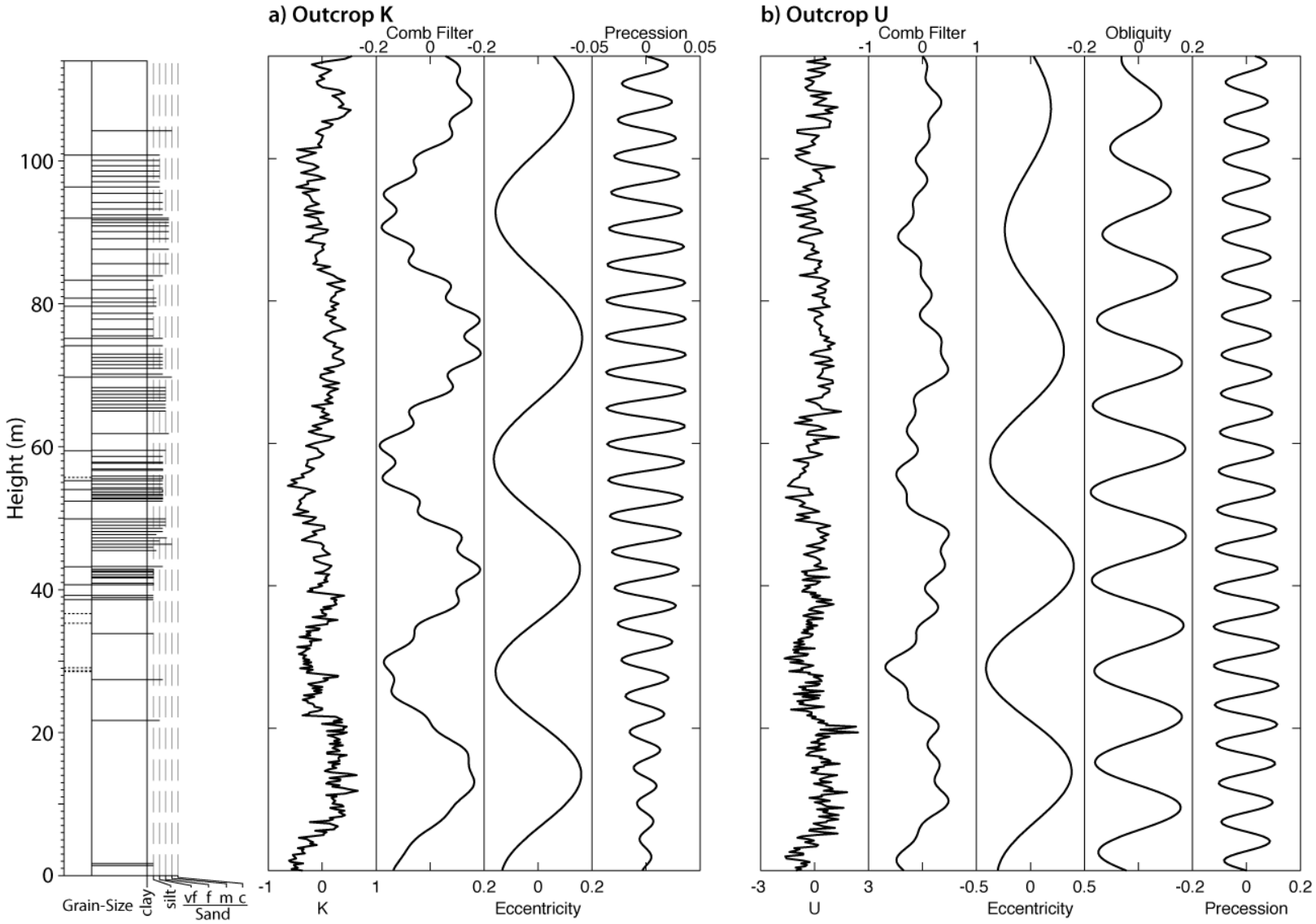
a) Outcrop K
Comb Filter
Precession
-0.2 0 -0.2
-0.05 0 0.05
Height (m)
0
20
40
60
80
100
Grain-Size
clay
silt
vf f m c
Sand
-1 0 1
K
0.2 0 0.2
Eccentricity
b) Outcrop U
Comb Filter
Obliquity
-1 0 1
-0.2 0 0.2
-3 0 3
U
-0.5 0 0.5
Eccentricity
-0.2 0 0.2
Precession

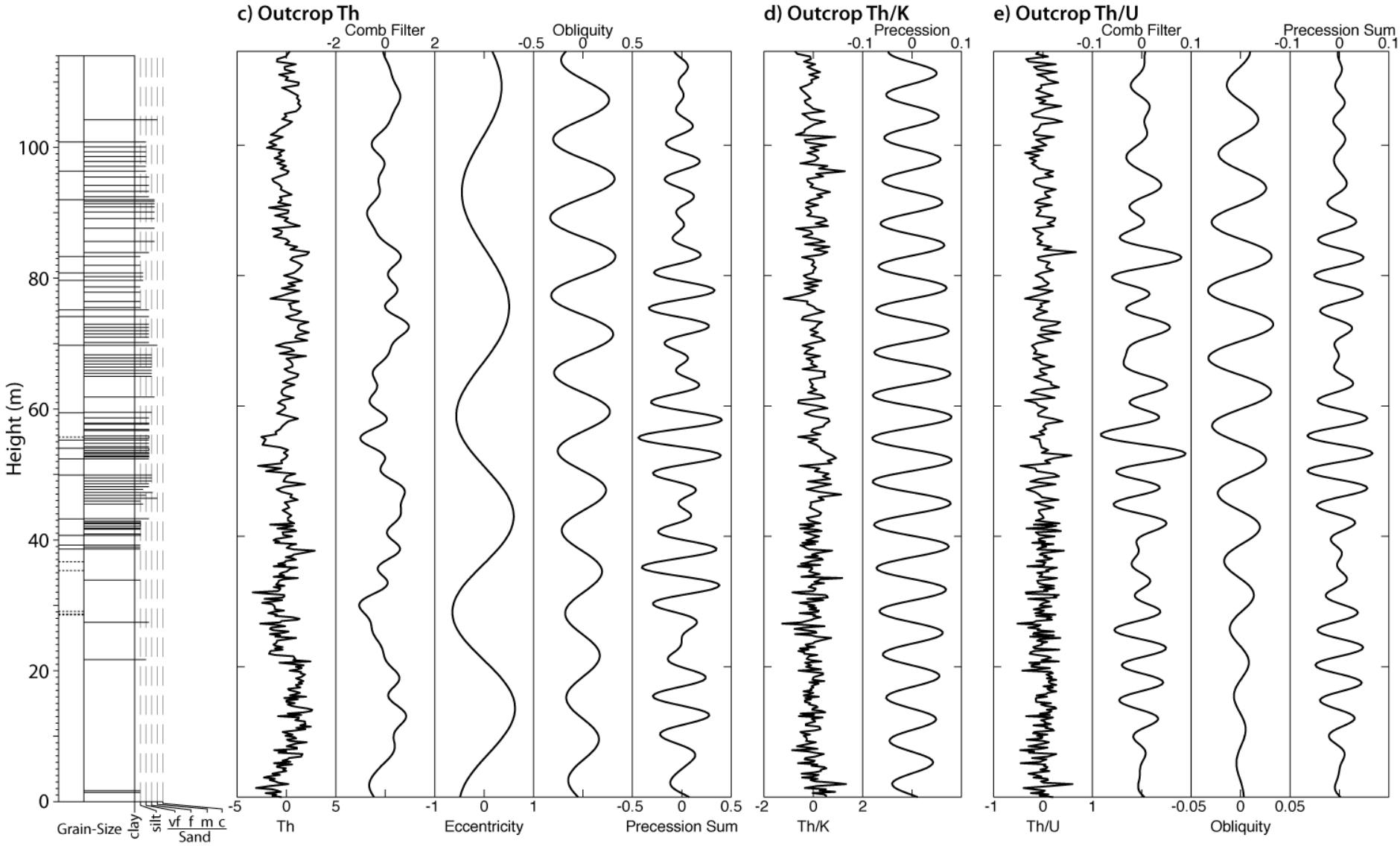
c) Outcrop Th
d) Outcrop Th/K
e) Outcrop Th/U
Height (m)
0
20
40
60
80
100
Grain-Size
clay
silt
vf f m c
Sand
Comb Filter
Obliquity
Precession
Comb Filter
Precession Sum
-2 0 2
-0.5 0 0.5
-0.1 0 0.1
-0.1 0 0.1
-0.1 0 0.1
-5 0 5
-1 0 1
-0.5 0 0.5
-2 0 2
-1 0 1
-0.05 0 0.05
Th
Eccentricity
Precession Sum
Th/K
Th/U
Obliquity

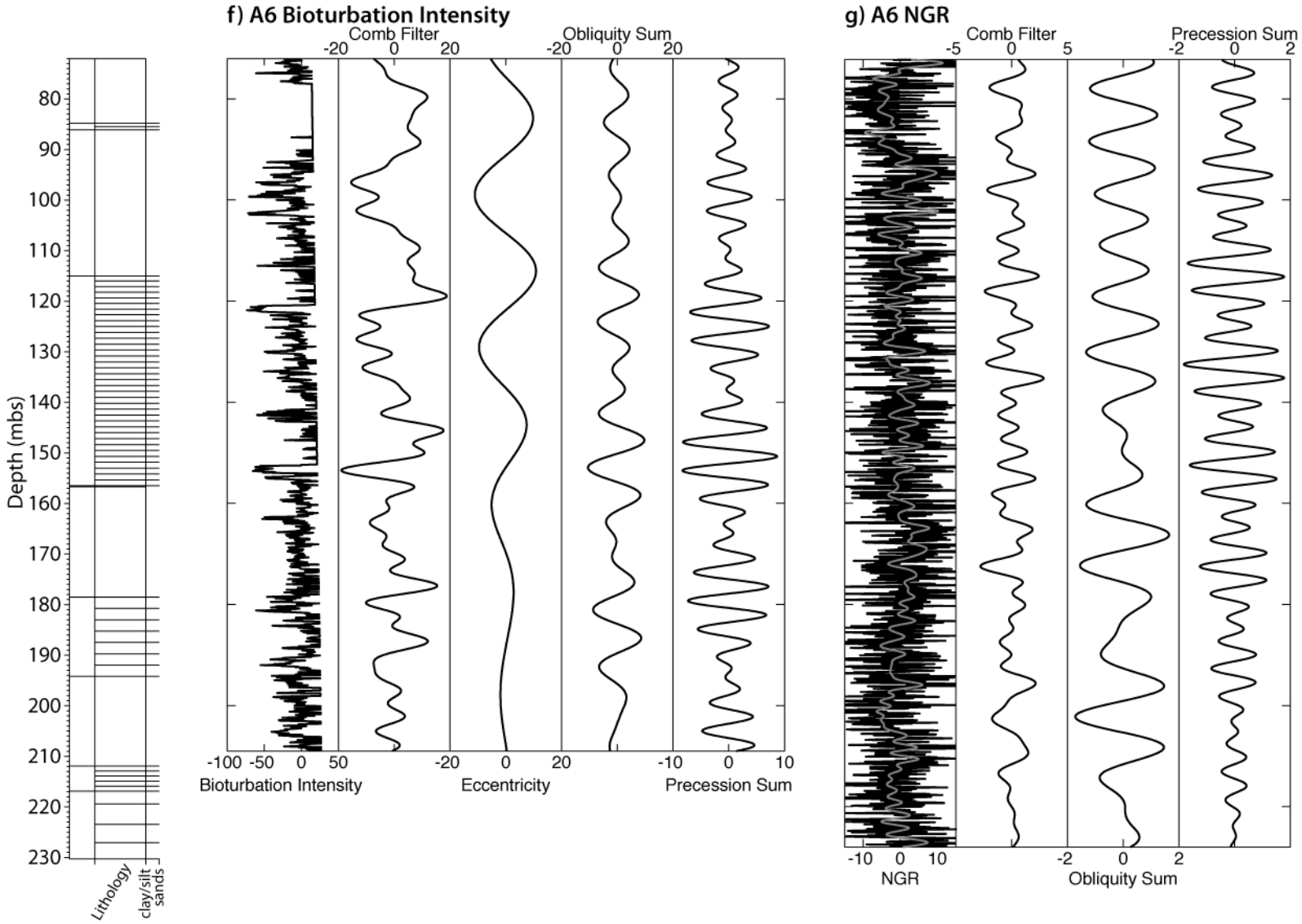
f) A6 Bioturbation Intensity
g) A6 NGR
Depth (mbs)
80
90
100
110
120
130
140
150
160
170
180
190
200
210
220
230
Lithology
clay/silt
sands
Comb Filter
Obliquity Sum
-20 0 20
-20 0 20
-100 -50 0 50
Bioturbation Intensity
-20 0 20
Eccentricity
-10 0 10
Precession Sum
Comb Filter
Precession Sum
-5 0 5
-2 0 2
-10 0 10
NGR
-2 0 2
Obliquity Sum

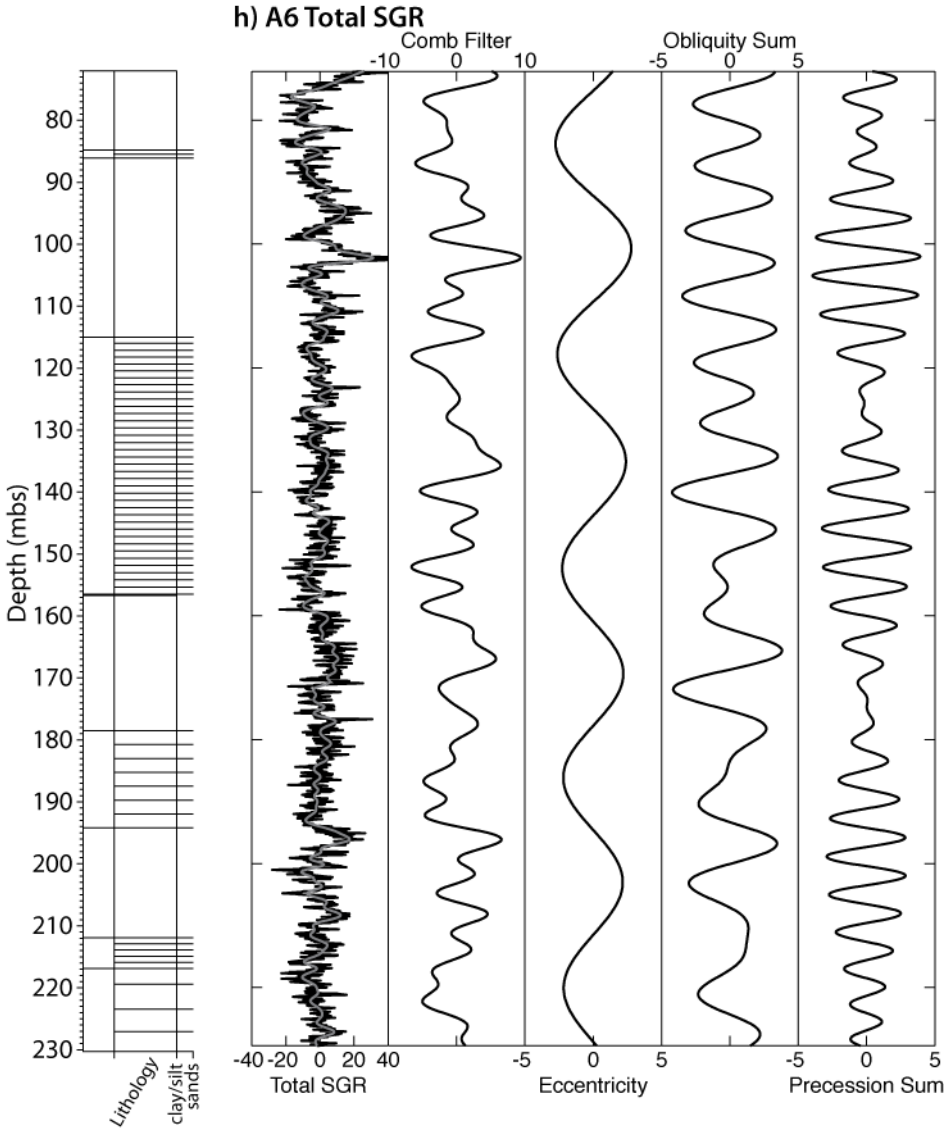

Figure 5.19 (previous three pages) | Band-pass filters of proposed orbital periods compared stratigraphic series and lithologic columns. Significant MTM harmonic F-test frequencies were isolated using band-pass filtering performed within Analyseries 2.0.4.2 (Paillard et al., 1996). Band-pass filter gain functions are illustrated in Figure 5.20. Where two frequencies are identified as representing precession and obliquity they were summed to create comb-filters. Outcrop Th/U and A6 bioturbation intensity and total SGR precession comb-filters reveal likely amplitude modulation (AM) by the proposed eccentricity frequency. The A6 NGR and total SGR plot contains the stratigraphic time series (black solid line) and the low-pass filter (grey solid line).

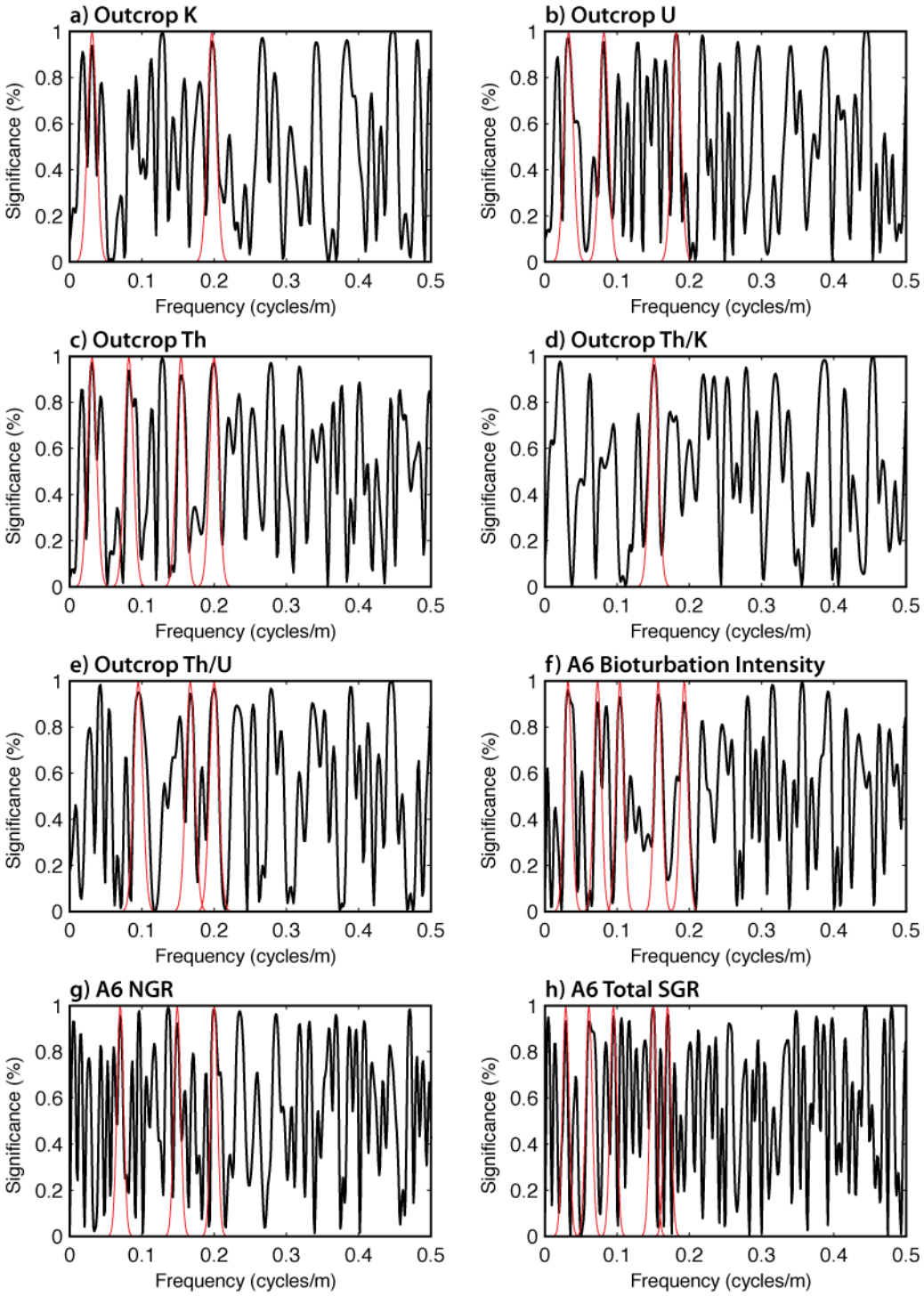

Figure 5.20 | Gain functions of the pass-band filters applied to outcrop and A6 well time series. Pass-band filters were applied to each time series within Analyseries 2.0.4.2 (Paillard et al., 1996). The Gaussian pass-band (red solid line) is centred about the frequency to be filtered. The width of the pass-band is determined by the bandwidth of the MTM harmonic F-test. The filtered frequencies and bandwidth information for each time series are provided within Tables 5.7 and 5.8.

5.5 Discussion

5.5.1 Precision and accuracy of SGR data

The above interpretation of the SGR data obtained from outcrop and A6 well depends upon the reliability of these data. Comparison between outcrop (Fig. 5.10a) and subsurface (Fig. 5.10b) K/U and Th/U correlations reveal striking relationship inversions. As only relationships involving U are affected it suggests that this radioelement is responsible, explanations for this variation involving relative radioelement mobility within the sediments, redox state or the precision of their measurement.

For radioelement mobility to be responsible, differential stratigraphic enrichment and/or depletion would be required. With U being the most mobile within the sediments (Chapter 2), the transition from the reducing subsurface to oxidising subaerial conditions would likely result in the preferential leaching of U from the exposed sediments. However, a uniform leaching of U would not invert the Th/U and K/U correlations. For this to occur, both relative U depletion and enrichment would be required, altering peaks to troughs and troughs to peaks thus creating an inverted U profile. Depletion of U is possible within outcrop via leaching (Myers and Bristow, 1989). Relative or absolute enrichment of U however is unlikely, as this would involve either the leaching of the more stable Th and K elements or authigenic enrichment under reducing conditions.

The variable precision between outcrop and subsurface SGR data could also be responsible for the correlation inversions observed in Figure 5.10. Factors affecting the precision of SGR data obtained from the subsurface include drilling mud composition, logging speed, variations in well width, data processing and low count rates (Rider, 1996). Unfortunately, information on these factors is unavailable for the A6 well and therefore it is unclear how element concentrations were determined from the total SGR spectra. It is assumed that the SGR data was additionally processed to remove the affects of well conditions, especially drilling mud. Without this processing the presence drilling mud has been shown to cause relative enrichment of K and Th whilst depleting U concentrations (Rider, 1996). Over compensating for the presence of drilling mud however, can introduce negative SGR values and distort results (Bristow and Williamson, 1998). However, even with these considerations taken into account the precision of subsurface SGR data is variable. Hurst (1990) and Rider (1996) demonstrate this by comparing multiple runs from a well to show that the precision is poor for U, variable for Th and good for K. However, if poor precision was responsible for the inversion of relationships then U would be expected to be highly variable and not consistently the inverse of Th and K.

In comparison, the precision of outcrop SGR data is affected by weathering of surface material, outcrop geometry, sampling time and detector volume (Lovborg and Mose, 1987; Myers and Wignall, 1987). By following the method outlined in Chapter 2, the precision of the outcrop SGR data was maximised. Other studies to utilise the GR-320 spectrometer have demonstrated a precision of better than ±10% when sampling from an ideal plane (Lovborg and Mose, 1987; Van Buchem et al., 1992; Andersson and Worden, 2004; Koptikova et al., 2010). However, repeated measurement of a short stratigraphic section at outcrop using the two spectrometers illustrates that both K and Th are reliably reproduced whilst U is not (Fig. 5.9). These differences in recorded radioelement concentrations are most likely due to the differing detector crystal volumes of the GR-320 (21 cubic inch) and RS-125 (6.3 cubic inch) spectrometers.

To determine which of these explanations are correct, absolute elemental values of K, U and Th are required from the SGR sampling locations at both outcrop and the subsurface. However, only absolute elemental abundances of K and Th exist for the basins submarine fan sandstones (Das Gupta, 2008), which show that Th/K share a poor positive correlation (Fig. 5.21).

Considering the possible causes for the inversion of K/U and Th/U relationships between outcrop and the subsurface data, it is apparent that these data obtained using different spectrometers and processing techniques and are therefore not directly comparable. Without further details upon the subsurface SGR collection, and absolute elemental abundance data, individual A6 radioelement data should be treated as suspect. SGR data collected form outcrop are likely to be more representative of the absolute elemental concentrations due to the method of data acquisition.

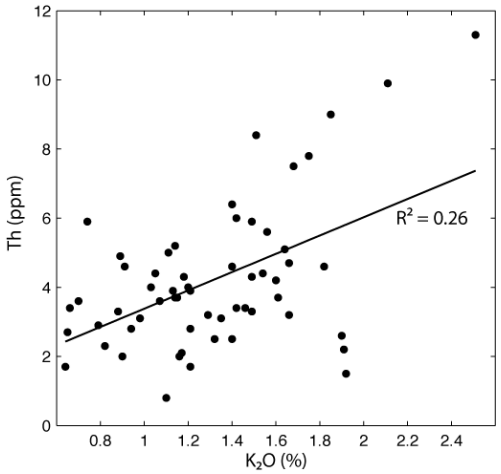

Figure 5.21 | Cross-plot of Th/K_2O obtained from XRF bulk analysis of basin wide submarine fan sandstones (Das Gupta, 2008). The poor positive correlation coefficient between Th and K_2O within the basins sandstones illustrate that the inverse correlation within the A6 well data is potentially erroneous. However, as no bulk geochemistry analysis has been performed upon the inter-fan deposits it is not possible to verify the outcrop and subsurface data.

5.5.2 Orbital forcing within the Ainsa System

Based upon the above spectral interpretation, the studied sediments between Ainsa-II and Morillo-I are shown to contain oscillations, within both radioelement concentration and ichnological data, that correspond to the average short eccentricity, obliquity and precession orbital periods (Tables 5.3, 5.5). The variation in radioelement concentration (K, Th, total SGR and natural GR data) is interpreted as reflecting the amount of terrigenous material being introduced to inter-fan sediments of the Ainsa System. The orbital forcing of terrigenous sediment supply to the basin was likely controlled by variation in precipitation rates. During the Eocene precipitation and continental run-off rates, which control terrestrial input to the basin, are shown to be strongly influenced by orbital precession (Sloan and Huber, 2001; Lawrence et al., 2003).

The orbitally paced variability within the U, Th/U and bioturbation intensity data are here interpreted as reflecting changes in bottom water redox conditions. Oscillations within bottom water redox conditions may be the result from the affect of insolation changes upon latitudinal temperature gradients. With relatively weak meridional circulation during the Eocene (Zachos et al., 1994), variation in these gradients could have affected intermediate- and deep-water formation (Wade et al., 2001). Surface upwelling rates have also been shown to have been influenced by orbital changes in insolation (Sloan and Huber, 2001). These oceanic responses to orbital forcing could have affected the oxygenation of the bottom waters, which is subsequently recorded in the bioturbation intensity and Th/U results.

Of the orbital oscillations within the above data, the short eccentricity cycle appears to have the greatest influence upon both terrigenous input (K, Th, total SGR and natural GR) and bottom water oxygenation (U, Th/U and bioturbation intensity). However, the A6 bioturbation intensity short eccentricity band-pass filters do not appear to be directly influenced by the short eccentricity cycle demonstrated by the offset between filter and data variability (Fig. 5.19). Instead, the maximum variability is associated with periods of greatest amplitude within the precession signal. The increased amplitude in the precession band (0.157-0.200 cycles/m) filters occur over periods of ~30 m which is consistent with the period of the short eccentricity cycle. This is consistent with amplitude modulation of the precession band by short eccentricity is predicted within the Milankovitch theory and climatic records (Hinnov, 2000; Pälike et al., 2001; Huybers and Aharonson, 2010).

5.5.3 Additional periods of interest

With the temporal duration of each of the significant frequency identified from both the A6 well and its lateral equivalent outcrop, it is apparent that the majority contain durations matching the predicted orbital periods (Table 1.1). When applying the optimal SAR to the remaining significant frequencies, periods of ~200 kyr, ~30 kyr and ~12 kyr are identified mainly within the outcrop stratigraphic series (Tables 5.3 and 5.5). The ~200-kyr period (0.017 cycles/m) may represent the 204 kyr component of the amplitude modulation of precession by long eccentricity (Hinnov, 2000). Support for this interpretation is provided from the identification of amplitude modulation within the precession frequency band (Fig. 5.19). Alternately, this could represent the first harmonic of the average short eccentricity frequency (0.03 cycle/m).

The ~30-kyr period (~0.128 cycles/m) is commonly identified within palaeoclimatic records and is interpreted as representing the non-linear interaction between the eccentricity and obliquity (Rodriguez-Tovar and Pardo-Iguzquiza, 2003; Huybers and Wunsch, 2004; Lisiecki and Raymo, 2005).

The ~12-kyr period (~0.28 cycles/m) may represent half precession cycles commonly observed within equatorial regions and potentially higher latitudes (Short et al., 1991; Hagelberg et al., 1994; Berger et al., 2006). Half precession cycles (~11 kyr) are believed the result of the twice-yearly passage of the Sun across equatorial sites during the spring and autumn equinox. The result is a twice-yearly maxima in insolation received within the tropics and sub-tropics when the Sun is over the equator resulting in the spring and autumn equinox, the magnitude of which is controlled by precession (Berger and Loutre, 1997; Berger et al., 2006).

5.5.4 Uncertainty within spectral results

5.5.4.1 Frequency stability

Applying the average SAR to the significant frequencies identified within both outcrop and the stratigraphically equivalent A6 well indicate the likely presence of the average short eccentricity (~110 kyr), obliquity (~40 kyr) and precession (~22 to 18 kyr) periods. However, with less than six complete oscillations present, the accuracy of the eccentricity cycles ~0.030 cycles/m frequency is uncertain (Chapter 2). Despite this, the consistency in these frequencies independent identification within outcrop SGR, well SGR and bioturbation intensity records support the cycles predominance.

5.5.4.2 Potential fault zone

Further concern surrounds the proposed fault identified at ~156 mbs within the A6 core (Plate 5.2d). The presence of this fault plane may potentially create a hiatus thereby juxtaposing sections containing oscillations of different frequencies or duplicate stratigraphy within the time series data. Wavelet spectra (Fig. 5.14), however, reveals that there is no significant shift in frequency across the fault's position suggesting that two segments with similar scale oscillations exist either side of the fault zone. If a depositional hiatus, frequency shift or duplication was present within the stratigraphic series due to thrusting then evidence for this should exist within wavelet spectral results (Lau and Weng, 1995).

The thrust identified within the subsurface should feasibly be present within the equivalent outcrop and therefore has the potential to affect spectral results. If present, based upon correlations (Fig. 5.6), it should be located between 40 to 50 m. Wavelet spectra (Fig. 5.14) however do not reveal a significant shift in frequency at within this interval suggesting that would correspond to missing or duplicated stratigraphy. Wavelet spectral analysis therefore suggests that the presence of the proposed fault plane within the well and potentially outcrop stratigraphy does not appear to have distorted the stratigraphic series.

5.5.5 Ainsa System submarine fan timing and duration

The identification of orbital oscillations within the Ainsa-II and Ainsa-III inter-fan and off-axis sediments enables the temporal duration between the coarser-grained and thicker-bedded submarine fan deposits to be determined. Using these temporal estimates, the hypothesis that the 404-kyr long eccentricity cycle was the primary driver on sediment flux and sediment calibre to the deep-marine Ainsa basin, can be tested. This hypothesis proposes that each submarine fan was forced by a 404-kyr eccentricity paced glacio-eustatic mechanism (refer to Section 3.4.5 for details). The hypothesis suggests, therefore, that approximately 404-kyr should exist between the deposition of each submarine fan and its associated finer-grained inter-fan deposits.

Testing of this hypothesis is achieved by firstly calculating the temporal spacing between stratigraphic events interpreted as reflecting glacio-eustatic base-level changes, which include the initiation or termination of submarine fan and MTC deposits (Fig. 1.17). Within the studied stratigraphy, the distance between cessation of the Ainsa-II and Ainsa-III submarine fan sediments is approximately 115 m based upon the A6 core (Fig. 5.6). The second stratigraphic interval encompasses the sediments between the initiation of the Ainsa-III off-axis sediments and the base of the first sizable

(>5 m) type-I MTC is represented by an identical 115 m thickness within the A6 core (Fig. 5.6). Application of the average SAR of 28.12 cm/kyr to the two 115 m intervals yield temporal durations of 409 kyr. Applying the biostratigraphic age model to the same stratigraphic sections provides durations of 0.26-0.40 and <0.71 Myr respectively (Table 5.9). These estimates are based upon the assumption that the SAR was relatively constant with no hiatuses or fault duplication present. Assuming that these assumptions are correct, then they are consistent with the hypothesised 404-kyr driver for coarse clastic supply to the Ainsa Basin.

During the Greenhouse climate of the middle Eocene however, glacio-eustatic processes may not have occurred regularly every 404 kyr. Instead low-stand conditions likely occurred during periods preferential to ice accumulation. These conditions included the maximisation of the distance between the Earth and the Sun. During these periods of low eccentricity the amount of insolation is reduced therefore enabling the accumulation of ice over several seasons (further details within Section 3.4.5).

Table 5.9 – Complex age estimates

		Orbital age model	Biostratigraphic age model[§]		
Complex	**Height (m)***	**Age (Ma)[†]**	**Min age (Ma)**	**Mid age (Ma)**	**Max age (Ma)**
Top of section	1295	45.05	45.07	45.16	44.98
Ainsa-III off axis-sand	1266	45.16	45.15	45.22	45.26
Ainsa-II marl	1210	45.36	45.31	45.34	45.35
Ainsa-II sand	1137	45.62	45.52	45.54	45.55

*Height represents that to top of complex determined within Chapter 3.
[†]Orbital age estimates based upon the application of the 28.12 cm/kyr SAR to the studied section and tied to the geological time scale (Gradstein et al., 2004).
[§]Biostratigraphic age estimates those from Table 3.4.

Testing the orbitally paced glacio-eustatic forcing mechanism can be accomplished by fitting the orbital age model to the geological time scale. With no nannofossil data point present within the measured section, the mid point between the nearest two is used. The resultant the mid age (45.225 Ma) and mid height (1,247.02 m) is thereby determined using the maxima and minima height error values of FO of *C. gigas* and *S. furcatolithoides*, respectively. Using this tie point and the average SAR of 28.12 cm/kyr, the top (1,137 m) and base (1,295 m) of the studied section within the biostratigraphic age model can be estimated (Fig. 5.3). The resultant three data points enable the equation of the line to be determined:

Equation 5.1

$$y = -281.2x + 13964.2825$$

where y is the stratigraphic height (m) within the biostratigraphic age model and x is the age to be calculated (Ma). Using Equation 5.1 it is possible to determine the orbitally derived age of the Ainsa-III off-axis submarine fan initiation therefore enabling

comparison with the orbital and insolation curves calculated for the relevant time interval (Table 5.9; Fig. 5.22).

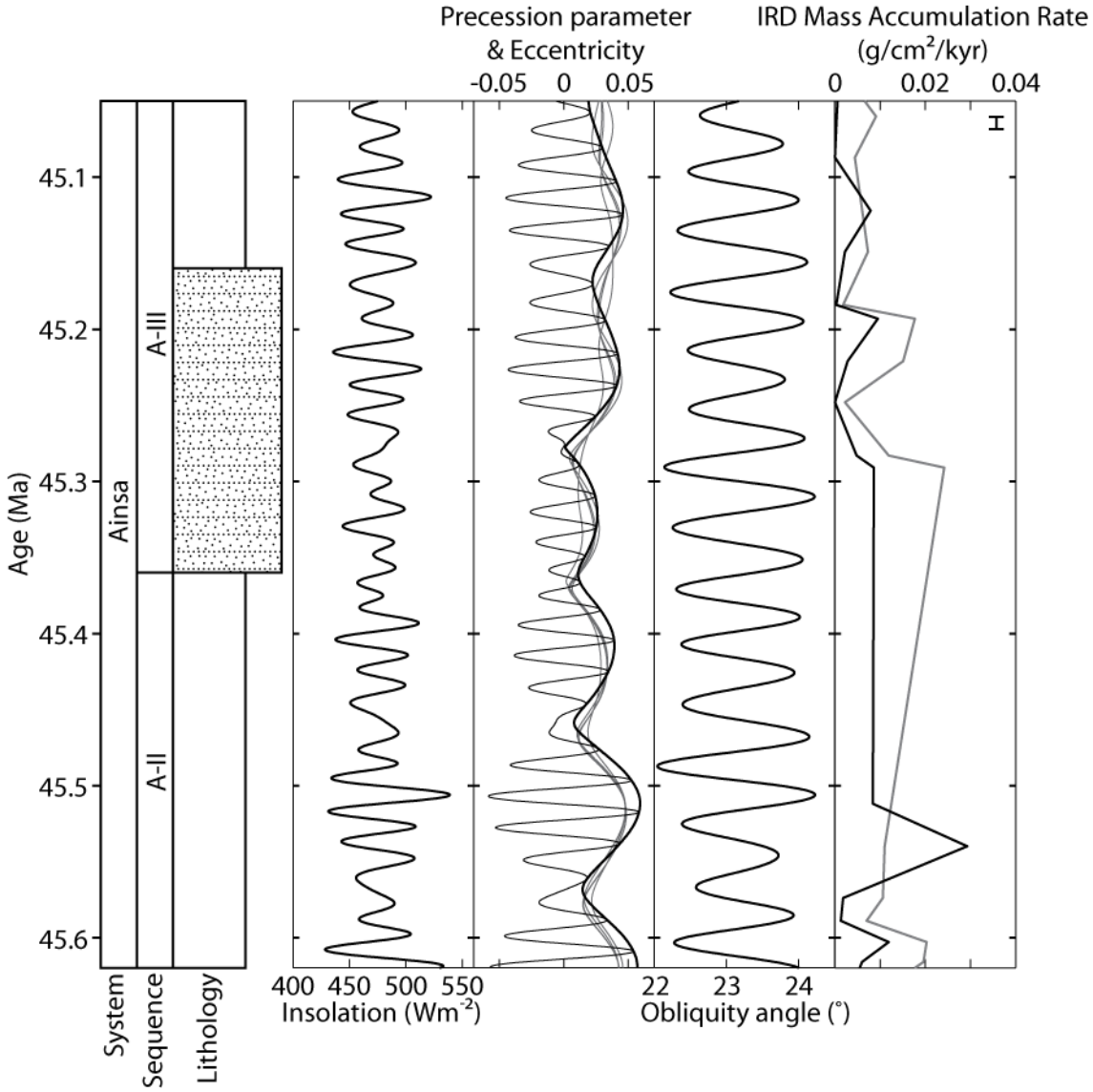

Figure 5.22 | Calculated insolation, orbital curves and observed IRD accumulation during Ainsa-II and -III sequence deposition. With the orbital age model tied to the geological time scale of Gradstein et al. (2004), the testing of the 404-kyr forcing hypothesis of Pickering and Bayliss (2009) can be achieved. The vertical error bar represents age uncertainty from the biostratigraphic age model (0.08 Myr). Orbital and insolation curves (black curves) calculated using the equations of Laskar et al. (2004). Grey eccentricity curves represent the more recent estimates from Laskar et al. (2011). Ice rafted debris (IRD) data record the mass accumulation rates (MAR) of sediment obtained from the Lomonosov Ridge (St. John, 2008). IRD data divided into sediments between 150-250 μm (black) and >250 μm (grey). The timing of the Ainsa-III submarine fan appears to coincide with a period of eccentricity minima between ~45.36 and 45.27 Ma. The resultant reduction in the insolation received at 65˚N during June/July may provide conditions preferential to the formation of ephemeral polar ice. The presence of northern hemisphere ice sheets is suggested by the presence of IRD throughout the studied time interval. Such a relationship would indicate a possible glacio-eustatic forcing mechanism influenced the timing of submarine fan deposition.

Comparison between the estimated timing of the Ainsa-III off-axis submarine fan initiation and the calculated insolation and orbital parameters suggest that deposition coincided with a period of reduced insolation at 65˚N. The reduction of insolation, caused by the reduced eccentricity increasing the Earth-Sun distance, potentially created conditions preferential for the accumulation of ephemeral polar ice. Sufficient ice may have accumulated over this interval to cause a glacio-eustatic sea-level fall subsequently supplying coarse-grained sediment into the Ainsa basin. The presence of such ice within the Northern Hemisphere is demonstrated by the identification of IRD within the coeval Lomonosov Ridge sediments (Fig. 5.22; St. John, 2008). Although no IRD data is available at the commencement of the Ainsa-III fan complex, the presence of such sediment prior to and during the fans deposition supports the glacio-eustatic forcing mechanism.

An alternate mechanism for the supply of voluminous coarse-grained material to the basin may be via variation within the hydrological cycle as identified within the more distal Jaca basin (Kodama et al., 2010). However, for this to occur the submarine fan deposits should correspond to periods of increased insolation thereby amplifying the hydrological cycle. Further autocyclic or tectonic events may have also supplied sediment to the basin. Such scenarios shall be discussed further within Chapter 8.

The affect of tectonics upon the development of the Ainsa System can be determined using palaeomagnetically-dervied rotation rates for the period (Holl and Anastasio, 1993; Mochales et al., 2012). The continuous tightening of the Mediano anticline during the deposition of the Ainsa System accounts for the overall south-westward migration of the individual sequences. Tectonic activity associated with the Boltaña anticline is believed to be responsible for the unconformities located at the top and base of the Ainsa System (Pickering and Bayliss, 2009). The timing of the unconformity marking the termination of the Ainsa System corresponds with increased rotation of the blind-thrust underlying the Boltaña anticline, which may have led to anticlinal uplift (Mochales et al. 2012; Fig. 3.7). Based upon these observations, it is suggested that tectonics controlled the lateral distribution of coarse-grained sediments.

The above duration and timing of proposed glacio-eustatic events within the Ainsa System appear to correspond with those proposed within the Pickering and Bayliss (2009) orbital forcing and “see-saw” tectonic hypothesis. However, despite the above supporting the orbitally forced glacio-eustatic mechanism for the timing of the Ainsa basins submarine fan, uncertainties within the proposed age model remain. Further work is required to constrain the timing of submarine fan deposits within the Ainsa System such as orbital tuning. Despite this, this study indicates that whilst climate controlled the timing of submarine fan deposition, their lateral distribution was

influenced by tectonics. Such a result is similar to those observed within other deep-marine basins where, researchers identify glacio-eustasy as being the dominant control on the timing of coarse-clastic sediment supply whilst tectonics influenced their spatial distribution (Manley and Flood, 1988; Feeley et al., 1990; Pickering et al., 1999; Prins and Postma, 2000; Normark et al., 2006).

5.6 Summary

The immediate conclusions from this chapter are here outlined. The wider interpretation and context of these results shall be discussed in Chapter 8.

Spectral analysis of new and pre-existing SGR and ichnological data obtained from both outcrop and subsurface inter-fan stratigraphy are here shown to contain evidence of orbital forcing (eccentricity, obliquity and precession). Variability within these data is here interpreted as reflecting orbitally forced changes in terrigenous input and bottom water oxygenation. Using the identification of the orbital parameters, an average SAR of 28.12 cm/kyr was determined for the stratigraphic interval. Applying this SAR to the stratigraphy between Ainsa-II and Morillo-I, the temporal spacing of submarine fan growth and abandonment is consistent with the proposed 404-kyr long-eccentricity driver. Placing the proposed orbital age model within the geological time scale, the timing of the Ainsa-III off-axis submarine fan initiation appears consistent with orbital conditions ideal for the formation of ephemeral ice-sheets and hence low-stand conditions. The presence of ice rafted debris within coeval Arctic Ocean sediments during the Ainsa Systems deposition further support the glacio-eustatic forcing mechanism. The evidence provided within this chapter lends credence to a global climatic forcing of coarse clastic material to the Ainsa basin as proposed by Pickering & Bayliss (2009).

Whilst the timing of submarine fan deposition within the Ainsa System is attributed to climatic factors, their lateral distribution is attributed to the “see-saw” tectonic mechanism proposed by Pickering and Bayliss (2009). The interaction between the basin bounding Mediano and Boltaña anticlines potentially resulted in the overall south-westward migration of the basin depocenter and unconformities between the systems, respectively.

Other instructive conclusions to be drawn from this study mainly involve radioelement reproducibility. Comparison between SGR data collected at outcrop and subsurface show that radioelement trends vary significantly, possibly due to high noise levels, well conditions and processing. Of these, outcrop data is here considered more reliable with both K and Th being adequately reproduced at outcrop. In both cases U appears the more variable.

Chapter 6
The Banaston System

6.1 Introduction

6.1.1 Chapter objectives

The Banaston System represents the lower-most deep-water depositional system within the Upper Hecho Group. Within this chapter, spectral analysis techniques shall be employed to identify whether orbital periods are recorded within spectral gamma ray data collected from the Banaston System off-axis fan and inter-fan sediments. The presence of orbital cyclicity shall be used to create a floating time scale through these deposits via the identification of a sediment accumulation rate (SAR). The resultant orbital age model shall be compared to that previously defined biostratigraphic age model (Chapter 3). Ultimately, it should be possible to test the predictions of the orbital forcing hypothesis that the timing of each submarine fan complex is paced by a 404-kyr paced glacio-eustatic cycle.

6.1.2 The Banaston System

The Banaston System is one of the eight deep-marine systems within the Ainsa basin and defines the base of the Upper Hecho Group (Fig. 1.8). These sediments record the incision and subsequent backfill of six highly confined channelised submarine fan and inter-fan marl intervals (Bayliss, 2010). Banaston System deposition coincided with a second phase of basin reorganisation associated with continued emplacement of the Lower Thrusting Sheets/Complex (Munoz, 1992; Remacha et al., 2003; Remacha et al., 2005; Bayliss, 2010).

Banaston System sediments outcrop in a SE-NW orientated transect around the villages of Banaston-Usana, Labuerda and Boltaña-San Vincente (Figs. 1.18, 6.1). Each outcrop illustrates a differing environment of deposition. From the southeast to northwest environments have been interpreted as representing mid-slope canyon-channel transition (Banaston-Usana), intermediate overbank (Labuerda) and lower-slope to proximal basin floor channel (Boltaña-San Vincente) deposits (Remacha et al., 2003; Bayliss, 2010).

The base of the Banaston System is marked by an unconformity associated with significant erosion into the underlying Gerbe System (Remacha et al., 2003; Bayliss, 2010). Sediments are divided into six unconformity bound sequences referred to as Banaston-I to Banaston-VI (B-I to B-VI) (Pickering and Bayliss, 2009; Bayliss,

2010). Axially, the base of each sequence is marked by a mappable erosional surface created by extensive mass wasting of the fine-grained basin slope marlstones and thin-bedded silty to fine-grained turbidites. Following each erosional surface the systems depositional axis is observed to shift subtly within the Banaston area compared to a more significant WSW shift is observed within the San Vincente area (Bayliss, 2010). Basal sediments within each submarine fan complex consist of mainly type-II MTC deposits ranging in thickness from 12-42 m. These initial sediments consist of contorted intra-formational sediment slides, localised sandy conglomerates and gravels, large-scale olisotoliths (metres to hundreds-of-metres in length), fossiliferous material and intra- and extra-formational components set within a sandy mudstone matrix. Subsequent thick-bedded, amalgamated, very-coarse to granule sandstone turbidite beds are observed to infill topography created by the underlying MTC deposits (Bayliss, 2010). Within the Banaston System most submarine fan complex beds are thick- to medium-bedded, coarse- to medium-grained and amalgamated (Bayliss, 2010). Each submarine fan complex commonly displays a thinning and fining upward trend linked to waning sediment supply which is consistent with the basin generic depositional model (Pickering and Bayliss, 2009; Bayliss, 2010). The cessation of the Banaston System coincides with an ESE shift of the basins depositional axis and the subsequent deposition of the Ainsa System potentially related to tectonic processes (Fig. 1.15).

Off-axis submarine fan complex deposition within the system consists of laterally extensive, very thin- and thin-bedded, current-rippled, very fine-grained sandstones and parallel laminated, thin-bedded siltstones inter-bedded with marls. These deposits have been interpreted as originating from traction and suspension deposits from low-concentration turbidity currents (Remacha et al., 2003; Bayliss, 2010). Within these off-axis sediments, Bayliss (2010) uses the presence of well-defined *Arenicolites* burrows to indicate the possible development of firm-grounds at the top of B-I and B-II sequences. Bayliss (2010) links these firm-grounds to periods of waning sediment supply coincident with the fining upward patterns within the more axial deposits. The preservation of these structures suggests that these off-axis deposits are mainly non-erosive (Bayliss, 2010).

High-frequency cyclic stacking patterns have previously been identified within the systems off-axis sediments (Remacha et al., 2003). Each cycle is composed of a 12-13 m fining upward cycle showing a concurrent decrease in sand and increase in marl content. Laterally, these deposits can be traced from the systems channel axis to levee-overbank deposits within the Banaston-Usana and Labuerda areas respectively (Remacha et al., 2003).

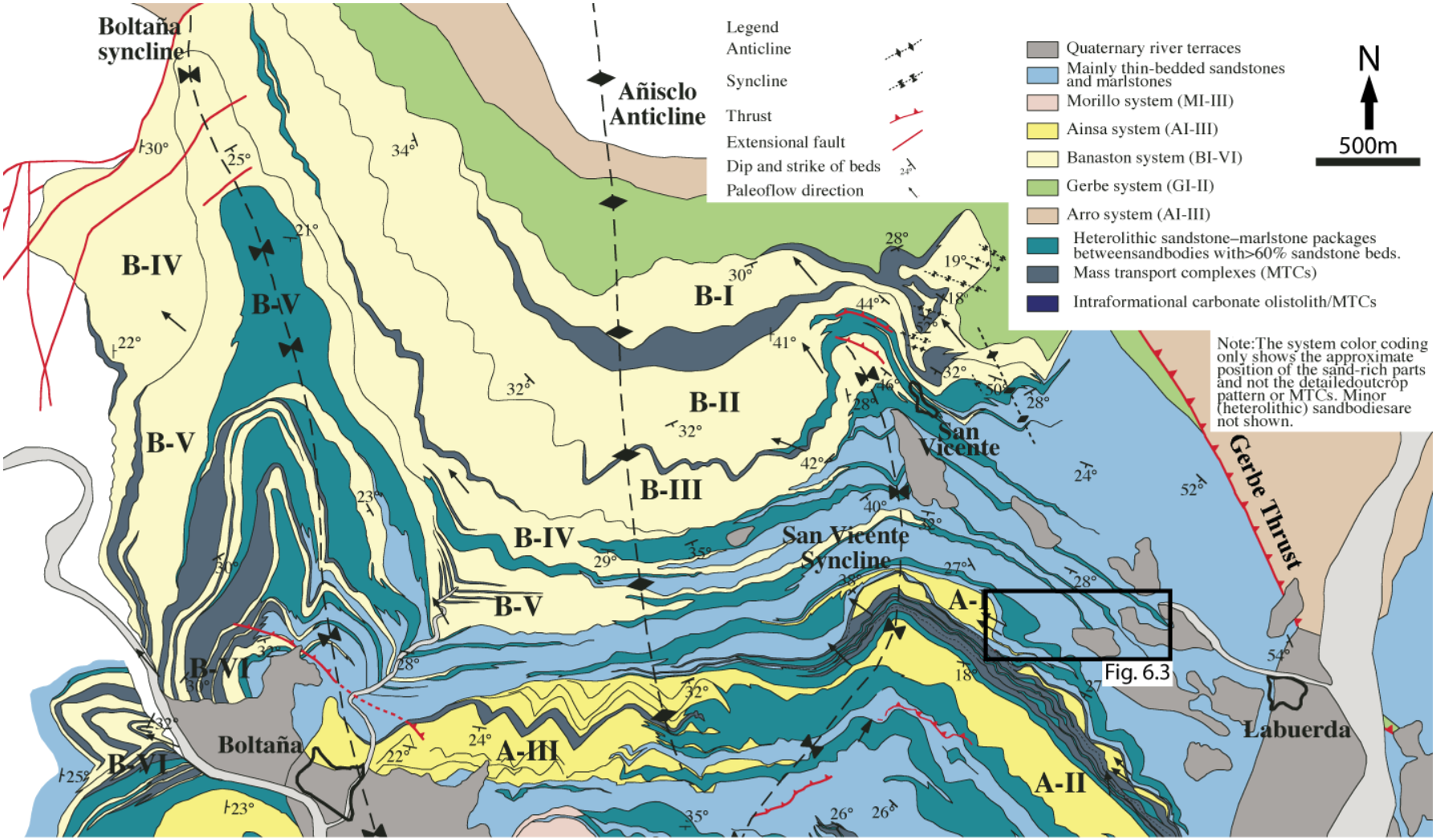

Figure 6.1 | Geological map of the Ainsa basin between Boltaña and Labuerda (Pickering and Bayliss, 2009). Studied off-axis sediments of the Banaston System were measured within the area highlighted consisting of intermediate overbank deposits.

6.1.3 System dating

The deposition of the Banaston System, based upon the biostratigraphic age model (Chapter 3; Fig. 6.2), occurred between 45.9-48.4 Ma on the GTS 2004 time-scale (Gradstein et al., 2004). Analyses of calcareous nannofossil assemblages indicate that the systems sediments contain the first and last occurrence (FO and LO) of *Blackites inflatus* dated at 47.92 and 46.67 Ma respectively. The first occurrence of *Nannotetrina fulgens* is also observed corresponding to 46.57 Ma. The identification of these marker species suggest that the Banaston System deposition spans nannofossil zones NP14b-15a of Martini (1971).

Large benthic foraminifera collected from the system indicate deposition occurred within the coeval shallow benthic zone SBZ13 of Serra-Kiel et al. (1998) based upon an assembalge including *Nummulites laevigatus, N. obesus, N. syrticus, Assilina abrardi, N. lehneri, N. messinae,* and *Alveolina elliptica*.

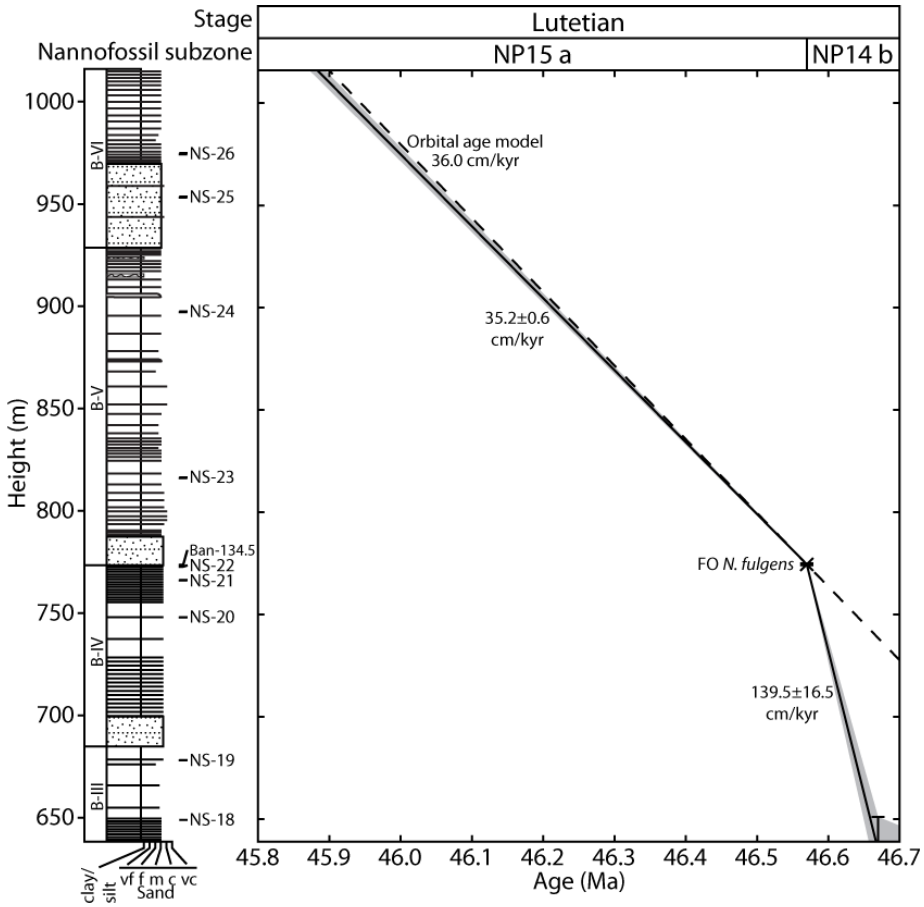

Figure 6.2 | Banaston System age model determined from nannofossil data. Detailed description of age model provided in Chapter 3. Solid lines between nannofossil data points represent mid-point ages whilst grey shaded areas constitute age error envelope. Dashed line represents proposed age-height relationship based upon the orbital age model tied to the geological time scale by the FO of *N. fulgens*.

6.1.4 Tectonic setting

Deposition of the Banaston System coincided with the initiation of a second phase of activity within the Ainsa basins tectono-sequence 2 (TS-2) of Bayliss (2010). This second phase of activity commenced during the late Ypresian-Lutetian (Puigdefabregas and Souquet, 1986; Verges and Burbank, 1996; Remacha et al., 2003) with the emplacement of the Larra-Boltaña thrust (Teixell, 1996). Later the Gavarnie thrust emplacement resulted in the thickening of the Pyrenean Axial Zone and the transformation of the southern foreland into a series of compartmentalised piggyback basins (Munoz, 1992; Verges and Burbank, 1996; Remacha et al., 2003).

Within the Ainsa basin the syn-depositional growth of the Boltaña and Añisclo submarine highs, along with the pre-existing Mediano anticline, structurally confined early Banaston System (B-I to B-III) system sediments (Bayliss, 2010). Post deposition of the B-I submarine fan the Boltaña seafloor high began to affect the systems deposition as documented by the change from easterly palaeocurrent directions. Within the B-IV to B-VI submarine fans, confinement is observed to decrease with a wider dispersion of palaeocurrents either due to the cessation of activity in Boltaña and Añisclo submarine highs or an increase of sediment supply (Bayliss, 2010). The interaction between these anticlines is hypothesised to have controlled the Banaston System development potentially via “see-saw” tectonics (Figs. 1.15, 1.16) (Pickering and Bayliss, 2009; Bayliss, 2010).

6.1.5 Sediment provenance and petrography

Sediments supplying the Banaston System originated from over the Mediano anticline from the Tremp-Graus basin to southeast (Figs. 1.13, 1.14). Sediments are believed to have originated from the terrestrial Campanùe fan which consists of conglomerates and sandstones derived from Mesozoic and Palaeozoic source rocks (Weltje et al., 1996; Caja et al., 2010). Further refinement of correlation with Tremp-Graus sediments is proposed by Bayliss (2010) who links Banaston System sediments with those of the UM-B megasequence of Nijman (1998) (Figs. 1.8, 1.9).

The Banaston System submarine fan sands consist of sub-arkose arenites with a mean $Q_{61}F_{21}L_{18}$ (Das Gupta and Pickering, 2008). Disagreement however exists over the analysis of the clastic carbonate grains with the systems sediments being either described as hybrid arenites (enriched carbonate intra-basinal carbonate grains; Gupta and Pickering, 2008) or calclithites (enriched carbonate extra-basinal carbonate grains; Caja et al., 2010). Despite this disagreement, workers have been able to trace Banaston System sediments from the proximal deposits within the Ainsa Basin with the

distal deposits of the Jaca Basin using sediment petrography (Fig. 1.9) (Remacha et al., 2003; Remacha et al., 2005; Das Gupta and Pickering, 2008; Bayliss, 2010).

6.2 Materials and methods

6.2.1 Spectral gamma ray logging

Inter-fan and off-axis fan sediments of the Banaston-III to Banaston-VI sequences were studied within an area ~1 km northwest of Labuerda. Spectral gamma ray (SGR) data were collected from exposed sediments within the Barranco Solaneta Espluga and Barranco Pinar (Figs. 6.1, 6.3). Spectral gamma ray data were collected during three sampling campaigns during August 2009, April 2010 and August 2010. Undergraduate students R. Quarmby and P. Warburton collected the August 2009 and 2010 data respectively whilst J. Scotchman collected data during April 2010.

Spectral gamma ray data were collected using a Radiation Solutions RS-125 Super-Spec spectrometer following the general procedure outlined in Section 2.2.3. The Quarmby and Warburton high-resolution SGR data were collected, where possible, using a sampling interval of 0.2 m. With this being less than the detection radii of the spectrometer a moving average was created through the stratigraphy. Low-resolution data collected during April 2010 were collected every ~1 m. SGR readings in all cases were collected over a 3-minute period providing a precision of ±1.5%, 6.7%, 24.1% and 9.6% for total, K, U and Th respectively (Table 2.5). Accuracy error bars were calculated using the `rs125error_est.m` MATLAB script (Appendix) based upon the estimates provided in Table 2.4. Average 1-sigma errors calculated for accuracy were ±0.090%, ±0.483 ppm and ±0.900 ppm for K, U and Th, respectively.

6.2.2 Constructing a composite SGR time series

The construction of a composite stratigraphic series was achieved by correlating total SGR events between the three overlapping SGR data sets (Fig. 6.4). The composite stratigraphic time series data is based upon the identification of similar SGR minima within both the Quarmby and Warburton total data at 143.2 m and 11 m, respectively (Fig. 6.5). Using this SGR event as a tie point, a 376 m high-resolution composite stratigraphic series is formed encompassing sediments from the B-III to B-VI sequences. Litho-stratigraphy for the stratigraphic series was obtained during the low-resolution SGR logging during April 2010. Correlating the low- and high-resolution data links the SGR data to the litho-stratigraphy (Fig. 6.4).

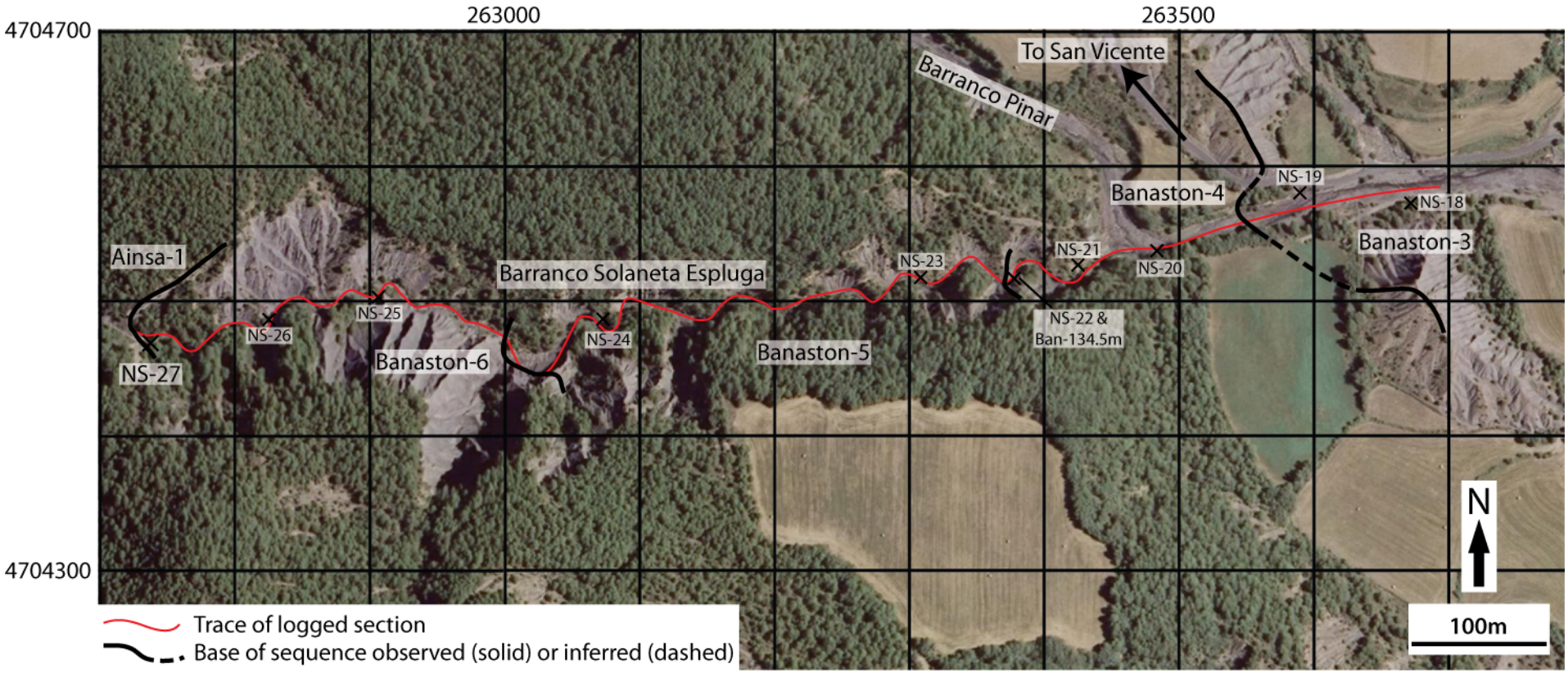

Figure 6.3 | Aerial image of the study area showing location of logged sediments. Banaston System sediments were studied within both the Barranco Solaneta Espluga and Barranco Pinar. SGR data were collected from ~376 m of stratigraphy located between the upper B-III sequence and the top of the Banaston System. The red solid line represents the approximate trace of the logged section. The base of each submarine fan complex is positioned (bold black lines) based upon increased frequency of sandstone deposits interpreted as representing off-axis submarine fan sediments. Bulk sediment samples were also collected from the section with the aim to constrain the age of the system. UTM zone 31 coordinates are used, aerial image obtained from http://sigpac.mapa.es/fega/visor/ during September 2011.

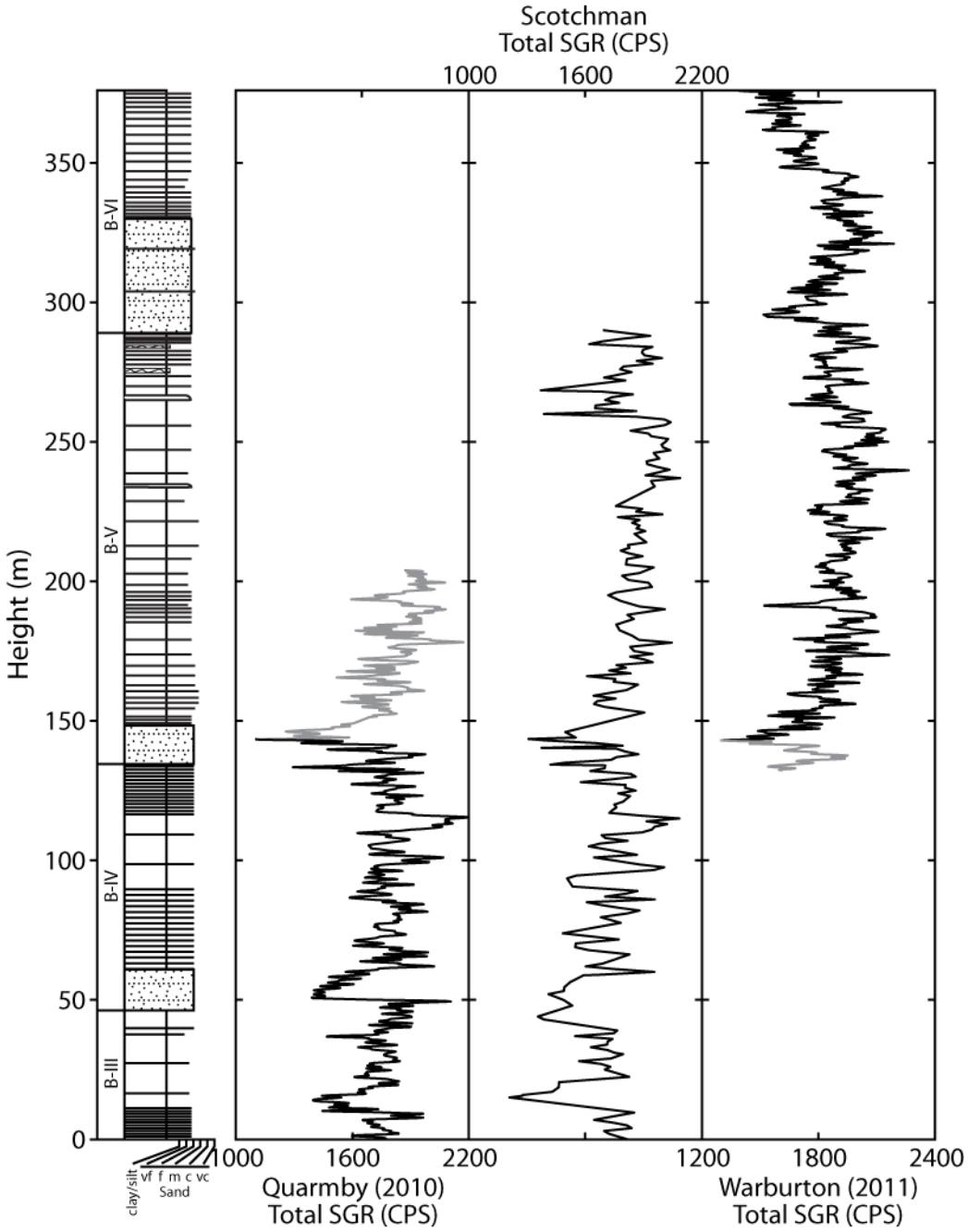

Figure 6.4 | Correlation between the Quarmby, Scotchman and Warburton total SGR data sets. Both the Quarmby and Warburton datasets were smoothed using a 12th order Butterworth low-pass filter with a cut-off frequency of 1.0 cycles/m. The visual correlation between the three data sets indicates reliable data reproducibility throughout the studied section. Combination of the two high-resolution data sets enabled the construction of a composite time series. Assuming that the total SGR depletion events at 134.2 and 11 m are identical then Quarmby data >134.2 m and Warburton data <11 m are discarded (grey line). The remaining data (black line) are combined to create a composite SGR time series (Fig. 6.5).

Figure 6.5 (next page) | Composite SGR time series obtained from the combination of Quarmby and Warburton data. Original data are presented (black lines) along with smoothed data from the application of a 12th order Butterworth low-pass filter with a cut-off frequency of 0.4 cycles/m (grey lines). Vertical dashed lines within Th/K and Th/U ratio data represent average shale values (see text for interpretation).

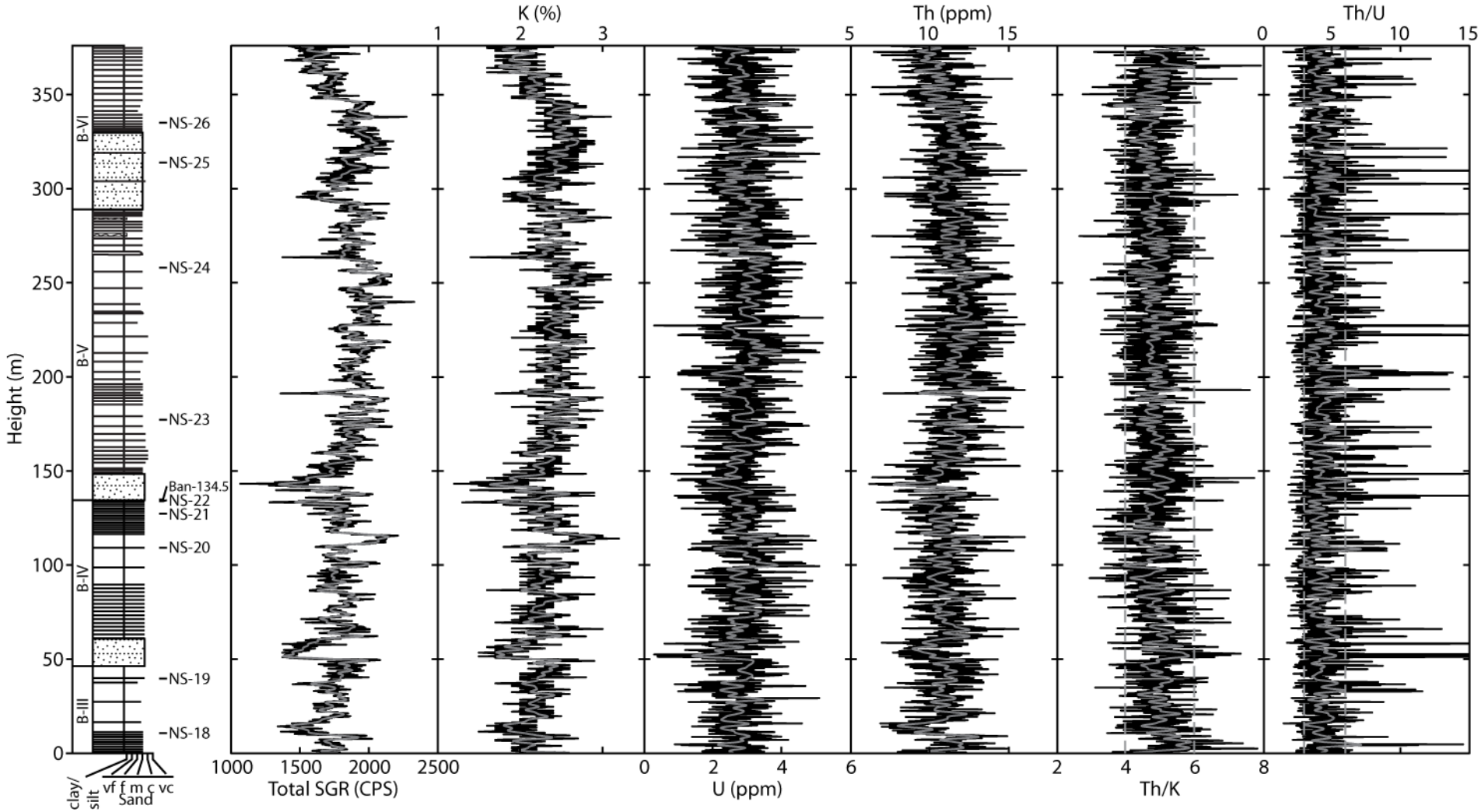
Height (m)
B-VI
B-V
B-IV
B-III
NS-26
NS-25
NS-24
NS-23
Ban-134.5
NS-22
NS-21
NS-20
NS-19
NS-18
clay/
silt
vf f m c vc
Sand
K (%)
Th (ppm)
Th/U
Total SGR (CPS)
U (ppm)
Th/K

6.2.3 Spectral analyses

Prior to spectral analyses, data were screened to remove data collected whilst the RS-125 spectrometer was non-stabilised to background conditions. Outliers within the SGR data were absent apart from the Th/U data where values >15 were deleted to avoid spurious spectral results (refer to Section 2.5.2.2). Although assumed instantaneous, minor MTC deposits remained within the measured stratigraphy, as this should enable their timing to be approximated.

Following screening, each stratigraphic series was de-trended, interpolated and low-pass filtered using MATLAB scripts (Appendix; `process.m` MATLAB code) creating data suitable each spectral estimation technique.

With the majority of the stratigraphic series being unevenly spaced, the REDFIT algorithm (Schulz and Mudelsee, 2002) was utilised to determine statistically significant frequencies. REDFIT spectral analyses were performed using an over-sampling factor (ofac) of 4, a hifac of 1, and 6 WOSA rectangular segments yielding 8 degrees of freedom.

To determine the spatial distribution of regular oscillations within these stratigraphic series, the online tool (http://paos.colorado.edu/research/wavelets/) was utilised, which applies the continuous wavelet algorithms (CWT) of Torrence and Compo (1998). The continuous wavelet spectra were calculated using the de-trended and interpolated stratigraphic series. CWT calculations used a Morlet mother wavelet with a parameter of 6, a start scale of 2, a scale width of 0.1, 11 powers-of-2. Data were not zero-padded therefore not requiring a cone of influence.

With the stratigraphic time series potentially containing records of orbital cyclicity, their objective identification and quantification is achieved using the Average Spectral Misfit (ASM) method of Meyers and Sageman (2007). Based upon significant frequencies identified by the MTM harmonic F-test (Thomson, 1982; Thomson, 1990), the ASM method provides a null hypothesis significance level of there being no orbital periods present. An objective sediment accumulation rate (SAR) is also provided.

MTM analyses required for the ASM method were performed upon the interpolated and de-trended stratigraphic series within Analyseries 2.0.4.2 (Paillard et al., 1996) using a time bandwidth product of 4 and 6 data tapers. Two sets of F-test frequencies of ≥90% confidence were isolated within a frequency range corresponding to ≥80% total variance within the relevant MTM spectra. Based upon these frequencies, the ASM was calculated for each stratigraphic series based upon their Rayleigh (R_f) and Nyquist (N_f) frequencies (Table 6.1). The range of SARs used was 5-100 cm/kyr with a step size of 0.95 cm/kyr resulting in 100 ASM and H_o estimates for each analysis. The number of orbital terms used during ASM analyses included all 7

orbital terms. ASM calculations were calculated for 47 Ma (Table 6.2) based upon available dating for the Banaston System (Fig. 6.2; Chapter 3).

Table 6.1 – Time series properties

Stratigraphic time series*	N	Sample Interval (m)†	Nyquist Frequency (cycles/m)	Rayleigh Frequency (cycles/m)
K	1813	0.2073	2.4120	0.0027
U	1813	0.2073	2.4120	0.0027
Th	1813	0.2073	2.4120	0.0027
Th/K	1813	0.2073	2.4120	0.0027
Th/U	1801	0.2087	2.3958	0.0027

*Properties of the individual time series after the removal of major outliers from the data.
†Sample interval applied during linear interpolation of time series for wavelet and MTM F-test algorithms.

Table 6.2 – Calculated orbital periods for the Banaston System

Orbital Parameter	Period (kyr)*
Precession	18.81
Precession	22.62
Obliquity	39.97
Obliquity	52.21
Short Eccentricity	94.78
Short Eccentricity	123.82
Long Eccentricity	404.18

*Orbital periods calculated for 47 Ma using equations of Berger et al (1992).

6.3 Results

6.3.1 Sedimentology

The sediments measured within the Barranco Solaneta Espluga and Barranco Pinar (Figs. 6.1, 6.3) included inter-fan and off-axis submarine fan deposits belonging to the B-III, IV, V and VI sequences. A total of 376 m of stratigraphy was measured including both inter-fan and off-axis submarine fan deposits.

Inter-fan sediments were dominated by parallel laminated, very-thin bedded calcareous mudstones and siltstones with intermittent, centimetre-scale, very fine- to medium-grained sandstones throughout (Plate 6.1a). The frequency, thickness and grain-size of these sandstone beds increase toward the off-axis submarine fan deposits.

Off-axis submarine fan deposits consist of 5 to 20 cm thick, medium- to very coarse-grained sandstone beds separated by <10 cm of marl and silty marls (Plate 6.1b). The transition from the off-axis to inter-fan sediments is gradual with a decrease in sand frequency, thickness and grain size.

Mass transport complexes (MTCs) within the studied sediment are mainly associated with the heterolithic deposits above ~250 m and rarely exceed 1 m in

thickness. The majority are type-Ib MTCs containing intra-formational sandstone olistoliths (Plate 6.1c). Type-Ia and -III MTCs are also present within the system.

6.3.2 Outcrop SGR

Spectral gamma ray data obtained from the 376 m of outcropping sediments are displayed in Figure 6.5. The statistics for each stratigraphic series are provided in Table 6.3.

Depletions within the SGR data, especially within the total SGR and K, appear to broadly correspond with intervals of increased sandstone frequency associated with off-axis submarine fan deposits. The SGR signatures of these deposits are characterised by a rapid depletion at their base followed by a gradual enrichment in both total SGR and K concentrations as the frequency of sandstone beds decrease. Although dominated by noise, the low-pass filter results for U and Th radioelement concentrations demonstrate a similar response to sandstone bed frequency as total SGR and K. The two Th/K and Th/U ratios however, show little major variation throughout the stratigraphic series with high noise levels.

Table 6.3 – Summary statistics of SGR data

	Min	Max	Mean	Stdev
Total	1066.10	2331.30	1822.31	163.84
K	1.20	3.20	2.32	0.29
U	0.30	5.20	2.85	0.80
Th	6.20	16.10	11.19	1.64
Th/K	2.67	7.94	4.87	0.72
Th/U*	1.33 (1.33)	51.00 (14.56)	4.44 (4.31)	2.52 (1.79)

*Statistics calculated for Th/U prior to removal of outliers. Bracketed values represent those calculated once outliers removed.

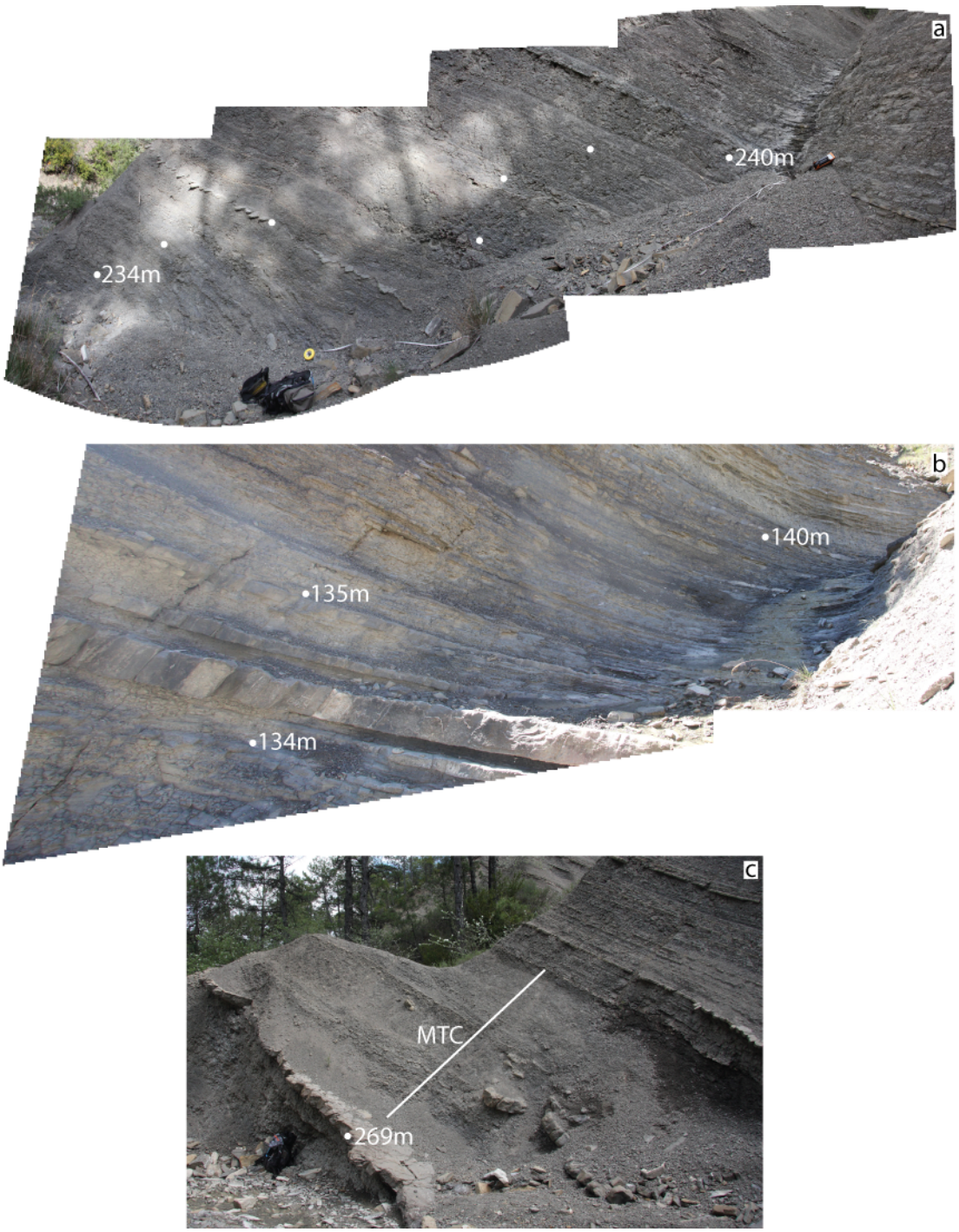

Plate 6.1 | Example images of typical inter-fan, off-axis fan and MTD/MTC deposits of the Banaston System exposed within the Barranco Solaneta Espluga and Barranco Pinar. (a) Inter-fan sediments are dominated by laminated silty marlstones, very-thin and thin-bedded and infrequent centimetre-scale turbidite deposits. **(b)** Off-axis fan deposits consist of 5 to 20 cm thick medium-very coarse-grained sandstone beds separated by generally <10 cm of marlstones. **(c)** MTC deposits within the section are sparse with the example here representing a type-1b MTC containing intra-formational sandstone olistoliths. Positions marked are height measurements from where low-resolution SGR data was collected during April 2010.

6.3.3 Spectral and ASM results

The three spectral analysis techniques applied to the Banaston System gamma ray stratigraphic series identify the presence of abundant significant frequencies (Table 6.4). REDFIT spectra are dominated by five frequency bands centred about 0.012, 0.025, 0.054, 0.067, 0.080, 0.092 and 0.122 cycles/m (Fig. 6.6; Table 6.4). Of these the 0.012, 0.025 and 0.054 cycle/m frequencies exceed the 99% and critical (<99%) confidence levels whilst the remainder lie between 90% and 99% confidence.

Near identical frequencies to those recognised within the REDFIT spectra, along with numerous others, are identified within MTM F-test spectra (Fig. 6.7; Table 6.4). The F-test methods reduced bandwidth (±0.001 cycles/m) enables the 0.024, 0.028, 0.053, 0.058, 0.069 cycles/m frequencies to be discerned from within the previously identified frequency ranges.

Wavelet spectra identified significant frequencies similar to, and in addition to those identified by the REDFIT and MTM F-test spectra at 0.005, 0.008, 0.013, 0.023, 0.052 and 0.065 cycle/m to above the 90% confidence level (Fig. 6.8; Table 6.4). Spatially the lower frequencies appear continuous throughout the wavelet spectra except for Th/K and Th/U stratigraphic series, which appear more variable. Within the lower ~150 m of stratigraphy the ~0.028 cycles/m (~1/35 m) frequency decreases with height to ~0.018 cycles/m (~1/56 m) whilst adjacent frequencies show little signs of spatial variability. The 0.052 cycles/m frequency (~1/19 m period) appears spatially continuous throughout the stratigraphic series although the majority of power is present within the lower 100 m.

ASM results obtained from the stratigraphic series, except for Th/K, contain a wide range of SAR estimates between 5.95 and 99.05 cm/kyr that exceed the minimum null hypothesis significance level of 0.99% (Table 6.5; Fig. 6.7). Of the numerous SAR estimates identified, the two most significant and consistent ASM results of ~15 to 20 and ~35 to 36 cm/kyr with null hypothesis significant levels <0.053%.

Table 6.4a – Spectral results

Spectral Estimation Method	Frequency (cycles/m)*	Period (m)	Confidence Level (%)	Temporal Period (kyr)†	Spectral Estimation Method	Frequency (cycles/m)	Period (m)	Confidence Level (%)	Temporal Period (kyr)
Total SGR					**K**				
Wavelet	0.005	200.02	90.0	555.1	**Wavelet**	0.005	199.13	90.0	552.7
	0.008	125.81	90.0	349.2		0.008	125.39	90.0	348.0
	0.013	77.39	90.0	214.8		0.013	77.88	90.0	216.1
	0.051	19.50	90.0	54.1		0.053	18.96	90.0	52.6
REDFIT§	0.012	85.94	Critical	238.5	**REDFIT**	0.009	107.43	Critical	298.2
	0.026	39.07	99.0	108.4		0.028	35.81	Critical	99.4
	0.054	18.68	Critical	51.9		0.056	17.91	Critical	49.7
						0.067	14.82	95.0	41.1
						0.081	12.28	99.0	34.1
						0.123	8.11	99.0	22.5
MTM F-test#	0.013	75.48	96.6	209.5	**MTM F-test**	0.013	75.48	97.4	209.5
	0.024	41.93	97.0	116.4		0.024	41.93	94.6	116.4
	0.029	34.66	91.4	96.2		0.042	24.09	95.3	66.9
	0.041	24.26	95.4	67.3		0.058	17.33	99.9	48.1
	0.054	18.66	92.7	51.8		0.068	14.64	90.1	40.6
	0.058	17.33	99.8	48.1		0.086	11.59	90.7	32.2
	0.095	10.48	97.3	29.1		0.096	10.45	98.5	29.0
	0.110	9.11	95.1	25.3		0.110	9.13	91.3	25.3
	0.123	8.11	99.9	22.5		0.124	8.09	99.6	22.4
	0.135	7.40	99.3	20.5		0.135	7.42	90.9	20.6
	0.148	6.75	97.0	18.7		0.148	6.74	94.4	18.7
	0.172	5.82	97.8	16.1		0.171	5.86	98.3	16.3
	0.181	5.52	94.5	15.3		0.181	5.52	94.9	15.3
	0.193	5.17	98.3	14.3		0.191	5.23	90.8	14.5

Table 6.4b – Spectral results

Spectral Estimation Method	Frequency (cycles/m)	Period (m)	Confidence Level (%)	Temporal Period (kyr)	Spectral Estimation Method	Frequency (cycles/m)	Period (m)	Confidence Level (%)	Temporal Period (kyr)
U					**Th**				
Wavelet	0.005	200.14	90.0	555.5	**Wavelet**	0.005	197.39	90.0	547.8
	0.008	125.88	90.0	349.4		0.008	125.42	90.0	348.1
	0.013	77.43	90.0	214.9		0.013	76.99	90.0	213.7
	0.023	44.17	90.0	122.6		0.049	20.28	90.0	56.3
	0.055	18.29	90.0	50.8					
	0.148	6.75	90.0	18.7					
REDFIT	0.005	214.86	Critical	596.3	**REDFIT**	0.012	85.94	Critical	238.5
	0.021	47.75	99.0	132.5		0.026	39.07	Critical	108.4
	0.037	26.86	99.0	74.5		0.051	19.53	Critical	54.2
	0.054	18.68	99.0	51.9		0.067	14.82	99.0	41.1
	0.070	14.32	95.0	39.8		0.079	12.64	90.0	35.1
	0.081	12.28	90.0	34.1		0.091	11.02	90.0	30.6
	0.093	10.74	95.0	29.8		0.123	8.11	95.0	22.5
	0.107	9.34	95.0	25.9		0.230	4.34	90.0	12.0
	0.123	8.11	90.0	22.5		0.251	3.98	90.0	11.0
	0.156	6.41	99.0	17.8		0.265	3.77	95.0	10.5
MTM F-test	0.007	141.52	93.3	392.8	**MTM F-test**	0.024	41.93	98.2	116.4
	0.012	80.87	91.9	224.4		0.041	24.43	95.8	67.8
	0.028	35.75	91.1	99.2		0.054	18.66	91.8	51.8
	0.037	27.17	97.5	75.4		0.058	17.15	99.7	47.6
	0.053	18.97	96.9	52.7		0.069	14.51	97.1	40.3
	0.074	13.48	96.0	37.4		0.081	12.40	97.5	34.4
	0.085	11.79	91.2	32.7		0.123	8.11	99.9	22.5
	0.094	10.65	91.4	29.6		0.173	5.80	94.5	16.1
	0.108	9.28	99.3	25.8					
	0.122	8.20	97.0	22.8					
	0.145	6.92	91.7	19.2					
	0.158	6.31	96.9	17.5					
	0.173	5.77	99.9	16.0					
	0.184	5.43	100.0	15.1					
	0.195	5.14	92.7	14.3					
	0.200	4.99	97.2	13.9					

Table 6.4c – Spectral results

Spectral Estimation Method	Frequency (cycles/m)	Period (m)	Confidence Level (%)	Temporal Period (kyr)	Spectral Estimation Method	Frequency (cycles/m)	Period (m)	Confidence Level (%)	Temporal Period (kyr)
Th/K					**Th/U**				
Wavelet	0.005	198.15	90.0	549.9	**Wavelet**	0.005	197.26	90.0	547.5
	0.013	77.85	90.0	216.1		0.008	125.61	90.0	348.6
	0.063	15.83	90.0	43.9		0.037	27.25	90.0	75.6
						0.066	15.08	90.0	41.8
REDFIT	0.005	214.86	Critical	596.3	**REDFIT**	0.023	42.92	95.0	119.1
	0.030	33.06	95.0	91.7		0.037	26.83	95.0	74.5
	0.061	16.53	90.0	45.9		0.068	14.80	99.0	41.1
	0.119	8.43	90.0	23.4		0.123	8.10	95.0	22.5
MTM F-test	0.013	75.48	90.8	209.5	**MTM F-test**	0.007	148.67	99.3	412.6
	0.057	17.42	94.3	48.3		0.024	41.70	99.3	115.7
	0.074	13.48	91.4	37.4		0.037	26.92	99.8	74.7
	0.105	9.57	93.7	26.6		0.074	13.46	98.1	37.4
	0.109	9.15	94.5	25.4		0.085	11.75	99.6	32.6
	0.119	8.43	95.9	23.4		0.096	10.42	93.9	28.9
	0.159	6.29	97.6	17.5		0.123	8.14	97.7	22.6
	0.170	5.90	98.8	16.4		0.140	7.15	95.2	19.9
	0.182	5.50	95.8	15.3		0.158	6.32	94.4	17.5
						0.173	5.79	97.3	16.1
						0.183	5.45	98.1	15.1
						0.199	5.01	98.2	13.9

*Frequencies between 0-0.2 cycles/m provided. Full results located within Appendix.
†Temporal period determined using the average SAR of 36.03 cm/kyr identified from ASM analyses.
§All REDFIT analyses have bandwidth (BW) = ±0.0056 cycles/m. REDFIT critical level = 99.8%.
#All MTM F-test analyses have bandwidth (BW) = ±0.013 cycles/m.

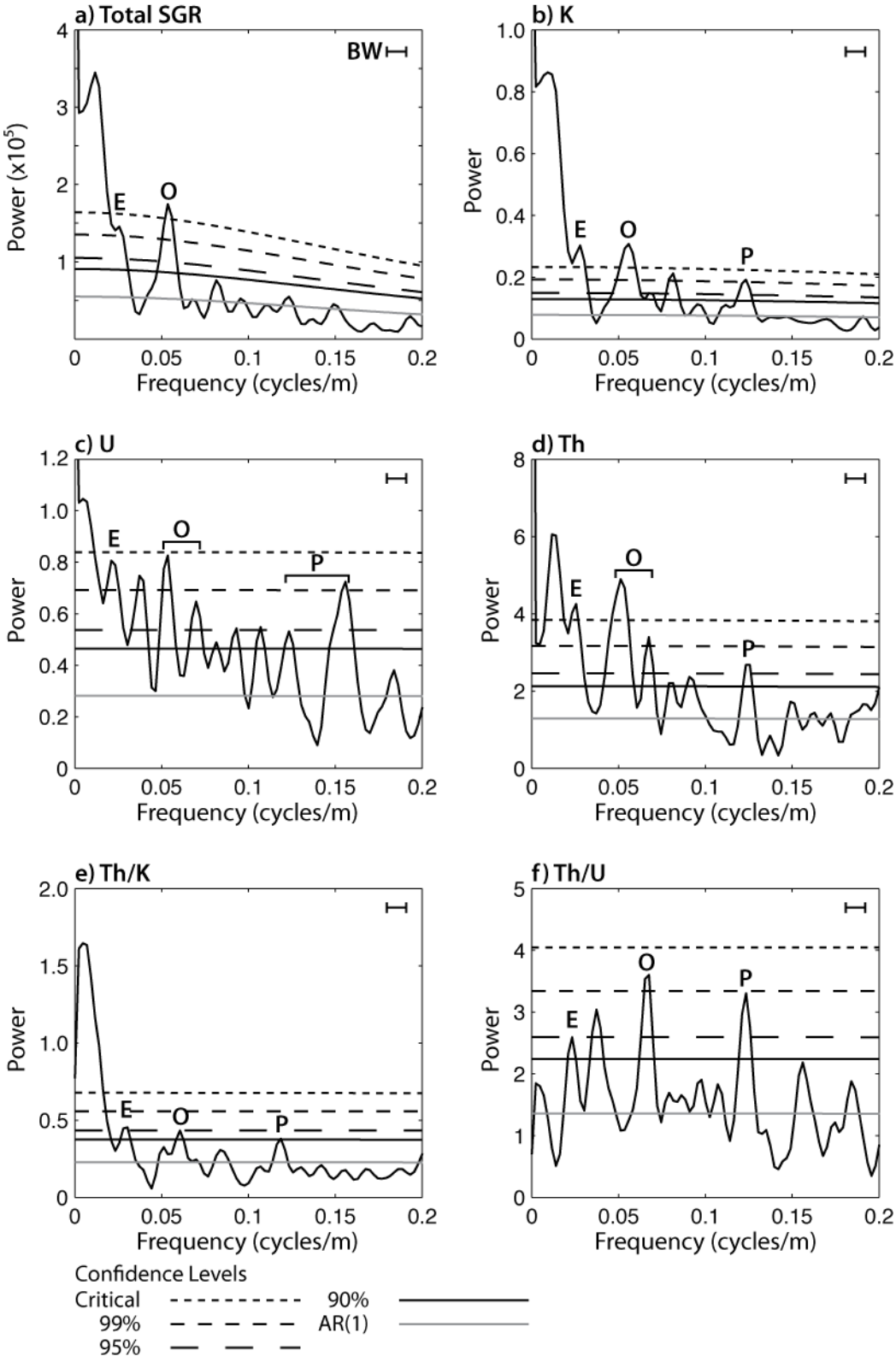

Figure 6.6 | REDFIT spectra calculated from the SGR time series. Spectra for each time series were calculated using an ofac of 4 and 6 WOSA segments providing 8 degrees of freedom. Significant frequencies thought to represent the main eccentricity (E), obliquity (O) and precession (P) Milankovitch periods are marked. The horizontal bar in each spectrum represents a bandwidth of 0.011 cycles/m.

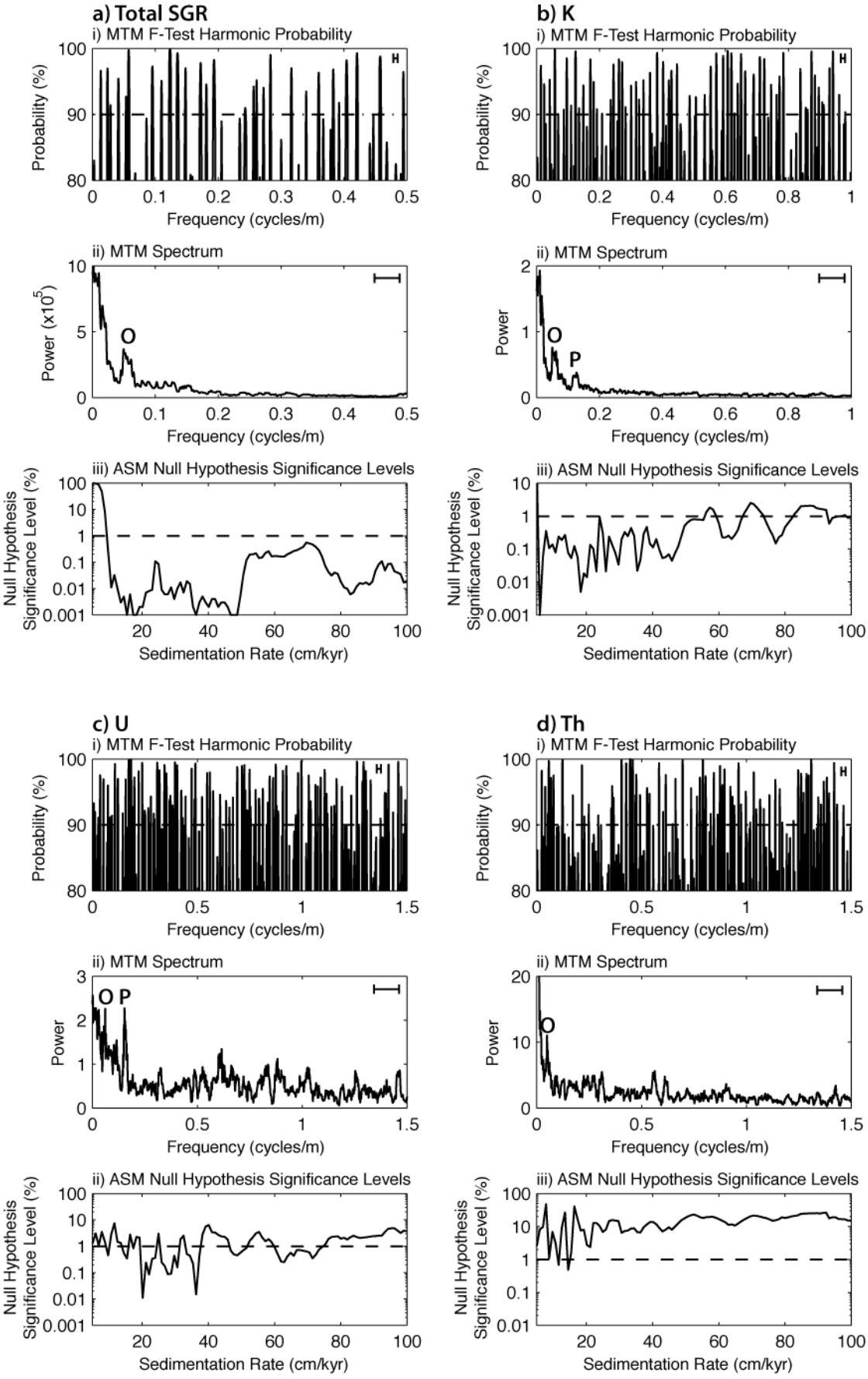
a) Total SGR
i) MTM F-Test Harmonic Probability
Probability (%)
Frequency (cycles/m)
H
ii) MTM Spectrum
Power (x10^5)
O
iii) ASM Null Hypothesis Significance Levels
Null Hypothesis Significance Level (%)
Sedimentation Rate (cm/kyr)
b) K
i) MTM F-Test Harmonic Probability
ii) MTM Spectrum
Power
O
P
iii) ASM Null Hypothesis Significance Levels
c) U
i) MTM F-Test Harmonic Probability
ii) MTM Spectrum
O P
ii) ASM Null Hypothesis Significance Levels
d) Th
i) MTM F-Test Harmonic Probability
ii) MTM Spectrum
O
iii) ASM Null Hypothesis Significance Levels

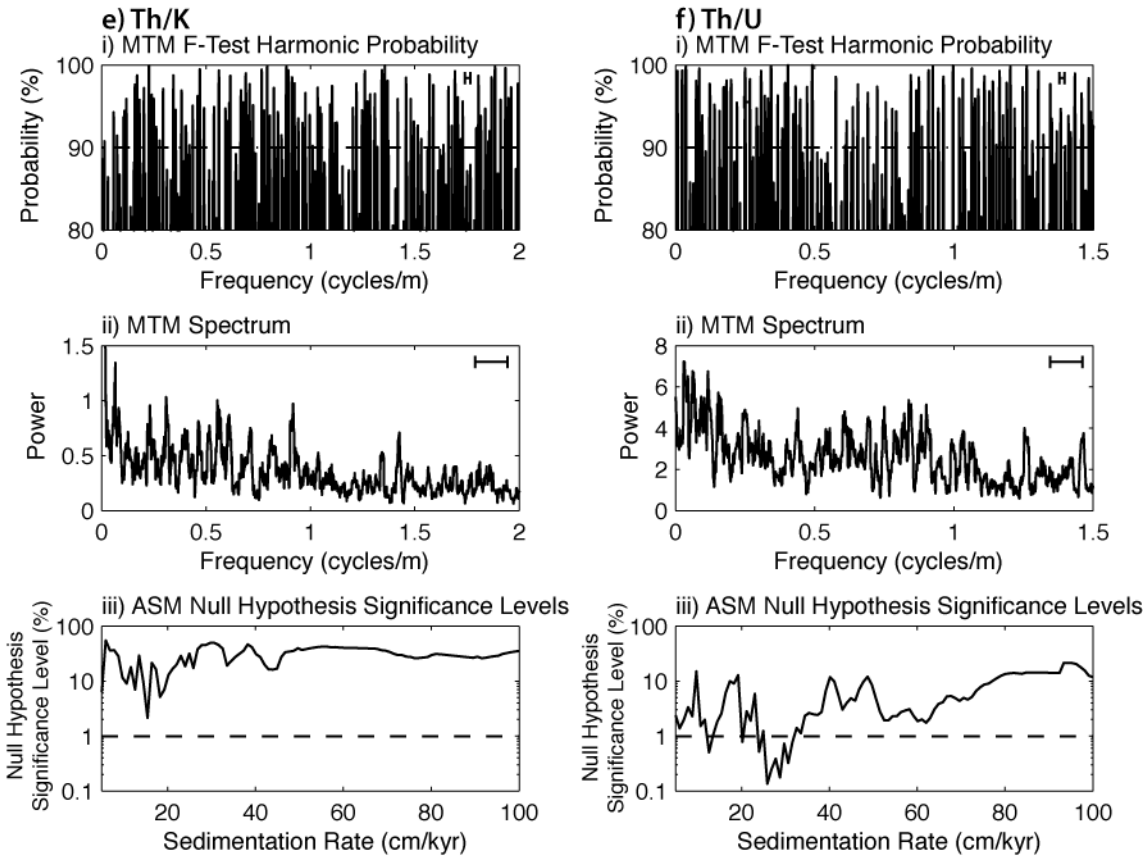

Figure 6.7 | Multi-Taper Method spectral and Average Spectral Misfit results. (i) Significant frequencies (>90%) were identified from each time series using the MTM harmonic F-test (Table 6.4). Bandwidth represented by horizontal bar. (ii) The MTM spectra was utilised to determine the frequency range that corresponded with ~80% of the total variance. The variance (area below the curve) was calculated for every 0.5 cycles/m increment. Bandwidth represented by horizontal bar. Significant peaks thought to represent the main eccentricity (E), obliquity (O) and precession (P) Milankovitch periods are marked. (iii) ASM calculations were run using all orbital terms (black solid line). Only those SAR estimates with H_o significance levels below the critical level (0.99009901%; dashed line) are included within Table 6.5. ASM analyses were not performed for Th/K as insufficient significant frequencies were identified (Table 6.4).

Figure 6.8 (next two pages) | Wavelet spectra calculated for each time series. (i) Wavelet spectra illustrate the spatial distribution of frequencies throughout the individual time series. Bold contours represent the 90% confidence level. (ii) Global wavelet spectra represent the average variance throughout the entire time series. Those frequencies exceeding the 90% confidence level (solid line) and corresponding to the predicted eccentricity (E), obliquity (O) and precession (P) periods are marked.

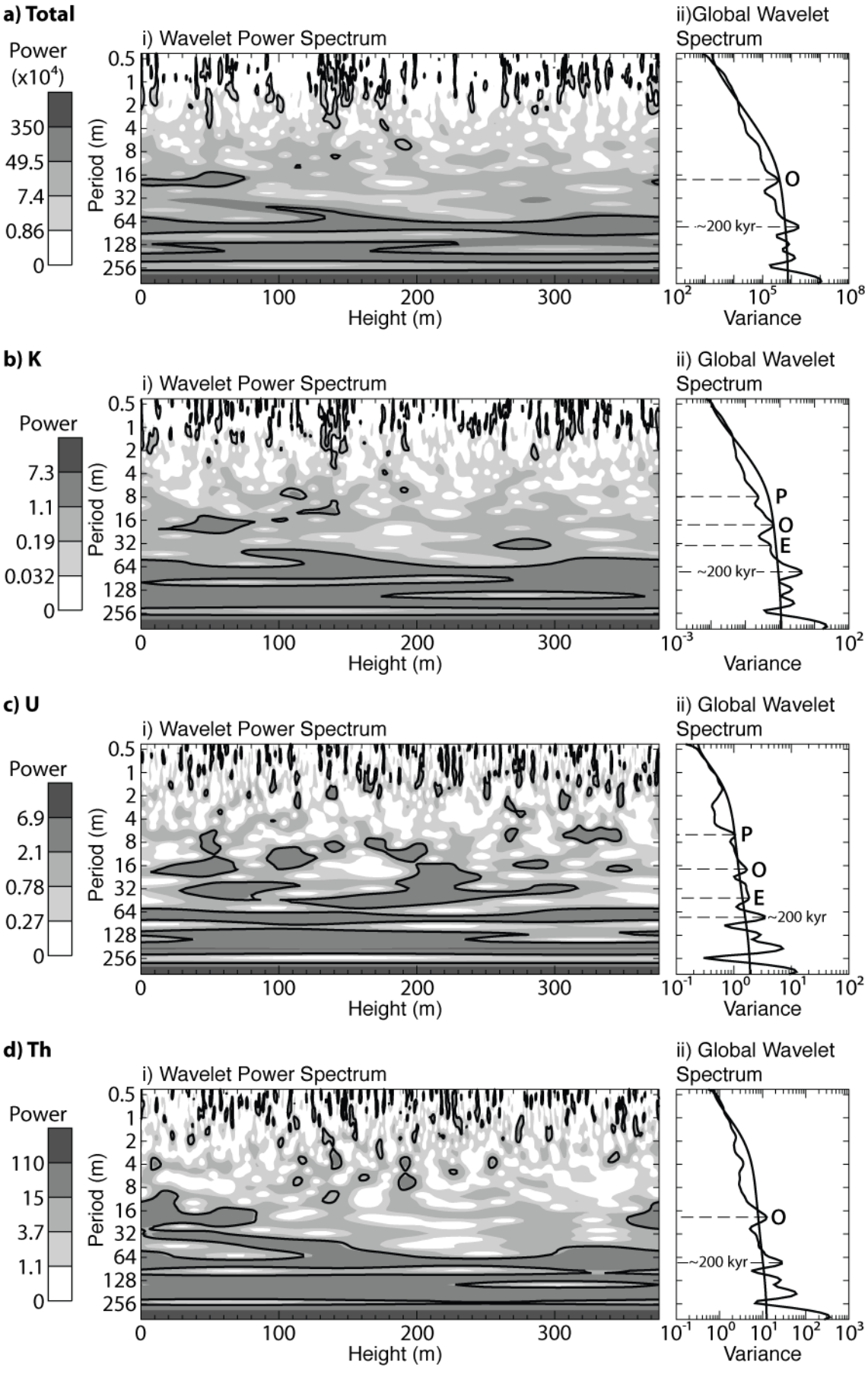
a) Total
i) Wavelet Power Spectrum
ii)Global Wavelet Spectrum
Power (x10^4)
350
49.5
7.4
0.86
0
Period (m)
0.5
1
2
4
8
16
32
64
128
256
0
100
200
300
Height (m)
O
~200 kyr
10^2
10^5
10^8
Variance
b) K
i) Wavelet Power Spectrum
ii) Global Wavelet Spectrum
Power
7.3
1.1
0.19
0.032
0
P
O
E
~200 kyr
10^-3
10^2
c) U
i) Wavelet Power Spectrum
ii) Global Wavelet Spectrum
Power
6.9
2.1
0.78
0.27
0
~200 kyr
10^-1
10^0
10^1
10^2
d) Th
i) Wavelet Power Spectrum
ii) Global Wavelet Spectrum
Power
110
15
3.7
1.1
0
~200 kyr
10^-1
10^0
10^1
10^2
10^3

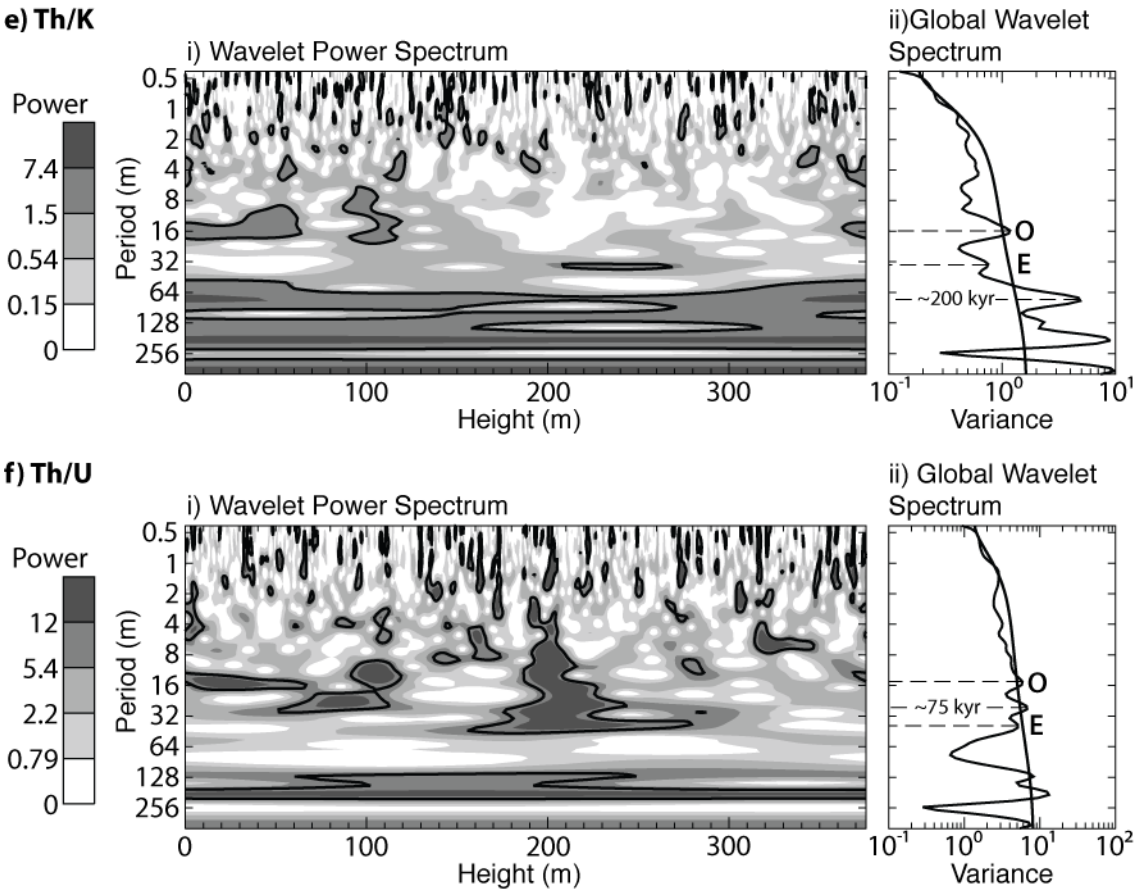
e) Th/K
i) Wavelet Power Spectrum
ii)Global Wavelet Spectrum
Power
7.4
1.5
0.54
0.15
0
Period (m)
0.5
1
2
4
8
16
32
64
128
256
0
100
200
300
Height (m)
O
E
~200 kyr
10^{-1}
10^{0}
10^{1}
Variance
f) Th/U
i) Wavelet Power Spectrum
ii) Global Wavelet Spectrum
Power
12
5.4
2.2
0.79
0
Period (m)
0.5
1
2
4
8
16
32
64
128
256
0
100
200
300
Height (m)
O
~75 kyr
E
10^{-1}
10^{0}
10^{1}
10^{2}
Variance

Table 6.5 – ASM Results

Stratigraphic time series*	SAR (cm/kyr)	H_o Level (%)	ASM (cm/kyr)	No. of Orbital Terms
Total	10.70	0.011	6.57E-04	7
	13.55	0.003	8.36E-04	7
	15.45	0.001	7.11E-04	7
	29.70	0.004	1.32E-03	7
	32.55	0.007	1.66E-03	7
	36.35	0.001	1.14E-03	7
	40.15	0.002	1.50E-03	7
	43.00	0.002	1.43E-03	7
	55.35	0.143	3.16E-03	7
	59.15	0.165	3.29E-03	7
	77.20	0.031	2.93E-03	7
	82.90	0.006	2.30E-03	7
	86.70	0.015	2.73E-03	7
	88.60	0.014	2.86E-03	7
	93.35	0.049	2.81E-03	6
	99.05	0.017	2.56E-03	6
K	5.95	0.001	1.15E-04	7
	8.80	0.106	3.78E-04	7
	10.70	0.079	4.31E-04	7
	12.60	0.188	5.98E-04	7
	15.45	0.053	5.73E-04	7
	18.30	0.005	5.01E-04	7
	20.20	0.014	5.99E-04	7
	23.05	0.021	7.16E-04	7
	25.90	0.021	7.15E-04	7
	29.70	0.034	9.18E-04	7
	32.55	0.245	1.41E-03	7
	35.40	0.022	1.04E-03	7
	40.15	0.111	1.47E-03	7
	43.00	0.053	1.34E-03	7
	45.85	0.044	1.41E-03	7
	55.35	0.755	2.51E-03	7
	61.05	0.223	2.18E-03	7
	63.90	0.201	2.22E-03	7
	77.20	0.147	2.29E-03	7
	93.35	0.589	2.75E-03	6
	99.05	0.881	3.11E-03	6

Stratigraphic time series	SAR (cm/kyr)	H_o Level (%)	ASM (cm/kyr)	No. of Orbital Terms
U	9.75	0.448	3.20E-04	7
	15.45	0.342	4.76E-04	7
	17.35	0.836	6.27E-04	7
	20.20	0.011	3.14E-04	7
	22.10	0.086	4.95E-04	7
	27.80	0.087	5.87E-04	7
	30.65	0.159	7.48E-04	7
	36.35	0.015	5.68E-04	7
	48.70	0.452	1.39E-03	7
	62.95	0.252	1.51E-03	7
	65.80	0.439	1.72E-03	7
	71.50	0.351	1.75E-03	7
Th	11.65	0.687	5.83E-04	7
	14.50	0.483	6.69E-04	7
Th/U	12.60	0.502	5.05E-04	7
	20.20	0.784	8.51E-04	7
	24.00	0.52	9.28E-04	7
	25.90	0.135	7.65E-04	7
	28.75	0.175	8.73E-04	7
	30.65	0.323	1.05E-03	7

*Only stratigraphic time series with significant SAR estimates are provided.

6.4 Interpretation

6.4.1 Outcrop SGR

The initial interpretation of the SGR data would suggest an inverse relationship between radioelement concentration and the abundance of coarse-grained turbiditic sandstone deposits. However, to ensure the correct interpretation, SGR data obtained from sand and marl lithologies should be interpreted separately (Rider, 1996; Ruffell and Worden, 2000).

The SGR data obtained from the coarse-grained submarine fan deposits indicate their initiation is characterised by a rapid depletion in values, especially within total SGR and K concentrations. The observed depletion in radioelement concentrations is likely associated with an increased abundance of relatively non-radioactive quartz (Table 2.2). Petrographic studies of the systems submarine fan sediments suggest an average quartz contents of 43.9% (Das Gupta and Pickering, 2008) supporting such an interpretation. The subsequent gradual increase in SGR values likely reflects the decreasing abundance of quartz and the concurrent increase in fine-grained sediments, which typically are associated with more radioactive minerals (Rider, 1996). The resultant SGR trend creates a characteristic bell-shaped curve similar to that expected for a fining-upward deposit with increasing shale volume (Rider, 1990; Rider, 1996).

Interpretation of the SGR variation observed within the inter-fan marl sediments is likely similar to that described for the younger Guaso System (Chapter 4). With both the Banaston and Guaso systems sharing the same source area (Caja et al., 2010) the causes of SGR variability are likely comparable. Such a scenario suggests that variation in terrigenous run-off from the nearby Tremp-Graus basin controlled radioelement concentrations.

Calculated Th/K and Th/U ratios obtained from the sediments can also be used to identify mineralogical and palaeoenvironmental variability. The majority of Th/K compositions (mean Th/K value 4.9) lie within the usual 4 to 6 range indicating a mix of both kaolinite and illite/muscovite (Fig. 6.5) (Myers, 1989; Rider, 1996). Short intervals do however exceed this range suggesting the possible dominance of either kaolinite (Th/K > 6) or illite/muscovite (Th/K < 4).

Mean Th/U values of 4.4 are within the average values expected for mudrocks of 3 to 6 which suggests the majority of the systems sediments were deposited within a ‘normal’ environment (Rider, 1996). The range of values within the Th/U record does however suggest benthic conditions varied between oxygenated and reducing over short periods although these may be the result of detrital heavy mineral concentrations (Rider, 1996).

6.4.2 Spectral interpretation

Interpretation of the spectral results, in terms of orbital cyclicity, is achieved using the independently determined SAR estimates from the ASM method. Of the numerous SAR estimates identified, the two most significant and consistent ASM results of ~15 to 20 (mean = 18.54 cm/kyr) and ~35 to 36 cm/kyr (mean = 36.03 cm/kyr) shall be considered. Using these SAR estimates it is possible to calculate a temporal period for each dominant frequency. From these calculations it is apparent that these two SAR estimates depend upon different orbital periods being assigned to a frequency For example, the 0.053-0.058 cycles/m frequency being assigned the short eccentricity (18.54 cm/kyr) or long obliquity (36.03 cm/kyr). Further temporal constraint provided by the biostratigraphic age model (Fig. 6.2) is therefore required to determine which of these assignments is more realistic.

The biostratigraphic age model suggests that of the two significant ASM results, only those within the ~35 to 36 cm/kyr range correspond to both the models 26.59±14.67 and 35.18±0.56 cm/kyr SAR estimates. The corroboration between these estimates indicates that the ~0.025 and ~0.055 cycles/m frequencies correspond to eccentricity and obliquity respectively. However, the model also suggests that between 11 to 134.5 m sediments accumulated at a rate of 139.49±16.49 cm/kyr prior to a decrease in SAR to 35.18±0.56 cm/kyr. Such a drop in SAR should be accompanied by a decrease in orbital frequencies and therefore visible within the wavelet spectra (Lau and Weng, 1995; Weedon, 2003). Although a frequency change is observed within the lower 150 m, the frequencies actually decrease from ~0.024 to ~0.018 cycles/m indicate a potential increasing SAR, contradicting the age model. The stability of the bounding 0.013 and 0.053 cycles/m frequencies (Fig. 6.8) however, suggest that the SAR remained within the 35-36 cm/kyr range throughout.

An explanation, other than a change in SAR, for the differential frequency stability within the lower ~150 m is provided by Rial (1999). Using a tuned $\delta^{18}O$ time series, Rial (1999) demonstrated that differential frequency stability can exist between obliquity and eccentricity due to a contrasting climate response to orbital forcing (e.g., frequency modulation). Assuming a similar encoding of orbital forcing by the Banaston System sediments, the differential frequency stability may be interpreted as reflecting a non-linear response to orbital forcing rather than a shift in SAR.

Based upon the SAR being continuous throughout the stratigraphic series at 36.03 cm/kyr, the temporal period of each significant frequency can be determined (Table 6.4). The ~0.024, ~0.056, ~0.068 and ~0.123 cycles/m frequencies are therefore interpreted as reflecting the average short eccentricity (109-kyr), long and short obliquity (52 and 40 kyr) and average precession (23 kyr) Milankovitch cycles

(Table 6.2). Other consistent frequencies representing periods of ~200, ~70 and ~30 kyr are also commonly identified within orbitally forced climatic spectra and likely represent the non-linear response of the climate system to periodic forcing (Ruddiman et al., 1989; Clemens et al., 1991; Hinnov, 2000; Huybers and Wunsch, 2004).

6.5 Discussion

6.5.1 Age model discrepancy

The observed discrepancy between the biostratigraphic and orbital SAR estimates, within the lower 134.5 m, are likely explained by the biostratigraphic age models method of construction. The contested 139.49±16.49 cm/kyr SAR within this interval is due to the estimated position of sample BB013 containing the LO of *B. inflatus* compared to that of the FO of *N. fulgens* contained within the Ban-134.5m sample. The SAR calculated between these samples is based upon the assumed lateral stratigraphic correlation between the top of the B-III off-axis heterolithic deposit (located here at 11 m height in Figure 6.5) with the top of the coeval axial fan and MTC deposits located ~7 km to the southeast (Fig. 3.2). With the axial sediments likely being deposited at a higher rate compared to the off-axis position studied here, along with correlation over a large distance, significant uncertainty therefore exists within this SAR estimate. The overlying FO of *N. fulgens* and FO of *C. gigas* used to calculate the 35.18±0.56 cm/kyr SAR, are far more accurate as these samples are collected directly from the stratigraphy used to construct the biostratigraphic age model. Support for the reliability of this upper interval is provided by the independent identification of a similar 36.03 cm/kyr SAR using orbital cyclicity. The prevalence of these orbital frequencies demonstrates that the 36.03 cm/kyr SAR was dominant throughout the measured section, leaving the 139.49±16.49 cm/kyr SAR as being unlikely.

With the biostratigraphic age model below the FO of *N. fulgens* being potentially unreliable, an alternate age model is constructed based around the 36.03 cm/kyr SAR identified from orbital cyclicity. The floating orbital time scale is tied to the geological time scale of Gradstein et al. (2004) using the 46.57 Ma FO of *N. fulgens* as a datum (Fig. 6.2). Age estimates determined from the biostratigraphic and orbitally derived age models are compared in Table 6.6.

Within this orbital age model the basal age estimates for the B-V sequence are likely to be the most accurate as this located only 0.5 m from the LO of *N. fulgens* tie point. As this distance from the tie point increases so does the uncertainty within the age model due to potential varying accumulation rates, hiatuses, etc. Only with an orbitally tuned record will the timing of the coarse clastic supply to the basin be adequately determined.

Table 6.6 – Complex age estimates

Complex	Height (m)*	Orbital age model Age (Ma)†	Biostratigraphic age model§ Min age (Ma)	Mid age (Ma)	Max age (Ma)
Banaston-VI marl	1016	45.90	45.87	45.88	45.89
Banaston-VI sand	970	46.03	46.01	46.01	46.02
Banaston-V marl	929	46.14	46.12	46.13	46.14
Banaston-V sand	789	46.53	46.53	46.53	46.53
Banaston-IV marl	775	46.57	46.57	46.57	46.57
Banaston-IV sand	700	46.78	46.62	46.62	46.63
Banaston-III marl	685	46.82	46.63	46.63	46.64
Banaston-III heterolithic	650	46.92	46.65	46.66	46.67
Base of section	639	46.95			

*Height represents that to top of complex determined within Chapter 3.
†Orbital age estimates based upon the application of the 36.03 cm/kyr SAR to the studied section and tied to the geological time-scale (Gradstein et al., 2004) using the LO of *N. fulgens*.
§Biostratigraphic age estimates those from Table 3.4.

Table 6.7 – Sequence durations*

Sequence	Height§ (m)	Orbital Duration (Myr)	Biostratigraphic model Duration (Myr) Min	Mid	Max	Expected† Duration (Myr)
Banaston-VI	1016	0.24	0.23	0.25	0.27	0.40
Banaston-V	929	0.43	0.43	0.44	0.45	0.40
Banaston-IV	775	0.25	0.06	0.07	0.08	0.40

*Only durations of complete sequence calculated from age estimates in Table 6.6.
†Expected sequence durations of Pickering and Bayliss (2009).
§Height represents that to top of complex determined within Chapter 3.

6.5.2 Banaston System sequence timing and duration

According to the orbital forcing hypothesis of Pickering and Bayliss (2009) each submarine fan is paced by the 404-kyr-long eccentricity Milankovitch cycle. Testing of this hypothesis can be achieved using the proposed age model to estimate the timing and duration of each sequence (Fig. 6.2; Table 6.7). The cessation of the Banaston System is estimated to have occurred at 45.90 Ma whilst the basal age of the Banaston-III sequence heterolithic package is estimated at 46.95 Ma. The duration of the stratigraphic series is therefore 1.05 Myr.

The orbital forcing hypothesis predicts that the three complete sequences, each being 404 kyr in duration, should have accumulated over a 1.21 Myr period. Based upon the proposed age model, the Banaston-IV to VI sequences were instead deposited over a shorter period of 0.92 Myr. Discrepancy also exists between the predicted and calculated sequence durations with only the Banaston-V sequence accumulating over a period similar to that expected (Table 6.7). The observed duration of the entire measured section and individual sequence are therefore largely inconsistent with the 404 kyr orbital forcing hypothesis of Pickering and Bayliss (2009).

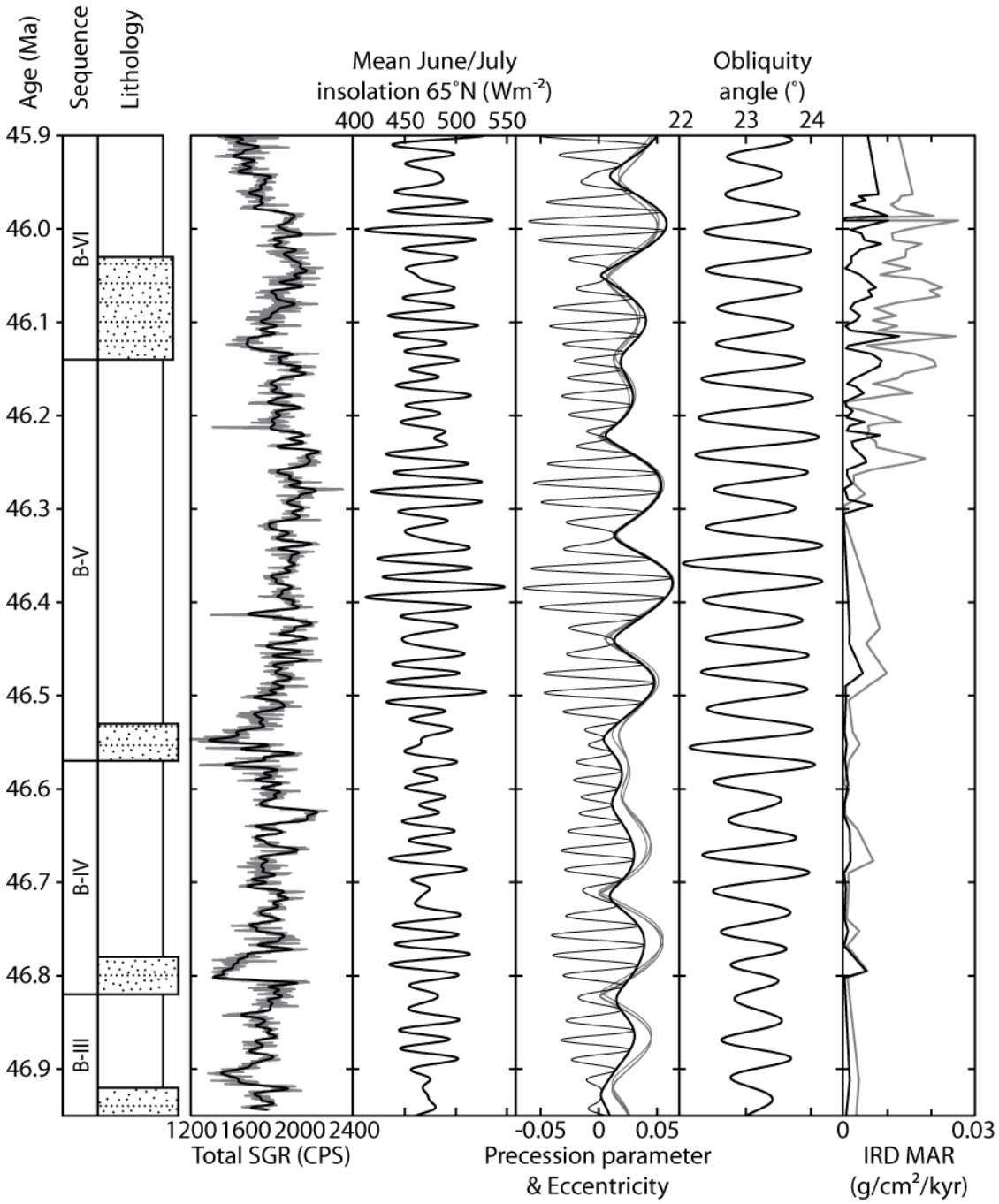

Figure 6.9 | Calculated insolation, orbital curves and observed periods of IRD accumulation compared with periods of submarine fan complex deposition. Using the orbital age model the height scale of the total SGR stratigraphic time series was place onto the geological time scale (Fig. 6.2). Orbital and insolation curves calculated using the equations of Laskar et al. (2004; 2011). Grey eccentricity curves represent the more recent estimates from Laskar et al. (2011). Ice rafted debris (IRD) data record the mass accumulation rates (MAR) of sediment obtained from the Lomonosov Ridge (St. John, 2008). IRD data separated into sediment grain-size between 150-250 μm (black) and >250 μm (grey). Based solely upon the timing of the submarine fan complexes (Section 6.5.2), the 404-kyr pacing is refuted. However, the timing of each submarine fan complex (periods of depleted total SGR values) appears to coincide with periods of eccentricity minima. Such a relationship, along with the coeval presence of IRD within the Arctic Ocean, would indicate a possible glacio-eustatic forcing mechanism operated during deposition of the Banaston System. The irregular pacing of these events are likely dependant upon the occurrence of ideal orbital conditions providing conditions beneficial for polar ice accumulation (for details refer to Chapter 3).

6.5.3 Forcing of system sediments

6.5.3.1 Inter-fan

The observed radioelement variations within the inter-fan sediments likely correspond to orbitally forced changes in run-off from the adjacent Tremp-Graus basin. Modelling the affect of obliquity and precession during the Eocene indicates that between periods of intensified and muted seasonality, both precipitation and surface run-off varied significantly (Sloan and Huber, 2001). Contrasts between these two climatic settings will have conceivably influenced the supply of terrigenous material to the Ainsa basin. With radioelement concentration being closely linked to terrigenous minerals (Chapter 4), the oscillations recorded within the SGR data likely represent both obliquity and precession.

6.5.3.2 Submarine fan

The ~250 and ~430 kyr pacing of the Banaston System submarine fan complexes (Table 6.7), unlike the inter-fan sediments, do not appear regularly paced and thereby appear initially inconsistent with the orbital forcing model of Pickering and Bayliss (2009). However, as discussed in Chapter 3, the proposed orbitally paced glacio-eustatic mechanism supplying voluminous coarse clastics to the basin may still be valid. It is proposed that orbitally forced periods of insolation minima lead to the formation of ephemeral ice sheets and hence a lowering of sea-level. Such a mechanism suggests that the timing of voluminous coarse clastic sediment supply to the basin would correspond to periods of insolation minima brought about by certain combination of orbital conditions.

Testing the above hypothesis is achieved by comparing the significant SGR depletions, here interpreted as reflecting periods of increased coarse clastic supply to the basin, with the calculated orbital and insolation parameters (calculated for the 45.90 to 46.95 Ma period) along with IRD records obtained from the Arctic Ocean (Fig. 6.9; St. John, 2008). Comparisons between these records indicate that the base of the off-axis fan and heterolithic deposits broadly correspond to intervals of low eccentricity, diminished insolation variability but inconsistent obliquity and precession conditions. Of these only the eccentricity parameter shall be considered, as the uncertainties within the orbital age model will have a greater affect upon the accurate determination of the higher frequency obliquity and precession orbital conditions.

The potential coincidence between the supply of coarse-grained clastic sediment to the basin and intervals of IRD accumulation and low eccentricity, although irregularly paced, are consistent with the glacio-eustatic mechanism proposed by

Pickering and Bayliss (2009). During these intervals of eccentricity minima, the Earth-Sun distance was maximised thereby reducing the total insolation resulting in conditions beneficial for ice accumulation. The presence of IRD within middle Eocene Arctic Ocean sediments, coeval to the deposition of the B-IV to B-VI sequences clearly indicate the existence of Northern Hemisphere polar ice. The irregular timing of these events may indicate certain background conditions were required that enabled ice to accumulate. These may include atmospheric CO_2 concentrations being below ~280 to 750 ppmv (Pearson and Palmer, 2000; Royer, 2006; DeConto et al., 2008) and the coincidence of ideal orbital conditions.

Inter- and intra-basinal tectonics will have also influenced submarine fan deposition within the Banaston System. Deposition of the Banaston System immediately followed a period of basin reorganisation represented within the basin as the angular unconformity separating the Lower and Upper Hecho groups (Figs. 1.8, 1.18). Following this pulse of tectonic activity, increased denudation within the hinterland will have increased the volume and calibre of the sediments available for transport. Within the Banaston System this is evident from the presence of six submarine fans compared to the other systems, which consistently contain two to three. The increased calibre of sediment is also apparent within the system with the initial B-I and B-II submarine fan complexes dominated by large limestone olistoliths, pebbly conglomerates and very-coarse sandstones (Bayliss, 2010).

Tectonic activity of the bounding Mediano and Boltaña anticlines will have also influenced the spatial development of the Banaston System. Bayliss (2010) indicates that the continuous uplift of the Mediano anticline forced the migration of the individual submarine fans toward the southwest consistent with the “see-saw” tectonic model (Figs. 1.15, 1.16) (Pickering and Bayliss, 2009). According to this model, the termination of the Banaston System is linked to uplift of the Boltaña anticline forcing the basins depositional axis to the northeast. Using available palaeomagnetic data (thrust rotation and anticlinal tightening) for the two anticlines it is possible to test this mechanism by comparing the expected timing of the unconformity associated with the termination of the Banaston System (45.9 Ma) and the thrust rotational data (Fig. 3.7). A peak in rotational rates is observed within the Mediano anticline, which is inconsistent with the “see-saw” tectonic mechanism. However, the lack of blind thrust rotation beneath the Boltaña anticline at ~45.9 Ma prevents the mechanism from being adequately tested.

The study of the Banaston System indicates that whilst climate may have controlled the timing of submarine fan deposition, their lateral distribution was likely influenced by tectonics. Such a result is similar to those observed within other deep-marine basins where, researchers identify glacio-eustasy as being the dominant control

on the timing of coarse-clastic sediment supply whilst tectonics influenced their spatial distribution (Manley and Flood, 1988; Feeley et al., 1990; Pickering et al., 1999; Prins and Postma, 2000; Normark et al., 2006).

6.5.4 Application of results to previous records

With both a reliable SAR estimate and the timing of submarine fan complex deposition determined, local cyclic records and correlations between the Banaston System's sequences and other sequence stratigraphic interpretations can be attempted.

Locally, applying the 36.03 cm/kyr SAR to the proposed 12-13 m sedimentary cycles observed by Remacha et al. (2003), suggests they occurred over a 33-36 kyr period which is similar to the expected 39-kyr obliquity period (Table 6.2). With these deposits being located a further ~1 km from the depositional axis, the supply of sediment and hence the SAR would have been likely reduced therefore accounting for the discrepancy in age. Assuming that these 12-13 m cycles correspond to obliquity this would enable an SAR of ~30-33 cm/kyr to be estimated for the section studied by Remacha et al. (2003).

The presence of firm-grounds located a the top of the B-I and II fining-upward sequences were interpreted as reflecting periods of waning sediment supply possibly linked to glacio-eustatic processes by Bayliss (2010). Using the observed association between the overlying (B-III to B-VI) submarine fan complexes and periods preferential to ice accumulation lends supports this interpretation. The timing of submarine fan deposition throughout the Banaston System was therefore likely controlled by an irregular orbitally paced glacio-eustatic forcing mechanism.

Using the timing of low-stand conditions within Banaston System, it should be possible to link their occurrence with other middle Eocene glacio-eustatic records. Using the records from the New Jersey margin and South Tasman Rise (Browning et al., 1996; Pekar et al., 2005) the Banaston System may have coincided with the stratigraphic sequence boundaries (periods of relative lowered sea-level) between the E5 to E7 and Yp5 to Lu2 sequences respectively. These sequence boundaries correspond to proposed oxygen isotope events, which are suggested to represent periods of ice growth and 20 to 40 m sea-level change (Pekar et al., 2005). Although these records are of a lower resolution they lend support for the proposed glacio-eustatic mechanism for the supply of voluminous coarse-sediment supply to the Ainsa basin.

6.6 Summary

The immediate conclusions from this chapter are here outlined. The wider interpretation and context of these results shall be discussed in Chapter 8.

Spectral gamma ray data collected from the Banaston System inter-fan and off-axis fan deposits are here shown to contain cyclic components consistent with orbital eccentricity, obliquity and precession. During inter-fan deposition the supply of terrigenous material to the basin and potentially bottom water redox conditions were dominantly paced by the obliquity orbital cycle.

Identification of orbital periods within the stratigraphic time series enabled the average SAR of 36.03 cm/kyr to be determined. The orbital age model enabled the construction of new time scale tied to the geological time scale of Gradstein et al. (2004) using the FO of the nannofossil *N. inflatus*. The age model suggests the studied sediments were deposited between 45.90 and 46.95 Ma during nannofossil zones NP14b and NP15a of Martini (1971).

Using the age model, the variable pacing of the submarine fan complexes, between 240 and 430 kyr, appear inconsistent with the 404-kyr long eccentricity forcing proposed by Pickering and Bayliss (2009). However, comparing the timing of each submarine fan complex with the insolation curve for June/July at 65˚N, calculated orbital conditions and IRD records, indicate their timing may have coincided with periods preferential to ice accumulation. The formation of ephemeral ice-sheets and resultant lowering of sea-level could have caused the mobilisation of voluminous coarse-grained clastic sediment from the shelf into the deep-marine Ainsa basin depositing a low-stand submarine fan complex. The pacing of submarine fan complexes, therefore, appears consistent with an orbitally forced glacio-eustatic mechanism similar to the model of Pickering and Bayliss (2009) but apparently less regular than they envisaged, for reasons that cannot be fully explained at this stage.

Chapter 7
Sub-Milankovitch Cyclicity

7.1 Introduction

7.1.1 Chapter objectives

Evidence exists for the presence of sub-Milankovitch millennial-scale cycles as far back as the Cambrian (Anderson, 1982; Elrick et al., 1991; Williams, 1991; Dansgaard et al., 1993; Elrick and Hinnov, 1996, 2007; Mawson and Tucker, 2009; Tucker et al., 2009; Franco et al., 2012). If such cycles are an intrinsic part of the Earth's climatic system then (like Milankovitch cycles) they should be present in the geological record, irrespective of the average climatic state of the planet. This idea can be tested through examination of stratigraphically expanded sedimentary records from so-called 'greenhouse' periods in Earth history during which time the continental cryosphere was likely minimal in extent.

In this chapter, the elemental composition of the Ainsa System's Well A6 core is presented at high-resolution in order to investigate the presence of any sub-Milankovitch cyclicity.

7.1.2 The Ainsa System

An opportunity to investigate the presence of sub-Milankovitch cyclicity within siliciclastic deposits that accumulated at an active convergent plate margin is present in sediment cores from the Middle Eocene deep-marine Ainsa basin, Spanish Pyrenees. Drilling took place as part of the FORCE Deep Water Clastic Workgroup based at University College London (Pickering and Corregidor, 2005). This research focused on the Ainsa System, one of eight depositional systems that accumulated in the deep-marine Ainsa basin (Chapter 5). The Ainsa System is interpreted as three stacked, structurally-confined, sandy and channelised submarine fans separated by tens of metres of fine-grained marlstones and very thin-bedded, fine- to very fine-grained sandy and silty turbidites (Pickering and Corregidor, 2005; Pickering and Bayliss, 2009). Deposition is interpreted as having occurred in water depths of 400-800 m, mainly as proximal basin-floor fans in a relatively narrow and structurally confined, NNW-SSE orientated sedimentary basin (Pickering and Corregidor, 2005; Pickering and Bayliss, 2009). Deposition of the Ainsa System's sediments occurred between 43.9 and 45.9 Ma, coinciding with nannofossil zone NP15 of Martini (1971; Chapter 3).

Detailed mapping of the Ainsa basin fill shows that there was no routing for the fine-grained sediment gravity flows to bypass the depositional site, and therefore,

crucially, the core represents an archive of geologically near continuous environmental change (Pickering and Corregidor, 2005; Pickering and Bayliss, 2009). The preservation of eccentricity- and obliquity-paced variability within the core bioturbation-intensity record support this view (Heard et al., 2008). Without a near continuous record of environmental change this record would not be retained.

The Well A6 core records fan lateral-margin in the lower half, and inter-fan deposition in the upper half, where sand supply to the deep-marine basin was much reduced, and comprises laminated marlstones, fine-grained, mm-scale turbidites and hemipelagic sediments, which have a consistent structural dip of 20˚, apart from bedding dips in local and thin sediment slide deposits (Fig. 7.1). Laminated sections of the A6 core inter-fan sediments were selected for high-resolution geochemical analysis in order to investigate the presence of sub-Milankovitch cyclicity.

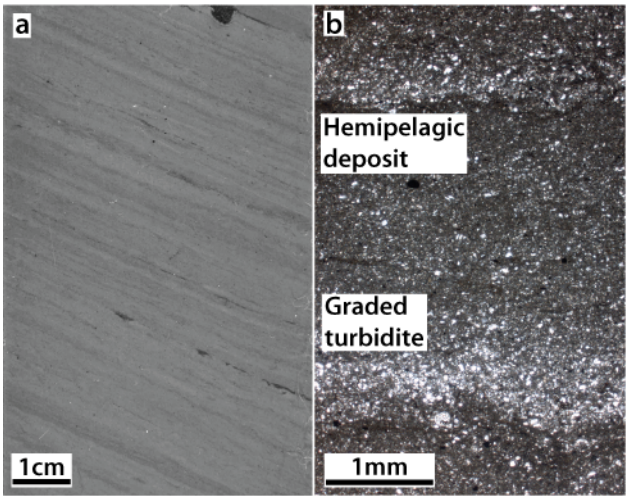

Figure 7.1 | Representative image of A6 core and petrographic thin-section. (a) Laminated sections of core are interpreted as reflecting low-oxygen benthic conditions possibly likely controlled by Milankovitch orbital pacing (Heard et al., 2008). Thin mm-scale turbidites are visible as dark laminae. **(b)** Petrographic thin-sections reveal mm-scale laminations composed of fine-grained turbidites consisting of coarser siliciclastic grains, including reworked carbonate grains, grading up into hemipelagic material. Foraminifera and organic matter (OM) appear to be concentrated at base of each very thin-bedded turbidite.

Figure 7.2 (next page) | Ainsa System geological map and location of Well A6. The Ainsa System is one of eight submarine-fan depositional systems within the Ainsa basin. Well A6 sediments were recovered from the stratigraphy between the top of the Ainsa-II submarine fan and the overlying mass-transport complex (MTC) associated with the off-axis basal parts of the Morillo system. Detailed analysis of the core in terms of Milankovitch cyclicity is provided in Chapter 5.

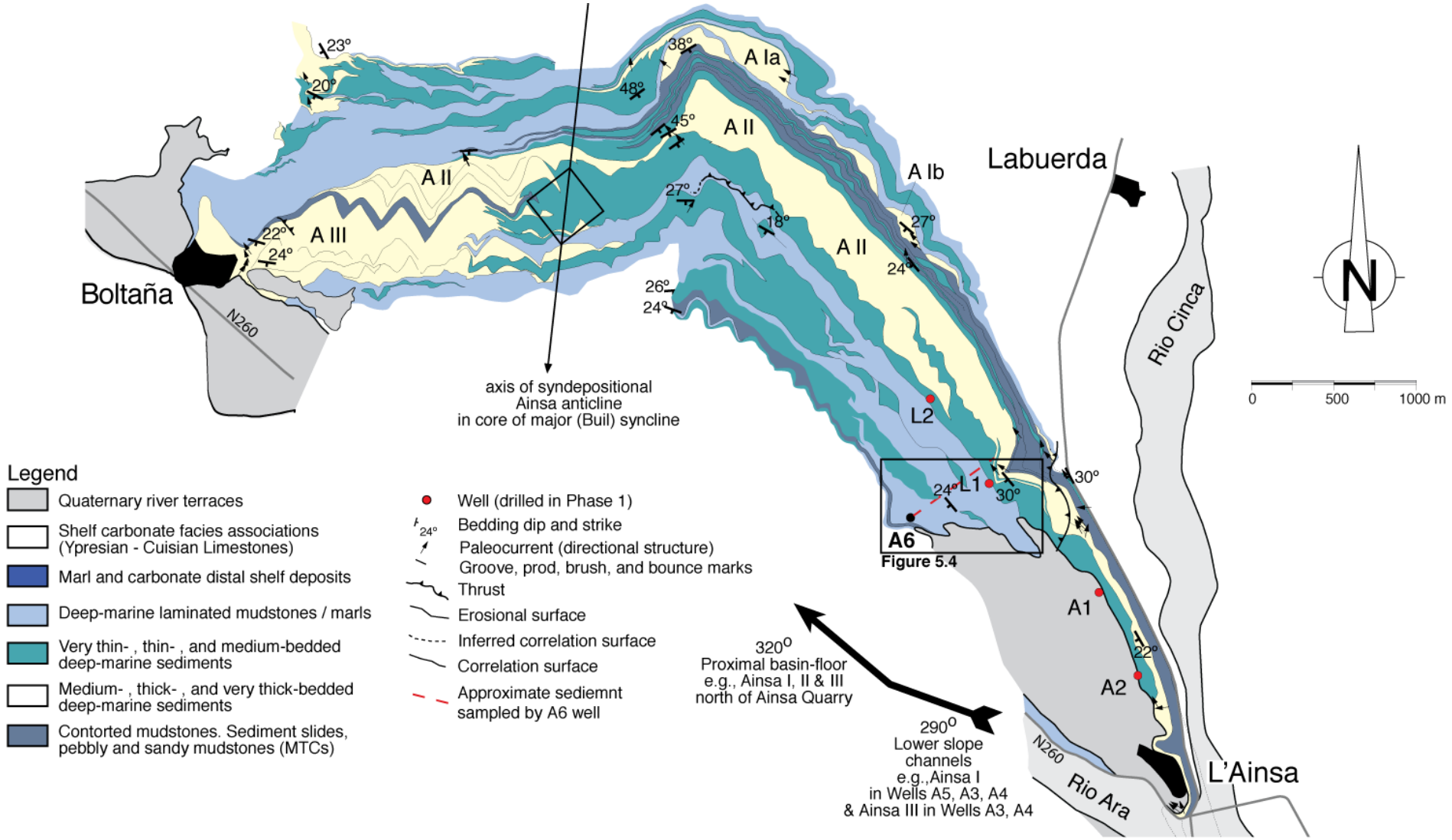
Boltaña
N260
Labuerda
Rio Cinca
Rio Ara
L'Ainsa
A Ia
A Ib
A II
A III
axis of syndepositional
Ainsa anticline
in core of major (Buil) syncline
L1
L2
A1
A2
A6
Figure 5.4
320°
Proximal basin-floor
e.g., Ainsa I, II & III
north of Ainsa Quarry
290°
Lower slope
channels
e.g.,Ainsa I
in Wells A5, A3, A4
& Ainsa III in Wells A3, A4
N
0
500
1000 m
Legend
Quaternary river terraces
Shelf carbonate facies associations
(Ypresian - Cuisian Limestones)
Marl and carbonate distal shelf deposits
Deep-marine laminated mudstones / marls
Very thin- , thin- , and medium-bedded
deep-marine sediments
Medium- , thick- , and very thick-bedded
deep-marine sediments
Contorted mudstones. Sediment slides,
pebbly and sandy mudstones (MTCs)
Well (drilled in Phase 1)
Bedding dip and strike
Paleocurrent (directional structure)
Groove, prod, brush, and bounce marks
Thrust
Erosional surface
Inferred correlation surface
Correlation surface
Approximate sediemnt
sampled by A6 well


A6/22
A6/23
2
3
03
4
5
6
1
2
3
4_short
4_long
5
6
Top
10 cm
10 cm
Kodak
Kodak
Increasing depth (m)


A6/24
1
2
3
4
5
6
A6/25
1
2
3
4
5
10 cm
10 cm
Increasing depth (m)

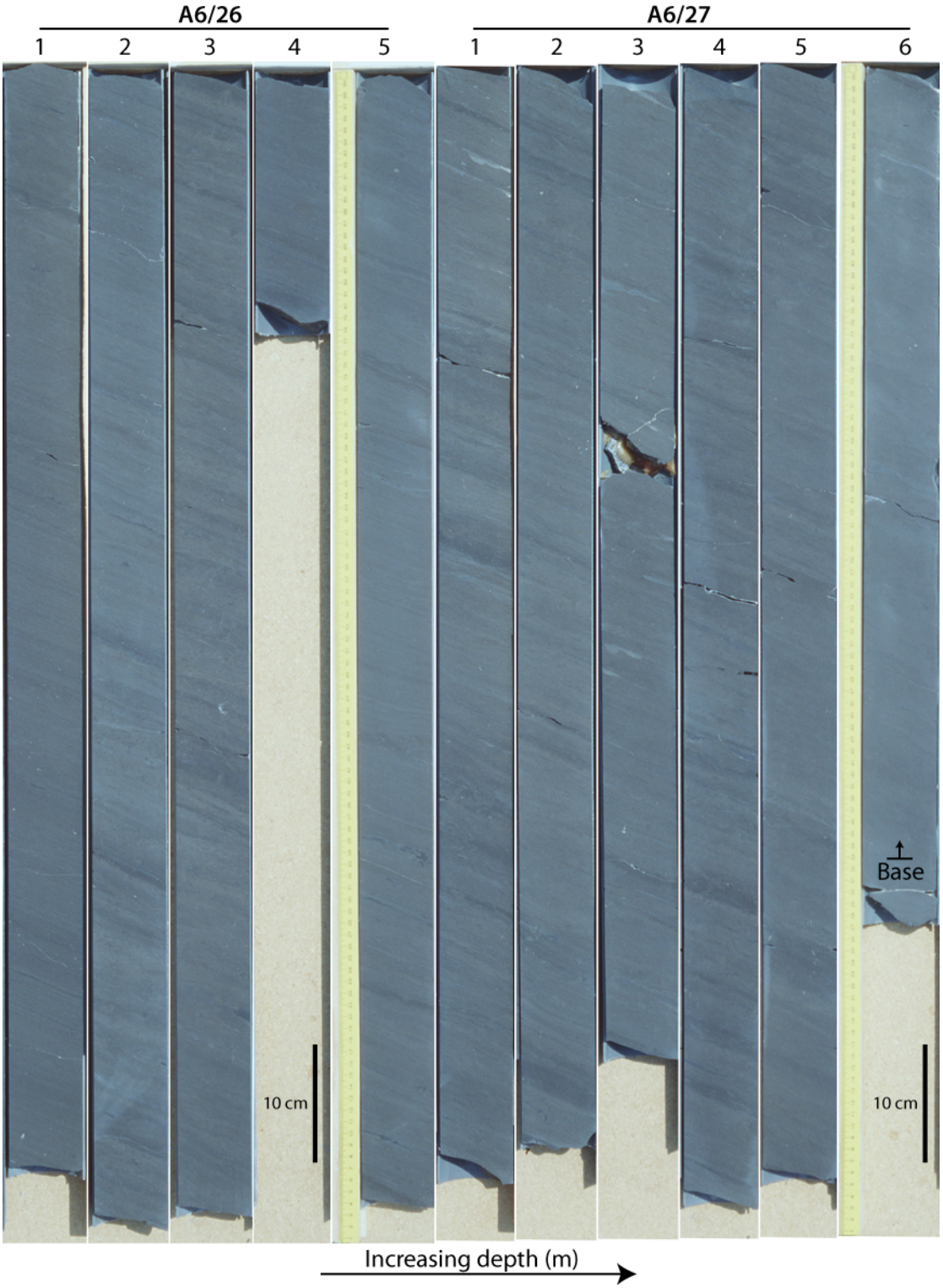

Plate 7.1 (previous three pages) | Photographs of the 36 individual Well A6 core sections discussed in this chapter. Positions associated with fractures, glue and the top and base of each core section were avoided during XRF elemental scanning to avoid spurious results.

7.2 Materials and methods

7.2.1 Studied sediments

The A6/22 to A6/27 core interval was selected for this study corresponding to well depths of 103.44 and 131.55 metres below surface (mbs) (Plate 7.1). This 28-m-core interval consists of 36 individual core sections ranging between 0.21 and 0.99 m in length. The recovered sediments comprise thin-bedded sandstones, siltstone-mudstone laminae and intervals of intensely bioturbated siltstone and silty mudstones associated with the waning of the Ainsa-III off-axis submarine fan (Fig. 5.6).

7.2.2 X-ray fluorescence core scanning

Semi-quantitative element scanning of polished core intervals was undertaken at the UCL Environmental Sedimentology Facility using an Avaatech X-ray fluorescence (XRF) split-core scanner. Core sections were scanned at both 10 kV (600μA) and 30kV (1000μA) allowing elemental range of Al to Bi to be analysed. Discrete XRF samples were taken using a 30-second sampling time, 2 mm slit size and a 2 cm sampling interval. For each 10kV and 30kV scan these settings yielded average total counts of ~7,000 and ~800 counts per second (CPS) and dead-times of ~13% and ~2% respectively.

7.2.3 Data processing

XRF count data were converted from the raw accumulating spectra to elemental counts per second using the standard UCL 10kV and 30kV processing models. Based upon the XRF precision estimates provided in Chapter 2, only those elements with a precision of >10% were used except for Ti (Table 2.8). Values with chi-squared values of ≥3, which indicate a bad fit between the collected data and model, were discarded. Where necessary, data points clearly associated with fractures, glue, core edges and secondary mineralisation (e.g., pyrite) were removed from each of the elemental profiles.

Prior to spectral analysis, each elemental data set requires pre-processing to create a stratigraphic time series. During this process, major outliers and any linear trends were removed and, depending upon the spectral technique, linear interpolated to create an evenly spaced depth-scale. The statistics of each time series are provided within Table 7.1.

Table 7.1 – XRF data properties*

Time series	N	Min (area)	Max (area)	Mean (area)	Standard Deviation	SI (m)†	Nyquist Frequency (cycles/m)
Al	1333	1153	3114	2098	232.89	0.02100	23.81
Si	1330	12808	20433	17367	843.33	0.02104	23.76
K	1332	3261	11476	7205	874.14	0.02101	23.80
Ca	1329	64025	130123	104210	8059.30	0.02105	23.75
Fe	1333	11647	24288	15811	1481.10	0.02100	23.81
Sr	1327	584	1905	1091	145.37	0.02108	23.72
Zr	1327	184	412	282	34.19	0.02109	23.71

*Properties with chi-squared values ≥3 and outliers removed. Original number of data points 1333.
†Sample interval applied during interpolation using the `process.m` MATLAB script (Appendix).

7.2.4 Spectral analyses

With the majority of the stratigraphic time series being unevenly spaced, the REDFIT algorithm (Schulz and Mudelsee, 2002) was utilised (Section 2.6.4) to determine statistically significant frequencies. REDFIT spectral analyses were performed using an over-sampling factor (ofac) of 4 and a hifac of 1. To maintain the required 8 degrees of freedom 6 WOSA rectangular segments were used.

To determine the spatial distribution of regular oscillations within these stratigraphic series, the online tool (http://paos.colorado.edu/research/wavelets/) was utilised, which applies the continuous wavelet algorithms (CWT) of Torrence and Compo (1998). The continuous wavelet spectra were calculated using the de-trended and interpolated outcrop and well stratigraphic series. CWT calculations used a Morlet mother wavelet with a parameter of 6, a start scale of 2, scale width of 0.1, 11 powers-of-2 with no zero padding therefore not requiring a cone of influence.

7.2.5 Band-pass filtering

Where persistently significant frequencies were identified, their visualisation is achieved via band-pass filtering. Isolation of individual frequencies was achieved using a Gaussian band-pass filter performed within Analyseries 2.0.4.2 (Paillard et al., 1996).

Figure 7.3 (next page) | A6/22-27 semi-quantitative elemental data. Un-smoothed elemental data represented by grey line whilst the black line illustrates the 5-point moving average (`moving_average.m` MATLAB script within the Appendix) calculated for each element. The positions of the 36 individual core intervals are also identified.

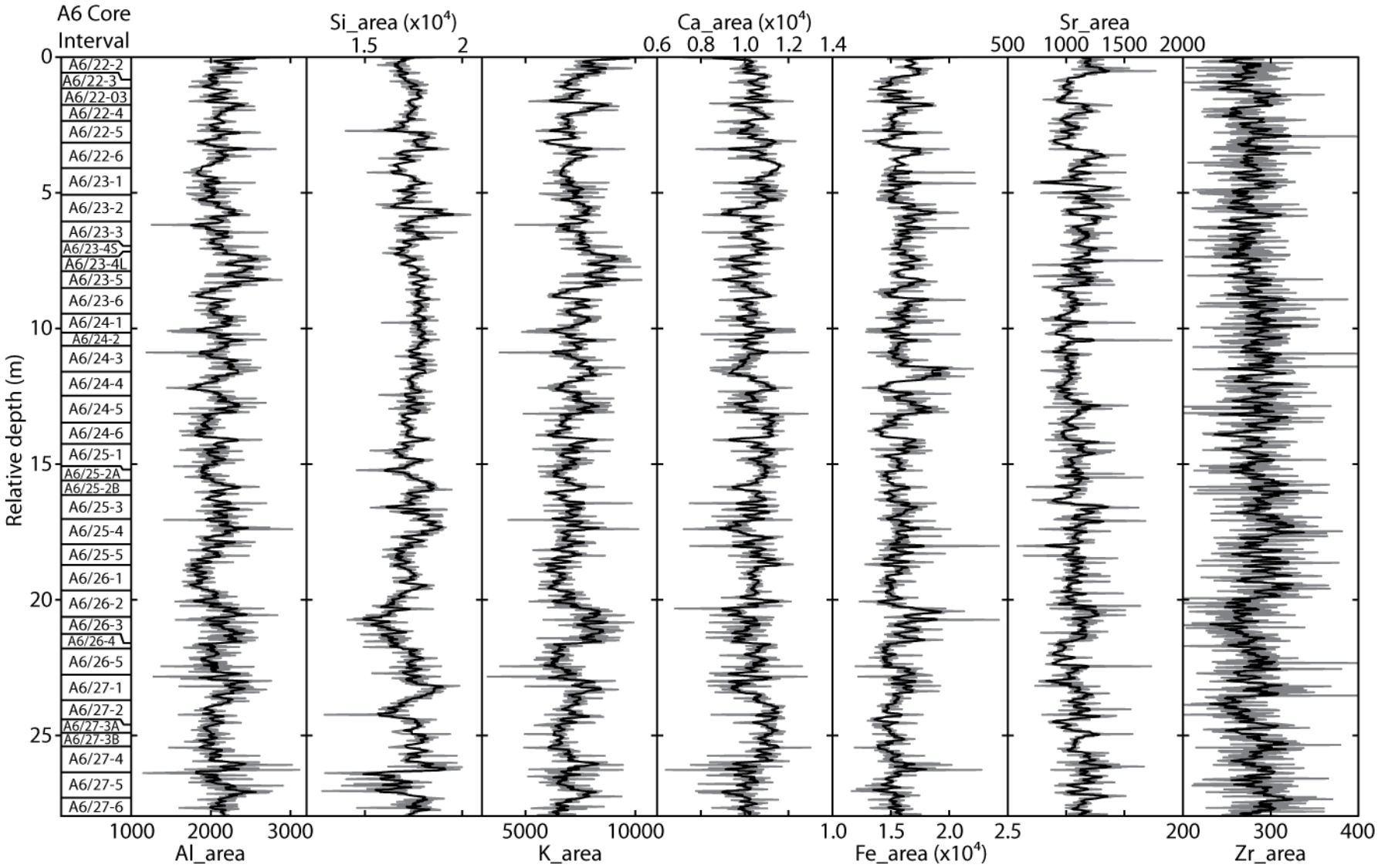
A6 Core Interval
Relative depth (m)
0
5
10
15
20
25
A6/22-2
A6/22-3
A6/22-03
A6/22-4
A6/22-5
A6/22-6
A6/23-1
A6/23-2
A6/23-3
A6/23-4S
A6/23-4L
A6/23-5
A6/23-6
A6/24-1
A6/24-2
A6/24-3
A6/24-4
A6/24-5
A6/24-6
A6/25-1
A6/25-2A
A6/25-2B
A6/25-3
A6/25-4
A6/25-5
A6/26-1
A6/26-2
A6/26-3
A6/26-4
A6/26-5
A6/27-1
A6/27-2
A6/27-3A
A6/27-3B
A6/27-4
A6/27-5
A6/27-6
Si_area (x10^4)
1.5
2
Ca_area (x10^4)
0.6
0.8
1.0
1.2
1.4
Sr_area
500
1000
1500
2000
1000
2000
3000
Al_area
5000
10000
K_area
1.0
1.5
2.0
2.5
Fe_area (x10^4)
200
300
400
Zr_area

7.3 Results

7.3.1 A6 core elemental data

A total of 27.97 m of semi-quantitative elemental data was collected from the A6/22-27 core interval and is illustrated in Figure 7.3. The XRF results demonstrate that Ca dominates the sediments chemical composition, with a mean of 104,200 counts per second.

Comparison between the elemental data and the core sedimentology indicate that significant Ca depletion events coincide with intervals characterised by dark grey shale deposits containing, in some instances, prevalent micro-bioturbation (Fig. 7.5). Within the 5-point smoothed Ca data, the most significant depletion events occur at 5.79, 11.65, 17.36, 22.74 and 27.09 m down core. The mean spacing of these events is 5.33 m. Within each of these 5.33 m intervals, additional reductions in Ca are observed with shorter periods between 2 and 3 m. Within the Al, Si, K and Fe elemental profiles, concurrent relative enrichment events are observed at these positions.

Relationships between the relative elemental concentrations indicate that significant inverse trends exist between Ca vs. Al and K counts. In contrast, correlations between Al and K show a strong positive relationship (Fig. 7.4; Table 7.2).

Table 7.2 – Elemental correlation coefficient table*

	Si	K	Ca	Fe	Sr	Zr
Al	0.04	0.67	0.63	0.26	0.01	0.01
Si		0.01	0.07	0.02	0.00	0.04
K			0.46	0.33	0.00	0.03
Ca				0.38	0.01	0.00
Fe					0.00	0.00
Sr						0.24

*Pearson correlation coefficients (R^2) calculated from data prior to processing.

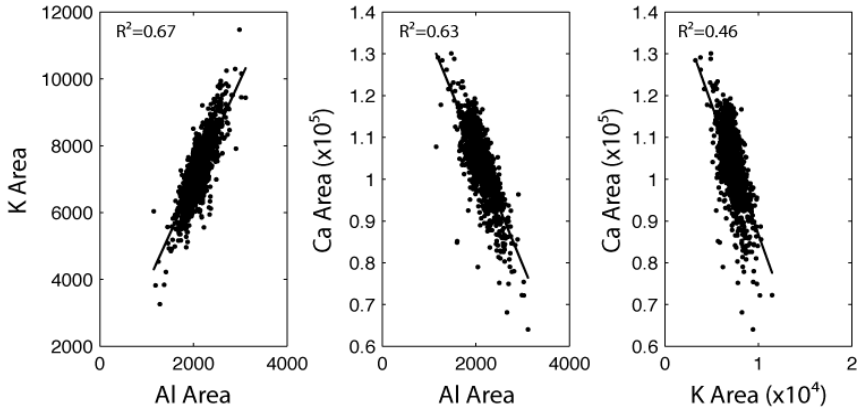

Figure 7.4 | X-plots of elements with significant correlation coefficients. The most significant correlation coefficients (R^2) are those between K/Al and Ca/Al. The strong positive correlation between K/Al is likely due to the occurrence of both these elements within common minerals such as muscovite and K-feldspar. Inverse relationships between Ca/Al and Ca/K are probably indicative of carbonate dilution by alumino-silicate minerals.

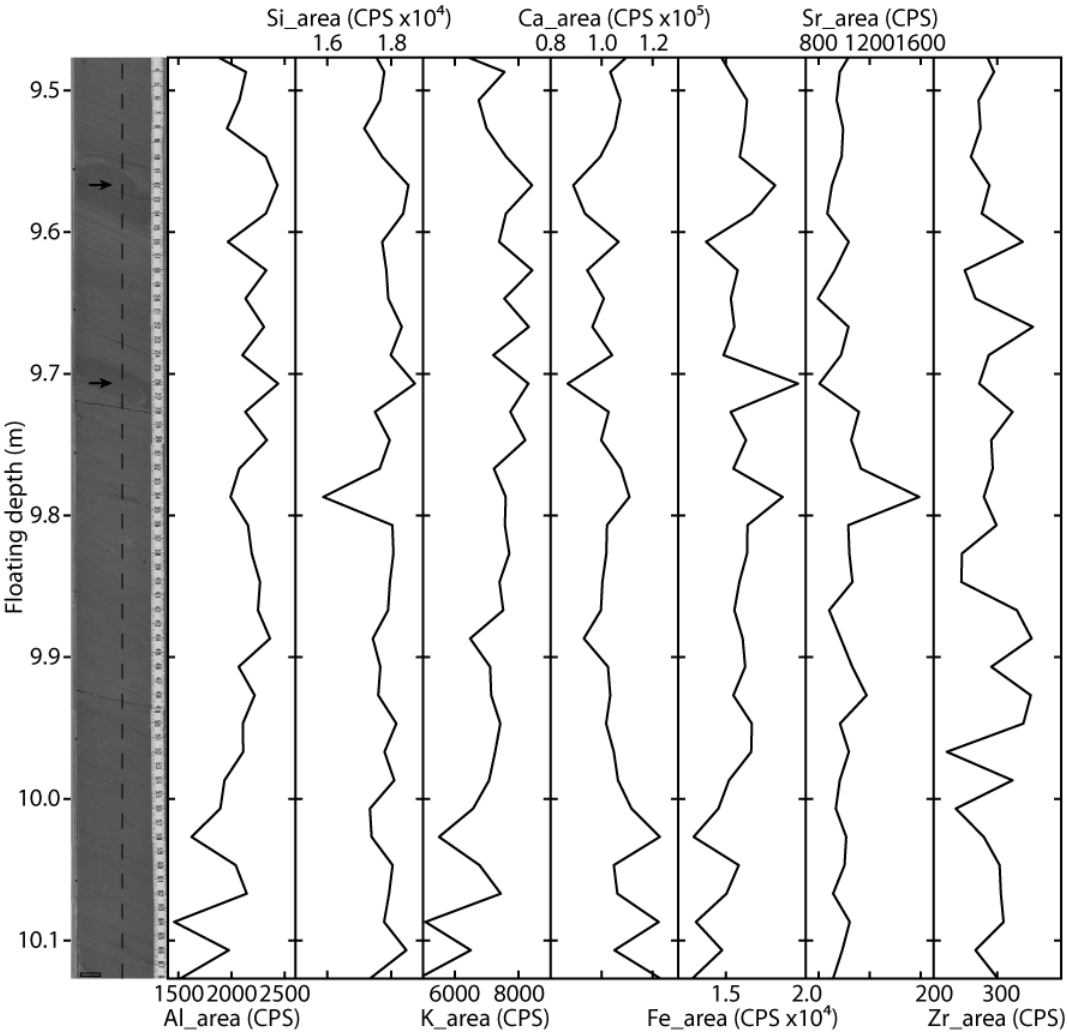

Figure 7.5 | Comparison between A6/24-1 core and semi-quantitative elemental results. The dashed vertical line overlying the core image represents the line, along which the XRF measurements were taken. The 2 x 14 mm area exposed to the X-ray radiation is represented by the rectangle in the bottom left of the core image. Comparison between the elemental results and the sediments illustrate that horizons of dark shale correspond to significant Ca depletion events. Identical relationships are observed within the remainder of the core.

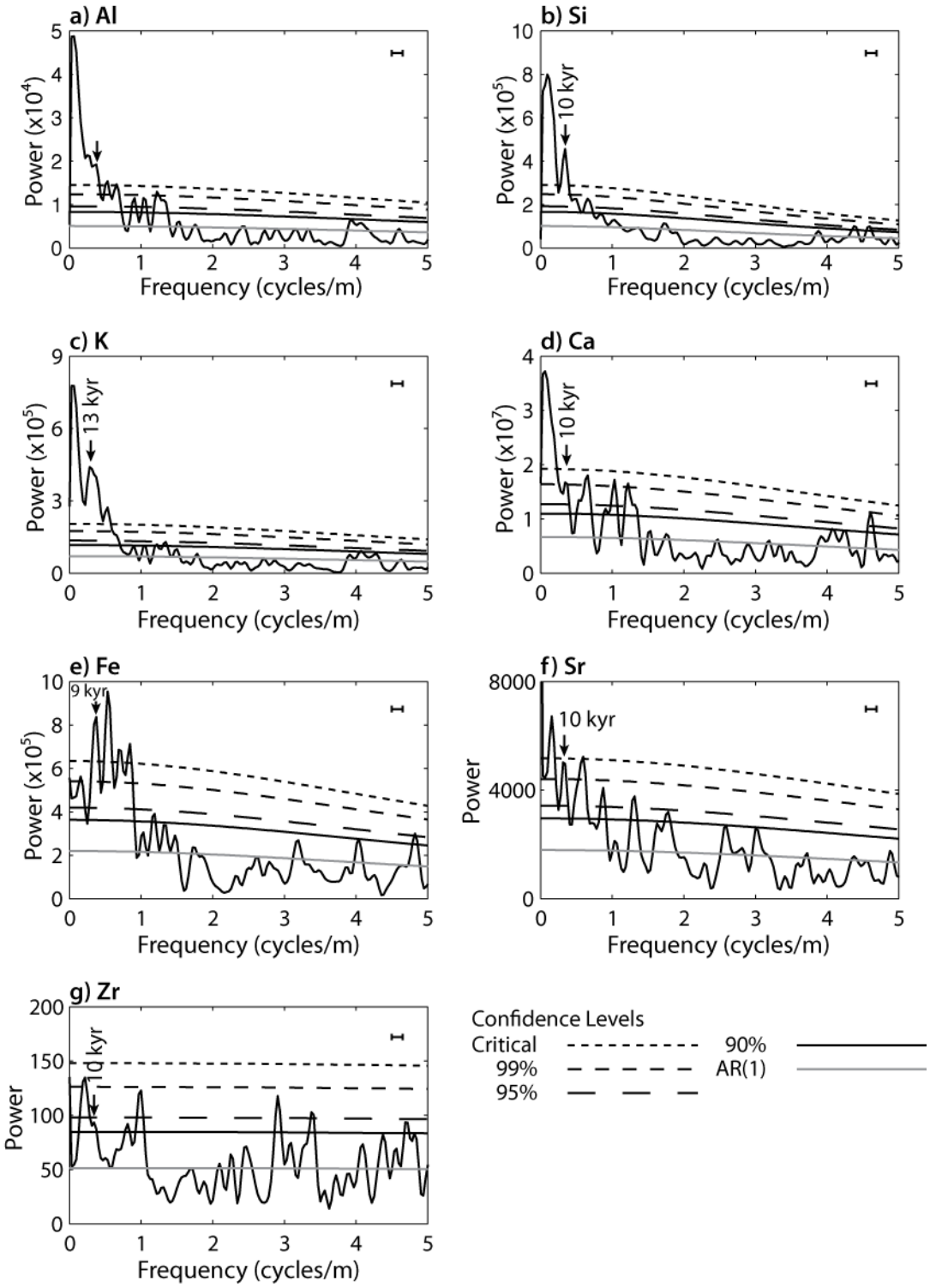

Figure 7.6 | REDFIT spectra calculated from the elemental time series. Spectra for each time series were calculated using an ofac of 4 and 6 WOSA segments providing 8 degrees of freedom. The horizontal bar in each spectrum represents a bandwidth of 0.152 cycles/m. Using the SAR of 28.12 cm/kyr identified for the Ainsa System (Chapter 5) it is possible to determine the temporal duration of spectral peaks.

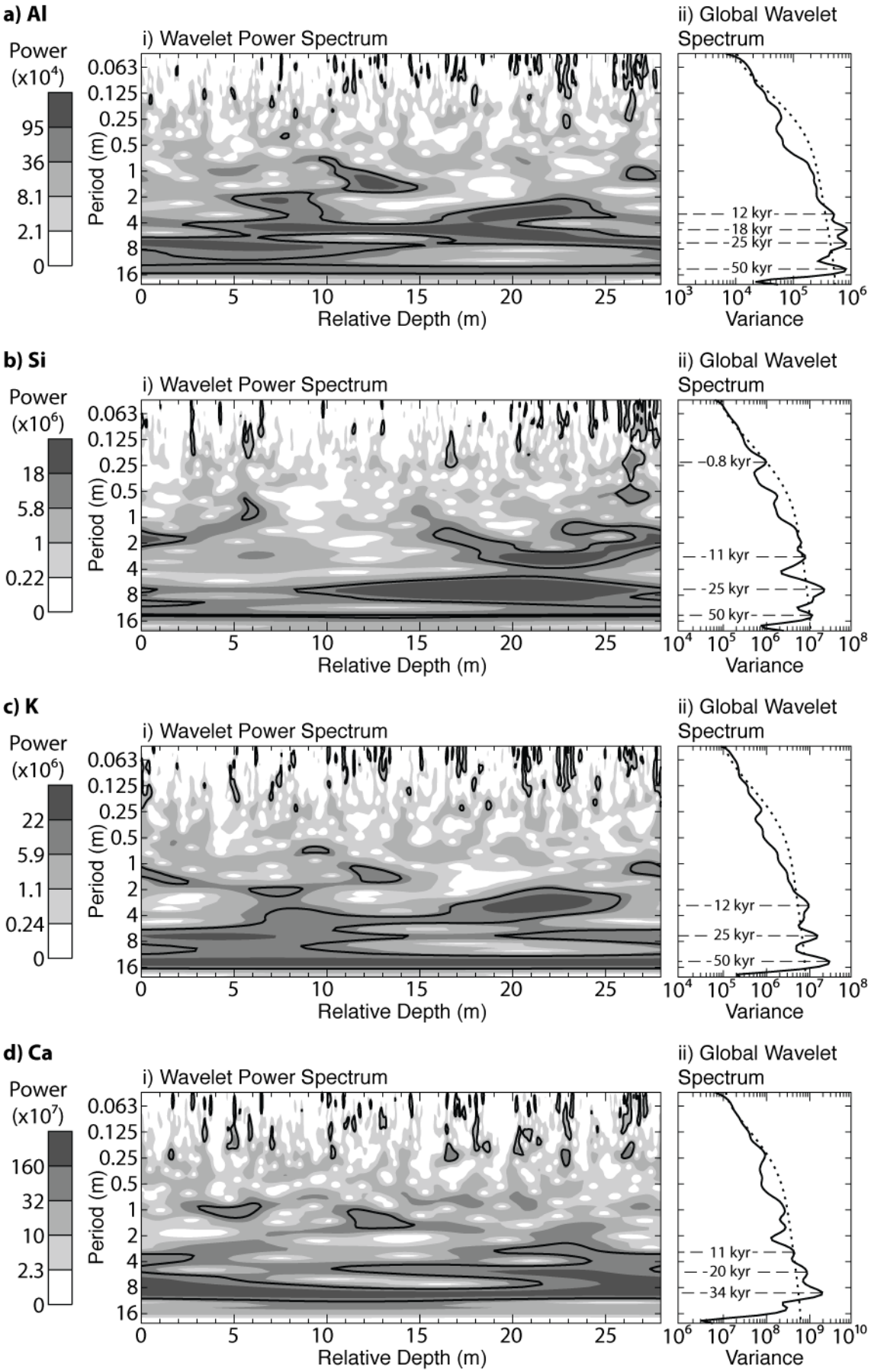
a) Al
i) Wavelet Power Spectrum
ii) Global Wavelet Spectrum
Power (x10^4)
95
36
8.1
2.1
0
Period (m)
0.063
0.125
0.25
0.5
1
2
4
8
16
0
5
10
15
20
25
Relative Depth (m)
12 kyr
18 kyr
25 kyr
50 kyr
10^3
10^4
10^5
10^6
Variance
b) Si
i) Wavelet Power Spectrum
ii) Global Wavelet Spectrum
Power (x10^6)
18
5.8
1
0.22
0
Period (m)
0.063
0.125
0.25
0.5
1
2
4
8
16
0
5
10
15
20
25
Relative Depth (m)
0.8 kyr
11 kyr
25 kyr
50 kyr
10^4
10^5
10^6
10^7
10^8
Variance
c) K
i) Wavelet Power Spectrum
ii) Global Wavelet Spectrum
Power (x10^6)
22
5.9
1.1
0.24
0
Period (m)
0.063
0.125
0.25
0.5
1
2
4
8
16
0
5
10
15
20
25
Relative Depth (m)
12 kyr
25 kyr
50 kyr
10^4
10^5
10^6
10^7
10^8
Variance
d) Ca
i) Wavelet Power Spectrum
ii) Global Wavelet Spectrum
Power (x10^7)
160
32
10
2.3
0
Period (m)
0.063
0.125
0.25
0.5
1
2
4
8
16
0
5
10
15
20
25
Relative Depth (m)
11 kyr
20 kyr
34 kyr
10^6
10^7
10^8
10^9
10^10
Variance

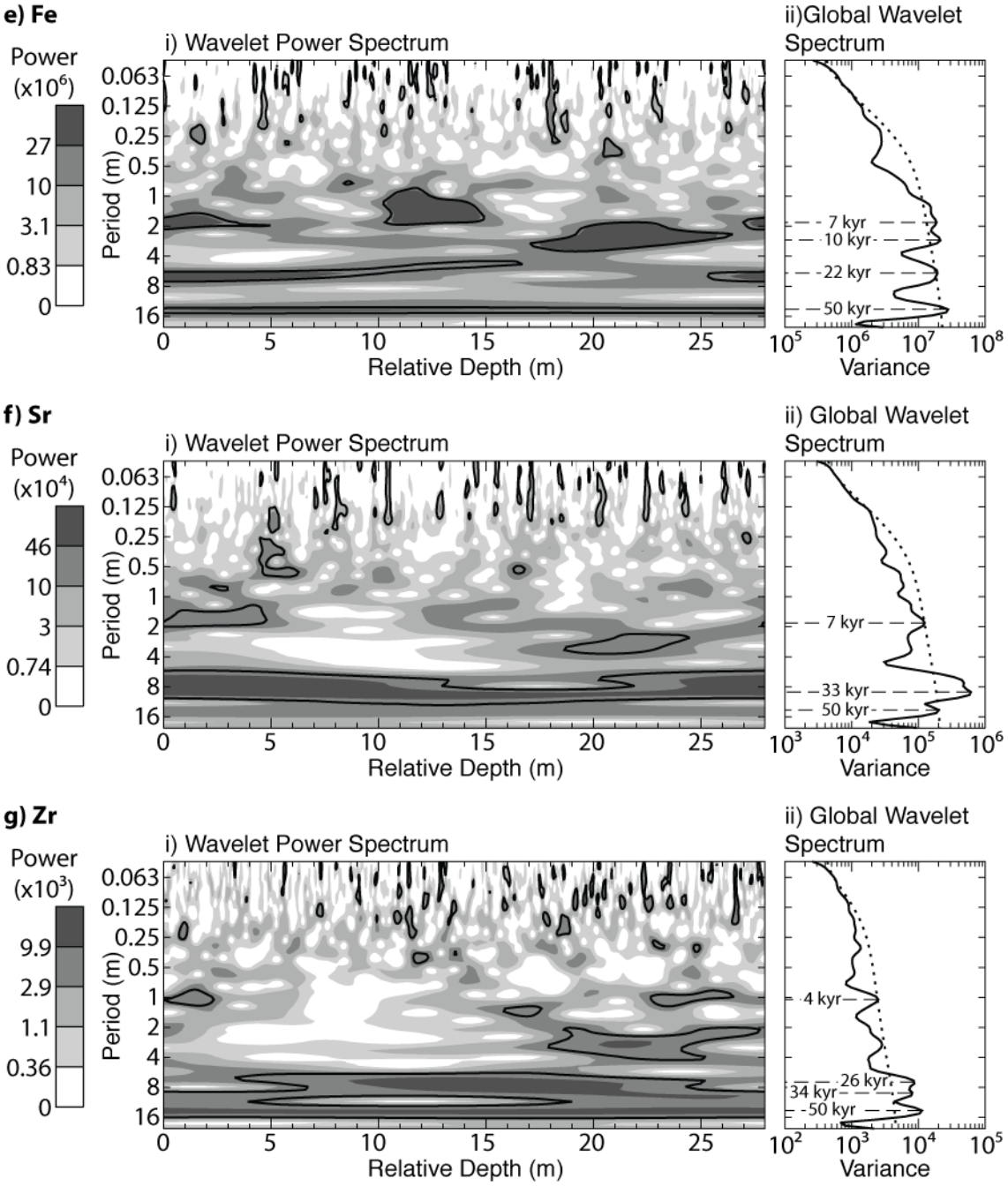

Figure 7.7 (previous two pages) | Wavelet spectra calculated for each time series. (i) Wavelet spectra illustrate the spatial distribution of frequencies throughout the individual time series. Bold contours represent the 95% confidence level. (ii) Global wavelet spectra represent the average variance throughout the entire time series. Those frequencies exceeding the 95% confidence level (dashed line) have their temporal durations estimated using the 28.12 cm/kyr SAR estimated for the Ainsa System (Chapter 5).

Table 7.3a – Spectral results

Spectral Estimation Method	Frequency (cycles/m)*	Period (m)	Confidence Level (%)	Temporal period (kyr)†	Spectral Estimation Method	Frequency (cycles/m)	Period (m)	Confidence Level (%)	Temporal period (kyr)
Al					**Si**				
Wavelet	0.070	14.22	95.0	50.6	**Wavelet**	0.070	14.20	95.0	50.5
	0.141	7.08	95.0	25.2		0.141	7.10	95.0	25.2
	0.198	5.05	95.0	18.0		0.329	3.04	95.0	10.8
	0.301	3.32	95.0	11.8		4.348	0.23	95.0	0.8
REDFIT§	0.063	15.96	Critical	56.8	**REDFIT**	0.094	10.66	Critical	37.9
	0.251	3.99	Critical	14.2		0.344	2.91	Critical	10.3
	0.376	2.66	Critical	9.5		0.469	2.13	95	7.6
	0.533	1.88	Critical	6.7		0.656	1.52	95	5.4
	0.658	1.52	Critical	5.4		4.376	0.23	95.0	0.8
	0.909	1.10	95.0	3.9		4.595	0.22	95.0	0.8
	1.034	0.97	95.0	3.4					
	1.222	0.82	99.0	2.9					
	1.316	0.76	95.0	2.7					
K					**Ca**				
Wavelet	0.071	14.15	95.0	50.3	**Wavelet**	0.104	9.65	95.0	34.3
	0.142	7.02	95.0	25.0		0.178	5.62	95.0	20.0
	0.310	3.22	95.0	11.5		0.306	3.27	95.0	11.6
REDFIT	0.031	31.94	Critical	113.6		0.063	15.97	Critical	56.8
	0.282	3.55	Critical	12.6	**REDFIT**	0.344	2.90	99.0	10.3
	0.532	1.88	Critical	6.7		0.532	1.88	95.0	6.7
	1.221	0.82	90.0	2.9		0.658	1.52	99.0	5.4
	1.346	0.74	90.0	2.6		0.908	1.10	90.0	3.9
	4.070	0.25	90.0	0.9		1.033	0.97	99.0	3.4
						1.221	0.82	99.0	2.9
						1.315	0.76	95.0	2.7
						4.071	0.25	90.0	0.9
						4.604	0.22	99.0	0.8

Table 7.3b – Spectral results

Spectral Estimation Method	Frequency (cycles/m)	Period (m)	Confidence Level (%)	Temporal period (kyr)
Fe				
Wavelet	0.071	14.12	95.0	50.2
	0.160	6.25	95.0	22.2
	0.342	2.93	95.0	10.4
	0.533	1.88	95.0	6.7
REDFIT	0.157	6.38	99.0	22.7
	0.376	2.66	Critical	9.5
	0.533	1.88	Critical	6.7
	0.689	1.45	Critical	5.2
	0.846	1.18	Critical	4.2
	1.190	0.84	90.0	3.0
	4.041	0.25	90.0	0.9
	4.825	0.21	95.0	0.7
Zr				
Wavelet	0.071	14.15	95.0	50.3
	0.106	9.47	95.0	33.7
	0.138	7.27	95.0	25.9
	0.935	1.07	95.0	3.8
REDFIT	0.219	4.57	99.0	16.2
	0.344	2.91	90.0	10.3
	0.813	1.23	90.0	4.4
	1.001	1.00	95.0	3.6
	2.908	0.34	95.0	1.2
	3.377	0.30	95.0	1.1
	4.690	0.21	90.0	0.8
	4.816	0.21	90.0	0.7
Sr				
Wavelet	0.070	14.2	95.0	50.5
	0.107	9.33	95.0	33.2
	0.534	1.87	95.0	6.7
REDFIT	0.156	6.40	Critical	22.7
	0.313	3.20	99.0	11.4
	0.594	1.68	Critical	6.0
	0.876	1.14	95.0	4.1
	1.313	0.76	95.0	2.7
	1.782	0.56	90.0	2.0

*Frequencies between 0 to 5 cycles/m provided. Full results located within Appendix.

[†]Temporal period determined using the average SAR of 28.12 cm/kyr identified from Chapter 5.

[§]All REDFIT analyses have bandwidth (BW) = ±0.076 cycles/m. REDFIT critical level = 99.75%.

7.3.2 Spectral results

REDFIT spectral results suggest the presence of a range of significant frequencies between 0 and 5 cycle/m (Fig. 7.6; Table 7.3). Of these frequencies, those that exceed the critical significance level (99.7%), and, therefore, distinct from the background noise, are identified within several frequency bands at 0.063 to 0.094, 0.313 to 0.376, 0.532 to 0.594, 0.658 to 0.689 and 0.846 cycles/m (Table 7.3). Wavelet spectra identify similar frequency bands at ~0.070, 0.138 to 0.178, 0.301 to 0.342 and 0.533 cycles/m (Table 7.3; Fig. 7.7). The most spatially continuous of these is the 0.070 cycle/m frequency.

Comparing the above spectral results with the observed Ca depletion events, it is possible to confirm the estimated 5.33 m spacing between events with the identification of the 0.178 (1/5.62 m) cycles/m frequency within wavelet spectrum. The shorter 2 to 3 m variability is also represented within both the REDFIT and wavelet spectra by the 0.344 (1/2.90 m) cycles/m frequency. Further higher frequency cycles are also identified at 0.532 (1/1.88 m) and 0.658 (1/1.52 m) cycles/m with confidence levels of 95 and 99%.

7.4 Interpretation

7.4.1 Elemental variation and mineralogy

The variation in the elemental abundance observed within the A6/22-27 core interval is interpreted using the mineralogy previously identified within the younger Guaso System (Table 4.5). These data suggest that the inter-fan sediments, similar to those studied here, contain calcium carbonate ($CaCO_3$), quartz (SiO_2), muscovite ($K_2Al_4[Si_6Al2O_{20}](OH,F)_4$), chlorite ($(Mg,Al,Fe)_{12}[(Si,Al)_8O_{20}](OH)_{16}$), pyrite ($FeS_2$), dolomite ($CaMg(CO_3)_2$) and rutile ($TiO_2$).

The dominant element identified within the XRF data is Ca, which considering the above mineralogy is most likely contained within the sediment calcium carbonate and, to a lesser extent, dolomite. With Sr being commonly substituted into the carbonate structure, this element is also likely to closely reflect the sediment carbonate content. However, the lack of a convincing correlation coefficient suggests another source of Sr may be present (Table 7.2).

The strong positive correlation between Al and K is most likely due to their concurrent presence within the both muscovite and chlorite and other clay minerals. Although both these minerals contain Si and Fe, their lack of a positive correlation with Al and K is probably due to their co-existing presence within quartz and pyrite.

The Zr is most likely contained within the zircon mineral, which is commonly associated with the presence of silica. The absence of a significant correlation coefficient between Si and Zr (Table 7.2), however, is likely due to the presence of Si within alumino-silicate minerals and the potential poor precision of Zr due to the relatively low number of counts.

Taking the above associations between elemental abundance and mineralogy into account, the depletion events where an ~80% decrease in Ca counts is observed (from ~104,000 to 80,000 counts), likely represent a decrease in carbonate content and a concurrent increase in muscovite and chlorite minerals. Such a relationship suggests that these events represent either a reduction of carbonate production and/or increased carbonate dilution by alumino-silicate minerals, most likely due to changing riverine input linked to temporally varying terrestrial suspended-load input.

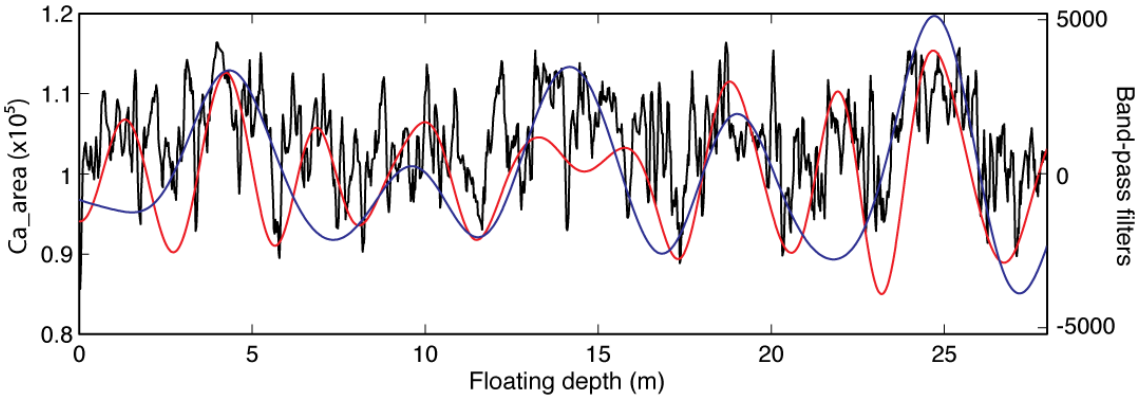

Figure 7.8 | Five-point moving average Ca data and band-pass filters. Band-pass filters of the significant 0.178 (blue) and 0.344 (red) cycles/m Ca frequencies using a bandwidth of ±0.076 cycles/m. Comparing the band-pass filters with the 5-point smoothed Ca data indicate a good visual correlation.

7.4.2 Spectral variability

Spectral results obtained from the A6/22-27 core interval illustrate that Ca depletion events are present with a spacing of 5.62 and 2.90 m (0.178 and 0.344 cycles/m) corresponding to the events identified within Figure 7.3. Although these frequencies are below the critical confidence level with the Ca REDFIT spectra, these frequencies commonly exceed this level within the other elemental spectra (e.g., Al, Si and Fe). Band-pass filtering of the 0.178 and 0.344 cycles/m frequencies within the Ca time series indicate a good correspondence with the original data (Fig. 7.8).

Conversion of the identified frequencies into temporal duration is achieved using the orbital age model proposed for the Well A6 core (Chapter 5). The age model is based on the identification of orbital periods within the A6 core, allowing an average sediment accumulation rate (SAR) of 28.12 cm/kyr to be determined. Application of this

SAR to the significant frequencies in Table 7.3 enables their temporal duration to be calculated. The pacing of the significant Ca depletion events occurred over periods of 20 and 10 kyr, which is interpreted to correspond to precession and hemi-precession cycles (Berger et al., 1993; Berger and Loutre, 1997; Wade et al., 2001; Weber et al., 2010). Other significant frequencies that exceed the critical confidence level within the Al, Si, K, Ca, Fe and Sr REDFIT spectra have temporal durations ranging between 4.2 and 113 kyr.

7.5 Discussion

7.5.1 Carbonate depletion events

The 5-point average Ca data obtained from the A6/22-27 core interval suggests possible carbonate productivity or dilution cycles occurring over 4 to 20 kyr periods. Based upon the inverse relationship between Ca versus Al and K, and the lack of a correlation between carbonate and TOC within the A6 core (Heard et al., 2008), the carbonate depleted shale intervals (marlstones) are probably the result of dilution cycles.

The mechanism driving these dilution cycles is likely varying precipitation over the nearby continental Tremp-Graus basin and its watershed. Periods of intensified precipitation could have conceivably led to an increase in the supply of terrigenous minerals (e.g., muscovite and chlorite) to the basin, therefore, diluting the carbonate content of the Ainsa basins inter-fan sediments. In essence, such temporally varying terrestrial input to the marine Ainsa basin is well explained by changing storminess and terrestrial run-off, mainly as suspended load in the drainage system. Something that has been shown to be prevalent within the area during the middle Eocene (Payros et al., 2010).

The most significant dilution events appear to have occurred every ~20 kyr, corresponding to the expected orbital precession cycle (Table 1.1). During the Eocene, the effect of precession has been shown to be dominant and strongly influenced continental run-off rates (Sloan and Huber, 2001; Lawrence et al., 2003; Westerhold and Röhl, 2009). Eocene climate models indicate precession also influences the strength of south-westerly winds, the intensity of which effect the frequency of cyclones tracking toward the Iberian plate. The clear effect of precession upon the middle Eocene Pyrenean climate (Section 1.7.6) favours the orbital pacing of the ~5 m spaced dilution events.

7.5.2 Sub-Milankovitch and millennial scale cyclicity

In addition to the ~20 kyr precession pacing, the presence of ~10 kyr cyclicity may represent hemi-precession dilution cycles. Hemi-precession cycles are commonly identified within spectral analysis of orbital time series. Explanations for these cycles include the non-linear response of the sedimentary system to external forcing (Kroon et al., 2000); the response of the climate system to the double peak in insolation occurring at the equator when equinoxes are in perihelion and aphelion (Short et al., 1991; Berger and Loutre, 1997; Preto and Hinnov, 2003; Berger et al., 2006; Ashkenazy and Gildor, 2008); or an alternating glaciation of the Northern and Southern hemispheres during each precession cycle (Eberli, 2000). Of these the double peak in insolation occurring at the equator during each precession cycle is currently the most accepted. According to the theory half precession cycles (~11 kyr) are the result of the twice-yearly passage of the Sun across equatorial sites during the spring and autumn equinox. The result is a twice-yearly maxima in insolation received within the tropics and sub-tropics when the Sun is over the equator resulting in the spring and autumn equinox, the magnitude of which is controlled by precession (Berger and Loutre, 1997; Berger et al., 2006).

Higher frequency and lower amplitude depletion cycles also appear to have occurred over millennial time scales ranging between 4 and 6 kyr. Such time scales are consistent with the recently proposed quarter precession cycles (Berger et al., 2006). These ~5 kyr changes in insolation are associated with the twice-yearly variation in the amount of insolation received within the tropics and sub-tropics. The maxima occur when the Sun is over the equator (spring and autumn equinox) whilst the minima occur when the Sun is over the Tropic of Cancer and Capricorn (summer and winter solstice). The result are four seasonal contrasts between the maxima and minima insolation received in the tropics occurring every ~5 kyr (Berger et al., 2006).

Despite the mechanism of sub-precessional changes in insolation having identified their effects are mainly restricted to the tropics (Berger et al., 2006). It is therefore necessary to determine how these half and quarter precession cycles influenced the climate at 35˚N where the Ainsa basin was located during the middle Eocene.

Variation in the amount of insolation received at the equator will alter the meridional temperature gradient thereby effecting atmospheric and oceanic circulation and exporting these changes to higher latitudes (Short et al., 1991; Crowley et al., 1992; Kukla and Gavin, 2004; Berger et al., 2006). Ashkenazy and Gildor (2008) provide a possible mechanism based around the precessional changes in the meridional temperature gradient. They suggest that relatively small changes in the

pattern of maximum zonally averaged tropical temperature may lead to changes in Hadley cell circulation. With the amount of insolation received within the equatorial region being dominated by precession, they argue that the pattern of maximum zonally averaged tropical temperature will alter in accord, which will affect the intensity of winter Hadley circulation. Subsequent changes in Hadley cell circulation intensity will increase mid-latitude cyclone activity therefore delivering moisture and hence precipitation northwards. With half-precession creating two insolation maxima at the equator during a season, it is therefore conceivable that the meridional transport of moisture may vary on ~10-12 kyr time scales. Supportive evidence is provided from the Pleistocene Chinese Loess Plateau (Sun and Huang, 2006). In this study the authors suggest that changes in equatorial heating influenced the strength of the summer monsoon over the Chinese Loess Plateau in the mid-latitudes.

With the possibility that changes in the insolation received within the tropics can be exported to extra-tropical regions, the ~10 and ~5 kyr cycles observed within the A6 core likely relate to quarter and half precessional changes in the meridional temperature gradient. These changes potentially altered the amount of moisture being transported northward and subsequently precipitated over the Pyrenean region. Changing run-off patterns into the Ainsa basin potentially created full, half and quarter precession driven carbonate dilution cycles.

Another explanation for the presence of sub-Milankovitch frequencies is the potential non-linear distortion of the time series. The regular spacing of 0.157 cycles/m between the 0.376, 0.533, 0.689 and 0.846 cycles/m peaks within the Fe REDFIT spectrum indicates the potential presence of non-linear distortion of the time series by either amplitude or frequency modulation (refer to Section 2.8). In the case of the Fe spectrum, the spacing of 0.157 cycles/m between peaks would suggest non-linear distortion occurring over a time period of ~23 kyr corresponding to orbital precession. Despite this coincidence, the spacing between significant peaks within the other REDFIT spectra are inconsistent, varying between 0.125 and 0.188 cycles/m. The shorter scale sub-Milankovitch cycles therefore more likely represent climatic variation rather than spectral artefacts.

7.6 Summary

High-frequency semi-quantitative elemental scanning of a 28-m-thick interval of Well A6 core reveal cyclic variations ranging between 2 and 5 m periods. Of particular interest are the Ca depletion events where concentrations decrease by ~80% every ~5 m and, to a lesser extent every 2 to 3 m. At these intervals a concurrent increase within the concentration of Al, Si, K, Fe and Zr is observed. The negative relationship when comparing Ca (interpreted as reflecting carbonate content) with Al and K (interpreted as representing concentration of muscovite and chlorite) are interpreted as reflecting carbonate dilution cycles. Spectral analyses of these element profiles confirm the presence of variability at these scales along with additional higher frequency oscillations above the 99.75% confidence level.

Application of an orbitally derived age model suggests that carbonate dilution events appear to have been paced by orbital precession. Additional half and quarter precession dilution cycles are also identified and linked to variability within the meridional transport of moisture due to changes in equatorial insolation.

Chapter 8

Ainsa basin framework

8.1 Introduction

8.1.1 Hypothesis outline

Following the identification of Milankovitch scale oscillations within the Ainsa System (Heard et al., 2008), Pickering and Bayliss (2009) suggested that the timing of coarse clastic supply to the Ainsa basin was orbitally paced by the 404 kyr long eccentricity cycle. The hypothesis is based upon the identification of 25 discrete submarine fan deposits, within ~4 km of deep-marine sediments deposited over a 10 to 12 Myr period. The resultant average of 400 to 480 kyr per submarine fan is coincident with the duration of the 404-kyr Milankovitch long eccentricity cycle. This coincidence prompted Pickering and Bayliss (2009) to suggest that a 404-kyr paced glacio-eustatic process controlled the timing of each submarine fan deposit. The above hypothesis presented a number of predictions:

- each sequence (comprised of a sandy submarine fan and its associated fine-grained, thin- to very thin-bedded deposits) spans ~404 kyr;
- the duration of a system (containing grouped sandy submarine fans) can be estimated based upon the number of constituent sequences;
- the base of each sequence should coincide with a period of eccentricity minima, or at some unspecified time after that minima;
- tectonics controlled the locus of coarse-clastic sediment deposition;
- average sediment accumulation rate for Ainsa basin was ~40 cm/kyr.

This research aimed to test these predictions via the construction of a basin age model (Chapter 3) and the identification of Milankovitch orbital oscillations within the Upper Hecho Group (Fig. 1.8). The derivation of an accurate age for each system, and its constituent submarine fans, permitted the preliminary testing of the above predictions. The identification of orbital periods enabled the creation of more accurate floating time scales within selected systems. Once tied to the geological time scale, these records allowed the more robust validation of the above hypothesis.

Within this chapter, the main conclusions from each of the data chapters are outlined and subsequently compared to the original hypothesis. Following a discussion upon whether the Ainsa basin submarine fans were paced by orbital cyclicity, an updated depositional model is proposed for the basin. The remainder of the chapter is dedicated to the identification of limitations within this study and suggested further research.

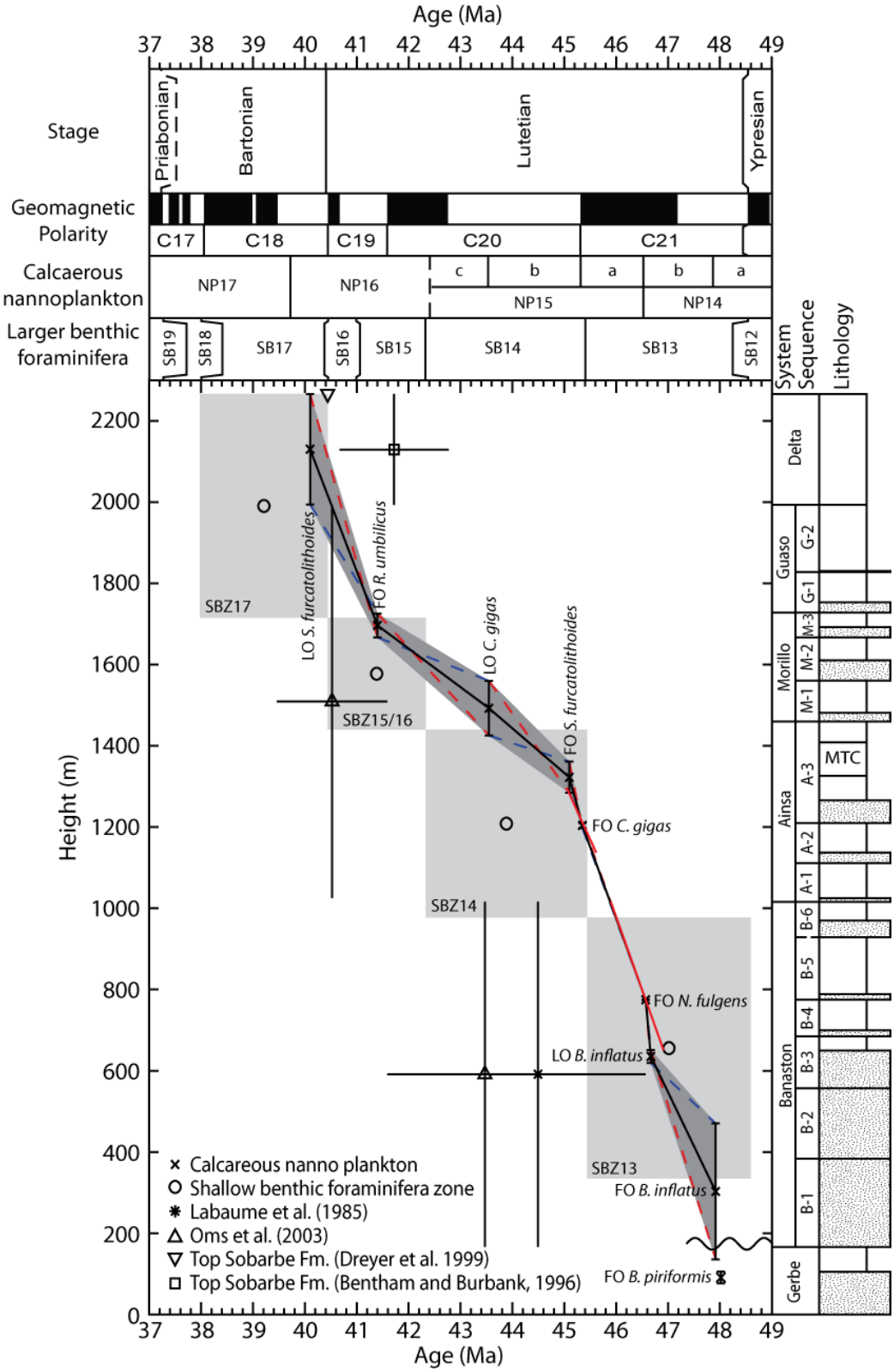

Figure 8.1 | Modified Upper Hecho Group age model. Using the composite Upper Hecho Group stratigraphy and biostratigraphic events an age model was constructed. Nannofossil events are here utilised to construct the age model as these represent discrete points in time rather than broad shallow benthic zones (grey boxes). Mean (black solid line), minimum (blue dashed line) and maximum (red dashed line) sediment accumulation rates are determined from height error bars for each numbered interval (1-7). Dark grey shaded area represents age uncertainty. The red solid lines represent the orbitally-derived age models for the studied sections within the Ainsa and Banaston systems.

8.2 Chapter overview

8.2.1 Upper Hecho Group age model

Within Chapter 3, biostratigraphic data collected from the Upper Hecho Group of the Ainsa basin was used to construct an age model based around calcareous nannofossil and large benthic foraminifera. Applying the calculated age model to the Upper Hecho Group enabled the orbital forcing hypothesis to be tested via estimation of the age and duration of each system and their constituent sequences. Additionally these data enabled their timing to be compared with the calculated orbital parameters, ice-rafted debris (IRD) and oxygen isotope ($\delta^{18}O$) curves of the middle Eocene (Laskar et al., 2004; St. John, 2008; Tripati et al., 2008; Zachos et al., 2008; Laskar et al., 2011).

A composite basin stratigraphy was constructed from detailed measured sections (Chapters 4, 5 and 6), well data (Pickering and Clark, 2012, under review) and published geological maps (Pickering and Bayliss, 2009). Palaeontological samples were collected from throughout the stratigraphy and analysed for calcareous nannofossil and larger benthic foraminifera events. Identified nannofossil events span the zones of NP14 to NP16 (Martini, 1971) and shallow benthic foraminifera zones SBZ13 to SBZ17 (Serra-Kiel et al., 1998). The resultant age model suggests that the 2.3 km of Upper Hecho Group stratigraphy accumulated over a 6.0-8.3 Myr period between ~40.5-48.4 Ma (Fig. 8.1). Sediment accumulation rates (SAR) are determined between adjacent nannofossil event points and range between 9.5±4.5 and 139.5±16.5 cm/kyr, with an average of 43.2±10.5 cm/kyr. These age and SAR estimates correspond well with those previously proposed for the individual systems within the Ainsa basin. Although the Upper Hecho Group intra-basin ages are isochronous, those between inter-basin systems (Ainsa basin) and allogroups (Jaca basin) appear diachronous indicating they require further review.

Applying the orbital forcing hypothesis to the 6.0-8.3 Myr Upper Hecho Group duration would suggest that between 15-20 sequences should exist, each potentially corresponding to an insolation minima every 404 kyr. With only 14 sequences being identified, and only 8 of these corresponding to the predicted 404-kyr duration, the orbital forcing hypothesis appears uncertain. However, when taking into account the less voluminous heterolithic deposits, the number of sequences and their durations may more closely correspond to those predicted.

Comparison between calculated orbital parameters, IRD and $\delta^{18}O$ curves with the estimated age of the submarine fan complexes; suggests that several eccentricity minima and IRD events may coincide with individual submarine fan complexes. The temporal spacing between the submarine fan complexes is shown to be irregular rather than the predicted 404-kyr intervals. However, with the average age uncertainty being

±180 kyr the relationship between eccentricity minima and submarine fan deposition remains uncertain. Only the age estimates for the Banaston System are small enough to enable a reliable correlation, even then they do not consistently correspond to eccentricity minima.

Despite variable results, the large uncertainties present within the Upper Hecho Group age model prevent the orbital forcing hypothesis from being adequately tested. Higher resolution floating age models, based upon the identification of orbital cyclicity, were therefore created between individual submarine fans to enable more reliable testing of the orbital forcing hypothesis.

8.2.2 The Guaso System

The Guaso System is the youngest of the eight, unconformity-bound depositional systems within the Upper Hecho Group (Fig. 1.8) and represents a delta-fed, structurally-confined, low-gradient clastic system deposited prior to the onset of mainly deltaic conditions across the basin (Sutcliffe and Pickering, 2009). The system consists of a 250-350 m thick succession of deep-marine deposits divided into the Guaso-I and Guaso-II (G-I and G-II) sequences (Pickering and Bayliss, 2009; Sutcliffe and Pickering, 2009).

Based upon the proposed Upper Hecho Group age model (Fig 8.1; Chapter 3), the Guaso System was deposited during nannofossil zone NP16 (Martini, 1971) and shallow benthic foraminifera zone SBZ17 (Serra-Kiel et al., 1998) with deposition between 41.39 and 40.10 Ma, placing the system within the latest Lutetian to earliest Bartonian stages.

Study of the Guaso System inter-fan sediments provided a 44 m long geochemical time series, constructed from spectral gamma ray (K, U and Th content) and bulk sediment geochemical ($CaCO_3$, TOC, $\delta^{18}O$ and $\delta^{13}C$) data. Spectral and ASM analyses of these data identified obliquity and precession orbital periods as being present with respective periods of approximately ~10 and ~6 m. ASM analyses suggest the inter-fan sediments accumulated at an average rate of 24.95 cm/kyr, with a >99.9% confidence level of orbital cycles being present.

Using limited mineralogical and petrographic analyses of bulk rock samples; an inverse relationship between carbonate and terrigenous minerals (quartz and muscovite) was identified and interpreted as reflecting carbonate dilution cycles. Hence the SGR data (concentration of K, U and Th) is assumed to reflect the terrigenous input to the basin. The associated increase of terrigenous inorganic carbon to the basin likely account for depletion in $\delta^{13}C$ compositions via the relative enrichment in isotopically depleted terrestrial dissolved inorganic carbonate. The reliability of the isotopic data is

however questionable with $\delta^{18}O$ reflecting only secondary values whilst $\delta^{13}C$ is assumed to reflect a 'memory' of climatic change. Based upon these geochemical interpretations it is suggested that run-off from the adjacent Tremp-Graus basin was influenced by both orbital precession and obliquity.

Application of the orbitally derived floating orbital time scale to the inter-fan sediments separating the submarine fan complexes corroborates the ~200-kyr duration predicted by the Upper Hecho Group age model. Average sediment accumulation rates calculated for the infer-fan and entire Guaso System are 24.95 cm/kyr and 33.4±12.7 cm/kyr, respectively.

With the Guaso System biostratigraphic age model regarded as reliable, the temporal duration of the entire system, Guaso-I and Guaso-II stratigraphic components are calculated as 0.40-1.29, <0.63 and <1.05 Myr, respectively. Despite errors existing within the age model, these estimates are consistent with the predicted sequence (404 kyr) and system (808 kyr) durations of Pickering and Bayliss (2009).

Using the system age estimates it is possible to compare the timing of the Guaso deposits with the calculated insolation, eccentricity and tectonic activity curves. Despite uncertainty existing within the age model, the Guaso-I and Guaso-II coarse-grained siliciclastic fan deposits potentially coincide with periods of eccentricity minima and periods of increased IRD mass accumulation rates (MAR). The base of the system is shown to correspond with a period of increased rotation of the blind-thrust underlying the Boltaña anticline, which may or may not have led to anticlinal uplift. The continuous uplift of the Mediano anticline is believed to have caused the overall south-westward migration of the Guaso-I and Guaso-II sequences. Despite the uncertainty within the age model, the evidence supports the glacio-eustatic control on coarse-clastic sediment supply to the basin with tectonics influencing their lateral distribution.

8.2.3 The Ainsa System

The Ainsa System (Fig. 1.8) is amongst the most studied deep-marine submarine fan system within the Ainsa basin. The Ainsa System contains ~180 m of stratigraphy consisting of three linear lower-slope and basin-floor submarine fan deposits (Ainsa-I, Ainsa-II and Ainsa-III). Each submarine fan is on average some tens of metres thick, and laterally offset-stacked in an east-to-west foreland stepping direction.

The deposition of the Ainsa System, based upon the analysis of calcareous nannofossil and large benthic foraminifera assemblages (Fig. 8.1; Chapter 3), places it within biozones NP15 and SBZ15 to 16, respectively. The resultant biostratigraphic age model suggests that Ainsa System deposition occurred between 43.9 and 45.9 Ma.

The Ainsa System stratigraphy between the top of the Ainsa-II and the upper Ainsa-III sequences were studied to test the orbital forcing hypothesis. New chemo-stratigraphic time series were constructed for this interval with data obtained from both outcrop and the laterally equivalent A6 well. Spectral and ASM analyses of these data identified the presence of short eccentricity, obliquity and precession orbital periods approximately 30, 12 and 7 m in length, respectively. The SAR of 28.12 cm/kyr was estimated using the ASM method, which indicates orbital cyclicity was present with a confidence level >99.72%. Using the floating orbital time scale, the 115 m interval between the cessation of the Ainsa-II and Ainsa-III submarine fans approximates 409 kyr, which corroborates the estimated duration by the biostratigraphic age model of 0.26 to 0.40 Myr (Fig. 8.1).

Comparing the estimated timing of the Ainsa-III off-axis submarine fan initiation and calculated orbital parameters, suggests that deposition may have coincided with a period of reduced summer insolation at the latitudes of 65˚N. The timing of IRD mass accumulation rates despite not coinciding with submarine fan deposition does, however, indicate the presence of ice within the Eocene Arctic Ocean.

The affect of tectonics upon the development of the Ainsa System is shown to have influenced the lateral distribution of submarine fan deposition. The unconformity marking the termination of the Ainsa System is linked to periods of increased rotation of the blind-thrust underlying the Boltaña anticline (Mochales et al. 2012; Fig. 3.7). The overall south-westward migration of the individual submarine fans is ascribed to the continuous uplift of the Mediano anticline.

The above duration and timing of proposed glacio-eustatic and tectonic events within the Ainsa basin appear to somewhat ambiguous, but, within the errors and uncertainties, potentially support with the Pickering and Bayliss (2009) orbital forcing and “see-saw” tectonic hypotheses. However, this corroboration is tenuous and further work is required to constrain the timing of the Ainsa Systems submarine fan deposits such as orbital tuning.

8.2.4 The Banaston System

The Banaston System represents the oldest deep-marine depositional system within the Upper Hecho Group (Fig. 1.8). The base of the Banaston System is marked by an unconformity associated with significant erosion of the underlying Gerbe System. This is linked to the second phase of basin reorganisation associated with continued emplacement of the Lower Thrusting Sheet (Munoz, 1992; Remacha et al., 2003; Remacha et al., 2005; Bayliss, 2010). The system’s sediments are divided into six unconformity-bound sequences referred to as Banaston-I to Banaston-VI (B-I to B-VI).

Each sequence records the incision and subsequent backfill of highly confined channelised submarine fan and inter-fan marl sediments (Pickering and Bayliss, 2009; Bayliss, 2010).

The deposition of the Banaston System, is dated using the analysis of calcareous nannofossil and large benthic foraminifera, as occurring during the NP14b to 15a and SBZ13 biozones, respectively (Fig. 8.1; Chapter 3). The resultant biostratigraphic age model suggests deposition occurred between 45.9 between 48.4 Ma.

Study of the Banaston System sediments involved the construction of a composite stratigraphic time series from two SGR data sets collected by undergraduate M.Sci students (Quarmby, 2010; Warburton, 2011). The SGR data used to construct the time series was collected from off-axis fan and inter-fan deposits ~1 km north of the village of Labuerda. The resultant 376 m long composite time series encompassed sediments from the B-III to the upper B-VI sequences. Spectral and ASM analyses indicate the presence of the short eccentricity, obliquity and precession orbital periods as being present with respective periods of approximately 40, 15 and 8 m. The SAR of 36.03 cm/kyr was estimated using the ASM method, which suggests orbital cyclicity was likely to be present with a confidence level >99.98%. Using the floating orbital age model it was possible to determine the relative timing of submarine fan deposition.

According to the orbital forcing hypothesis the three complete sequences (B-IV to B-VI), each of 404 kyr duration, should have accumulated over a 1.21 Myr period. Based upon the proposed age model, the Banaston-IV to VI sequences was however, deposited over a shorter period of 0.92 Myr. Using the age model adopted here, there are discrepancies between the predicted and calculated sequence durations, with only the Banaston-V sequence accumulating within a period similar to the expected 404 kyr. The remaining Banaston-IV and Banaston-VI sequences accumulated over 250 and 240 kyr periods, respectively. The observed duration of the entire measured section and individual sequences is, therefore, somewhat inconsistent with the 404 kyr orbital forcing hypothesis of Pickering and Bayliss (2009).

Testing whether the timing of submarine fan deposition coincide with periods of insolation minima indicates that the base of the off-axis fan and heterolithic deposits broadly correspond to intervals of low eccentricity. The coincidence between the supply of coarse-grained clastic sediment to the basin and intervals of low eccentricity and increased IRD MAR, although irregularly paced, are consistent with the glacio-eustatic mechanism proposed.

Tectonic activity of the bounding Mediano and Boltaña anticlines will have also influenced the development of the Banaston System. However, the lack of Boltaña

anticline rotational data coincident with the termination of the Banaston System prevents the “see-saw” forcing mechanism from being adequately tested.

8.2.5 Sub-Milankovitch cyclicity

The presence of sub-Milankovitch cyclicity was investigated within this study using the recovered A6 well core sediments from the Ainsa System. The A6 well mainly records inter-fan deposition, where sand supply to the deep-marine basin was much reduced. Sediments consist of laminated marls, fine-grained, mm-scale turbidites and hemipelagic sediments. Laminated sections of the A6 core were selected for high-resolution geochemical analysis in order to investigate the presence of sub-Milankovitch cyclicity.

Using semi-quantitative XRF scanning, a 28 m elemental time series was constructed from the A6/22-2 to A6/27-6 core sections (corresponding to well depths of ~103.44 and 131.55 metres below surface). Of the analysed elements (Al to Bi), only Al, Si, K, Ca, Fe, Sr and Zr were identified as being reliable. Relationships between these relative elemental concentrations indicate that significant inverse trends exist between Ca vs. Al and K counts. In contrast, correlations between Al and K show a strong positive relationship.

Within the elemental time series, counts of Ca were observed to decrease by ~80% at regular intervals of ~5 m, and to a lesser extent every 2-3 m, and coincide with dark shale deposits. Spectral analysis confirms the presence of regular cyclicity within Ca and the remaining elements with frequencies of 0.178 and 0.344 cycles/m, which correspond to the 5.62 and 2.90 m events observed within the Ca record.

The dominant element identified within the XRF data is Ca which, considering the mineralogy identified within Chapter 4, is most likely present as calcium carbonate, and to a lesser extent, dolomite. The strong positive correlation between Al and K is most likely to be due to their concurrent presence within the both muscovite and chlorite and within other clay minerals. Based upon the above associations between elemental abundance and mineralogy, the Ca depletion events are interpreted as representing a decrease in carbonate content with a concurrent increase in muscovite and chlorite. Such a relationship was taken to indicate the depletion events were either due to decreased carbonate production and/or increased dilution.

Using the average sediment accumulation rate (SAR) derived from the orbital age model proposed for the A6 core, the temporal spacing of the observed carbonate depletion events can be estimated. Applying the 28.12 cm/kyr SAR to the 5.62 and 2.90 m event periods indicates temporal durations of 20 and 10 kyr, respectively. The duration of these periods are similar to orbital precession (~23 kyr) and half precession

(~12 kyr). Additional higher frequency and lower amplitude depletion cycles also appear to have occurred over millennial time scales ranging between 4 and 6 kyr and may correspond to quarter precession cycles.

The inverse relationship between Ca vs. Al and K and the lack of a correlation between carbonate and TOC within the A6 core (Heard et al., 2008), suggests the carbonate depleted shale intervals are likely the result of dilution cycles. These dilution events are believed to have been paced by precession, half-precession and quarter-precession changes in insolation received at the equator. Variation in the amount of insolation received at the equator will alter the meridional temperature gradient thereby effecting atmospheric and oceanic circulation and exporting these changes to higher latitudes (Short et al., 1991; Crowley et al., 1992; Kukla and Gavin, 2004; Berger et al., 2006). Ashkenazy and Gildor (2008) propose that changes in the meridional temperature gradient results in an increase in mid-latitude cyclone activity therefore delivering moisture and hence precipitation northwards. These changes in precipitation over the adjacent Tremp-Graus basin and its watershed would have subsequently affected run-off and the supply of terrigenous material to the basin creating carbonate dilution cycles.

8.3 Controls on Ainsa basin sedimentation

Combining the above results from this study, it should be possible to test the predictions (Section 8.1.1) made by the orbital forcing hypothesis of Pickering and Bayliss (2009).

8.3.1 Basin chronostratigraphy

The creation of the Upper Hecho Group age model enabled the proposed average sediment accumulation rate (SAR) for the Ainsa basin of 40 cm/kyr to be also tested. A composite 2.3 km stratigraphic section was constructed through the Upper Hecho Group which was determined to have accumulated over a 6.0-8.3 Myr period between ~40.5-48.4 Ma (Fig. 8.1). Using the identified nannofossil events within the stratigraphy the average SAR for the basin was determined as being 43.2±10.5 cm/kyr, therefore confirming the proposed 40 cm/kyr.

The above results show a good correspondence with the previously suggested 10 to 12 Myr duration and 40 cm/kyr average SAR for the entire Hecho Group (Heard et al., 2008; Pickering and Bayliss, 2009). The 6.0-8.3 Myr duration of the Upper Hecho Group indicates that the four systems of the Lower Hecho Group accumulated over a 1.7-6.0 Myr period. This is assuming that the 10-12 Myr duration of the entire Hecho

Group is correct. The biostratigraphic age model constructed within this study supports the previously proposed general chronostratigraphic predictions for the Hecho Group within the Ainsa basin (Heard et al., 2008; Pickering and Bayliss, 2009; Sutcliffe and Pickering, 2009).

8.3.2 Pacing of submarine fans

According to the orbital forcing hypothesis of Pickering and Bayliss (2009), each of the 14 submarine fans identified within the Upper Hecho Group, were likely paced by the 404 kyr long eccentricity Milankovitch cycle. The testing of this hypothesis, using the biostratigraphic age model, suggests that the majority of submarine fans were irregularly paced. However, substantial errors within the age model leave a significant level of uncertainty surrounding this conclusion and, therefore, this study has not disproved the forcing by the Milankovitch long-eccentricity mode. There are relatively thin heterolithic packages of sediments within the Ainsa basin that Pickering and Bayliss (2009, their Fig. 4) mapped but did not assign to a specific (numbered) submarine fan. It might be that if these were to be interpreted as discrete fans, albeit relatively thin and volumetrically less significant, then the hypothesis of Pickering and Bayliss (2009) could be strengthened.

However, the construction of floating orbital age models for the Guaso, Ainsa and Banaston systems enabled a more accurate temporal duration of each sequence to be determined. The identification of orbital cyclicity within selected inter-fan sediments of these systems indicate that the duration between the initiation, or cessation of submarine fan deposition was either ~250 or ~400 kyr. The temporal spacing between each submarine fan within these systems is therefore somewhat inconsistent with the proposed 404 kyr pacing of coarse-clastic supply. The identification of a ~250 kyr interval may indicate that during certain periods, the short eccentricity (~95-125 kyr) orbital cycle also influenced the pacing of submarine fan deposition. Another explanation for the ~250 kyr interval between submarine fans, may be the modulation of the precession cycle by eccentricity creating a transient 204 kyr signal (Hinnov, 2000).

The variable duration of each sequence suggests that the 404-kyr long eccentricity cycle may not be the sole factor in controlling coarse-clastic sediment supply to the basin. Additional controlling factors may be shorter orbital cycles or tectonic variability to release large volumes of coarse clastic sediments into the deep-marine basin. However, the pacing of the Upper Hecho Groups submarine fans will remain uncertain until an improved age model is produced.

8.3.3 Glacio-eustatic forcing of submarine fans

The proposed mechanism pacing low-stand submarine fan deposition within the Ainsa basin was hypothesised by Pickering and Bayliss (2009) to have been glacio-eustatic. However, the prerequisite for the proposed glacio-eustatic forcing mechanism is the presence of ice-sheets, something long assumed by many researchers as absent from the middle Eocene so-called "greenhouse" climate. Despite this opinion, there is increasing evidence to suggest that conditions for ephemeral ice-sheet formation, and hence glacio-eustatic sea-level change, may have prevailed since at least 45 Ma (Pekar et al., 2005; Tripati et al., 2005; Moran et al., 2006; St. John, 2008; Tripati et al., 2008; Dawber and Tripati, 2011). The timing of these ephemeral ice-sheets has been linked to orbitally forced periods of reduced insolation (Sangiorgi et al., 2008; St. John, 2008; Westerhold and Röhl, 2009). With the amount of insolation received by the Earth being controlled by the integration of the three Milankovitch orbital periods (Berger et al., 1993; Laskar et al., 2004), the latter can be utilised to estimate the timing of these insolation minima and hence periods of potential ice accumulation during the middle Eocene.

Orbital conditions resulting in periods of insolation minima require a combination of; low eccentricity and angle of obliquity reducing the seasonal contrast and the northern hemisphere summer to coincide with the aphelion (greatest Earth-Sun distance). The integration of these conditions reduces the total insolation received by the Earth sufficiently to enable the formation of winter ice at high latitudes. The reduced seasonality would enable any ice formed to survive the following summer and accumulate over consecutive seasons (Milankovitch, 1941). The potential accumulation of ice could therefore result in a glacio-eustatic sea-level fall leading to low-stand conditions. During such conditions, coarse clastic material would be re-mobilised from the shelf (terrestrial and shallow marine Tremp-Graus basin) into the deep-marine Ainsa basin, resulting in low-stand fan accumulation. Extensive evidence exists, especially from the Pliocene-Pleistocene, linking orbitally-paced glacio-eustatic low-stand conditions to submarine fan accumulation (Shanmugam and Moiola, 1982; Weaver and Kuijpers, 1983; Manley and Flood, 1988; Feeley et al., 1990; Pickering et al., 1999; Ridente and Trincardi, 2002; Marsaglia et al., 2004; Normark et al., 2006; Covault and Graham, 2010).

Using the orbital equations of Laskar et al. (2004; 2011) it is possible to identify when in the geological past these conditions coexisted and enable the potential timing of ice accumulation and subsequent low-stand conditions to be predicted. Comparing these events with the timing of the Upper Hecho Group submarine fan complexes allows testing of the glacio-eustatic forcing mechanism. The comparison suggests that

several submarine fans potentially coincide with periods of low eccentricity but inconsistent precessional settings. During such minima, the seasonal contrast in the amount of insolation received is reduced thereby enabling snow from the previous winter to survive and accumulate over several seasons. Such conditions are ideal for the formation of ephemeral ice-sheets potentially leading to sea-level low-stand conditions and subsequent submarine fan deposition as during the Pleistocene (Hays et al., 1976). However, the large uncertainties within the age model are sufficient to prevent the potential correlations being confidently determined within both the Upper Hecho Group and the groups individual systems. With such uncertainty, it is impossible to definitively determine whether the timing of Upper Hecho Group submarine fans correspond to eccentricity minima.

Despite the correlation between the timing of submarine fan deposits and eccentricity minima being ambiguous, circumstantial evidence indicates that coarse-clastic sedimentation was glacio-eustatically forced within the Ainsa basin. The main lines of evidence are the reported presence of IRD deposits within the Arctic Ocean indicating the presence of ephemeral ice-sheets coeval to the Upper Hecho Groups deposition; sequence stratigraphic and stable isotope data suggesting glacio-eustatic sea-level variability (Browning et al., 1996; Miller et al., 1998; Pekar et al., 2005; Dawber et al., 2011); and the possible link between turbidite deposition and periods of apparent climatic cooling within the coeval and more distal Pamplona and Basque basins (Payros et al., 2006).

Where the combined effects of climatic and tectonic forcing on a deep-marine basin have been studied within glacial climates, researchers have identified glacio-eustasy was the dominant control on the timing of coarse-clastic sediment supply (Manley and Flood, 1988; Feeley et al., 1990; Pickering et al., 1999; Prins and Postma, 2000; Normark et al., 2006). Applying this to the circumstantial evidence outlined above, it is therefore likely that the Upper Hecho Group submarine fans were paced by glacio-eustasy. However, until a refined age model for the Upper Hecho Group along with the detailed dating of middle Eocene ephemeral ice sheet formation is achieved, the link between the submarine fan deposition and glacio-eustasy within the Ainsa basin will remain uncertain.

8.3.4 Orbital forcing of inter-fan sediments

Although the orbital pacing of the Ainsa basin submarine fan deposits appears uncertain, significant evidence exists supporting the presence of orbital forcing within inter-fan sediments. The study of three systems within the Upper Hecho Group indicate the presence of the average short eccentricity, obliquity and precession orbital cycles

within their inter-fan sediments. The interpretation of these cycles, based upon geochemical evidence presented in chapters 4 and 7, suggests that the flux of terrestrial material (quartz, muscovite and chlorite) to the basin varied over time creating carbonate dilution cycles (Harris and Mix, 1999; Koptikova et al., 2010).

The presence of orbitally induced carbonate dilution cycles within the Ainsa basin is consistent with the identification of orbitally forced waxing and waning of coarse-grained sediment supply within the coeval Montanyana Group of the Tremp-Graus basin (de Boer et al., 1991; Weltje et al., 1996; Nijman, 1998). With the Montanyana Group acting as the source area for the Ainsa basin (Caja et al., 2010), these variations in coarse clastic sediment flux should have propagated through to the deep-marine environment if these sediments were directly sourced from the continent (van Tassell, 1987; Weltje and de Boer, 1993). However, the orbital signal may be lost where sediment is stored on a continental shelf and then re-mobilised during a fall in base-level, which may or may not have been orbitally forced (Posamentier et al., 1988; Posamentier and Vail, 1988; Van Wagoner et al., 1988). Although the majority of coarse-grained sediment may be stored on the shelf during high-stand conditions, the supply of sediment to the deep-marine environment should continue albeit much reduced (Covault and Graham, 2010).

The proposed mechanism responsible for the cyclical flux of coarse-grained sediment is regular, possibly orbital controlled, climatic changes between arid and wet periods (de Boer et al., 1991). Eocene climate modelling indicates that significant variations in surface run-off may have occurred within the South Pyrenean region thereby substantiating the advocated wet/dry alternation in climate (Sloan and Huber, 2001; Lawrence et al., 2003). The mechanism for sediment delivery to the basin floor was likely via hyperpycnal flows and seismically (“seismites”) or storm (“tempestites”) triggered turbidity currents (Pickering and Corregidor, 2000).

8.3.5 Tectonic forcing

An alternative mechanism driving the deposition of the Ainsa basins low-stand fans may have been tectonic processes (Pickering and Corregidor, 2000, 2005). Within the Ainsa basin, tectonic controls must have occurred over a rage of scales affecting the entire Hecho Group down to the individual sequences.

The largest scale of tectonic variability within the Ainsa basin is the overall south-westward stacking of the individual Hecho Group systems away from the South Central Pyrenean Units (SCPUs) deformation front (Pickering and Bayliss, 2009). The tectonic development of the SCPU and associated Pyrenean thrust sheets are however, unlikely to have influenced the pacing of the Ainsa basins submarine fan

deposition. Instead, the increased relief of the Pyrenean orogen, and subsequent enhanced erosional rates, will have most likely led to long-term changes in sediment flux and provenance through time.

Long-term tectonic variability with a period of approximately 4 Myr has been suggested, based upon discrete element models of Pyrenean thrust sheets (Naylor and Sinclair, 2007), as being responsible for the angular-unconformity separating the Upper and Lower Hecho Groups within the Ainsa basin (Heard et al., 2008; Pickering and Bayliss, 2009; Sutcliffe and Pickering, 2009). The 4 Myr thrusting cycle is incompatible with the proposed duration of each system and their constituent sequences, identified within the Upper Hecho Group age model and, therefore, unlikely to have influenced their timing.

However, this phase of major basin reorganisation will have resulted in enhanced denudation within the hinterland thereby increasing the volume and calibre of the sediment available for transport in the Ainsa basin. This is evident within the Banaston System sediments that immediately overly the angular unconformity marking the base of the Upper Hecho Group (Figs. 1.8, 1.18). The six submarine fans that comprise the Banaston System, compared to the usual two to three within the remainder of the Hecho Group, illustrate the increase in sediment volume available following this event. The increased calibre of sediment immediately following the angular unconformity is also apparent within the Banaston System with the initial B-I and B-II submarine fan complexes dominated by large limestone olistoliths, pebbly conglomerates and very-coarse sandstones (Bayliss, 2010). Subsequent systems are shown to contain a decreasing amount of these deposits often associated with MTC deposits (Bayliss, 2009; their Fig. 7.4).

Shorter-term syn-depositional tectonic activity is identified within the basin-bounding Boltaña and Mediano anticlines (Holl and Anastasio, 1993; Mochales et al., 2012). At the system scale, the south-westward stacking of individual systems and their constituent sequences illustrate the effects of syn-depositional tectonics. The position of the depositional axis of each system and their constituent sequences are believed to have been controlled by the uplift of the Boltaña and Mediano anticlines in a process described as “see-saw” tectonics (Figs. 1.15, 1.16) (Pickering and Bayliss, 2009). According to the “see-saw” tectonic process, continuous thrust-tip advancement of the blind thrust underlying the Mediano anticline led to syn-depositional uplift therefore forcing the basins depositional axis to migrate toward the southwest (Figs. 1.15, 1.16) (Pickering and Bayliss, 2009). Periodically this continuous south-westward migration was punctuated by activity of the thrust underlying the Boltaña anticline causing the basins depositional axis to migrate ~1 km toward the northeast. The

resultant unconformities are utilised by Pickering and Bayliss (2009) to define the upper and lower boundaries of each system (Fig. 1.16).

With both of these anticlines being related to underlying thrusts (Figs. 1.8, 1.11), the “see-saw” hypothesis infers that thrust-tip advancement and hence anticlinal uplift was continuous and periodic for the Mediano and Boltaña anticlines, respectively. However, the Boltaña anticline did not develop until the early Lutetian with the initial thrusting (Larra-Boltaña thrust) of the Lower Thrust Sheets (Teixell, 1996). Only the Mediano anticline formed early enough to influence the deposition of the entire Hecho Group (mid-late Ypresian; Holl and Anastasio, 1993). It is therefore unlikely that the proposed “see-saw” tectonic process was active during the deposition of the Lower Hecho Group. This may explain the limited lateral migration of the depositional axis within the Fosado, Los Molinos, Arro and Gerbe systems (Fig. 1.15). However, the later distribution of these systems remains unclear due to their poor exposure and tectonic deformation (Fig. 1.18).

With the early Lutetian development of the Boltaña anticline, the tectonic conditions were present for the “see-saw” tectonic mechanism to influence the deposition of the Upper Hecho Group. The increased lateral variability in the locus of submarine fan deposition, especially within the Banaston System, indicates the increased tectonic influence upon deep-marine sedimentation (Fig. 1.15).

Further supportive evidence supporting the effect of “see-saw” tectonics upon the Upper Hecho Group is provided by palaeomagnetic studies of the Boltaña and Mediano anticlines. Folding rates determined from the Mediano anticline indicate that uplift was continuous throughout the late Ypresian to early Bartonian (Chrons 22r to 18r) thereby supporting the hypothesis (Holl and Anastasio, 1993). However, Holl and Anastasio (1993) also identify periods of intensified uplift lasting periods of ~1.5 Myrs linked to the emplacement of the Cotiella thrust, which is not consistent with the “see-saw” tectonic hypothesis. Such periods of intensified uplift would theoretically force the deposition of the Ainsa basin toward the southwest.

The rate and timing of Boltaña anticline uplift is not clearly defined but may be estimated from the rotation of the underlying blind-thrust (Mochales et al., 2012). Thrust rotation data indicate that activity was continuous with an average of ~1.2˚/Myr during the Lutetian which increased to ~2.6˚/Myr during the late Lutetian to late Bartonian stages. Periods of intensified rotation are observed and potentially may relate to the timing of the observed unconformities separating the Hecho Group systems. However, without a detailed palaeomagnetic study determining the folding rates of the Boltaña anticline the proposed system bounding unconformities cannot be confidently linked to anticlinal uplift.

With the pacing of submarine fans <2 Myr, the longer term tectonic processes identified within the Ainsa basin (2 to >10 Myr) are unlikely to have paced coarse-clastic supply. Instead, the locus of deposition was likely controlled by these tectonic events. Where tectonic and eustatic controls upon sedimentation have been successfully decoded, glacio-eustasy is demonstrated to control the timing of sediment deposition whilst tectonics influences the loci of deposition (Houck, 1997; Prins and Postma, 2000; Ridente and Trincardi, 2002).

8.3.6 Autocyclic forcing

Autogenic events are self-induced aperiodic perturbations within a depositional system that can occur over a range of temporal and spatial scales, examples range from millimetre-scale ripple migration to the regional-scale switching of deltaic systems (Cecil, 2003).

On a basin scale, the autogenic response of a sedimentary system has been shown to be strongly dependant upon the basin geometry and setting (Peper and Cloetingh, 1995). The presence of autocyclic events within a basin has been linked to irregular shifts in sedimentation rates, thereby creating additional frequencies within stratigraphic spectral analyses that are not associated with orbital forcing (Peper and Cloetingh, 1995). The identification of such non-orbitally related cyclic periods and other unexplained sedimentary cycles within the Ainsa basin might, therefore, indicate the potential presence of autogenic processes.

The Upper Hecho Groups submarine fan deposits are not believed to have been paced by autogenic cycles due to evidence obtained from mapping and sedimentological data. Pickering and Corregidor (2005) suggest that the submarine fans of the Ainsa System were not paced by autocyclic compensational stacking but instead result from the sediment supply to the basin being “switched on and off” by eustatic processes. However, the cycles of channel incision, bypass and subsequent backfill (Fig. 1.17) identified within the individual submarine fan complexes may represent an autogenic channel avulsion process linked to a compensational stacking model (Allen, 1979; Deptuck et al., 2008; Straub et al., 2009) rather than an allogenic control (suggested for the fan channels by Pickering and Clark, 2012, in review). The compensational stacking model suggests that following the creation of relief by the deposition of a channelised submarine fan; subsequent fan deposits would bypass this area, resulting in deposition in adjacent areas. The process would create channel incision, bypass and backfill (Popescu et al., 2001; Jerolmack and Paola, 2007) followed by a lateral shift in the channel depositional axis (Deptuck et al., 2008; Straub et al., 2009; Ganti et al., 2011), thereby creating the cyclical intra-fan features observed

within the Ainsa System (Pickering and Corregidor, 2005; Pickering and Bayliss, 2009). The consistent westward offset-stacking, even of individual submarine channels, as well as for the submarine fans, tends to favour a tectonic control on shifting depositional axes as outlined by Pickering and Bayliss (2009).

Despite these cycles potentially being the result of an autogenic process, the change in energy commonly associated with the triggering of these processes may be associated with allogenic forcing (e.g., changing sea-level, fluvial discharge etc.) (Cecil, 2003). If correct, then autogenic events may be responsible for the lateral distribution of sediment (e.g. compensational stacking of lobe deposits) with allogenic cycles, such as orbitally forced changes in climate, ultimately controlling the underlying timing of these events.

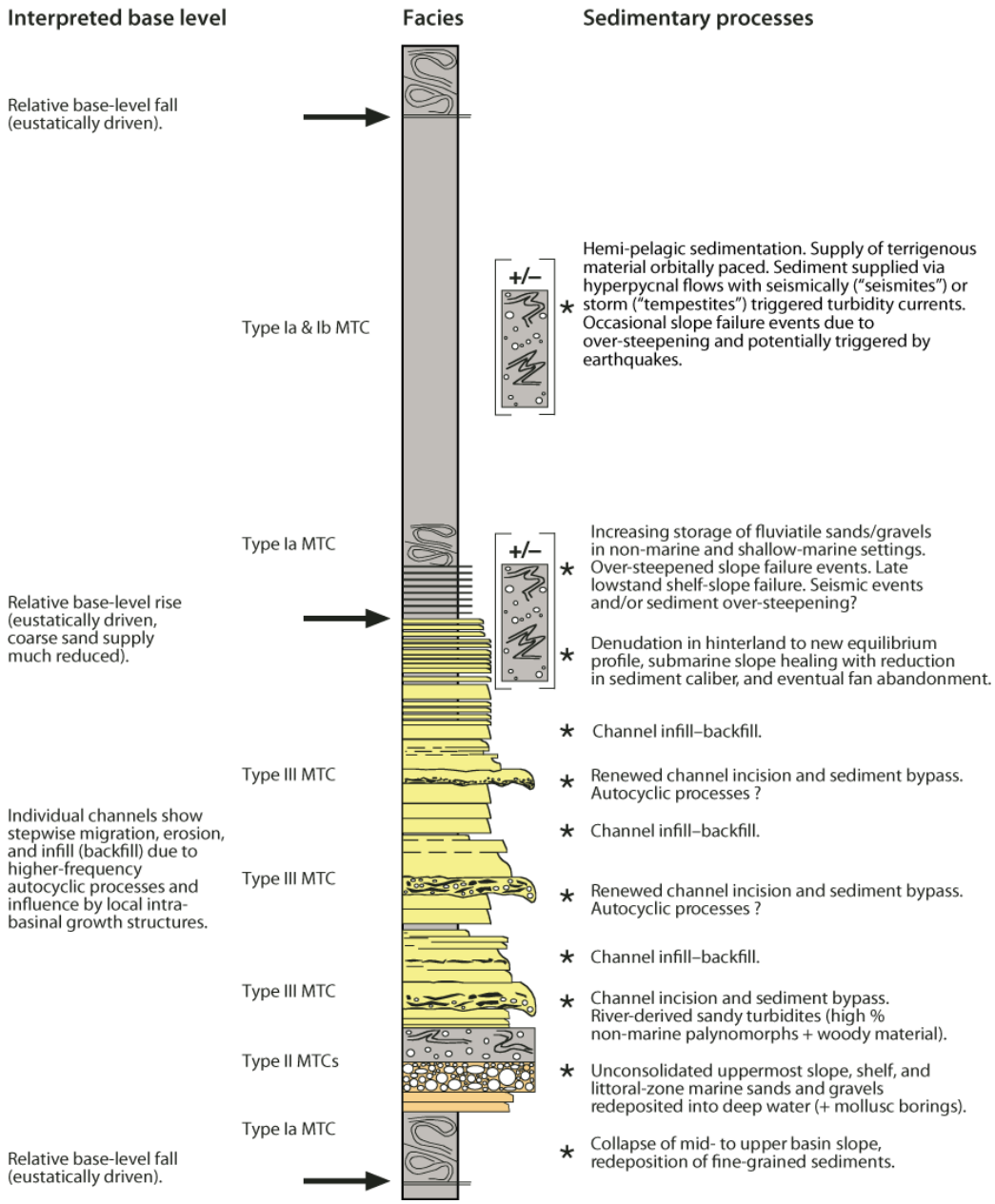

Figure 8.2 (previous page) | Generalised Ainsa basin depositional sequence and interpretation modified from Pickering and Bayliss (2009). Note, an earlier model of Pickering and Corregidor (2005) suggested tectonically forced base-level changes. For definitions of MTC deposits see Pickering and Corregidor (2005).

8.4 An updated Ainsa basin model

8.4.1 Ainsa basin depositional model

Incorporating the results from this study with the existing Ainsa basin depositional models (Pickering and Corregidor, 2005; Pickering and Bayliss, 2009) allows the following framework to be constructed for the Upper Hecho Group (Fig. 8.2). The deposition of each sequence commenced with low-stand conditions, potentially the result of orbitally paced glacio-eustasy, which triggered the collapse of mid- to upper basin slope depositing basal type-Ia MTCs and created a truncation surface (Pickering and Corregidor, 2005). Following sequence initiation, sediment stored on the adjacent shelf (Tremp-Graus basin) was re-mobilised over the Mediano anticline into the deep-marine Ainsa basin. These initial sediments comprise unconsolidated littoral zone (molluscan bored pebbles and boulders) and fluvial sands and gravels deposits incorporated within type-II MTCs. The main body of the submarine fan developed with the supply of fluvio-deltaic derived sandy turbidites creating several cycles of incision, sediment bypass and backfill. These cycles may represent either an orbital (Weltje and de Boer, 1993) or autocyclic (Popescu et al., 2001; Jerolmack and Paola, 2007; Pickering and Bayliss, 2009) control upon channel avulsion.

As the sea-level (likely glacio-eustatic?) cycle continued, the gradual denudation of the hinterland formed a new equilibrium profile. The delivery of coarse-grained sediment to the basin was reduced and began to accumulate on the shelf, leading to submarine fan abandonment. Subsequent inter-fan sedimentation was dominated by hemipelagic sedimentation with the supply of terrigenous material being orbitally paced (average short eccentricity, obliquity and precession). These orbital periods are proposed to have caused cyclical variations in run-off from the Tremp-Graus basin into the deep-marine Ainsa basin. The mechanism for sediment delivery to the basin floor was via hyperpycnal flows and seismically (“seismites”) or storm (“tempestites”) triggered turbidity currents (Pickering and Corregidor, 2000). The occurrence of type-II MTCs within these inter-fan sediments is ascribed to slope failure events due to over-steepening, potentially triggered by earthquakes.

Each of these complete cycles may have been regularly paced by the long eccentricity (~404 kyr), and possibly short eccentricity Milankovitch orbital periods (multiple ~95-125 kyr). The reduced insolation during these periods potentially caused

glacio-eustatic low-stand conditions triggering the commencement to the above depositional cycle.

Syn-depositional tectonics during the Upper Hecho Groups deposition was likely dominated by the interaction of the basin bounding Boltaña and Mediano anticlines creating a "see-saw" tectonic regime (Pickering and Bayliss, 2009). During the deposition of the Upper Hecho Group, the Mediano anticline was undergoing continuous uplift (Holl and Anastasio, 1993) resulting in the WSW migration of the depositional systems and their constituent sequences (Fig. 8.4). The intermittent uplift of the Boltaña anticline potentially caused the observed ~1 km shift toward the ENE of the depositional axis, thereby creating angular unconformities between each system proposed by Pickering and Bayliss (2009).

8.4.2 Age and pacing of Ainsa basin submarine fans

The Upper Hecho Group within the Ainsa basin is shown to have accumulated during middle Eocene nannofossil zones NP14 to 16 and shallow benthic foraminiferal zones SBZ13 to 17 (Martini, 1971; Serra-Kiel et al., 1998). The age model constructed from these palaeontological events indicates that Upper Hecho Group deep-marine sedimentation occurred at an average rate of 43.2±10.5 cm/kyr between 40.5 and 48.4 Ma (Fig. 8.1).

Figure 8.3 (next page) | Summary diagram outlining the main results from this thesis. The palaeontological study of the Upper Hecho Group enabled the improved dating of the submarine fan systems of the Ainsa basin (Fig. 8.1; Chapter 3). Results indicate the Upper Hecho Group spanned biozones SBZ13-16 and NP14a-16 with the overlying Sobarbe deltaic complex continuing into SBZ17 and NP17. The age model enabled the timing of the Guaso, Morillo, Ainsa and Banaston systems to be estimated. Testing the 400 kyr orbital pacing of submarine fan deposition was achieved by identifying shorter term orbital cycles within inter-fan and off-axis fan deposits. The Guaso, Ainsa and Banaston systems were studied and from the identification of the main orbital parameters (E2&3 – average short eccentricity; O – obliquity; P – precession; 1/2P – half precession; 1/4P – quarter precession) average sediment accumulation rates (SAR) were calculated. The SAR range for the Morillo System (*) is based upon those calculated for intervals 2 and 3 within the age model (Fig. 8.1; Table 3.7). Using these SAR estimates it was possible to determine whether the fans were separated by ~400 kyr of stratigraphy. With climate proposed to have controlled the timing of submarine fan deposition, tectonics is believed to have influenced the locus deposition via the "see-saw" tectonics (Fig. 1.16). This involves the alternation of uplift between the flanking Boltaña and Mediano anticlines. Individual depositional sequences migrate away from the continuously growing Mediano anticline. Uplift of Boltaña anticline potentially created unconformities separating the individual systems. Systems expanded for clarity. Figure based around the "see-saw" stacking diagram of Pickering and Bayliss (2009).

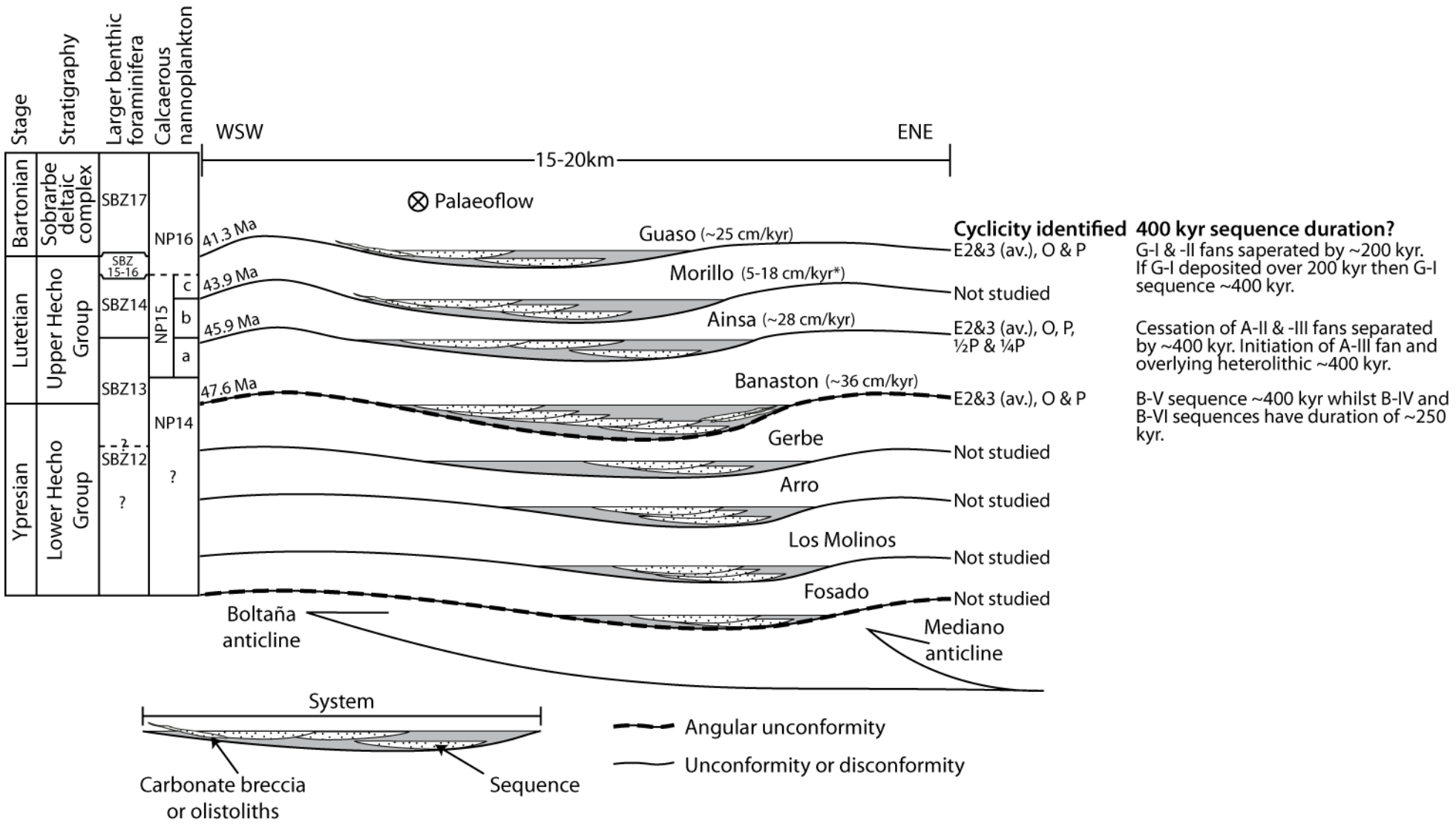
Stage
Stratigraphy
Larger benthic foraminifera
Calcaerous nannoplankton
WSW
ENE
15-20km
Palaeoflow
Bartonian
Lutetian
Ypresian
Sobrarbe deltaic complex
Upper Hecho Group
Lower Hecho Group
SBZ17
SBZ 15-16
SBZ14
SBZ13
SBZ12
NP16
NP15
c
b
a
NP14
41.3 Ma
43.9 Ma
45.9 Ma
47.6 Ma
Guaso (~25 cm/kyr)
Morillo (5-18 cm/kyr*)
Ainsa (~28 cm/kyr)
Banaston (~36 cm/kyr)
Gerbe
Arro
Los Molinos
Fosado
Boltaña anticline
Mediano anticline
Cyclicity identified
E2&3 (av.), O & P
Not studied
E2&3 (av.), O, P, ½P & ¼P
E2&3 (av.), O & P
Not studied
Not studied
Not studied
Not studied
400 kyr sequence duration?
G-I & -II fans saperated by ~200 kyr. If G-I deposited over 200 kyr then G-I sequence ~400 kyr.
Cessation of A-II & -III fans separated by ~400 kyr. Initiation of A-III fan and overlying heterolithic ~400 kyr.
B-V sequence ~400 kyr whilst B-IV and B-VI sequences have duration of ~250 kyr.
System
Carbonate breccia or olistoliths
Sequence
Angular unconformity
Unconformity or disconformity

8.5 Wider applications

Ancient deep-water clastic systems are an important economic resource, containing >15% of the worlds total hydrocarbon reserves (Richards et al., 1998). It is estimated that between 1,200 and 1,300 turbidite systems around the world contain hydrocarbons (Stow and Mayall, 2000), with 43 of these being classified as 'giants' containing the equivalent of over 500 million barrels of oil (Pettingill, 1998) (Fig. 8.4).

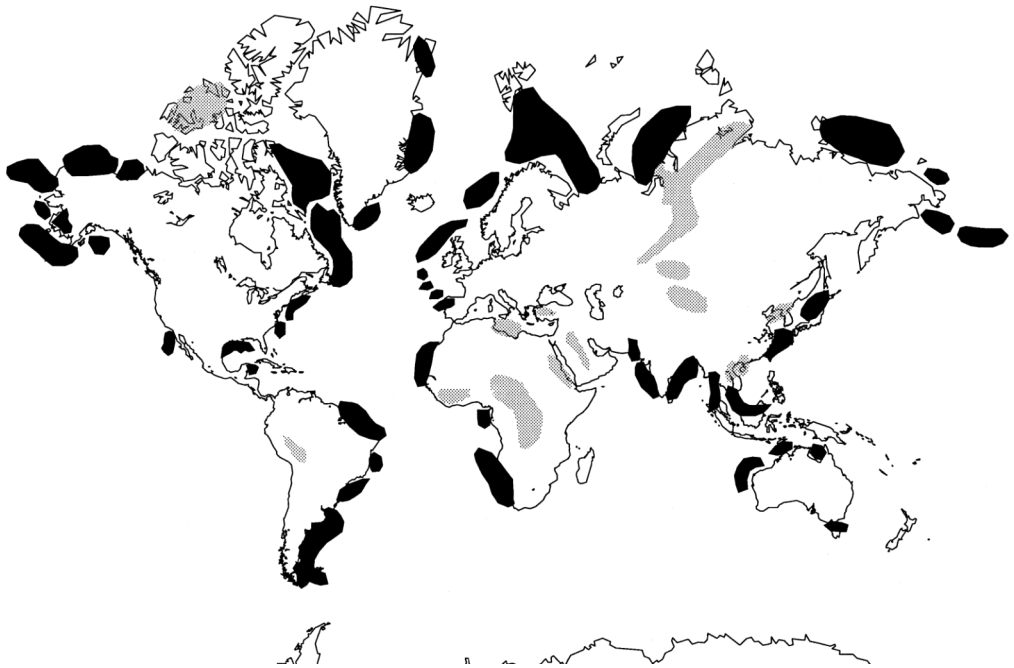

Figure 8.4 | Global distribution of turbidite systems (Stow and Mayall, 2000).

Prior to oil field development, the internal architecture of a deep-marine depositional system needs to be determined to enable the most efficient extraction of hydrocarbons from the system. The internal reservoir architecture of clastic systems is highly variable in geometry, size and internal character, due to sediment flux, sea-level fluctuations and regional basin tectonics.

Currently, determination of the internal architecture of a depositional system is difficult, as widely spaced well and seismic data (typically <60 Hz) lack adequate resolution to identify potential baffles and barriers to flow and relatively minor reservoir sands. A simple method to overcome these difficulties is to study the internal architecture of analogous systems and develop predictive models. Here the model determined from the study of the Ainsa basin, may be applicable to similar analogous basins such as offshore Angola (Bakke et al., 2008) or the Norwegian Vøring and Møre basins (Fugelli and Olsen, 2005). Such a model should enable the prediction of features below current seismic resolution including the position of potential reservoirs

(submarine fan) or barriers and baffles to flow (MTCs) within chronostratigraphically well constrained, deep-marine basins.

With new hydrocarbon deposits becoming increasingly scarce, the ability to improve the understanding of basin development via the study of analogous basins is of utmost importance. Beside the obvious economic aspects, there are good academic reasons for understanding the relative importance of climatic *versus* tectonic processes, their timing and magnitudes, in order to better read the stratigraphic record in deep time and, therefore, understand more about the evolution of the Earth as recorded in surface and crustal processes.

8.6 Limitations of this study

The major limitations of this study are associated with the relatively short time series and the relatively large age uncertainties within the Upper Hecho Group age model. The relatively short outcrop time series collected from the Guaso and Ainsa systems reduced the potential accuracy of the spectral results, while the length of these sections was too short to allow the confident identification of eccentricity cycles. Usually at least six complete oscillations are required to enable the confident isolation of a frequency (Section 2.6.1; Weedon, 2003).

The construction of the age model was hampered by the method of data collection, mainly from the estimation of stratigraphic thickness and the placement of some palaeontological samples. The resultant age model therefore limits the accurate placing of the floating orbital time scales within the geological time scale. Without an accurate time scale for each of the studied sections, uncertainty exists when comparing the timing of the Ainsa basin submarine fans with specific orbital events and other climatic records. However, even with a more accurate age model, the reliability of the calculated curves would still remain an issue. An illustration of this point is made by comparing the La2004, La2010a, La2010b, La2010c and La2010d eccentricity curves of Laskar et al. (2004; 2011).

8.7 Further work

With the results of this study being largely supportive of the initial hypothesis, but remaining inconclusive, further research is required to determine whether the deposition of the submarine fans within the Ainsa basin coincided with a middle Eocene 404 kyr paced glacio-eustatic cycle. Based upon the limitations identified above and the knowledge gained during this investigation, the following research is proposed:

- Robust testing of the 404-kyr glacio-eustatic hypothesis requires the creation of an continuous lithostratigraphic column throughout the entire Upper Hecho Group. This would probably require the lateral correlation of several individual sections. Ideally, the sections should concentrate within the inter-fan and off-axis facies to enable the identification of orbital forcing.
- Within the measured stratigraphy, the high-resolution measurement of radioelement concentrations would be carried out to identify orbital cyclicity. Additional or alternative geochemical measurements could also be performed analysing the sediments calcium carbonate content, magnetic susceptibility and stable isotopic composition. The sampling strategy should enable the amplitude and temporal variation of the shortest precession (23 kyr) cycle to be identified. To ensure that this could be achieved, a sampling resolution of <4 kyr should be used with 8 samples per oscillation (Herbert, 1994). Using the minimum SAR value of 32.7 cm/kyr from the basin average (43.2±10.5 cm/kyr), the suggested 4-kyr sampling interval equates to 1.3 m of stratigraphy. Based upon this sampling interval and the 2.3 km of Upper Hecho Group stratigraphy identified within this thesis, the resultant time series will contain approximately 1769 measurements. Spectral analysis of the resultant time series could then be used to determine whether any orbital cyclicity is present.
- The formation of a robust time scale for the measured stratigraphy should also be constructed via the high-resolution study of nannofossil and large benthic foraminifera. An additional palaeomagnetic study could also be performed to increase the accuracy of the age model. With this temporal framework in place, the time series, potentially ~6 to 8 Myr in duration, can be orbitally tuned using the orbital curves of Laskar et al. (2004; 2011). The resultant orbitally tuned time scale will then be able to definitively determine the pacing and timing of each submarine fan deposit.

Additional analyses should include determining whether the base of each submarine fan is isochronous with their equivalent off-axis deposits, the identification of how SGR

or other geochemical variability is represented within the sediment, and a high-resolution analysis to test whether millennial-scale cyclicity is recorded within inter-fan sediments.

Given unlimited resources, the above could be achieved by the drilling of several additional wells through the entire Upper Hecho Group. High-resolution geophysical time series data could be collected simultaneously using downhole tools. The recovered sediment cores could then be utilised for the construction of palaeo- and magneto-biostratigraphic age models and to construct a high-resolution semi-quantitative elemental time series using an XRF split-core scanner. As above, the elemental time series could be used to construct an orbitally-tuned age scale to test the pacing and timing of the Upper Hecho Group submarine fans.

With a new generic model proposed for the Ainsa basin, it may be possible to predict the timing of sand supply, and hence potential reservoirs within other deep-marine foreland basins. Such an investigation would provide the ideal rigorous test of the above generic model is also applicable to other basins or restricted only to the Ainsa basin.

References

Adams, J.A.S., and Weaver, C.E., 1958, Thorium-to-uranium ratios as indicators of sedimentary processes; example of concept of geochemical facies: AAPG Bulletin, v. 42, p. 387-430.

Agnini, C., Fornaciari, E., Giusberti, L., Grandesso, P., Lanci, L., Luciani, V., Muttoni, G., Pälike, H., Rio, D., Spofforth, D.J.A., and Stefani, C., 2011, Integrated biomagnetostratigraphy of the Alano section (NE Italy): A proposal for defining the middle-late Eocene boundary: Geological Society of America Bulletin, v. 123, p. 841-872.

Agnini, C., Macri, P., Backman, J., Brinkhuis, H., Fornaciari, E., Giusberti, L., Luciani, V., Rio, D., Sluijs, A., and Speranza, F., 2009, An early Eocene carbon cycle perturbation at ~52.5 Ma in the Southern Alps: Chronology and biotic response: Paleoceanography, v. 24, p. PA2209.

Aigner, T., Schauer, M., Junghans, W.D., and Reinhardt, L., 1995, Outcrop gamma-ray logging and its applications: examples from the German Triassic: Sedimentary Geology, v. 100, p. 47-61.

Allen, J.R.L., 1979, Studies in fluviatile sedimentation: An elementary geometrical model for the connectedness of avulsion-related channel sand bodies: Sedimentary Geology, v. 24, p. 253-267.

Anadón, P., and Roca, E., 1996, Geological setting of the Tertiary basins of Northeast Spain, *in* Friend, P.F., and Dabrio, C.J., eds., The Tertiary Basins of Spain: the stratigraphic record of crustal kinematics: Cambridge, Cambridge University Press, p. 153-160.

Anderson, R.F., Lehuray, A.P., Fleisher, M.Q., and Murray, J.W., 1989, Uranium deposition in saanich inlet sediments, vancouver island: Geochimica et Cosmochimica Acta, v. 53, p. 2205-2213.

Anderson, R.Y., 1982, A Long Geoclimatic Record From the Permian: J. Geophys. Res., v. 87, p. 7285-7294.

Anderson, T.F., and Arthur, M.A., 1983, Stable isotopes of oxygen and carbon and their application to sedimentologic and palaeoenvironmental problems, *in* Arthur, M.A., Anderson, T.F., Kaplam, I.R., Veizer, J., and Land, L.S., eds., Stable Isotopes in Sedimentary Geology: Dalas, Society of Economic Palaeontologists and Mineralogists Short Course No. 10.

Andersson, P.O.D., and Worden, R.H., 2004, Mudstones of the Tanqua Basin, South Africa: an analysis of lateral and stratigraphic variations within mudstones, and a comparison of mudstones within and between turbidite fans: Sedimentology, v. 51, p. 479-502.

Andreasson, F.P., and Schmitz, B., 2000, Temperature seasonality in the early middle Eocene North Atlantic region: Evidence from stable isotope profiles of marine gastropod shells: Geological Society of America Bulletin, v. 112, p. 628-640.

Antico, A., Marchal, O., Mysak, L.A., and Vimeux, F., 2010, Milankovitch Forcing and Meridional Moisture Flux in the Atmosphere: Insight from a Zonally Averaged Ocean-Atmosphere Model: Journal of Climate, v. 23, p. 4841-4855.

Ashkenazy, Y., and Gildor, H., 2008, Timing and significance of maximum and minimum equatorial insolation: Paleoceanography, v. 23, p. PA1206.

Bakke, K., Gjelberg, J., and Agerlin Petersen, S., 2008, Compound seismic modelling of the Ainsa II turbidite system, Spain: Application to deep-water channel systems offshore Angola: Marine and Petroleum Geology, v. 25, p. 1058-1073.

Barron, E.J., Hay, W.W., and Thompson, S., 1989, The hydrologic cycle: A major variable during earth history: Palaeogeography, Palaeoclimatology, Palaeoecology, v. 75, p. 157-174.

Bartlett, M.S., 1948, Smoothing periodograms from time series with continuous spectra: Nature, v. 161, p. 686-687.

Bassinot, F.C., Beaufort, L., Vincent, E., Labeyrie, L.D., Rostek, F., M¸ller, P.J., Quidelleur, X., and Lancelot, Y., 1994, Coarse Fraction Fluctuations in Pelagic

Carbonate Sediments from the Tropical Indian Ocean: A 1500-Kyr Record of Carbonate Dissolution: Paleoceanography, v. 9, p. 579-600.
Bayliss, N.J., 2010, Architecture and processes of deep-marine sandbodies, Ainsa basin, Spanish Pyrenees (PhD thesis): London, University College London.
Beamud, E., Muñoz, J.A., Fitzgerald, P.G., Baldwin, S.L., Garcés, M., Cabrera, L., and Metcalf, J.R., 2011, Magnetostratigraphy and detrital apatite fission track thermochronology in syntectonic conglomerates: constraints on the exhumation of the South-Central Pyrenees: Basin Research, v. 23, p. 309-331.
Beaumont, C., Muñoz, J.A., Hamilton, J., and Fullsack, P., 2000, Factors controlling the Alpine evolution of the central Pyrenees inferred from a comparison of observations and geodynamical models: Journal of Geophysical Research, v. 105, p. 8121-8145.
Bentham, P.A., and Burbank, D.W., 1996, Chronology of Eocene foreland basin evolution along the western margin of the South-Central Pyrenees, *in* Friend, P.F., and Dabrio, C.J., eds., Tertiary basins of Spain, the stratigraphic record of crustal kinematics: Cambridge, Cambridge University Press, p. 144-152.
Bentham, P.A., Burbank, D.W., and Puigdefabregas, C., 1992, Temporal and spatial controls on the alluvial architecture of an axial drainage system: late Eocene Escanilla Formation, southern Pyrenean foreland basin, Spain: Basin Research, v. 4, p. 335-352.
Berger, A., 1978a, Long-term variations of caloric insolation resulting from the earth's orbital elements: Quaternary Research, v. 9, p. 139-167.
Berger, A., Loutre, M.-F., and Tricot, C., 1993, Insolation and Earth's Orbital Periods: Journal of Geophysical Research, v. 98, p. 10341-10362.
Berger , A., and Loutre, M.F., 1997, Intertropical Latitudes and Precessional and Half-Precessional Cycles: Science, v. 278, p. 1476-1478.
Berger, A., Loutre, M.F., and Laskar, J., 1992, Stability of the Astronomical Frequencies Over the Earth's History for Paleoclimate Studies: Science, v. 255, p. 560-566.
Berger, A., Loutre, M.F., and Melice, J.L., 2006, Equatorial insolation: from precession harmonics to eccentricity frequencies: Climate of the Past, v. 2, p. 131-136.
Berger, A.L., 1978b, Long-Term Variations of Daily Insolation and Quaternary Climatic Changes: Journal of the Atmospheric Sciences, v. 35, p. 2362-2367.
Bijl, P.K., Houben, A.J.P., Schouten, S., Bohaty, S.M., Sluijs, A., Reichart, G.-J., Sinninghe Damsté, J.S., and Brinkhuis, H., 2010, Transient Middle Eocene Atmospheric CO2 and Temperature Variations: Science, v. 330, p. 819-821.
Bijl, P.K., Schouten, S., Sluijs, A., Reichart, G.-J., Zachos, J.C., and Brinkhuis, H., 2009, Early Palaeogene temperature evolution of the southwest Pacific Ocean: Nature, v. 461, p. 776-779.
Bloomfield, P., 2000, Fourier Analysis of Time Series: An Introduction: New York, Wiley.
Bohaty, S.M., and Zachos, J.C., 2003, Significant Southern Ocean warming event in the late middle Eocene: Geology, v. 31, p. 1017-1020.
Bohaty, S.M., Zachos, J.C., Florindo, F., and Delaney, M.L., 2009, Coupled greenhouse warming and deep-sea acidification in the middle Eocene: Paleoceanography, v. 24, p. PA2207.
Boillot, G., 1986, Comparison between the Galicia and Aquitaine margins: Tectonophysics, v. 129, p. 243-255.
Boudagher-Fadel, M., 2008, Chapter 1 Biology and evolutionary history of larger benthic foraminifera, *in* Boudagher-Fadel, M.K., ed., Developments in Palaeontology and Stratigraphy, Volume Volume 21, Elsevier, p. 1-37.
Boulila, S., Galbrun, B., Hinnov, L.A., and Collin, P.-Y., 2008, High-resolution cyclostratigraphic analysis from magnetic susceptibility in a Lower Kimmeridgian (Upper Jurassic) marl-limestone succession (La Méouge, Vocontian Basin, France): Sedimentary Geology, v. 203, p. 54-63.
Bown, P.R., and Young, J.R., 1998, Techniques, *in* Bown, P.R., ed., Calcareous Nannofossil Biostratigraphy: London, Chapman & Hall, p. 16-28.

Breien, H., De Blasio, F.V., Elverhoi, A., Nystuen, J.P., and Harbitz, C.B., 2010, Transport Mechanisms of Sand in Deep-Marine Environments--Insights Based on Laboratory Experiments: JOURNAL OF SEDIMENTARY RESEARCH, v. 80, p. 975-990.

Bristow, C.S., and Williamson, B.J., 1998, Spectral gamma ray logs: core to log calibration, facies analysis and correlation problems in the Southern North Sea: Geological Society, London, Special Publications, v. 136, p. 1-7.

Broecker, W.S., 2003, The Oceanic CaCO3 Cycle, *in* Heinrich, D.H., and Karl, K.T., eds., Treatise on Geochemistry: Oxford, Pergamon, p. 529-549.

Browning, J.V., Miller, K.G., and Pak, D.K., 1996, Global implications of lower to middle Eocene sequence boundaries on the New Jersey coastal plain: The icehouse cometh: Geology, v. 24, p. 639-642.

Brunet, M.F., 1986, The influence of the evolution of the Pyrenees on adjacent basins: Tectonophysics, v. 129, p. 343-354.

Burbank, D.W., Puigdefabregas, C., and Munoz, J.A., 1992a, The chronology of the Eocene tectonic and stratigraphic development of the eastern Pyrenean foreland basin, northeast Spain: Geological Society of America Bulletin, v. 104, p. 1101-1120.

Burbank, D.W., Verges, J., Munoz, J.A., and Bentham, P., 1992b, Coeval hindward- and forward-imbricating thrusting in the south-central Pyrenees, Spain: Timing and rates of shortening and deposition: Geological Society of America Bulletin, v. 104, p. 3-17.

Burgess, C.E., Pearson, P.N., Lear, C.H., Morgans, H.E.G., Handley, L., Pancost, R.D., and Schouten, S., 2008, Middle Eocene climate cyclicity in the southern Pacific: Implications for global ice volume: Geology, v. 36, p. 651-654.

Caja, M.A., Marfil, R., Garcia, D., Remacha, E., Morad, S., Mansurbeg, H., Amorosi, A., Martínez-Calvo, C., and Lahoz-Beltrá, R., 2010, Provenance of siliciclastic and hybrid turbiditic arenites of the Eocene Hecho Group, Spanish Pyrenees: implications for the tectonic evolution of a foreland basin: Basin Research, v. 22, p. 157-180.

Cecil, C.B., 2003, The Comcept of autocyclic and allocyclic controls on sedimentation and stratigaphy, emphasizing the climatic variable, Climate Controls on Stratigraphy, Volume 77, SEPM (Society for Sedimentary Geology), p. 13-20.

Choukroune, P., 1992, Tectonic Evolution of the Pyrenees: Annual Review of Earth and Planetary Sciences, v. 20, p. 143-158.

Choukroune, P., and Team, E., 1989, The Ecors Pyrenean deep seismic profile reflection data and the overall structure of an orogenic belt: Tectonics, v. 8, p. 23-39.

Chowning, J.M., 1973, The Synthesis of Complex Audio Spectra by Means of Frequency Modulation: Journal of the Audio Engineering Society, v. 21, p. 526-534.

Clemens, S., Prell, W., Murray, D., Shimmield, G., and Weedon, G., 1991, Forcing mechanisms of the Indian Ocean monsoon: Nature, v. 353, p. 720-725.

Colley, S., and Thomson, J., 1985, Recurrent uranium relocations in distal turbidites emplaced in pelagic conditions: Geochimica et Cosmochimica Acta, v. 49, p. 2339-2348.

Cooley, J.W., and Tukey, J.W., 1965, An Algorithm for the Machine Calculation of Complex Fourier Series: Mathematics of Computation, v. 19, p. 297-301.

Cooper, A.K., Barrett, P.J., Hinz, K., Traube, V., Letichenkov, G., and Stagg, H.M.J., 1991, Cenozoic prograding sequences of the Antarctic continental margin: a record of glacio-eustatic and tectonic events: Marine Geology, v. 102, p. 175-213.

Covault, J.A., and Graham, S.A., 2010, Submarine fans at all sea-level stands: Tectono-morphologic and climatic controls on terrigenous sediment delivery to the deep sea: Geology, v. 38, p. 939-942.

Cramer, B.S., Wright, J.D., Kent, D.V., and Aubry, M.-P., 2003, Orbital climate forcing of ∂13C excursions in the late Paleocene-early Eocene (chrons C24n-C25n): Paleoceanography, v. 18, p. 1097.

Croll, J., 1867, XVII. On the excentricity of the Earth's orbit, and its physical relations to the glacial epoch: The Philosophical magazine, v. 33, p. 119.

Cronin, B., Owen, D., Hartley, A., and Kneller, B., 1998, Slumps, debris flows and sandy deep-water channel systems: implications for the application of sequence stratigraphy to deep water clastic sediments: Journal of the Geological Society, v. 155, p. 429-432.

Crowley, T.J., Kim, K.-Y., Mengel, J.G., and Short, D.A., 1992, Modeling 100,000-Year Climate Fluctuations in Pre-Pleistocene Time Series: Science, v. 255, p. 705-707.

Curnelle, R., Dubois, P., Seguin, J.C., Whitaker, D., Matthews, D.H., Roberts, D.G., Kent, P., Laughton, A.S., and Kholief, M.M., 1982, The Mesozoic-Tertiary Evolution of the Aquitaine Basin [and Discussion]: Philosophical Transactions of the Royal Society of London. Series A, Mathematical and Physical Sciences, v. 305, p. 63-84.

Dansgaard, W., Johnsen, S.J., Clausen, H.B., Dahl-Jensen, D., Gundestrup, N.S., Hammer, C.U., Hvidberg, C.S., Steffensen, J.P., Sveinbjornsdottir, A.E., Jouzel, J., and Bond, G., 1993, Evidence for general instability of past climate from a 250-kyr ice-core record: Nature, v. 364, p. 218-220.

Das Gupta, K., 2008, Petrography and chemostratigraphy of the Mid Eocene deep-marine clastic sediments, Ainsa and Jaca basins, Spanish Pyrenees (PhD thesis): London, University College London.

Das Gupta, K., and Pickering, K.T., 2008, Petrography and temporal changes in petrofacies of deep-marine Ainsa-Jaca basin sandstone systems, Early and Middle Eocene, Spanish Pyrenees: Sedimentology, v. 55, p. 1083-1114.

Davies, S.J., and Elliott, T., 1996, Spectral gamma ray characterization of high resolution sequence stratigraphy: examples from Upper Carboniferous fluvio-deltaic systems, County Clare, Ireland: Geological Society, London, Special Publications, v. 104, p. 25-35.

Dawber, C.F., and Tripati, A.K., 2011, Constraints on glaciation in the middle Eocene (46-37 Ma) from Ocean Drilling Program (ODP) Site 1209 in the tropical Pacific Ocean: Paleoceanography, v. 26, p. PA2208.

Dawber, C.F., Tripati, A.K., Gale, A.S., MacNiocaill, C., and Hesselbo, S.P., 2011, Glacioeustasy during the middle Eocene? Insights from the stratigraphy of the Hampshire Basin, UK: Palaeogeography, Palaeoclimatology, Palaeoecology, v. 300, p. 84-100.

de Boer, P.L., Pragt, J.S.J., and Oost, A.P., 1991, Vertically persistent sedimentary facies boundaries along growth anticlines and climate-controlled sedimentation in the thrust-sheet-top South Pyrenean Tremp-Graus Foreland Basin: Basin Research, v. 3, p. 63-78.

de Boer, P.L., and Smith, D.G., 1994, Orbital forcing and cyclic sequences, *in* de Boer, P.L., and Smith, D.G., eds., Orbtial Forcing and Cyclic Sequences: Special Publication of the International Assocaition of Sedimentologists: Oxford, Blackwell Scientific Publications, p. 1-14.

De Visser, J.P., Ebbing, J.H.J., Gudjonsson, L., Hilgen, F.J., Jorissen, F.J., Verhallen, P.J.J.M., and Zevenboom, D., 1989, The origin of rhythmic bedding in the Pliocene Trubi Formation of Sicily, southern Italy: Palaeogeography, Palaeoclimatology, Palaeoecology, v. 69, p. 45-66.

Dean, W.E., and Gardner, J.V., 1986, Milankovitch Cycles in Neogene Deep-Sea Sediment: Paleoceanography, v. 1, p. 539-553.

Dean, W.E., Gardner, J.V., and Cepek, P., 1981, Tertiary carbonate-dissolution cycles on the Sierra Leone Rise, eastern equatorial Atlantic Ocean: Marine Geology, v. 39, p. 81-101.

DeConto, R.M., and Pollard, D., 2003, Rapid Cenozoic glaciation of Antarctica induced by declining atmospheric CO2: Nature, v. 421, p. 245-249.

DeConto, R.M., Pollard, D., Wilson, P.A., Pälike, H., Lear, C.H., and Pagani, M., 2008, Thresholds for Cenozoic bipolar glaciation: Nature, v. 455, p. 652-656.

Deptuck, M.E., Piper, D.J.W., Savoye, B., and Gervais, A., 2008, Dimensions and architecture of late Pleistocene submarine lobes off the northern margin of East Corsica: Sedimentology, v. 55, p. 869-898.

Dickens, G.R., O'Neil, J.R., Rea, D.K., and Owen, R.M., 1995, Dissociation of Oceanic Methane Hydrate as a Cause of the Carbon Isotope Excursion at the End of the Paleocene: Paleoceanography, v. 10, p. 965-971.

Diester-Haass, L., 1991, Rhythmic carbonate content variations in Neogene sediments above the oceanic lysocline, *in* Einsele, G., Ricken, W., and Seilacher, A., eds., Cycles and Events in Stratigraphy: Berlin, Springer-Verlag.

Dreyer, T., Corregidor, J., Arbues, P., and Puigdefabregas, C., 1999, Architecture of the tectonically influenced Sobrarbe deltaic complex in the Ainsa Basin, northern Spain: Sedimentary Geology, v. 127, p. 127-169.

Eberle, J.J., Fricke, H.C., Humphrey, J.D., Hackett, L., Newbrey, M.G., and Hutchison, J.H., 2010, Seasonal variability in Arctic temperatures during early Eocene time: Earth and Planetary Science Letters, v. 296, p. 481-486.

Eberli, G.P., 2000, The record of Neogene sealevel changes in the prograding carbonates along the Bahamas transect-Leg 166 synthesis, *in* Swart, P.K., Eberli, G.P., Malone, M.J., and Sarg, J.F., eds., Proc. ODP, Sci. Results, Volume 166, Ocean Drilling Program.

Ehrmann, W.U., and Mackensen, A., 1992, Sedimentological evidence for the formation of an East Antarctic ice sheet in Eocene/Oligocene time: Palaeogeography, Palaeoclimatology, Palaeoecology, v. 93, p. 85-112.

Einsele, G., 1982, Limestone-marl cycles (periodites): Diagnosis, significance, causes - a review, *in* Einsele, G., and Seilacher, A., eds., Cyclic and Event Stratification: Berlin, Springer-Verlag, p. 8-53.

Elrick, M., and Hinnov, L.A., 1996, Millennial-scale climate origins for stratification in Cambrian and Devonian deep-water rhythmites, western USA: Palaeogeography, Palaeoclimatology, Palaeoecology, v. 123, p. 353-372.

—, 2007, Millennial-scale paleoclimate cycles recorded in widespread Palaeozoic deeper water rhythmites of North America: Palaeogeography, Palaeoclimatology, Palaeoecology, v. 243, p. 348-372.

Elrick, M., Read, J.F., and Coruh, C., 1991, Short-term paleoclimatic fluctuations expressed in lower Mississippian ramp-slope deposits, southwestern Montana: Geology, v. 19, p. 799-802.

Emery, D., 1987, Trace-element source and mobility during limestone burial diagenesis - example from the Middle Jurassic of eastern England: Geological Society, London, Special Publications, v. 36, p. 201-217.

Erba, E., and Premoli Silva, I., 1994, Orbitally driven cycles in trace-fossil distribution from the Piobbico core (late Albian, central Italy), *in* de Boer, P.L., and Smith, D.G., eds., Orbital Forcing and Cyclic Sequences, Volume 19: Special Publication of the International Assocaition of Sedimentologists: Oxford, Blackwell Scientific Publications, p. 211-225.

Falivene, O., Arbues, P., Gardiner, A., Pickup, G., Munoz, J.A., and Cabrera, L., 2006a, Best practice stochastic facies modeling from a channel-fill turbidite sandstone analog (the Quarry outcrop, Eocene Ainsa basin, northeast Spain): AAPG Bulletin, v. 90, p. 1003-1029.

Falivene, O., ArbuÈs, P., Howell, J., MuÒoz, J.A., Fern·ndez, O., and Marzo, M., 2006b, Hierarchical geocellular facies modelling of a turbidite reservoir analogue from the Eocene of the Ainsa basin, NE Spain: Marine and Petroleum Geology, v. 23, p. 679-701.

Falivene, O., Arbues, P., Ledo, J., Benjumea, B., Munoz, J.A., Fernandez, O., and Martinez, S., 2010, Synthetic seismic models from outcrop-derived reservoir-scale three-dimensional facies models: The Eocene Ainsa turbidite system (southern Pyrenees): AAPG Bulletin, v. 94, p. 317-343.

Farge, M., 1992, Wavelet Transforms and their Applications to Turbulence: Annual Review of Fluid Mechanics, v. 24, p. 395-458.
Farrell, S.G., 1984, A dislocation model applied to slump structures, Ainsa Basin, South Central Pyrenees: Journal of Structural Geology, v. 6, p. 727-736.
Farrell, S.G., Williams, G.D., and Atkinson, C.D., 1987, Constraints on the age of movement of the Montsech and Cotiella Thrusts, south central Pyrenees, Spain: Journal of the Geological Society, v. 144, p. 907-914.
Feeley, M.H., Moore, T.C., Loutit, T.S., and Bryant, W.R., 1990, Sequence Stratigraphy of Mississippi Fan Related to Oxygen Isotope Sea Level Index: AAPG Bulletin, v. 74, p. 407-424.
Fenton, J.P.G., 1999, Ainsa Deep Water Channel Project, Spanish Pyrenees: Biostratigraphic Analysis of Core Samples from Six Shallow Boreholes (unpublished): Llandudno, Robertson Research International Limited.
Fernandez, O., Munoz, J.A., Arbues, P., Falivene, O., and Marzo, M., 2004, Three-dimensional reconstruction of geological surfaces: An example of growth strata and turbidite systems from the Ainsa basin (Pyrenees, Spain): AAPG Bulletin, v. 88, p. 1049-1068.
Fischer, A.G., 1986, Climatic Rhythms Recorded in Strata: Annual Review of Earth and Planetary Sciences, v. 14, p. 351-376.
—, 1995, Cyclostratigraphy, Quo Vadis?: Geological Society, London, Special Publications, v. 85, p. 199-204.
Fischer, A.G., Herbert, T.D., Napoleone, G., Premoli Silva, I., and Ripepe, M., 1991, Albian pelagic rhythms (Piobbico Core): Journal of Sedimentary Petrology, v. 61, p. 1164-1172.
Fischer, M.W., 1984, Thrust tectonics in the North Pyrenees: Journal of Structural Geology, v. 6, p. 721-726.
Fontana, D., Zuffa, G.G., and Garzanti, E., 1989, The interaction of eustacy and tectonism from provenance studies of the Eocene Hecho Group Turbidite Complex (South-Central Pyrenees, Spain): Basin Research, v. 2, p. 223-237.
Franco, D.R., Hinnov, L.A., and Ernesto, M., 2012, Millennial-scale climate cycles in Permian-Carboniferous rhythmites: Permanent feature throughout geologic time?: Geology, v. 40, p. 19-22.
Fugelli, E.M.G., and Olsen, T.R., 2005, Screening for deep-marine reservoirs in frontier basins: Part 1--Examples from offshore mid-Norway: AAPG Bulletin, v. 89, p. 853-882.
Galeotti, S., Krishnan, S., Pagani, M., Lanci, L., Gaudio, A., Zachos, J.C., Monechi, S., Morelli, G., and Lourens, L., 2010, Orbital chronology of Early Eocene hyperthermals from the Contessa Road section, central Italy: Earth and Planetary Science Letters, v. 290, p. 192-200.
Ganti, V., Straub, K.M., Foufoula-Georgiou, E., and Paola, C., 2011, Space-time dynamics of depositional systems: Experimental evidence and theoretical modeling of heavy-tailed statistics: J. Geophys. Res., v. 116, p. F02011.
Gaspar-Escribano, J.M., Van Wees, J.D., Ter Voorde, M., Cloetingh, S., Roca, E., Cabrera, L., Muñoz, J.A., Ziegler, P.A., and Garcia-Castellanos, D., 2001, Three-dimensional flexural modelling of the Ebro Basin (NE Iberia): Geophysical Journal International, v. 145, p. 349-367.
Ghil, M., Allen, M.R., Dettinger, M.D., Ide, K., Kondrashov, D., Mann, M.E., Robertson, A.W., Saunders, A., Tian, Y., Varadi, F., and Yiou, P., 2002, Advanced spectral methods for climatic time series: Rev. Geophys., v. 40, p. 1003.
Gilman, D.L., Fuglister, F.J., and Mitchell, J.M., 1963, On the Power Spectrum of Red Noise: Journal of the Atmospheric Sciences, v. 20, p. 182-184.
Goodwin, P.W., and Anderson, E.J., 1985, Punctuated Aggradational Cycles: A General Hypothesis of Episodic Stratigraphic Accumulation: The Journal of Geology, v. 93, p. 515-533.
Gradstein, F.M., Ogg, J.G., Smith, A.G., Agterberg, F.P., Bleeker, W., Cooper, R.A., Davydov, V., Gibbard, P., Hinnov, L., House, M.R., Lourens, L., Luterbacher, H.-P., McArthur, J., Melchin, M.J., Robb, L.J., Shergold, J., Villenueve, M.,

Wardlaw, B.R., Ali, J., Brinkhuis, H., Hilgen, F.J., Hooker, J., Howarth, R.J., Knoll, A.H., Laskar, J., Monechi, S., Powell, J., Plumb, K.A., Raffi, I., Rohl, U., Sanfilipo, A., Schmitz, B., Schakleton, N.J., Shields, G.A., Strauss, H., van Dam, J., Veizer, J., van Kolfschoten, T., and Wilson, D., 2004, A Geologic Time Scale 2004: Cambridge, Cambridge University Press, 384 p.

Greenwood, D.R., and Wing, S.L., 1995, Eocene continental climates and latitudinal temperature gradients: Geology, v. 23, p. 1044-1048.

Grinsted, A., Moore, J.C., and Jevrejeva, S., 2004, Application of the cross wavelet transform and wavelet coherence to geophysical time series: Nonlinear Processes in Geophysics, v. 11, p. 561-566.

Grutzner, J., Giosan, L., Franz, S.O., Tiedemann, R., Cortijo, E., Chaisson, W.P., Flood, R.D., Hagen, S., Keigwin, L.D., Poli, S., Rio, D., and Williams, T., 2002, Astronomical age models for Pleistocene drift sediments from the western North Atlantic (ODP Sites 1055-1063): Marine Geology, v. 189, p. 5-23.

Grutzner, J., and Higgins, S.M., 2010, Threshold behavior of millennial scale variability in deep water hydrography inferred from a 1.1 Ma long record of sediment provenance at the southern Gardar Drift: Paleoceanography, v. 25, p. PA4204.

Hagelberg, T.K., Bond, G., and deMenocal, P., 1994, Milankovitch Band Forcing of Sub-Milankovitch Climate Variability during the Pleistocene: Paleoceanography, v. 9, p. 545-558.

Hagelberg, T.K., and Pisias, N., 1990, Nonlinear Response of Pliocene Climate to Orbital Forcing: Evidence from the Eastern Equatorial Pacific: Paleoceanography, v. 5, p. 595-617.

Hampson, G.J., Davies, W., Davies, S.J., Howell, J.A., and Adamson, K.R., 2005, Use of spectral gamma-ray data to refine subsurface fluvial stratigraphy: late Cretaceous strata in the Book Cliffs, Utah, USA: Journal of the Geological Society, v. 162, p. 603-621.

Haq, B.U., Hardenbol, J., and Vail, P.R., 1987, Chronology of Fluctuating Sea Levels Since the Triassic: Science, v. 235, p. 1156-1167.

Hardenbol, J.A.N., Thierry, J., Farley, M.B., Jacquin, T., De Graciansky, P.-C., and Vail, P.R., 1998, Mesozoic and Cenozoic sequence chronostratigaphic framework of European basins, Mesozoic and Cenozoic Sequence Stratigraphy of European Basins, Volume 60, SEPM (Society for Sedimentary Geology), p. 3-13.

Harris, F.J., 1978, On the use of windows for harmonic analysis with the discrete Fourier transform: Proceedings of the IEEE, v. 66, p. 51-83.

Harris, S.E., and Mix, A.C., 1999, Pleistocene Precipitation Balance in the Amazon Basin Recorded in Deep Sea Sediments: Quaternary Research, v. 51, p. 14-26.

Hays, J.D., Imbrie, J., and Shackleton, N.J., 1976, Variations in the Earth's Orbit: Pacemaker of the Ice Ages: Science, v. 194, p. 1121-1132.

Heard, T.G., and Pickering, K.T., 2008, Trace fossils as diagnostic indicators of deep-marine environments, Middle Eocene Ainsa-Jaca basin, Spanish Pyrenees: Sedimentology, v. 55, p. 809-844.

Heard, T.G., Pickering, K.T., and Robinson, S.A., 2008, Milankovitch forcing of bioturbation intensity in deep-marine thin-bedded siliciclastic turbidites: Earth and Planetary Science Letters, v. 272, p. 130-138.

Herbert, T.D., 1994, Reading orbital signals distorted by sedimentation: models and examples, *in* de Boer, P.L., and Smith, D.G., eds., International Association of Sedimentologists Special Publication 19: Oxford, Blackwell, p. 483-507.

Herbert, T.D., and Fischer, A.G., 1986, Milankovitch climatic origin of mid-Cretaceous black shale rhythms in central Italy: Nature, v. 321, p. 739-743.

Herbert, T.D., and Mayer, L.A., 1991, Long climatic time series from sediment physical property measurements: Journal of Sedimentary Petrology, v. 61, p. 1089-1108.

Hesselbo, S.P., Deconinck, J.-F., Huggett, J.M., and Morgans-Bell, H.S., 2009, Late Jurassic palaeoclimatic change from clay mineralogy and gamma-ray

spectrometry of the Kimmeridge Clay, Dorset, UK: Journal of the Geological Society, v. 166, p. 1123-1133.
Hinnov, L.A., 2000, New Perspectives on Orbitally Forced Stratigraphy: Annual Review of Earth and Planetary Sciences, v. 28, p. 419-475.
Hinnov, L.A., and Park, J., 1998, Detection of astronomical cycles in the stratigraphic record by frequency modulation (FM) analysis: JOURNAL OF SEDIMENTARY RESEARCH, v. 68, p. 524-539.
Hogan, P.J., Burbank, D.W., Friend, P.F., and Dabrio, C.J., 1996, Evolution of the Jaca piggyback basin and emergence of the External Sierra, southern Pyrenees
Tertiary Basins of Spain, Cambridge University Press.
Holl, J.E., and Anastasio, D.J., 1993, Paleomagnetically derived folding rates, southern Pyrenees, Spain: Geology, v. 21, p. 271-274.
—, 1995, Kinematics around a large-scale oblique ramp, southern Pyrenees, Spain: Tectonics, v. 14, p. 1368-1379.
Hollis, C.J., Dickens, G.R., Field, B.D., Jones, C.M., and Percy Strong, C., 2005, The Paleocene-Eocene transition at Mead Stream, New Zealand: a southern Pacific record of early Cenozoic global change: Palaeogeography, Palaeoclimatology, Palaeoecology, v. 215, p. 313-343.
Houck, K.J., 1997, Effects of sedimentation, tectonics, and glacio-eustasy on depositional sequences, Pennsylvanian Minturn Formation, north-central Colorado: AAPG Bulletin, v. 81, p. 1510-1533.
Howell, D., and Vedder, J., 1983, Ferrelo Fan, California: Depositional system influenced by Eustatic sea level changes: Geo-Marine Letters, v. 3, p. 187-192.
Huber, M., and Sloan, L.C., 2001, Heat transport, deep waters, and thermal gradients: Coupled simulation of an Eocene greenhouse climate: Geophysical Research Letters, v. 28, p. 3481-3484.
Hurst, A., 1990, Natural gamma-ray spectrometry in hydrocarbon-bearing sandstones from the Norwegian Continental Shelf: Geological Society, London, Special Publications, v. 48, p. 211-222.
Huybers, P., and Aharonson, O., 2010, Orbital tuning, eccentricity, and the frequency modulation of climatic precession: Paleoceanography, v. 25, p. PA4228.
Huybers, P., and Wunsch, C., 2004, A depth-derived Pleistocene age model: Uncertainty estimates, sedimentation variability, and nonlinear climate change: Paleoceanography, v. 19, p. PA1028.
Hyun, S., Ahagon, N., and Yoon, H.-I., 2005, Milankovitch cycles and paleoceanographic evolution within sediments from ODP Sites 980 and 983 of the North Atlantic Ocean: Geosciences Journal, v. 9, p. 235-242.
Ifeachor, E.C., and Jervis, B.W., 2002, Digital Signal Processing: A Practical Approach: London, Prentice Hall.
Itambi, A.C., von Dobeneck, T., Mulitza, S., Bickert, T., and Heslop, D., 2009, Millennial-scale northwest African droughts related to Heinrich events and Dansgaard-Oeschger cycles: Evidence in marine sediments from offshore Senegal: Paleoceanography, v. 24, p. PA1205.
Jansen, J.H.F., Van der Gaast, S.J., Koster, B., and Vaars, A.J., 1998, CORTEX, a shipboard XRF-scanner for element analyses in split sediment cores: Marine Geology, v. 151, p. 143-153.
Jarrard, R.D., and Arthur, M.A., 1989, Milankovitch Paleoceanographic Cycles in Geophysical Logs from ODP Leg 105, Labrador Sea and Baffin Bay: Proceedings of the Ocean Driiling Program, Scientific Results, v. 105, p. 757-772.
Jarvis, I., Mabrouk, A., Moody, R.T.J., and de Cabrera, S., 2002, Late Cretaceous (Campanian) carbon isotope events, sea-level change and correlation of the Tethyan and Boreal realms: Palaeogeography, Palaeoclimatology, Palaeoecology, v. 188, p. 215-248.
Jenkins, G.M., and Watts, D.G., 1968, Spectral Analysis and its Applications: San Francisco, Holden-Day.

Jenkins, R., and De Vries, J.L., 1970, Practical X-ray Spectrometry: London, Macmillan.
Jenkyns, H.C., Jones, C.E., Grocke, D.R., Hesselbo, S.P., and Parkinson, D.N., 2002, Chemostratigraphy of the Jurassic System: applications, limitations and implications for palaeoceanography: Journal of the Geological Society, v. 159, p. 351-378.
Jerolmack, D.J., and Paola, C., 2007, Complexity in a cellular model of river avulsion: Geomorphology, v. 91, p. 259-270.
Jones, R.W., Pickering, K.T., Boudagher-Fadel, M., and Matthews, S., 2005, Preliminary observations on the micropalaeontological characterization of submarine fan/channel sub-environments, Ainsa System, south-central Pyrenees, Spain, *in* Powell, A.J., and Riding, J.B., eds., Recent Developments in Applied Biostratigraphy: London, The Micropalaeontological Society.
Kapellos, C., and Schaub, H., 1973, Zur Korrelation von Biozonierungen mit Grossforaminiferen und Nannoplankton im Palaogen der Pyrenaen: Eclogae Geologicae Helvetiae, v. 66, p. 687-737.
Keating-Bitonti, C.R., Ivany, L.C., Affek, H.P., Douglas, P., and Samson, S.D., 2011, Warm, not super-hot, temperatures in the early Eocene subtropics: Geology, v. 39, p. 771-774.
Keener, V.W., Feyereisen, G.W., Lall, U., Jones, J.W., Bosch, D.D., and Lowrance, R., 2010, El-Nino/Southern Oscillation (ENSO) influences on monthly NO3 load and concentration, stream flow and precipitation in the Little River Watershed, Tifton, Georgia (GA): Journal of Hydrology, v. 381, p. 352-363.
Kennett, J.P., and Stott, L.D., 1991, Abrupt deep-sea warming, palaeoceanographic changes and benthic extinctions at the end of the Palaeocene: Nature, v. 353, p. 225-229.
King, T., 1996, Quantifying nonlinearity and geometry in time series of climate: Quaternary Science Reviews, v. 15, p. 247-266.
Kleiven, H.F., Hall, I.R., McCave, I.N., Knorr, G., and Jansen, E., 2011, Coupled deep-water flow and climate variability in the middle Pleistocene North Atlantic: Geology, v. 39, p. 343-346.
Klinkhammer, G.P., and Palmer, M.R., 1991, Uranium in the oceans: Where it goes and why: Geochimica et Cosmochimica Acta, v. 55, p. 1799-1806.
Kodama, K.P., Anastasio, D.J., Newton, M.L., Pares, J.M., and Hinnov, L.A., 2010, High-resolution rock magnetic cyclostratigraphy in an Eocene flysch, Spanish Pyrenees: Geochemistry, Geophysics, Geosystems, v. 11, p. Q0AA07.
Koptikova, L., Babek, O., Hladil, J., Kalvoda, J., and Slavik, L., 2010, Stratigraphic significance and resolution of spectral reflectance logs in Lower Devonian carbonates of the Barrandian area, Czech Republic; a correlation with magnetic susceptibility and gamma-ray logs: Sedimentary Geology, v. 225, p. 83-98.
Kroon, D., Williams, T., Pirmez, C., Spezzaferri, S., Sato, T., and Wright, J.D., 2000, Coupled early Pliocene-middle Miocene bio-cyclostratigraphy of Site 1006 reveals orbitally induced cyclicity patterns of Great Bahama Bank carbonate production, *in* Swart, P.K., Eberli, G.P., Malone, M.J., and Sarg, J.F., eds., Proc. ODP, Sci. Results, Volume 166, Ocean Drilling Program.
Kukla, G., and Gavin, J., 2004, Milankovitch climate reinforcements: Global and Planetary Change, v. 40, p. 27-48.
Kump, L.R., and Arthur, M.A., 1999, Interpreting carbon-isotope excursions: carbonates and organic matter: Chemical Geology, v. 161, p. 181-198.
Kurtz, A.C., Kump, L.R., Arthur, M.A., Zachos, J.C., and Paytan, A., 2003, Early Cenozoic decoupling of the global carbon and sulfur cycles: Paleoceanography, v. 18, p. 1090.
Kutzbach, J.E., and Otto-Bliesner, B.L., 1982, The Sensitivity of the African-Asian Monsoonal Climate to Orbital Parameter Changes for 9000 Years B.P. in a Low-Resolution General Circulation Model: Journal of the Atmospheric Sciences, v. 39, p. 1177-1188.

Labaume, P., Mutti, E., and Seguret, M., 1987, Megaturbidites: A depositional model from the eocene of the SW-Pyrenean Foreland basin, Spain: Geo-Marine Letters, v. 7, p. 91-101.
Labaume, P., SÈguret, M., and Seyve, C., 1985, Evolution of a turbiditic foreland basin and analogy with an accretionary prism: Example of the Eocene South-Pyrenean Basin: Tectonics, v. 4, p. 661-685.
Labourdette, R., Crumeyrolle, P., and Remacha, E., 2008, Characterisation of dynamic flow patterns in turbidite reservoirs using 3D outcrop analogues: Example of the Eocene Morillo turbidite system (south-central Pyrenees, Spain): Marine and Petroleum Geology, v. 25, p. 255-270.
Lamy, F., Kaiser, J.r.m., Ninnemann, U., Hebbeln, D., Arz, H.W., and Stoner, J., 2004, Antarctic Timing of Surface Water Changes off Chile and Patagonian Ice Sheet Response: Science, v. 304, p. 1959-1962.
Laskar, J., Fienga, A., Gastineau, M., and Manche, H., 2011, La2010: A new orbital solution for the long term motion of the earth: Astronomy and Astrophysics.
Laskar, J., Joutel, F., and Boudin, F., 1993, Orbital, precessional, and insolation quantities for the Earth from -20Myr to 20 Myr: Astronomy and Astrophysics, v. 270, p. 522-533.
Laskar, J., Robutel, P., Joutel, F., Gastineau, M., Correia, A.C.M., and Levrard, B., 2004, A long-term numerical solution for the insolation quantities of the Earth: Astronomy and Astrophysics, v. 428, p. 261-285.
Lau, K.M., and Weng, H., 1995, Climate Signal Detection Using Wavelet Transform: How to Make a Time Series Sing: Bulletin of the American Meteorological Society, v. 76, p. 2391-2402.
Laurin, J.ô., Meyers, S.R., Sageman, B.B., and Waltham, D., 2005, Phase-lagged amplitude modulation of hemipelagic cycles: A potential tool for recognition and analysis of sea-level change: Geology, v. 33, p. 569-572.
Lawrence, K.T., Sloan, L.C., and Sewall, J.O., 2003, Terrestrial climatic response to precessional orbital forcing in the Eocene: Geological Society of America Special Papers, v. 369, p. 65-77.
Le, J., and Shackleton, N.J., 1992, Carbonate Dissolution Fluctuations in the Western Equatorial Pacific During the Late Quaternary: Paleoceanography, v. 7, p. 21-42.
Leeder, M., Raiswell, R., Al-Biatty, H., McMahon, A., and Hardman, M., 1990, Carboniferous stratigraphy, sedimentation and correlation of well 48/3-3 in the southern North Sea Basin: integrated use of palynology, natural gamma/sonic logs and carbon/sulphur geochemistry: Journal of the Geological Society, v. 147, p. 287-300.
Lees, J.M., and Park, J., 1995, Multiple-taper spectral analysis: A stand-alone C-subroutine: Computers & Geosciences, v. 21, p. 199-236.
Lisiecki, L.E., and Raymo, M.E., 2005, A Pliocene-Pleistocene stack of 57 globally distributed benthic d18O records: Paleoceanography, v. 20, p. PA1003.
Lomb, N.R., 1976, Least-squares frequency analysis of unequally spaced data: Astrophysics and Space Science, v. 39, p. 447-462.
Lourens, L.J., Sluijs, A., Kroon, D., Zachos, J.C., Thomas, E., Röhl, U., Bowles, J., and Raffi, I., 2005, Astronomical pacing of late Palaeocene to early Eocene global warming events: Nature, v. 435, p. 1083-1087.
Lovborg, L., and Mose, E., 1987, Counting statistics in radioelement assaying with a portable spectrometer: Geophysics, v. 52, p. 555-563.
Lovborg, L., Nyegaard, P., Christiansen, E.M., and Nielsen, B.L., 1980, Borehole logging for uranium by gamma-ray spectrometry: Geophysics, v. 45, p. 1077-1090.
Lovborg, L., Wollenberg, H., Srensen, P., and Hansen, J., 1971, Field determination of uranium and thorium by gamma-ray spectrometry, exemplified by measurements in the Ilmaussaq alkaline intrusion, south Greenland: Economic Geology, v. 66, p. 368-384.

Lovley, D.R., Phillips, E.J.P., Gorby, Y.A., and Landa, E.R., 1991, Microbial reduction of uranium: Nature, v. 350, p. 413-416.
Lowenstein, T.K., and Demicco, R.V., 2006, Elevated Eocene Atmospheric CO2 and Its Subsequent Decline: Science, v. 313, p. 1928.
Lu, H., Zhang, F., and Liu, X., 2003, Patterns and frequencies of the East Asian winter monsoon variations during the past million years revealed by wavelet and spectral analyses: Global and Planetary Change, v. 35, p. 67-74.
Lüning, S., and Kolonic, S., 2003, Uranium spectral gamma-ray response as a proxy for organic richness in black shales: Applicability and limitations: Journal of Petroleum Geology, v. 26, p. 153-174.
Lunsen, V., 1970, Geology of the Ara-Cinca Region, Spanish Pyrenees, Province of Huesca, Utrecht University.
MacDonald, G.J., 1989, Spectral analysis of time series generated by nonlinear processes: Reviews of Geophysics, v. 27, p. 449-469.
Machlus, M.L., Olsen, P.E., Christie-Blick, N., and Hemming, S.R., 2008, Spectral analysis of the lower Eocene Wilkins Peak Member, Green River Formation, Wyoming: Support for Milankovitch cyclicity: Earth and Planetary Science Letters, v. 268, p. 64-75.
Manley, P.L., and Flood, R.D., 1988, Cyclic Sediment Deposition Within Amazon Deep-Sea Fan: AAPG Bulletin, v. 72, p. 912-925.
Mansurbeg, H., Caja, M.A., Marfil, R., Morad, S., Remacha, E., Garcia, D., Martin-Crespo, T., El-Ghali, M.A.K., and Nystuen, J.P., 2009, Diagenetic Evolution and Porosity Destruction of Turbiditic Hybrid Arenites and Siliciclastic Sandstones of Foreland Basins: Evidence from the Eocene Hecho Group, Pyrenees, Spain: JOURNAL OF SEDIMENTARY RESEARCH, v. 79, p. 711-735.
Marsaglia, K.M., Fukusawa, H., Cornell, W.C., Skilbeck, C.G., Meyers, P.A., Prasad, M., and Klaus, A., 2004, Eustatic Signals in Deep-Marine Sedimentary Sequences Recovered at ODP Site 978, Alboran Basin, Western Mediterranean Sea: JOURNAL OF SEDIMENTARY RESEARCH, v. 74, p. 378-390.
Marshall, J.D., 1992, Climatic and oceanographic isotopic signals from the carbonate rock record and their preservation: Geological Magazine, v. 129, p. 143-160.
Martinez, P., and Casas, S., 2003, Cretaceous-Tertiary tectonic inversion of the Cotiella Basin (southern Pyrenees, Spain): International Journal of Earth Sciences, v. 92, p. 99-113.
Martini, E., 1971, Standard Tertiary and Quaternary calcareous nannoplankton zonation, *in* Farinacci, A., ed., Proceedings of the Second Planktonic Conference Roma 1970, Volume 2: Rome, Edizioni Tecnoscienza, p. 739-785.
Marzo, M., Nijman, W., and Puigdefabregas, C.A.I., 1988, Architecture of the Castissent fluvial sheet sandstones, Eocene, South Pyrenees, Spain: Sedimentology, v. 35, p. 719-738.
Maslin, M.A., and Ridgwell, A.J., 2005, Mid-Pleistocene revolution and the 'eccentricity myth': Geological Society, London, Special Publications, v. 247, p. 19-34.
Mawson, M., and Tucker, M., 2009, High-frequency cyclicity (Milankovitch and millennial-scale) in slope-apron carbonates: Zechstein (Upper Permian), North-east England: Sedimentology, v. 56, p. 1905-1936.
Mayer, H., and Appel, E., 1999, Milankovitch cyclicity and rock-magnetic signatures of palaeoclimatic change in the Early Cretaceous Biancone Formation of the Southern Alps, Italy: Cretaceous Research, v. 20, p. 189-214.
McClay, K., Mu√±oz, J.-A., and Garc√≠a-Senz, J., 2004, Extensional salt tectonics in a contractional orogen: A newly identified tectonic event in the Spanish Pyrenees: Geology, v. 32, p. 737-740.
Meigs, A.J., and Burbank, D.W., 1997, Growth of the South Pyrenean orogenic wedge: Tectonics, v. 16, p. 239-258.
Meigs, A.J., Vergés, J., and Burbank, D.W., 1996, Ten-million-year history of a thrust sheet: Geological Society of America Bulletin, v. 108, p. 1608-1625.

Melice, J.L., Coron, A., and Berger, A., 2001, Amplitude and Frequency Modulations of the Earth's Obliquity for the Last Million Years: Journal of Climate, v. 14, p. 1043-1054.
Meyers, S.D., Kelly, B.G., and O'Brien, J.J., 1993, An Introduction to Wavelet Analysis in Oceanography and Meteorology: With Application to the Dispersion of Yanai Waves: Monthly Weather Review, v. 121, p. 2858-2866.
Meyers, S.R., 2008, Resolving Milankovitchian controversies: The Triassic Latemar Limestone and the Eocene Green River Formation: Geology, v. 36, p. 319-322.
Meyers, S.R., and Sageman, B.B., 2007, Quantification of deep-time orbital forcing by average spectral misfit: American Journal of Science, v. 307, p. 773-792.
Milankovitch, M., 1941, Kanon der Erdbestrahlungen und seine Anwendung auf das Eiszeitenproblem: Belgrade.
Millan, H., Bezemer, T.D., Verges, J., Marzo, M., Munoz, J.A., Roca, E., Cires, J., Zoetemeijer, R., Cloetingh, S., and Puigdefabregas, C., 1995, Palaeo-elevation and effective elastic thickness evolution at mountain ranges: inferences from flexural modelling in the Eastern Pyrenees and Ebro Basin: Marine and Petroleum Geology, v. 12, p. 917-928.
Miller, K.G., Mountain, G.S., Browning, J.V., Kominz, M., Sugarman, P.J., Christie-Blick, N., Katz, M.E., and Wright, J.D., 1998, Cenozoic global sea level, sequences, and the New Jersey Transect: Results From coastal plain and continental slope drilling: Reviews of Geophysics, v. 36, p. 569-601.
Miller, K.G., Wright, J.D., and Browning, J.V., 2005, Visions of ice sheets in a greenhouse world: Marine Geology, v. 217, p. 215-231.
Millington, J.J., and Clark, J.D., 1995, The Charo/Arro canyon-mouth sheet system, south-central Pyrenees, Spain; a structurally influenced zone of sediment dispersal: JOURNAL OF SEDIMENTARY RESEARCH, v. 65, p. 443-454.
Mix, A.C., and Ruddiman, W.F., 1984, Oxygen-isotope analyses and Pleistocene ice volumes: Quaternary Research, v. 21, p. 1-20.
Mochales, T., Casas, A.M., Pueyo, E.L., and Barnolas, A., 2012, Rotational velocity for oblique structures (Boltaña anticline, Southern Pyrenees): Journal of Structural Geology, v. 35, p. 2-16.
Mochales, T., Pueyo, E.L., Casas, A.M., Barnolas, A., and Oliva-Urcia, B., 2010, Anisotropic magnetic susceptibility record of the kinematics of the Boltaña Anticline (Southern Pyrenees): Geological Journal, v. 45, p. 562-581.
Molina, E., Alegret, L., Apellaniz, E., Bernaola, G., Caballero, F., Dinarès-Turell, J., Hardenbol, J., Heilmann-Clausen, C., Larrasoaña, J.C., Luterbacher, H., Monechi, S., Ortiz, S., Orue-Etxebarria, X., Payros, A., Pujalte, V., Rodríguez-Tovar, F.J., Tori, F., Tosquella, J., and Uchman, A., 2011, The Global Stratotype Section and Point (GSSP) for the base of the Lutetian Stage at the Gorrondatxe section, Spain: Episodes, v. 34, p. 86-108.
Mommersteeg, H.J.P.M., Loutre, M.F., Young, R., Wijmstra, T.A., and Hooghiemstra, H., 1995, Orbital forced frequencies in the 975 000 year pollen record from Tenagi Philippon (Greece): Climate Dynamics, v. 11, p. 4-24.
Moran, K., Backman, J., Brinkhuis, H., Clemens, S.C., Cronin, T., Dickens, G.R., Eynaud, F., Gattacceca, J., Jakobsson, M., Jordan, R.W., Kaminski, M., King, J., Koc, N., Krylov, A., Martinez, N., Matthiessen, J., McInroy, D., Moore, T.C., Onodera, J., O'Regan, M., Pälike, H., Rea, B., Rio, D., Sakamoto, T., Smith, D.C., Stein, R., St John, K., Suto, I., Suzuki, N., Takahashi, K., Watanabe, M., Yamamoto, M., Farrell, J., Frank, M., Kubik, P., Jokat, W., and Kristoffersen, Y., 2006, The Cenozoic palaeoenvironment of the Arctic Ocean: Nature, v. 441, p. 601-605.
Morris, Sinclair, and Yell, 1998, Exhumation of the Pyrenean orogen: implications for sediment discharge: Basin Research, v. 10, p. 69-85.
Morse, J.W., 2003, Formation and Diagenesis of Carbonate Sediments, *in* Heinrich, D.H., and Karl, K.T., eds., Treatise on Geochemistry: Oxford, Pergamon, p. 67-85.

Muller, R.A., and MacDonald, G.J., 2000, Ice Ages and Astronomical Causes: Data, Spectral Analysis, and Mechanisms: London, Springer-Praxis, 318 p.
Munoz, J.A., 1992, Evolution of a continental collision belt: ECORS-Pyrenees crustal balanced corss-section, *in* McClay, K.R., ed., Thrust Tectonics: London, Chapman and Hall, p. 235-246.
Munoz, J.A., Arbues, P., and Serra-Kiel, J., 1998, The Ainsa Basin and the Sobrarbe oblique thrust system: sedimentological and tectonic processes controlling slope platform sequences deposited synchronously with a submarine emergent thrust system, *in* Melendez Hevia, A., and Soria, A.R., eds., 15th International Sedimentological Congress, Volume Excursion B2 Guidebook: Alicante, International Association of Sedimentologists, p. 213-223.
Munoz, J.A., Martinez, A., and Vergés, J., 1986, Thrust sequences in the eastern Spanish Pyrenees: Journal of Structural Geology, v. 8, p. 399-405.
Munoz, J.A., McClay, K.R., and Poblet, J., 1994, Synchronous extension and contraction in frontal thrust sheets of the Spanish Pyrenees: Geology, v. 22, p. 921-924.
Mutti, E., 1977, Distinctive thin-bedded turbidite facies and related depositional environments in the Eocene Hecho Group (South-central Pyrenees, Spain): Sedimentology, v. 24, p. 107-131.
—, 1983, The Hecho Eocene Submarine Fan System, South-Central Pyrenees, Spain: Geo-Marine Letters, v. 3, p. 199-202.
Mutti, E., Luterbacher, H.P., Ferrer, J., and Rossell, J., 1972, Schema stratigrafico e lineamenti di facies del Paleogene marino della zona centrale sudpirenaica tra Tremp (Catalogna) e Pamplona (Navarra): Memorie della scoieta geologica italiana, v. 11, p. 391-416.
Mutti, E., Remacha, E., Sgavetti, M., Rosell, J., Valloni, R., and Zamorano, M., 1985, Stratigraphy and facies characteristics of the Eocene Hecho Group turbidite systems, south-central Pyrenees, *in* Mila, M.D., and Rosell, J., eds., 6th European Regional Meeting of the International Assocaiation of Sedimentologists, Volume Excursion Guidebook, 12: Lleida, International Assocaiation of Sedimentologists, p. 521-576.
Myers, K.J., 1989, The origin of the Lower Jurassic Cleveland Ironstone Formation of North-East England: evidence from portable gamma-ray spectrometry: Geological Society, London, Special Publications, v. 46, p. 221-228.
Myers, K.J., and Bristow, C.S., 1989, Detailed sedimentology and gamma-ray log characteristics of a Namurian deltaic succession II: Gamma-ray logging: Geological Society, London, Special Publications, v. 41, p. 81-88.
Myers, K.J., and Wignall, P.B., 1987, Understanding Jurassic Organic-rich Mudrocks-New Concepts using Gamma-ray Spectrometry and Palaeoecology: Examples from the Kimmeridge Clay of Dorset and the Jet Rock of Yorkshire, *in* Leggett, J.K., and Zuffa, G.G., eds., Marine Clastic Sedimentology: Concepts and case Studies: London, Grahman & Trotman, p. 172-189.
Nador, A., Lantos, M., Toth-Makk, A., and Thamo-Bozso, E., 2003, Milankovitch-scale multi-proxy records from fluvial sediments of the last 2.6 Ma, Pannonian Basin, Hungary: Quaternary Science Reviews, v. 22, p. 2157-2175.
Naylor, M., and Sinclair, H.D., 2007, Punctuated thrust deformation in the context of doubly vergent thrust wedges: Implications for the localization of uplift and exhumation: Geology, v. 35, p. 559-562.
Nicolo, M.J., Dickens, G.R., Hollis, C.J., and Zachos, J.C., 2007, Multiple early Eocene hyperthermals: Their sedimentary expression on the New Zealand continental margin and in the deep sea: Geology, v. 35, p. 699-702.
Nijman, W., 1998, Cyclicity and basin axis shift in a piggyback basin: towards modelling of the Eocene Tremp-Ager Basin, South Pyrenees, Spain: Geological Society, London, Special Publications, v. 134, p. 135-162.
Nijman, W., and Nio, S.D., 1975, The Eocene Montanana Delta (Tremp-Graus Basin, Provinces Lerida and Huesca, Southern Pyrenees, N. Spain) *in* Rosell, J., and Puigdefabregas, C., eds., 9th International Sedimentological Congress Volume

Excursion Guidebook 19, Part B: Nice, International Assocaition of Sedimentologists.
Normark, W.R., Piper, D.J.W., and Sliter, R.A.Y., 2006, Sea-level and tectonic control of middle to late Pleistocene turbidite systems in Santa Monica Basin, offshore California: Sedimentology, v. 53, p. 867-897.
Norris, R.D., and Röhl, U., 1999, Carbon cycling and chronology of climate warming during the Palaeocene/Eocene transition: Nature, v. 401, p. 775-778.
North, C.P., and Boering, M., 1999, Spectral gamma-ray logging for facies discrimination in mixed fluvial-eolian successions; a cautionary tale: AAPG Bulletin, v. 83, p. 155-169.
Ogg, J.G., Lugowski, A., and Gradstein, F.M., 2010, Earth History databases and visualization - the TimeScale Creator system, EGU General Assembly, 2-7 May: Vienna, EGU.
Olsen, H., 1990, Astronomical forcing of meandering river behaviour: Milankovitch cycles in Devonian of East Greenland: Palaeogeography, Palaeoclimatology, Palaeoecology, v. 79, p. 99-115.
—, 1994, Orbital forcing on continental depositonal systems - lacustrine and fluvial cyclicity in the Devonian of east Greenland, *in* de Boer, P.L., and Smith, D.G., eds., Orbital Forcing and Cyclic Sequences: Special Publication of the International Assocaition of Sedimentologists: Oxford, Blackwell Scientific Publications, p. 429-438.
Olsen, P.E., and Kent, D.V., 1999, Long-period Milankovitch cycles from the Late Triassic and Early Jurassic of eastern North America and their implications for the calibration of the Early Mesozoic time,Äìscale and the long,Äìterm behaviour of the planets: Philosophical Transactions of the Royal Society of London. Series A: Mathematical, Physical and Engineering Sciences, v. 357, p. 1761-1786.
Oms, O., Dinarès-Turell, J., and Remacha, E., 2003, Magnetic Stratigraphy from Deep Clastic Turbidites: An Example from the Eocene Hecho Group (Southern Pyrenees): Studia Geophysica et Geodaetica, v. 47, p. 275-288.
Pagani, M., Pedentchouk, N., Huber, M., Sluijs, A., Schouten, S., Brinkhuis, H., Sinninghe Damste, J.S., Dickens, G.R., and Expedition, S., 2006, Arctic hydrology during global warming at the Palaeocene/Eocene thermal maximum: Nature, v. 442, p. 671-675.
Paillard, D., Labeyrie, L., and Yiou, P., 1996, Macintosh program performs time-series analysis: EOS, Transactions American Geophysical Union, v. 77, p. 379.
Pälike, H., Nishi, H., Lyle, M., Raffi, I., Gamage, K., Klaus, A., and Scientists, E., 2009, Expedition 320: Pacific equatorial transect, Integrated Ocean Drilling Program Preliminary Report, Volume 320.
Pälike, H., Shackleton, N.J., and Röhl, U., 2001, Astronomical forcing in Late Eocene marine sediments: Earth and Planetary Science Letters, v. 193, p. 589-602.
Parkinson, D.N., 1996, Gamma-ray spectrometry as a tool for stratigraphical interpretation: examples from the western European Lower Jurassic: Geological Society, London, Special Publications, v. 103, p. 231-255.
Payros, A., Orue-Etxebarria, X., and Pujalte, V., 2006, Covarying sedimentary and biotic fluctuations in Lower-Middle Eocene Pyrenean deep-sea deposits: Palaeoenvironmental implications: Palaeogeography, Palaeoclimatology, Palaeoecology, v. 234, p. 258-276.
Payros, A., Pujalte, V., and Orue-Etxebarria, X., 1999, The South Pyrenean Eocene carbonate megabreccias revisited: new interpretation based on evidence from the Pamplona Basin: Sedimentary Geology, v. 125, p. 165-194.
Payros, A., Pujalte, V., Tosquella, J., and Orue-Etxebarria, X., 2010, The Eocene storm-dominated foralgal ramp of the western Pyrenees (Urbasa,ÄìAndia Formation): An analogue of future shallow-marine carbonate systems?: Sedimentary Geology, v. 228, p. 184-204.
Pearson, P.N., and Palmer, M.R., 2000, Atmospheric carbon dioxide concentrations over the past 60 million years: Nature, v. 406, p. 695-699.

Pekar, S.F., Hucks, A., Fuller, M., and Li, S., 2005, Glacioeustatic changes in the early and middle Eocene (51-42 Ma): Shallow-water stratigraphy from ODP Leg 189 Site 1171 (South Tasman Rise) and deep-sea ∂18O records: Geological Society of America Bulletin, v. 117, p. 1081-1093.

Peper, T., and Cloetingh, S., 1995, Autocyclic perturbations of orbitally forced signals in the sedimentary record: Geology, v. 23, p. 937-940.

Percival, D.B., and Walden, A.T., 1993, Spectral Analysis for Physical Applications: Multitaper and Conventional Univariate Techniques: Cambridge, Cambridge University Press.

Percival, D.P., 1995, On estimation of the wavelet variance: Biometrika, v. 82, p. 619-631.

Petit, J.R., Jouzel, J., Raynaud, D., Barkov, N.I., Barnola, J.M., Basile, I., Bender, M., Chappellaz, J., Davis, M., Delaygue, G., Delmotte, M., Kotlyakov, V.M., Legrand, M., Lipenkov, V.Y., Lorius, C., Pepin, L., Ritz, C., Saltzman, E., and Stievenard, M., 1999, Climate and atmospheric history of the past 420,000 years from the Vostok ice core, Antarctica: Nature, v. 399, p. 429-436.

Pettingill, H., 1998, Lessons learned from 43 turbidite giant fields: Oil and Gas Journal, v. 96.

Pickering, K.T., and Bayliss, N.J., 2009, Deconvolving tectono-climatic signals in deep-marine siliciclastics, Eocene Ainsa basin, Spanish Pyrenees: Seesaw tectonics versus eustasy: Geology, v. 37, p. 203-206.

Pickering, K.T., and Boudagher-Fadel, M., 2004, Micropalaeontology of the Mid Eocene Ainsa I Fan Channel-Levee-Overbank Complex, Ainsa System, South Central Pyrenees, Spain (unpublished): London, University College London.

Pickering, K.T., and Clark, J.D., 2012, Architecture and stacking patterns of lower-slope and proximal basin-floor channelized submarine fans, Middle Eocene Ainsa system, Spanish Pyrenees: An Integrated outcrop - subsurface study: Sedimentology.

Pickering, K.T., and Corregidor, J., 2000, 3D Reservoir Scale Study of Eocene Confined Submarine Fans, South Central Spanish Pyrenees, *in* Weimer, P., Slatt R.M., Coleman, J., Rosen, N.C., Nelson, H., Bouma, A.H., Styzen, M.J., & Lawrence, D.T., ed., Deep Water Reservoirs of the World: Houston, Gulf Coast Section, Society of Economic Palaeontologists and Mineralogists, p. 776-781.

—, 2005, Mass-Transport Complexes (MTCs) and Tectonic Control on Basin-Floor Submarine Fans, Middle Eocene, South Spanish Pyrenees: JOURNAL OF SEDIMENTARY RESEARCH, v. 75, p. 761-783.

Pickering, K.T., Souter, C., Oba, T., Taira, A., Schaaf, M., and Platzman, E., 1999, Glacio-eustatic control on deep-marine clastic forearc sedimentation, Pliocene-mid-Pleistocene (c. 1180-600 ka) Kazusa Group, SE Japan: Journal of the Geological Society, v. 156, p. 125-136.

Pisias, N.G., and Mix, A.C., 1988, Aliasing of the geological record and the search for long-period Milankovitch cycles: Paleoceanography, v. 3, p. 613-619.

Plaziat, J.-C., 1981, Late cretaceous to late eocene palaeogeographic evolution of southwest Europe: Palaeogeography, Palaeoclimatology, Palaeoecology, v. 36, p. 263-320.

Poblet, J., Mu√±oz, J.A., Trav√©, A., and Serra-Kiel, J., 1998, Quantifying the kinematics of detachment folds using three-dimensional geometry: Application to the Mediano anticline (Pyrenees, Spain): Geological Society of America Bulletin, v. 110, p. 111-125.

Popescu, I., Lericolais, G., Panin, N., Wong, H.K., and Droz, L., 2001, Late Quaternary channel avulsions on the Danube deep-sea fan, Black Sea: Marine Geology, v. 179, p. 25-37.

Posamentier, H.W., Jervey, M.T., and Vail, P.R., 1988, Eustatic controls on clastic deposition I - conceptual framework, *in* Wilgus, C.K., Posamantier, H.W., Ross, C.A., and Kendall, C.G.S.C., eds., Sea-Level Changes, Volume 42, SEPM (Society for Sedimentary Geology), p. 109-124.

Posamentier, H.W., and Vail, P.R., 1988, Eustatic controls on clastic deposition II - sequence and systems tract models, *in* Wilgus, C.K., Posamantier, H.W., Ross, C.A., and Kendall, C.G.S.C., eds., Sea-Level Changes, Volume 42, SEPM (Society for Sedimentary Geology), p. 125-154.

Postma, G., 2001, Physical climate signatures in shallow- and deep-water deltas: Global and Planetary Change, v. 28, p. 93-106.

Postma, G., and ten Veen, J.H., 1999, Astronomically and tectonically linked variations in gamma-ray intensity in Late Miocene hemipelagic successions of the Eastern Mediterranean Basin: Sedimentary Geology, v. 128, p. 1-12.

Pous, J., Munoz, J.A., Ledo, J.J., and Liesa, M., 1995, Partial melting of subducted continental lower crust in the Pyrenees: Journal of the Geological Society, v. 152, p. 217-220.

Prell, W., and Hays, J.D., 1976, Late Pleistocene faunal and temperature patterns of the Colombia basin, Caribbean Sea, *in* Cline, R.M., and Hays, J.D., eds., Investigation of Late Quaternary Paleoceanography and Paleoclimatology, Volume Memoir 145: Boulder, Colorado, The Geological Society of America.

Press, W.H., Teukolsky, S.A., Vetterling, W.T., and Flannery, B.P., 1992, Numerical Recipes in C: The Art of Scientific Computing: Cambridge, Cambridge University Press, 994 p.

Preto, N., and Hinnov, L.A., 2003, Unraveling the Origin of Carbonate Platform Cyclothems in the Upper Triassic Dürrenstein Formation (Dolomites, Italy): JOURNAL OF SEDIMENTARY RESEARCH, v. 73, p. 774-789.

Priestly, M.B., 1981, Spectral Analysis and Time Series: London, Academic Press.

Prins, M.A., and Postma, G., 2000, Effects of climate, sea level, and tectonics unraveled for last deglaciation turbidite records of the Arabian Sea: Geology, v. 28, p. 375-378.

Prokoph, A., and Agterberg, F.P., 2000, Wavelet Analysis of Well-Logging Data from Oil Source Rock, Egret Member, Offshore Eastern Canada: AAPG Bulletin, v. 84, p. 1617-1632.

Prokoph, A., and Barthelmes, F., 1996, Detection of nonstationarities in geological time series: Wavelet transform of chaotic and cyclic sequences: Computers & Geosciences, v. 22, p. 1097-1108.

Prokoph, A., and Thurow, J., 2000, Diachronous pattern of Milankovitch cyclicity in late Albian pelagic marlstones of the North German Basin: Sedimentary Geology, v. 134, p. 287-303.

Puigdefabregas, C., Munoz, J.A., and Verges, J., 1992, Thrusting and foreland basin evolution in the Southern Pyrenees, *in* McClay, K.R., ed., Thrust Tectonics: London, Chapman & Hall.

Puigdefabregas, C., and Souquet, P., 1986, Tecto-sedimentary cycles and depositional sequences of the Mesozoic and Tertiary from the Pyrenees: Tectonophysics, v. 129, p. 173-203.

Quarmby, R., 2010, Investigating high-resolution environmental change using outcrop spectral gamma-ray logging: Middle Eocene Spanish Pyrenees: London, UCL.

Quinn, T.R., Tremaine, S., and Duncan, M., 1991, A three million year integration of the earth's orbit: Astronomical Journal, v. 101, p. 2287-2305.

Raymo, M.E., Lisiecki, L.E., and Nisancioglu, K.H., 2006, Plio-Pleistocene Ice Volume, Antarctic Climate, and the Global d18O Record: Science, v. 313, p. 492-495.

Raymo, M.E., and Nisancioglu, K., 2003, The 41 kyr world: Milankovitch's other unsolved mystery: Paleoceanography, v. 18, p. 1011.

Remacha, E., Fernandez, L.P., and Maestro, E., 2005, The Transition Between Sheet-Like Lobe and Basin-Plain Turbidites in the Hecho Basin (South-Central Pyrenees, Spain): JOURNAL OF SEDIMENTARY RESEARCH, v. 75, p. 798-819.

Remacha, E., Fernandez, L.P., Maestro, E., Oms, O., Estrada, R., and Teixell, A., 1998, The Upper Hecho Group turbidites and their vertical evolution to deltas (Eocene, South-Central Pyrenees), *in* Melendez Hevia, A., and Soria, A.R.,

eds., 15th International Sedimentological Congress, Volume Excursion A1 Guidebook: Alicante, International Assocaition of Sedimentologists, p. 1-23.
Remacha, E., Oms, O., Gual, G., Bolano, F., Climent, F., Fernandez, L.P., Crumeyrolle, P., Pettingill, H., Vicente, J.C., Suarez, J., and Arcuri, M., 2003, Geological Field Trip 12, South-Central Pyrenees, Spain, AAPG International Conference and Exhibition: Barcelona, Spain, Total.
Rial, J.A., 1999, Pacemaking the Ice Ages by Frequency Modulation of Earth's Orbital Eccentricity: Science, v. 285, p. 564-568.
Rial, J.A., and Anaclerio, C.A., 2000, Understanding nonlinear responses of the climate system to orbital forcing: Quaternary Science Reviews, v. 19, p. 1709-1722.
Richards, M., Bowman, M., and Reading, H., 1998, Submarine-fan systems i: characterization and stratigraphic prediction: Marine and Petroleum Geology, v. 15, p. 689-717.
Richter, T.O., van der Gaast, S., Koster, B., Vaars, A., Gieles, R., de Stigter, H.C., De Haas, H., and van Weering, T.C.E., 2006, The Avaatech XRF Core Scanner: technical description and applications to NE Atlantic sediments: Geological Society, London, Special Publications, v. 267, p. 39-50.
Ricken, W., 1985, Epicontinental marl-limestone alternations: Event deposition and diagenetic bedding (Upper Jurassic, southwest Germany), *in* Bayer, U., and Seilacher, A., eds., Lecture Notes in Earth Sciences, Volume 1: Berlin, Springer-Verlag, p. 127-162.
—, 1987, The carbonate compaction law: a new tool: Sedimentology, v. 34, p. 571-584.
Ridente, D., and Trincardi, F., 2002, Eustatic and tectonic control on deposition and lateral variability of Quaternary regressive sequences in the Adriatic basin (Italy): Marine Geology, v. 184, p. 273-293.
Rider, M.H., 1990, Gamma-ray log shape used as a facies indicator: critical analysis of an oversimplified methodology: Geological Society, London, Special Publications, v. 48, p. 27-37.
—, 1996, The Geological Interpretation of Well Logs: Caithness, Whittles Publishing.
Rodriguez-Tovar, F.J., and Pardo-Iguzquiza, E., 2003, Strong evidence of high-frequency (sub-Milankovitch) orbital forcing by amplitude modulation of Milankovitch signals: Earth and Planetary Science Letters, v. 210, p. 179-189.
Röhl, U., and Abrams, L.J., 2000, High-resolution, downhole, and nondestructive core measurements from Sites 999 and 1001 in the Caribbean Sea: application to the Late Paleocene Thermal Maximum, *in* Leckie, R.M., Sigurdsson, H., Acton, G.D., and Draper, G., eds., Proceedings of the Ocean Drilling Program, Scientific Results, Volume 165.
Röhl, U., Westerhold, T., Bralower, T.J., and Zachos, J.C., 2007, On the duration of the Paleocene-Eocene thermal maximum (PETM): Geochemistry, Geophysics, Geosystems, v. 8, p. Q12002.
Roure, F., Choukroune, P., Berastegui, X., Munoz, J.A., Villien, A., Matheron, P., Bareyt, M., Seguret, M., Camara, P., and Deramond, J., 1989, Ecors deep seismic data and balanced cross sections: Geometric constraints on the evolution of the Pyrenees: Tectonics, v. 8, p. 41-50.
Royer, D.L., 2006, CO2-forced climate thresholds during the Phanerozoic: Geochimica et Cosmochimica Acta, v. 70, p. 5665-5675.
Ruddiman, W.F., and McIntyre, A., 1984, Ice-age thermal response and climatic role of the surface Atlantic Ocean, 40˚N to 63˚N: Geological Society of America Bulletin, v. 95, p. 381-396.
Ruddiman, W.F., Raymo, M.E., Martinson, D.G., Clement, B.M., and Backman, J., 1989, Pleistocene Evolution: Northern Hemisphere Ice Sheets and North Atlantic Ocean: Paleoceanography, v. 4, p. 353-412.
Ruffell, A., McKinley, J.M., and Evans, R., 2004, Distinguishing faults from flooding surfaces on spectral gamma-ray logs: American Association of Petroleum Geologists, v. 88, p. 1239-1254.

Ruffell, A., and Worden, R., 2000, Palaeoclimate analysis using spectral gamma-ray data from the Aptian (Cretaceous) of southern England and southern France: Palaeogeography, Palaeoclimatology, Palaeoecology, v. 155, p. 265-283.
Sagasti, G., 2005, Hemipelagic record of orbitally-induced dilution cycles in Lower Cretaceous sediments of the Neuquen Basin: Geological Society, London, Special Publications, v. 252, p. 231-250.
Sangiorgi, F., van Soelen, E.E., Spofforth, D.J.A., Pälike, H., Stickley, C.E., St. John, K., Koç, N., Schouten, S., Sinninghe Damsté, J.S., and Brinkhuis, H., 2008, Cyclicity in the middle Eocene central Arctic Ocean sediment record: Orbital forcing and environmental response: Paleoceanography, v. 23, p. PA1S08.
Scargle, J.D., 1982, Studies in astronomical time series analysis. II. Statistical aspects of spectral analysis of unevenly spaced data: The Astrophysical Journal, v. 263, p. 835-853.
Schidlowski, M., 1988, A 3,800-million-year isotopic record of life from carbon in sedimentary rocks: Nature, v. 333, p. 313-318.
Schiffelbein, P., and Dorman, L., 1986, Spectral Effects of Time-Depth Nonlinearities in Deep Sea Sediment Records: A Demodulation Technique for Realigning Time And Depth Scales: Journal of Geophysical Research, v. 91.
Scholle, P.A., and Arthur, M.A., 1980, Carbon Isotope Fluctuations in Cretaceous Pelagic Limestones: Potential Stratigraphic and Petroleum Exploration Tool: AAPG Bulletin, v. 64, p. 67-87.
Schrag, D.P., DePaolo, D.J., and Richter, F.M., 1995, Reconstructing past sea surface temperatures: Correcting for diagenesis of bulk marine carbonate: Geochimica et Cosmochimica Acta, v. 59, p. 2265-2278.
Schulz, M., and Mudelsee, M., 2002, REDFIT: estimating red-noise spectra directly from unevenly spaced paleoclimatic time series: Computers & Geosciences, v. 28, p. 421-426.
Schulz, M., and Stattegger, K., 1997, Spectrum: spectral analysis of unevenly spaced paleoclimatic time series: Computers & Geosciences, v. 23, p. 929-945.
Schuppers, J.D., 2009, Quantification of Turbidite Facies in a Reservoir-Analogous Submarine-Fan Channel Sandbody, South-Central Pyrenees, Spain, Blackwell Publishing Ltd., 99-111 p.
Schwarzacher, W., 1975, Sedimentation models and quantitative stratigraphy: Amsterdam, Elsevier.
Serra-Kiel, J., Canudo, J.I., Dinarès, J., Molina, E., Ortiz, N., Pascual, J.O., Samso, J.M., and Tosquella, J., 1993, Cronostratigrafia de los sedimentos marinos del Terciario inferior de la Cuenca de Graus-Tremp (Zona Central Surpirenaica): Revista de la Sociedad Geológica de España, v. 7, p. 273-297.
Serra-Kiel, J., Hottinger, L., Caus, E., Drobne, K., Ferrandez, C., Jauhri, A.K., Less, G., Pavlovec, R., Pignatti, J., Samso, J.M., Schaub, H., Sirel, E., Strougo, A., Tambareau, Y., Tosquella, J., and Zakrevskaya, E., 1998, Larger foraminiferal biostratigraphy of the Tethyan Paleocene and Eocene: Bulletin de la Societe Geologique de France, v. 169, p. 281-299.
Sexton, P.F., Norris, R.D., Wilson, P.A., Pälike, H., Westerhold, T., Röhl, U., Bolton, C.T., and Gibbs, S., 2011, Eocene global warming events driven by ventilation of oceanic dissolved organic carbon: Nature, v. 471, p. 349-352.
Sexton, P.F., Wilson, P.A., and Norris, R.D., 2006, Testing the Cenozoic multisite composite ∂18O and ∂13C curves: New monospecific Eocene records from a single locality, Demerara Rise (Ocean Drilling Program Leg 207): Paleoceanography, v. 21, p. PA2019.
Shackleton, N., and Boersma, A., 1981, The climate of the Eocene ocean: Journal of the Geological Society, v. 138, p. 153-157.
Shackleton, N.J., 1987, The carbon isotope record of the Cenozoic: history of organic carbon burial and of oxygen in the ocean and atmosphere: Geological Society, London, Special Publications, v. 26, p. 423-434.
—, 2000, The 100,000-Year Ice-Age Cycle Identified and Found to Lag Temperature, Carbon Dioxide, and Orbital Eccentricity: Science, v. 289, p. 1897-1902.

Shackleton, N.J., Hall, M.A., Pate, D., Meynadier, L., and Valet, P., 1993, High-Resolution Stable Isotope Stratigraphy from Bulk Sediment: Paleoceanography, v. 8, p. 141-148.

Shackleton, N.J., and Imbrie, J., 1990, The δ 18O spectrum of oceanic deep water over a five-decade band: Climatic Change, v. 16, p. 217-230.

Shackleton, N.J., Le, J., Mix, A., and Hall, M.A., 1992, Carbon isotope records from pacific surface waters and atmospheric carbon dioxide: Quaternary Science Reviews, v. 11, p. 387-400.

Shanmugam, G., and Moiola, R.J., 1982, Eustatic control of turbidites and winnowed turbidites: Geology, v. 10, p. 231-235.

Shimmield, G.B., and Mowbray, S.R., 1991, The inorganic geochemical record of the Northwest Arabian Sea; a history of productivity variation over the last 400 k.y. from sites 722 and 724, *in* Prell, W.L., Niitsuma, N., Emeis, K.-C., Al-Sulaiman, Z.K., Al-Tobbah, A.N.K., Anderson, D.M., Barnes, R.O., Bilak, R.A., Bloemendal, J., Bray, C.J., Busch, W.H., Clemens, S.C., de Menocal, P., Debrabant, P., Hayashida, A., Hermelin, J.O.R., Jarrard, R.D., Krissek, L.A., Kroon, D., Murray, D.W., Nigrini, C.A., Pedersen, T.F., Ricken, W., Shimmield, G.B., Spaulding, S.A., Takayama, T., ten Haven, H.L., and Weedon, G.P., eds., Proceedings of the Ocean Drilling Program, Scientific Results, Volume 117: College Station, Texas A & M University, Ocean Drilling Program.

Short, D.A., Mengel, J.G., Crowley, T.J., Hyde, W.T., and North, G.R., 1991, Filtering of milankovitch cycles by earth's geography: Quaternary Research, v. 35, p. 157-173.

Slatt, R.M., Jordan, D.W., D'Agostino, A.E., and Gillespie, R.H., 1992, Outcrop gamma-ray logging to improve understanding of subsurface well log correlations: Geological Society, London, Special Publications, v. 65, p. 3-19.

Sloan, L.C., and Huber, M., 2001, Eocene Oceanic Responses to Orbital Forcing on Precessional Time Scales: Paleoceanography, v. 16, p. 101-111.

Sloan, L.C., and Morrill, C., 1998, Orbital forcing and Eocene continental temperatures: Palaeogeography, Palaeoclimatology, Palaeoecology, v. 144, p. 21-35.

Smith, A.G., 1996, Cenozoic latitudes, positions and topography of the Iberian Peninsula, *in* Friend, P.F., and Dabrio, C.J., eds., Tertiary Basins of Spain: The Stratigraphic Record of Crustal Kinematics: Cambridge, Cambridge University Press, p. 6-8.

Soto, R., and Casas, A.M., 2001, Geometría y cinemática de las estructuras norte-sur de la cuenca de Aínsa: Revista de la Sociedad Geológica de España, v. 14, p. 199-211.

Speelman, E.N., Sewall, J.O., Noone, D., Huber, M., der Heydt, A.v., DamstÈ, J.S., and Reichart, G.-J., 2010, Modeling the influence of a reduced equator-to-pole sea surface temperature gradient on the distribution of water isotopes in the Early/Middle Eocene: Earth and Planetary Science Letters, v. 298, p. 57-65.

St. John, K., 2008, Cenozoic ice-rafting history of the central Arctic Ocean: Terrigenous sands on the Lomonosov Ridge: Paleoceanography, v. 23, p. PA1S05.

Stap, L., Lourens, L.J., Thomas, E., Sluijs, A., Bohaty, S., and Zachos, J.C., 2010, High-resolution deep-sea carbon and oxygen isotope records of Eocene Thermal Maximum 2 and H2: Geology, v. 38, p. 607-610.

Stickley, C.E., St John, K., Koc, N., Jordan, R.W., Passchier, S., Pearce, R.B., and Kearns, L.E., 2009, Evidence for middle Eocene Arctic sea ice from diatoms and ice-rafted debris: Nature, v. 460, p. 376-379.

Stoll, H.M., and Schrag, D.P., 2000, High-resolution stable isotope records from the Upper Cretaceous rocks of Italy and Spain: Glacial episodes in a greenhouse planet?: Geological Society of America Bulletin, v. 112, p. 308-319.

Stow, D., Howell, D., and Nelson, C., 1984, Sedimentary, tectonic, and sea-level controls on submarine fan and slope-apron turbidite systems: Geo-Marine Letters, v. 3, p. 57-64.

Stow, D.A.V., and Mayall, M., 2000, Deep-water sedimentary systems: New models for the 21st century: Marine and Petroleum Geology, v. 17, p. 125-135.

Straub, K.M., Paola, C., Mohrig, D., Wolinsky, M.A., and George, T., 2009, Compensational Stacking of Channelized Sedimentary Deposits: JOURNAL OF SEDIMENTARY RESEARCH, v. 79, p. 673-688.
Sun, J., and Huang, X., 2006, Half-precessional cycles recorded in Chinese loess: response to low-latitude insolation forcing during the Last Interglaciation: Quaternary Science Reviews, v. 25, p. 1065-1072.
Sussman, A.J., Butler, R.F., Dinarés-Turell, J., and Vergés, J., 2004, Vertical-axis rotation of a foreland fold and implications for orogenic curvature: an example from the Southern Pyrenees, Spain: Earth and Planetary Science Letters, v. 218, p. 435-449.
Sutcliffe, C., and Pickering, K.T., 2009, End-signature of deep-marine basin-fill, as a structurally confined low-gradient clastic system: the Middle Eocene Guaso system, South-central Spanish Pyrenees: Sedimentology, v. 56, p. 1670-1689.
Svendsen, J.B., and Hartley, N.R., 2001, Comparison between outcrop-spectral gamma ray logging and whole rock geochemistry: implications for quantitative reservoir characterisation in continental sequences: Marine and Petroleum Geology, v. 18, p. 657-670.
Svensen, H., Planke, S., Malthe-Sorenssen, A., Jamtveit, B., Myklebust, R., Rasmussen Eidem, T., and Rey, S.S., 2004, Release of methane from a volcanic basin as a mechanism for initial Eocene global warming: Nature, v. 429, p. 542-545.
Tavani, S., Storti, F., Fernández, O., Muñoz, J.A., and Salvini, F., 2006, 3-D deformation pattern analysis and evolution of the Añisclo anticline, southern Pyrenees: Journal of Structural Geology, v. 28, p. 695-712.
Teixell, A., 1996, The Anso transect of the southern Pyrenees: basement and cover thrust geometries: Journal of the Geological Society, v. 153, p. 301-310.
—, 1998, Crustal structure and orogenic material budget in the west central Pyrenees: Tectonics, v. 17, p. 395-406.
ten Veen, J.H., and Postma, G., 1996, Astronomically forced variations in gamma-ray intensity: Late Miocene hemipelagic successions in the eastern Mediterranean basin as a test case: Geology, v. 24, p. 15-18.
Thomson, D.J., 1982, Spectrum estimation and harmonic analysis: Proceedings of the IEEE, v. 70, p. 1055-1096.
—, 1990a, Quadratic-Inverse Spectrum Estimates: Applications to Palaeoclimatology: Philosophical Transactions: Physical Sciences and Engineering, v. 332, p. 539-597.
—, 1990b, Time Series Analysis of Holocene Climate Data: Philosophical Transactions of the Royal Society of London. Series A, Mathematical and Physical Sciences, v. 330, p. 601-616.
Tindall, J., Flecker, R., Valdes, P., Schmidt, D.N., Markwick, P., and Harris, J., 2010, Modelling the oxygen isotope distribution of ancient seawater using a coupled ocean-atmosphere GCM: Implications for reconstructing early Eocene climate: Earth and Planetary Science Letters, v. 292, p. 265-273.
Tjallingii, R., Röhl, U., Kölling, M., and Bickert, T., 2007, Influence of the water content on X-ray fluorescence core-scanning measurements in soft marine sediments: Geochemistry, Geophysics, Geosystems, v. 8, p. Q02004.
Torrence, C., and Compo, G.P., 1998, A Practical Guide to Wavelet Analysis: Bulletin of the American Meteorological Society, v. 79, p. 61-78.
Trauth, M.H., 2007, MATLAB Recipes for Earth Sciences: Berlin, Springer.
Trave, A., Labaume, P., Calvet, F., and Soler, A., 1997, Sediment dewatering and pore fluid migration along thrust faults in a foreland basin inferred from isotopic and elemental geochemical analyses (Eocene southern Pyrenees, Spain): Tectonophysics, v. 282, p. 375-398.
Trave, A., Labaume, P., Calvet, F., Soler, A., Tritlla, J., Buatier, M., Potdevin, J.-L., Seguret, M., Raynaud, S., and Briqueu, L., 1998, Fluid migration during Eocene thrust emplacement in the south Pyrenean foreland basin (Spain): an integrated

structural, mineralogical and geochemical approach: Geological Society, London, Special Publications, v. 134, p. 163-188.
Tripati, A., Backman, J., Elderfield, H., and Ferretti, P., 2005, Eocene bipolar glaciation associated with global carbon cycle changes: Nature, v. 436, p. 341-346.
Tripati, A.K., Eagle, R.A., Morton, A., Dowdeswell, J.A., Atkinson, K.L., Bahé, Y., Dawber, C.F., Khadun, E., Shaw, R.M.H., Shorttle, O., and Thanabalasundaram, L., 2008, Evidence for glaciation in the Northern Hemisphere back to 44 Ma from ice-rafted debris in the Greenland Sea: Earth and Planetary Science Letters, v. 265, p. 112-122.
Tucker, M.E., Gallagher, J., and Leng, M.J., 2009, Are beds in shelf carbonates millennial-scale cycles? An example from the mid-Carboniferous of northern England: Sedimentary Geology, v. 214, p. 19-34.
Turney, C., Baillie, M., Clemens, S., Brown, D., Palmer, J., Pilcher, J., Reimer, P., and Leuschner, H.H., 2005, Testing solar forcing of pervasive Holocene climate cycles: Journal of Quaternary Science, v. 20, p. 511-518.
Vacher, P., and Souriau, A., 2001, A three-dimensional model of the Pyrenean deep structure based on gravity modelling, seismic images and petrological constraints: Geophysical Journal International, v. 145, p. 460-470.
Van Buchem, F.S.P., Melnyk, D.H., and McCave, I.N., 1992, Chemical cyclicity and correlation of Lower Lias mudstones using gamma ray logs, Yorkshire, UK: Journal of the Geological Society, v. 149, p. 991-1002.
Van der Weijden, C.H., Middelburg, J.J., De Lange, G.J., Van der Sloot, H.A., Hoede, D., and Woittiez, J.R.W., 1990, Profiles of the redox-sensitive trace elements As, Sb, V, Mo and U in the Tyro and Bannock Basins (eastern Mediterranean): Marine Chemistry, v. 31, p. 171-186.
Van der Zwan, C.J., 2002, The impact of Milankovitch-scale climatic forcing on sediment supply: Sedimentary Geology, v. 147, p. 271-294.
van Tassell, J., 1987, Upper Devonian Catskill Delta margin cyclic sedimentation: Brallier, Scherr, and Foreknobs Formations of Virginia and West Virginia: Geological Society of America Bulletin, v. 99, p. 414-426.
Van Wagoner, J.C., Mitchum, J.C., Campion, K.M., and Rahmanian, V.D., 1990, Siliciclastic Sequence Stratigraphy in Well Logs, Core, and Outcrops: Concepts for High-Resolution Correlation of Time and Facies: Tulsa, The American Association of Petroleum Geologists.
Van Wagoner, J.C., Posamentier, H.W., Mitchum, R.M., Vail, P.R., Sarg, J.F., Loutit, T.S., and Hardenbol, J., 1988, An overview of the fundamentals of sequence stratigraphy and key definitions, Sea-Level Changes, Volume 42, SEPM (Society for Sedimentary Geology), p. 39-45.
Veeh, H.H., Calvert, S.E., and Price, N.B., 1974, Accumulation of uranium in sediments and phosphorites on the South West African shelf: Marine Chemistry, v. 2, p. 189-202.
Veizer, J., and Mackenzie, F.T., 2003, Evolution of Sedimentary Rocks, *in* Heinrich, D.H., and Karl, K.T., eds., Treatise on Geochemistry: Oxford, Pergamon, p. 369-407.
Veizer, J.n., Ala, D., Azmy, K., Bruckschen, P., Buhl, D., Bruhn, F., Carden, G.A.F., Diener, A., Ebneth, S., Godderis, Y., Jasper, T., Korte, C., Pawellek, F., Podlaha, O.G., and Strauss, H., 1999, 87Sr/86Sr, d13C and d18O evolution of Phanerozoic seawater: Chemical Geology, v. 161, p. 59-88.
Verges, J., and Burbank, D.W., 1996, Eocene-Oligocene thrusting and basin configuration in the eastern and central Pyrenees (Spain), *in* Friend, P.F., and Dabrio, C.J., eds., The Tertiary basins of Spain: the stratigraphic record of crustal kinematics: Cambridge, Cambridge Universtiy Press.
Verges, J., Fernandez, M., and Martinez, A., 2002, The Pyrenean orogen: pre-, syn-, and post-collisional evolution: Journal of the Virtual Explorer, v. 8, p. 57-76.
Verges, J., Mill·n, H., Roca, E., MuÒoz, J.A., Marzo, M., CirÈs, J., Bezemer, T.D., Zoetemeijer, R., and Cloetingh, S., 1995, Eastern Pyrenees and related

foreland basins: pre-, syn- and post-collisional crustal-scale cross-sections: Marine and Petroleum Geology, v. 12, p. 903-915.
Vissers, R.L.M., 1992, Variscan extension in the Pyrenees: Tectonics, v. 11, p. 1369-1384.
Voigt, S., and Hilbrecht, H., 1997, Late Cretaceous carbon isotope stratigraphy in Europe: Correlation and relations with sea level and sediment stability: Palaeogeography, Palaeoclimatology, Palaeoecology, v. 134, p. 39-59.
Volat, J.-L., Pastouret, L., and Vergnaud-Grazzini, C., 1980, Dissolution and carbonate fluctuations in Pleistocene deep-sea cores: A review: Marine Geology, v. 34, p. 1-28.
Wade, B.S., and Kroon, D., 2002, Middle Eocene regional climate instability: Evidence from the western North Atlantic: Geology, v. 30, p. 1011-1014.
Wade, B.S., Kroon, D., and Norris, R.D., 2001, Orbitally forced climate change in late mid-Eocene time at Blake Nose (Leg 171B): evidence from stable isotopes in foraminifera: Geological Society, London, Special Publications, v. 183, p. 273-291.
Wade, B.S., and Pälike, H., 2004, Oligocene climate dynamics: Paleoceanography, v. 19, p. PA4019.
Warburton, P.R.C., 2011, Investigating High-Resolution Environmental Change Using Outcrop Spectral Gamma-Ray Logging, Middle Eocene Ainsa Basin, Spanish Pyrenees, Earth Sciences: London, UCL.
Weaver, P.P.E., and Kuijpers, A., 1983, Climatic control of turbidite deposition on the Madeira Abyssal Plain: Nature, v. 306, p. 360-363.
Weber, M.E., Tougiannidis, N., Kleineder, M., Bertram, N., Ricken, W., Rolf, C., Reinsch, T., and Antoniadis, P., 2010, Lacustrine sediments document millennial-scale climate variability in northern Greece prior to the onset of the northern hemisphere glaciation: Palaeogeography, Palaeoclimatology, Palaeoecology, v. 291, p. 360-370.
Weedon, G.P., 2003, Time-Series Analysis and Cyclostratigraphy: Cambridge, Cambridge University Press.
Welch, P., 1967, The use of fast Fourier transform for the estimation of power spectra: A method based on time averaging over short, modified periodograms: Audio and Electroacoustics, IEEE Transactions on, v. 15, p. 70-73.
Weltje, G., and de Boer, P.L., 1993, Astronomically induced paleoclimatic oscillations reflected in Pliocene turbidite deposits on Corfu (Greece): Implications for the interpretation of higher order cyclicity in ancient turbidite systems: Geology, v. 21, p. 307-310.
Weltje, G.J., and Tjallingii, R., 2008, Calibration of XRF core scanners for quantitative geochemical logging of sediment cores: Theory and application: Earth and Planetary Science Letters, v. 274, p. 423-438.
Weltje, G.J., Van Ansenwoude, S.O.K.J., and de Boer, P.L., 1996, High-frequency detrital signals in Eocene fan-delta sandstones of mixed parentage (south-central Pyrenees, Spain); a reconstruction of chemical weathering in transit: JOURNAL OF SEDIMENTARY RESEARCH, v. 66, p. 119-131.
Westerhold, T., and Röhl, U., 2009, High resolution cyclostratigraphy of the early Eocene - new insights into the origin of the Cenozoic cooling trend: Climate of the Past, v. 5, p. 309-327.
Westerhold, T., Röhl, U., Laskar, J., Raffi, I., Bowles, J., Lourens, L.J., and Zachos, J.C., 2007, On the duration of magnetochrons C24r and C25n and the timing of early Eocene global warming events: Implications from the Ocean Drilling Program Leg 208 Walvis Ridge depth transect: Paleoceanography, v. 22, p. PA2201.
Westphal, H., Head, M.J., and Munnecke, A., 2000, Differential Diagenesis of Rhythmic Limestone Alternations Supported by Palynological Evidence: JOURNAL OF SEDIMENTARY RESEARCH, v. 70, p. 715-725.

Westphal, H., Hilgen, F., and Munnecke, A., 2010, An assessment of the suitability of individual rhythmic carbonate successions for astrochronological application: Earth-Science Reviews, v. 99, p. 19-30.
Wignall, P.B., and Myers, K.J., 1988, Interpreting benthic oxygen levels in mudrocks: A new approach: Geology, v. 16, p. 452-455.
Williams, G.E., 1991, Milankovitch-band cyclicity in bedded halite deposits contemporaneous with Late Ordovician-Early Silurian glaciation, Canning Basin, Western Australia: Earth and Planetary Science Letters, v. 103, p. 143-155.
Wilson, R.C.L., Drury, S.A., and Chapman, J.L., 2000, The Great Ice Age: Climate Change and Life: London, Routledge/Open University.
Wunsch, C., 2000, On Sharp Spectral Lines in the Climate Record and the Millennial Peak: Paleoceanography, v. 15.
Yiou, P., Baert, E., and Loutre, M.F., 1996, Spectral analysis of climate data: Surveys in Geophysics, v. 17, p. 619-663.
Zachos, J., Pagani, M., Sloan, L., Thomas, E., and Billups, K., 2001, Trends, Rhythms, and Aberrations in Global Climate 65 Ma to Present: Science, v. 292, p. 686-693.
Zachos, J.C., Dickens, G.R., and Zeebe, R.E., 2008, An early Cenozoic perspective on greenhouse warming and carbon-cycle dynamics: Nature, v. 451, p. 279-283.
Zachos, J.C., McCarren, H., Murphy, B., Röhl, U., and Westerhold, T., 2010, Tempo and scale of late Paleocene and early Eocene carbon isotope cycles: Implications for the origin of hyperthermals: Earth and Planetary Science Letters, v. 299, p. 242-249.
Zachos, J.C., Röhl, U., Schellenberg, S.A., Sluijs, A., Hodell, D.A., Kelly, D.C., Thomas, E., Nicolo, M., Raffi, I., Lourens, L.J., McCarren, H., and Kroon, D., 2005, Rapid Acidification of the Ocean During the Paleocene-Eocene Thermal Maximum: Science, v. 308, p. 1611-1615.
Zachos, J.C., Stott, L.D., and Lohmann, K.C., 1994, Evolution of Early Cenozoic Marine Temperatures: Paleoceanography, v. 9, p. 353-387.

Appendix

The printed appendix to this research contains full-scale versions of Figures 4.4 and 4.15 along with nannofossil and thin-section images referred to within chapters 3 and 4 (Appendix Plates 1.1, 1.2). The remainder of the appendix (see contents to attached CD-ROM) contains the data generated during this research along with MathWorks MATLAB scripts.

The contents of the digital appendix are as follows:

Chapter 2

Chapter 2 - Orthoclase XRF data Table 2.7.xls

Chapter 2 - SGR data.xls

Chapter 3

Chapter 3 - Nannofossil assemblage data.xls

Chapter 3 - Nannofossil images.jpg

Chapter 3 - Table 3.1 sample list.xls

Chapter 4

Chapter 4 - Guaso geochemical and SGR data.xls

Chapter 4 - Guaso thin-section images

guaso 20 - 005_PPL.tiff

guaso 28 - 001_PPL.tiff

guaso 32 - 002_PPL.tiff

guaso 35 - 002_PPL.tiff

guaso 40 - 001_PPL.tiff

guaso 57 - 001_PPL.tiff

guaso 58 - 001_PPL.tiff

guaso 59 - 001_PPL.tiff

guaso 60 - 002_PPL.tiff

guaso 61 - 001_PPL.tiff

guaso 62 - 001_PPL.tiff

guaso 63 - 001_PPL.tiff

guaso 64 - 001_PPL.tiff

guaso 65 - 001_PPL.tiff

guaso 66 - 001_PPL.tiff

guaso 67 - 001_PPL.tiff

guaso 91 - 003_PPL.tiff

Chapter 4 - Guaso time series data.xls

Chapter 4 - Guaso XRD results.xls

Chapter 4 - Spectral and ASM results

CaCO3.xls

d13C.xls

d18O.xls

K.xls

Th.xls

ThK.xls

ThU.xls

TOC.xls

U.xls

Chapter 4 - Time series data.xls

Chapter 5

A6 well data

A6 Well Data.xls

A6CALP.LAS

A6SPEC.LAS

Heard & A6 well data.xls

Chapter 5 - Spectral and ASM results

A6 Bioturbation.xls

A6 K.xls

A6 NGR.xls

A6 Th.xls

A6 ThK.xls

A6 ThU.xls

A6 Total.xls

A6 U.xls

Ouctrop_K.xls

Outcrop_Th.xls

Outcrop_ThK.xls

Outcrop_ThU.xls

Outcrop_U.xls

Chapter 5 – Time series data.xls

Chapter 6

Chapter 6 - Correlate banaston data.xls

Chapter 6 - Quarmby 2009 data.xls

Chapter 6 - Scotchman 2010 data.xls

Chapter 6 - Spectral and ASM results

K.xls

Th.xls

ThK.xls

ThU.xls

Total.xls

U.xls

Chapter 6 - Time series data.xls

Chapter 6 - Warburton 2010 data.xls

Chapter 7

Chapter 7 - A622-27 XRF data.xls

Chapter 7 - REDFIT spectral results.xls

MATLAB Scripts

AM.m

FM.m

lowpass.m

moving_average.m

mtm_variance.m

process.m

RS-125 error estimation

k_gamma_error_data.mat

rs125error_est.m

th_gamma_error_data.mat

u_gamma_error_data.mat

save_REDFIT.m

synthetic_milankovitch.m

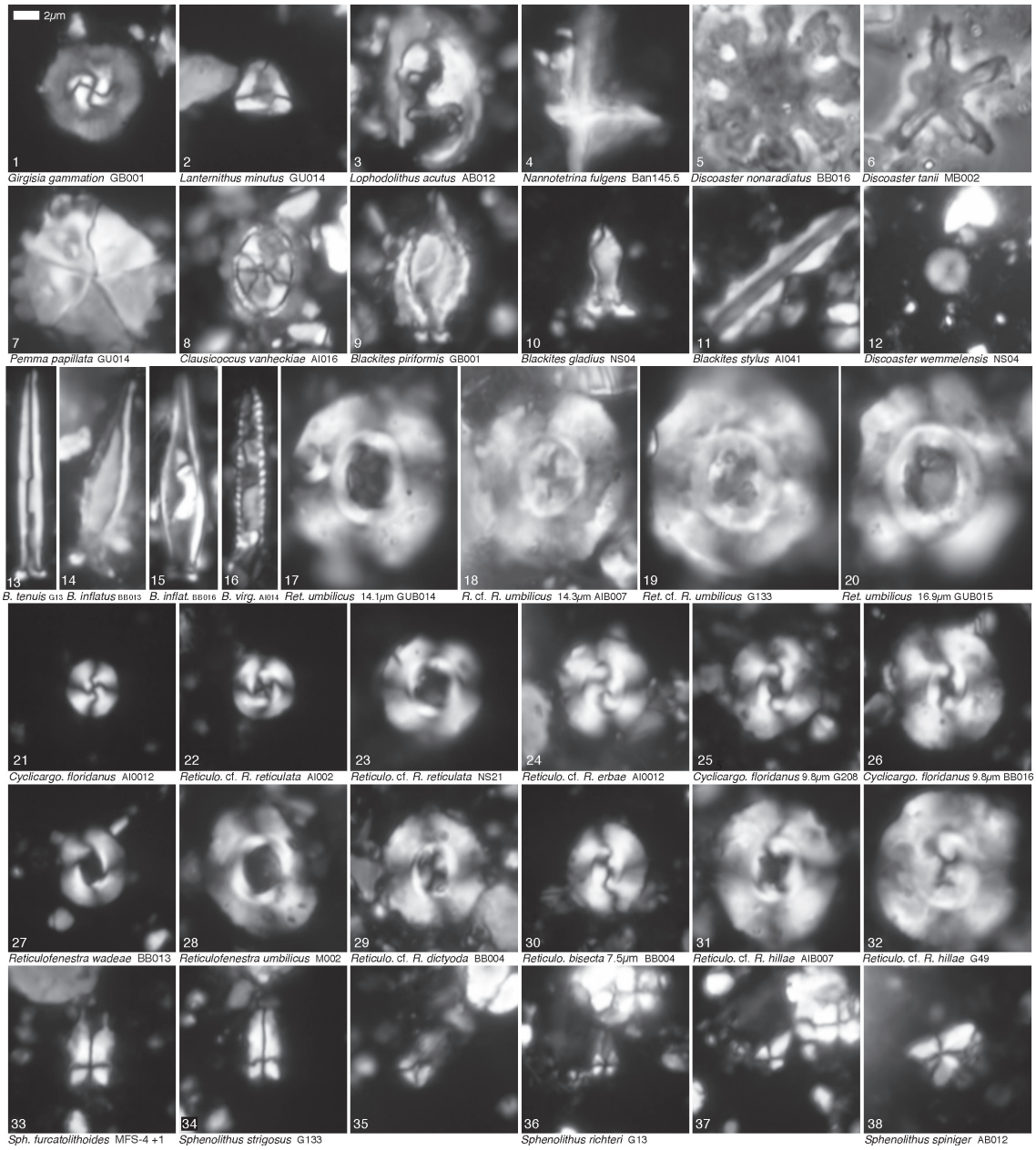

Appendix Plate 1.1 | Age-diagnostic nannofossil taxa used to construct the Upper Hecho Group palaeontological age model. Calcareous nannofossils were analysed using simple smear slides and standard light microscope techniques (Bown & Young, 1998). Data was collected semi-quantitatively using a Zeiss Axiophot photomicroscope at x1000 magnification, with a minimum of 1000 fields of view examined for each sample.

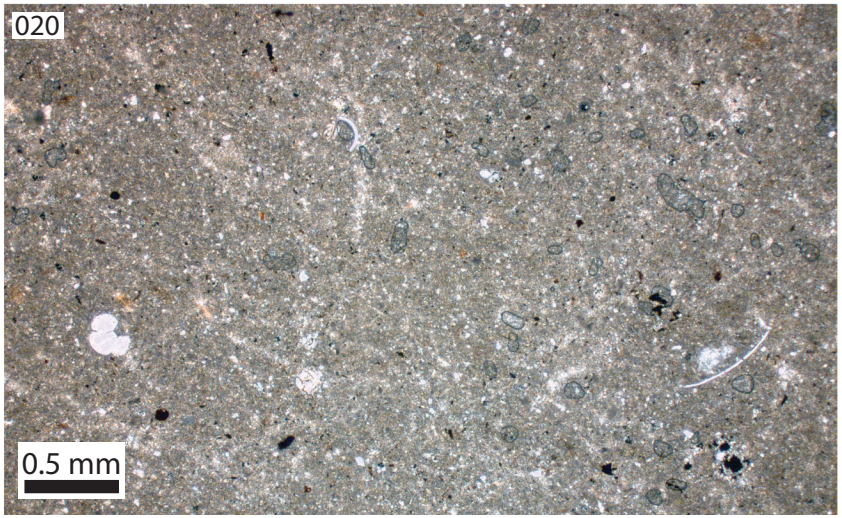
020
0.5 mm

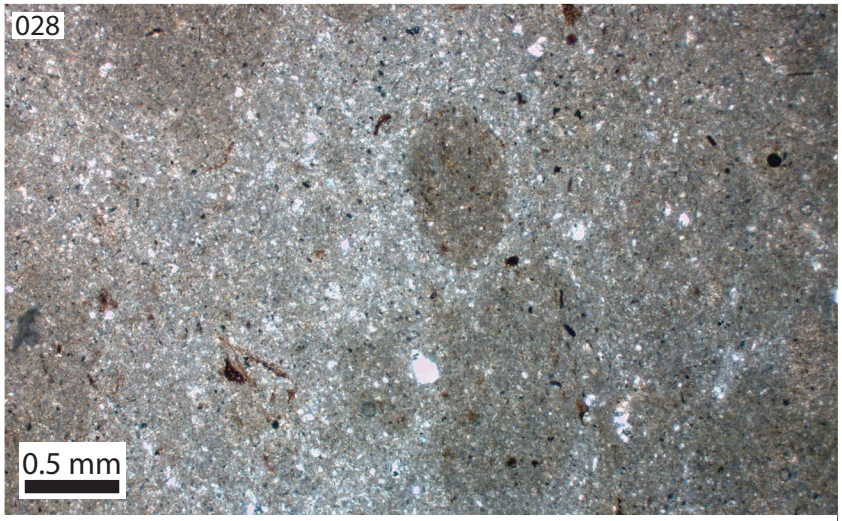
028
0.5 mm

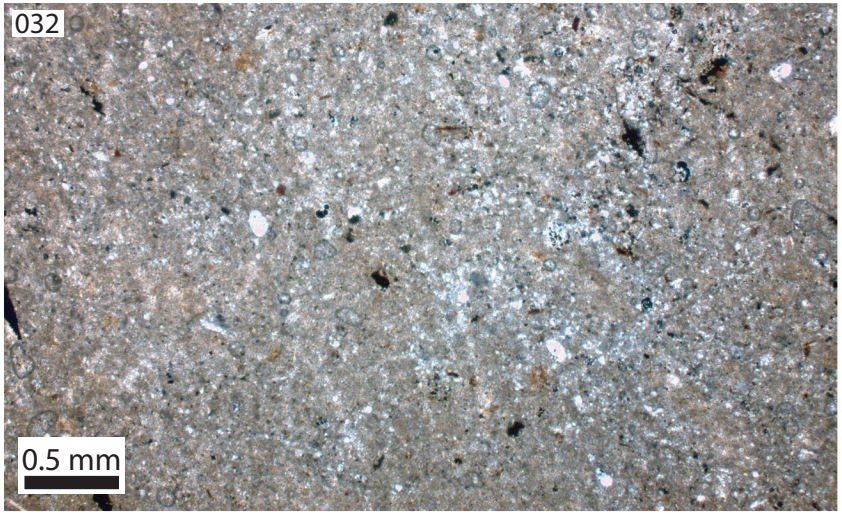
032
0.5 mm

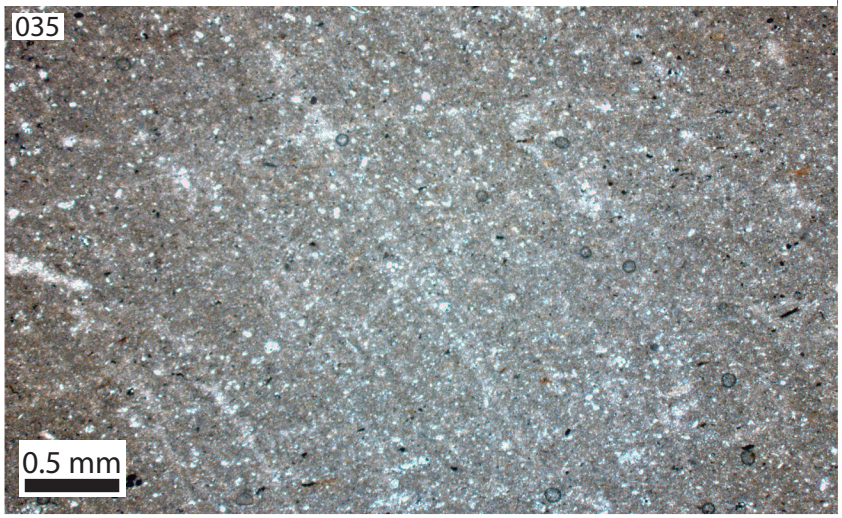
035
0.5 mm

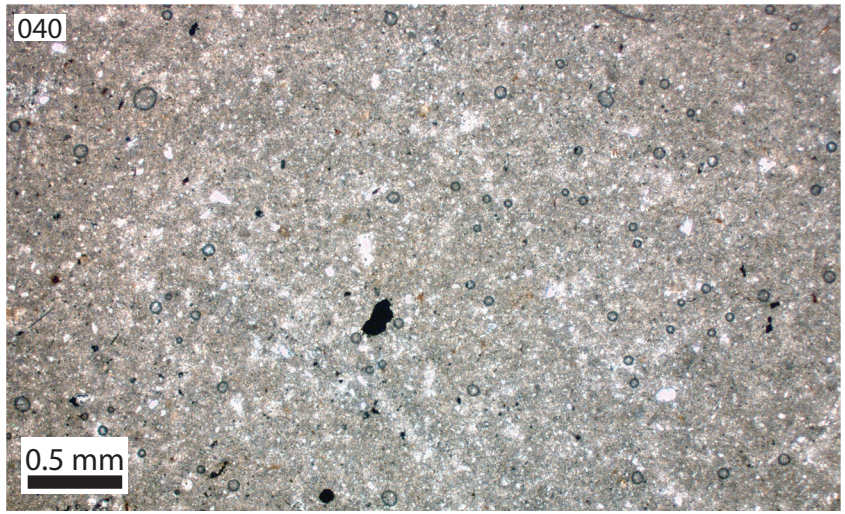
040
0.5 mm

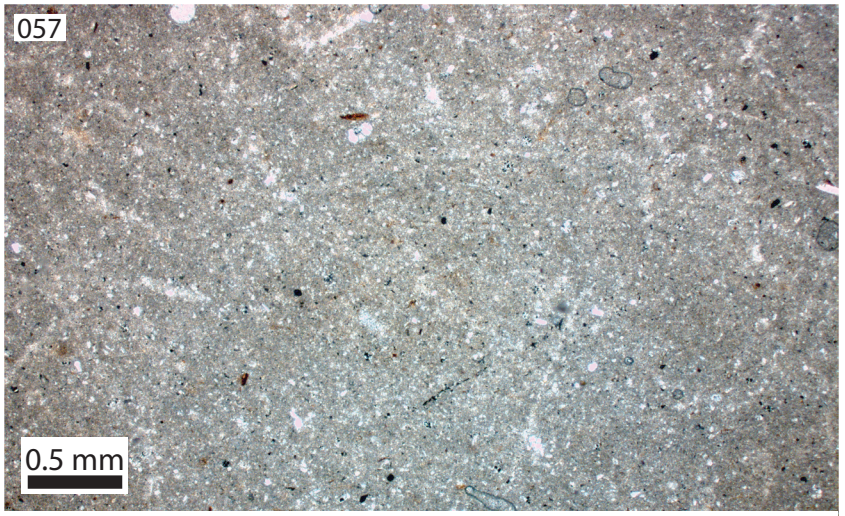
057
0.5 mm

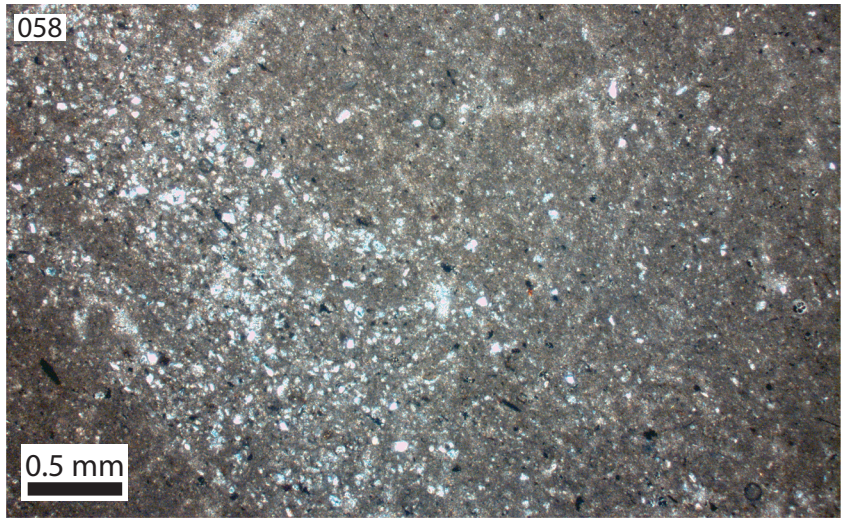
058
0.5 mm

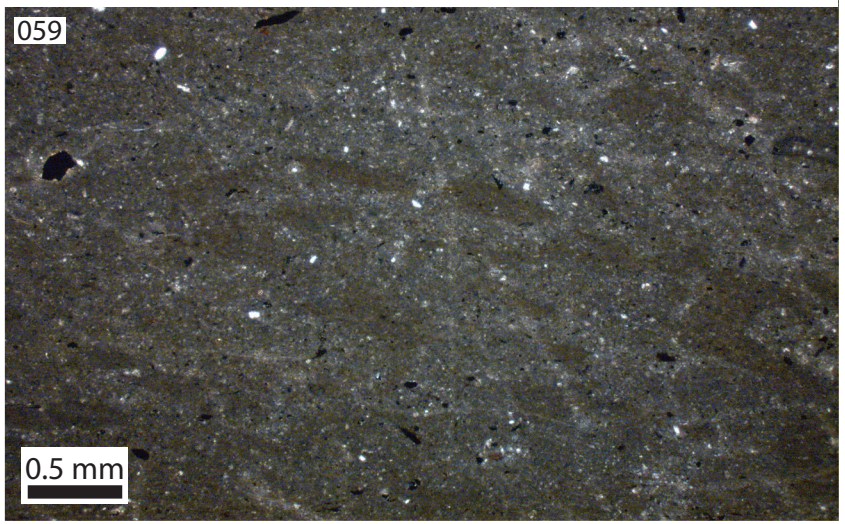
059
0.5 mm

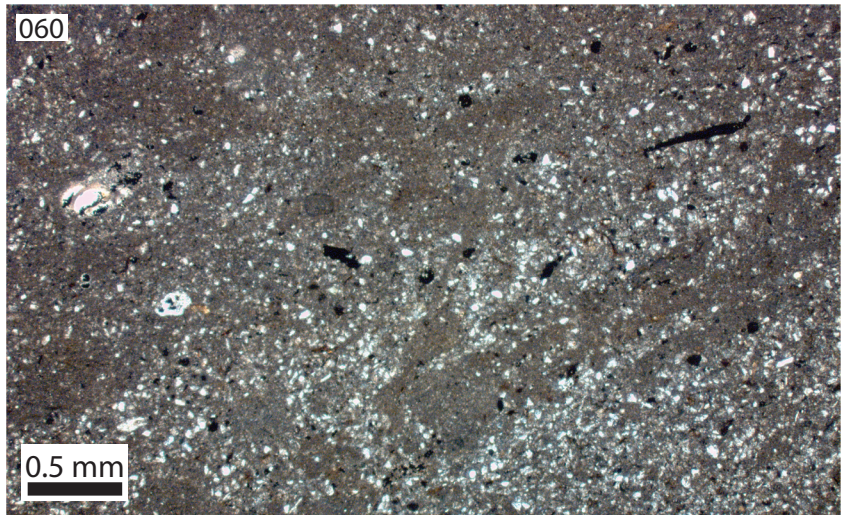
060
0.5 mm


061
0.5 mm

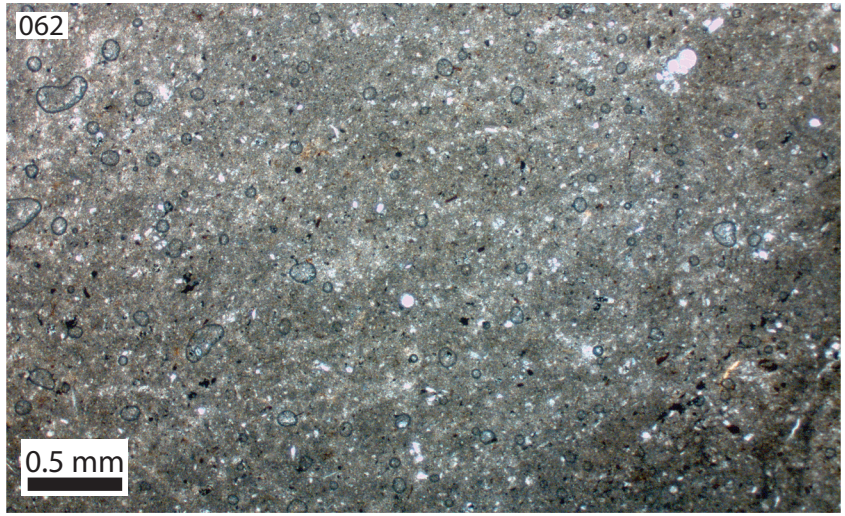
062
0.5 mm


063
0.5 mm

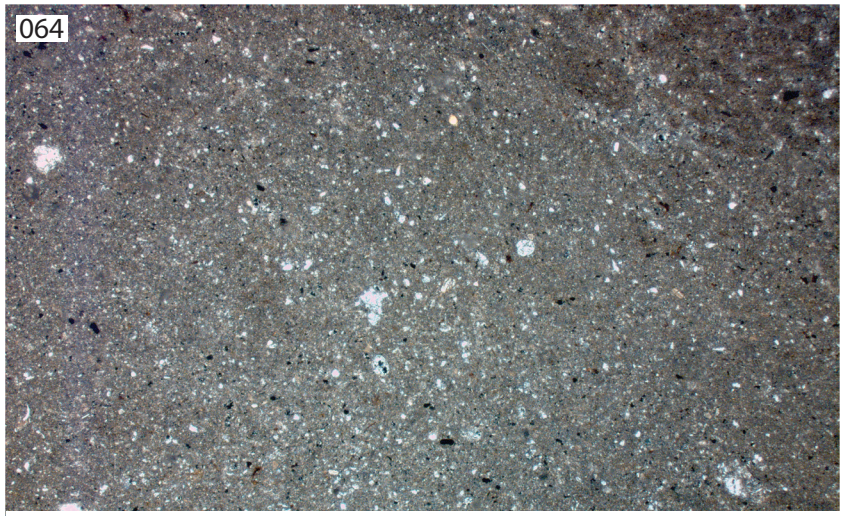
064

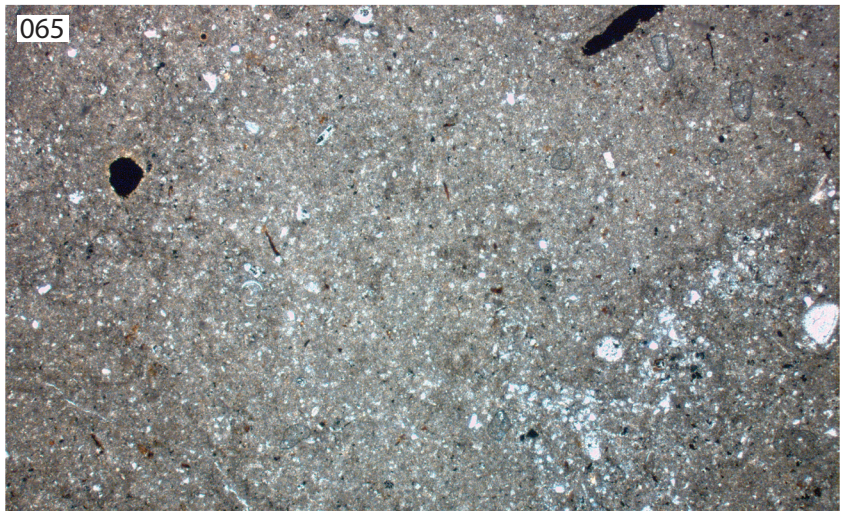
065


066


067

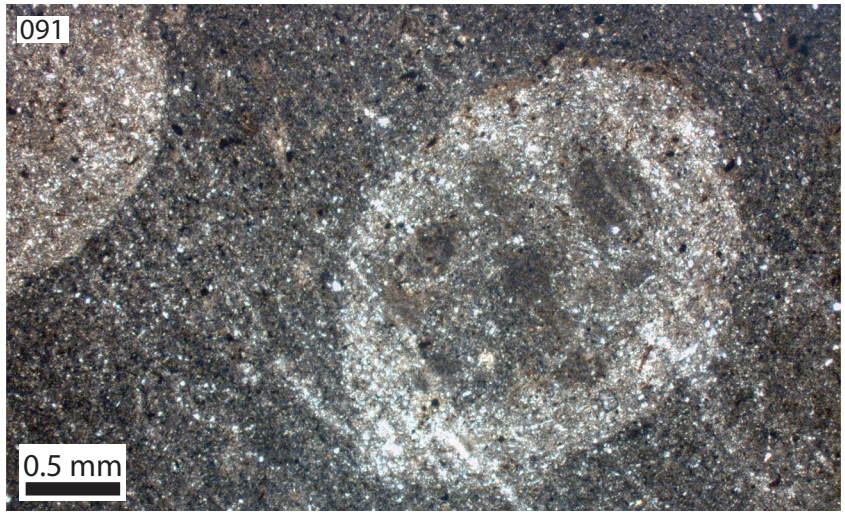

Appendix Plate 1.2 (left and previous four pages) | Petrographic thin section images of 17 Guaso System inter-fan sediment samples. Images taken using plain polarised light. Sample numbers correspond to those analysed within Chapter 4. See Figure 4.5 for sample stratigraphic position.

Figure 4.4 | Measured sections (1-7 and 9) obtained from localities 1 and 2. Numerous laterally offset stratigraphic sections were measured to ensure the entire inter-fan stratigraphy was sampled (Figure 4.3). Bulk sediment and spectral gamma ray samples were collected every 0.2 m where possible. Several bulk sediment samples were used for XRD (*), petrographic (#) and palaeontological (†) analysis.

Locality 1

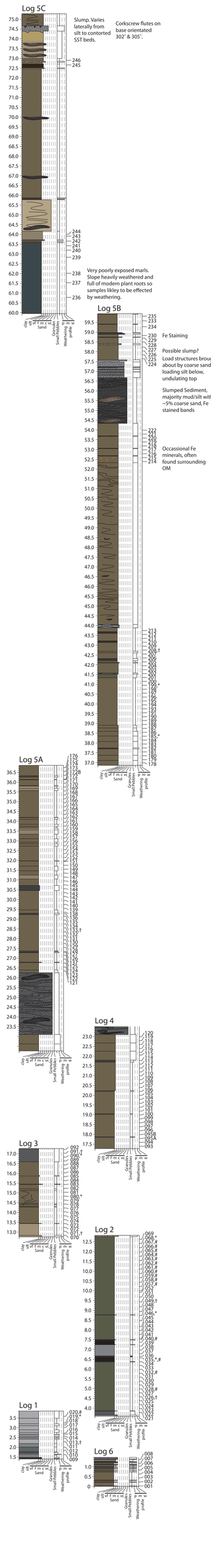

Locality 2

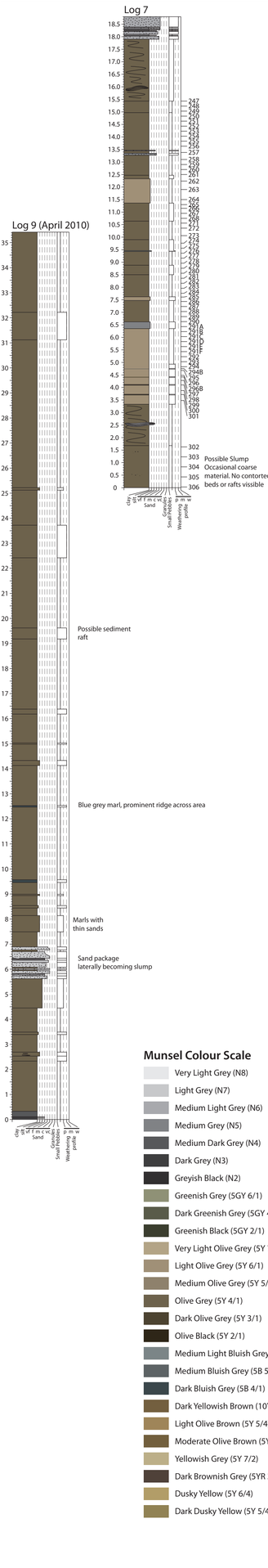

Munsell Colour Scale

- Very Light Grey (N8)
- Light Grey (N7)
- Medium Light Grey (N6)
- Medium Grey (N5)
- Medium Dark Grey (N4)
- Dark Grey (N3)
- Greyish Black (N2)
- Greenish Grey (5GY 6/1)
- Dark Greenish Grey (5GY 4/1)
- Greenish Black (5GY 2/1)
- Very Light Olive Grey (5Y 7/1)
- Light Olive Grey (5Y 6/1)
- Medium Olive Grey (5Y 5/1)
- Olive Grey (5Y 4/1)
- Dark Olive Grey (5Y 3/1)
- Olive Black (5Y 2/1)
- Medium Light Bluish Grey (5B 6/1)
- Medium Bluish Grey (5B 5/1)
- Dark Bluish Grey (5B 4/1)
- Dark Yellowish Brown (10YR 4/2)
- Light Olive Brown (5Y 5/4)
- Moderate Olive Brown (5Y 4/4)
- Yellowish Grey (5Y 7/2)
- Dark Brownish Grey (5YR 3/1)
- Dusky Yellow (5Y 6/4)
- Dark Dusky Yellow (5Y 5/4)

Figure 4.15 | Proposed correlations between measured sections taken from localities 1, 2 and 4. With the DB-1 bed being present at each section it was used as a datum. The remaining correlations are based upon colour, mapping or expected lateral facies variations.